Microgear Robots

Characterization and Control of shapeable microparticles in an Optoelectronic Tweezer setup

G.J. Gorsse

Master Thesis
MSc System & Control
MSc Applied Physics

TU Delft

Delft Center for Systems and Control

Microgear Robots

Characterization and Control of shapeable microparticles in an Optoelectronic Tweezer setup

by

G.J. Gorsse

to obtain the degree of Master of Science
at the Delft University of Technology,
to be defended publicly on Wednesday April 16, 2025 at 12:30 PM.

Student number:	4691407	
Project duration:	April 1, 2024 – April 16, 2025	
Thesis committee:	Prof. dr. ir. C.S. Smith,	TU Delft, supervisor
	Prof. dr. J. Kalkman,	TU Delft
	Prof. dr. ir. S.F. Pereira,	TU Delft
	Prof. dr. G.J. Verbiest	TU Delft

This thesis is confidential and cannot be made public until April 16, 2025.

An electronic version of this thesis is available at `http://repository.tudelft.nl/`.

TU Delft

Abstract

The growing demand for scalable biomedical solutions calls for precise, programmable, and cost-effective manipulation techniques at the microscale. While mechanical and magnetic methods have been explored, they often face limitations in flexibility, biocompatibility, or scalability. Optical tweezers offer high precision, but suffer from thermal side effects and complex, expensive setups. Optoelectronic tweezers (OET), by contrast, utilize patterned light to induce dielectrophoretic forces, enabling flexible, energy-efficient, and scalable control of microscopic particles using relatively simple hardware.

To support advanced biomedical research at Delft University of Technology, a fully functional OET platform was developed from the ground up. It integrates a custom transparent photoconductive microfluidic chip with a DMD-based optical system for real-time, reconfigurable actuation. Custom-fabricated PDMS microgear robots were successfully manipulated under varying electrical and optical conditions. Using precise motion tracking and calibration, the generated dielectrophoretic forces were quantified, with peak values approaching 500 pN, and benchmarked against theoretical models and literature estimates.

This research demonstrates that complex-shaped microbots can be effectively actuated within a custom-built OET system, paving the way for future applications in automated diagnostics, single-cell manipulation, and intelligent lab-on-a-chip platforms. By combining hardware innovation with theoretical insight, this work lays a robust foundation for microscale robotics in next-generation biomedical technologies.

Preface

It has been 7 years and 7 months since I arrived in Delft to pursue an engineering degree. Throughout these years, I've had many experience outside the educational field, always trying to find new ways to include personal development during my time at university. I had long been curious about the world of academia—how it works, and whether it would be a good fit for me. That's why I feel very lucky to have stumbled upon Prof. Smith, who inspired me to set up this amazing project. This past year has been a huge learning experience: working with new technologies, working on a project independently, applying my theoretical knowledge from both Applied Physics and Systems & Control, teaching and supervising students, and having insightful discussions with many experts.

I especially want to thank Dimitri Kromm for always being there to help me develop the optical system, for sharing his extensive knowledge in the field of optics, and for our small chats about everything. Another big thanks goes to Daniel Fan, who helped me build the theoretical framework of this research and sent me the printed microbots all the way from Melbourne. It was especially nice to have so many conversations, not just online, but even in real life here in Delft.

I want to thank Yabin Wang for teaching me the ways of the chemical lab and helping me create the microfluidic chip. He supported me with feedback and advice throughout the entire project. I also want to thank Liam Cool for taking the time to sit with me so often, discussing hardware and research life in general. Thanks to Dylan Kalisvaart and Federico Berto as well, for giving me feedback on the storyline of this thesis and sharing valuable tips.

My thanks also go to Aurèle Adam, Jacob Hoogenboom, Arno Smets, Roderick Tas, and Martijn Tijssen for taking the time to share their expert knowledge. Your input helped me bridge gaps in my understanding of OET principles and pointed me toward the right solutions—pushing this project further. I especially want to thank Roderick for offering me space in the chemical lab to work on the microfluidic chips, and Martijn for depositing the photoconductive layers on the ITO glasses at the Else Kooi Lab.

A special thanks to Dion Jetulahi, Rens van Elk, and Mirthe Folkerts for helping me out with different parts of the project. It was a lot of fun working alongside you all toward a functional OET setup. I'd also like to thank Kristian Blokhuis for making the lab feel more lively—seeing you sitting in the dark all day doing fluorescence imaging always brightened my days.

Special thanks to Jeroen Kalkman, Silvania Pereira, and Gerard Verbiest for taking the time to read my report, give feedback, and grade my work.

A personal thanks to all friends and family who stood by me—not just during this project, but throughout my entire time as a student. Big thanks to JC de Stropers, Huize A.D.A.M., my friends from IRP Delft, and my wonderful colleagues and friends from ORAS. Another big thanks and shout-out to my family and my girlfriend's family for always being interested and supporting me during the project. And, of course, the biggest thanks goes to my girlfriend Hadassah, for spending the most time with me, patiently listening to all my talk about microbots and optoelectronic tweezers.

This journey has been valuable, insightful, tough, but also fun. I wrote this research, and especially the supplementary document "Fundamental Principles of Optoelectronic Tweezers", with the goal not just to inspire, but to teach you something about this subject, no matter what your prior knowledge is. The topic is heavy on theoretical physics, so I challenged myself to make it understandable for readers of all levels, hoping to spark curiosity for science and its applications.

G.J. Gorsse
Delft, April 2025

Contents

Abstract iii

Preface v

1 Introduction 1

2 Theory 5
2.1 Dielectrophoretic force . . . 6
2.1.1 Maxwell stress tensor and electric dipole force . . . 6
2.1.2 Electric dipole force on a spherical particle . . . 7
2.2 Microfluidic Chip . . . 10
2.2.1 Dielectric medium . . . 10
2.2.2 Electrodes . . . 10
2.3 Photoconductive layer . . . 12
2.3.1 Electron dispersion in a semiconductor . . . 12
2.3.2 Hydrogenated amorphous silicon . . . 13
2.3.3 Absorption coefficient . . . 14
2.4 The dynamics of the dielectric particle . . . 16
2.4.1 Forces on the particle . . . 16
2.4.2 Forces on the medium . . . 18
2.4.3 Situational forces . . . 20
2.4.4 State space . . . 20
2.5 Optical setup . . . 21
2.5.1 The light microscope . . . 21
2.5.2 Resolution . . . 22
2.5.3 Light source . . . 24
2.5.4 Optical components . . . 25
2.6 Instrumentation . . . 26
2.6.1 Applied signal . . . 26

3 Methods 27
3.1 Design of the microfluidic chip . . . 27
3.1.1 Dimensionality . . . 27
3.1.2 Transmitting electrodes . . . 29
3.1.3 Photoconductive layer . . . 31
3.1.4 Electrical properties . . . 32
3.1.5 Robust design . . . 34
3.2 Design of the optical setup . . . 37
3.2.1 Illumination source . . . 41
3.2.2 Characterization of the optical setup . . . 42
3.2.3 Optical Alignment . . . 47
3.2.4 Other instrumentation . . . 48
3.3 Design of the dielectric particle . . . 48
3.3.1 Frequency range . . . 52
3.3.2 Dielectrophoretic force . . . 53
3.3.3 Controlling the DMD . . . 54
3.3.4 Measuring and analyzing the DEP force . . . 55

4 Results 57
4.1 Microfluidic chip. 57
4.1.1 Robust design 57
4.1.2 Electrical properties 58
4.1.3 Reflection and absorption 58
4.2 Optical setup 61
4.2.1 Magnification 61
4.2.2 Optical efficiency 62
4.2.3 Resolution 65
4.3 Dielectric particle dynamics 68
4.3.1 Dielectrophoretic force 68
4.3.2 Frequency range 72

5 Discussion 73
5.1 Microfluidic chip. 73
5.1.1 Benchmarking results 73
5.1.2 Design opportunities 74
5.2 Optical setup 75
5.2.1 Benchmarking results 75
5.2.2 Design opportunities 76
5.3 Dielectric particle 77
5.3.1 Dielectrophoretic force 77
5.3.2 Design opportunities 78

6 Conclusion 81

Bibliography 85

A Experimental 127
A.1 Intensity Spectra 127
A.2 Fluorescent Spectra 131
A.3 Code for controlling the DMD 132
A.3.1 Creating the sweep animation 132
A.3.2 Showing the sweep animation on the DMD 133
A.3.3 Dynamically creat a ring animation on the DMD 134

B Results 137
B.1 Microfluidic chip. 137
B.1.1 The thickness of the double-sided tape 137
B.1.2 The electrical resistances of the microfluidic chip components 139
B.1.3 Capacitance of tape 141
B.1.4 Capacitance photoconductive layer 142
B.1.5 Capacitance medium 143
B.2 Reflection 147
B.2.1 Reflection of ITO glass using 470 nm LED 147
B.2.2 Reflection of ITO glass using 635 nm laser 149
B.2.3 Reflection of ITO glass using 715 nm filtered lamp 151
B.2.4 Reflection of ITO glass using 470 nm LED in the absorption measurement experimental setup with beamsplitter 153
B.2.5 Reflection of ITO glass using 635 nm laser in the absorption measurement experimental setup with beamsplitter 155
B.2.6 Reflection of ITO glass using 715 nm filtered lamp in the absorption measurement experimental setup with beamsplitter 157
B.3 Absorption coefficient 159
B.3.1 Absorption by a-Si:H on ITO covered microscope slides with different resistances using 470 nm LED 159
B.3.2 Absorption by a-Si:H on ITO covered microscope slides with different resistances using 635 nm laser 160

B.3.3 Absorption by a-Si:H on ITO covered microscope slides with different resistances using 715 nm filtered lamp . . . 162

C Results: Optical setup 165
C.1 Magnification . . . 165
C.1.1 Magnification Chip to Camera . . . 165
C.1.2 Magnification DMD to camera . . . 167
C.2 Optical efficiency . . . 168
C.2.1 Optical power . . . 168
C.2.2 Intensity measurements 445 nm . . . 169
C.2.3 Intensity measurements 480 nm . . . 172
C.3 Resolution . . . 177
C.3.1 4 μm TetraSpeck Fluorescent bead . . . 177
C.3.2 1 μm TetraSpeck Fluorescent bead . . . 178
C.3.3 0.5 μm TetraSpeck Fluorescent bead . . . 179
C.4 DMD measurements . . . 180
C.4.1 DMD PSF measurements . . . 180
C.4.2 Measurements on differently sized pixel grids . . . 184
C.4.3 Intensity map . . . 190

D Results: Dielectric particle 191
D.1 MATLAB code to calculate the DEP motion . . . 191
D.2 DEP motion . . . 208
D.2.1 Bead motion . . . 208
D.2.2 Gear motion . . . 228
D.2.3 Pattern motion . . . 249
D.3 DEP force . . . 260
D.3.1 DEP force on the microbot, calculated using Stokes's law . . . 260
D.3.2 DEP force on the microbot, compared to literature . . . 280
D.4 Electrolysis . . . 301

List of Abbreviations

This abbreviation section outlines the definitions of all abbreviations appearing in this report, presented in order of occurrence.

Abbreviation	Meaning
COVID-19	Coronavirus Disease 2019
GDP	Gross Domestic Product
OET	Optoelectronic Tweezer
DEP	Dielectrophoretic
PL	Photoconductive Layer
OS	Optical setup
CM	Clausius-Mossotti
ITO	Indium Tin Oxide
a-Si:H	Hydrogenated Amorphous Silicon
c-Si	Crystalline silicon
a-Si	Amorphous silicon
BHJ	Bulk-Heterojunction polymer
TiOPc	Titanium Oxide Phthalocyanine
EP	Electrophoresis
LACE	Light-actuated AC electroosmosis
AC	Alternating current
ACET	AC electrothermal flow
BSA	Bovine Serum Albumin
PEG	Polyethylene Glycol
Vpp	Peak-to-peak voltage
NA	Numerical Aperture
DoF	Depth of Focus
LED	Light Emitting Diode
Laser	Light Amplification by Stimulated Emission of Radiation
RoI	Region of Interest
DMD	Digital Micromirror Device
FoV	Field of View
PECVD	Plasma Enhanced Chemical Vapor Deposition
2PP	Two-Photon Polymerization
PDMS	Polydimethylsiloxane
FWHM	Full Width at Half Maximum
Std	Standard deviation
RCF	Relative Centrifugal Force

Nomenclature

This nomenclature section outlines the definitions of all parameters appearing in the functions discussed in this report, presented in order of occurrence.

Symbol	Description	Unit
∇	Del operator	[-]
$\mathbf{E}$	Electrical field vector	[V·m^{-1}]
ρ	Electrical charge density	[C·m^{-3}]
ϵ_0	The permittivity of free space	[F·m^{-1}]
$\mathbf{B}$	Magnetic field vector	[T]
∂	Partial derivative operator	[-]
t	Time	[s]
μ_0	The permeability of free space	[N·A^{-2}]
$\mathbf{j}$	The current density vector	[A·m^{-2}]
c	The speed of light in free space	[m·s^{-1}]
$\mathbf{D}$	The electrical displacement field	[C·m^{-2}]
$\hat{\epsilon}$	Complex permittivity	[F·m^{-1}]
$\mathbf{H}$	The magnetization field	[A·m^{-1}]
μ	The permeability of a medium	[N·A^{-2}]
i	The complex number	[-]
ω	The angular frequency	[rad $\cdot$ s^{-1}]
$\mathbf{F}$	The force vector	[N]
V	The volume of a particle	[m^3]
$\mathbf{r}$	A direction in an integral	[m]
$\mathbf{S}$	The Poynting vector	[W $\cdot$ m^{-2}]
$\mathbb{I}$	The identity matrix	[-]
$\mathbf{T}$	The Maxwell stress tensor	[N·m^{-2}]
$\hat{n}$	The outward pointing unit vector on surface	[-]
$\mathbf{E}_{\parallel}$	The electrical field parallel to surface	[V·m^{-1}]
$\mathbf{E}_{\perp}$	The electrical field perpendicular to surface	[V·m^{-1}]
$\hat{b}$	Introduced complex number for calculation	[-]
s	Order in Maclaurin series	[-]
K	Clausius-Mossotti factor	[-]
$\mathbf{p}$	Electric dipole moment vector	[C·m]
I	Electric current	[A]
V	Electric potential difference	[V]
R	Electric resistance	[Ω]
P	Optical power	[W]
Z	Electric impedance	[Ω]
ϵ_r	The relative permittivity	[-]
A	Effective area in parallel plate capacitor	[m^2]
d	The distance between parallel plates	[m]
C	Capacitance of material	[F]
$\hbar$	The reduced Planck constant	[kg $\cdot$ m^2·s^{-1}]
Ψ	The wave function	[m$^{-3/2}$]
m	The mass of a particle	[kg]
E	The eigenenergy of a particle	[J]
C	Arbitrary constant	[-]
$\mathbf{k}$	The quantum wavenumber vector	[m^{-1}]
k	The quantum wavenumber	[m^{-1}]
L	The length of a cubic box	[m]
N	The number of states	[-]
g	Density of states	[J^{-1}]
D^+	Donor-like gap states per unit volume	[m^{-3}]
I	Intensity of light	[W·m-2]

Symbol	Description	Unit
x	The penetration depth	[m]
α	The absorption coefficient	[m^{-1}]
λ	The wavelength of light in vacuum	[m]
h	The Planck constant	[$kg \cdot m^2 \cdot s^{-1}$]
A	The illuminated area	[m^2]
g	The generation rate of free electrons	[$m^{-3} \cdot s^{-1}$]
η	The quantum efficiency	[-]
σ	The conductivity	[$S \cdot m^{-1}$]
e	Electron charge	[C]
μ	Electron mobility	[$m^2 \cdot V^{-1} s$]
n	The amount of holes	[m^{-3}]
p	The amount of electrons	[m^{-3}]
r	The recombination rate	[$m^{-3} \cdot s^{-1}$]
$c_{c,v}$	The recombination coefficient	[$m^6 \cdot s^{-1}$]
τ_n	The lifetime of an electron	[s^{-1}]
S	The optical power	[$W \cdot m^{-2}$]
f	The frequency of light	[Hz]
ρ	The density of a material	[$kg \cdot m^{-3}$]
g	The gravity constant	[$m \cdot s^{-2}$]
k_b	The Boltzmann constant	[$J \cdot K^{-1}$]
T	Temperature	[T]
η	Viscosity of medium	[Pa ·s]
$\mathbf{V}$	Fluid velocity vector	[$m \cdot s^{-1}$]
p	Pressure	[Pa]
L	Characteristic length	[m]
S	Surface area	[m^2]
σ_s	Viscous stress tensor	[Pa]
C_d	Drag coefficient	[-]
ω	Rotational velocity	[$rad \cdot s^{-1}$]
C_T	Rotational drag coefficient	[-]
q	Electrical charge	[C]
ζ	The zeta-potential	[V]
$f(\kappa r)$	The Henry coefficient	[-]
κ	The Debye length	[m^{-1}]
λ_d	The thickness of the double layer	[m]
$\mathbf{f}$	Body force	[$N \cdot m^{-3}$]
k_ϵ	Temperature change of permittivity	[T^{-1}]
M	Magnification	[-]
f	Focal length	[m]
n	Refractive index	[-]
θ	The angle with the optical axis	[rad]
NA	The numerical aperture	[-]
ρ	The lateral resolution	[m]
ΔZ	Half of the depth of focus	[m]
e	The smallest resolvable distance in camera	[m]
Φ	The collimation angle	[rad]
d	The size of the LED	[m]
FoV	Field of View	[m]
x	The size of a camera pixel	[m]
ρ	The resistivity of a medium	[$\Omega \cdot m$]
η	The optical efficiency	[-]
a	The acceleration of a dielectric particle	[$m \cdot s^{-2}$]

1 Introduction

The outbreak of COVID-19 in late 2019 marked the beginning of a global crisis that would claim the lives of over 7 million people worldwide, including 23,000 in the Netherlands alone [1]. Beyond the tragic death toll, the pandemic deeply affected mental well-being: nearly 1 in 10 Dutch citizens reported feeling severely lonely during this period [2]. The social impact was paralleled by massive economic disruption, with the costs of the pandemic estimated at $12 trillion for the global economy, equivalent to roughly 10% of global GDP [3]. Many pharmaceutical companies worked hard to create a vaccine to counter the rising number of infected people. While traditional vaccine development often spans 10 to 15 years, the first COVID-19 vaccines were approved within just one year [4].

The development of vaccines relies heavily on manual laboratory procedures such as pipetting, cell handling, and microscopic analysis. These workflows are labor-intensive, time-consuming, and spatially demanding. Automating such processes could drastically accelerate vaccine development and biomedical research. This resulted in a great ambition in the lab of Prof. Smith at Delft University of Technology, where the goal is to automate cell sorting, selection, imaging, and transfer for the development of antibodies. To achieve this, a precise and controllable method for microscale manipulation is essential.

Over the years, several techniques have been developed to manipulate microscopic objects with high precision. Among them, optical tweezers exploit the momentum carried by photons of a focused laser beam to trap and move transparent particles [5]. However, their reliance on high-power lasers often leads to undesirable thermal effects. This limitation has initiated the emergence of alternative tweezing techniques, including optothermal, plasmonic, optoacoustic, and optoelectronic tweezers.

OET offers a compelling combination of high precision, low power requirements, and controllability [6]. The technology has progressed from fundamental research to commercial application—for instance, in Bruker's Beacon® system, which reduces timelines for cell analysis by months [7]. Moreover, OET systems can manipulate complex-shaped polymer microstructures fabricated via two-photon polymerization [8], unlocking dynamic and reconfigurable environments at the microscale. Such capabilities pave the way for lab-on-a-chip platforms that could revolutionize biomedical workflows by increasing throughput, minimizing spatial and labor demands, and lowering costs—ultimately enabling faster, more affordable, and more sophisticated diagnostics and therapeutics.

Creating an OET setup compatible with custom-shaped microbots is non-trivial. It requires the design of a microfluidic chip that forms the foundation of the envisioned lab-on-a-chip system. This microfluidic chip functions as a capacitor, with a dielectric liquid containing the target microparticles as a dielectric material. By integrating a photoconductive layer on one side of the chip, we can dynamically shape the internal electric field by projecting patterned light, forming virtual electrodes. These light-induced virtual electrodes generate a spatially non-uniform electric field, exerting dielectrophoretic forces on nearby dielectric particles. The optical setup provides the illumination pattern, enables real-time imaging, and delivers the electrical periodic signal to the chip.

In this thesis, we first present the theoretical framework governing the physical phenomena involved in OET. This includes an analysis of the key variables that influence system performance, providing a solid foundation for design decisions across the entire setup. The theoretical derivation is extended by a dedicated document, ”The Fundamental Principles of Optoelectronic Tweezer”, written in parallel and included as supplementary material, offering a more in-depth and accessible explanation of the underlying physics.

Subsequently, we describe the methodology used to design, implement, and benchmark each component of the OET system. The results are summarized in the main chapters and presented in full detail in the appendix. Finally, we reflect on the findings by comparing them to theoretical predictions and literature, and offer recommendations for future improvements.

By following this structure, this work aims to contribute to the foundation for ongoing research at Delft University of Technology in the field of optoelectronic manipulation. Ultimately, it opens up new possibilities—not only for advancing microfluidic and biomedical research, but also for enabling more accessible, affordable, and scalable healthcare technologies worldwide.

To guide this research in a structured and goal-oriented manner, we formulate the following central research question:

> **What are the characteristics of a microgear microbot in a self-made optoelectronic tweezer system, and how can it be manipulated accurately?**

Although this question may appear straightforward at first, it encompasses multiple complex challenges. Therefore, it is divided into the following subquestions:

1. **How can an optoelectronic tweezer system be realized at TU Delft?**
   a. How can the optical system be aligned?
   b. Which illumination source is most optimal for the OET setup?
   c. How can a working fluorescence microscope be integrated into the OET setup?
   d. How can the microfluidic chip be provided with the appropriate electric potential, fluid velocity, and thermal stability?
2. **How can a suitable microfluidic chip be developed for OET?**
   a. Which materials (conductive layer, photoconductive layer, medium, etc.) are suitable for use in the OET chip?
   b. What dimensions are appropriate for the microfluidic chip, considering the optical setup and particles of interest?
   c. How can a reliable and reproducible fabrication method be established?
3. **How can the microbot be manipulated optimally in the OET system?**
   a. What are the optimal design parameters (size, material, geometry) for the microbots?
   b. How can the characteristics of the microbots be measured to determine the DEP force acting on them?
   c. What are the ideal OET settings (voltage, frequency, illumination) for effective control?
   d. How can appropriate patterning be implemented for precise microbot manipulation?

Together, these subquestions provide a comprehensive and structured approach toward the development, implementation, and evaluation of a functional OET system, laying the groundwork for future exploration in microscale actuation and smart biomedical technologies.

2
Theory

The physics underlying an OET system is complex and multifaceted. A clear understanding of these principles is crucial to explain system behavior and ensure effective design choices. This chapter introduces the key physical mechanisms behind each component of the OET setup, following the schematic overview in Figure 2.1.

Section 1 covers the dielectrophoretic (DEP) force, the primary mechanism for particle manipulation in OET, highlighting its dependence on the electric field, frequency, particle shape, and material properties. Section 2 discusses the microfluidic chip, focusing on the dielectric medium and passive electronic elements. Section 3 introduces the photoconductive layer (PL), which enables dynamic shaping of the electric field through light-induced conductivity. The section includes the PL's absorption characteristics and resulting photoconductivity. Section 4 explores the dynamics of the dielectric particle, including all relevant forces beyond DEP. Section 5 outlines the optical setup (OS) used for imaging and control, and Section 6 describes the instrumentation required to fabricate and operate the system.

This chapter presents only the theory essential to this thesis. A more detailed theoretical background can be found in the supplementary document, "Fundamental Principles of Optoelectronic Tweezers", developed alongside this work.

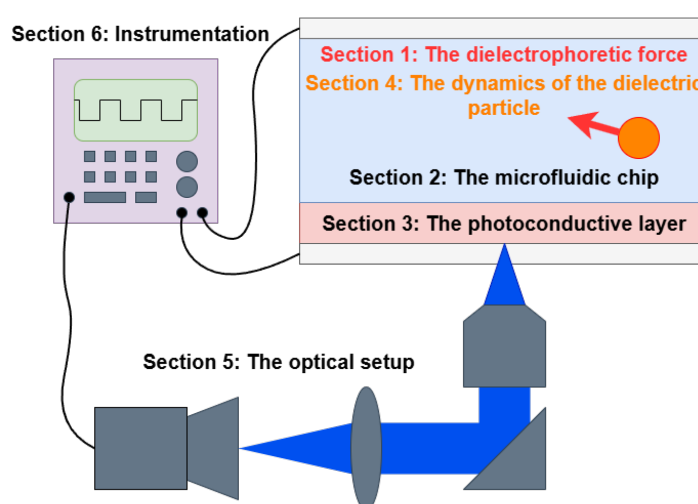

Figure 2.1: A schematic depiction of an OET setup. This depiction shows the layout of the sections, describing the theory of all the OET components in this chapter.

2.1. Dielectrophoretic force

The primary purpose of the OET is to move a microparticle accurately. To do this, the OET exerts the DEP force. The underlying physics of this DEP force originates from the field of electrodynamics. The 4 Maxwell equations govern this field [9].

$$\begin{aligned} \nabla \cdot \mathbf{E} &= \frac{\rho}{\epsilon_0} \qquad & \nabla \times \mathbf{E} &= -\frac{\partial \mathbf{B}}{\partial t} \\ \nabla \cdot \mathbf{B} &= 0 \qquad & \nabla \times \mathbf{B} &= \mu_0 \mathbf{j} + \frac{1}{c^2}\frac{\partial \mathbf{E}}{\partial t} \end{aligned} \tag{2.1}$$

The del operator ∇ is used for differential equations in vectors, with the dot product denoting the divergence and the cross product denoting the curl of the field. The electrical and magnetic fields are given by $\mathbf{E}$ and $\mathbf{B}$. The density of charge is given as ρ. The permittivity of free space is given by ϵ_0, and the permeability of free space is given as μ_0. The speed of light is given by c. The current density is given by $\mathbf{j}$, and $\frac{\partial}{\partial t}$ denotes the derivative with respect to time. When the electrical field is residing in a dielectric medium, it is convenient to rewrite Maxwell's equation in macroscopic form by introducing the auxiliary fields $\mathbf{D}$ and $\mathbf{H}$ defined as:

$$\mathbf{D} = \hat{\epsilon}\mathbf{E} \qquad \mathbf{H} = \mu \mathbf{B} \tag{2.2}$$

The magnetic permeability of the dielectric medium is given by μ. The complex permittivity of a homogeneous dielectric medium in a time-dependent input field is defined as $\hat{\epsilon} = \epsilon + i\frac{\sigma}{\omega}$. The real part is known as the permittivity of the medium ϵ. $i = \sqrt{-1}$ denotes the imaginary unit. The imaginary part of $\hat{\epsilon}$ consists of the conductivity of the medium σ and the angular frequency of the electric field ω. If we put a dielectric in between two charged electrodes, a field will exist within this dielectric material. The negative charges bound to the atoms of the dielectric will orient themselves in the direction of the negatively charged electrode and vice versa for the positive charges. This effect is called polarization and is accounted for in the definition of the auxiliary field $\mathbf{D}$. When the field would alternate because, e.g., an alternating current would be applied on the electrodes, the charges need to orient themselves with the corresponding charged electrodes. Because this effect is not instantaneous, the charges have some delay in orienting to the right electrode. This orientation creates a loss of electrical energy depending on the frequency, which is covered by the imaginary part of the complex permittivity [10]. Using the permeability and the real part of the permittivity in a medium, we can derive the speed of light in a material as $c_m^2 = \frac{1}{\epsilon\mu}$.

2.1.1. Maxwell stress tensor and electric dipole force

To determine the force on a dielectric particle in a dielectric medium due to the electromagnetic fields, we need to start at the Coulomb-Lorentz force [9].

$$\mathbf{F}_{mech} = \int_V (\rho \mathbf{E} + \mathbf{j} \times \mathbf{B}) d^3 r \tag{2.3}$$

This integral is taken over a volume V in each direction r. For a dielectric particle, the force equation can be more conveniently expressed in terms of the electric and magnetic fields alone. We can eliminate the charge density and the current using the Maxwell equations from equation 2.1 and change the permittivity and permeability as we did for the auxiliary fields in equation 2.2.

$$\begin{aligned} \mathbf{F}_{mech} &= \int_V d^3 r (\rho \mathbf{E} + \mathbf{j} \times \mathbf{B}) \\ &= \int_V d^3 r \left[(\hat{\epsilon} \cdot \mathbf{E})\mathbf{E} + \left(\frac{1}{\mu} \nabla \times \mathbf{B} - \frac{\mu\hat{\epsilon}}{\mu}\frac{\partial \mathbf{E}}{\partial t} \right) \times \mathbf{B} \right] \\ &= \int_V d^3 r \left[\hat{\epsilon} \left((\nabla \cdot \mathbf{E})\mathbf{E} + (\mathbf{E} \cdot \nabla)\mathbf{E} - \frac{1}{2}\nabla(\mathbf{E} \cdot \mathbf{E}) \right) + \frac{1}{\mu} \left((\nabla \cdot \mathbf{B})\mathbf{B} + (\mathbf{B} \cdot \nabla)\mathbf{B} - \frac{1}{2}\nabla(\mathbf{B} \cdot \mathbf{B}) \right) - \hat{\epsilon}\frac{\partial}{\partial t}(\mathbf{E} \times \mathbf{B}) \right] \\ &= \int_V d^3 r \left[\nabla \cdot \mathbf{T} - \frac{1}{c_m^2}\mathbf{S} \right] \end{aligned} \tag{2.4}$$

In the last step, we see a substitution of $\mathbf{S}$, which is also known as the Poynting vector. The substituted $\mathbf{T}$ is the Maxwell stress tensor and describes the volume force on a dielectric particle.

$$\mathbf{T} = \hat{\epsilon}(\mathbf{EE} - \frac{1}{2}\mathbb{I}|\mathbf{E}|^2) + \mu(\mathbf{BB} - \frac{1}{2}\mathbb{I}|\mathbf{B}|^2) \tag{2.5}$$

The identity matrix $\mathbb{I}$ has the size necessary to match the size of the tensor. If we consider a parallel plate capacitor, which the OET essentially is very similar to, we can derive the expected limits of the electrical and magnetic fields [11]. The first term of the stress tensor is many orders of magnitude larger than the second term, which allows us to neglect the effects of the magnetic field. Assuming the electric field takes the form of a complex harmonic function $\mathbf{E_c}(\mathbf{r}, t) = \mathbf{E}(\mathbf{r})e^{i\omega t}$, we can further simplify the Maxwell stress tensor.

$$\begin{aligned}
\text{Re}\,[\mathbf{T}(\mathbf{r}, t)] &= \text{Re}(\hat{\epsilon})\text{Re}\left[\mathbf{E_c}\mathbf{E_c} - \frac{1}{2}(\mathbf{E_c}\cdot\mathbf{E_c})\right] \\
&= \frac{1}{4}\text{Re}(\hat{\epsilon})\left[\mathbf{EE}^* + \mathbf{E}^*\mathbf{E} - \mathbb{I}|\mathbf{E}|^2\right] + \\
&\quad + \frac{1}{4}\text{Re}(\hat{\epsilon})\left[\mathbf{EE}e^{2i\omega t} + \mathbf{E}^*\mathbf{E}^*e^{-2i\omega t} - \frac{1}{2}(|\mathbf{E}|^2e^{2i\omega t} + |\mathbf{E}|^2e^{-2i\omega t})\mathbb{I}\right] \\
&= \mathbf{T}_1(\mathbf{r}) + \mathbf{T}_2(\mathbf{r}, t)
\end{aligned} \tag{2.6}$$

The force on a dielectric particle depends on the real part of the Maxwell stress tensor. We can take the time average[1] to analyze the effects of multiple periods of the applied electric field on the particle. Using the divergence theorem on the real part of the Maxwell stress tensor from Equation 2.6, we can rewrite the time-average force as an integral over the particle's surface.

$$\begin{aligned}
\langle\mathbf{F}_{mech}\rangle = \int_V \text{Re}\left[\nabla\cdot\mathbf{T} - \frac{1}{c^2}\mathbf{S}\right]d^3r &\approx \int_V [\nabla\cdot\mathbf{T}_1]\,d^3r \\
&= \oint_A \mathbf{T}_1\cdot\hat{n}dS \\
&= \frac{1}{4}\text{Re}(\hat{\epsilon})\oint_A \left[\mathbf{EE}^* + \mathbf{E}^*\mathbf{E} - |\mathbf{E}|^2\mathbb{I}\right]\cdot\hat{n}dS
\end{aligned} \tag{2.7}$$

The total force is given as the summation of the forces on all infinitely small surface elements dS. The particle's surface is given as A, and the unit vector pointing outward from the particle at each surface dS is given as $\hat{n}$.

2.1.2. Electric dipole force on a spherical particle

We have derived the force of the electrical field on a dielectric particle in the form of a surface integral. To solve this integral requires the electric field outside the particle, $\mathbf{E}_1$. The electrical field inside the particle is given as $\mathbf{E}_2$. A schematic depiction of these fields in a spherical dielectric particle in a dielectric medium is shown in Figure 2.2. We use the boundary conditions of a dielectric particle in a dielectric medium to find the electrical field outside the particle [12]. The permittivity of the materials is given as $\hat{\epsilon}_1$ for the medium and as $\hat{\epsilon}_2$ for the particle.

$$\begin{aligned}
\hat{\epsilon}_1\mathbf{E}_1\cdot\hat{n} = \hat{\epsilon}_2\mathbf{E}_2\cdot\hat{n} \quad &\Rightarrow \quad \mathbf{E}_1\cdot\hat{n} = \frac{\hat{\epsilon}_2}{\hat{\epsilon}_1}\mathbf{E}_2\cdot\hat{n} \\
\mathbf{E}_1\times\hat{n} = \mathbf{E}_2\times\hat{n} \quad &\Rightarrow \quad \mathbf{E}_{1,\parallel} = \mathbf{E}_{2,\parallel}
\end{aligned} \tag{2.8}$$

Using these boundary conditions, we can fully relate the field outside the particle to the field inside the particle.

$$\mathbf{E}_1 = \mathbf{E}_{1,\perp} + \mathbf{E}_{1,\parallel} = \mathbf{E}_2 + \hat{b}(\mathbf{E}_2\cdot\hat{n})\hat{n} \tag{2.9}$$

[1] We assume that the frequency of oscillation is much higher than the particle dynamics.

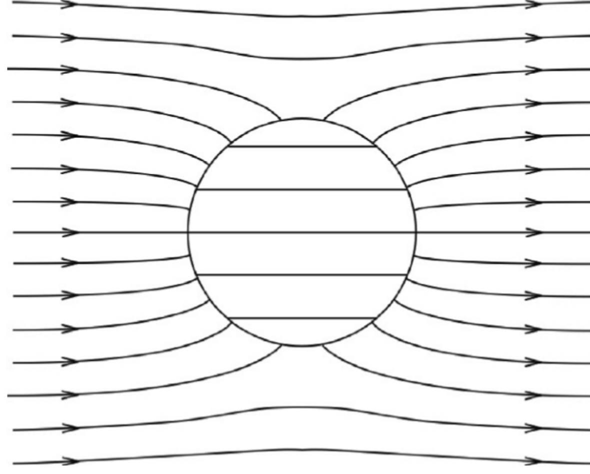

Figure 2.2: A schematic depiction of the field $\mathbf{E}_1$ outside the particle and the field $\mathbf{E}_2$ inside the particle. The uniform field $\mathbf{E}_0$, which we would expect in a capacitor, is disturbed by the dielectric particle [13].

The introduced complex number is related to the permittivity of the materials $\hat{b} = \frac{\hat{\epsilon}_2 - \hat{\epsilon}_1}{\hat{\epsilon}_1}$. To arrive at the formula for the DEP force, we need to solve equation 2.6 using the electrical field outside the particle, i.e., $\mathbf{E} = \mathbf{E}_1$. We can relate the electrical fields $\mathbf{E}_1$ and $\mathbf{E}_2$ to the applied electrical field $\mathbf{E}_0$ by incorporating the boundary equation 2.9 and relating the fields to each other using spherical harmonics [14]. To solve this integral, we must assume that the field can be linearized using a Maclaurin series.

$$\begin{aligned}
\mathbf{E}_2(\mathbf{r}) &= \mathbf{E}_2(r\hat{n}) \\
&= \sum_{s=0} \frac{1}{s!} r^s (\hat{n} \cdot \nabla)^s \mathbf{E}_2(0) \\
&= \underbrace{\mathbf{E}_2(0) + r(\hat{n} \cdot \nabla)\mathbf{E}_2(0)}_{\text{first-order}} + \underbrace{\frac{1}{2} r^2 (\hat{n} \cdot \nabla)^2 \mathbf{E}_2(0)}_{\text{second-order}} + \ldots
\end{aligned} \tag{2.10}$$

When we consider only the first-order linearization of the electrical field, we arrive at the first-order DEP force for a spherical dielectric particle.

$$\begin{aligned}
\langle \mathbf{F}_{DEP}^{(1)} \rangle &= \frac{1}{4} \mathrm{Re}(\hat{\epsilon}_1) \oint_A \left[(\hat{b}^* + 1)(\mathbf{E}_2^* \cdot \hat{n})\mathbf{E}_2 + (\hat{b} + 1)(\mathbf{E}_2 \cdot \hat{n})\mathbf{E}_2^* + \hat{b}\hat{b}^* |\mathbf{E}_2 \cdot \hat{n}|^2 \hat{n} - |\mathbf{E}_2| \hat{n} \right] dS \\
&= \pi r^3 \mathrm{Re}(\hat{\epsilon}_1) \left[K(\omega)(\mathbf{E}_0 \cdot \nabla)\mathbf{E}_0^* + K^*(\omega)(\mathbf{E}_0^* \cdot \nabla)\mathbf{E}_0 \right]
\end{aligned} \tag{2.11}$$

The K-factor is the so-called first-order Clausius-Mossotti (CM) factor, which is dependent on the field frequency ω and the permittivities of both the dielectric particle and the medium. It determines the direction of the DEP force, as shown in Figure 2.3.

$$K(\omega) = \frac{\hat{b}}{\hat{b} + 3} = \frac{\hat{\epsilon}_2 - \hat{\epsilon}_1}{\hat{\epsilon}_2 + 2\hat{\epsilon}_1} = \frac{(\epsilon_2 - \epsilon_1) + \frac{1}{\omega}(\sigma_2 - \sigma_1)i}{(\epsilon_2 + 2\epsilon_1) + \frac{1}{\omega}(\sigma_2 + 2\sigma_1)i} \tag{2.12}$$

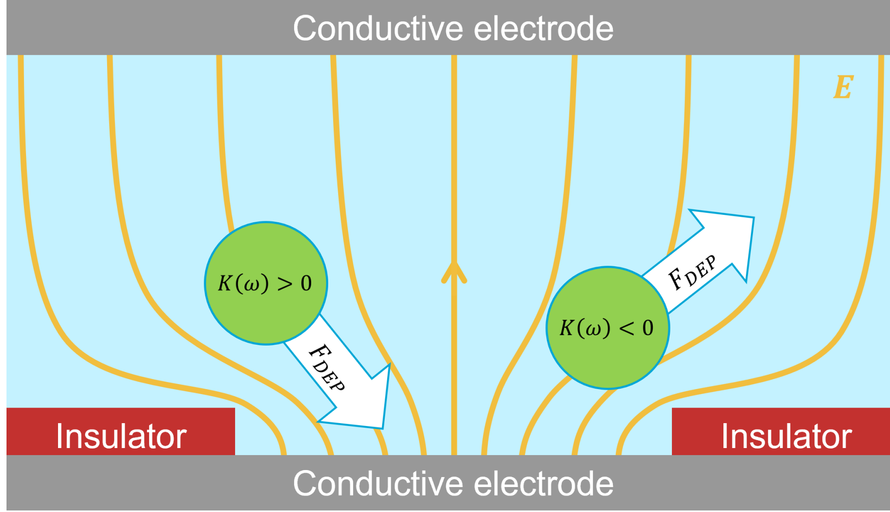

Figure 2.3: A schematic depiction of the effect of the Clausius-Mossotti factor on the direction of the DEP force in an OET. When the CM factor is positive, the DEP force will point towards the illuminated spot and vice versa.

If we assume that the applied electrical field is a complex harmonic of the form $\mathbf{E}_0 = E_j(\mathbf{r})e^{i\omega t}\hat{e}_j$ with $E_j(\mathbf{r})$ being the magnitude of the field at position $\mathbf{r}$ in the direction of $\hat{e}_j$, we arrive at a special form of the DEP form defined as conventional dielectrophoresis (cDEP), which is the most used expression in literature for the DEP force.

$$\begin{aligned}\langle \mathbf{F}^{(1)}_{cDEP}\rangle &= \pi r^3 \mathrm{Re}(\hat{\epsilon}_1)\left[K(\omega)(E_j(\mathbf{r})e^{i\omega t}\hat{e}_j\cdot\nabla)E_j(\mathbf{r})e^{-i\omega t}\hat{e}_j + K^*(\omega)(E_j(\mathbf{r})e^{-i\omega t}\hat{e}_j\cdot\nabla)E_j(\mathbf{r})e^{i\omega t}\hat{e}_j\right]\\ &= \pi r^3 \mathrm{Re}(\hat{\epsilon}_1)\left[K(\omega)+K^*(\omega)\right]E_j(\mathbf{r})\partial_j E_j(\mathbf{r})\hat{e}_j\\ &= \pi r^3 \mathrm{Re}(\hat{\epsilon}_1)\mathrm{Re}(K(\omega))\nabla|\mathbf{E}_0|^2\\ &= 2\pi r^3 \mathrm{Re}(\hat{\epsilon}_1)\mathrm{Re}(K(\omega))\nabla\mathbf{E}_{rms}\end{aligned} \tag{2.13}$$

In the last step, the squared norm of the field was replaced by the root mean square, assuming the applied field is sinusoidal. The DEP force can also be described as a dipole force resulting from the induced dipole moment in the dielectric particle. This derivation is often used in literature, using a dipole moment that results in the same DEP force as is derived by using the Maxwell stress tensor.

$$\begin{aligned}\langle \mathbf{F}_{cDEP}\rangle &= \mathrm{Re}\left[(\mathbf{p}\cdot\nabla)\mathbf{E}_0\right]\\ &= \mathrm{Re}\left[\left(4\pi\hat{\epsilon}_1 r^3\frac{\hat{\epsilon}_2-\hat{\epsilon}_1}{\hat{\epsilon}_2-2\hat{\epsilon}_1}\mathbf{E}_0\cdot\nabla\right)\mathbf{E}_0\right]\end{aligned} \tag{2.14}$$

It is important to note that this formula is incorrect for particles of different shapes (e.g., ellipsoids), particles with layered boundaries (e.g., cells), and electrical fields where the linear approximation is not valid. For an accurate description of an arbitrary shape, the integral equation 2.7 has to be integrated numerically.

2.2. Microfluidic Chip

The electric field needed to induce a DEP force can be generated by placing two plate electrodes in close proximity, similar to a parallel plate capacitor. Since the DEP force depends on the permittivity of both medium and particle, it is important to choose a medium that induces a big enough DEP while allowing for easy manipulation and engineering.

2.2.1. Dielectric medium

The DEP force depends linearly on the real part of the complex permittivity of the medium. Besides that, the real part of the CM factor determines the direction of the DEP force depending on the complex permittivities in the system. Therefore, we need to ensure that the dielectric properties of the medium and the particle fit the required dynamics of the OET. The simplest media, often used in literature, is deionized water, often containing 0.05% Tween-20 [15]. Deionized water is free of impurities and has relatively low conductivity, allowing the dielectric medium to function as a low-loss capacitor. The Tween-20 has been shown to increase the hydrophilicity of the particles which prevent the adhesion to each other and to the photoconductive layer [16].

The choice of medium also has a limiting effect on the minimum frequency of the electric field that can be used. This is due to the bubbles that form in the medium due to the separation of hydrogen and oxygen molecules when low-frequency voltages are applied. This phenomenon is known as electrolysis [17]. The electrolysis regions must be avoided because the bubbles can interfere with the OET by limiting or degrading its performance. In OET setups, electrolysis often occurs at frequencies below 1 kHz [18].

For live cell manipulation using OET, deionized water is not sufficient. Cells require a specialized medium with specific properties, including salts, a controlled pH level, and an appropriate temperature. The principle of the OET has proven itself to work at different dielectric media [19].

2.2.2. Electrodes

Because the microfluidic chip works similarly to a parallel plate capacitor, we can model the chip as an electrical circuit. Since a light source is used to both operate the OET and image the sample, electrodes must be both electrically conductive and optically transparent. This is typically achieved by sputtering a small layer of Indium Tin Oxide (ITO) on a microscope glass with a silver contact strip [20]. The transmittance and reflectance of different ITO layer thicknesses can be seen in Figure 2.4. Figure 2.5 shows the resistivity of different ITO layer thicknesses.

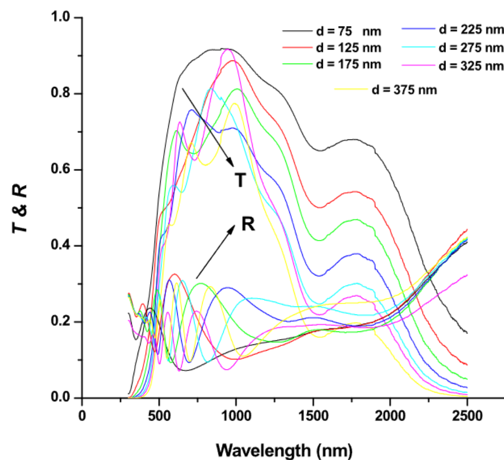

Figure 2.4: The transmittance and absorbance of different thicknesses of ITO film [21].

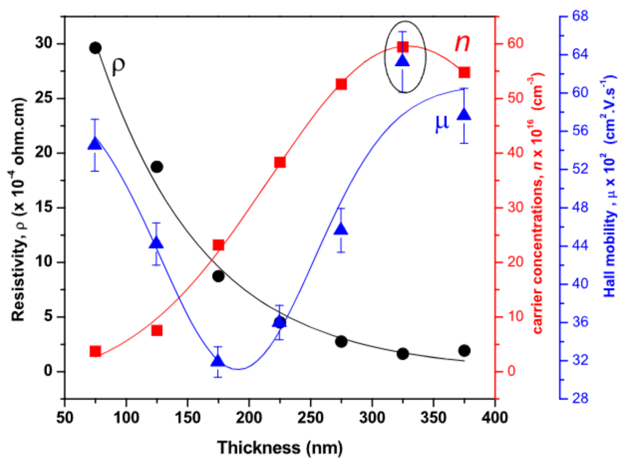

Figure 2.5: The resistance, carrier concentration, and Hall mobility of different thicknesses of ITO film [21].

To be able to project specific patterns on the OET, which in turn would allow us to move and position the particles in the trap to our liking, a photoconductive layer (PL) is placed on one of the electrodes. This layer is described in detail in the following section. From an electrical point of view, we can model the conductive and PL layers as series resistances, and the medium as a capacitance. This leads to the circuit shown in Figure 2.6.

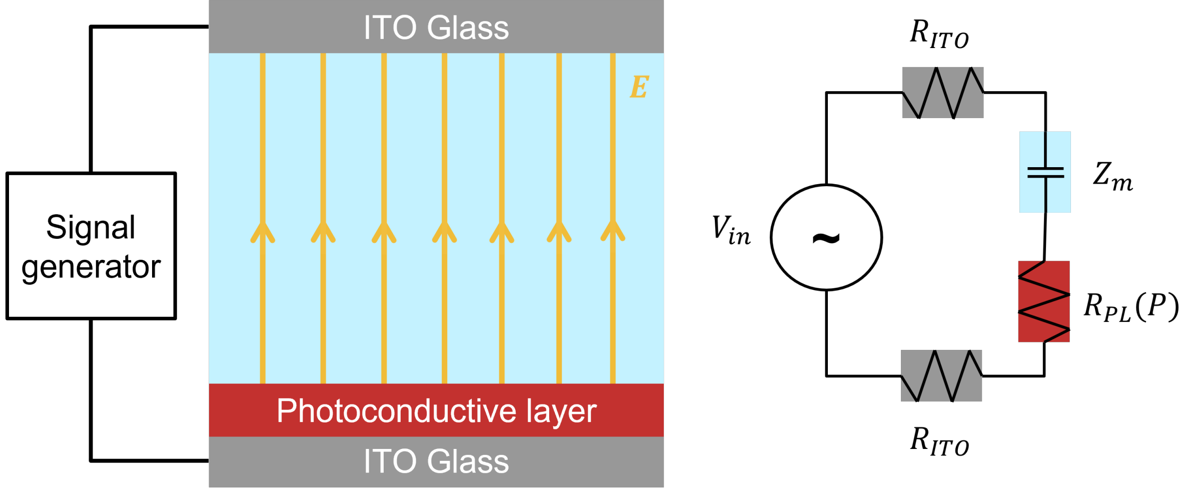

Figure 2.6: The OET is modeled as an electrical circuit with the most important resistances and impedances.

Using the fact that the current is constant in a series circuit, we can calculate the voltage drop over the impedance of the medium [22].

$$
\begin{aligned}
I &= \frac{V_{in}}{2R_{ITO} + R_{PL}(P) + Z_m} = \frac{V_m}{Z_m} \\
V_m &= \frac{V_{in} Z_m}{2R_{ITO} + R_{PL}(P) + Z_m}
\end{aligned}
\tag{2.15}
$$

The voltage drop over the medium V_m is related to the total input voltage V_{in}. The resistances of the ITO glasses and the PL are given by R_{ITO} and R_{PL}, for which the PL depends on the projection[2] of light P. The impedance of the capacitor with the medium depends on the frequency of the applied signal, the medium's material properties, and the microfluidic chamber's geometry [23].

$$
Z_m = \left(i\omega\epsilon_r\epsilon_0 \frac{A}{d} \right)^{-1} = (i\omega C)^{-1} \tag{2.16}
$$

ω is the frequency of the applied electrical signal. ϵ_r is the relative permittivity of the medium. A is the area of the microfluidic chip, and d is the height of the microfluidic chamber. The formula can be rewritten to the capacitance C, which can be measured using the right measuring device. In the absence of dielectric particles, the uniform field of this capacitor can be calculated from the voltage drop across the medium:

$$
E = \frac{V_m}{d} = \frac{V_{in} \left(i\omega\epsilon_r\epsilon_0 \frac{A}{d} \right)^{-1}}{d \left[2R_{ITO} + R_{PL}(P) + \left(i\omega\epsilon_r\epsilon_0 \frac{A}{d} \right)^{-1} \right]} \tag{2.17}
$$

[2] The dependency of the R_{PL} on the projection will be discussed in more detail in the next section.

2.3. Photoconductive layer

The photoconductive layer used in OET is often hydrogenated amorphous silicon (a-Si:H) [6]. This material is a semiconductor with a sufficiently small bandgap that visible or infrared photons can be used to promote electrons from the valence band to the conduction band. Effectively, this allows us to switch the material behavior from insulating to conducting by photo-activation [24]. This property enables the electrical field inside the microfluidic chip to be shaped. We will now discuss the physics behind these properties of a-Si:H, which will inform us of the ideal design choices for the PL layer.

2.3.1. Electron dispersion in a semiconductor

An electron in a solid has dynamics, as described by Schrödinger's equation. This equation can be solved in steady state by setting the potential $V(\mathbf{r})$ to 0. When using the ansatz that the electron's wavefunction can be written as a complex exponential, we can find the eigenvalues [25]. These are the eigenenergies that depend on the wave number k of the electron.

$$
\begin{aligned}
i\hbar\frac{\partial}{\partial t}\Psi(\mathbf{r},t) &= \left[-\frac{\hbar^2}{2m}\nabla^2 + V(\mathbf{r})\right]\Psi(\mathbf{r},t) \\
&\downarrow \text{Steady state and } V(\mathbf{r}) = 0 \\
-\frac{\hbar^2}{2m}\nabla^2\Psi(\mathbf{r}) &= E\Psi(\mathbf{r}) \\
&\downarrow \text{Ansatz: } \Psi(\mathbf{r}) = Ce^{i\mathbf{k}\cdot\mathbf{r}} \\
E &= \frac{\hbar^2 k^2}{2m}
\end{aligned}
\tag{2.18}
$$

The reduced Planck constant is given by $\hbar$. The electron has a mass m and a wavenumber k. This wavenumber has a direction but is assumed to be equal in every direction. Assuming that each electron occupies a cubic box with sidelength L, we can find how many energy states we can have in a given total volume and an amount of energy. This number of states $N(E)$ can be translated to a density of states $g(E) = \frac{dN(E)}{dE}$ [26].

$$
\begin{aligned}
N(\mathbf{k}) &= \left(\frac{L}{2\pi}\right)^3 \int_V d\mathbf{k} = \frac{L^3}{2\pi^2}\int_0^\infty k^2 dk \\
&\downarrow E(\mathbf{k}) < E \\
N(E) &= \frac{L^3\sqrt{2}m^{3/2}}{\pi^2\hbar^3}\int \sqrt{E}dE = \int g(E)dE \\
g(E) &= \frac{L^3\sqrt{2}m^{3/2}}{\pi^2\hbar^3}\sqrt{E}
\end{aligned}
\tag{2.19}
$$

We used the eigenenergy $E(k)$ from equation 2.18 to rewrite the number of states from depending on the wavenumber to the eigenenergy. In this formulation, we added a factor of 2 to account for the spin degeneracy of the electron. To arrive at the eigenenergy and the density of states, we assumed that the electron is free to move in the solid. This is the case for conductors but not for semiconductors or insulators. The effect of this nearly free electron is that it is more confined to its cubic box, as we defined previously. This effect is visualized in Figure 2.7. We can see that the eigenenergy is periodic with a total length of 2π times the cubic box side length L. When an electron is in a conductor and is free to move, it can enter eigenenergies in other boxes easily denoted by the blue line. When an electron is in a semiconductor, it is not entirely free to move between the boxes, which opens up gaps between the allowed amounts of energy. These gaps are called band gaps and are one of the distinguishing qualities of semiconductors and insulators.

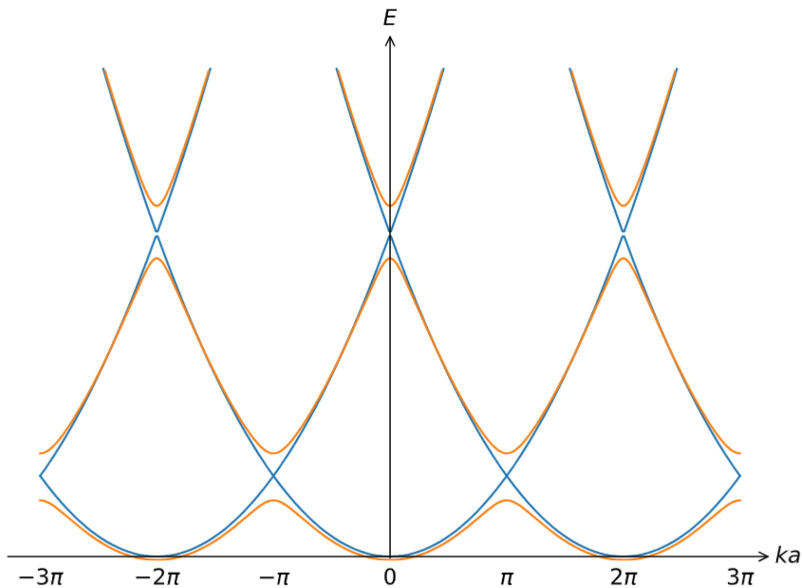

Figure 2.7: The dispersion relation of a free electron in blue and a nearly-free electron in orange. The dispersion relation is periodic in ka with a being the length of the cubic box, which we denote as L [27].

In their ground state, electrons are confined to the low-energy band, known as the valence band. If sufficient energy is provided to the electron, e.g., by absorbing a photon, the electron is promoted to higher energy bands. This allows the electron to move (almost) freely within the solid, making the material a better conductor. For this reason, the higher energy band is referred to as the conduction band.

2.3.2. Hydrogenated amorphous silicon

Solids tend to form ordered crystals. This is the case for crystalline silicon (c-Si), where silicon atoms are neatly organized in a lattice. When the atoms are randomly removed from the lattice, the regular structure is broken and amorphous silicon (a-Si) is obtained. The random distribution leaves some bonds that are not attached. These are called dangling bonds and capture moving electrons in the amorphous silicon. When hydrogen atoms are added to cap the dangling bonds to compensate for this phenomenon, hydrogenated amorphous silicon (a-Si:H) is created. Figure 2.8 shows a schematic depiction of the types of silicon.

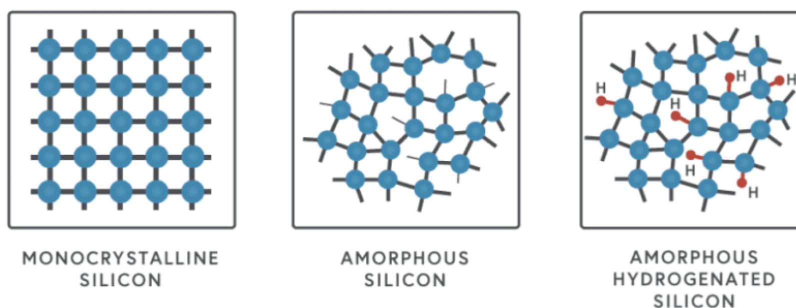

Figure 2.8: An illustration of the difference in crystal lattice structure. From left to right, monocrystalline silicon, amorphous silicon, and hydrogenated amorphous silicon [28].

The density of states is different for each type of silicon. The disorder in the a-Si results in localized states, which decrease the band gap by allowing some states between the valence and conduction bands, known as the Urbach tails, as shown in Figure 2.9.

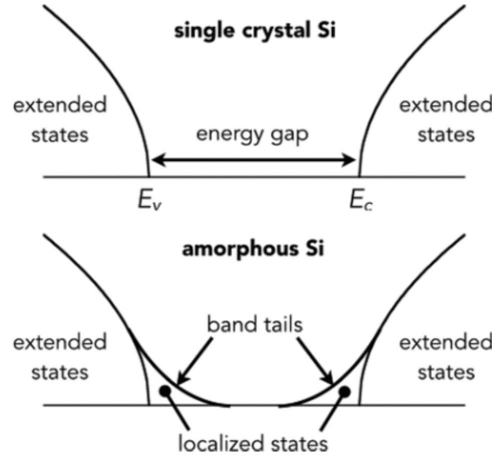

Figure 2.9: A schematic density of states for crystal silicon and amorphous silicon. E_v is the maximum energy of the valence band. E_c is the minimum energy of the conduction band. The band tails are due to disorder in the structure [29].

In a-Si:H, the localized states are often described as having the Urbach tails with an addition of two Gaussian distributions. These localized states are shown in Figure 2.10. The specific band gaps depend on the material properties of the a-Si:H. It changes with different amounts of chaotic distribution and doping of hydrogen to cap the dangling bonds [30].

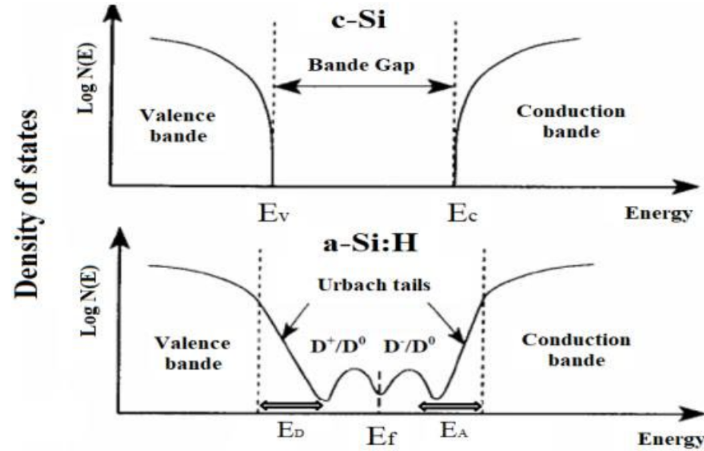

Figure 2.10: A schematic depiction of the difference in density of states between crystallized silicon and amorphous hydrogenated silicon. ED and EA describe the tails of the Urbach tails. E_v, E_c, and E_f are the valence band energy, conduction band energy, and the Fermi energy. D^+/D^0 and D^-/D^0 represent the donor-like gap states per unit volume and the acceptor-like gap states per unit volume [31].

2.3.3. Absorption coefficient

To determine how the electric field in the OET will be affected by the PL layer while exposed to illumination, a relation between the change in electrical conductivity, the photon absorption coefficient, and the illumination power must be established. When photons collide with electrons in a material, the energy can be absorbed, and the electrons can jump to a higher energy state. This phenomenon is called the photoelectric effect and was first discovered by Albert Einstein. The energy of a photon depends on its wavelength [32]. The amount of photons absorbed by the material is given by the Lambert-Beer law [33].

$$\begin{aligned} \frac{dI}{dx} &= -I(x)\alpha(\lambda) \\ I(x) &= I(0)e^{-\alpha(\lambda)x} = \frac{hc}{\lambda A t}e^{-\alpha(\lambda)x} \end{aligned} \tag{2.20}$$

The absorption coefficient is given by α and depends on the wavelength of the photon λ. The intensity of light I is the energy per area A per unit of time t. The energy of a photon is given by the Planck constant h, the speed of light c, and the wavelength of light. The higher the depth x the light travels inside the material, the lower the light intensity due to absorption. When a photon is absorbed in the material, it can excite an electron with sufficient energy for it to leave the surface of the material. The generation rate is given using the quantum efficiency η as $g(x,\lambda) = \eta(\lambda)\alpha(\lambda)I_0(\lambda)e^{-\alpha(\lambda)x}$ when disregarding the reflectance of the material [34]. These free electrons leave behind a hole, which creates more space for electrons to move in the valence band. The material's conductivity is determined by the initial conductivity at ground energy with the addition of the created electrons and holes.

$$\begin{aligned}\sigma &= \sigma_0 + \delta\sigma \\ &= |e|(\mu_n n_0 + \mu_p p_0) + |e|(\mu_n \delta n + \mu_p \delta p)\end{aligned} \tag{2.21}$$

The conductivity σ depends on the electron charge e, which is moved by electrons n and holes p with their respective mobilities μ_n and μ_p. The change in electrons can be calculated using the generation rate.

$$\frac{dn}{dt} = g(t) - r(t) = g(t) - c_{c,v}np \tag{2.22}$$

The carriers, i.e., holes or electrons, can be recombined, removing their contribution to the conductivity. This happens at a certain recombination rate $r(t)$, which is, for intrinsic photoconductivity, depending on the recombination coefficient $c_{c,v}$ and the number of holes and electrons. More factors can influence the change of conductivity of the material, such as trapping of electrons [35]. The increase in conductivity has been experimentally found to be linearly dependent on the optical power [36].

$$\Delta\sigma = e\eta\alpha\mu_n\tau_n\frac{S}{hf} \tag{2.23}$$

The increase in conductivity depends on the quantum efficiency η, which is the conversion efficiency of a photon with enough energy into a free electron. τ_n is the lifetime of the free electron. S is the optical power and f is the frequency of the light. In Table 2.1, the absorption coefficient and the photoconductivity given a certain wavelength of light are shown. The absorption coefficient increases with decreasing wavelength of the photons. This translates to a bigger increase in photoconductivity with higher energies of light.

Color	Wavelength (nm)	Averaged Absorption Coefficient (m^{-1})	Photoconductivity (S/m)
Red	Max: 700	1.0×10^6	1.1×10^{-5}
	Mean: 660	1.7×10^6	1.8×10^{-5}
	Min: 620	3.1×10^6	3.1×10^{-5}
Orange	Mean: 605	4.3×10^6	4.2×10^{-5}
Yellow	Mean: 580	5.7×10^6	5.3×10^{-5}
Green	Max: 570	6.8×10^6	6.3×10^{-5}
	Mean: 530	1.1×10^7	9.6×10^{-5}
	Min: 495	1.7×10^7	1.3×10^{-4}
Cyan	Mean: 485	1.9×10^7	1.5×10^{-4}
Blue	Mean: 463	2.5×10^7	1.8×10^{-4}
Purple	Max: 450	2.8×10^7	2.0×10^{-4}
	Mean: 415	3.6×10^7	2.5×10^{-4}
	Min: 380	4.5×10^7	2.9×10^{-4}

Table 2.1: The photoconductivity of a-Si:H depends on the wavelength of the photons. For this data, an optical power of $S = 0.2$ mW/cm^2 was used [36].

Besides a-Si:H, more possible photoconductive layers exist for OET. A bulk-heterojunction polymer (BHJ) has been shown to work, which is less complicated and expensive to fabricate [37]. In addition to that, BHJ can be used to create flexible photoconductive layers [38]. The downside of BHJ is its relatively short lifetime. Another material used as the photoconductive layer is the organic photosensitive material titanium oxide phthalocyanine (TiOPc). This material is promising, for it can be fabricated within 40 minutes [39]. The most promising photoconductive layer material is a phototransistor-based junction of differently doped a-Si:H [40]. This material is complex to fabricate but showed a bigger conductivity difference between illuminated and non-illuminated spots. This results in stronger electrical fields overall and, therefore, stronger DEP forces, which opens up the OET more to living cell manipulation.

2.4. The dynamics of the dielectric particle

Precise control of dielectric particles in OET actually requires considering more forces than just the DEP force. The DEP force is the controllable input force, but we also need to consider forces such as friction and fluid forces. A free-body diagram of the dielectric particle with all possible forces working on it can be seen in Figure 2.11. We will discuss all these possible forces in this section.

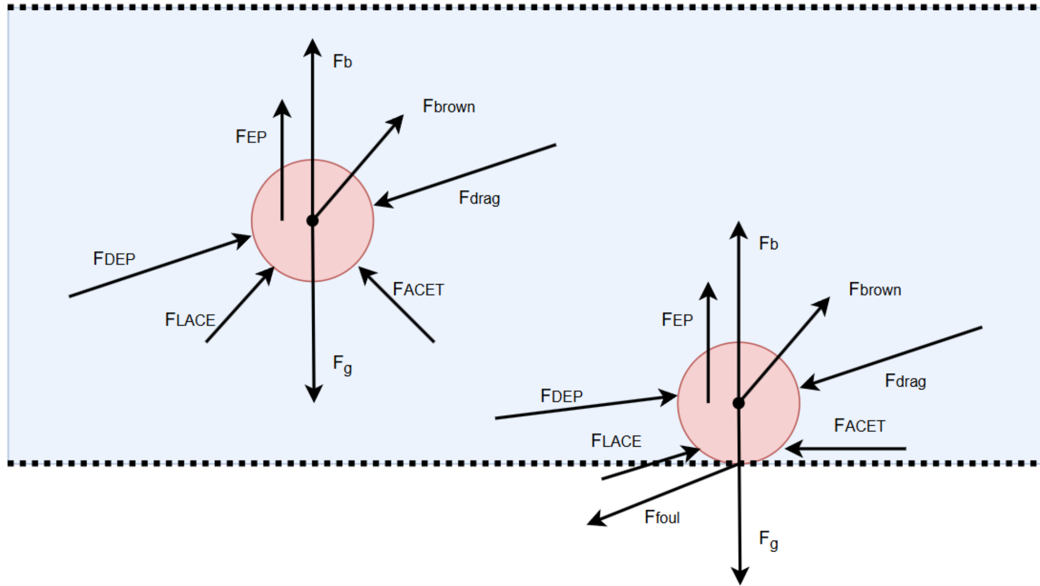

Figure 2.11: The OET forces that are working on a particle submerged in a medium, free to move (left) and stuck to the bottom (right).

2.4.1. Forces on the particle

Gravity and Buoyancy

The gravity and buoyancy forces push the particle down and up, respectively. Both depend on the gravity constant and the particle's volume. The gravity force pulls the particle down due to its weight, while the buoyancy force pushes the particle up due to the weight of water that needs to be displaced.

$$\mathbf{F}_g = -V\rho_p g\hat{z} \qquad \mathbf{F}_b = V\rho_m g\hat{z} \tag{2.24}$$

with the volume of the particle V, the density of the particle ρ_p, the density of the medium ρ_m, the gravitational constant $g = 9.81$ m/s^2 and the unit vector $\hat{z}$ pointing upwards.

Brownian motion

When particles are small enough, they collide with other small particles that move due to their entropy. This collision randomly moves the particle in any direction. This can be described using Brownian motion and taken as a stochastic disturbance with decreasing expected motion with the increasing size of a spherical particle [41].

$$\langle\frac{d\mathbf{x}_{brown}}{dt}\rangle = \sqrt{\frac{k_bT}{3\pi\eta r}} \qquad \langle\mathbf{F}_{brown}\rangle = m\langle\frac{d^2\mathbf{x}_{brown}}{dt^2}\rangle \tag{2.25}$$

where the random movement in $\mathbf{x}$ direction is depending on the Boltzmann constant k_b, the temperature T, the viscosity of the medium η and the radius of particle r. The Brownian force depends on the time derivative of this Brownian motion and the mass of the particle m.

Drag force

When a particle moves in a fluid, it will be slowed down by the fluid's resistance, called drag. The Navier-Stokes equation describes the dynamics of a fluid [42].

$$\rho_m\left(\frac{\partial\mathbf{V}}{\partial t} + (\mathbf{V}\cdot\nabla)\mathbf{V}\right) = -\nabla p + \mu\nabla^2\mathbf{V} + \mathbf{F} \tag{2.26}$$

The Navier-Stokes equation gives the velocity of the fluid $\mathbf{V}$ and the pressure on the fluid p due to an external force F. This equation is difficult to solve and often requires simplification to arrive at an analytical result. We can simplify the Navier-Stokes formula by substituting the Reynolds number Re.

$$Re = \frac{\rho_m|\mathbf{V}|L}{\mu} \rightarrow Re\left(\frac{\partial\mathbf{V}}{\partial t} + (\mathbf{V}\cdot\nabla)\mathbf{V}\right) = |\mathbf{V}|L\nabla^2\mathbf{V} - \frac{|\mathbf{V}|L}{\mu}\nabla p + \frac{|\mathbf{V}|L}{\mu}\mathbf{F} \tag{2.27}$$

L is the particle's characteristic length. The external forces are ignored in full dynamics, meaning we will ignore them when deriving the drag force. If we consider the Reynolds number small, we can ignore the left side of the modified Navier-Stokes equation. This results in the relation between the pressure and velocity of the fluid.

$$\mu\nabla^2\mathbf{V} = \nabla p \tag{2.28}$$

Another relation can be found by the steady-state continuity equation of a fluid with a homogeneous density, which results from the conservation of mass [43].

$$\frac{d\rho}{dt} + \nabla\cdot(p\mathbf{V}) = 0 \rightarrow \nabla\cdot\mathbf{V} = 0 \tag{2.29}$$

To find the force on a particle due to the viscous stress of the fluid, we need to solve the surface integral of the viscous stress tensor σ_v.

$$\mathbf{F}_{drag} = \oint_S \sigma_v \cdot d\mathbf{S} \qquad \sigma_v = -p\mathbb{I} + \mu(\nabla\mathbf{V} + (\nabla\mathbf{V})^\top) \tag{2.30}$$

When we assume the particle to be spherical and the fluid's velocity relative to the particle to move in a single direction far from the particle, we can solve this integral and arrive at Stokes's law.

$$\mathbf{F}_{drag} = 6\pi\mu r\mathbf{V}_\infty \tag{2.31}$$

The particle has a radius r, and the relative velocity of the fluid at a large distance from the center of the particle is given as $\mathbf{V}_\infty$. If we cannot assume a small Reynolds number, we can describe the drag force with the drag coefficient C_d [42].

$$\mathbf{F}_{drag} = \frac{1}{2}\rho_m C_d A|\mathbf{V}_\infty|\hat{v} \tag{2.32}$$

The cross-sectional area is given as A, and the direction of the fluid with respect to the particle is given as $\hat{v}$. The drag coefficient can be experimentally found and differs at different Reynolds numbers. At small Reynolds numbers, the drag forces from the drag coefficient and Stokes law are the same for spherical particles. A rotational drag due to a spherical particle rotating with angular velocity ω can be found that is similar to the linear drag, including a formulation of the drag torque on a spherical particle at large Reynolds numbers using a rotational drag coefficient C_T [44][45].

$$\mathbf{T}_{drag} = 8\pi\mu r^3|\omega|\hat{\omega} \underset{Re>>0}{\longrightarrow} \mathbf{T}_{drag} = \rho_m \pi r^5 C_T|\omega|^2\hat{\omega} \tag{2.33}$$

Electrophoresis

When we put a charged particle inside an electrical field at low frequencies (i.e., <10 Hz) in a vacuum, it feels a force due to the electromagnetic interaction, also known as Coulomb's law. When the particle is positively charged with charge q, the force is in the same direction as the electrical field [12].

$$\mathbf{F}_{EP} = q\mathbf{E} \tag{2.34}$$

When a charged particle is submerged in a dielectric medium and subject to an electrical field, similar to the OET, a double boundary layer appears around the charged particle. These layers, also shown in Figure 2.12, form due to the ions of the medium being attracted to the particle's charge. The outside layer is called the slipping plane. The electromagnetic interaction at the slipping plane moves the particle depending on the ζ-potential [46] [47].

$$\mu_e = \frac{|\mathbf{V}_{EP}|}{|\mathbf{E}|} = \frac{2\epsilon_r\epsilon_0}{3\mu}\zeta f(\kappa r) \tag{2.35}$$

The electrophoretic mobility μ_e couples the electrophoretic particle velocity $\mathbf{V}_{EP}$ to the ζ-potential and to the Henry coefficient $f(\kappa r)$, which depends on the Debye length κ.

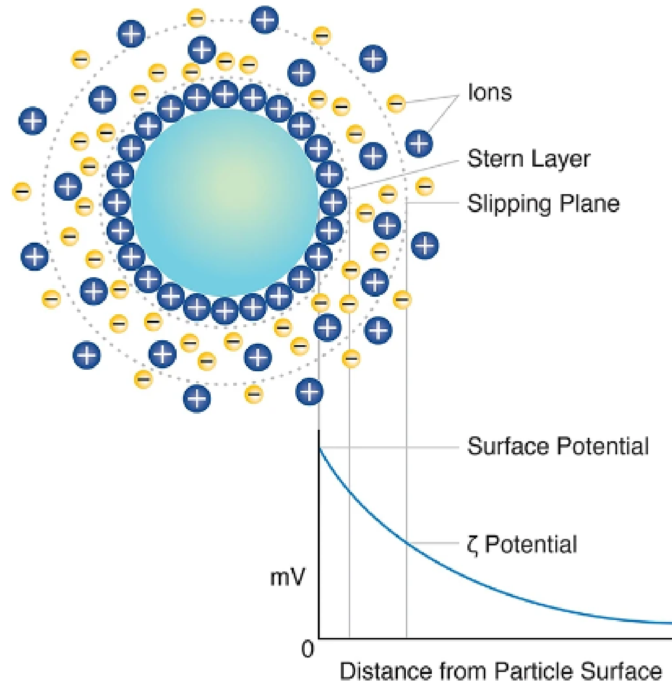

Figure 2.12: The electric double layer around a submerged negatively charged particle. The surface charge decreases with radial distance. At the Stern layer, the potential is the Stern potential. At the slipping plane, the potential is the ζ-potential [48].

2.4.2. Forces on the medium

The particle is directly subject to forces due to the electromagnetic and fluid phenomena in the OET setup. The dielectric medium itself is also subject to forces from these phenomena. The dynamics of the fluid directly create the dynamics of the particle as described by the drag force.

Light-actuated AC electroosmosis

Similar to electrophoresis, the charges created at the electrodes of the OET move due to electromagnetic phenomena. At the slipping plane of the electrodes, the ions move towards the illuminated spot, for it has a bigger surface potential. This induced flow is called light-actuated AC electroosmosis (LACE) [49]. Figure 2.13 shows a schematic of the LACE flow. The LACE depends on the ζ-potential of the electrodes and moves the fluid with velocity $\mathbf{V}_{LACE}$ to the tangential component to the electrode of the non-uniform electrical field $\mathbf{E}_{\perp}$.

$$\mathbf{V}_{LACE} = \frac{\epsilon_r \epsilon_0}{\mu_m} \mathbf{E}_{\perp} \tag{2.36}$$

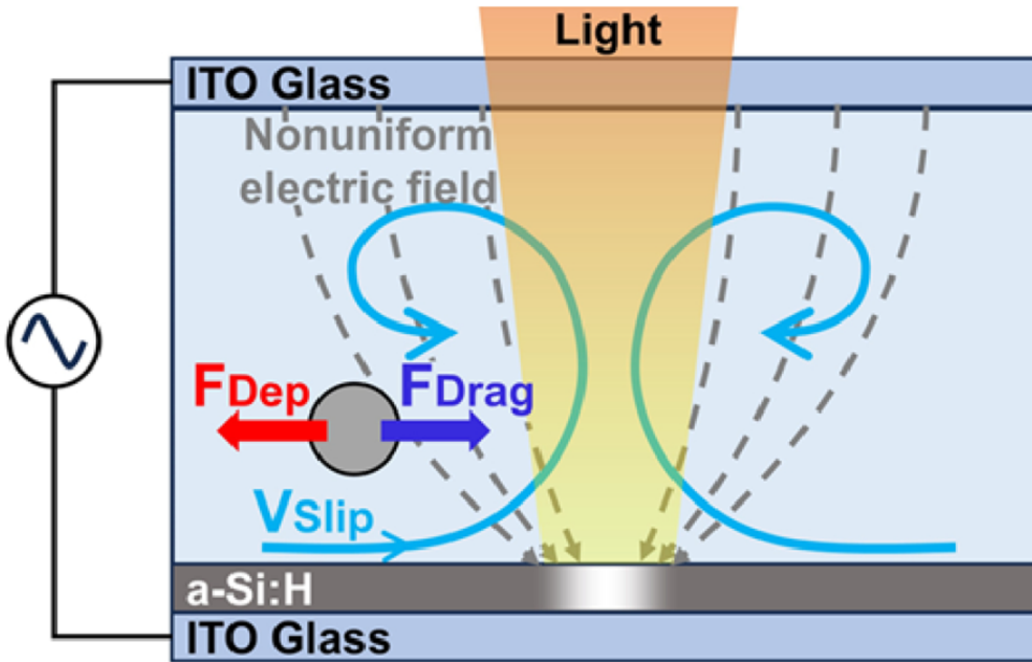

Figure 2.13: The fluid has a certain slip velocity due to the light-induced AC electroosmosis [49].

Because the LACE depends on the AC field, the effect changes at different frequencies. The optimal frequency f_{opt} relies on the conductivity of the medium σ_m, the thickness of the double layer λ_d, and the height of the medium L [50].

$$f_{opt} = \frac{\sigma_m \lambda_d}{2\pi \epsilon_m L} \tag{2.37}$$

Electrothermal flow

The conductivity of the medium heats the fluid when subject to an electrical field. This can be found from the internal energy of the fluid at steady state with a small Peclet number [51] [52].

$$\begin{gathered} \rho_m c_p \left(\frac{dT}{dt} + (\mathbf{V} \cdot \nabla) T \right) = k \nabla^2 T + \sigma_m |\mathbf{E}| \\ \underbrace{\frac{\rho_m c_p \mathbf{V}}{k}}_{Pe} \cdot \nabla T = \nabla^2 T + \sigma_m |\mathbf{E}| \approx 0 \end{gathered} \tag{2.38}$$

The specific heat and the thermal conductivity of the fluid are given as c_p and k. We can solve this equation by linearizing the electrical field and assuming incompressibility; we can derive the electrothermal (ACET) body force depending on the frequency of the applied electrical field. We can also find a cross-over frequency that switches the sign of the ET body force [53].

$$\langle \mathbf{f}_{ET} \rangle = \frac{1}{2}\text{Re}\left[\left(\left(\frac{\epsilon_m \sigma_m}{i\omega\epsilon_m + \sigma_m}\right)(k_\epsilon - k_\sigma)\nabla T \cdot \mathbf{E}\right)\mathbf{E}^*\right] - \frac{1}{4}|\mathbf{E}^2|\epsilon_m k_\epsilon \nabla T$$
$$f_{ET,cross-over} \approx \frac{\sigma_m}{2\pi\epsilon_m}\sqrt{2\frac{|\frac{1}{\sigma_m}(\frac{\partial\sigma_m}{\partial T})|}{|\frac{1}{\epsilon_m}(\frac{\partial\epsilon_m}{\partial T})|}} \tag{2.39}$$

k_ϵ and k_σ are empirically found constants that relate the change in ϵ_m and σ_m to the change in temperature [54].

$$\nabla\epsilon_m = k_\epsilon \epsilon_m \nabla T \qquad \nabla\sigma_m = k_\sigma \sigma_m \nabla T \tag{2.40}$$

Thermal flow

A temperature change in the fluid influences its density. This induces natural convection inside the fluid, which can be described by a temperature-dependent version of the buoyancy force [55].

$$\mathbf{f}_{nc} = \frac{\partial\rho_m}{\partial T}\nabla T g\hat{z} \tag{2.41}$$

2.4.3. Situational forces

When a particle is stationary at the bottom of the chip, it could be adhered, making it difficult to move. The friction or adhesion from the surface interaction between the boundaries of the chip and the dielectric particle can be modeled as a step-like situational force depending on the particle's velocity. The surface adhesion can be prevented by creating an antifouling layer on the photoconductive layer. Bovine serum albumin (BSA) and polyethylene glycol (PEG) can be used to reduce the adhered particles to up to 90% [56]. Another way to reduce the adhesion is by putting 0.05% Tween-20 in a medium of deionized water [16].

2.4.4. State space

The full dynamics of the particle can be found by putting together all the forces directly influencing the dielectric particle. The same can be done with the forces working on the fluid, which affect the dynamics of the dielectric particle through the drag force. Temperature influences the dynamics of the fluid. The states that we are interested in in the system are, therefore, the dynamics of the center of mass of the particle $\mathbf{x}$ and the dynamics of the rotation of the particle's center of mass $\theta_m\hat{\theta}_m$. Other states are the dynamics of the velocity $\mathbf{V}_m$, and angular velocity $\omega_m\hat{\omega}_m$ of the fluid. The last state of interest is the dynamics of the temperature of the fluid T. The input states of the OET system are the optical power P, the frequency f, and voltage V of the applied electrical signal, and optionally, externally applied heat power P_{ext}. Different forces are dominant in the OET setup in different operational regimes. Figure 2.14 shows an example of these regimes.

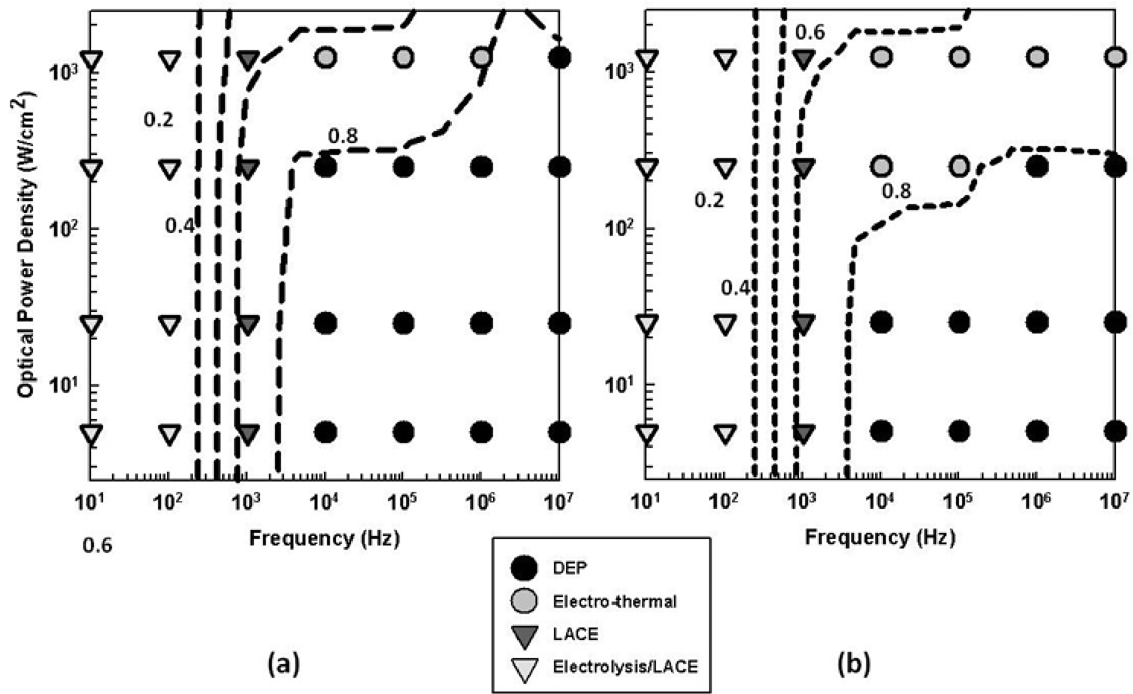

Figure 2.14: Regions in the frequency/optical power plot show where certain forces dominate. The particle in this system is in a liquid solution with a conductivity of 1 mS/m. The applied AC frequency is 100 kHz. In (a), the applied voltage is 20 Vpp. In (b), the applied voltage is 10 Vpp [54].

2.5. Optical setup

To image and control the dielectric particle, we need to build the OET setup, which is essentially an optical setup. This setup appends the light path so that we can magnify the microfluidic chip and demagnify the patterned illumination used to control the dielectric particle.

2.5.1. The light microscope

The OET is a light microscope that demagnifies the illuminated pattern created by a digital micromirror device using a 4f system. A 4f-system consists of 2 lenses separated by the sum of their focal lengths. The total length of the optical path on the optical axis is four focal lengths long [57]. An example of magnification by a 4f-system is shown in Figure 2.15. The magnification depends on the focal lengths of the two used lenses.

$$M = \frac{y_2}{y_1} = -\frac{f_2}{f_1} \tag{2.42}$$

If we want to increase the size of a projection, i.e., $\frac{y_2}{y_1} > 1$, we need to have $f_2 > f_1$. The negative sign is due to the image being flipped after the 4f system.

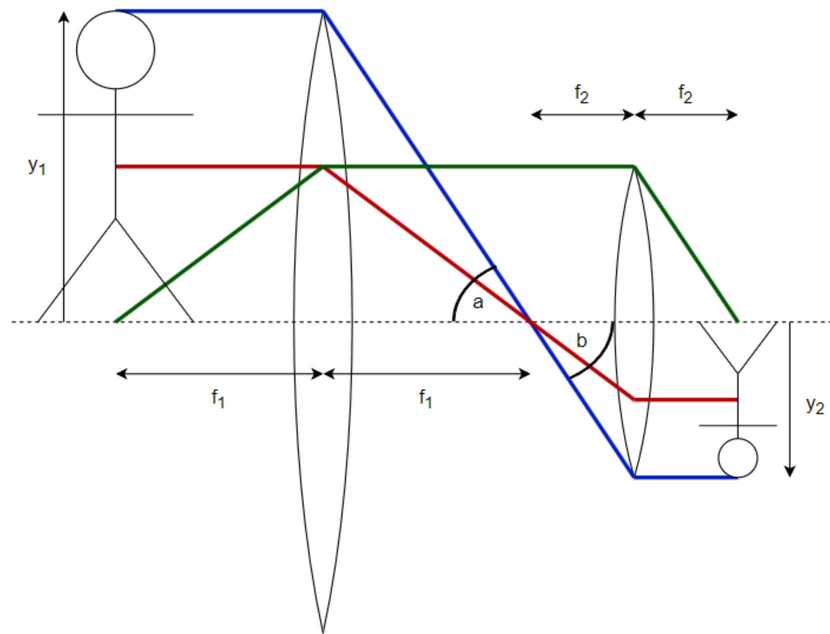

Figure 2.15: A schematic depiction of a telescope with two lenses. The left lens has a focal length f_1, and the second lens has a focal length f_2. On the left side, the stick figure stands at f_1 distance from the first lens. This object, the stick figure, is imaged, translated, and demagnified on the right side.

The image in the optical setup can be considered a plane. We talk about aberrations when the optical setup distorts this plane, e.g., bends or tilts it. These aberrations reduce the quality of the images and should be avoided as much as possible. Therefore, a microscope objective is used to prevent aberrations while imaging the sample. To increase the quality of the images, the source light should be as collimated as possible to ensure that the focus of the illumination is in the same focal plane as the objective.

2.5.2. Resolution

In general, all the optical elements in the optical setup should be aligned and put at the right intermediate distances to get a clear image. The distance the particles can be spread out while we can still distinguish them is called the resolution of the optical setup. The resolution is highly dependent on the numerical aperture (NA), which is defined by the maximum angle θ_{max} the light rays can make before exiting the lens entrance pupil and the refractive index of the medium outside of the lens n. The maximum angle is due to Snell's law, for which larger angles will not escape a lens anymore. Each optical element has its own NA. The smallest NA determines the NA of the full optical system among all elements [57].

$$NA = n\sin(\theta_{max}) \tag{2.43}$$

When light moves through an aperture, it is diffracted due to the Huygens principle. Using Fourier optics, we can find that this diffraction results in a pattern in the image plane [58]. This pattern is called the Airy pattern and shows how small objects can be and how close together they can be to be still able to distinguish them [59]. This is called the lateral resolution[3]. The intensity pattern of a single point through a 4f-system results in a first-order Bessel function, as shown in Figure 2.16. The first zero of this Bessel function is found at a radius ρ from the pattern's center. This radius depends on the NA of the optical system and the wavelength λ of the light source used to image the spot.

$$\rho = 0.61\frac{\lambda}{NA} \tag{2.44}$$

[3]This is sometimes also denoted as the spatial resolution.

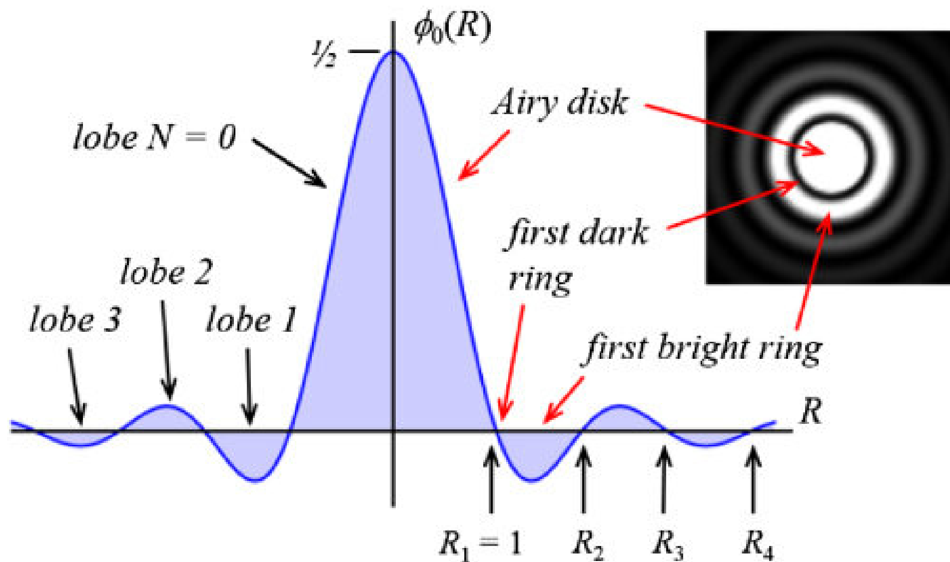

Figure 2.16: The field due to a circular aperture. This shape is called the Airy disk and consists of multiple circles. Each circle is separated due to the minima in the Airy disk function [60].

Two spots need to be separated by at least ρ distance to be able to distinguish them. This is called the Rayleigh criterion and can be seen in Figure 2.17.

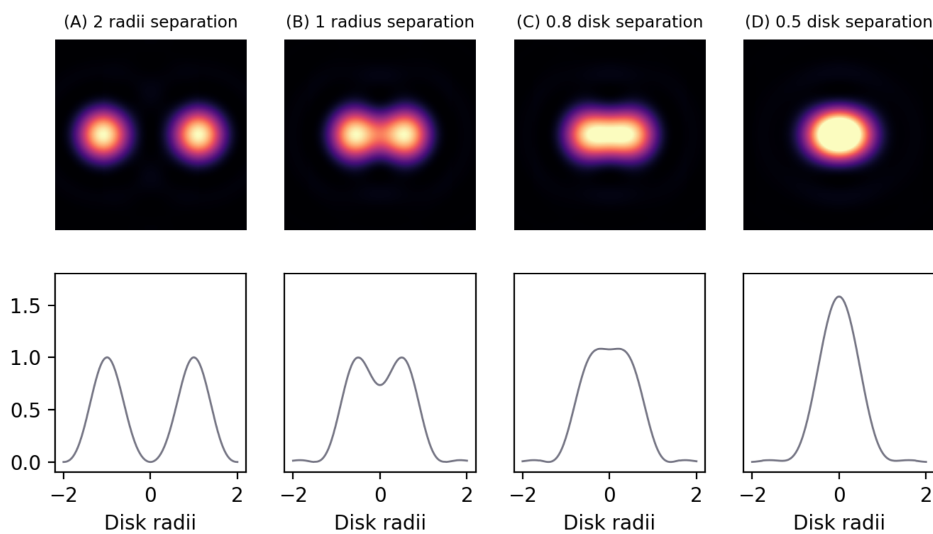

Figure 2.17: The effects of separation of the Airy disks are shown. If we separate the spots with a distance of at least 1 one radius, the spot centers can be distinguished as two separate spots. When the separation is less than a distance of 1 radius, it is impossible to recognize individual spots anymore [61].

One also has to consider the resolution in depth, along the optical axis. This is called the depth of focus (DoF) and depends on the NA, the refractive index of the medium n, and the wavelength of the optical source λ. This DoF can be found geometrically by finding the distance a wavefront can be out of focus to still be able to distinguish a particle. Figure 2.18 shows the schematic depiction of this out-of-focus wavefront. When the maximum distance W is taken to be $\frac{\lambda}{4n}$, we can find the maximum distance ΔZ at which an object can still be distinguished[4] [62].

[4]At a quarter wavelength for a monochromatic wavefront, we have $\sin(\frac{\pi}{2}) = 0$, resulting in 0 amplitude.

$$\Delta Z \leq \frac{\lambda}{4n\left(1-\sqrt{1-\left(\frac{NA}{n}\right)^2}\right)}$$
$$\downarrow \text{NA small}$$
$$\Delta Z \leq \frac{\lambda n}{2(NA)^2} \tag{2.45}$$

The limit when NA is small is often taken in the literature [58]. The DoF goes in two directions, meaning the total resolution in depth is $2\Delta Z$. When using a small NA, another term could be added to correct the geometrical optical circle of confusion, which is due to aberrations from the objective lens. This formula uses the magnification between the camera and the chip M and the smallest distance e that can be resolved by the camera [63].

$$2\Delta Z \leq \frac{\lambda n}{(NA)^2} + \frac{n}{M(NA)}e \tag{2.46}$$

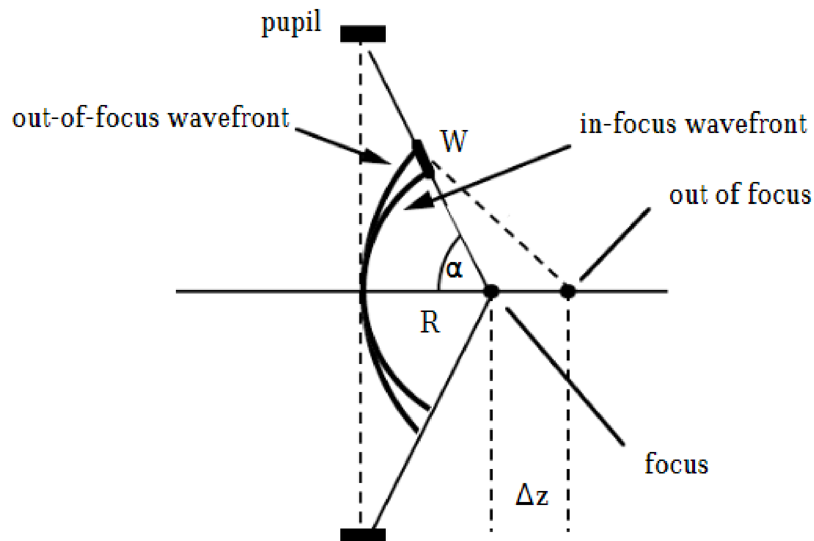

Figure 2.18: A schematic depiction of a wavefront compared to an out-of-focus wavefront. The wavefronts are distanced with a distance W as seen from the focal point of the focused wavefront [62].

2.5.3. Light source

In the optical setup, we have a choice of different light sources we can use. Important light sources are light-emitting diodes (LED), Light Amplification by Stimulated Emission of Radiation (laser), or incandescent lamps. Incandescent lamps work by radiation from Joule heating [64]. They are usually not expensive, have low power, high temperatures, and have a broad light spectrum. LEDs have a sharper peaked spectrum and a higher optical power. The LED works by electroluminescence. Photons are emitted from the excess energy of electrons and holes recombining in the LED [65]. The light from an LED is not a point source, making it difficult to collimate. The divergence angle can be decreased by placing a lens after the LED [66]. The expected beam divergence of the LED with the lens is schematically shown in Figure 2.19. The divergence angle Φ depends on the size of the LED d and the lens's focal length f.

$$\frac{\Phi}{2} = \tan^{-1}\left(\frac{d}{2f}\right) \tag{2.47}$$

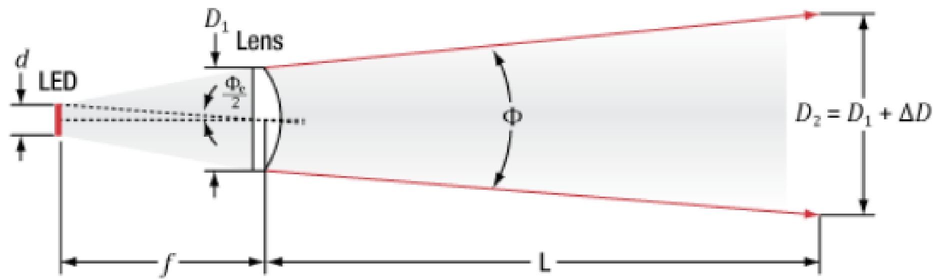

Figure 2.19: The expected beam divergence of an LED with size d after a distance L [66]

A laser has a very sharply peaked optical spectrum. Photons are emitted in phase with one another, thanks to the stimulated emission process, making laser beams highly coherent. The laser's collimation angle depends on the diameter D of the exit pupil as $\theta = \frac{\lambda}{D}$. The coherence, monochromatic, and collimation make lasers good optical sources for precise imaging [57]. The sharply peaked optical spectrum makes lasers good optical sources for fluorescence microscopy. The difference between the laser light and the output photons from the emission spectrum could be juxtaposed due to the Stokes shift of the particles of interest [67]. A fluorescence microscope could be implemented in an OET to create distinguished imaging [8].

2.5.4. Optical components

Besides light sources and lenses, there are more necessary optical elements in an OET setup. For precise control of the focal point and the region of interest (RoI), we can use a (motorized) stage. The patterning illumination and the particles of interest must be visible simultaneously. Therefore, the light must return to a camera from the microfluidic chip. We can use a beam splitter to split the light path. For fluorescence microscopes, dichroic beam splitters can filter out the emitted photons from the laser photons. Optical elements can be put on (motorized) stages to align and calibrate them properly. Movable mirrors can align or redirect the light path when necessary. We can use a digital micromirror device (DMD) to create the patterns used for control. A DMD consists of multiple small mirrors that can switch to two different sides, as shown in Figure 2.20. For example, when a circle of mirrors in the center of the DMD is switched on, and all other mirrors are switched off, and light at a certain angle illuminates the DMD, the circular pattern and the rest of the DMD will be directed differently. This principle is shown in Figure 2.21.

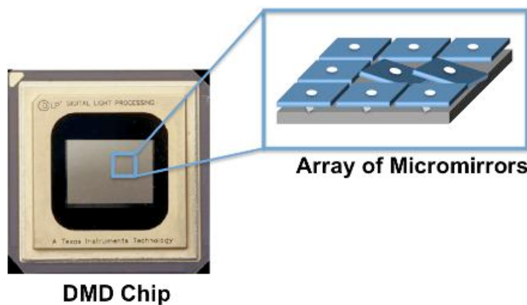

Figure 2.20: A digital micromirror device with a part of the array schematically shown [68].

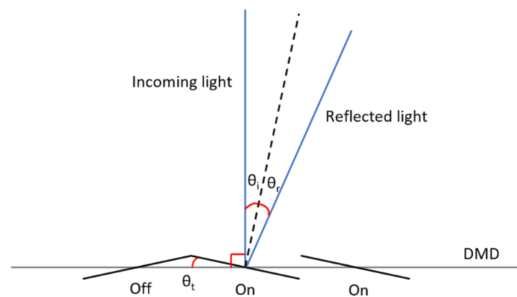

Figure 2.21: A schematic depiction of a DMD showing the on and off state. Light reflects on the DMD with $2\theta_t$ in the on state and with $-2\theta_t$ in the off state [69].

Because the DMD is a grating pattern of small square mirrors, the light gets diffracted as well as reflected. Using a highly collimated monochromatic light source could result in a diffraction pattern that could be undesired [70]. Besides the diffraction, this also decreases the amount of photons reflected due to the gaps between the mirrors. This results in an overall efficiency of the DMD that needs to be considered. The created pattern and the moving particles of interest need to be imaged using a camera if we want to be able to see and control them. The light from the objective has to return and be magnified using a lens to use as much of the camera's sensor as possible. The size of the camera sensor and the number of pixels, respectively, influence the field of view (FoV) and the resolution of the OET setup. The FoV is defined by the size of the sides[5] x of the sensor and the magnification M of the 4f-system between the chip and the camera.

$$FoV = \frac{x}{M} \tag{2.48}$$

Another important characteristic of the camera is the framerate. This is the speed at which images are updated. If, e.g., the movement of the beads oscillates with a frequency of 1 Hz and the camera's framerate is 2 Hz, the camera's image output does not seem to be moving. Therefore, if every movement needs to be captured well using the camera, a framerate should be chosen at least the Nyquist frequency, which is two times the highest frequency of movement that needs to be captured [71].

2.6. Instrumentation

To create the OET setup, we need to use a precise sputtering machine to create a conductive layer of ITO on a microscope glass. The photoconductive layer can be deposited using a Plasma Enhanced Chemical Vapor Deposition machine (PECVD). This machine uses plasma to precisely deposit a thin film of the wanted photoconductive layer [72]. To create a complex dielectric particle, we can use the Nanoscribe [73]. This lithography device uses two-photon polarization (2PP), where a precise laser hardens illuminated parts in a layer of photoresist. This principle is similar to 3D printing in that it builds up the structure in layers. Polystyrene beads with extremely precise sizes can be used for calibration and benchmarking of the OET and are readily available from specialized manufacturers.

2.6.1. Applied signal

The system's applied signals are the electrical and optical signals. A signal generator can create a specifically shaped oscillating electrical signal that induces the DEP force. An oscilloscope can measure this signal to measure the input voltage. The input voltage can be amplified using a waveform amplifier to create a stronger electrical field inside the microfluidic chip. To control the DMD, we must send a signal with a certain frequency using a computer. This signal can be created and sent using Python or MATLAB.

[5]The sides of the sensor are not always square, which means that the FoV is defined by both the sidelength and the side-width.

3 Methods

In the previous chapter, we explored the theoretical framework and key design considerations for constructing an OET system with maximum effectiveness. Since the OET is being developed from the ground up, all relevant factors must be carefully integrated into the system design. This chapter outlines the experimental approach taken to translate theory into practice. It describes the design process in detail and explains how the system's performance was evaluated.

By benchmarking the OET's capabilities, we not only validate the design choices but also gain a deeper understanding of the physical mechanisms governing the system. Given that an OET setup consists of multiple interconnected components, this experimental section is structured to reflect its modular nature. Specifically, the chapter is divided into three main parts: the microfluidic chip, the optical setup, and the dielectric particle. Each section provides both practical implementation details and explains how we can benchmark the designed parts against the literature.

This work also benefited from contributions by three bachelor students who carried out their Bachelor's End Projects (BEP) on subtopics related to this thesis. Dion Jetulahi contributed to the design and testing of the microfluidic chip [74], Mirthe Folkerts focused on the characterization of the photoconductive layer [75], and Rens van Elk worked on the development of the optical setup [69].

3.1. Design of the microfluidic chip

3.1.1. Dimensionality

When designing the microfluidic chip for the OET, the first step is determining its dimensionality. As discussed, the chip must meet specific criteria, such as accommodating the dielectric particles and allowing for effective imaging. To minimize boundary effects and prevent particle blockage within the channel, its length and width are set to be at least ten times the size of the dielectric particles. Different designs have been tried for the microfluidic chip, iterating towards a final design. The first iteration is shown schematically in Figure 3.1.a where the channel was designed for a small ITO microscope cover glass. The area of the channel is 12 mm × 5 mm $= 60$ mm^2. The two 2 mm diameter holes are included to add inlets for the microfluidic chip. These holes decrease the effective area of the parallel plate capacitor. To increase the effective area, the channel was laid diagonally with respect to the ITO-covered microscope slide, resulting in an area of 20 mm × 5 mm $= 100$ mm^2. This design is shown in 3.1.b. The final design using the 22 mm × 26 mm ITO cover glasses is shown in Figure 3.1.c. This iteration removed the inlet holes to increase the effective area to 26 mm × 12 mm $= 312$ mm^2. The sides of the channel that are not covered by tape are closed off by two-component epoxy glue. To get dielectric particles inside the chip, they need to be added before closing the chip off using the glue.

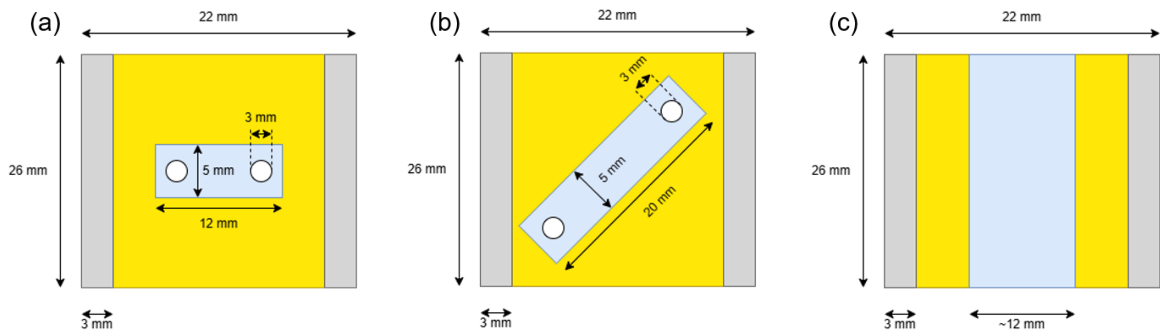

Figure 3.1: Different iterations for the design of the microfluidic chip. Yellow shows the double-sided tape, gray shows the silver contact strips of the ITO-covered glass, blue shows where the microfluidic channel is positioned, and white denotes the inlets for the channel. In (a), the first design was made to have a microfluidic channel fit on an ITO-coated microscope cover glass. (b) depicts a design of the microfluidic channel with an increased channel area. (c) shows the third design of the microfluidic channel without inlets to test if another design can increase the robustness.

When using bigger ITO microscope coverslips, with dimensions 26 mm$\times 40$ mm, there is more room to create bigger and more robust microfluidic channels. Therefore, a fourth iteration for the microfluidic chip was created and is shown in Figure 3.2.a. The increased area is 30 mm $\times$ 9 mm $= 180$ mm^2. Figure 3.2.b shows a cross-sectional view of the microfluidic chip. The height of the microfluidic chip is created by double-sided yellow tape with a height of 90 μm. This means that, for the final iteration, the channel of the microfluidic chip can contain 30 mm$\times 9$ mm$\times 90$ μm $= 24.3$ nL of the dielectric medium.

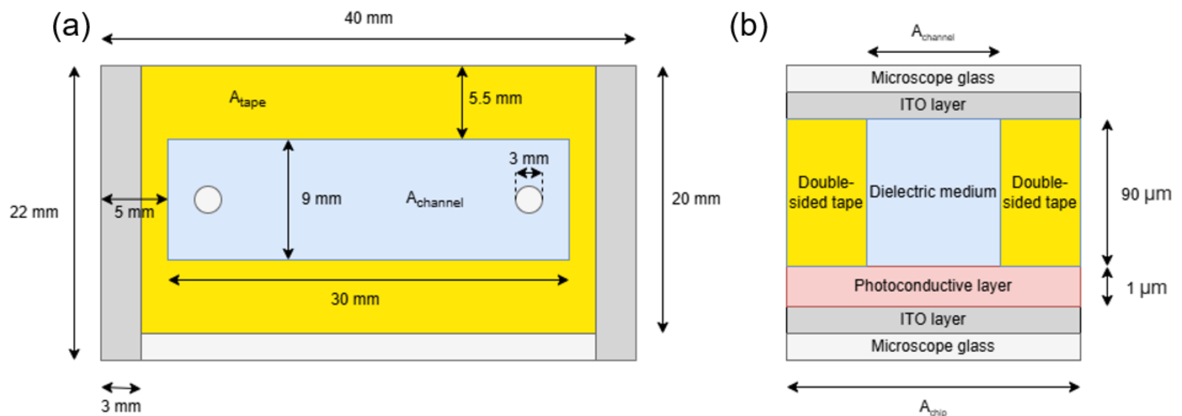

Figure 3.2: Schematic dimensionalities of the microfluidic chip. (a) shows the fourth and final iteration using the bigger ITO-covered microscope slides. (b) depicts a cross-sectional view of the microfluidic channel, which is true for all iterations that include the ITO-covered glasses and the photoconductive layer.

Figure 3.3 shows the realized iterations before the final design. In Figure 3.3.a, an initial chip was created on a normal microscope slide with a normal microscope coverslip to test the microfluidic channel before working with the more expensive ITO-coated glasses. The inlets of this microfluidic chip are created by cutting pipetting tips such that one side has a flat surface, and one side can be attached to a syringe pump. The inlets are glued on the microfluidic chips using two-component epoxy glue. This chip follows the design from Figure 3.1.a. The design from Figure 3.1.b is implemented in Figure 3.3.b, 3.3.c, 3.3.d, and in Figure 3.3.e.

In Figure 3.3.c, a third chip was created to make a microfluidic chip using two ITO-coated coverslips with No 1.5 thickness, i.e., 170 μm, without the photoconductive layer to avoid spilling useful coated chips. After this was successful, a fourth chip iteration was created, as shown in Figure 3.3.d. These chips were operational for OET, although very fragile. When putting just a bit too much pressure while attaching conductive wires to the electrodes on the chips, the chips often break, making them useless for OET purposes. Therefore, a new design was tried using ITO-covered microscope slides that were 1.1 mm thick to increase the robustness of the microfluidic chip. This design is shown in Figure 3.3.e. Iteration 3 from Figure 3.1.c without the inlets are shown in Figure 3.3.e.

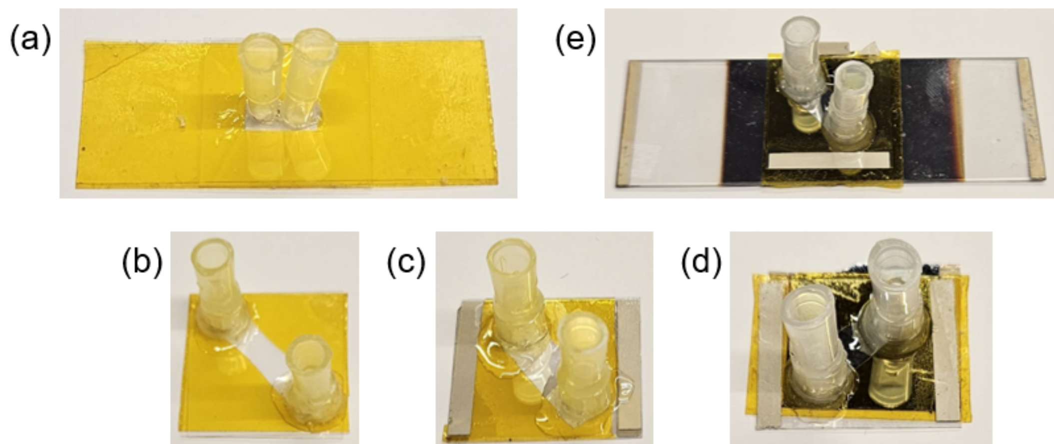

Figure 3.3: Different iterations for the design of the microfluidic chip. (a) shows the microfluidic chip without ITO-covered glass with the parallel channel design from Figure 3.1.a. (b) shows the second channel design from 3.1.b without the ITO-covered glass. (c) is the third realization with ITO-covered glass. (d) shows the first operational OET chip with the ITO-covered glass and the photoconductive layer. (e) shows the operational OET chip with a more robust bottom ITO glass.

The design from Figure 3.1.c is realized in Figure 3.4.a. Figure 3.4.b shows the final chip design. The chip is placed in a specialized chip holder to connect two wires to the microfluidic chip.

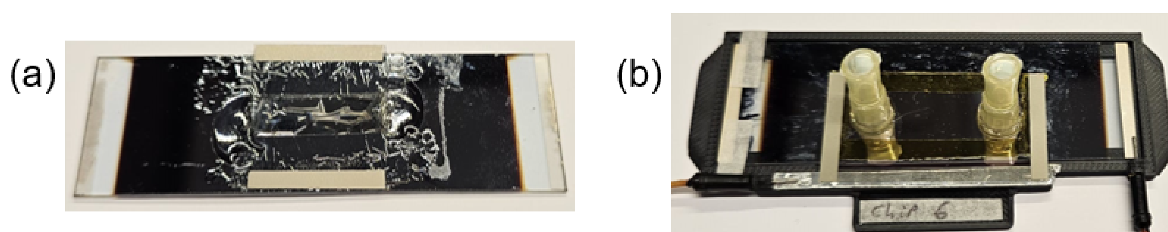

Figure 3.4: The final realizations of the microfluidic chip. (a) shows the chip from the design shown in Figure 3.1.c. The final design of the microfluidic chip with a 3D-printed chip holder is shown in (b). This chips fits the design from Figure 3.2.a.

3.1.2. Transmitting electrodes

As already mentioned, the transmittive electrodes are created by covering microscope glass with ITO. As shown in Figure 2.4 and Figure 2.5, the resistance and the transmittance seem to depend on the thickness of the ITO layer. Ideally, we want glass that transmits as much as possible to let as much light through as possible to create the virtual electrodes in the photoconductive layer. On the other hand, we want a resistance that is as low as possible to have the electrical field in the chip be as strong as possible. This can be derived from equation 2.17. When R_{ITO} is small, the part in the denominator becomes smaller, making the E larger. Therefore, we want to find a tradeoff between the ITO glasses' resistance and transmittance.

We will use the ITO glasses from Diamond Coatings Ltd, which specializes in transparent electrodes. They sell ITO glass with resistances of 8-12 Ohms, 15-30 Ohms, and 70-100 Ohms. The transmittance of all three types of different resistances was measured using the setup shown schematically in Figure 3.5 and pictured in Figure 3.6. When assuming no absorption of the ITO glass, the resulting reflectance is given by $I_r = I_0 - I_t$. We can find the ITO glass from Diamond Coating Ltd that is most suitable for the OET microfluidic chip by trying different wavelengths.

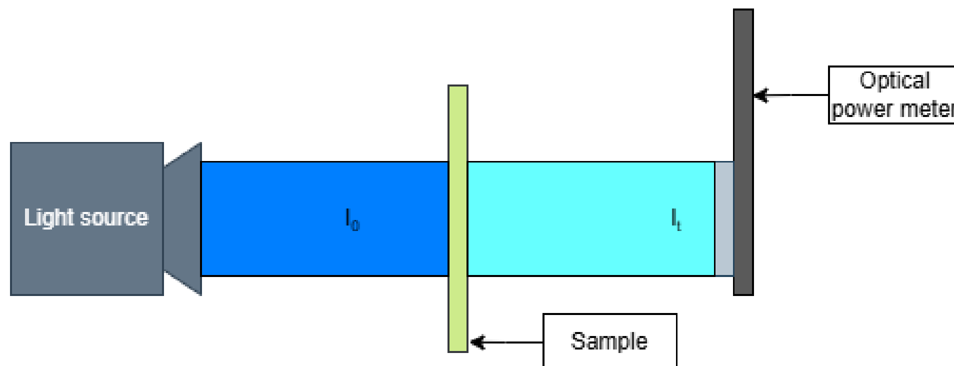

Figure 3.5: A schematic depiction of an experimental setup to measure the transmittance of a sample using a light source with a certain frequency. The initial optical intensity from the light source I_0 partially passes through the sample, resulting in the transmitted intensity I_t. The intensity can be measured using an optical power meter.

The LED light source was collimated as well as possible using an AC254-035-A-ML Thorlabs lens with a focal length of 35 mm. This light beam was demagnified using an AC254-200-A-ML Thorlabs lens with a focal length of 200 mm and an RMS4X Olympus objective with a focal length of 45 mm. This results in a theoretical magnification of $M = -\frac{45}{200} \approx -0.225$. The intensity of the light was measured by a PM130D Thorlabs optical power meter. By putting the sensor first in front of the sample and then just after the sample, we can find how much light is transmitted through the ITO glass sample. Three different light sources were used in this experiment. The blue LED M470L3-C1 from Thorlabs with a nominal wavelength of 470 nm, a red laser CPS635R from Thorlabs with a nominal wavelength of 635 nm, and a candescent light source QTH10/M from Thorlabs was used in combination with a 2 inch Red Optical Cast Plastic Filter from Edmund Optics, resulting in an expected wavelength of 700 nm. The true wavelengths of the light sources are verified using a CCS200/M Thorlabs compact spectrometer.

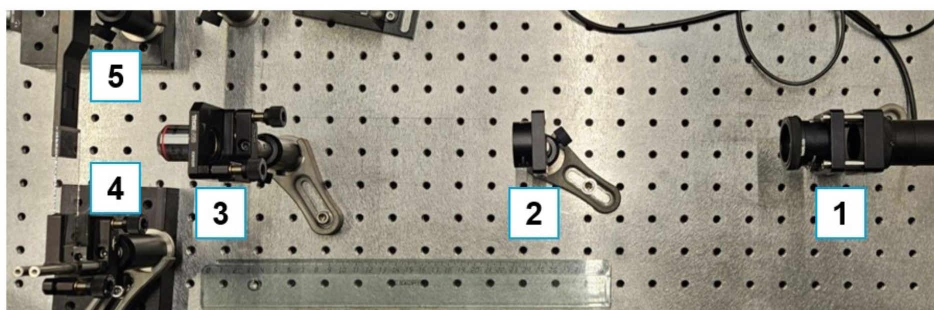

Figure 3.6: A top view of the experimental setup to measure the transmittance and reflectance of different ITO glasses. (1) shows the LED, (2) and (3) show lenses to create a demagnified illumination spot on the optical power meter. (4) is the sample in the sample holder, and (5) is the optical power meter.

To measure the resistance of the ITO glasses, a TENMA 72-7780 multimeter was used. To create a clean microfluidic chip, we must ensure the ITO glasses we want to use are clean. This can be done by rinsing the glass carefully with acetone and isopropanol. Using a SHE-UT8031-EUK ultrasonic cleaner at 40 kHz for 3 minutes after each rinsing process has also been tested, but, in some cases, this resulted in a broken chip or partially removed ITO layer. Therefore, most glasses used were carefully taken out of the package with gloves to avoid making them dirty in the first place.

3.1.3. Photoconductive layer

To create virtual electrodes in the OET microfluidic chip, we must put a photoconductive layer on one of the ITO-covered glasses. Because the DEP force is the strongest close to the virtual electrodes, and because the particles sink to the bottom of the chip due to gravity, we decided to place the photoconductive layer on the bottom of the microfluidic chip. The material chosen for the photoconductive layer is hydrogenated amorphous silicon, a-Si:H, which has been deposited at the Else Kooi Laboratory at the TU Delft. This was done using a PECVD with the substrate temperature at 180 °C, the process pressure at 0.7 mbar, and an RF source at 13.56 MHz with a power density of 20 mW/cm^2. The PECVD was done with no dilution of the gas flow. The deposited photoconductive layer is 1 μm thick, which takes 100 minutes to deposit using the PECVD. The absorbed light inside the a-Si:H creates free electrons, resulting in a certain photoconductivity.

To select the light source for the OET setup, we must know which light is absorbed best to create the strongest virtual electrodes. To calculate the absorption of the photoconductive layer, we use an experimental setup as shown in Figure 3.7. This setup is similar to the setup from Figure 3.5, however, the main difference is the 50/50 beam splitter before the sample. The light reflected from the ITO glass and the a-Si:H returns to the beam splitter, after which 50% is sent to the second optical power meter. This way, the reflected intensity and the transmitted intensity can be measured. Using these intensities, we can derive the absorbed intensity as $I_a = I_0 - I_t - I_r$. Using the Lambert-Beer law from equation 2.20.

$$\begin{aligned} I_a = I_0 - I_t - I_r &= I_{0,a} e^{-\alpha(\lambda)x} \\ &= (I_0 - I_{r,ITO}) e^{-\alpha(\lambda)x} \\ \alpha(\lambda) &= \frac{-1}{x} \ln\left(\frac{I_0 - I_t - I_r}{I_0 - I_{r,ITO}}\right) \end{aligned} \tag{3.1}$$

The thickness x is 1 μm. The transmitted intensity of the ITO glass $I_{r,ITO}$ is experimentally derived from the experiment in Figure 3.5.

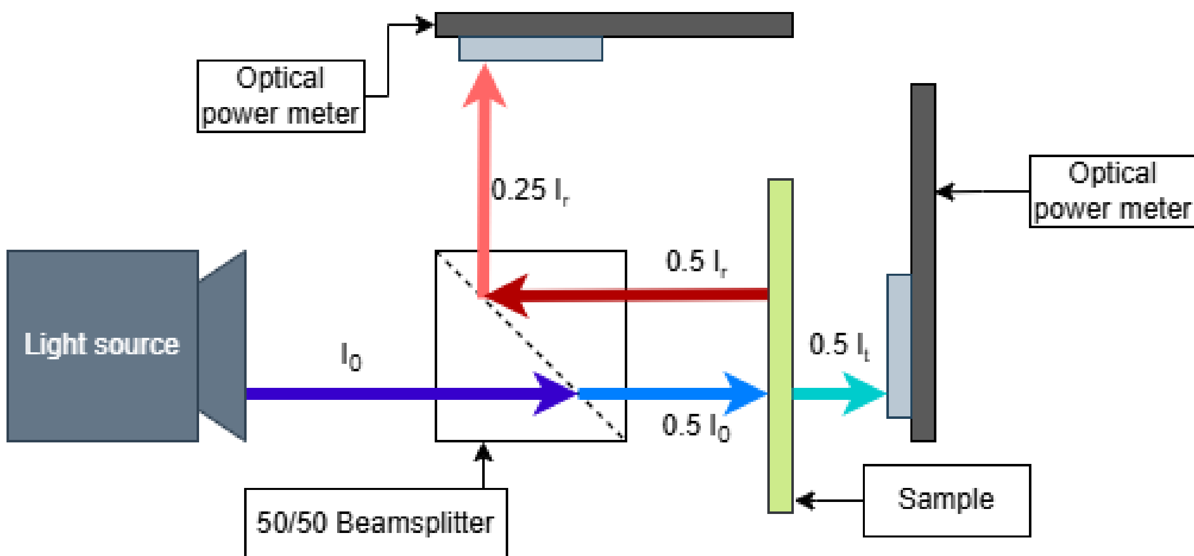

Figure 3.7: A schematic depiction of an experimental setup to measure the transmittance and reflectance of a sample using a light source with a certain frequency. The initial optical intensity from the light source I_0 is decreased by 50% due to the 50-50 beamsplitter. The remaining intensity partially passes through the sample, resulting in the transmitted intensity I_t, depicted in robin's egg blue, and the reflected intensity I_r, depicted in dark red. Both intensities can be measured using an optical power meter. The fractions displayed in the light beams are due to passing the beam splitter.

The realization of the experimental setup described in Figure 3.7 is shown in Figure 3.8. Because there was only one optical power meter, the transmitted and reflected intensities were measured separately. The 50/50 beam splitter is a CCM1-BS013/M from Thorlabs. The sample consists of a single ITO glass with a 1 μm layer of a-Si:H. The glass side is pointed towards the light source so that the reflected light does not traverse the a-Si:H twice. The rest of the setup uses the same components as in the experiment of Figure 3.5.

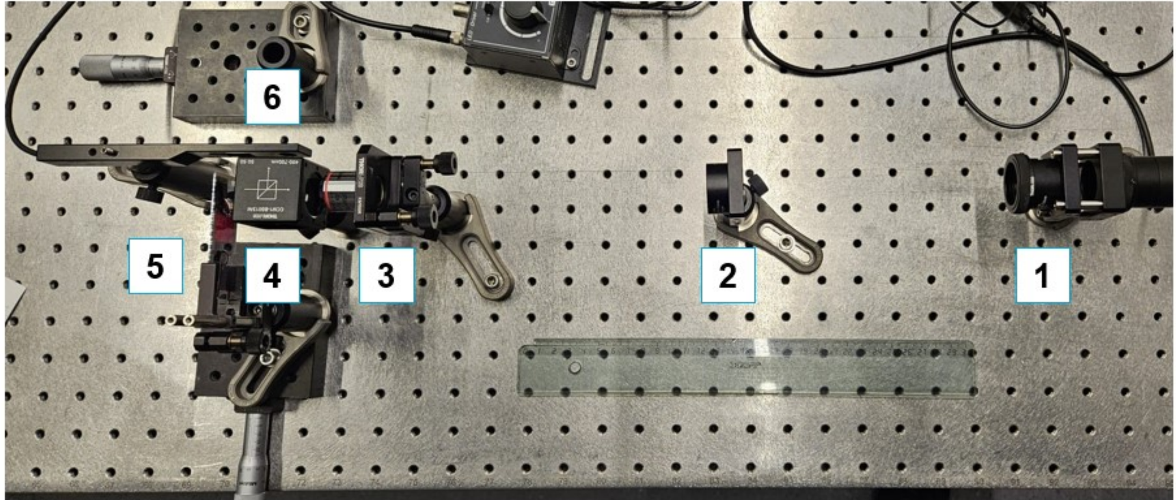

Figure 3.8: A top view of the experimental setup to measure the absorption of the photoconductive a-Si:H layer. (1) shows the LED whose illumination is demagnified using the lenses in (2) and (3). The beamsplitter is shown by (4). The sample is located at (5), and the optical power meter measures the light at (6).

3.1.4. Electrical properties

The dielectric medium inside the microfluidic chip determines the DEP force directly by its real permittivity and contributes to the CM-factor with its complex permittivity, as can be seen in equation 2.13. The dielectric medium can also determine how well the particles move due to Stokes' law from equation 2.31. As already described in section 2.2.1, deionized water is often used as the dielectric medium. We use deionized water from an Ultra Puur Water LWTN Genie Purist type 1 machine from Laboratorium Water Technologie Nederland with a resistivity of 18.2 MOhm-m and a relative permittivity of 78.

The particle adhesion in the microfluidic chip can be reduced by adding a layer of PEG on the a-Si:H. This is what we will try as well. Another way to reduce the adhesion is by adding a percentage of Tween-20 to the dielectric medium, which is also a type of PEG. The conductivity of pure Tween-20 is 50 μS/cm [76]. We will measure the conductivity of the microfluidic medium by measuring the resistance over a certain distance and comparing it to the known conductivity of deionized water. The resistivity is given by the resistance times the cross-sectional area divided by the distance between the probes, making it have the unit Ohm-m. However, due to the fact that electric current will move from one probe to the other, traversing the full volume of the liquid, estimating the correct cross-sectional area is difficult. Therefore, because we know the true conductivity, calculated by the Ultra Puur Water LWTN Genie Purist type 1 [77], we can find a factor F at a certain distance between the wires in the fluid, such that we can relate the measured resistance of the fluid to the known resistivity of the deionized water. The conductivity is the inverse of the resistivity. The resistance was measured by the Keysight 34465A 6.5 Digit Multimeter Truevolt.

$$\begin{aligned} R_{H2O,measured} &= F\rho_{H2O,true} \\ \rho_{medium,true} &= \frac{R_{medium,measured}}{F} = \frac{R_{medium,measured}}{R_{H2O,measured}}\rho_{H2O,true} \end{aligned} \tag{3.2}$$

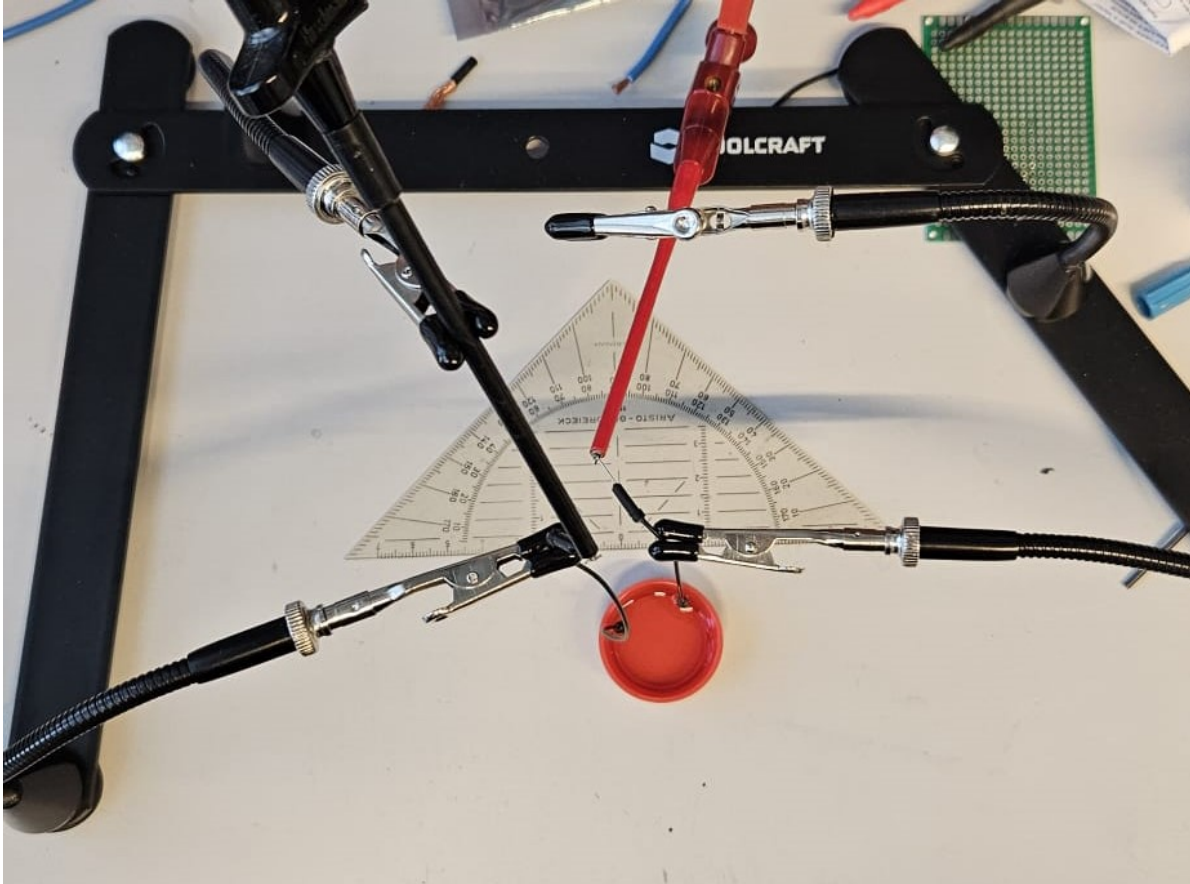

Figure 3.9: An experimental setup to measure the relative conductivity of a fluid.

The permittivity of the medium determines the strength of the electrical field in the capacitance, as can be seen in equation 2.17. The capacitance of the chip is determined by the mixture of dielectric material, such as the tape and the photoconductive layer [78]. The permittivity of the tape, the photoconductive layer, the medium, and all dimensions give the capacitance of the fully combined chip.

$$
\begin{aligned}
\frac{1}{C_{full}} &= \frac{1}{C_{pl}} + \frac{1}{C_{tape} + C_{medium}} \\
C_{pl} &= \epsilon_{pl}\epsilon_0 \frac{A_{chip}}{d_{pl}} \\
C_{tape} &= \epsilon_{tape}\epsilon_0 \frac{A_{chip} - A_{channel}}{d_{tape}} \\
C_{medium} &= \epsilon_{medium}\epsilon_0 \frac{A_{channel} - 2A_{hole}}{d_{tape}}
\end{aligned}
\tag{3.3}
$$

The area of the full chip is given by $A_{chip} = 40$ mm × 20 mm $= 8 * 10^{-4}$ m^2. The area of the channel is given by $A_{channel} = 30$ mm × 9 mm $= 27 * 10^{-5}$ m^2. The area of the tape is given by $A_{tape} = A_{chip} - A_{channel} = 8 * 10^{-4}$ m^2 $- 27 * 10^{-5}$ m^2 $= 53 * 10^{-5}$ m^2. The area of the medium is given by $A_{medium} = A_{channel} - 2A_{hole} = 27 * 10^{-5}$ m^2 $- 2\pi * (1.5$ mm$)^2 = 25.59 * 10^{-5}$ m^2. The relative permittivities of the photoconductive layer, the tape, and the medium are respectively given by ϵ_{pl}, ϵ_{tape}, and ϵ_{medium}. The permittivity of a vacuum is given by $\epsilon_0 = 8.854 * 10^{-12}$ F/m. The thickness of the photoconductive layer and the tape are given as $d_{pl} = 1$ μm and $d_{tape} = 90$ μm.

To find the capacitance of the double-sided tape, we made two chips from 2 ITO-covered microscope coverglasses sandwiching a layer of tape. The relative permittivity of the tape is given as $\epsilon_{tape} = \frac{A_{measured}\epsilon_0}{d_{tape}C_{measured}}$. The area can be more exactly calculated using ImageJ [79]. The capacitance can be measured using the same Keysight 34465A 6.5 Digit Multimeter Truevolt as was used for measuring the resistance of the fluid. The multimeter calculates the capacitance by measuring the change in voltage (DV) that occurs over a short time. It measures the change in voltage at two different times, and then fits an exponential to calculate the capacitance. Therefore, the capacitance is measured independently of frequency [80]. Using the found relative permittivity of the double-sided tape, the relative permittivity of the photoconductive layer can be measured using a chip with 2 ITO coverglasses sandwiching a photoconductive layer and a layer of tape. The relative permittivity of the photoconductive layer is given as $\epsilon_{pl} = d_{pl}\left(\frac{\epsilon_0 A_{measured}}{C_{measured}} - \frac{d_{tape}}{\epsilon_{tape}}\right)^{-1}$. The expected relative permittivities are 78 for the deionized water and for the mix of deionized water and Tween-20, between 2.8 and 4.5 for the double sided tape and between 11 and 12 for a-Si:H [81].

When using different materials, we need to account for electrolysis in the chip. Therefore, we need to find the upper and lower limits of frequencies at certain voltages for different chips to establish a safe frequency window with varying types of dielectric media. This can be done by finding the threshold frequency at which bubbles start to form at different applied voltages.

3.1.5. Robust design

To ensure the constant realization and robustness of the microfluidic chip, we created some 3D printed tools to help out with the fabrication process. These tools also went through multiple optimization iterations. One of the problems in fabricating the OET chip was applying the wires to the contact strips on the ITO glass. When trying to tape it on, the pressure applied cracked the glass, or when not enough pressure was applied, the wires did not stick. Silver glue 9410 from MG Chemical was used to try to get the wires to stick to the contact strips. It was not possible to harden the glue since it requires curing at high temperatures (≥ 90°C) which would have damaged the chip [82]. An easy solution was found in the chip holder, of which the 3D model is shown in Figure 3.10.

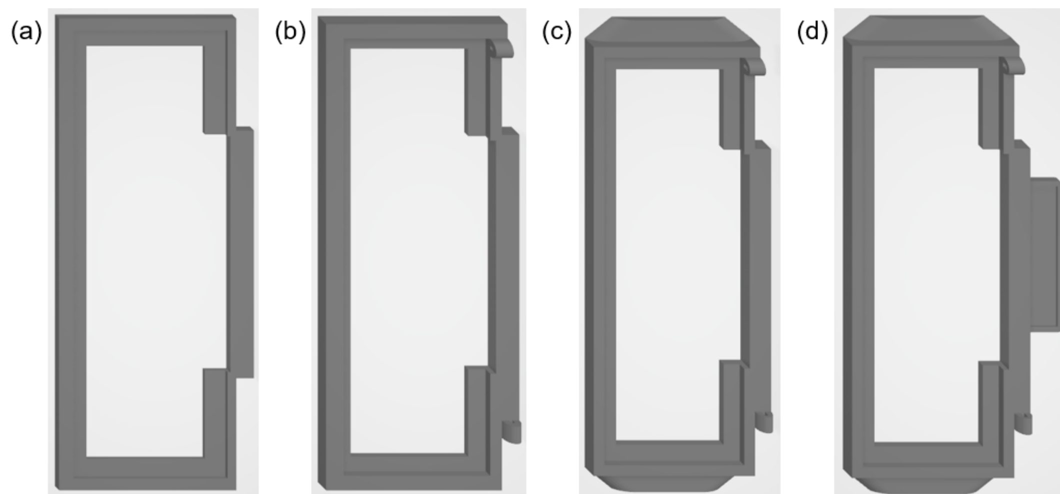

Figure 3.10: Four iterations of the chip holder for fabricating constant spaced chips. (a) shows version 1 of the iteration, which was used to test the dimensions of the chip. (b) shows iteration 4 of the chip holder. It includes a deeper cut for the microfluidic chip to be positioned in. The small cavities on the top right and bottom right are for electronic wires to be applied. (c) shows iteration 5 of the chip holder with small grips for eventual storage possibilities. (d) shows the final chip holder design, including a small space to put on a label.

Version 1, shown in Figure 3.10.a was created to get a good grasp of the initial dimensions. The rectangular piece on the right is covered by conductive tape on which the top ITO glass electrode lies. The next three versions added a deeper slot for the chip to lie in and added two wire holders to attach electrical components to the microfluidic chip safely. Versions 2,3, and 4 look very similar but differ in the depth of the chip hole. This was done to fine-tune the height at which the top glass electrodes lie on the chip holder. Version 4 is shown in Figure 3.10.b. A new version was designed to create the possibility of storing the chips. This version 5 can be seen in Figure 3.10.c. The final version, version 6, of the chip holder adds a small patch to put on a label. This way, the chips can be distinguished from each other. The final version is shown in Figure 3.10.d.

Cutting the double-sided tape is not easy. We cannot cut the tape directly on the roll, for it can cut through other layers of tape as well. A solution to cut the microfluidic chip is to stretch the double-sided tape and cut the channel in the air. This resulted in many differently shaped and many non-functional microfluidic channels. To make a more robust channel design, we created a 3D printed OET ”cookie-cutter”. A piece of double-sided tape can be applied to this template. Using a sharp knife, the hole in the template can be outlined to cut out a consistent channel. This channel cutter is shown in Figure 3.11. The second version of this cutter is shown in Figure 3.11.c and differs from the first version by decreasing the surface area of the tape and by making it possible to cut over the small patches between the outer ring and the inner piece.

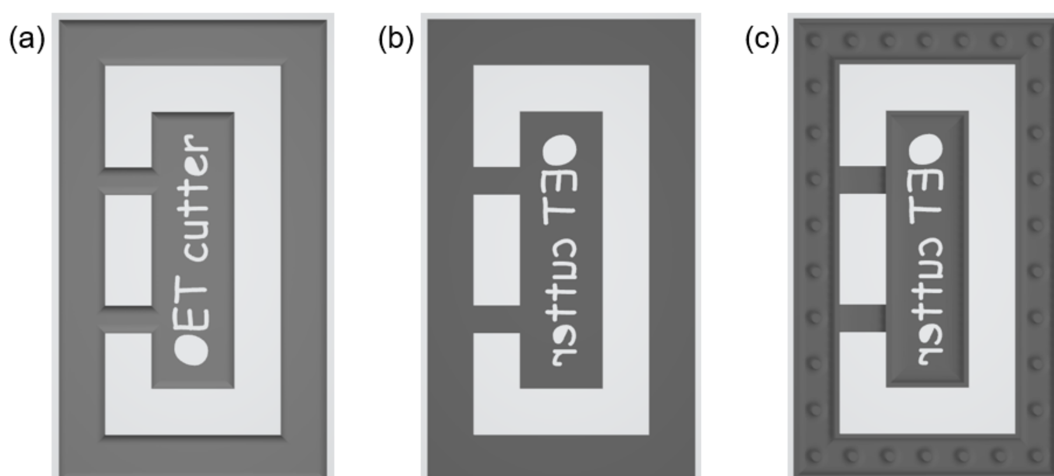

Figure 3.11: Two iterations of the channel cutter for cutting constantly sized microfluidic chambers. (a) shows the front view of both iterations. (b) shows the back side of the first iteration, which has a flat surface. (c) shows the back side of the second iteration, which has less surface area to make the tape easier to remove.

To make sure each chip fits well in the chip holder, we need to make sure that the channel in each chip is aligned properly. This is done by a 3D printed alignment tool [1], as shown in Figure 3.12. This alignment tool fits over the big microscope slide and leaves a hole the same size as the cut-out double-sided tape. The second version, shown in Figure 3.12.b adds the possibility to also align the ITO coverglass by removing the middle lower part. The diagonal lines are added to compensate for the loss in strength.

[1] There is no spelling check in SolidWorks.

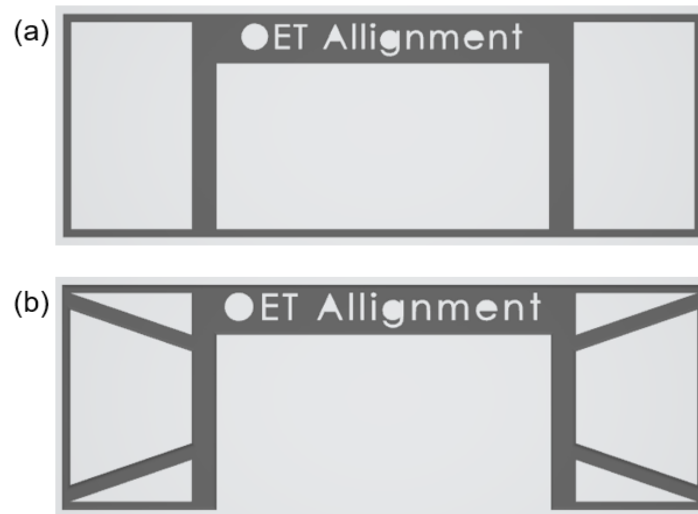

Figure 3.12: Two iterations of the alignment tool. (a) shows the front view of the initial design. (b) shows the front view of the second iteration, which makes it possible to be left on the big ITO microscope slide when putting on the ITO coverglass.

The 3D parts were designed in SolidWorks and 3D printed with PLA using a Bambu lab X1-Carbon 3D printer. The 3D printed versions of the chip holder are shown in Figure 3.13. The 3D printed versions of the channel cutter are shown in Figure 3.14. The 3D printed versions of the alignment tool are shown in Figure 3.15.

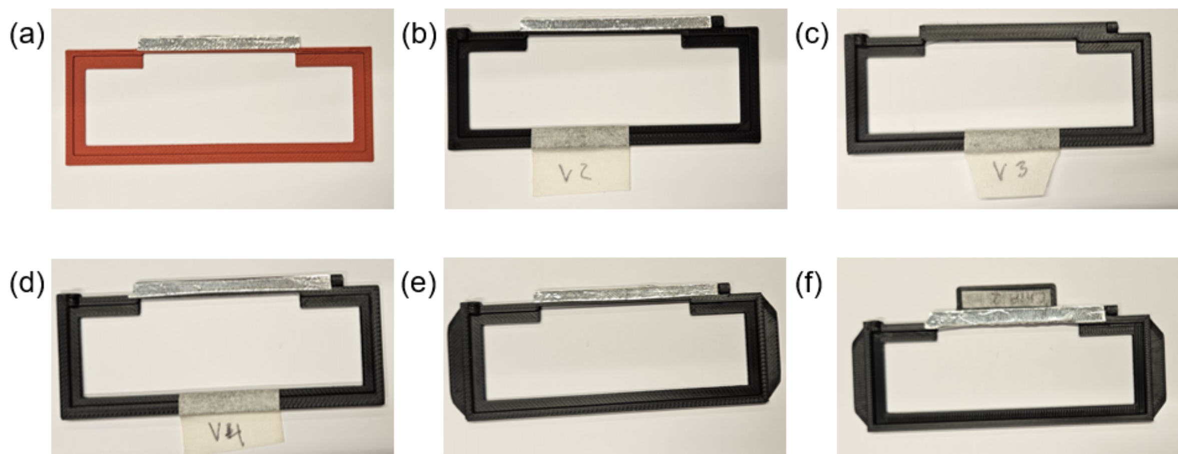

Figure 3.13: The 3D printed chip holders. Each design fits a 25mm by 75mm ITO microscope slide inside. (a) shows version 1. (b) shows version 2. (c) shows version 3. (d) shows version 4. (e) shows version 5. (f) shows version 6.

Figure 3.14: The 3D printed channel cutters. (a) shows the front side of version 1. (b) shows the back side of version 1. (c) shows the back side of version 2.

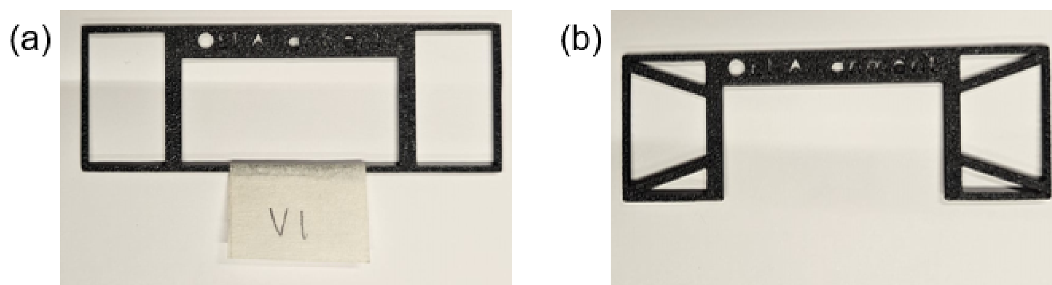

Figure 3.15: The 3D printed alignment tools that fit a 25mm by 75mm ITO microscope slide. (a) shows version 1. (b) shows version 2.

To assemble a full OET chip, the ITO glasses first need to be cleaned properly. After this, the a-Si:H layer has to be deposited on the ITO microscope slide using the PECVD machine. Using the 3D printed channel cutter, a channel must be cut from the double-sided tape. This channel must be applied to the photoconductive layer using the 3D printed alignment tool. The ITO coverglass with the laser cut holes needs to be put on this tape with its silver contact strips facing the photoconductive layer. On the holes, the small pipette inlets need to be carefully glued on using the two-component epoxy glue. Be careful not to get glue inside the microfluidic chip. After hardening, the microfluidic chip can be placed into the 3D printed chip holder. A small piece of conductive tape needs to be applied to this chip holder so that it touches the contact strips of the ITO coverglass. Two wires need to be put inside the holes of the chip holder such that one wire touches the conductive tape and one wire touches the contact strip of the big ITO microscope slide. The fully assembled chip can be seen in Figure 3.4.b.

3.2. Design of the optical setup

The optical setup had multiple iterations before the final design, just as the microfluidic chip did. The optical setup was first created to try to incorporate a DMD in a simple microscope. This setup is shown schematically in Figure 3.16. The light from the LED is collimated using lens L1 before it illuminates the DMD. The mirrors that are selected to be in the on-state reflect the image through lens L2. Two mirrors, M1 and M2, move the light path up such that the microfluidic chip can be illuminated from above. The light is partly reflected due to the beamsplitter BS. The objective collimates the light, demagnifies the light, and illuminates the microfluidic chip due to the 4f-system of L2 and the objective. The light returns from the microfluidic chip to the objective, which is then partly passed through the beamsplitter BS. The transmitted light is collimated by lens L3, which magnifies the light and illuminates the camera sensor.

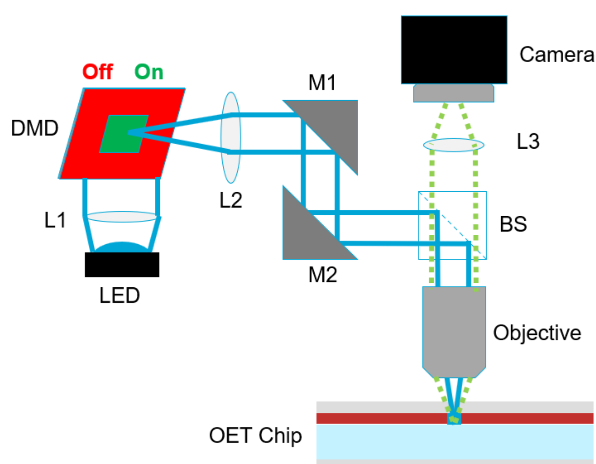

Figure 3.16: The first iteration of the optical setup design. The light originates from the LED and is collimated by lens L1. After the DMD partly reflects it, it passes through lens L2, two mirrors M1 and M2, a beamsplitter BS, and through the objective on the OET chip. After illumination, it returns inside the objective and the beamsplitter to enter lens L3 to image in the sensor of the camera.

The second iteration illuminates the chip from below and is shown in Figure 3.17. The light passes lens L2 similarly to the setup from Figure 3.16. The light is directly reflected by the beamsplitter BS and illuminated on the microfluidic chip using the objective. In the imaging path, the light passes the objective, the beamsplitter BS, the mirror M1, and the lens L3 before illuminating the camera sensor. This iteration removed one optical element, making it more efficient. This improved iteration also includes a manual moving stage for the chipholder to get particles in focus.

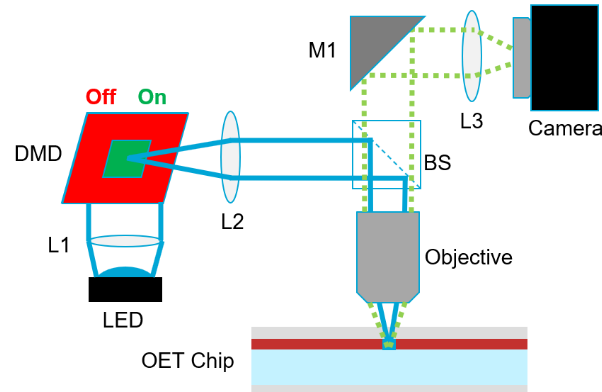

Figure 3.17: The second iteration of the optical setup design. The light originates from the LED and is collimated by lens L1. After the DMD partly reflects it, it passes through lens L2, a beamsplitter BS, and through the objective on the OET chip. After illumination, it returns inside the objective, and the beamsplitter is reflected by mirror M1 to enter lens L3 to image in the sensor of the camera.

The third iteration, as shown in Figure 3.18, adds a lamp for imaging the microfluidic chip and a filter before the camera to decrease the intensity on the sensor to avoid saturation. In the previous iterations, the only sources of light on the chip were the illuminated pattern from the LED and the environmental light. The second was found to be weak compared to the illuminated pattern, making it hard to image the particles in the microfluidic chip. Therefore, the third iteration incorporates a lamp above the microfluidic chip and a neutral density filter before the camera.

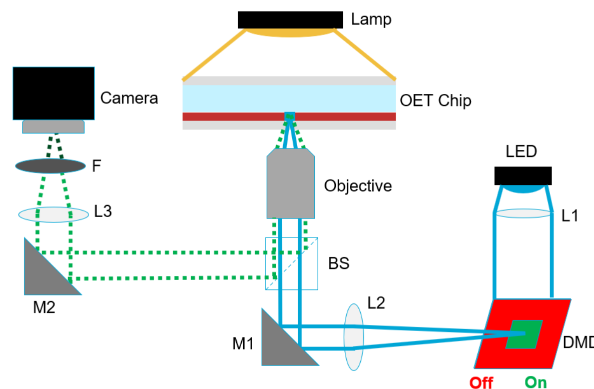

Figure 3.18: The third iteration of the optical setup design. The light originates from the LED and is collimated by lens L1. After the DMD partly reflects it, it passes through lens L2, a mirror M1, a beamsplitter BS, and through the objective on the OET chip. After illumination, it returns inside the objective together with light from the lamp to pass the beamsplitter and be reflected by mirror M2 to enter lens L3 to image in the sensor of the camera after being filtered by neutral density filter F.

Because the lamp has a broad spectrum, unwanted virtual electrodes could be created in the photoconductive layer. The photoconductive layer increases in photoconductivity more towards the UV wavelengths than the IR wavelengths. The unwanted virtual electrodes can therefore be avoided by making the lamp have a spectrum with a cut-off at higher energies than red light, which is done by putting a red filter on the lamp. The ND filter was removed to capture clearer images. These changes are incorporated in the fourth iteration, as shown in Figure 3.19.

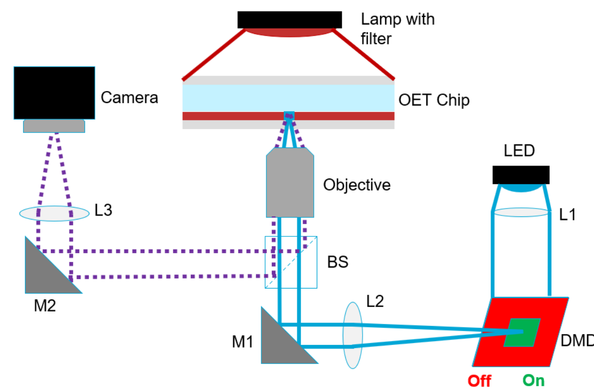

Figure 3.19: The fourth iteration of the optical setup design. The light originates from the LED and is collimated by lens L1. After the DMD partly reflects it, it passes through lens L2, a mirror M1, a beamsplitter BS, and the objective on the OET chip. After illumination, it returns inside the objective together with the red light from the lamp to pass the beamsplitter and be reflected by mirror M2 to enter lens L3 to image in the sensor of the camera.

The final iteration is shown in Figure 3.20. Two mirrors, M1 and M2, are added after collimation lens L1 to align the LED light correctly on the DMD. Because the DMD needs to be aligned at a specific angle while the micromirrors are oriented at a different specific angle, this alignment tool helps us find the correct angles. Besides the alignment mirrors between the LED and the DMD, the DMD is also placed on two translation stages to align it properly. Because the DMD is rotated, the camera is also rotated to get an image aligned with the illumination from the DMD.

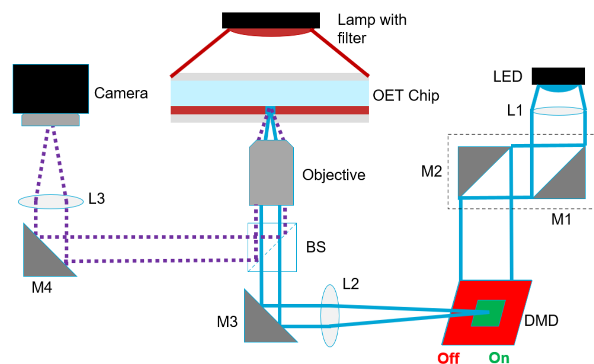

Figure 3.20: The final iteration of the optical setup design. The light originates from the LED and is collimated by lens L1. The lens L1 and the DMD are aligned by mirrors M1 and M2. After the DMD partly reflects it, it passes through lens L2, a mirror M1, a beamsplitter BS, and the objective on the OET chip. After illumination, it returns inside the objective together with the red light from the lamp to pass the beamsplitter and be reflected by mirror M2 to enter lens L3 to image in the sensor of the camera.

The realizations of the optical setups can be seen in Figure 3.21, 3.22, 3.23, and Figure 3.24. The mirrors in the optical setup are all Thorlabs BBE1-E02 in the mirror cage Thorlabs KCB1EC/M. The beamsplitter used in all setups is the 50/50 beamsplitter Thorlabs CCM1-BS013/M. The objective used for this setup is the Olympus RMS4X. The DMD is the V-9501 from Vialux. The camera used for imaging is the IDS Imaging U3-3070CP-M-GL. The ND filter used in the third iteration is the NE10A from Thorlabs. The lamp from iteration 3 is the Thorlabs QTH10/M. The red filter on the lamp from iteration 4 is the Edmund Optics red 2-inch Plastic Color Filter. The LEDs used in the optical setup are all housed in the Thorlabs M470L3-C1 LED housing. Because this LED burned out, the LED inside was first replaced by the Star-BL475-03-00-00 from Conrad and later by the Thorlabs M455D3. The light power from the LED is controlled by the LEDD1B from Thorlabs. All the mechanical elements, such as cage systems, moveable stages, optical tables, lens holders, and irises, are from Thorlabs. The lenses used in each iteration, besides the objective lens, are shown in Table 3.1.

	L1	L2	L3
Iteration 1	Thorlabs AC254-050-A-ML	Thorlabs AC254-200-A-ML	Thorlabs AC254-100-A-ML
Iteration 2	Thorlabs AC254-050-A-ML	Thorlabs AC254-300-A-ML	Thorlabs AC254-200-A-ML
Iteration 3	Thorlabs AC254-050-A-ML	Thorlabs AC254-300-A-ML	Thorlabs AC254-200-A-ML
Iteration 4	Thorlabs AC254-050-A-ML	Thorlabs AC254-300-A-ML	Thorlabs AC254-200-A-ML
Iteration 5	Thorlabs AC254-035-A-ML	Thorlabs AC254-300-A-ML	Thorlabs AC254-200-A-ML

Table 3.1: The lenses used in the five optical setup iterations.

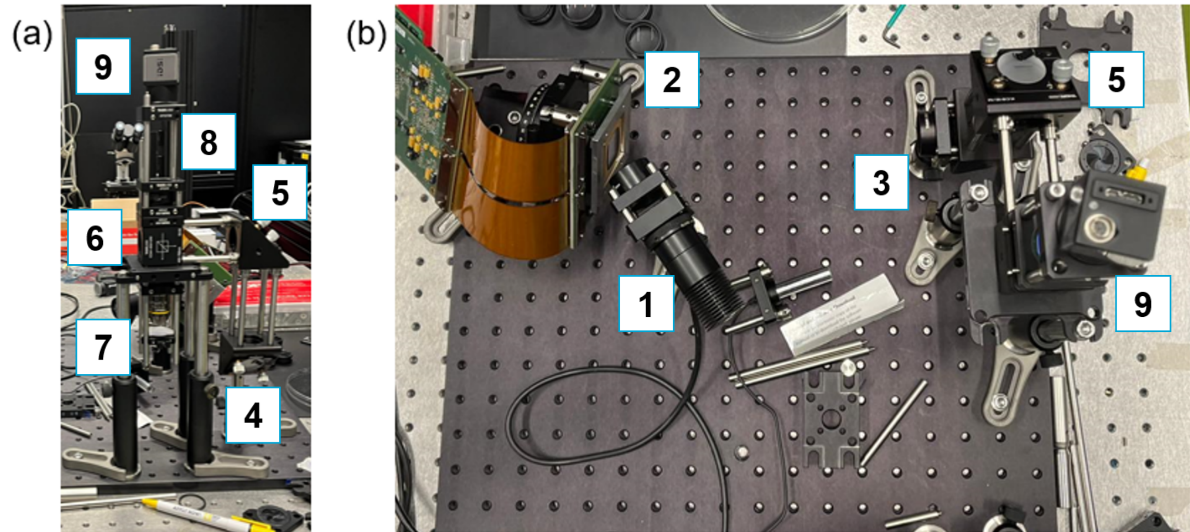

Figure 3.21: The realization of the first iteration of the optical setup. (1) shows the LED with the collimation lens L1, and (2) shows the DMD. (3) shows lens L2. (4) and (5) are the mirrors M1 and M2. (6) is the beamsplitter. (7) shows the objective and the OET chip holder. (8) and (9) are the lens L3 and the camera. (a) shows the side view of the microscope. The camera on top is opposite to the chip, which is imaged using the objective pointing down. (b) shows a top view of the microscope where the DMD is well visible.

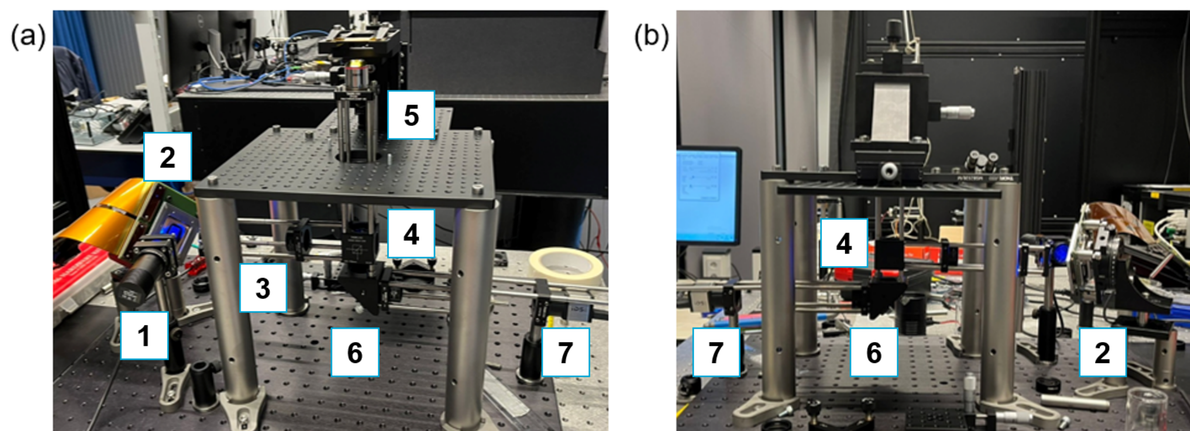

Figure 3.22: The realization of the second iteration of the optical setup. (1) shows the LED with the collimation lens L1, and (2) shows the DMD. (3) shows lens L2. (4) is the beamsplitter. (5) shows the objective and the OET chip holder. (6) shows the mirror M1 and the lens L3. (7) shows the camera. (a) shows a back view of the microscope. The microscope has two stages. The top stage has a platform on which the chip holder can be placed. The chip is illuminated from below. (b) shows a front view of the microscope.

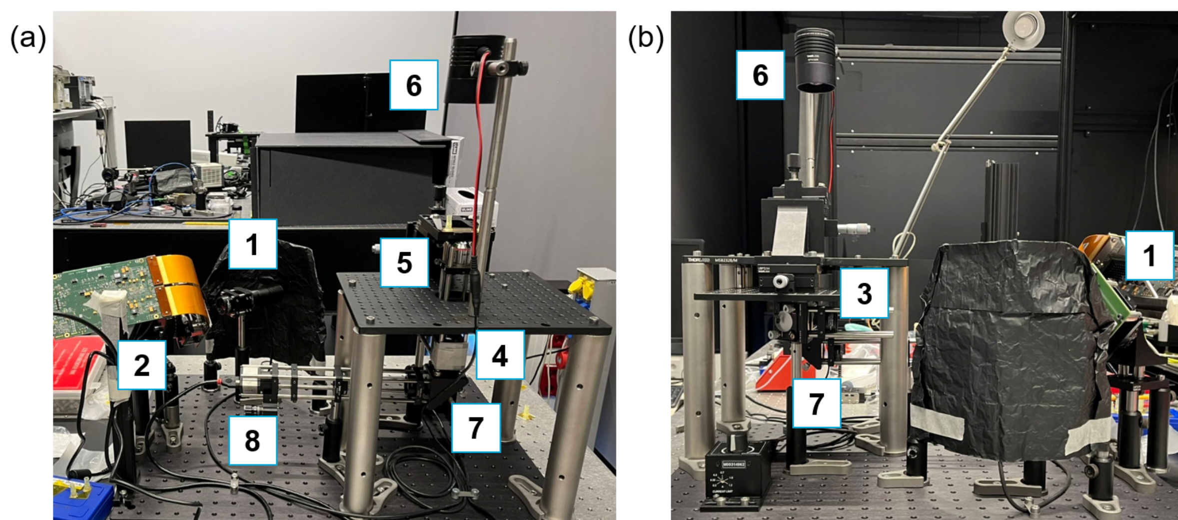

Figure 3.23: The realization of the third and fourth iterations of the optical setup. In terms of looks, the third and fourth iterations only differ by the filters. (1) shows the LED with the collimation lens L1, and (2) shows the DMD. (3) shows lens L2. (4) is the beamsplitter. (5) shows the objective and the OET chip holder, and (6) shows the lamp. (7) shows the mirror M1 and the lens L3, and (8) shows the camera with the neutral density filter. (a) shows a back view of the microscope. The lamp illuminates the microfluidic chip from above. The black aluminum foil is to block the stray light from the DMD. (b) shows the front view of the microscope.

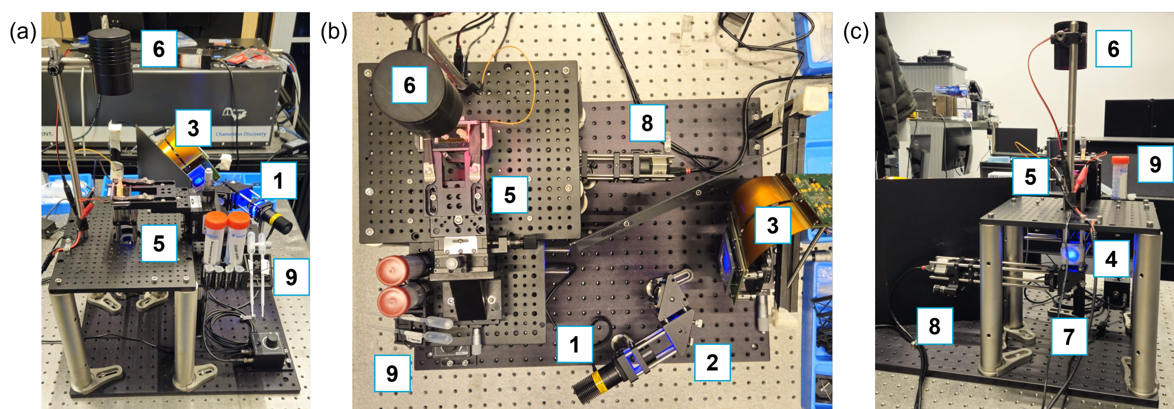

Figure 3.24: The realization of the final iteration of the optical setup. (1) shows the LED with the collimation lens L1, and (2) shows the alignment mirrors M1 and M2. (3) shows the DMD, which reflects the unwanted illumination on a black aluminum plate. (4) shows the beamsplitter BS, of which the stray light is blocked using tape. (5) shows the objective, the stage, and the microfluidic chip. (6) shows the lamp that illuminates the chip using red filtered light. (7) shows the mirror M4 with the lens L3 that focuses the light on the camera sensor. This camera is shown in (8). To store the dielectric media and the dielectric particles safely, a 3D-printed tube holder was designed, which is shown in (9). (a) shows a front view of the microscope, (b) shows the top view of the microscope, and (c) shows the back view of the microscope.

3.2.1. Illumination source

As has already been shown, two light sources are needed in this optical setup. The most important one is the illumination source for the patterning on the OET chip. Because a laser induces a lot of diffraction at the DMD, we need to choose a different light source. Since LEDs also have a sharply peaked nominal wavelength and a relatively high optical power, they make for a good patterning light source. Because we expect the a-Si:H to have a higher conductivity at a smaller wavelength, we choose a blue LED. Initially, we used a Thorlabs M470L3-C1 with a nominal wavelength of 470 nm and a total beam power of 350 mW. In the final iteration, we first swapped the LED for the Roschwege HighPower LED Koningsblauw with a wavelength of 480 nm and a total beam power of 340 mW. Later, we replaced this LED with the Thorlabs M455D3 with a nominal wavelength of 455 nm and a total beam power of 1150 mW. The first LED was used for the absorption measurement of the photoconductive layer. The other two LEDs were used to calculate the efficiency of the optical setup.

To create a clear image, we added a candescent light source in iteration 3 with an additional red plastic filter in iteration 4. This red light source was used unfocused on the OET chip to illuminate the whole chip while inducing as little photoconductivity as possible. This red lamp was used for the absorption measurement of the photoconductive layer.

A collimated red laser, the Thorlabs CPS635R, with a wavelength of 635 nm and a total beam power of 1.2 mW, was used to align the optical setup and measure the absorption of the photoconductive layer. The spectra of the light sources were all measured using the Thorlabs CCS200/M Compact Spectrometer. The measured spectra can be found in Appendix A.1

3.2.2. Characterization of the optical setup

In the optical setup, we characterize five different metrics. The magnification, the field of view, the lateral resolution, the depth of focus, and the optical efficiency. The magnification of a 4f-system can be easily calculated using equation 2.42 for each combination of lenses. The objective used in all setups has a focal length of 45 mm. The theoretically derived magnifications of the optical setup iterations are shown in Table 3.2.

	$M_{DMD\to Chip}$	$M_{Chip\to Camera}$	$M_{DMD\to Camera}$
Iteration 1	$M = -45/200 = -0.225$	$M = -100/45 = -2.22$	$M = -0.225 \times -4.44 = 0.5$
Iteration 2	$M = -45/300 = -0.15$	$M = -200/45 = -4.44$	$M = -0.15 \times -4.44 = 0.67$
Iteration 3	$M = -45/300 = -0.15$	$M = -200/45 = -4.44$	$M = -0.15 \times -4.44 = 0.67$
Iteration 4	$M = -45/300 = -0.15$	$M = -200/45 = -4.44$	$M = -0.15 \times -4.44 = 0.67$
Iteration 5	$M = -45/300 = -0.15$	$M = -200/45 = -4.44$	$M = -0.15 \times -4.44 = 0.67$

Table 3.2: The theoretical magnifications of each optical setup iteration.

Since lenses' focal lengths commonly have small deviations from their nominal values due to the manufacturing process, the true system magnification should be measured. This can be done by measuring how many pixels it takes on the camera sensor to image a polystyrene bead of a known size. This gives the true magnification using the number of pixels used for the bead $N_{cam,pix}$, the size of a camera pixel $d_{cam,pix}$, and the size of the bead d_{bead}.

$$M_{Chip\to Camera} = \frac{N_{cam,pix} d_{cam,pix}}{d_{bead}} \tag{3.4}$$

The true magnification of the DMD to the chip must be calculated in parts. We can measure the magnification of a DMD pixel to a camera pixel. This gives the true magnification using the number of pixels used by the DMD $N_{DMD,pix}$ and the size of a DMD pixel $d_{DMD,pix}$.

$$M_{DMD\to Camera} = \frac{N_{cam,pix} d_{cam,pix}}{N_{DMD,pix} d_{DMD,pix}} \tag{3.5}$$

Using the found magnification from the DMD to the camera and the magnification from the chip to the camera, we can calculate the magnification from the DMD to the chip.

$$M_{DMD\to Chip} = \frac{M_{DMD\to Camera}}{M_{Chip\to Camera}} \tag{3.6}$$

The FoV is closely related to the magnification. The FoV of the chip is related to the size of the sensor L_{cam} and the magnification from the chip to the camera $M_{Chip\to Camera}$.

$$FoV_{Chip} = \frac{L_{cam}}{M_{Chip\to Camera}} \tag{3.7}$$

The amount of the DMD pixels $N_{DMD,FoV}$ we can see using the camera is related to the calculated FoV_{Chip}, the size of a DMD pixel $d_{DMD,pix}$ and the magnification from the DMD to the chip $M_{DMD\to Chip}$.

$$N_{DMD,FoV} = \frac{FoV_{Chip}}{d_{DMD} M_{DMD\to Chip}} \tag{3.8}$$

To characterize the lateral resolution, we need to use the numerical aperture. The NA of the used objective is equal to 0.1. This means that the maximum allowed angle in the optical setup that the light can make with the optical axis is 5.74 °, assuming that we can use the refractive index of air, $n = 1$. We can calculate the lateral resolution using equation 2.44. The lateral resolution, setting NA=0.1, is theoretically given as $\rho = 6.1\lambda$, depending on the wavelength of the used LED.

It is not trivial to measure the resolution of the created OET microscope. Because the sample is illuminated and imaged from below, we are observing shadows. Therefore, to get a better estimation of the resolution, we need to add a fluorescence microscope to the setup, with fluorescent beads small enough to be diffraction-limited. The fluorescent beads that we will use to measure the resolution are from the TetraSpeck Fluorescent Microspheres Size Kit. This microscope slide consists of 6 different chambers with differently sized fluorescent beads. The beads in the first chamber have a diameter of 4 μm, in the second chamber a diameter of 1 μm, and in the third chamber a diameter of 0.5 μm. If we want to image the beads of chamber two clearly, we would need a light source with a wavelength of 164 nm, which is much smaller than the LEDs we use. We did, however, do a measurement as well on the 0.5 μm beads to compare the results to the 1 μm beads. Each chamber we investigate has beads of a similar size but with four different fluorescent colors. The colors are called ”FluoSpheres blue”, ”FluoSpheres yellow-green”, ”FluoSpheres orange”, and ”FluoSpheres dark red”. The excitation and emission spectra of these colors are shown in Figure 3.25.

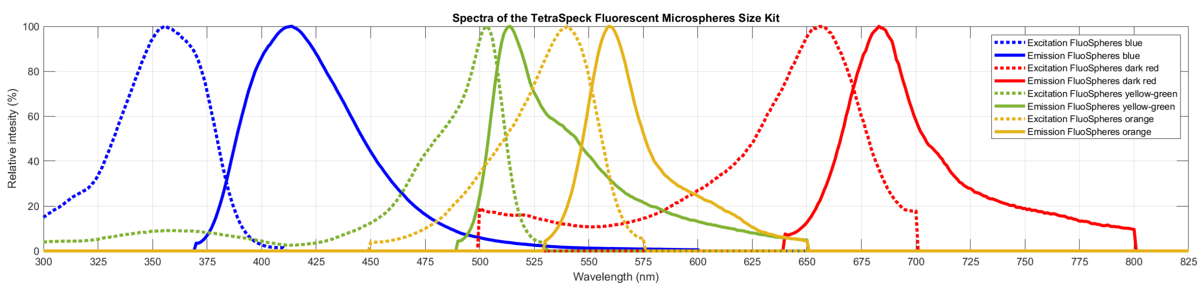

Figure 3.25: The spectra of the fluorescent beads in the TetraSpeck Fluorescent Microspheres Size Kit. The data is retrieved from the manufacturer [83].

The measurements were taken to establish the resolution of the system using the final optical setup. The LED that we use in this setup is in the blue spectrum with an expected wavelength of 455 nm. We can see in Figure 3.25, this wavelength sits between two excitation peaks of the TetraSpeck beads. Even using a Brightline Basic 525/39 filter, this LED did not seem to activate the fluorescence. Using the flashlight of a Samsung Galaxy S24, the beads emitted a signal strong enough to be captured by the camera. This fluorescence setup is shown in Figure 3.26. The illumination is put at an angle to avoid directly shining inside the objective to avoid saturating the camera sensor. The light used for excitation is a white light source, meaning that it excites all types of fluorescence colors.

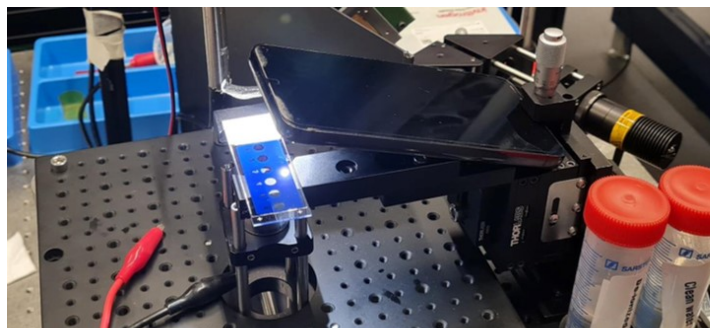

Figure 3.26: The fluorescence microscope setup to measure the resolution using the TestraSpeck Fluorescent Microspheres Size Kit and white light source.

To filter out some of the light before the camera, we use an EdgeBasic Long Wave Pass 488 filter, which cuts off all the light with a shorter wavelength than 488 nm. This means that the emission from the ”yellow-green”, the ”orange”, and the ”dark red” fluorescent colors must be taken into account. Using the data from the Fluorescence SpectraViewer from ThermoFischer, we can determine the center of mass (CoM) of the emission spectra [84]. The CoM will be located at the average wavelength for each of the spectra. These CoMs and spectra are shown in Appendix A.2. The average wavelength of the three spectra is found to be 597 nm. We therefore expect a lateral resolution of $\rho = 3.64$ µm.

By using Fiji[2], we could select individual beads of the 4 µm, the 1 µm, and the 0.5 µm beads measurements to estimate the point spread function (PSF). This PSF should be a first-order Bessel function, which we can approximate to first order with a Gaussian distribution. Therefore, we can additionally fit a Gaussian distribution on the found PSF. In practice, the resolution can be taken from the PSF as the full width at half maximum (FWHM). Using this method, we are also able to measure the resolution and precision of the illumination from the DMD on the OET chip.

The DoF is similarly calculated as the lateral resolution. Because we have a small NA, we can use the second formula from equation 2.46. Assuming again the refractive index of air, we find that theoretically, the total resolution in depth is given as $2\Delta Z = 100\lambda + \frac{10}{4.44}e$, depending on the wavelength of the used LED. Because the magnification between the chip and the camera is calculated to be 4.44, we can establish the smallest distance the camera is able to resolve by the lateral resolution. A diffracted limit spot has a size of $\rho = 6.1\lambda$, which is the theoretical lower limit of the smallest resolvable distances of the camera. Using this limit, we can say that our DoF can be approximated as $2\Delta Z = 100\lambda + 2.25 \times 6.1\lambda = 113.86\lambda$. Using the average wavelength from the fluorescent beads, we find that we would expect our DoF to be $2\Delta Z = 70$ µm.

To measure the DoF is even less trivial than measuring the lateral resolution. Using the fluorescence imaging method, as was done for measuring the lateral resolution, at certain distances from the focal point on the optical axis, we can create a z-stack showing how the particles get in- and out of focus. Due to the defocusing, the center of the particle loses intensity, which we can map in a PSF in the z-direction[3]. To create images with different z distances, we will use a moving stage with a micrometric screw. The lines on the screw allow us to move the the stage up and down with an accuracy of 10 µm. At the focus, we take 14 steps (0.14 mm) from the focus point down, and 13 steps (0.13 mm) from the focus point up. The stacked images are first aligned using the ”Linear Stack Alignment with SIFT” plugin on Fiji. We then reslice the image with steps of 0.5 µm to create a 3D profile of the image. Using this, we can see how the intensity at a single pixel changes over the distance on the optical axis. An example of this is shown in Figure 3.27.

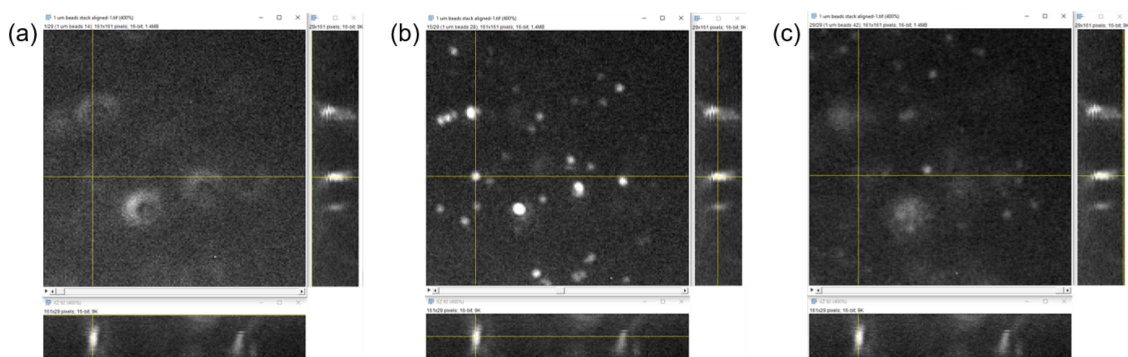

Figure 3.27: An example of using reslice in Fiji. (a) shows a 1 µm diameter bead around 0.14 mm out of focus. In the lower plot, we can see that this matches the intensity at the top of this lower plot. In the small plot to the right, this matches the left. (b) shows the same bead but now in focus. The intensities in both smaller plots are now also at maximum. (c) shows the same bead but 0.13 mm out of focus. This matches the lower part of the small plot below and the right part of the small plot on the right.

[2]Also known as ImageJ.
[3]The z-direction is the name used for the optical axis in literature.

Again, using the FWHM of the PSF in the z-direction, we can estimate the DoF for beads that are diffraction limited. We do these measurements again on 4 μm, 1 μm, and 0.5 μm diameter beads. Using Fiji, we fit a Gaussian on the measured PSF. We can relate the standard deviation σ of this fitted Gaussian to the FWHM [85]. This is given by $FWHM = 2\sigma\sqrt{2\ln 2}$.

The last metric, the optical efficiency, tells about how much light is left after passing an optical element in the optical setup. To quantify, we will measure this efficiency at different points of the final optical setup. We will first measure the total LED power when focused on the PM130D Thorlabs optical power meter. The lens used for focusing is the AC254-035-A-ML from Thorlabs. The setup of this measurement is shown in Figure 3.28. The lights in the room were turned off, except for the LED, at all power measurements.

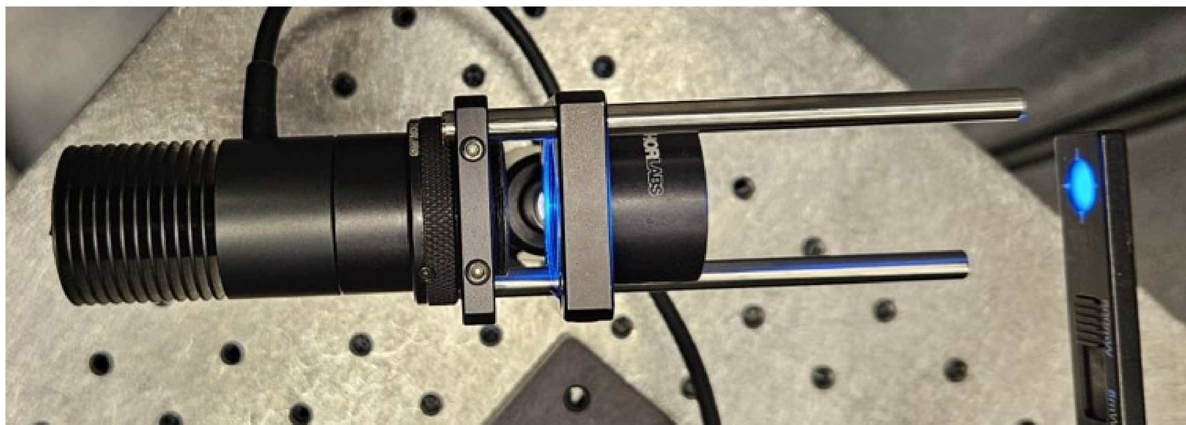

Figure 3.28: The blue LED focused on the optical power sensor such that the full sensor is illuminated.

After this, the light power after the alignment mirrors is measured twice. Once while focusing on the sensor and once without focusing on the sensor. The focused measurement allows us to compare all the efficiencies with less loss. The second measurement is more representative of the real optical power. The setup for both these measurements is shown in Figure 3.29.

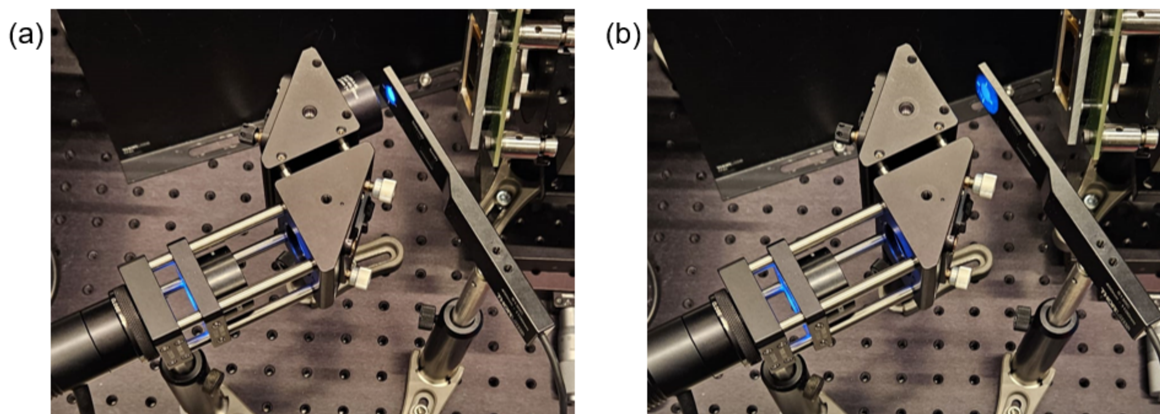

Figure 3.29: The power sensor after the alignment mirrors. (a) shows the blue light focused on the sensor so that the full sensor is illuminated. (b) shows the sensor at the same location without the focusing lens.

Six more measurements are done after the DMD. The first three are with the sensor in focus, as can be seen in Figure 3.30. The first measurement of these three is with all the DMD mirrors in the on-state. This means that the maximum power can be measured after the DMD. The second measurement is done with the DMD having tiles of 64×65 pixels switched on in a checkered pattern on the DMD. This means that half of the micromirrors are switched on and half are turned off in a relatively uniform manner. The third measurement is done with only a single pixel in the center of the DMD turned on. These three measurements are repeated with the sensor not focused by the lens. In addition to these measurements, the noise was measured after the DMD without a focusing lens and without illumination from the LED.

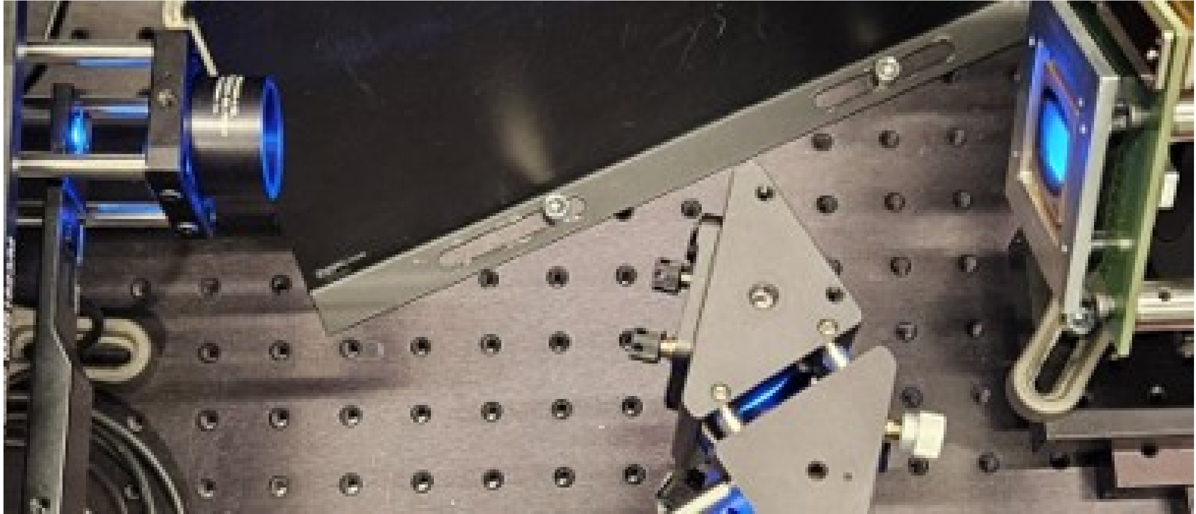

Figure 3.30: The power sensor placed on the optical path after the DMD and after a lens that focuses the light on the full sensor.

After the measurements were taken to calculate the efficiency of the DMD, three measurements were made before the objective lens, with a lens focusing the blue light on the full power meter sensor. This experimental setup is shown in Figure 3.31.a. The power is measured with the DMD fully on, with the 64×64 checker pattern, and with the single switched-on mirror in the center of the DMD. Again, the noise was measured in this setup with no light switched on. Finally, three measurements were done with the optical power sensor placed in the same location where the microfluidic chip would be located. This is a good representation of the real power on the photoconductive layer. This experimental setup is shown in Figure 3.31.b. A measurement was done with the DMD fully on, with the 64×64 checker pattern, and with the single switched on mirror in the center of the DMD. Additionally, the noise in this setup was measured as well.

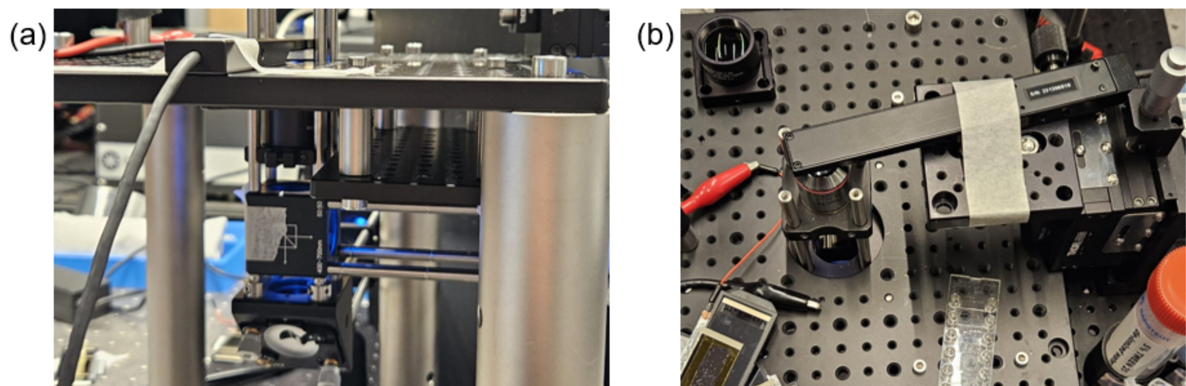

Figure 3.31: The optical power meter on the last part of the optical path. (a) shows the sensor placed between the objective lens and a lens that focuses the blue light such that the full sensor is illuminated. (b) shows the optical sensor placed at the place where the microfluidic chip would be set.

By comparing the power before each optical path piece P_{before} and after each optical path piece P_{after}, the efficiency η of this piece can be measured.

$$\eta = \frac{P_{after}}{P_{before}} \times 100\% \tag{3.9}$$

We expect all the achromatic doublet lenses from Thorlabs to have an efficiency of around 80% for the blue wavelengths [86]. We expect the mirrors to have a reflectance of 99% [87]. We expect the 50/50 beamsplitter to have an efficiency of 50% [88]. We have no information on the Vialux DMD, but for a different DMD, from Texas Instruments, we find an estimated efficiency around 60-70% [89]. There was no information available on the objective, so we will expect its efficiency to be comparable to that of the achromatic doublet lenses. This gives us an expected total efficiency from the LED to the objective $\eta_{LED->chip}$.

$$\begin{aligned} \eta_{LED->chip} &\approx \eta_{L1} \times \eta_{M1} \times \eta_{M2} \times \eta_{DMD} \times \eta_{L2} \times \eta_{M3} \times \eta_{BS} \times \eta_{Obj} \\ &\approx 80\% \times 99\% \times 99\% \times 65\% \times 80\% \times 99\% \times 50\% \times 80\% \\ &\approx 16.15\% \end{aligned} \tag{3.10}$$

3.2.3. Optical Alignment

To obtain a sharp and clear image, it's necessary to follow a precise optical alignment protocol for each individual element of the setup. For this, we can make use of a beamwalk. The beamwalk makes use of an aligned red laser (Thorlabs CPS635R). To align the laser, we need to place the laser on two movable stages and a tilt stage so that we can adjust all the degrees of freedom that define the laser beam axis. We then place 2 SM1D12D irises from Thorlabs some distance apart after the laser using the Thorlabs cage system. This setup is shown in Figure 3.32. If the light passes through both irises, we know the laser is correctly aligned with the optical axis. The end of this cage system is connected to an adapter, such that we can connect this tool to the cage system in the optical setup.

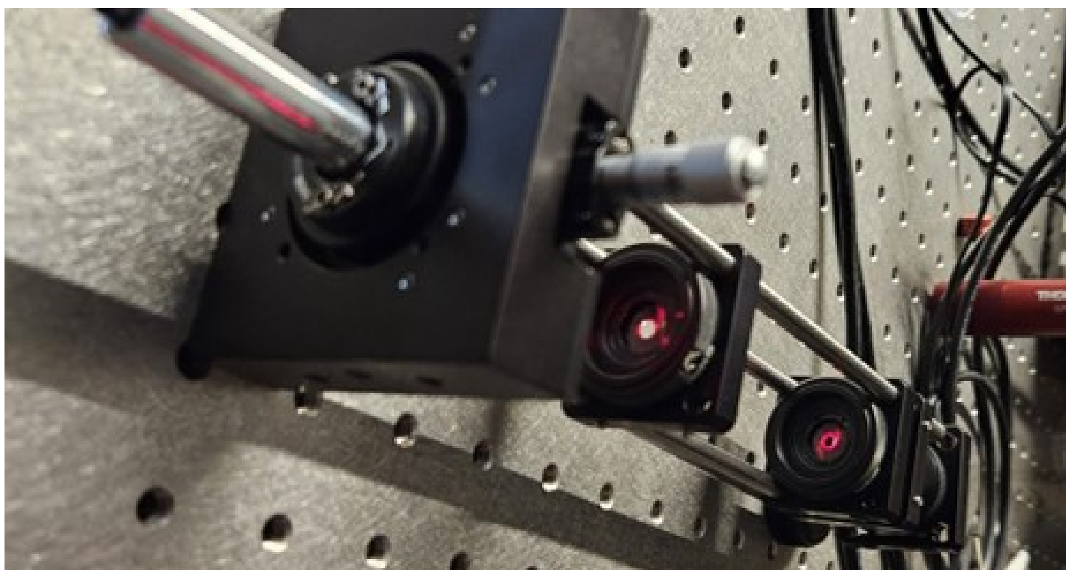

Figure 3.32: The alignment tool using the red CPS635R laser and two SM1D12D irises. The irises make sure that the laser light passes straight through the center of the cage system. Two movable translation stages and a single tilt stage can be used to align the laser.

Using the aligned laser, we can first fix the lens L3 before the camera by moving the lens L3 so that the smallest possible focal spot is formed on the camera sensor. This is the correct distance between the sensor and the L3 Lens. To avoid damaging the camera pixels, some absorptive ND filters are used to reduce the laser intensity. When L3 is fixed, we can put the aligned laser at the top of the microscope, where the chip is supposed to be. When aligning this path without the objective, we can calibrate the mirror M4. Using the beamsplitter, we can focus the light directly on a testing chip, which we need to see in focus on the camera as well. With this, we can set the objective at the focal length, making the 4f-system between the camera and the chip complete. By putting an iris in between M3 and L2, we align mirror M3 without the objective. We can align L2 by again creating a focus on the chip using the objective. Still without placing the objective lens, we can align the DMD through L2 by putting it in focus. All the mirrors of the DMD should be in the on-state to make sure that most of the light is reflected in the right direction. By placing the center of the alignment mirror M2 in the reflected focus from the DMD after L2, we can align M2 and M1. By turning on the LED and illuminating a certain pattern on the chip in focus, we can align the mirrors M1 and M2. These two alignment mirrors give us the freedom to slightly tune the focus of the optical setup. The alignment of the optical setup is made more complex due to the DMD. The DMD needs to be at an angle of 45°around the optical axis. The DMD also needs to be put at an angle of 12°between L2 and M2. The DMD has no built-in kinematic mount, meaning that the sensor is fixed with the casing. Therefore, to make the alignment easier, we put the DMD on two movable stages.

3.2.4. Other instrumentation

The OET setup not only consists of optical elements, but also needs to be able to supply an electric signal to the microfluidic chip and to the DMD to be functional. The Agilent 3320A function generator provides the electric signal that we apply to the chip. This function generator is coupled in series with a Thurlby Thandar Instruments WA301 Wideband Amplifier 30V pk-pk to increase the amplitude of the electrical signal to more than 30V peak to peak. The microfluidic chip is coupled to the amplifier in parallel together with an Agilent DSO3202A oscilloscope. This allows us to measure the output voltage and the signal form of the signal inside the microfluidic chip. The microfluidic chip is attached to the amplifier and back to the function generator using simple electronic breadboard wires. The DMD is controlled using the ”ALP Demo” program to put in predefined images for quick and easy focusing. The ”EasyProj” program can be used to load single pictures easily in the DMD. For more complex control of the DMD, Python with the ALP4 library was used on a computer with an Intel(R) Xeon(R) CPU E5-2630 @ 2.30 GHz and 64 GB installed RAM. The image from the camera is captured in the uEye cockpit. For control of the liquid flow in the microfluidic chip, we tried to use a NE-4002X syringe pump, but this pumped the liquid too fast to be useful due to a syringe that was too big.

3.3. Design of the dielectric particle

After discussing the microfluidic chip and the optical setup, we come to the last part of the OET setup. The dielectric particle that we want to control. The particles that we want to control using the OET need to fit in the microfluidic chamber and flow in and out using the inlets. A dielectric particle often used in literature is a polystyrene bead. Since the beads are almost perfect spheres, we are able to use the first-order DEP force formula with good confidence. Because the setup we use is likely to be diffraction limited around 3.64 μm, we will use beads of a bigger size. In this thesis, we used beads with a diameter of 15 μm. The expected polystyrene conductivity is around 2×10^{-3}S/m [90] and the relative permittivity is around 2.6 [91].

If we want to put more complex forms of dielectric particles, we need to take into account that the DEP force approximation will be less accurate. We will use PDMS microbots that are created by a Nanoscribe at the Delft University of Technology and the University of Melbourne. The microbots are heavily inspired by the microgear robots found in literature [8]. This creates the possibility to benchmark against, and possibly improve on the state-of-the-art. The robots are designed as small gears with eight teeth and a hole in the center. The outer diameter of the gears is 200 μm. The teeth have a length of 37.5 μm and a width of 25 μm. The hole in the circle has a diameter of 75 μm. The design for the microgears in the literature often presents an opening formed by removing one tooth from the gear, so that it is able to scoop up other particles. This "mouth" is designed to have an opening of 50 μm. The design of the robots is created in SolidWorks, of which a screenshot is shown in Figure 3.33. The nominal thickness of the microbots is 50 μm.

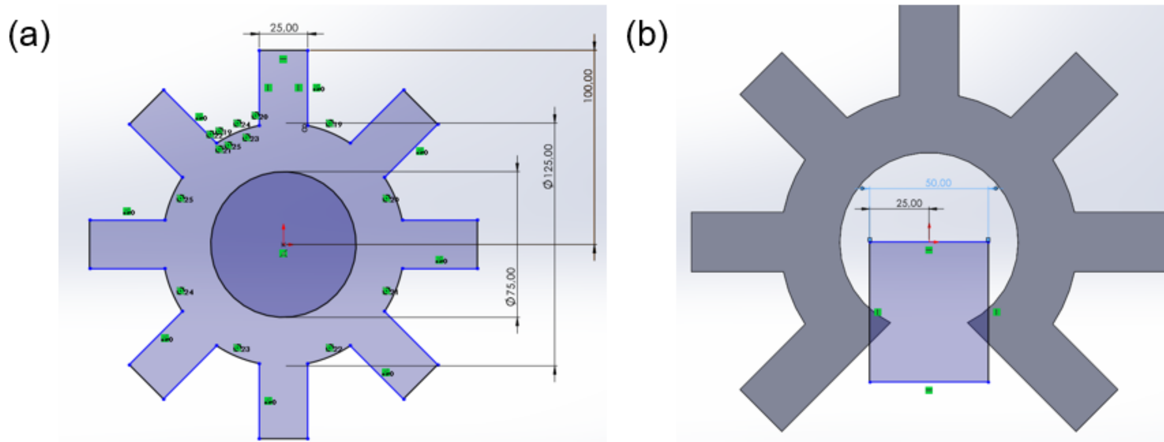

Figure 3.33: The design of the microgear robots. (a) shows the initial design of the microgear with all the dimensions denoted. (b) shows the microgear design with the "mouth".

To realize these robots, our collaborator Dr. Fan from the University of Melbourne created a Nanoscribe file and helped me print them using polydimethylsiloxane (PDMS). We expect the conductivity of the PDMS to be around 2.5×10^{-14} S/m and the relative permittivity to be around 2.55 [92]. To decrease the adhesion of the microbots on the photoconductive layer, we included small semispheres on the microbots to reduce the contact area, as shown in Figure 3.34.a. In another iteration, we tried to decrease the thickness to 10 μm, as shown in Figure 3.34.b. A preview of the Nanoscribe is shown in Figure 3.34.c, which shows 144 robots to be printed.

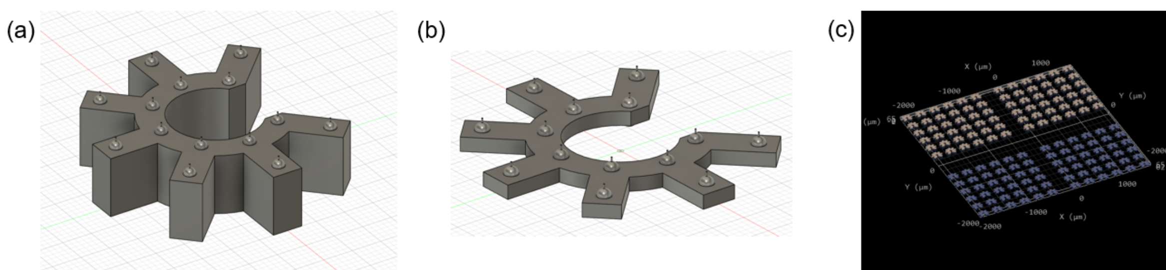

Figure 3.34: The STL files of the second iteration of the microbot design. (a) shows the new microbot with a thickness of 50 μm. The small dots are semispheres with a diameter of 10 μm. (b) shows the same microbot but with a thickness of 10 μm. (c) shows a preview of the Nanoscribe where 144 microbots are to be printed in a matrix. 72 microbots with a thickness of 50 μm and 72 microbots with a thickness of 10 μm.

In Figure 3.35.a, we see an image from an optical microscope of the original microbot design. In Figure 3.35.b, we see a realized microbot with the adhesion decreasing semispheres. In order to test the OET with different microbot geometries, we designed a different type of robot. For this, we designed a small platform with an adhesion-decreasing semisphere. This platform has four legs, which are connected to a hinge on the platform itself. This design has the potential to show moving parts of the microbot, which are to be controlled by the OET. This realized four-legged microbot is shown in Figure 3.35.c.

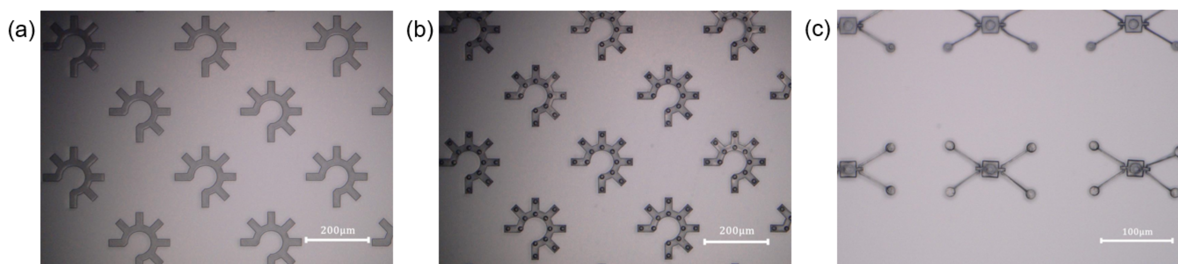

Figure 3.35: Images made of 3 different types of microbots using a microscope in the chemical laboratory of the faculty ME of the Delft University of Technology. (a) shows the initial design from Figure 3.33.a. (b) shows the same initial design with added 15 µm diameter semispheres. (c) shows the four-legged microbot.

When printed, the microbots are stuck to the substrate. We tried to remove them by first heating them using a Stuart UC150 hotplate at around 100 degrees while submerged in deionized water. This detached the robots after more than 4 hours of cooking. We then put small samples of this water, containing the loose robots, in small Eppendorf tubes, which we centrifuged using the Centrifuge 5420 from Eppendorf for 3 minutes at 2000 RCF[4]. This forced the robots to clump together at the bottom of the tubes due to the centrifugal force. By very carefully pipetting a small amount of the deionized water away from the centrifuged tubes, we then could increase the concentration of the microbots. To avoid losing the robots, we put the pipetted water away in tubes that we centrifuged again. The water was again carefully removed from these tubes to filter out the microbots in case we removed them from the first tube by accident. This process is then repeated until we are left with 30 tubes containing 2 µL of deionized water and as many microbots as possible. However, we found that this methodology led to a considerable amount of damaged or destroyed microbots.

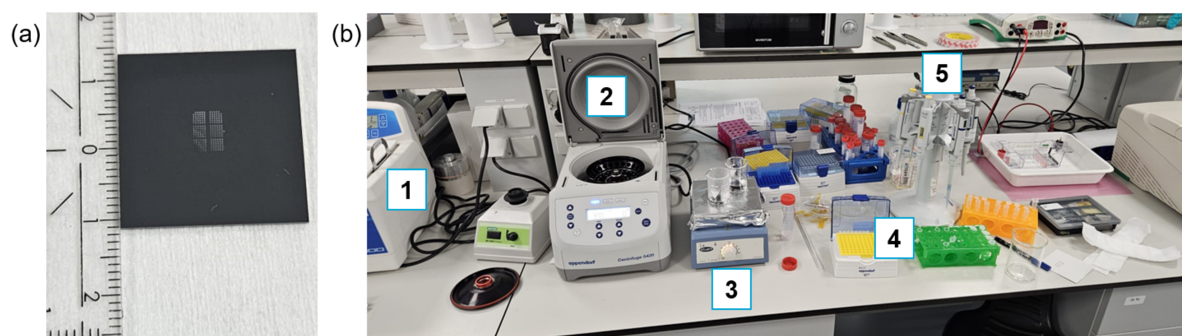

Figure 3.36: The setup used for separating the PDMS microbots from their substrate. (a) shows the printed robots still attached to the substrate. (b) shows the equipment used to detach the microbots. (1) is the sonicator, (2) is the centrifuge. (3) shows the hot plate with two filled beakers. (4) are the tubes in which the PDMS microbots are deposited using the Eppendorf pipettes shown in (5).

[4] RCF is the relative centrifugal force also known as g-forces.

With the second iteration of robots, from Figure 3.34, we again tried to separate the microbots from the substrate. After 10 minutes of being submerged in hot water, not only were the microbots detaching from the substrate, but also small chunks of debris. After carefully rinsing the substrate, we put the substrate in a small glass beaker submerged in a small volume of deionized water. By placing the small glass beaker with the substrate in the Branson 1800 ultrasonic cleaner for just 10 seconds, the microbots popped right off. After again centrifuging and pipetting to increase the concentration, we put around 2 μL of the deionized water containing the microbots inside 10 small tubes. In the assembly of the microfluidic chip, we put the water containing the microbots directly on the photoconductive layer before putting it on the small ITO glass with the laser-cut holes. Using a microscope in the chemical lab, we could make sure that the created microfluidic chips contained the microbots. An image of a robot is shown in Figure 3.37. The robot on the left is missing a tooth, which could have resulted from the centrifuging process. The small circles are the 15 μm diameter polystyrene beads. The straight line on the top right is the border of the microfluidic channel created by the double-sided tape. The big circles on the lower right are air bubbles.

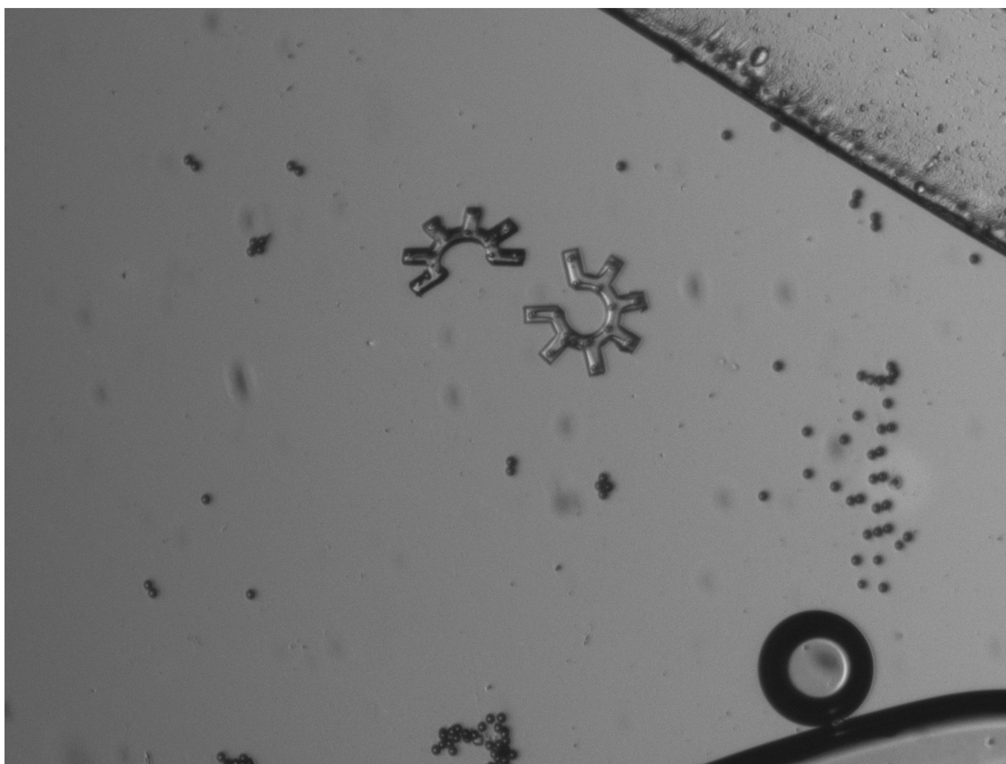

Figure 3.37: An image of 2 microbots with polystyrene beads inside a microfluidic OET chip created using the OET optical setup.

3.3.1. Frequency range

The DEP force in the OET depends on the frequency via the Clausius-Mossotti (CM) factor. This comes from the CM factor depending on the complex permittivities of the dielectric particle and the dielectric medium. The CM factor has two limits, one at $\omega = 0$ and one at $\omega = \infty$.

$$K(\omega = 0) = \frac{\sigma_2 - \sigma_1}{\sigma_2 + 2\sigma_1} \qquad K(\omega = \infty) = \frac{\epsilon_2 - \epsilon_1}{\epsilon_2 + 2\epsilon_1} \tag{3.11}$$

The cross-over frequency, where $K(\omega_{co}) = 0$, can also be found by using the material properties of the dielectric particle and the dielectric medium.

$$f_{co} = \frac{\omega_{co}}{2\pi} = \frac{1}{2\pi}\sqrt{\frac{(\sigma_2 - \sigma_1)(\sigma_2 + 2\sigma_1)}{(\epsilon_1 - \epsilon_2)(\epsilon_2 + 2\epsilon_1)}} \tag{3.12}$$

The cross-over frequency can only exist[5] when $\sigma_2 > \sigma_1$ and $\epsilon_1 > \epsilon_2$ or when $\sigma_2 < \sigma_1$ and $\epsilon_1 < \epsilon_2$.

We can calculate the system's expected CM factors by using the conductivities and permittivities of deionized water, polystyrene, and deionized water. With $\sigma_1 = 5.4945 \times 10^{-8}$ S/m, and $\epsilon_1 = 6.9030 \times 10^{-10}$ F/m. We can find that we expect the real part of the CM factor to be positive at $\omega = 0$ and negative at $\omega = \infty$. For the PDMS microbots, we expect the real part of the CM factor to be negative at both limits. Therefore, for the PDMS, the cross-over frequency does not exist. The expected real parts of the CM-factors of the PDMS and the polystyrene in deionized water can be seen in Figure 3.38.

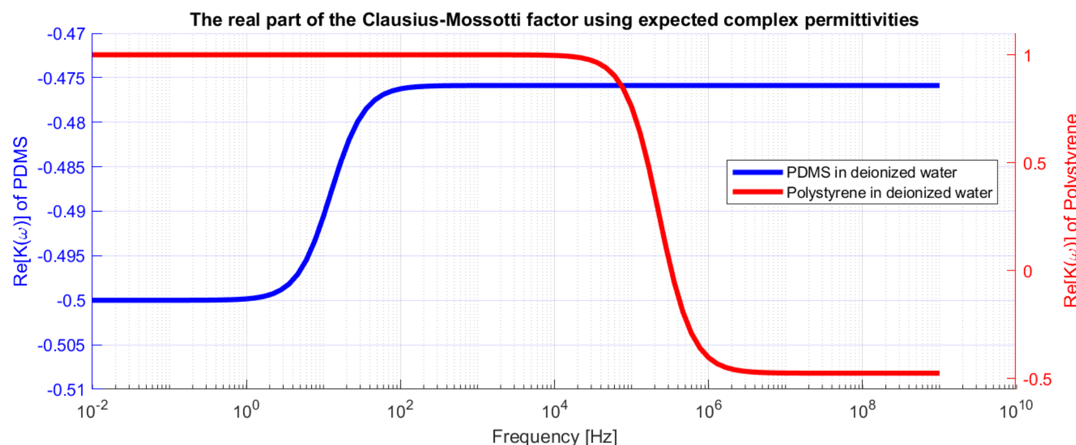

Figure 3.38: The expected real parts of the CM factors of PDMS, in blue, and polystyrene, in red, in deionized water. For the PDMS we have Re$[K(0)] = -0.5$ and Re$[K(\infty)] = -0.476$. For the polystyrene we have Re$[K(0)] = 1$ and Re$[K(\infty)] = -0.475$. For the polystyrene, we find an expected cross-over frequency of 328.9 kHz.

The Agilent 3320A function generator can output four different signals: a sinusoidal wave, a square wave, a triangular wave, and a pulse. The DEP force in equation 2.13 depends on the rms value of the electrical field. The rms value X of a harmonic signal $x(t)$ is given by the square root of the integral of the square of the harmonic signal divided by the period of the signal T.

$$X = \sqrt{\frac{1}{T}\int_0^T (x(t))^2 dt} \tag{3.13}$$

For all the types of signals, we can find the rms value. Assuming that the given amplitude is V_{pp} and we have a period of $T = 2\pi$, we find that the rms value of the sinusoidal wave is given as $X = V_{pp}\frac{1}{\sqrt{2}}$. The rms value of the square wave is given as $X = V_{pp}$. The rms value of the triangular wave is given as $X = V_{pp}\frac{1}{\sqrt{3}}$ and the rms value of the pulse wave is given as $X = V_{pp}\frac{1}{\sqrt{2\pi}}$. Therefore, we will use the square wave input signal to maximize the DEP force. At high frequencies ($f > 5$MHz), the square wave seems less consistent and looks more like a sinusoidal function the higher the frequency gets.

[5] It only exists when it is not imaginary.

The last thing we need to consider regarding the input frequency is electrolysis. At low and high frequencies, bubbles can start forming inside the microfluidic chip, deteriorating it. Therefore, we will need to establish a window of frequencies that are safe to work in to avoid breaking the OET chips.

3.3.2. Dielectrophoretic force

If we want to establish the dynamics of a dielectric particle in the OET setup, we need to look back at section 2.4.1. We will simplify this complete image to make it easier to distinguish the DEP force, which is the main force of interest. We are not interested in the gravity and buoyancy forces because we can only image the spatial translation using the optical setup. Suppose we assume the medium to be deionized water with a temperature of 20 °C and a viscosity of 1 mPa-s [93]. In that case, the expected velocity due to Brownian motion is around $\langle \frac{d\mathbf{x}_{brown}}{dt} \rangle = \sqrt{\frac{k_b T}{3\pi\eta r}} = 6.56 \times 10^{-10} \frac{1}{\sqrt{r}}$. That means that if we have a bead with a radius of 7.5 μm, the effect would be 240 nm/s of movement, which will be negligible.

The electrophoretic effect happens at low frequencies. Because we want to avoid electrolysis, we will avoid low frequencies, making it credible that the electrophoretic force will also be negligible. The LACE effect has an optimal frequency that depends on the medium's conductivity and permittivity, as seen in equation 2.37. If we take deionized water as the medium with a height of 90 μm, the optimal frequency would be around $f_{opt} = 1.408 \times 10^5 \lambda$. If we want LACE to occur in the frequency range where we avoid electrolysis, it needs to have a frequency higher than 100 Hz. This means the electric double layer must be at least 710 μm. Because the thickness of the EDL λ can never be bigger than the thickness of the chip, we can neglect LACE when using deionized water. When using a medium with a much higher conductivity, we need to consider that LACE can play a role in the dynamics. The electrothermal effects are only dominant with optical power densities greater than 200 W/cm^2 as shown in Figure 2.14. If we assume that we could put all the optical power from an LED on an area of 1 mm^2, we would need the LED to have 2 W of power and an efficiency of 100%. The LEDs that we use are, therefore, not strong enough to induce ACET.

This leaves us with two main forces to describe the dynamics: the DEP force and the drag force. Therefore, we assume the dynamics of the dielectric particle depend on those two forces.

$$\begin{aligned} F_p &= ma_p = F_{DEP} - F_{drag} \\ F_{DEP} &= ma_p + F_{drag} \end{aligned} \tag{3.14}$$

Because the particle's speed is not large enough to create a large Reynolds number, we can assume that we can approximate the drag force by Stokes' law. As a dielectric medium, we used deionized water, deionized water with 0.05% Tween-20, and deionized water with 5% Tween-20. We assume that the Tween-20 does not influence the viscosity of the water much. Therefore, we take the viscosity of the dielectric medium to be 1 mPa-s. Using equation 2.31 and calculating the mass by the volume and density, we find a new formula for the DEP force.

$$\begin{aligned} F_{DEP,bead} &= \rho_{polystyrene} V_{bead} \frac{d^2\mathbf{x}_{bead}}{dt^2} + 6\pi r_{bead} \mu \frac{d\mathbf{x}_{bead}}{dt} \\ &= 1.856 \times 10^{-12} \frac{d^2\mathbf{x}_{bead}}{dt^2} + 1.414 \times 10^{-7} \frac{d\mathbf{x}_{bead}}{dt} \\ F_{DEP,microbot} &= \rho_{pdms} V_{microbot} \frac{d^2\mathbf{x}_{microbot}}{dt^2} + 6\pi r_{microbot} \mu \frac{d\mathbf{x}_{microbot}}{dt} \\ &= 6.588 \times 10^{-10} \frac{d^2\mathbf{x}_{microbot}}{dt^2} + 1.885 \times 10^{-6} \frac{d\mathbf{x}_{microbot}}{dt} \end{aligned} \tag{3.15}$$

The density of polystyrene is 1060 kg/m³ [94]. The volume of the beads is given by $V_{bead} = \frac{4}{3}\pi r^3 = 5.625 \times 10^{-16}\text{m}^3$. The density of PDMS is found to be 1011 kg/m³ [95]. The volume of a microbot is calculated using SolidWorks to be 6.516×10^{-13} m³. In literature, for calculating the DEP force for the microbot using Stokes law, a different scaling is applied [8]. If we want to benchmark the DEP force with this paper, we need to use $F_{DEP,microbot,corrected} = 3.88 \times 10^{-7} \frac{d\mathbf{x}_{microbot}}{dt}$. This paper uses the same correction for calculating the DEP force on a 15 µm diameter polystyrene bead. In other literature, a DEP force of around 35 pN has been found for 15 µm diameter polystyrene beads [96]. Comparing this paper to an older paper from Ming C. Wu and Pei-Yu Chiou, we find that they could manipulate 45 µm beads with a speed of 40 µm/s, which would translate to 17 times lower compared to Shuailong Zhang et al. [97] [96]. Literature does not give a precise view of the DEP force we would expect, so we will refer to equation 3.15 to find the DEP force and benchmark the results in the section 5.3.

3.3.3. Controlling the DMD

As we already discussed in section 3.2.4, we can use multiple programs to control the DMD. For quantifying the DEP force on the dielectric particles, we will use Python and the ALP4lib module created by Sébastien M. Popoff [98]. This is not a library created by Vialux, the company producing the DMD. Therefore, the DMD is not optimally controlled this way. The DMD is more optimally controlled using C/C++, for which Vialux has developed an API. We did not use C/C++ to have everything controllable in Python. Listing 3.1 shows sample code for controlling the DMD using Python and the ALP4 library. For this code to work, the function "create_img_array" needs to be defined. The DMD also needs a pictureTime, which relates to how long an image is shown on the DMD. This particular code keeps running until the timer runs out.

```python
# Import needed libraries
    import numpy as np
    from ALP4 import *
    import time

# Load the Vialux .dll
    DMD = ALP4(version = '4.3')
# Initialize the device
    DMD.Initialize()

    img = np.zeros([DMD.nSizeY,DMD.nSizeX])

    # Create the animation for the DMD
    def create_img_array(img):
        # Put the code here to create an image array setting an image with the same size as "
    img" as a frame on the DMD
        # The mirrors go on at the values 1 in the img_array. They turn off at the value 0.
        img_array = ....
        return img_array

# Make each frame of the img_array 1D for the DMD and concatenate them into a sequence
    imgSeq = np.concatenate([frame.ravel() for frame in img_array])

# Allocate the memory on the DMD for the animation
    DMD.SeqAlloc(nbImg = 2, bitDepth = bitDepth)
# Send the image sequence to the DMD
    DMD.SeqPut(imgData = imgSeq)
# Set image rate to 10 Hz. The value is in microseconds
    DMD.SetTiming(pictureTime = 100000)

# Run the created animation for 10 seconds
    DMD.Run()
    time.sleep(10)

# Stop running the DMD
    DMD.Halt()
# Free allocated memory on the DMD
    DMD.FreeSeq()
# De-allocate the DMD
    DMD.Free()
```

Listing 3.1: A sample code in Python used for controlling the DMD.

3.3.4. Measuring and analyzing the DEP force

To measure the DEP force, we must first decide what patterning we will apply on the DMD. To create a steady movement, we created a sweep animation that goes from the left border of the FoV to the right border of the FoV and back. We can adjust the sweep pattern's speed and thickness to fit the measurement we want to do. The code for creating this sweep pattern animation is shown in Appendix A.3.1. The code for displaying the sweep animation on the DMD is shown in Appendix A.3.2. To make the code more efficient, we only use the part of the DMD that is in the FoV of the optical setup. The FoV is bounded by a rectangular ring with the same thickness as the sweep pattern. This ring avoids microgears and beads escaping from the FoV due to the sweep.

Because we did not seem to be able to control the framerate of the DMD accurately, we did some experiments on the DMD to establish the framerate when no assignment for the framerate was given in the Python code. The found framerate was around 72 fps. Using this framerate, we could adjust the number of frames for the sweep animation to fit the given sweep time. For measuring the DEP force, we used sweep animations with sweep times of 3 seconds, 5 seconds, 7 seconds, and 15 seconds. For the sweep thickness, we used a thickness of 30 DMD pixels, 60 DMD pixels, 90 DMD pixels, and 120 DMD pixels. We measured the DMD in some experiments using different light intensities, setting the LED at 1/3 power, 1/2 power, 2/3 power, 5/6 power, and full power using the Thorlabs LEDD1B LED driver. We did the experiments at different frequencies ranging between 1 and 100 kHz.

To control a dielectric particle dynamically, we wrote a Python script that prints a ring on the DMD that can be moved and reformed using keyboard inputs. The code for this ring is shown in Appendix A.3.3. This code seems to be inconsistent with the projected speeds on the DMD. Furthermore, this code seemed to require a lot of memory from Python, making it run out of memory after a short time. Therefore, this code was not eligible for quantifying the DEP force and needs to be optimized.

To quantify the code, we created videos of the movements using the uEye cockpit with a certain framerate. Using Fiji, we could manually track specific points by selecting them in each frame. We tracked the microbot at four different points for each measurement to find the average movement speed. We additionally tracked four separate beads in each experiment. Because the framerates of the camera and the DMD were not aligned, it was harder to track the sweep animation accurately. Therefore, to measure the actual sweep animation speed, we selected the right and left borders of the sweep line in each visible frame. The center of the borders was taken to be the approximate center of the sweep animation to compensate for the saturation blur. The tracking data is then processed in MATLAB to obtain the maximum velocities and accelerations for each set of parameters.

4 Results

This chapter presents the experimental results obtained from the development and evaluation of the optoelectronic tweezers (OET) system. Following the theoretical foundation laid out in the previous chapters, each component of the setup was systematically characterized and tested to measure its performance and validate the design.

The results are structured according to the main functional parts of the OET system. Section 4.1 covers the microfluidic chip, including its mechanical robustness, electrical behavior, and optical absorption properties. Section 4.2 focuses on the optical setup, with subsections addressing the resulting magnification, optical efficiency, and resolution. Finally, Section 4.3 discusses the dynamics of the dielectric particles, denoting the measured DEP forces on the particles and the effect of varying parameters.

Together, these results provide insight into the capabilities and limitations of the current OET implementation, and form the foundation for the analyses and conclusions presented in the subsequent chapters. In this chapter, the results are presented without detailed discussion; their interpretation is reserved for later chapters, where the underlying causes of the observed phenomena are examined.

4.1. Microfluidic chip

4.1.1. Robust design

As was explained in section 3.1, we created a microfluidic chip with a channel area of 270 mm^2. The thickness of the tape was measured by doing three experiments to be 0.096 mm $\pm$ 0.005 mm. This means the volume of a created chip is around 25.8 mm^3, not taking into account the accuracy in cutting the double-sided tape. The data for the thickness measurements can be found in Appendix B.1.1.

In the full project, a total of 52 functional microfluidic chips have been made. Of these 52, 10 chips were created using the design from iteration 1 as shown in Figure 3.3.a. These chips were not functional for OET, for they did not have ITO-covered glass and no photoconductive layer. From iteration 2, as shown in Figure 3.3.b, four chips without ITO-covered glass and 7 with ITO-covered glass were made. These chips were also not functional for OET, for they did not have a photoconductive layer. From the design of Figure 3.3.d. 5 chips were made using two small ITO coverslips. 2 chips were created using one big, and one small ITO glass, as shown in Figure 3.3.e. Both these designs were functional, having conductive glasses and a photoconductive layer. Six chips of the third design were made as shown in Figure 3.4.a. Half of the chips in this iteration had a PEGylated photoconductive layer to try to reduce the surface particle adhesion. 18 OET microfluidic chips were made from the final design as shown in Figure 3.4.b.

4.1.2. Electrical properties

We measured the resistance of three different liquid media with the experiment described in section 3.1.4. This was done using pure deionized water, deionized water with 0.05% Tween-20, and deionized water with 5% Tween-20. The results of these measurements, including the correction factor as described in equation 3.2, are shown in Table 4.1.

The corrected resistivities are calculated using the measured resistance per meter times the correction factor calculated. All measurements done on the resistance of the materials used for the microfluidic chip can be found in Appendix B.1.2.

Deionized Water			
Measurement Distance	**29 mm**	**23 mm**	**3 mm**
Measured resistance per meter [Ω/m]	7.34×10^{7}	7.94×10^{7}	3.55×10^{8}
Measured resistance per meter Std. [Ω/m]	3.12×10^{6}	1.75×10^{6}	2.41×10^{5}
Correction Factor in m^{-2}	2.48×10^{-3}	2.29×10^{-3}	5.13×10^{-4}
Corrected ρ [Ω·m]	1.82×10^{5}	1.82×10^{5}	1.82×10^{5}
Corrected ρ Std. [Ω·m]	7.74×10^{3}	4.01×10^{3}	1.23×10^{2}
Corrected Conductivity [S/m]	5.49×10^{-6}	5.49×10^{-6}	5.49×10^{-6}
Deionized Water + 0.05% Tween-20			
Measured resistance per meter [Ω/m]	1.04×10^{7}	1.15×10^{7}	7.04×10^{7}
Measured resistance per meter std. [Ω/m]	1.33×10^{5}	7.93×10^{5}	2.27×10^{5}
Corrected ρ [Ω·m]	2.58×10^{4}	2.65×10^{4}	3.61×10^{4}
Corrected ρ Std. [Ω·m]	3.30×10^{2}	1.82×10^{3}	1.16×10^{2}
Corrected Conductivity [S/m]	3.87×10^{-5}	3.78×10^{-5}	2.77×10^{-5}
Deionized Water + 5% Tween-20			
Measured resistance per meter [Ω/m]	4.50×10^{6}	4.72×10^{6}	2.40×10^{7}
Measured resistance per meter Std. [Ω/m]	1.49×10^{4}	1.31×10^{5}	2.05×10^{3}
Corrected ρ [Ω·m]	1.11×10^{4}	1.08×10^{4}	1.23×10^{4}
Corrected ρ Std. [Ω·m]	3.70×10^{1}	3.00×10^{2}	1.05×10^{0}
Corrected Conductivity [S/m]	8.97×10^{-5}	9.24×10^{-5}	8.11×10^{-5}

Table 4.1: Measured resistance per meter, correction factors, and conductivity for different concentrations of Tween-20 in deionized water.

The capacities measured in the microfluidic chip are shown in Table 4.2 and Table 4.3. These measurements are done by doing the experiment described in section 3.1.4. The relative permittivities of the double-sided tape, the a-Si:H, the air, and deionized water with 5%, 0.05%, and with no Tween-20 are calculated using the measured capacities and by using equation 3.3. The full measurement data regarding the capacities can be found in Appendix B.1.3 and in Appendix B.1.4 for the double-sided tape and the a-Si:H. The full measurement data regarding the capacities of the air and the different concentrations of Tween-20 in deionized water can be found in Appendix B.1.5.

4.1.3. Reflection and absorption

To calculate the reflection of the ITO glasses, we use the setup described in section 3.1.2 and in section 3.1.3. The initial light intensity of an LED of 470 nm, a laser of 635 nm, and a lamp of 715 nm is measured. The transmitted light is measured for these wavelengths using different ITO-covered microscope slides with various resistances. Using the incoming and transmitted light, the reflection percentage could be calculated. The results of these measurements are shown in Table 4.4 and in Figure 4.1. The full reflection measurement at 470 nm, 635 nm, and 715 nm is shown in Appendix B.2.1, B.2.2, and B.2.3, respectively. The reflection measurements of the ITO glasses in the setup with the beamsplitter to measure the absorption coefficient of a-Si:H at 470 nm, 635 nm, and 715 nm are shown in appendices B.2.4, B.2.5 and B.2.6 respectively.

	Tape	a-Si:H	Air
Measured capacitance average	1.6×10^{-10} F	6.5×10^{-10} F	1.4×10^{-10} F
Measured capacitance std	1.6×10^{-11} F	3.7×10^{-11} F	3.1×10^{-11} F
A_{eff}	4.8×10^{-4} m^2	7.3×10^{-4} m^2	2.6×10^{-4} m^2
d_{eff}	9.6×10^{-5} m	1.0×10^{-6} m	9.6×10^{-5} m
Calculated ϵ_r	3.50	0.10	5.94
Theoretical ϵ_r	3.65	11.5	1
Expected material capacitance	1.62×10^{-10} F	7.43×10^{-8} F	2.37×10^{-11} F
Expected total capacitance	1.62×10^{-10} F	2.35×10^{-10} F	1.95×10^{-10} F
Difference	6.71×10^{-12} F	4.17×10^{-10} F	5.43×10^{-11} F
Percentage of measured capacitance	4%	64%	39%

Table 4.2: Capacitance measurements and dielectric constant calculations for Tape, a-Si:H, and Air.

	0% Tween-20	5% Tween-20	0.05% Tween-20
Measured capacitance average	3.9×10^{-6} F	4.9×10^{-6} F	1.9×10^{-6} F
Measured capacitance std	1.7×10^{-6} F	1.8×10^{-7} F	1.2×10^{-7} F
A_{eff}	2.6×10^{-4} m^2	2.6×10^{-4} m^2	2.6×10^{-4} m^2
d_{eff}	9.6×10^{-5} m	9.6×10^{-5} m	9.6×10^{-5} m
Calculated ϵ_r	1.65×10^{5}	2.05×10^{5}	7.84×10^{4}
Theoretical ϵ_r	78	78	78
Expected material capacitance	1.85×10^{-9} F	1.85×10^{-9} F	1.85×10^{-9} F
Expected total capacitance	1.97×10^{-9} F	1.97×10^{-9} F	1.97×10^{-9} F
Difference	3.91×10^{-6} F	4.86×10^{-6} F	1.85×10^{-6} F
Percentage of measured capacitance	100%	100%	100%

Table 4.3: Capacitance measurements and dielectric constant calculations for different Tween-20 concentrations.

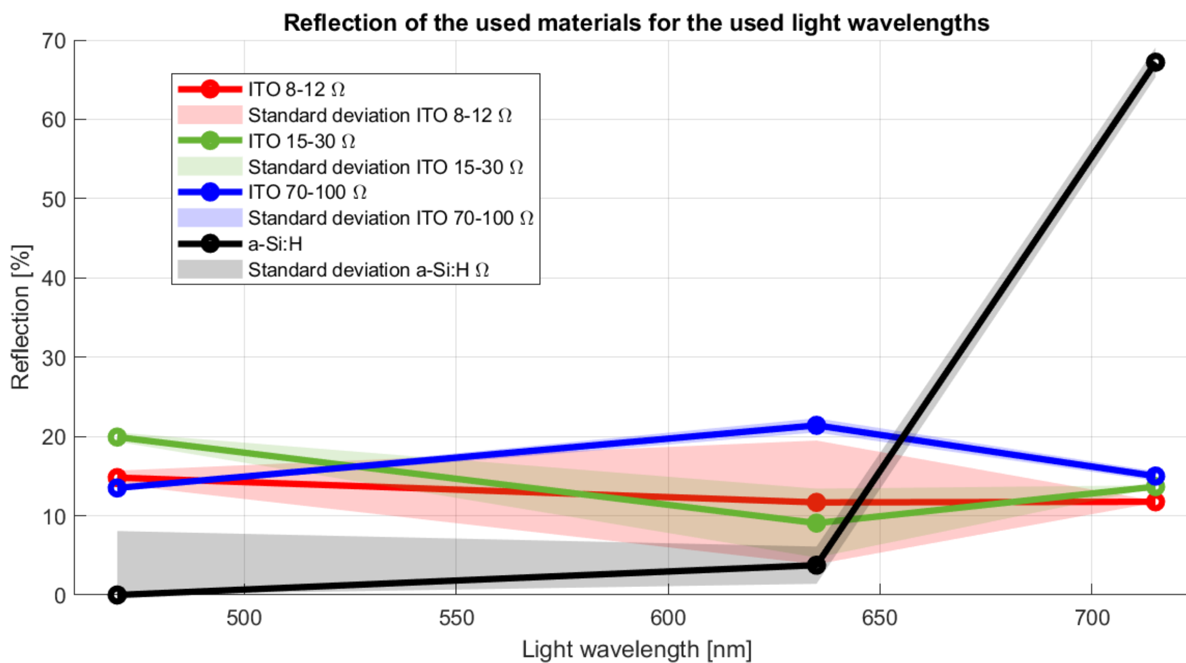

Figure 4.1: The measured reflection percentages of ITO covered microscope slides with resistances 8-12 Ω, 15-30 Ω, and 70-100 Ω for photons with wavelengths of 470 nm, 635 nm, and 715 nm. The black line denotes the measured reflection percentages of a-Si:H at the same photon wavelengths.

Material	Wavelength (nm)	I_0 (nW)	Avg. I_r (nW)	Std. I_r (nW)	Refl. % Avg.
ITO 8-12 Ω	470	6.69×10^6 nW	9.90×10^5 nW	5.80×10^4 nW	14.81%
	635	1.16×10^6 nW	1.36×10^5 nW	9.06×10^4 nW	11.68%
	715	3.07×10^6 nW	3.61×10^5 nW	3.51×10^3 nW	11.76%
ITO 15-30 Ω	470	6.69×10^6 nW	1.33×10^6 nW	3.86×10^4 nW	19.92%
	635	1.16×10^6 nW	1.05×10^5 nW	5.04×10^4 nW	9.07%
	715	3.07×10^6 nW	4.19×10^5 nW	5.29×10^3 nW	13.67%
ITO 70-100 Ω	470	6.69×10^6 nW	9.02×10^5 nW	1.63×10^4 nW	13.49%
	635	1.16×10^6 nW	2.49×10^5 nW	1.05×10^4 nW	21.42%
	715	3.07×10^6 nW	4.60×10^5 nW	1.89×10^4 nW	15.01%

Table 4.4: Reflected intensity measurements at different wavelengths for ITO-covered microscope slides with different resistances. All values are in nanowatts (nW) except for reflection percentages.

The absorption coefficient of the used a-Si:H has been measured using the experiment of section 3.1.3. At three different wavelengths: 470 nm, 635 nm, and 715 nm, we calculated the light power that was transmitted by the ITO-covered microscope slides using the measured incoming light and the measured reflected light. Both this transmitted light, the measured light transmitted by the a-Si:H, and the measured noise bias were used to calculate the absorption coefficient of the a-Si:H as is used in equation 2.20. The computed absorption coefficients are shown in Table 4.5 and in Figure 4.2. In this figure, two absorption coefficients at different wavelengths found in the literature are shown [36] [99]. The dashed black line shows the calculated absorption coefficient if the measured transmitted light is as big as the measured noise bias. The full data on the measured absorption coefficient at a photon wavelength of 470 nm, 635 nm, and 715 nm are shown in Appendix B.3.1, B.3.2, and B.3.3 respectively.

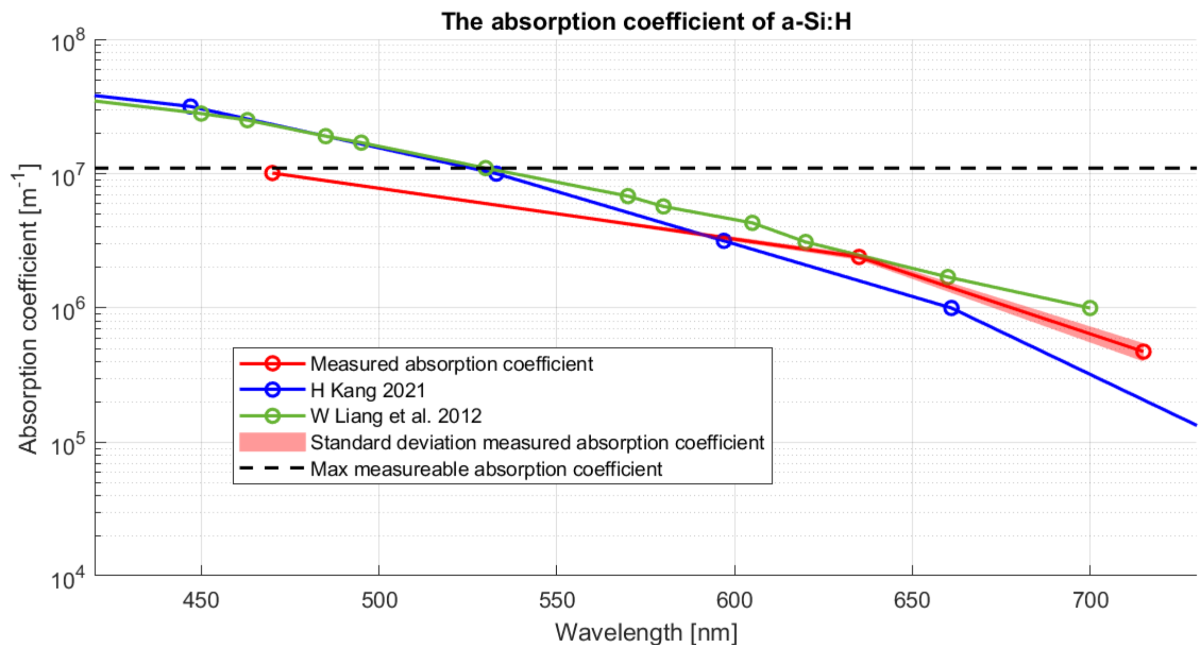

Figure 4.2: The measured absorption coefficient of the used a-Si:H shown in red with its standard deviation. The blue line shows the absorption coefficient of a-Si:H as found by H. Kang [99]. The green line shows the absorption coefficient of a-Si:H as found by W. Liang [36]. The black dashed line shows the maximum absorption coefficient that we are able to measure using the experimental setup.

Wavelength	α (m^{-1})	α Std. (m^{-1})	Refl. %	Refl. % Std.
470 nm	$1.01 \times 10^{7}\, m^{-1}$	$1.76 \times 10^{4}\, m^{-1}$	-0.35%	8.07%
635 nm	$2.40 \times 10^{6}\, m^{-1}$	$1.22 \times 10^{5}\, m^{-1}$	3.76%	2.35%
715 nm	$4.74 \times 10^{5}\, m^{-1}$	$7.41 \times 10^{4}\, m^{-1}$	67.20%	1.87%

Table 4.5: The measured absorption coefficient α of a-Si:H at different photon wavelengths with its standard deviation. The resulting reflection percentages with their standard deviations are calculated using this absorption coefficient and are also shown in Figure 4.1.

4.2. Optical setup

The created OET setup is a combination of the optical elements, the microfluidic chip, the dielectric particles, the dielectric media, and other elements of instrumentation. The full combined setup of the OET system can be seen in Figure 4.3. In this figure, the most important parts of the OET are highlighted. In this section, we will go into more detail on the characteristics of the optical setup.

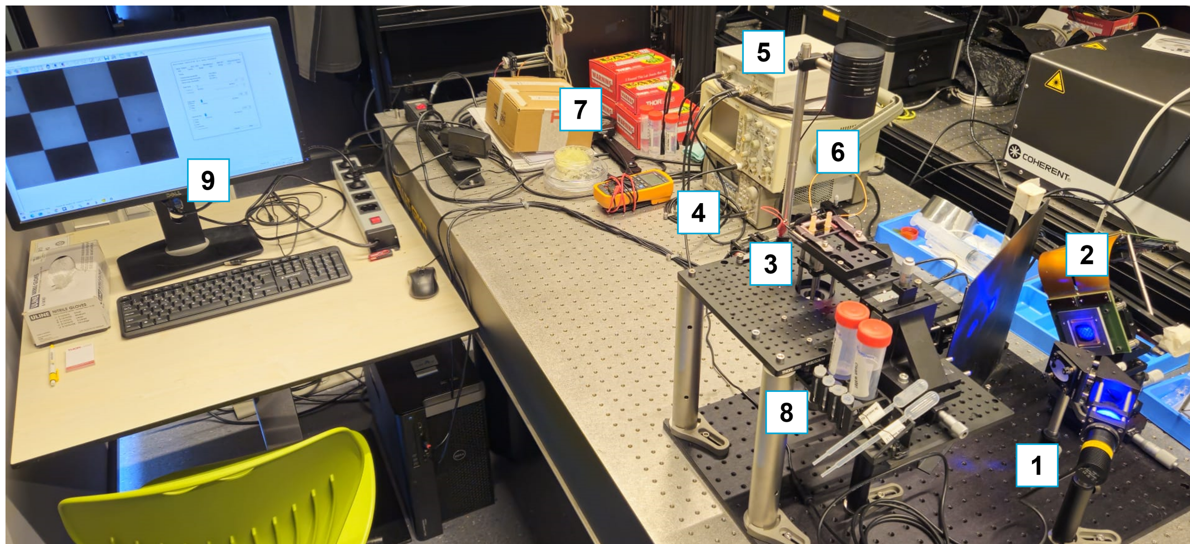

Figure 4.3: The full OET setup. (1) shows the blue LED, which provides light for the illumination of the photoconductive layer. (2) shows the DMD, which determines which pattern gets deflected. This created the control in the OET. (3) shows the microfluidic chip on the movable stage. In the microfluidic chip, the dielectric particles are imaged and manipulated by the DEP force. (4) shows the signal generator, which provides the electrical signal to the microfluidic chip with a particular shape and frequency. (5) shows the waveform amplifier, which increases the voltage, and thus also increases the strength of the electrical field inside the microfluidic chip. (6) shows the oscilloscope, which shows the electrical input signal of the OET. (8) shows the 3D-printed tube holder to safely store the dielectric media and the dielectric particle. (9) shows the computer used for control, imaging, and analysis of the DEP force.

4.2.1. Magnification

The magnification of the optical paths in the optical setup has been measured with the method described in section 3.2.2. The sizes of beads and DMD patterns were measured in terms of the number of pixels used on the camera sensor. Using this information and the known sizes of the measured object, we were able to retrieve the magnifications. The magnification from the microfluidic chip to the camera is found to be $M_{chip \to cam} = 4.2 \pm 0.2$ as can be seen in Table 4.6. The full data on the magnification from the chip to the camera can be found in Appendix C.1.1. The magnification from the DMD to the camera is found to be $M_{DMD \to cam} = 0.67 \pm 0.02$ as can be seen in Table 4.7. The full data on the magnification from the DMD to the camera can be found in Appendix C.1.2.

Using the found magnifications, we can find the magnification from the DMD to the chip to be $M_{DMD\rightarrow chip} = 0.16 \pm 0.06$. This means that a DMD pixel size of 10.8 µm should be 1.7 $\pm$ 0.6 µm in the microfluidic chip. A camera sensor pixel of 3.45 µm should be able to image 0.81 $\pm$ 0.042 µm of the microfluidic chip when not taking into account the diffraction of light. The camera sensor is 2056 by 1542 pixels which means that the FoV is found to be 1.67 $\pm$ 0.09 mm by 1.26 $\pm$ 0.07 mm. This FoV limits the amount of DMD pixels visible to be 984 $\pm$ 25 by 738 $\pm$ 19 pixels. The FoV of the DMD used in the sweep animation is 978 by 736 pixels, which almost fills up the entire camera FoV.

Object	**Conversion** (m/pix)	**Std. Conversion** (m/pix)	**Magnification** $M_{\text{Chip}\rightarrow\text{Camera}}$	**Std. Magnification**
Bead	8.43×10^{-7} m/pix	3.91×10^{-8} m/pix	4.10	0.19
Robot full length	7.87×10^{-7} m/pix	1.83×10^{-8} m/pix	4.39	0.10
Robot diameter circle	8.30×10^{-7} m/pix	2.46×10^{-8} m/pix	4.16	0.12
Robot tooth width	7.80×10^{-7} m/pix	3.80×10^{-8} m/pix	4.43	0.22
Combined data	8.15×10^{-7} m/pix	4.25×10^{-8} m/pix	4.24	0.22

Table 4.6: The measured distances in camera sensor pixels of objects in the microfluidic chip. Using the known ground truths of the lengths, the conversion and consequently, the magnification from the chip to the camera could be retrieved.

Size	**30 px**	**60 px**	**90 px**	**120 px**	**Combined**
m/pix	5.36×10^{-6}	5.10×10^{-6}	5.12×10^{-6}	5.09×10^{-6}	5.17×10^{-6}
Std. m/pix	8.89×10^{-8}	7.50×10^{-8}	5.04×10^{-8}	3.74×10^{-8}	1.30×10^{-7}
$M_{\text{Chip}\rightarrow\text{Camera}}$	0.644	0.677	0.674	0.677	0.668
Std. $M_{\text{Chip}\rightarrow\text{Camera}}$	0.011	0.010	0.007	0.005	0.016
DMD/Cam	0.496	0.472	0.474	0.472	0.478
Std. DMD/Cam	0.008	0.007	0.005	0.003	0.012

Table 4.7: The measured distances in camera sensor pixels of projected DMD sweep animations in the microfluidic chip with different thicknesses. Using the known ground truths of the lengths, the conversion and consequently, the magnification from the DMD to the camera could be retrieved. The last two columns give the ratio between a DMD pixel size and a camera sensor pixel size.

4.2.2. Optical efficiency

The optical efficiency of all optical elements is measured using the experiment as described in section 3.2.2 and in equation 3.9. Two different light sources were used, which resulted in the optical efficiency at two different wavelengths. The element clusters of which the efficiencies are calculated are shown in Figure 4.4 as red dashed rectangles. The efficiency of cluster 1 is found to be $\eta_{1,455nm} = 79\% \pm 6\%$ using a 455 nm LED, and $\eta_{1,480nm} = 70\% \pm 2\%$ using a 480 nm LED. The efficiency of cluster 2, i.e., the DMD, is found to be $\eta_{2,455nm} = 42.5\% \pm 0.6\%$ using a 455 nm LED and having the DMD fully reflecting. The efficiency of the same cluster with the same DMD setting is $\eta_{2,480nm} = 33.2\% \pm 0.7\%$ using a 480 nm LED. Finally, the efficiency of cluster 3, ending before the objective, is given as $\eta_{3,455nm} = 34.9\% \pm 0.5\%$ using a 455 nm LED and $\eta_{3,480nm} = 30.9\% \pm 0.9\%$ using a 480 nm LED. The six efficiency measurements were done, focusing the light on the sensor using a lens which is normally not used in the optical setup, as described in section 3.2.2. This lens has a theoretical efficiency of around 80% for both wavelengths [86].

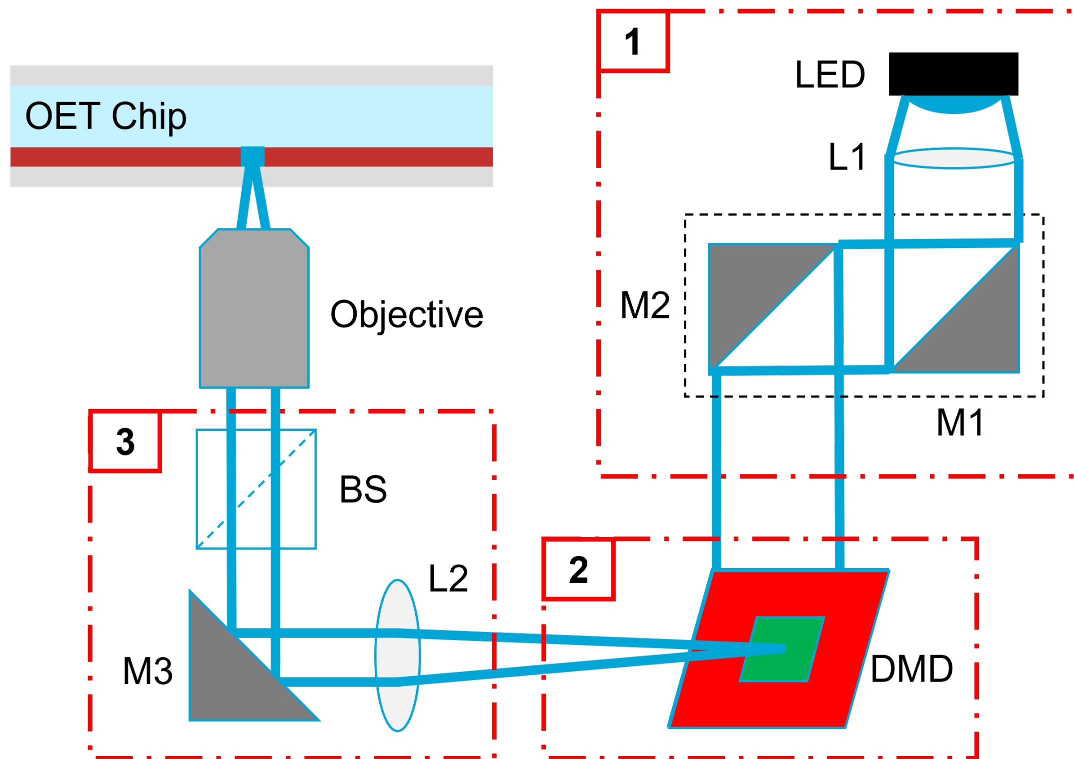

Figure 4.4: The optical setup used for the OET, denoting three clusters of optical elements by the red dashed rectangles. The efficiency of these three clusters is measured using two different wavelengths of light.

The total efficiency of the system is found to be $\eta_{455nm} = 11.7\% \pm 0.8\%$ using the 455 nm LED and $\eta_{480nm} = 8.4\% \pm 0.4\%$ using the 480 nm LED. The full measurements done on the optical efficiencies can be found in Appendix C.2. The efficiencies found after each particular cluster, measured with, and without focusing the output light on the power meter, is shown in Table 4.8 and Table 4.9 for respectively the 455 nm LED and the 480 nm LED. As can be seen in this table, the intensity of the DMD decreases by $49.8\% \pm 0.9\%$ using the 455 nm LED, and $50\% \pm 2\%$ using the 480 nm LED when patterning a 64 pixel by 64 pixel checker pattern on the DMD. The intensity of the DMD decreases by $0.008\% \pm 0.005\%$ using the 455 nm LED, and $0.008\% \pm 0.006\%$ using the 480 nm LED when patterning a single pixel on the center of the DMD.

Thorlabs M455D3 Efficiency Analysis			
Measurement	**Efficiency**	**Std. Efficiency**	**Theor. Efficiency**
Focussed after alignment mirrors	79%	5.18%	78%
Not focussed after alignment mirrors	27%	1.74%	98%
Focused after DMD with full white screen (FW)	42%	0.55%	52%
Focussed after DMD with 64-pixel checker (64p)	21%	0.35%	26%
Focused after DMD with single center pixel (SP)	0.00553%	0.0005%	0.00002%
Not focussed after DMD FW	41%	0.62%	65%
Not focussed after DMD 64p	20%	0.31%	33%
Not focussed after DMD SP	0.00470%	0.0002%	0.00003%
After the objective with DMD FW	48%	0.95%	32%
After the objective with DMD 64p	49%	0.90%	32%
After the objective with DMD SP	13%	0.95%	32%
Focussed before the objective with DMD FW	35%	0.47%	32%
Focussed before the objective with DMD 64p	35%	0.65%	32%
Focussed before the objective with DMD SP	8%	0.61%	32%
Total efficiency	12%	0.80%	13%
Total efficiency DMD corrected	14%	0.96%	-

Table 4.8: Efficiency measurements for the Thorlabs M455D3 at different stages in the optical setup. FW = full white screen pattern on the DMD. 64p = checker pattern with blocks with a side length of 64 pixels. SP = only a single pixel in the center of the DMD switched on.

Roschwege HighPower LED Koningsblauw Efficiency Analysis			
Measurement	**Efficiency**	**Std. Efficiency**	**Theor. Efficiency**
Focussed after alignment mirrors	70%	1.97%	78%
Not focussed after alignment mirrors	22%	0.50%	98%
Focused after DMD with full white screen (FW)	39%	0.72%	52%
Focussed after DMD with 64-pixel checker (64p)	21%	0.67%	26%
Focused after DMD with single center pixel (SP)	0.00282%	0.0002%	0.00002%
Not focussed after DMD FW	33%	0.71%	65%
Not focussed after DMD 64p	16%	0.81%	33%
Not focussed after DMD SP	0.00262%	0.0001%	0.00003%
After the objective with DMD FW	32%	1.33%	32%
After the objective with DMD 64p	33%	0.79%	32%
After the objective with DMD SP	47%	1.86%	32%
Focussed before the objective with DMD FW	31%	0.92%	32%
Focussed before the objective with DMD 64p	29%	0.92%	32%
Focussed before the objective with DMD SP	11%	0.49%	32%
Total efficiency	8%	0.38%	13%
Total efficiency DMD corrected	11%	0.46%	-

Table 4.9: Efficiency measurements for the Roschwege HighPower LED Koningsblauw at different stages in the optical setup. FW = full white screen pattern on the DMD. 64p = checker pattern with blocks with a side length of 64 pixels. SP = only a single pixel in the center of the DMD switched on.

4.2.3. Resolution

The resolution of the system is measured with the experimental setup as shown in Figure 3.26. The measured FWHMs of the PSFs in Fiji are calculated using a Gaussian fit over the PSF. The measured lateral resolution and the measured DoF are shown in Table 4.10. The z-stack to measure the DoF was created by taking 14 intervals of 10 µm in the optical axis below the focal length and 14 intervals above the focal length. Using these measured resolutions, we calculated the corresponding wavelength using the formula from equation 2.44 and equation 2.45. The full measurement data to establish the resolutions are found in Appendix C.3.

Derived Wavelength and Standard Deviation from Measurements				
Measurement (µm)	**ρ (µm)**	**Std. ρ (µm)**	**Derived λ (nm)**	**Std. derived λ (nm)**
4 µm	3.501 µm	0.166 µm	573.9 nm	27.2 nm
1 µm	3.345 µm	0.115 µm	548.4 nm	18.8 nm
0.5 µm	3.299 µm	0.140 µm	540.8 nm	22.9 nm

Measurement (µm)	**$2\Delta Z$ (µm)**	**ΔZ Std. (µm)**	**Derived λ (nm)**	**Std. derived λ (nm)**
4 µm	88.540 µm	5.201 µm	777.6 nm	45.7 nm
1 µm	89.691 µm	10.522 µm	787.7 nm	92.4 nm
0.5 µm	98.140 µm	2.889 µm	861.9 nm	25.4 nm

Table 4.10: Measured values for the lateral resolution ρ and DoF $2\Delta Z$ with their corresponding derived wavelength values using three differently sized TetraSpeck Fluorescent beads.

By creating a grid of 9 by 12 squares with different side lengths on the DMD, we were able to calculate the resolution of an individual DMD mirror. The light source for creating this DMD pattern was a 455 nm LED. The resolution was measured by taking the standard deviation of a Gaussian fit on the PSF of the squares as shown in Figure 4.5. The increase in lateral resolution and its standard deviation with increasing square side length is shown in Figure 4.6. A linear fit was made to show the linear trend in the second half of the figure. This linear function increases by 1.65 µm for each added pixel in the DMD squares. The full data on the resolution measurements can be found in Appendix C.4.

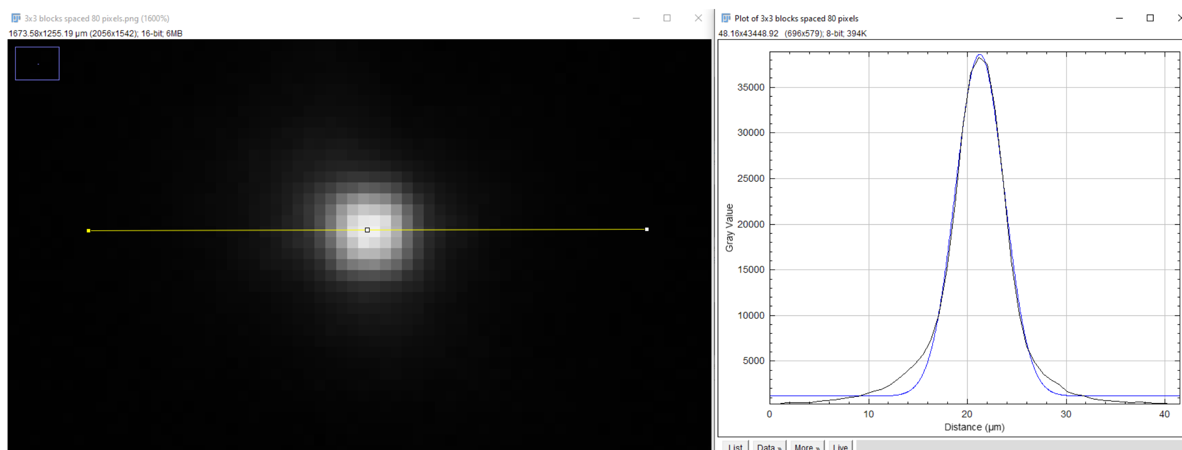

Figure 4.5: A view of Fiji where we measured the PSF of a single 3 by 3 pixel DMD square projection on the chip. The left screen shows the image of the DMD spot. The yellow line determines the cross-section at which the PSF on the right side is measured. A Gaussian fit is put on the PSF, shown as the blue line.

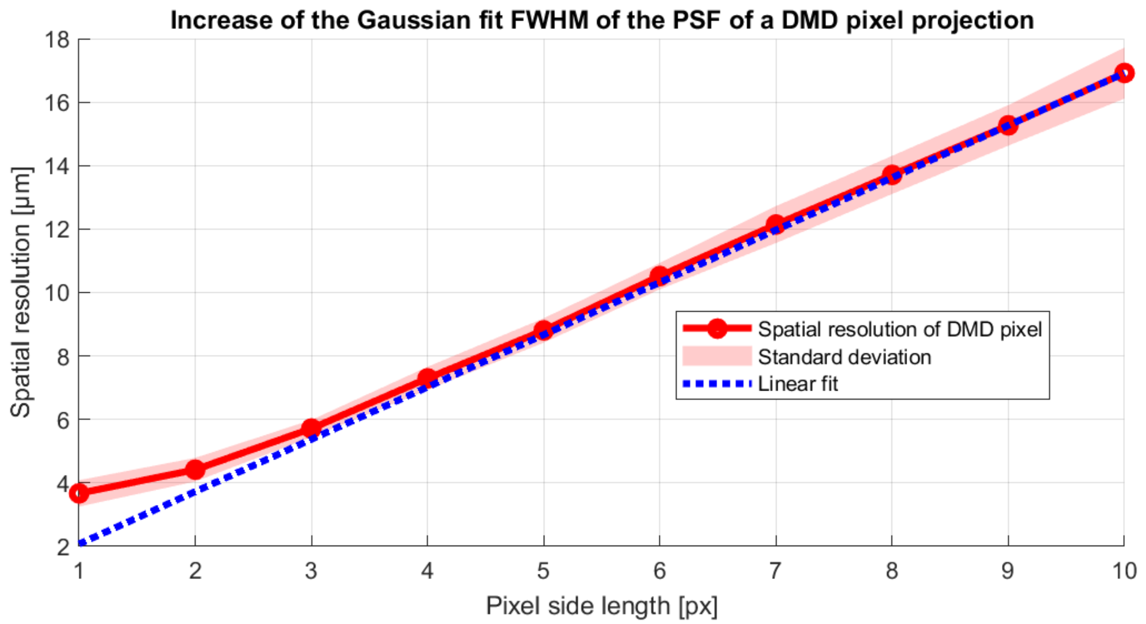

Figure 4.6: The lateral resolution and its standard deviation of a single DMD square. The horizontal axis shows the side length in the number of DMD pixels of this DMD square. The vertical axis shows the lateral resolution in µm. The blue dashed line shows a linear fit $y = ax + b$ with $a = 1.6487$ µm and $b = 0.4282$ µm.

The maximum intensities of the measured pixels in the grid are shown in Figure 4.7 together with their standard deviations. The intensity of the pixels is given in grey value, which is capped at 65535 and shown as the red dashed line. The average maximum intensity seems to converge to this capped maximum with increasing side length.

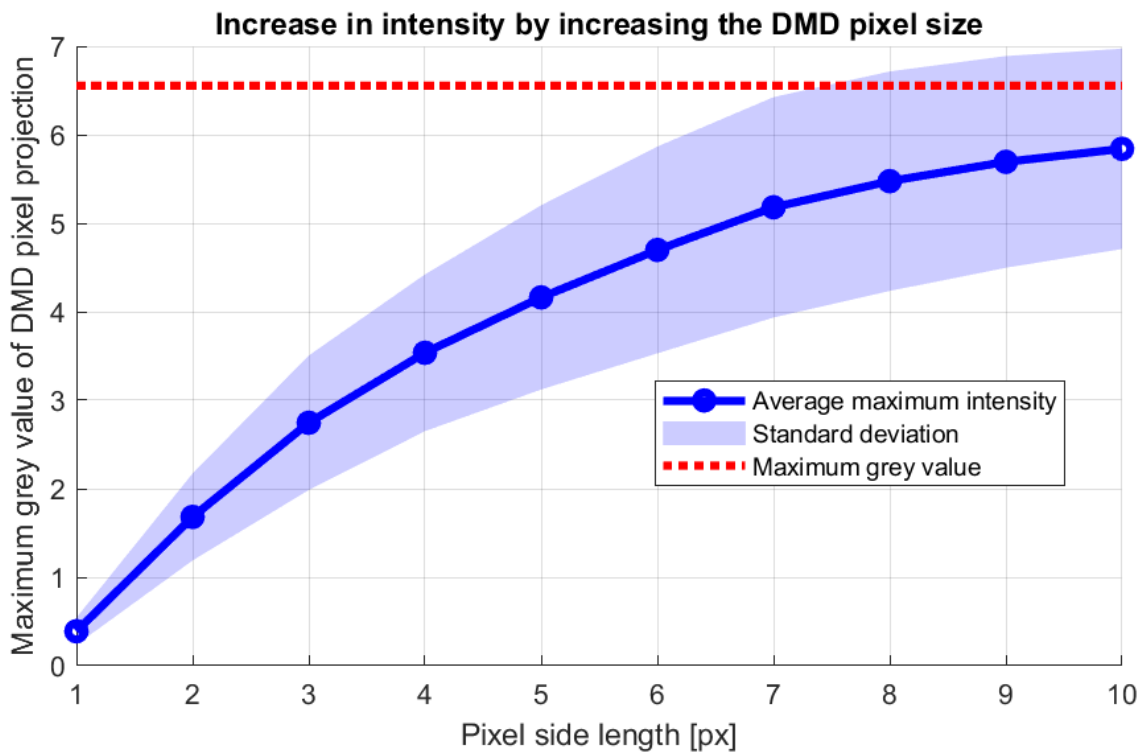

Figure 4.7: The increase in measured maximum intensity depending on the side length of the squares in the grid pattern. The horizontal axis shows the side length in the number of DMD pixels of this DMD square. The vertical axis shows the grey value $\times 10^4$.

To measure the spatial distribution of the intensity of a projection from the DMD, we measured the center intensity of all spots in a 7 by 7 pixel grid as shown in Figure 4.8. The intensity peaks differ in height depending on the location on the chip. The total intensity map is shown in Figure 4.9. The maximum values are all taken relative to the maximum found intensity. There seems to be a small tilt towards the north-west direction in the plot.

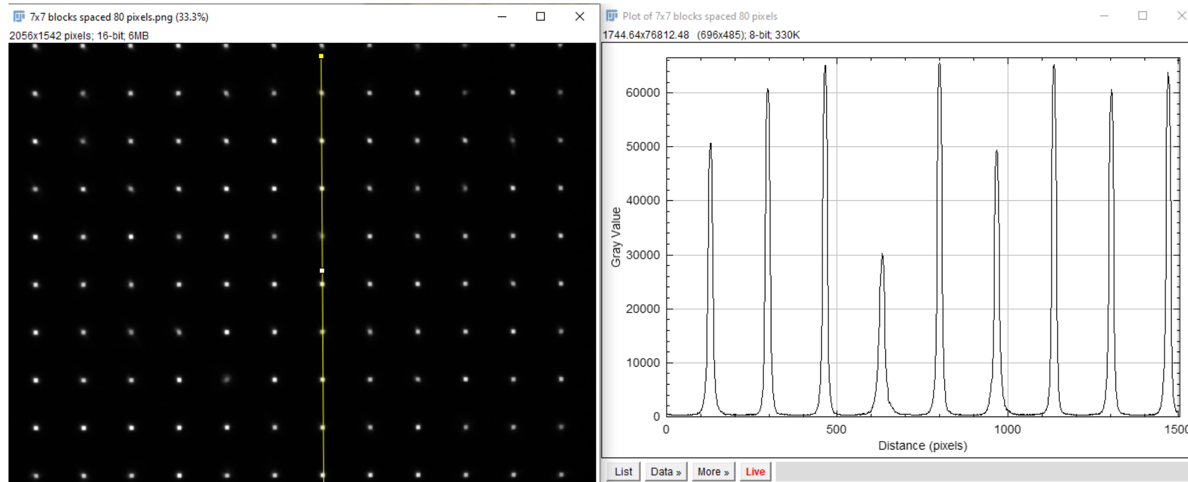

Figure 4.8: A view of Fiji where we show the PSF of nine 7 by 7 pixel DMD square projections on the chip. The left screen shows the image of the DMD spot. The yellow line determines the cross-section at which the PSF on the right side is measured.

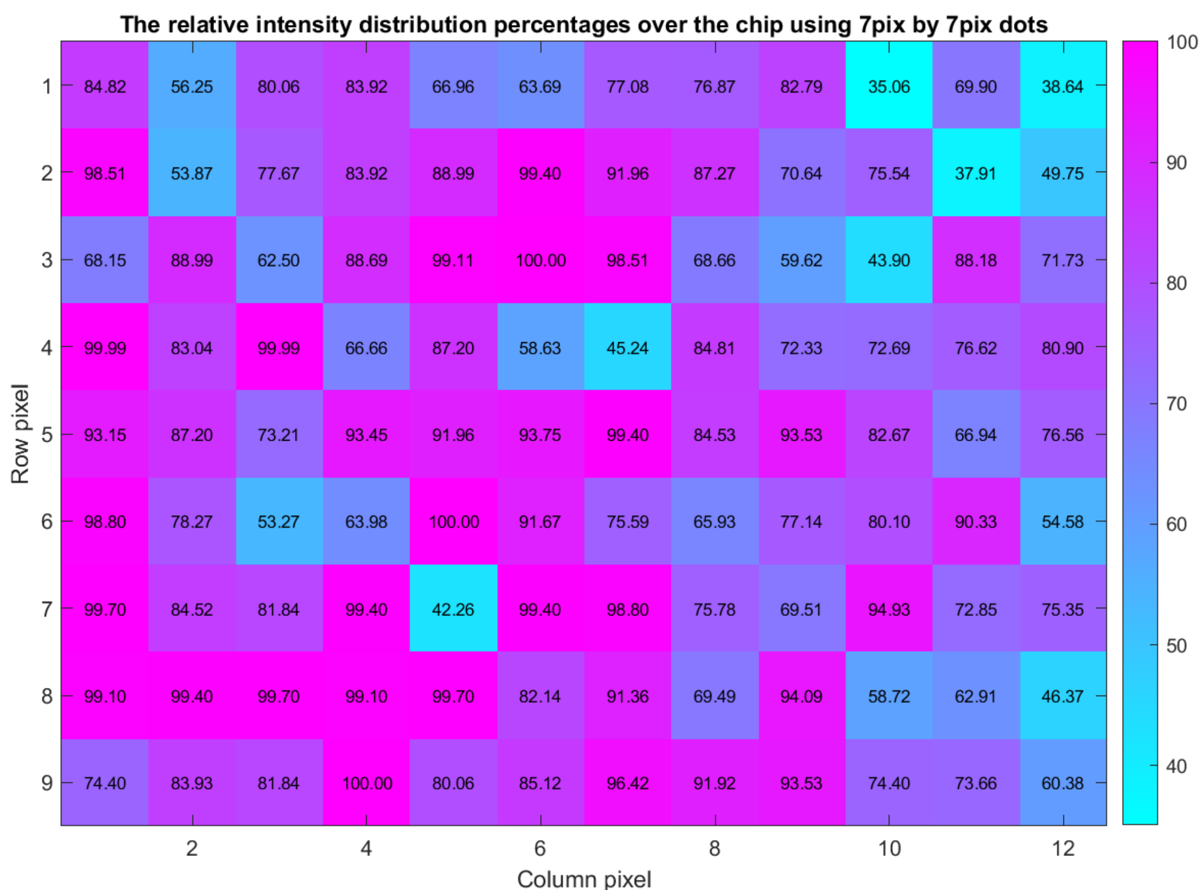

Figure 4.9: A plot showing the maximum intensity distribution of a DMD projection on the microfluidic chip using a 7 by 7 pixel grid as shown in Figure 4.8. The axes denote the positions of the projected dots in the grid. The values inside shown are the relative measured maximum intensities in percentage of the biggest measured intensity.

4.3. Dielectric particle dynamics

4.3.1. Dielectrophoretic force

We measured the DEP force using the method as described in section 3.3.2. In total, 48 measurements were made using different electrical signal frequencies, different DMD patterns, different illumination powers, and different sweep times. The measurements were saved in the uEye cockpit as an .avi file and manually tracked in Fiji to get the position data of four beads, the microbot at four positions, and the sweep pattern at two points in every frame. In total, 50270 positions were carefully selected to minimize the measurement error. Using the MATLAB code from Appendix D.1, the dynamics of the beads, the microbot, and the illumination pattern could be retrieved. Because the beads and/or microbot were not visible in every frame due to the oversaturation, the positions in those frames could not be selected, instead first-order interpolation between the adjacent frames was used. The center position of the microbot is calculated by taking a circle for each combination of 3 measured positions on the microbot and averaging them. Because we defined the DMD pattern animation, we were able to fit a function on the measured positions to recover the pattern dynamics. The fit is created by selecting the frame where the peak of the pattern location is expected, and by selecting the frame when the animation is expected to have started. The measured and calculated dynamics of the beads and the microbot can be found in Appendix D.2.1 and Appendix D.2.2. The fits on the pattern dynamics are shown in Appendix D.2.3.

The frequency dependence of the DEP force on the microbot can be seen in Figure 4.10. These experiments had the microbots submerged in deionized water with 0.05% Tween-20. The illumination power was set to maximum, and the sweep animation had a sweep time of 7 seconds and a thickness of 120 DMD pixels. The force magnitude increases sharply initially and seems to decrease exponentially with the increasing frequency of the electrical signal. The full DEP force measurements on the microbot can be found in Appendix D.3.

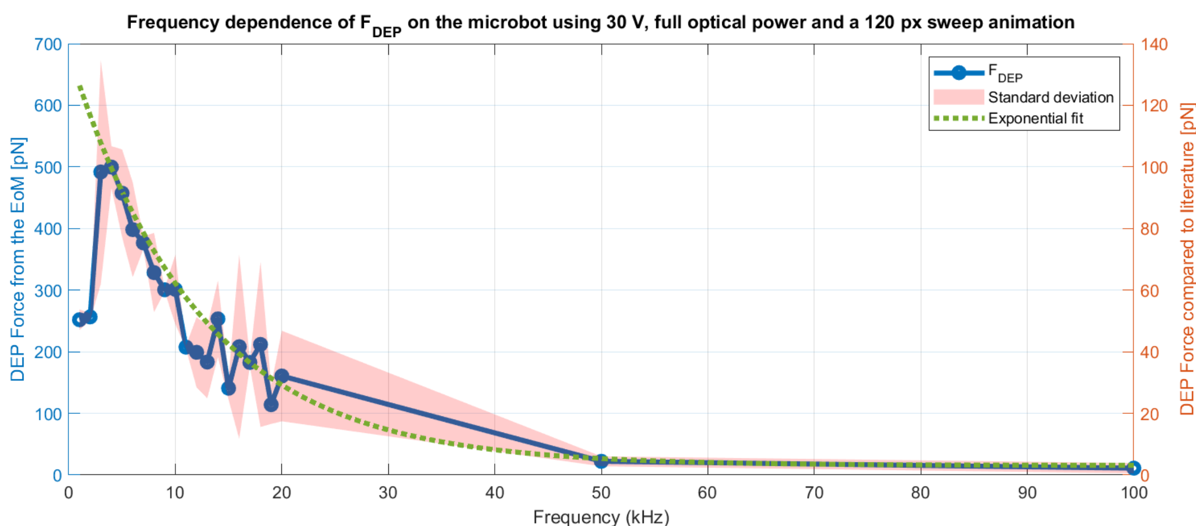

Figure 4.10: The measured DEP force exerted on the microbot using a sweep animation with a sweep time of 7 seconds and a thickness of 120 DMD pixels. The microbots are submerged in deionized water with 0.05% Tween-20. The electrical signal is a square wave with a Vpp of 30 V. The blue line shows the measured averaged DEP forces. The red patch shows the measured standard deviation. The green dashed line is an exponential fitted line of the form $y = ae^{-bx} + c$ with $a = 650$, $b = 0.0817$ and $c = 15$. The left vertical axis shows the DEP force magnitude in pN when calculated using the Stokes drag force. The right vertical axis shows the DEP force magnitude in pN when using the conversion rate from literature [8].

The frequency dependence of the DEP force on the polystyrene 15 µm diameter beads can be seen in Figure 4.11. These measurements were done simultaneously with the measurements of the DEP force of the microbot. The beads also seemed to decrease exponentially with increasing frequency. The fit for this exponential decrease is also shown in the figure as a green dashed line. The fit has the same exponent as the fit from Figure 4.10.

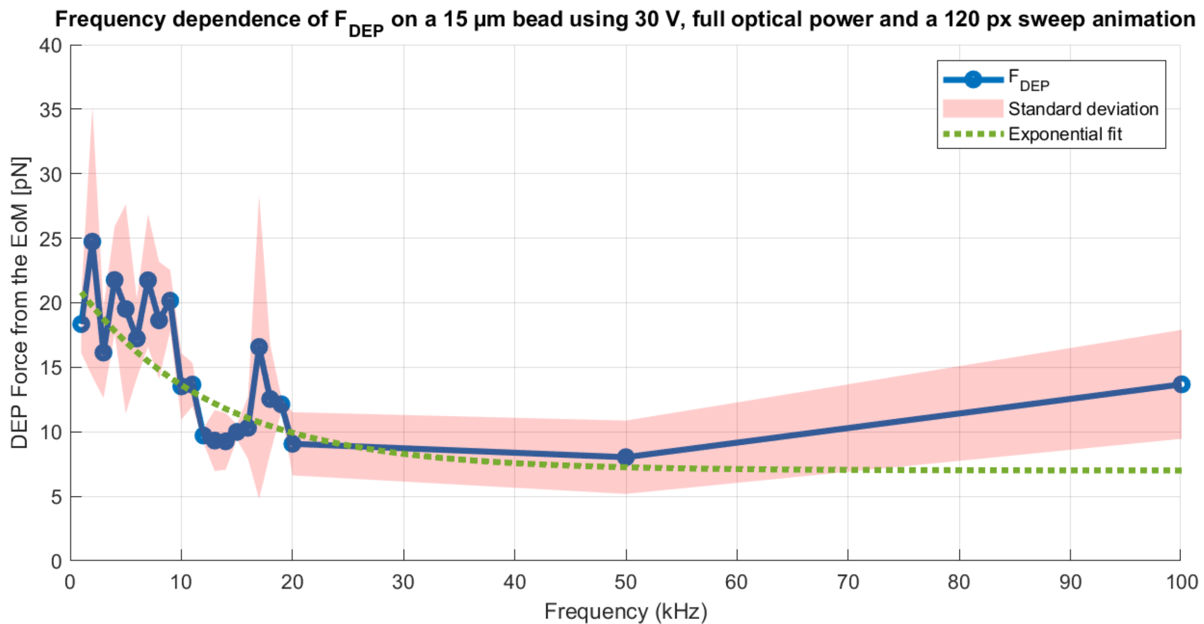

Figure 4.11: The measured DEP force exerted on the 15 µm polystyrene beads using a sweep animation with a sweep time of 7 seconds and a thickness of 120 DMD pixels. The beads are submerged in deionized water with 0.05% Tween-20. The electrical signal is a square wave with a Vpp of 30 V. The blue line shows the measured averaged DEP forces. The red patch shows the measured standard deviation. The green dashed line is an exponential fitted line of the form $y = ae^{-bx} + c$ with $a = 15$, $b = 0.0817$, and $c = 7$. The left vertical axis shows the DEP force magnitude in pN when calculated using the Stokes drag force.

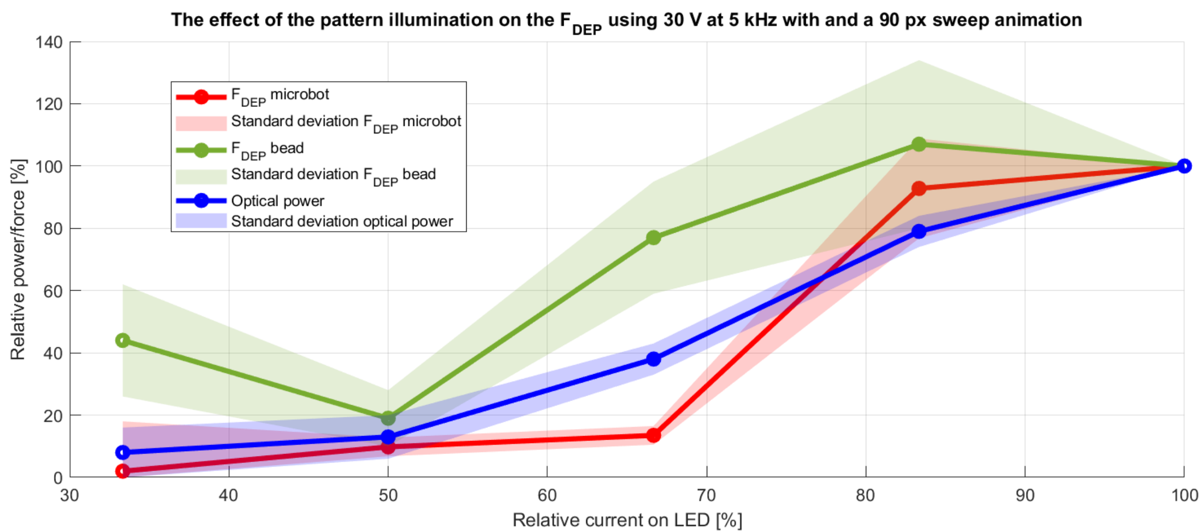

Figure 4.12: The effect of light intensity on the DEP force on the microbot and a 15 µm polystyrene bead. The measurements were done using a sweep animation with a sweep time of 15 seconds and a sweep thickness of 90 DMD pixels. All dielectric particles were submerged in deionized water with 0.05% Tween-20. The electrical signal was a square wave with a Vpp of 30 V and a frequency of 5 kHz. The relative current on the LED is given as a percentage of the current at full power. The relative power/force is given as a percentage of the power/force at full optical power.

The effect of the illumination power of the LED for creating the DMD pattern is shown in Figure 4.12. To see the connection to the optical power, the measured relative optical power is included in the figure, including its standard deviation. The microbot seems to be depending more on the illumination intensity than the beads do.

The effect of the sweep animation thickness is shown in Figure 4.13. Although the effect is not as strong as with the difference in light intensity, the DEP force on the microbot seems to increase with increasing pattern thickness. The standard deviation of the force on the beads is capped to magnify the area of interest.

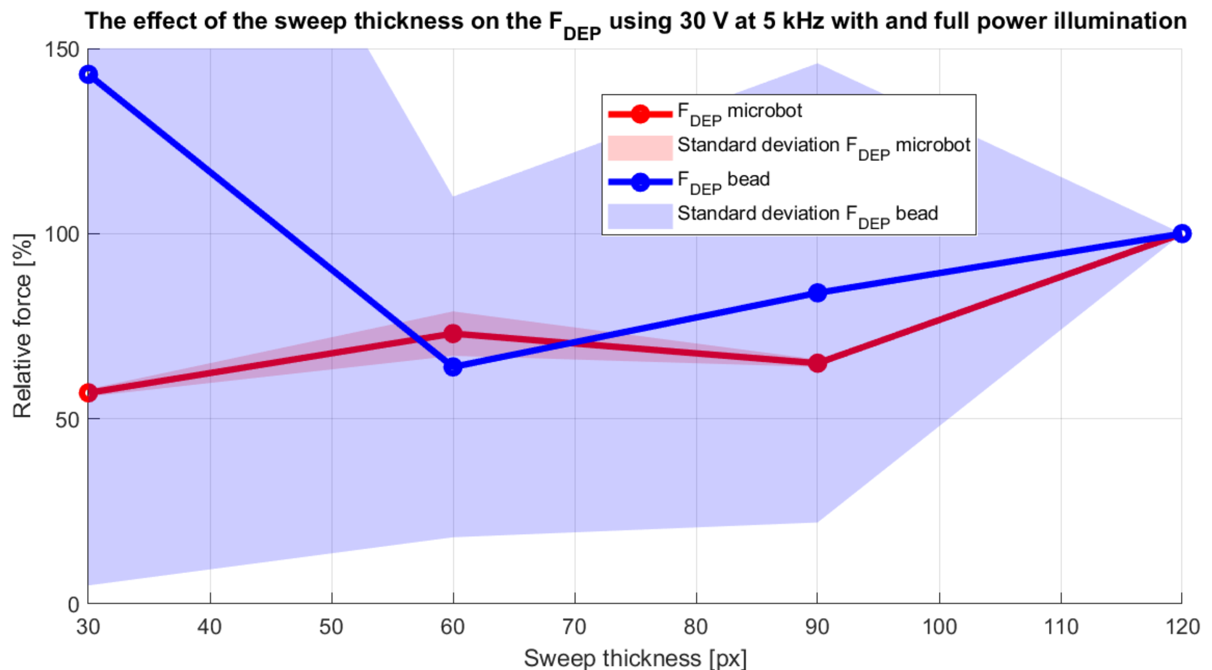

Figure 4.13: The effect of sweep thickness on the DEP force on the microbot and a 15 µm polystyrene bead. The measurements were done using a sweep animation with a sweep time of 15 seconds. All dielectric particles were submerged in deionized water with 0.05% Tween-20. The electrical signal was a square wave with a Vpp of 30 V and a frequency of 5 kHz. The optical power of the 455 nm LED was set to maximum output. The relative force is given as a percentage of the force at the sweep thickness of 120 pixels.

The 10 strongest DEP forces on the microbot found in our OET system are shown in Table 4.11. We can see that the frequencies in this table are all relatively low. The sweep thickness is found to be 120 DMD pixels, and the illumination power is set to maximum for all top DEP forces.

Highest DEP Forces Found for the Microbot					
Sweep (s)	**Freq (kHz)**	**Sweep (pix)**	$\mathbf{P_{L,rel}}$	**DEP (pN)**	**Std. DEP (pN)**
7	4	4	1	499.7	33.91
7	3	4	1	491.72	181.63
7	5	4	1	457.33	71.03
3	1	4	1	425.03	9.97
7	6	4	1	398.19	76.93
7	7	4	1	376.7	10.4
7	8	4	1	328.49	64.25
7	10	4	1	301.18	56.32
7	9	4	1	300.59	2.87
15	1	4	1	296.02	33.68

Table 4.11: Highest DEP forces found for the microbot under different experimental conditions. The DEP force is expressed in picoNewtons (pN).

The 10 weakest DEP forces on the microbot found in our OET system are shown in Table 4.12. We can mostly see low optical power and high frequencies, which are contrary to the experimental conditions found at the strongest DEP forces. The difference between the average DEP force and the standard deviation of the DEP force is small, showing a relatively large measurement error. The DEP force of 4.24 pN translates to a gear velocity of 3.72 μm/s.

Lowest DEP Forces Found for the Microbot					
Sweep (s)	**Freq (kHz)**	**Sweep (pix)**	$\mathbf{P_{L,rel}}$	**DEP (pN)**	**Std. DEP (pN)**
15	5	3	0.33	4.24	30.60
7	100	4	1.00	11.04	8.38
15	18	1	1.00	18.82	3.00
15	5	3	0.50	18.92	6.54
7	50	4	1.00	22.20	8.04
15	5	3	0.67	26.08	6.42
15	15	1	1.00	58.68	2.70
15	13	1	1.00	61.89	1.51
15	15	3	1.00	113.77	22.07
7	19	4	1.00	114.13	31.23

Table 4.12: Lowest DEP forces found for the microbot under different experimental conditions. The DEP force is expressed in picoNewtons (pN).

Measurements done by Dion Jetulahi showed a DEP force on a 15μm diameter polystyrene bead of 12.5 pN. This experiment was done using an older iteration of the optical setup and microfluidic chip, and pure deionized water was used as the dielectric medium. By creating an advance optical setup and microfluidic chip, we were able to push the maximum measured DEP force on the same type of bead to 29 $\pm$ 5 pN using deionized water with 0.05% Tween-20.

4.3.2. Frequency range

The real part of the derived Clausius-Mossotti factor using the found conductivities and using the theoretical permittivities is shown in Figure 4.14. The orange lines denote the real part of the CM-factor of the polystyrene beads. The blue lines denote the real part of the CM-factor of the PDMS microbot. The dashed lines indicate the CM-factors using 0.05% Tween-20. This addition seems to decrease the CM-factor at low frequencies for the beads and seems to shift the CM-factor to the right for the PDMS. The CM-factor for the beads can be both positive and negative in theory. The CM-factor for the PDMS microbots can only be negative and decrease in magnitude with increasing applied frequency. We measured the frequencies when the microfluidic chip started to deteriorate due to electrolysis. These measurements were done using different voltages, different Tween-20 concentrations, and different microfluidic chips. The resulting "danger zones" are shown in Figure 4.14 as the red patches. The full measurement data on the electrolysis can be found in Appendix D.4.

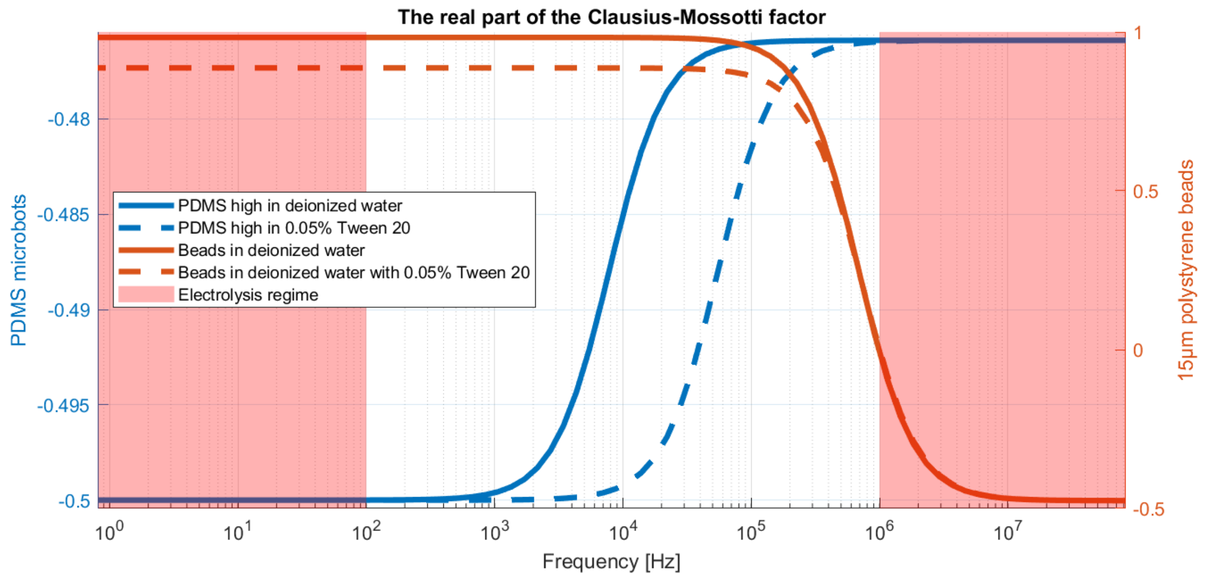

Figure 4.14: The real part of the Clausius-Mossotti factor of both the polystyrene beads and the PDMS microbots in both pure deionized water and deionized water containing 0.05% Tween-20, shown as dashed lines. The values of the CM-factor of the beads are shown on the right vertical axis in orange. The values of the CM-factor of the microbots are shown in blue on the left vertical axis. The red patches show the frequency regions where the chips started to deteriorate due to electrolysis.

5 Discussion

In this chapter, we critically reflect on the findings presented in Chapter 4 by benchmarking and evaluating the performance of the OET system to deepen our understanding of its underlying physical principles, identify limitations in the current implementation, and uncover opportunities for further optimization. The discussion follows the structure of the results chapter: starting with the microfluidic chip, moving to the optical setup, and concluding with the analysis of the dielectric particle and the DEP force. For each component, we interpret the outcomes, assess their significance, and propose concrete steps for improvement. In doing so, we lay the groundwork for future research toward more precise, scalable, and accessible biomedical technologies.

5.1. Microfluidic chip

5.1.1. Benchmarking results

Discovering how to make the microfluidic chips for the OET was a task that took many days. Applying just a little too much force on a part of the chip often resulted in breaking it, making it unusable. This was partly due to the fragility of the chip. When trying to remove a broken ITO cover slip, the glass would break into more pieces, making it necessary to remove the layer of double-sided tape to clear the debris. However, removing the double-sided tape often caused flakes of the a-Si:H photoconductive layer to come off as well, deteriorating the photoconductive properties. Using the improved chip design removed the problem of the chip breaking during wiring, but it did not eliminate the risk of breaking when placing the ITO cover glass on the tape, or when attaching the inlets to the cut-out holes.

The measured resistance of deionized water was previously benchmarked in the experiment [77]. The resulting conductivity of deionized water with 0.05% Tween-20 was found to be 35 ± 6 μS/m, which is 144 times lower than the conductivity reported in literature [8]. This discrepancy may be due to the experimental setup: the voltage from the wire inside the fluid does not travel directly to the other wire, but instead spreads across the small volume of fluid used in the measurement. This can also be due to the 2-probe measurement used, which measures, besides the resistance of the medium, also the resistances of the wires, probes, and contacts [100]. Nevertheless, this result confirms that the conductivity increases when Tween-20 is added. Limitations of the experimental setup to measure the electrical properties were also clearly visible in the experiments measuring the relative permittivities of materials inside the microfluidic chip. Measuring the permittivity of the tape was successful. The difference between the measured and theoretical value was only 4.3%. However, the measured capacitance of the photoconductive layer was 115 times smaller than expected. A likely cause is that ambient light in the lab partially activated the photoconductive layer, turning it into a capacitor with leakage current and affecting the measurement. The same issue likely influenced the capacitance measurements of the microfluidic chip filled with different dielectric media. The measured relative permittivity of water was much higher than expected. We could not find reliable reference values for the relative permittivity of water with low concentrations of Tween-20. Still, we expect it to be close to that of pure water, since the concentration percentages are small.

The reflectance of the ITO glasses was measured to be 15% $\pm$ 4% across all measurements. This corresponds well to the reflectance values found in literature, as shown in Figure 2.4. The difference in reflectance between the ITO layer with the highest resistance and the one with the lowest resistance is just over 2%, which is a very small variation. It is therefore justified to choose the ITO layer with the lowest resistance in the design of the microfluidic chip, since its effect on the strength of the electric field is proportionally greater than the impact of the slightly reduced transmittance.

The absorption coefficient of the a-Si:H appears to follow the same trend as the coefficients found in literature, as can be seen in Figure 4.2. Due to the limitations of the power sensor, the absorption coefficients theoretically higher than 1.1×10^7 m^{-1} are clipped, resulting in a flat line at that value. The main goal of this experiment was to determine which illumination source would be most suitable for creating a well-functioning OET system. Based on the results, we can conclude that a light source with the smallest possible wavelength in the visible spectrum should be used to generate a strong electric field gradient, and therefore a strong DEP force [101]. We also conclude that, for imaging purposes, a light source with the longest possible wavelength in the visible spectrum is preferred. Although this results in a weaker DEP force, due to the reduced contrast in conductivity between illuminated and non-illuminated areas, it allows for better visualization of the particles on the chip. The increase in reflectance of a-Si:H above 60% for wavelengths longer than 715 nm is consistent with values reported in literature [102]. To improve the accuracy of future measurements of the optical properties of a-Si:H, a stronger initial illumination is needed. This would increase the detected signal on the power meter and reduce measurement uncertainty.

5.1.2. Design opportunities

The microfluidic chip we designed in this thesis is a good starting point for creating a robust and reliable workspace for manipulating the dielectric particle in the OET. That does not mean there is no room for improvement; on the contrary. One area to explore is the wiring on the microfluidic chip, which could be improved by redesigning the 3D chip holder. This holder could apply a gentle force on the top ITO microscope cover slip to ensure proper contact with the conductive tape. Currently, the weight of the chip alone is not sufficient, causing it to hover just above the tape without closing the electrical circuit. To attach the wires to the conductive tape. This might be achieved by soldering or gluing the wires onto the conductive tape before placing the microfluidic chip. Another point of improvement lies in how the inlets are attached to the chip. At the moment, they are glued on manually using two-component epoxy. This occasionally results in small amounts of glue entering the channel, partially blocking it and preventing microbots from moving in or out. This could be solved by creating a simple alignment tool that allows precise placement of the inlets without exerting too much pressure, while still ensuring a leak-tight seal.

There is also room for improvement in the dimensionality of the microfluidic chip. We are currently limited by the size of the ITO-covered microscope slides, which restricts the distance between the two inlets. Suppose we want to use an additional objective with higher magnification and a larger numerical aperture for fluorescence imaging. In that case, the objective must fit between the inlets to focus on the particles. This means that, in order to enable fluorescence imaging, a larger microfluidic channel is required. Another potential improvement is the use of double-sided tape with greater thickness. While this reduces the electric field strength—and therefore the DEP force—it introduces the possibility of three-dimensional particle manipulation [103]. The increased thickness also makes it harder for the voltage to pass directly through the fluid from the photoconductive layer to the top electrode, resulting in a capacitor with reduced leakage current [104].

A third improvement that we can explore in future research is the use of a more complex photoconductive layer. Mirthe Folkerts investigated the possibility of using a p-i-n junction a-Si:H layer, which was also provided by the Else Kooi lab at Delft University of Technology [75]. A more advanced photoconductive layer showed higher photoconductivity, which allows the OET system to function with dielectric media that have higher conductivities, such as those used in research on biological cells [40]. Although the research was not yet sufficient for a fully functional OET, it provides a solid starting point for expanding the usability of the system in healthcare-related applications. If we want to use the OET setup to image living biological cells, we also need to be able to regulate the temperature of the dielectric medium. This can be controlled by connecting a Peltier heater to the microfluidic chip [105]. An additional improvement to the photoconductive layer could be the addition of a PEG layer to reduce particle adhesion. While the amount of adhesion has already been reduced by adding 0.05% Tween-20 to the dielectric medium, PEGylation has shown promising results in literature [56].

5.2. Optical setup

5.2.1. Benchmarking results

The found magnifications in the optical setup all seem to match the magnifications calculated using the theoretical focal lengths. The magnification from the chip to the camera has the largest relative standard deviation. This is most likely because the objects seen in the microfluidic chip are defined by the absence of light, rather than its reflection. The illumination used to measure the magnification from the chip to the camera was the lamp with the red plastic filter, placed on the opposite side of the microfluidic chip. This effect is most apparent in the measurement of the 15 μm diameter polystyrene beads. Due to the shadow cast by the beads on the chip, the beads appear slightly larger, resulting in a slightly smaller calculated magnification.

The theoretical efficiency of the full system was estimated at 16%. An additional achromatic lens with an efficiency of 80% was used during the measurement of the optical efficiency, lowering the theoretical efficiency of the full system to 13%. The measured optical efficiency using the Thorlabs M455D3 was found to match this value. The efficiency measured using the Roschwege HighPower LED Koningsblauw, however, was found to be below the theoretical estimate. One possible explanation is that the Roschwege LED has a larger beam angle than the more expensive LED from Thorlabs, resulting in a less collimated light beam and thus greater optical losses. Another reason for the discrepancy could be the theoretical optical efficiency assumed for the DMD. The actual measured efficiency of the DMD was around 15% lower than the value used in the calculations. The optical power density on the microfluidic chip was measured to be 4.45 ± 0.06 mW/cm^2 using the Roschwege LED, and 16.8 ± 0.1 mW/cm^2 using the Thorlabs M455D3. The measured power density of the Thorlabs LED is about 7.5 times lower than the value reported in literature for effective microbot manipulation [15]. Since the photoconductivity increases linearly with the optical power density, this could explain why the observed DEP forces were lower than expected [36].

The measured lateral resolution of the optical setup was found to be close to the expected one using the average wavelength of the used TetraSpeck fluorescent beads. The corrected wavelength that would have resulted from the measurement of the beads that were smaller than the found resolution is found to be 544.6 ± 5.4 nm. The reason why this wavelength is found to be smaller than the average wavelength could be because more yellow-green and orange beads were measured than the dark red colored ones, shifting the average to be smaller. Another reason could be that the bead dyes did not have the same brightness to begin with. The found DoF was found to be larger than the theoretical DoF, even when considering the corrected wavelength from the lateral resolution measurement. The reason for this could be the inaccuracy in the z-stack. The micrometric screw was manually operated, leaving a lot of possibility for introducing error. Another reason could be due to the beamsplitter inducing aberrations in the system, which depends on the distance [106]. We already saw in equation 2.46 that we needed a correction term to determine the DoF of a system with a low NA. Together with inaccuracy in the step size in the distance from the focal point, we find good evidence why this error is to be expected.

The measured resolution of the created DMD squares increases with the number of pixels added to the side length of these squares. The linear fit from Figure 4.6 shows that the projected square size increases by 1.65 μm for each added micromirror. We calculated that the size of a single micromirror should be 1.7 ± 0.6 μm on the microfluidic chip, which matches the linear fit very well. The average maximum intensity with increasing DMD square size appears to converge toward the maximum grey value, as seen in Figure 4.7. This is expected, since the PSFs of the pixels in the square overlap and add up due to diffraction. The spatial distribution of the DMD projection, shown in Figure 4.8, indicates that the DMD introduces a slight tilt aberration. This is not surprising, as the DMD was difficult to align optically. The projection used to generate this distribution was made on a microfluidic chip containing a photoconductive layer. Surface irregularities in the photoconductive layer, dust on the optical elements, or small alignment errors could explain the observed random spatial irregularities in the projection.

5.2.2. Design opportunities

The objective we used had an NA of 0.1 and a magnification of 4X when combined with a 180 mm tube lens. This works well for controlling microbots since they are relatively large. If we want to control more microbots simultaneously, we could consider using a camera with a larger sensor. This would increase not only the FoV of the camera, but also the FoV of the DMD. If we want more detailed imaging, we could include a separate fluorescence microscope with higher magnification, imaging from the top of the microfluidic chip to avoid the photoconductive layer. Since the blue LED does not excite fluorescence very effectively, fluorescence imaging would not interfere with the current optical path. By using a separate optical path, we could combine a wide FoV for control with high-magnification imaging for analysis.

The blue LED we used underperforms compared to the patterning illumination sources found in literature. We can increase the photoconductivity by replacing it with a stronger light source to match the state-of-the-art. To still be able to image the microfluidic chip properly, we can include a long-pass filter to reduce the intensity of blue light reaching the camera sensor. This prevents oversaturation and allows for better automatic tracking of the dielectric particles in the chip. Another way to improve tracking is by aligning the camera and DMD frame rates. In our experiments, the framerates were not synchronized, which resulted in frames where either the particles or the DMD pattern were missing. If we manage to connect these two devices, we can control how many frames the DMD pattern is visible per cycle. To reduce noise in the measurements, the optical setup should also be shielded from ambient light in the laboratory.

We can improve the overall optical setup by cleaning all optical elements and realigning them. To make it easier to align the DMD, we can place it flat, facing downward on a lifted stage, so that it doesn't rotate due to the weight of its control board. Once fixed, the entire optical path from the DMD should be positioned at the appropriate distance from it. We expect this to result in a more uniform intensity distribution on the microfluidic chip and a reduction of diffracted stray light from the micromirrors. The optical setup was built on a small working area, which challenged us to design it efficiently, but also prevented us from using the minimal number of optical elements, which potentially introduced aberrations. Therefore, a bigger working area is expected to improve the alignment and the optical efficiency.

To improve control over the DMD, we need to create more efficient input signals. The Python script we developed for pre-made animations works well, but for real-time control, it consumes a lot of memory, causing the computer to run out after a short time. To further automate the system, we can replace the manually operated micrometric screw with a motorized stage. This would allow us to make precise Z-stacks to find a more accurate DoF and automatically bring particles of interest into focus. Another improvement would be to control the electrical signal using the same code as the DMD and the camera. Centralizing this control would not only simplify the workflow but also make it possible to safeguard regions from electrolysis by avoiding the dangerous input signals.

5.3. Dielectric particle

5.3.1. Dielectrophoretic force

The main purpose of the OET was to create a controllable DEP force that moves dielectric particles. Implementing this successfully for the microbots proved to be a significant challenge. Getting the robots off the substrate in one piece took multiple attempts. We used three batches of microbots produced by the Nanoscribe. Since the microbots had to be shipped from the University of Melbourne, each failed attempt caused delays of several weeks before a new method could be tried. Using the final batch, we were able to remove the microbots using the ultrasonic cleaner successfully, but increasing their concentration by carefully pipetting out water was not very successful. This could be because the robots did not survive the centrifuge, or because they were lost in the pipetting process. The small number of microbots we managed to get into a microfluidic chip was not all functional, which severely limited our measurements. This was partly due to the microfluidic chips themselves not being operational. When the robots were flushed out of faulty chips, they were lost in the process. In working chips, some robots were stuck at the edges of the double-sided tape or adhered to the bottom, making them unusable for OET measurements. In the end, we succeeded in getting a single microbot to move properly, which enabled the measurements presented in Section 4.3.1. Unfortunately, after a day, the dielectric medium inside the functional chip had evaporated. When we carefully pipetted in new medium, the liquid did not spread across the full chip, making the microbots unreachable.

The maximum measured DEP force on the microbot was found to be 500 ± 30 pN when calculated using the described equations of motion, or 103 ± 7 pN when using the conversion factor from literature [8]. This measured DEP force using the conversion factor is roughly three times smaller than the value reported in the literature. A noteworthy difference between our measurement and the one in the literature is that they used an electrical signal at 20 kHz, which was not the optimal frequency in our case, as shown in Figure 4.10. Additionally, their optical intensity was 7.5 times higher than ours. They determined the DEP force by measuring the fluid velocity required to escape the OET trap. Since we did not have access to a precise pump, we were unable to use the same method. Another factor may have been the dielectric medium. Although they also used deionized water with 0.05% Tween-20, the conductivity in their case was 5 mS/m and thus significantly higher than in our setup. The DEP force measured on 15 µm beads in our system was 12.5 pN using deionized water in a chip of the second design [74], and 29 ± 5 pN using deionized water with 0.05% Tween-20 in a chip of the final design. In literature, a DEP force of around 35 pN has been reported for beads of the same size [96]. This suggests that, with the improved chip design, our measurements are approaching the expected values. The pattern used for bead manipulation in that study had an optical power density of 0.65 W/cm^2 [107], which is roughly 38 times higher than in our setup. This again could explain part of the performance gap. An interesting observation with the polystyrene beads was that they appeared to be attracted to the illuminated region from a much larger distance than expected based on the DEP range. This gave the impression that the beads were being influenced by LACE, which is known to dominate further away from the illuminated patterns [49]. The microbots, however, did not appear to respond to this effect, suggesting that further investigation is needed.

The effect of illumination power density was already apparent from Figure 4.12. For both the microbot and the polystyrene bead, the strength of the DEP force appears to increase with increasing light intensity. The relative force on the bead seems to follow the same curve as the relative power output of the LED. Interestingly, the relative force on the microbot shows a threshold behavior, increasing rapidly at 83% intensity. To better understand the influence of pattern intensity, more measurements are needed to map the exact shape of the intensity-response function in greater detail. The effect of pattern size was investigated as shown in Figure 4.13. The bead was manipulated most effectively using an illumination pattern of 30 DMD pixels. This observation aligns with findings in the literature, where the DEP force was strongest using a 20-pixel pattern, after which the force decreased [108]. The more constant effect of pattern size on the microbot has also been observed in literature, where the DEP force using a 30-pixel pattern was only slightly lower than that with 60 pixels [15].

The CM-factor shown in Figure 4.14 was measured for the beads in deionized water [74]. The attenuated CM-factor for beads in deionized water with 0.05% Tween-20 was estimated using the measured conductivities of the dielectric particle and medium, assuming constant relative permittivity. This estimate was not verified experimentally by observing the effect on the DEP force of the beads. One reason for this is that we avoided measuring too closely to regions where electrolysis occurs. This window makes the DEP force on the beads appear only positive. When comparing the CM-factor to the measured DEP forces in Figure 4.11, little correlation is found, making it difficult to assess how accurately the CM-factor describes the frequency dependence of the DEP force. For the microbots, the CM-factor was theorized to have negligible influence based on the dielectric properties of both the medium and the microbot itself. As a result, verifying the CM-factor would require many more measurements to reduce the standard deviation of the DEP force. The frequency regions at which chip deterioration began were determined experimentally. No clear theoretical model was found in the literature for the behavior of deionized water with Tween-20 in a capacitor-like configuration. Electrolysis at low frequencies was expected based on general electrochemical principles [17]. The deterioration observed at higher frequencies was less anticipated, but we speculate that these frequencies may break down the PEG in the water, releasing oxygen gas and forming bubbles in the dielectric medium. This hypothesis needs to be supported by further research, including both theoretical justification and experimental confirmation. It is important to take these deterioration frequency zones into account when applying different frequencies to an OET system, to avoid damaging and wasting functional microfluidic chips.

5.3.2. Design opportunities

The DEP force measurements in this research were limited by the scarce number of working microfluidic chips containing movable dielectric particles. Therefore, conducting more experiments with additional chips of the same design, and with more movable dielectric particles, would already greatly increase the accuracy and validity of the results. By applying the ultrasonic cleaner directly to the microbots and submerging the substrate in less water, we could avoid the need to concentrate the microbots manually. This would eliminate several processing steps and significantly increase the chances of recovering more functional microbots for use in the OET system. The measurements performed on the microbots and beads using varying illumination intensities and pattern thicknesses should be repeated with smaller step sizes to more precisely identify the actual dependencies. Another factor that is frequently studied in the literature is the effect of voltage on the DEP force [8], [96], [107]. Measuring this effect could help us benchmark the performance of our OET system more effectively. We could also improve the comparability to the literature by modifying the experiment to include measurements of the fluid velocity required to escape a DEP trap. This would require precise control of flow inside the microfluidic chip, which could theoretically be achieved using closed-loop flow control with a pump.

A measurement we wanted to explore was the effect of different microbot volumes, which would be a valuable novelty in the literature. All current measurements on the microbot were performed using a version with adhesion-reducing semispheres on its surface, making it impossible to compare the results to microbots without this surface adjustment. There are many possibilities for testing different designs using the Nanoscribe, opening up a wide range of interesting experiments that could help in characterizing and quantifying microbot design in great detail. The electrolysis measurements performed in this research were entirely experimental, meaning there is a significant opportunity to contribute new knowledge to this important aspect of the OET field. This could be better quantified by developing a reusable setup, which would avoid destroying working microfluidic chips in the process.

Finally, to make it easier—and much faster—to translate the measured movement from an .avi file into a calculated DEP force, we would need to implement a script that automatically and precisely tracks the movement of the dielectric particles. For this to work, the microbots and beads must be clearly visible and in focus. As discussed earlier, this requires synchronization between the framerate of the DMD and the camera. In our experiments, we used a relatively simple sweep animation with varying settings to measure the DEP force. However, the DMD offers a large degree of freedom in creating patterns and, therefore, designing a wide variety of experiments. One idea is to precisely measure the effect of the distance between a moving pattern and a moving dielectric particle on the resulting DEP force. By measuring the DEP force under many different conditions, and by using a grey-box estimation learning model, we could build an accurate representation of the dielectric particle within the OET setup [109]. This would not only deepen our understanding of the system's underlying dynamics, but also enable the creation of accurate simulations. These simulations could be used to design and optimize complex swarm control strategies for multiple printed microbots, serving as a strong catalyst in making OET a viable tool for the envisioned next generation of healthcare technology.

6 Conclusion

In this research, we built a functional optoelectronic tweezer (OET) setup capable of dynamically manipulating PDMS-printed microparticles. The system required the design of a transparent microfluidic capacitor, incorporating a photoconductive layer to enable active manipulation of the DEP force in the OET. The dynamic control patterns were generated by a custom-designed optical setup, developed to project specifically shaped light patterns onto the chip. The microparticle used in this study was an adapted microgear robot, inspired by the design presented by Zhang et al. [8]. To evaluate the system's performance and conclude this research, we reflect on the main research question by addressing the corresponding subquestions. These answers together form a well-reasoned and evidence-based conclusion to the central research question.

1. **How can an optoelectronic tweezer system be realized at TU Delft?**

   a. *How can the optical system be aligned?*
   To align the optical system, we developed a custom alignment tool based on a red collimated laser beam, which can be mounted on the Thorlabs cage system. This enabled precise placement and focusing of each optical element in the beam path, verified directly through the camera. To further improve alignment accuracy and reproducibility, we incorporated adjustable mirrors, making the alignment of the DMD significantly more manageable.

   b. *Which illumination source is most optimal for the OET setup?*
   Based on insights from literature and experimental validation, we found that the photoconductive response of the chip was strongest when using light with a shorter (bluer) wavelength. This informed our decision to select the most powerful available blue LED from Thorlabs, operating at 455 nm, to serve as the optimal patterning light source. For imaging the entire microfluidic chip without unintentionally exciting the photoconductive layer, we used a red-filtered incandescent light source at 715 nm. This allowed sufficient contrast to visualize the particles while minimizing interference with the DEP actuation.

   c. *How can a working fluorescence microscope be integrated into the OET setup?*
   We demonstrated that the optical setup is suitable for fluorescence imaging by successfully exciting fluorescent beads and capturing their emission using the existing OET system. The excitation spectra of the beads showed minimal overlap with the illumination wavelength used for DEP actuation, indicating that advanced fluorescence imaging can be performed without interfering with OET functionality.

d. *How can the microfluidic chip be provided with the appropriate electric potential, fluid velocity, and thermal stability?*

The electrical potential was generated using an Agilent 33220A function generator and amplified with a Thurlby Thandar Instruments WA301 Wideband Amplifier, allowing voltages of up to 30 Vpp. The function generator was configured to produce square waves at specific frequencies, providing a stable and flexible voltage source for creating the electric fields required for DEP manipulation. Fluid velocity within the microfluidic chip can be controlled using a syringe pump, which is connectable to the inlets, enabling precise flow regulation when needed. Temperature control of the dielectric medium could, in theory, be achieved by integrating a Peltier heater, allowing for localized heating or cooling of the chip environment.

An optoelectronic tweezer (OET) system, which consists of a custom-designed optical setup and microfluidic chip, was successfully built at TU Delft. The system achieved a magnification of 4.2 ± 0.2 from the chip to the camera, and 0.16 ± 0.06 from the DMD to the chip. A single DMD pixel was projected onto the microfluidic chip with a physical size of 1.7 ± 0.6 μm. The resulting field of view (FoV) of the optical system measured 1.67 ± 0.09 mm by 1.23 ± 0.07 mm. The optical efficiency of the system, using a 455 nm blue LED, was measured at $12 \pm 0.8\%$. The lateral resolution, determined using 1μm TetraSpeck fluorescent beads, was found to be 3.4 ± 0.1 μm, with a depth of field (DoF) of 90 ± 10 μm. The electrical signal applied to the microfluidic chip was sufficient to enable effective OET manipulation. Moreover, the DMD demonstrated high versatility in pattern generation, making it a powerful tool for future advanced particle control and microbot applications.

2. How can a suitable microfluidic chip be developed for OET?

a. *Which materials (conductive layer, photoconductive layer, medium, etc.) are suitable for use in the OET chip?*

For the transparent electrodes, ITO-coated microscope slides and coverslips were purchased from Daimon Coatings Ltd., with a specified resistance of 8–12 Ω and a measured optical transmittance of $15 \pm 4\%$. The photoconductive layer in the microfluidic chip consisted of a 1 μm thick hydrogenated amorphous silicon film, with an absorption coefficient consistent with values found in literature. As a dielectric medium, deionized water with 0.05% Tween-20 was used to reduce particle adhesion. The measured conductivity of this solution was 35 ± 6 μS/m. The spacer layer in the microfluidic chip was realized using double-sided adhesive tape with a measured thickness of 96 ± 5 μm.

b. *What dimensions are appropriate for the microfluidic chip, considering the optical setup and particles of interest?*

To ensure sufficient space for the microbots to move freely and to minimize boundary interactions, the microfluidic channel was designed with a length of 30 mm and a width of 9 mm. These dimensions are significantly larger than both the microbots and the FoV, allowing for extended manipulation without constraint.

c. *How can a reliable and reproducible fabrication method be established?*

The initial microfluidic chips were prone to breaking, which led to several design iterations aimed at improving their mechanical robustness. This process resulted in a larger chip with a well-aligned channel that is easier to handle during assembly. To standardize the channel dimensions and improve fabrication consistency, two 3D-printed tools were developed to assist in cutting and applying the double-sided adhesive tape. Additionally, to enable electrical connection without applying pressure to the fragile glass, a 3D-printed chip holder was designed. This holder uses conductive tape to establish contact with the electrodes, significantly reducing the risk of breakage during wire attachment.

Five design iterations were performed to develop a robust and effective microfluidic chip for OET applications, with each version improving the structural integrity and usable working area of the chip. In total, 52 chips were fabricated over the course of the project. To support consistent and efficient manufacturing, several 3D-printed tools were developed. These tools enabled more accurate assembly and alignment, further enhancing the reliability and performance of the final chip design.

3. How can the microbot be manipulated optimally in the OET system?

a. *What are the optimal design parameters (size, material, geometry) for the microbots?*

The dielectric particles manipulated in the system were commercially available 15 µm polystyrene beads, allowing for straightforward verification and benchmarking of the initial OET setup. For more advanced experiments, custom-shaped microparticles were used, designed to closely match the dimensions of microgear microbots found in the literature. This enabled performance benchmarking of the OET system with relevant micro-scale geometries. These microbots were fabricated using a NanoScribe two-photon polymerization system, which limits the choice of materials but offers a high degree of design flexibility. The microbots were printed in PDMS and featured small surface-mounted semispheres to reduce particle adhesion effects during manipulation.

b. *How can the characteristics of the microbots be measured to determine the DEP force acting on them?*

The equations of motion for the dielectric particles were derived using Newton's second law in combination with Stokes' law. This allowed us to determine the DEP force based on the measured velocity and acceleration of the microbot. To enable benchmarking against literature, an additional method was applied using a published conversion factor that relates particle speed to DEP force. Particle motion was recorded on video, and the velocity and acceleration were extracted by tracking the particle's position frame by frame. Multiple reference points were used to minimize measurement error and improve accuracy.

c. *What are the ideal OET settings (voltage, frequency, illumination) for effective control?*

Using an applied voltage of 30 Vpp, the DEP force acting on the microbot was found to peak at a frequency of 4 kHz, with a noticeable decrease at higher frequencies. The strongest DEP forces on the microbot were observed when both the optical power and the pattern thickness were maximized. To avoid deterioration of the microfluidic chip due to electrolysis, frequencies below 100 Hz and above 1 MHz should be avoided during operation.

d. *How can appropriate patterning be implemented for precise microbot manipulation?*

The pattern used to characterize the DEP force on the microbots in the OET setup was a customizable sweep. This approach was straightforward to implement and analyze, allowing for controlled variation in sweep velocity and pattern thickness. For more advanced, precise, and dynamic control, future patterns could involve the formation of a closed boundary around the microbot. By translating and rotating this boundary pattern across the field of view, the microbot could be guided with higher spatial accuracy and increased flexibility.

The microbots used in this research featured a more advanced design compared to those reported in the literature. This allowed for both meaningful benchmarking and a reduced likelihood of surface adhesion during DEP manipulation. Applying a 4 kHz, 30 Vpp square-wave signal to the microfluidic chip, combined with a sweep pattern of 120 DMD pixels at full optical power, resulted in a measured DEP force of 500 ± 34 pN using the equations of motion, and 103 ± 7 pN using the literature-based conversion factor. Under these conditions, the microbot was manipulated effectively within the OET setup, indicating that these parameters are near-optimal for actuation using the current system.

This research marks the successful foundation of a new field of study at Delft University of Technology, establishing a robust platform for future exploration into optoelectronic tweezer-based microsystems. It serves as a pivotal starting point for a wide range of promising investigations that can contribute directly to the advancement of next-generation healthcare technologies.

What began with the characterization of a single PDMS microbot now opens the door to building accurate simulations of microbot dynamics within the OET environment. Such simulations will enable complex control strategies, which are essential for the realization of advanced lab-on-chip systems. In the long term, these microbots should be capable of handling and testing living cells, assessing their function and suitability for biological research. This goal will influence future microparticle designs, making them increasingly application-specific and better characterized for targeted use-cases.

Improvements can be made across several domains to unlock the potential of OET systems further. The photoconductive layer should be optimized to support operation in high-conductivity environments such as cell-culture media. The DEP force strength can be significantly increased by implementing a more powerful patterning light source, enhancing the conductivity gradient, and resulting field gradients. The optical setup itself should be upgraded to improve optical efficiency and incorporate fluorescence microscopy for advanced real-time imaging.

As the system becomes more effective, it unlocks a world of possibilities—bringing us closer to a future of faster, more accessible, and more affordable healthcare worldwide. The ability to accelerate biological and medical experimentation holds the potential to save time, reduce costs, and most importantly, save lives during future epidemics. This thesis not only demonstrates the feasibility of such a system but also lays the groundwork for transformative innovations in biomedical technology at the Delft University of Technology.

Bibliography

[1] World Health Organization, *Number of covid-19 deaths reported to who (cumulative total)*, Accessed: 2025-03-24, 2025. [Online]. Available: https://data.who.int/dashboards/covid19/deaths.

[2] Centraal Bureau voor de Statistiek, *Almost 1 in 10 dutch people felt strongly lonely in 2019*, Accessed: 2025-03-24, original publication date: 2020-03-27, 2020. [Online]. Available: https://www.cbs.nl/en-gb/news/2020/13/almost-1-in-10-dutch-people-felt-strongly-lonely-in-2019.

[3] C. Vardavas, K. Zisis, K. Nikitara, *et al.*, "Cost of the covid-19 pandemic versus the cost-effectiveness of mitigation strategies in eu/uk/oecd: A systematic review," *BMJ Open*, vol. 13, no. 10, e077602, 2023. DOI: 10.1136/bmjopen-2023-077602. [Online]. Available: https://doi.org/10.1136/bmjopen-2023-077602.

[4] J. Solis-Moreira. "How did we develop a covid-19 vaccine so quickly?" Fact checked by Anna Guildford, Ph.D. Updated on November 13, 2021. Accessed: 2025-03-24. (2021), [Online]. Available: https://www.medicalnewstoday.com/articles/how-did-we-develop-a-covid-19-vaccine-so-quickly.

[5] LUMICKS. "What are optical tweezers?" Accessed: 2025-03-24. (2025), [Online]. Available: https://lumicks.com/knowledge/what-are-optical-tweezers/.

[6] S. Zhang, B. Xu, M. Elsayed, *et al.*, "Optoelectronic tweezers: A versatile toolbox for nano-/micro-manipulation," *Chem. Soc. Rev.*, vol. 51, pp. 9203–9242, 22 2022. DOI: 10.1039/D2CS00359G. [Online]. Available: http://dx.doi.org/10.1039/D2CS00359G.

[7] Bruker Cellular Analysis. "Beacon® optofluidic system." Accessed: 2025-03-24. (2025), [Online]. Available: https://brukercellularanalysis.com/products/instruments/the-beacon-optofluidic-system/.

[8] S. Zhang, E. Y. Scott, J. Singh, *et al.*, "The optoelectronic microrobot: A versatile toolbox for micromanipulation," *Proceedings of the National Academy of Sciences*, vol. 116, no. 30, pp. 14 823–14 828, 2019. DOI: 10.1073/pnas.1903406116. eprint: https://www.pnas.org/doi/pdf/10.1073/pnas.1903406116. [Online]. Available: https://www.pnas.org/doi/abs/10.1073/pnas.1903406116.

[9] A. Zangwill, *Modern Electrodynamics* (Modern Electrodynamics). Cambridge University Press, 2013, ISBN: 9780521896979. [Online]. Available: https://books.google.nl/books?id=tEYSUegp9WYC.

[10] O. Martinsen and A. Heiskanen, *Bioimpedance and Bioelectricity Basics*. Elsevier Science, 2023, ISBN: 9780128191071. [Online]. Available: https://books.google.nl/books?id=tzXLEAAAQBAJ.

[11] A. Adam. ""2023 - ap3071 advanced electrodynamics lecture 4 - electromagnetic energy. ap3071 advanced electrodynamics (2023/2024 q1)"." (), [Online]. Available: https://brightspace.tudelft.nl/d2l/le/content/593900/viewContent/3532986/View. "(accessed: 30.05.2024)".

[12] D. J. Griffiths, *Introduction to electrodynamics*. Pearson, 2013.

[13] T. Matsushita, "Dielectric materials," in *Electricity and Magnetism: New Formulation by Introduction of Superconductivity*. Cham: Springer International Publishing, 2021, pp. 81–106, ISBN: 978-3-030-82150-0. DOI: 10.1007/978-3-030-82150-0_4. [Online]. Available: https://doi.org/10.1007/978-3-030-82150-0_4.

[14] X. Wang, X.-B. Wang, and P. R. Gascoyne, "General expressions for dielectrophoretic force and electrorotational torque derived using the maxwell stress tensor method," *Journal of Electrostatics*, vol. 39, no. 4, pp. 277–295, 1997, ISSN: 0304-3886.

[15] S. Zhang, M. Elsayed, R. Peng, *et al.*, "Reconfigurable multi-component micromachines driven by optoelectronic tweezers," *Nature Communications*, vol. 12, Sep. 2021. DOI: 10.1038/s41467-021-25582-8.

[16] H. Pan, Y. Xia, M. Qin, Y. Cao, and W. Wang, "A simple procedure to improve the surface passivation for single molecule fluorescence studies," *Phys. Biol.*, vol. 12, no. 4, p. 045 006, 2015, Published June 29, 2015. DOI: 10.1088/1478-3975/12/4/045006.

[17] T. Smolinka, "Fuels – hydrogen production | water electrolysis," in *Encyclopedia of Electrochemical Power Sources*, J. Garche, Ed., Amsterdam: Elsevier, 2009, pp. 394–413, ISBN: 978-0-444-52745-5. DOI: https://doi.org/10.1016/B978-044452745-5.00315-4. [Online]. Available: https://www.sciencedirect.com/science/article/pii/B9780444527455003154.

[18] Y.-C. Tsai, Y.-H. Hong, S.-J. Zhang, and J.-N. Kuo, "Frequency-selective electrokinetic manipulation of microparticles in gold nanofilm optically-induced dielectrophoretic device," *Microsystem Technologies*, vol. 26, no. 4, pp. 1213–1222, 2020, ISSN: 1432-1858. DOI: 10.1007/s00542-019-04651-5. [Online]. Available: https://doi.org/10.1007/s00542-019-04651-5.

[19] C. Kua, Y. Lam, C. Yang, and K. Youcef-Toumi, "Review of bio-particle manipulation using dielectrophoresis," Dec. 2004.

[20] M. Toofan and J. Toofan, "Chapter 5 - a brief review of the cleaning process for electronic device fabrication," in *Developments in Surface Contamination and Cleaning*, R. Kohli and K. Mittal, Eds., Oxford: William Andrew Publishing, 2015, pp. 185–212, ISBN: 978-0-323-29961-9. DOI: https://doi.org/10.1016/B978-0-323-29961-9.00005-3. [Online]. Available: https://www.sciencedirect.com/science/article/pii/B9780323299619000053.

[21] M. Ahmed, A. Bakry, E. Shaaban, and H. Dalir, "Structural, electrical, and optical properties of ito thin films and their influence on performance of cds/cdte thin-film solar cells," *Journal of Materials Science: Materials in Electronics*, vol. 32, pp. 1–12, Apr. 2021. DOI: 10.1007/s10854-021-05777-x.

[22] C. Alexander and M. Sadiku, *Fundamentals of Electric Circuits*. McGraw-Hill Education, 2012, ISBN: 9780073380575. [Online]. Available: https://books.google.nl/books?id=OxRk5AAACAAJ.

[23] W. H. H. Jr. and J. A. Buck, *Engineering Electromagnetics*, 9th. New York, NY: McGraw-Hill Education, 2019, Late Emeritus Professor Purdue University; Georgia Institute of Technology, ISBN: 978-1-259-66097-9.

[24] J. Melskens, "Hydrogenated amorphous silicon: Nanostructure and defects," Promotors: M. Zeman, E.H. Bruck, A.H.M. Smets. Department: Electrical Sustainable Energy (EEMCS), Doctoral thesis, Delft University of Technology, 2015. [Online]. Available: http://resolver.tudelft.nl/uuid:13d60d5e-3d68-4ac7-b2b6-a867cc393231.

[25] D. Griffiths and D. Schroeter, *Introduction to Quantum Mechanics*. Cambridge University Press, 2018, ISBN: 9781107189638. [Online]. Available: https://books.google.nl/books?id=82FjDwAAQBAJ.

[26] S. Simon, *The Oxford Solid State Basics*. OUP Oxford, 2013, ISBN: 9780199680764. [Online]. Available: https://books.google.nl/books?id=QI8jLeTOBAsC.

[27] T. v. d. S. Anton Akhmerov, *Open solid state notes, the nearly free electron model bloch theorem*, Accessed: 05.09.2024, 2022. [Online]. Available: https://solidstate.quantumtinkerer.tudelft.nl/11_nearly_free_electron_model/#the-nearly-free-electron-model-bloch-theorem.

[28] G. O. Inc., *An overview of the materials used for solar cells*, [Online; accessed 2024-09-09], 2018. [Online]. Available: https://g2voptics.com/photovoltaics-solar-cells/solar-cell-materials/.

[29] G. Horowitz, "Validity of the concept of band edge in organic semiconductors," *Journal of Applied Physics*, vol. 118, p. 115 502, Sep. 2015. DOI: 10.1063/1.4931061.

[30] H. Li and M. Matsumoto, "Optical response of hydrogenated amorphous silicon: Investigation with electronic dynamics simulations," *Applied Physics A*, vol. 128, no. 10, p. 924, Sep. 2022, ISSN: 1432-0630. DOI: 10.1007/s00339-022-06029-3. [Online]. Available: https://doi.org/10.1007/s00339-022-06029-3.

[31] T. Belaroussi, D. Rached, W. L. Rahal, and F. Hamdache, "Sensitivity of a hit c-si solar cell to structural distortions of the hydrogenated amorphous silicon constituting the front face of the device," *Journal of Nano- and Electronic Physics*, vol. 12, p. 5023, Oct. 2020. DOI: 10.21272/jnep.12(5).05023.

[32] C.B.Honsberg and S.G.Bowden, *Photon energy*, Accessed: 29.08.2024, 2019. [Online]. Available: https://www.pveducation.org/pvcdrom/properties-of-sunlight/energy-of-photon.

[33] J. P. Thomas G. Mayerhofer Susanne Pahlow, *Understanding the limits of the bouguer-beer-lambert law*, [Online; accessed 2024-09-10], 2023. [Online]. Available: https://www.spectroscopyonline.com/view/understanding-the-limits-of-the-bouguer-beer-lambert-law.

[34] K. W. Boer and H. Pohl, "Semiconductor physics," in 2nd. Cham: Springer, 2018, ch. Photoconductivity, pp. 1182–1204, ISBN: 978-3-319-69607-0. DOI: 10.1007/978-3-319-69607-0_9. [Online]. Available: https://link.springer.com/book/10.1007/978-3-319-69607-0.

[35] TU Graz, *Electrical conductivity of silicon*, https://lampz.tugraz.at/~hadley/psd/L4/conductivity.php, Accessed: September 12, 2024, 2023.

[36] W. Liang, S. Wang, Z. Dong, G.-B. Lee, and W. Li, "Optical spectrum and electric field waveform dependent optically-induced dielectrophoretic (odep) micro-manipulation," *Micromachines*, vol. 3, pp. 492–508, Dec. 2012. DOI: 10.3390/mi3020492.

[37] W. Wang, Y.-H. Lin, R.-S. Guan, T.-C. Wen, T.-F. Guo, and G.-B. Lee, "Bulk-heterojunction polymers in optically-induced dielectrophoretic devices for the manipulation of microparticles," *Opt. Express*, vol. 17, no. 20, pp. 17 603–17 613, Sep. 2009. DOI: 10.1364/OE.17.017603. [Online]. Available: https://opg.optica.org/oe/abstract.cfm?URI=oe-17-20-17603.

[38] S.-J. Lin, S.-H. Hung, J.-Y. Jeng, T.-F. Guo, and G.-B. Lee, "Manipulation of micro-particles by flexible polymer-based optically-induced dielectrophoretic devices," *Opt. Express*, vol. 20, no. 1, pp. 583–592, Jan. 2012. DOI: 10.1364/OE.20.000583. [Online]. Available: https://opg.optica.org/oe/abstract.cfm?URI=oe-20-1-583.

[39] S.-M. Yang, T.-M. Yu, H.-P. Huang, M.-Y. Ku, L. Hsu, and C.-H. Liu, "Dynamic manipulation and patterning of microparticles and cells by using tiopc-based optoelectronic dielectrophoresis," *Opt. Lett.*, vol. 35, no. 12, pp. 1959–1961, Jun. 2010. DOI: 10.1364/OL.35.001959. [Online]. Available: https://opg.optica.org/ol/abstract.cfm?URI=ol-35-12-1959.

[40] H.-y. Hsu, A. T. Ohta, P.-Y. Chiou, A. Jamshidi, S. L. Neale, and M. C. Wu, "Phototransistor-based optoelectronic tweezers for dynamic cell manipulation in cell culture media," *Lab Chip*, vol. 10, pp. 165–172, 2 2010. DOI: 10.1039/B906593H. [Online]. Available: http://dx.doi.org/10.1039/B906593H.

[41] J. Thijssen, *Lecture Notes Statistical Physics, Summer 2022 Course AP3021*. TU Delft, 2022, Course material for AP3021, TU Delft.

[42] Y. Çengel and J. Cimbala, *Fluid Mechanics: Fundamentals and Applications*. McGraw-Hill Education, 2018, ISBN: 9781259921902. [Online]. Available: https://books.google.nl/books?id=DqFJvgAACAAJ.

[43] P. dr. ir. C. R. Kleijn and D. ing. S. Kenjeres, *Continuum physics*, Course Code: AP3032, 2024.

[44] M. Zastawny, G. Mallouppas, F. Zhao, and B. van Wachem, "Derivation of drag and lift force and torque coefficients for non-spherical particles in flows," *International Journal of Multiphase Flow*, vol. 39, pp. 227–239, 2012, ISSN: 0301-9322. DOI: https://doi.org/10.1016/j.ijmultiphaseflow.2011.09.004. [Online]. Available: https://www.sciencedirect.com/science/article/pii/S0301932211002047.

[45] A. Pantokratoras, “Lift, drag and torque on a rotating sphere in a stream of non-newtonian power-law fluid,” *Rheologica Acta*, vol. 60, no. 4, pp. 175–186, Apr. 2021, ISSN: 1435-1528. DOI: 10.1007/s00397-021-01259-3. [Online]. Available: https://doi.org/10.1007/s00397-021-01259-3.

[46] A. L. Polaczyk, J. E. Amburgey, A. Alansari, J. C. Poler, M. Propato, and V. R. Hill, “Calculation and uncertainty of zeta potentials of microorganisms in a 1:1 electrolyte with a conductivity similar to surface water,” *Colloids and Surfaces A: Physicochemical and Engineering Aspects*, vol. 586, p. 124 097, 2020, ISSN: 0927-7757. DOI: https://doi.org/10.1016/j.colsurfa.2019.124097. [Online]. Available: https://www.sciencedirect.com/science/article/pii/S0927775719310891.

[47] D. Hanaor, M. Michelazzi, P. Veronesi, C. Leonelli, M. Romagnoli, and C. Sorrell, “Anodic aqueous electrophoretic deposition of titanium dioxide using carboxylic acids as dispersing agents,” *Journal of the European Ceramic Society*, vol. 31, no. 6, pp. 1041–1047, 2011, ISSN: 0955-2219. DOI: https://doi.org/10.1016/j.jeurceramsoc.2010.12.017. [Online]. Available: https://www.sciencedirect.com/science/article/pii/S095522191000590X.

[48] W. Technology, *Zeta potential*, Wyatt’s line of multi-angle static light scattering products couple to size exclusion chromatography (SEC-MALS), field-flow fractionation (FFF-MALS) and stop-flow composition-gradient systems (CG-MALS). Accessed: 2024-11-19, 2024. [Online]. Available: https://www.wyatt.com/solutions/properties/charge-zeta-potential.html.

[49] J. Zhao, B. Chen, C. Gan, *et al.*, “Study of particle equilibrium based on the combination of light-actuated ac electroosmosis and light-actuated dielectrophoresis,” *Opt. Express*, vol. 32, no. 14, pp. 24 563–24 572, Jul. 2024. DOI: 10.1364/OE.523241. [Online]. Available: https://opg.optica.org/oe/abstract.cfm?URI=oe-32-14-24563.

[50] P.-Y. Chiou, A. Ohta, A. Jamshidi, H. Y. Hsu, and M. C. Wu, “Light-actuated ac electroosmosis for nanoparticle manipulation,” *Journal of Microelectromechanical Systems*, vol. 17, pp. 525–531, 2008. [Online]. Available: https://api.semanticscholar.org/CorpusID:2827857.

[51] A. Castellanos, A. Ramos, A. González, N. Green, and H. Morgan, “Electrohydrodynamics and dielectrophoresis in microsystems: Scaling laws,” *Journal of Physics D: Applied Physics*, vol. 36, Oct. 2003. DOI: 10.1088/0022-3727/36/20/023.

[52] R. Shah and A. London, “Chapter iii - dimensionless groups and generalized solutions,” in *Laminar Flow Forced Convection in Ducts*, R. Shah and A. London, Eds., Academic Press, 1978, pp. 37–60, ISBN: 978-0-12-020051-1. DOI: https://doi.org/10.1016/B978-0-12-020051-1.50008-5. [Online]. Available: https://www.sciencedirect.com/science/article/pii/B9780120200511500085.

[53] A. Salari, M. Navi, T. Lijnse, and C. Dalton, “Ac electrothermal effect in microfluidics: A review,” *Micromachines*, vol. 10, no. 11, 2019, ISSN: 2072-666X. DOI: 10.3390/mi10110762. [Online]. Available: https://www.mdpi.com/2072-666X/10/11/762.

[54] J. K. Valley, A. Jamshidi, A. T. Ohta, H. Y. Hsu, and M. C. Wu, “Operational regimes and physics present in optoelectronic tweezers,” *Journal of Microelectromechanical Systems: A Joint IEEE and ASME Publication on Microstructures, Microactuators, Microsensors, and Microsystems*, vol. 17, no. 2, pp. 342–350, 2008. DOI: 10.1109/JMEMS.2008.916335. [Online]. Available: https://doi.org/10.1109/JMEMS.2008.916335.

[55] C. Balaji, B. Srinivasan, and S. Gedupudi, “Chapter 6 - natural convection,” in *Heat Transfer Engineering*, C. Balaji, B. Srinivasan, and S. Gedupudi, Eds., Academic Press, 2021, pp. 173–198, ISBN: 978-0-12-818503-2. DOI: https://doi.org/10.1016/B978-0-12-818503-2.00006-X. [Online]. Available: https://www.sciencedirect.com/science/article/pii/B978012818503200006X.

[56] A. N. K. Lau, A. T. Ohta, H. L. Phan, *et al.*, “Antifouling coatings for optoelectronic tweezers,” *Lab Chip*, vol. 9, pp. 2952–2957, 20 2009. DOI: 10.1039/B907840A. [Online]. Available: http://dx.doi.org/10.1039/B907840A.

[57] S. Konijnenberg, A. Adam, and H. Urbach, *Bsc Optics*. TU Delft Open, Mar. 2024, ISBN: 9789463668477. DOI: 10.59490/tb.91.

[58] M. Born and E. Wolf, *Principles of Optics: Electromagnetic Theory of Propagation, Interference and Diffraction of Light*, 7th expanded edition. Cambridge, UK: Cambridge University Press, 2002, ISBN: 978-0521642224.

[59] C. Mack, "Fundamental principles of optical lithography: The science of microfabrication," *Fundamental Principles of Optical Lithography: The Science of Microfabrication*, pp. 1–515, Nov. 2007. DOI: 10.1002/9780470723876.

[60] I. Gris Sánchez, D. Ras, and T. Birks, "The airy fiber: An optical fiber that guides light diffracted by a circular aperture," *Optica*, vol. 3, Mar. 2016. DOI: 10.1364/OPTICA.3.000270.

[61] P. Bankhead, *Spatial formation in fluorescence imaging*, Accessed: 2024-10-26, 2022–2024. [Online]. Available: https://bioimagebook.github.io/chapters/3-fluorescence/2-formation_spatial/formation_spatial.html.

[62] I. Young, R. Zagers, L. Van Vliet, J. Mullikin, F. Boddeke, and H. Netten, "Depth-of-focus in microscopy," *8th Scandinavian Conference on Image Analysis, Tromso, Norway*, Jan. 1993.

[63] K. R. Spring and M. W. Davidson, *Depth of field and depth of focus*, Accessed: 2025-03-14, 2025. [Online]. Available: https://www.microscopyu.com/microscopy-basics/depth-of-field-and-depth-of-focus.

[64] A. Anvari, A. Azimi Yancheshme, K. M. Kekre, and A. Ronen, "State-of-the-art methods for overcoming temperature polarization in membrane distillation process: A review," *Journal of Membrane Science*, vol. 616, p. 118 413, 2020, ISSN: 0376-7388. DOI: https://doi.org/10.1016/j.memsci.2020.118413. [Online]. Available: https://www.sciencedirect.com/science/article/pii/S0376738820309911.

[65] D. Feezell and S. Nakamura, "Invention, development, and status of the blue light-emitting diode, the enabler of solid-state lighting," *Comptes Rendus Physique*, vol. 19, no. 3, pp. 113–133, 2018, LEDs: The new revolution in lighting / Les LED : la nouvelle révolution de l'éclairage, ISSN: 1631-0705. DOI: https://doi.org/10.1016/j.crhy.2017.12.001. [Online]. Available: https://www.sciencedirect.com/science/article/pii/S163107051730124X.

[66] Thorlabs, *Two collimation methods for leds*, Accessed 30 October 2024, 2024. [Online]. Available: https://www.thorlabs.com/newgrouppage9.cfm?objectgroup_id=2692&tabname=Collimation.

[67] D. Kromm, "Pushing Light-Sheet Microscopy to Greater Depths," Dissertation submitted to the Combined Faculty of Natural Sciences and Mathematics of the Ruperto Carola University Heidelberg, for the degree of Doctor of Natural Sciences. Oral examination: 17 December 2021, Ph.D. dissertation, Ruperto Carola University Heidelberg, Heidelberg, Germany, Dec. 2021.

[68] *How does a dlp projector work?* ProjectorScreen.com, 2024. [Online]. Available: https://www.projectorscreen.com/blog/How-does-a-DLP-projector-work (visited on 10/31/2024).

[69] R. van Elk, *Designing a microscope for an optoelectronic tweezer to trap polystyrene beads*, Project Supervisor: C.S. Smith, Project Report, Jul. 2024.

[70] C. Pereira, M. Abreu, A. Cabral, and J. Rebordão, "Characterization of light diffraction by a digital micromirror device," *Journal of Physics: Conference Series*, vol. 2407, p. 012 048, Dec. 2022. DOI: 10.1088/1742-6596/2407/1/012048.

[71] H. Austerlitz, "Chapter 4 - analog/digital conversions," in *Data Acquisition Techniques Using PCs (Second Edition)*, H. Austerlitz, Ed., Second Edition, San Diego: Academic Press, 2003, pp. 51–77, ISBN: 978-0-12-068377-2. DOI: https://doi.org/10.1016/B978-012068377-2/50004-8. [Online]. Available: https://www.sciencedirect.com/science/article/pii/B9780120683772500048.

[72] D. A. Smets and P. M. Zeman, *Solar energy: Photovoltaic (pv) technologies, pecvd*, https://ocw.tudelft.nl/courses/solar-energy-photovoltaic-pv-technologies/, Course info: Study load 121 hrs, Bachelor program, Licensed under a Creative Commons Attribution-NonCommercial-ShareAlike 4.0 International License. Last edited: 2020-03-03, Dec. 2017.

[73] J. R. Stair, *Introduction to the nanoscribe*, Online: https://dozuki.umd.edu/Guide/, Accessed: 2024-12-23, Nov. 2020.

[74] D. Jetulahi, *Designing and testing a microfluidic for an optoelectronic tweezers setup by trapping polystyrene beads*, Bachelor's Thesis, Jul. 2024.

[75] M. Folkerts, *Production of an a-si:h p-i-n junction thin film solar cell in order to test it's eligibility to work as a photoconductive layer in optoelectronic tweezers*, Bachelor's Thesis, Jan. 2025.

[76] Millipore, *Tween® 20 solution*, Productnummer: 655206, 2025. [Online]. Available: https://www.sigmaaldrich.com/NL/en/product/mm/655206.

[77] LWTN, *Ultra puur water lwtn genie purist*, © Cryo. ALL Rights Reserved. LWTN, 2013. [Online]. Available: https://lwtn.nl/Ultrapuur-Watersysteem-Type1.html.

[78] A. Krishnan, *How to calculate capacitance in capacitors with multiple dielectrics*, Accessed on March 11, 2025, 2017. [Online]. Available: https://www.emworks.com/blog/pcbs/capacitance-calculation-ems-solidworks.

[79] T. Ferreira and W. Rasband, *Imagej user guide*, IJ 1.46r, Last updated: October 2, 2012, 2012. [Online]. Available: https://imagej.net/ij/docs/guide/index.html.

[80] K. Technologies, *Keysight truevolt series dmm operating and service guide*, Accessed on March 11, 2025, n.d. [Online]. Available: https://www.keysight.com/nl/en/assets/9018-03876/service-manuals/9018-03876.pdf.

[81] The Engineering ToolBox, *Relative permittivity - the dielectric constant*, Accessed on March 11, 2025, 2010. [Online]. Available: https://www.engineeringtoolbox.com/relative-permittivity-d_1660.html.

[82] MG Chemicals, *9410 – 1 part epoxy, electrically conductive adhesive, high tg*, Copyright 2025 © MG Chemicals, 2025. [Online]. Available: https://mgchemicals.com/products/adhesives/electrically-conductive-adhesives/conductive-adhesive/.

[83] Thermo Fisher Scientific Inc., *TetraSpeck™ Fluorescent Microspheres Size Kit (mounted on slide)*, Accessed: 2025-04-01, 2025. [Online]. Available: https://www.thermofisher.com/order/catalog/product/T14792.

[84] Thermo Fisher Scientific, *Fluorescence spectraviewer*, Accessed: 2025-03-14, 2025. [Online]. Available: https://www.thermofisher.com/order/fluorescence-spectraviewer/?SID=srch-svtool&UID=tsorange#!/.

[85] L. Leo. "2.3 the gaussian or normal distribution." Accessed: 2025-03-24. (1995), [Online]. Available: https://ned.ipac.caltech.edu/level5/Leo/Stats2_3.html.

[86] Thorlabs, Inc., *Mounted achromatic doublets, ar coated: 400 - 700 nm*, Accessed: 2025-03-14, 2025. [Online]. Available: https://www.thorlabs.com/newgrouppage9.cfm?objectgroup_id=2696&pn=AC254-035-A-ML.

[87] Thorlabs, Inc., *Elliptical mirrors*, Accessed: 2025-03-14, 2025. [Online]. Available: https://www.thorlabs.com/newgrouppage9.cfm?objectgroup_id=5136&pn=BBE1-E02.

[88] Thorlabs, Inc., *Non-polarizing beamsplitter cubes in 30 mm cage cubes*, Accessed: 2025-03-14, 2025. [Online]. Available: https://www.thorlabs.com/newgrouppage9.cfm?objectgroup_id=4129&pn=CCM1-BS013/M.

[89] Texas Instruments Incorporated, *Dmd optical efficiency for visible wavelengths*, Accessed: 2025-03-14, 2023. [Online]. Available: https://www.ti.com/lit/an/dlpa083b/dlpa083b.pdf?ts=1741926945343.

[90] W. Ren, M. Zaman, M. Wu, M. Jensen, R. Davis, and L. Hesselink, "Microparticle electrical conductivity measurement using optoelectronic tweezers," *Journal of Applied Physics*, vol. 134, Sep. 2023. DOI: 10.1063/5.0169565.

[91] S. W. Ellingson, *10.1: Permittivity of some common materials*, Accessed: 2025-03-14, 2025. [Online]. Available: https://eng.libretexts.org/Bookshelves/Electrical_Engineering/Electro-Optics/Book%3A_Electromagnetics_I_(Ellingson)/10%3A_Appendices/10.01%3A_Permittivity_of_Some_Common_Materials.

[92] Massachusetts Institute of Technology, *6.777j/2.751j material property database: Pdms (polydimethylsiloxane)*, Accessed: 2025-03-14, 2025. [Online]. Available: https://www.mit.edu/~6.777/matprops/pdms.htm.

[93] D. A. Berstad, B. Knapstad, M. Lamvik, P. A. Skjølsvik, K. Tørklep, and H. A. Øye, "Accurate measurements of the viscosity of water in the temperature range 19.5–25.5°c," *Physica A: Statistical Mechanics and its Applications*, vol. 151, no. 2, pp. 246–280, 1988, ISSN: 0378-4371. DOI: 10.1016/0378-4371(88)90015-5. [Online]. Available: https://www.sciencedirect.com/science/article/pii/0378437188900155.

[94] Thermo Fisher Scientific Inc., *Invitrogen™ fluospheres™ polystyrene microspheres, 15 µm, red-orange fluorescent (565/580), for blood flow determination*, Accessed: 2025-03-14, 2025. [Online]. Available: https://www.fishersci.nl/shop/products/fluospheres-polystyrene-microspheres-15-m-red-orange-fluorescent-565-580-blood-flow-determination/11554796.

[95] M. Cutroneo, V. Havranek, V. Semian, *et al.*, "Porous polydimethylsiloxane filled with graphene-based material for biomedicine," *Journal of Porous Materials*, vol. 28, Oct. 2021. DOI: 10.1007/s10934-021-01095-z.

[96] S. Zhang, W. Li, M. Elsayed, *et al.*, "Size-scaling effects for microparticles and cells manipulated by optoelectronic tweezers," *Opt. Lett.*, vol. 44, no. 17, pp. 4171–4174, Sep. 2019. DOI: 10.1364/OL.44.004171. [Online]. Available: https://opg.optica.org/ol/abstract.cfm?URI=ol-44-17-4171.

[97] M. C. Wu and P.-Y. Chiou, "Optoelectronic tweezers," in *Proceedings of the Microoptics Group (OSJ/JSAP)*, Japan: Microoptics Group (OSJ/JSAP), 2007. [Online]. Available: https://api.semanticscholar.org/CorpusID:11938835.

[98] S. M. Popoff, *Alp4lib: Python control module for vialux dmds based on alp4.x api*, GitHub repository, MIT License, 2016. [Online]. Available: https://github.com/wavefrontshaping/ALP4lib.

[99] H. Kang, "Crystalline silicon vs. amorphous silicon: The significance of structural differences in photovoltaic applications," *IOP Conference Series: Earth and Environmental Science*, vol. 726, p. 012 001, Apr. 2021. DOI: 10.1088/1755-1315/726/1/012001.

[100] SURAGUS GmbH, *Four point probe measurement method*, Accessed: 2025-04-01, 2025. [Online]. Available: https://www.suragus.com/en/technology/four-point-probe/.

[101] H. Sayed, M. Al-Dossari, M. Ismail, N. El-Gawaad, and A. Aly, "Theoretical analysis of optical properties for amorphous silicon solar cells with adding anti-reflective coating photonic crystals," *Photonics*, vol. 9, p. 813, Oct. 2022. DOI: 10.3390/photonics9110813.

[102] X. Li, C. Zhang, Z. Yang, and A. Shang, "Broadband, polarization-insensitive and wide-angle absorption enhancement of a-si:h/µc-si:h tandem solar cells by nanopatterning a-si:h layer," *Optics Express*, vol. 21, A677–A686, May 2013. DOI: 10.1364/OE.21.00A677.

[103] G. Li, B. Xu, X. Wang, *et al.*, "Crossing the dimensional divide with optoelectronic tweezers: Multicomponent light□driven micromachines with motion transfer in three dimensions," *Advanced Materials*, Feb. 2025. DOI: 10.1002/adma.202417742.

[104] S. Gupta. "What is capacitor leakage current and how to reduce it." Accessed: 2025-03-24. (2019), [Online]. Available: https://circuitdigest.com/tutorial/what-is-capacitor-leakage-current-and-how-to-reduce-it.

[105] V. Miralles, A. Huerre, F. Malloggi, and M.-C. Jullien, "A review of heating and temperature control in microfluidic systems: Techniques and applications," *Diagnostics*, vol. 3, no. 1, pp. 33–67, 2013. DOI: 10.3390/diagnostics3010033.

[106] S. Mozaffari, F. LaRocca, V. Jaedicke, P. Tiruveedhula, and A. Roorda, “Wide-vergence, multi-spectral adaptive optics scanning laser ophthalmoscope with diffraction-limited illumination and collection,” *Biomedical Optics Express*, vol. 11, Feb. 2020. DOI: `10.1364/BOE.384229`.

[107] S. Zhang, J. Juvert, J. Cooper, and S. Neale, “Manipulating and assembling metallic beads with optoelectronic tweezers,” *Scientific Reports*, vol. 6, p. 32 840, Sep. 2016. DOI: `10.1038/srep32840`.

[108] S. Zhang, M. Elsayed, R. Peng, *et al.*, “Influence of light pattern thickness on the manipulation of dielectric microparticles by optoelectronic tweezers,” *Photonics Research*, vol. 10, Nov. 2021. DOI: `10.1364/PRJ.437528`.

[109] M. Verhaegen and V. Verdult, *Filtering and System Identification: A Least Squares Approach*. Jan. 2007, ISBN: 978-0-521-87512-7.

List of Figures

2.1 A schematic depiction of an OET setup. This depiction shows the layout of the sections, describing the theory of all the OET components in this chapter. 5
2.2 A schematic depiction of the field $\mathbf{E}_1$ outside the particle and the field $\mathbf{E}_2$ inside the particle. The uniform field $\mathbf{E}_0$, which we would expect in a capacitor, is disturbed by the dielectric particle [13]. 8
2.3 A schematic depiction of the effect of the Clausius-Mossotti factor on the direction of the DEP force in an OET. When the CM factor is positive, the DEP force will point towards the illuminated spot and vice versa. 9
2.4 The transmittance and absorbance of different thicknesses of ITO film [21]. 10
2.5 The resistance, carrier concentration, and Hall mobility of different thicknesses of ITO film [21]. 10
2.6 The OET is modeled as an electrical circuit with the most important resistances and impedances. 11
2.7 The dispersion relation of a free electron in blue and a nearly-free electron in orange. The dispersion relation is periodic in ka with a being the length of the cubic box, which we denote as L [27]. 13
2.8 An illustration of the difference in crystal lattice structure. From left to right, monocrystalline silicon, amorphous silicon, and hydrogenated amorphous silicon [28]. 13
2.9 A schematic density of states for crystal silicon and amorphous silicon. E_v is the maximum energy of the valence band. E_c is the minimum energy of the conduction band. The band tails are due to disorder in the structure [29]. 14
2.10 A schematic depiction of the difference in density of states between crystallized silicon and amorphous hydrogenated silicon. ED and EA describe the tails of the Urbach tails. E_v, E_c, and E_f are the valence band energy, conduction band energy, and the Fermi energy. D^+/D^0 and D^-/D^0 represent the donor-like gap states per unit volume and the acceptor-like gap states per unit volume [31]. 14
2.11 The OET forces that are working on a particle submerged in a medium, free to move (left) and stuck to the bottom (right). 16
2.12 The electric double layer around a submerged negatively charged particle. The surface charge decreases with radial distance. At the Stern layer, the potential is the Stern potential. At the slipping plane, the potential is the ζ-potential [48]. 18
2.13 The fluid has a certain slip velocity due to the light-induced AC electroosmosis [49]. . . 19
2.14 Regions in the frequency/optical power plot show where certain forces dominate. The particle in this system is in a liquid solution with a conductivity of 1 mS/m. The applied AC frequency is 100 kHz. In (a), the applied voltage is 20 Vpp. In (b), the applied voltage is 10 Vpp [54]. 21
2.15 A schematic depiction of a telescope with two lenses. The left lens has a focal length f_1, and the second lens has a focal length f_2. On the left side, the stick figure stands at f_1 distance from the first lens. This object, the stick figure, is imaged, translated, and demagnified on the right side. 22
2.16 The field due to a circular aperture. This shape is called the Airy disk and consists of multiple circles. Each circle is separated due to the minima in the Airy disk function [60]. 23
2.17 The effects of separation of the Airy disks are shown. If we separate the spots with a distance of at least 1 one radius, the spot centers can be distinguished as two separate spots. When the separation is less than a distance of 1 radius, it is impossible to recognize individual spots anymore [61]. 23
2.18 A schematic depiction of a wavefront compared to an out-of-focus wavefront. The wavefronts are distanced with a distance W as seen from the focal point of the focused wavefront [62]. 24

2.19 The expected beam divergence of an LED with size d after a distance L [66] 25
2.20 A digital micromirror device with a part of the array schematically shown [68]. 25
2.21 A schematic depiction of a DMD showing the on and off state. Light reflects on the DMD with $2\theta_t$ in the on state and with $-2\theta_t$ in the off state [69]. 25

3.1 Different iterations for the design of the microfluidic chip. Yellow shows the double-sided tape, gray shows the silver contact strips of the ITO-covered glass, blue shows where the microfluidic channel is positioned, and white denotes the inlets for the channel. In (a), the first design was made to have a microfluidic channel fit on an ITO-coated microscope cover glass. (b) depicts a design of the microfluidic channel with an increased channel area. (c) shows the third design of the microfluidic channel without inlets to test if another design can increase the robustness. 28
3.2 Schematic dimensionalities of the microfluidic chip. (a) shows the fourth and final iteration using the bigger ITO-covered microscope slides. (b) depicts a cross-sectional view of the microfluidic channel, which is true for all iterations that include the ITO-covered glasses and the photoconductive layer. 28
3.3 Different iterations for the design of the microfluidic chip. (a) shows the microfluidic chip without ITO-covered glass with the parallel channel design from Figure 3.1.a. (b) shows the second channel design from 3.1.b without the ITO-covered glass. (c) is the third realization with ITO-covered glass. (d) shows the first operational OET chip with the ITO-covered glass and the photoconductive layer. (e) shows the operational OET chip with a more robust bottom ITO glass. 29
3.4 The final realizations of the microfluidic chip. (a) shows the chip from the design shown in Figure 3.1.c. The final design of the microfluidic chip with a 3D-printed chip holder is shown in (b). This chips fits the design from Figure 3.2.a. 29
3.5 A schematic depiction of an experimental setup to measure the transmittance of a sample using a light source with a certain frequency. The initial optical intensity from the light source I_0 partially passes through the sample, resulting in the transmitted intensity I_t. The intensity can be measured using an optical power meter. 30
3.6 A top view of the experimental setup to measure the transmittance and reflectance of different ITO glasses. (1) shows the LED, (2) and (3) show lenses to create a demagnified illumination spot on the optical power meter. (4) is the sample in the sample holder, and (5) is the optical power meter. 30
3.7 A schematic depiction of an experimental setup to measure the transmittance and reflectance of a sample using a light source with a certain frequency. The initial optical intensity from the light source I_0 is decreased by 50% due to the 50-50 beamsplitter. The remaining intensity partially passes through the sample, resulting in the transmitted intensity I_t, depicted in robin's egg blue, and the reflected intensity I_r, depicted in dark red. Both intensities can be measured using an optical power meter. The fractions displayed in the light beams are due to passing the beam splitter. 31
3.8 A top view of the experimental setup to measure the absorption of the photoconductive a-Si:H layer. (1) shows the LED whose illumination is demagnified using the lenses in (2) and (3). The beamsplitter is shown by (4). The sample is located at (5), and the optical power meter measures the light at (6). 32
3.9 An experimental setup to measure the relative conductivity of a fluid. 33
3.10 Four iterations of the chip holder for fabricating constant spaced chips. (a) shows version 1 of the iteration, which was used to test the dimensions of the chip. (b) shows iteration 4 of the chip holder. It includes a deeper cut for the microfluidic chip to be positioned in. The small cavities on the top right and bottom right are for electronic wires to be applied. (c) shows iteration 5 of the chip holder with small grips for eventual storage possibilities. (d) shows the final chip holder design, including a small space to put on a label. 34
3.11 Two iterations of the channel cutter for cutting constantly sized microfluidic chambers. (a) shows the front view of both iterations. (b) shows the back side of the first iteration, which has a flat surface. (c) shows the back side of the second iteration, which has less surface area to make the tape easier to remove. 35

3.12 Two iterations of the alignment tool. (a) shows the front view of the initial design. (b) shows the front view of the second iteration, which makes it possible to be left on the big ITO microscope slide when putting on the ITO coverglass. 36

3.13 The 3D printed chip holders. Each design fits a 25mm by 75mm ITO microscope slide inside. (a) shows version 1. (b) shows version 2. (c) shows version 3. (d) shows version 4. (e) shows version 5. (f) shows version 6. 36

3.14 The 3D printed channel cutters. (a) shows the front side of version 1. (b) shows the back side of version 1. (c) shows the back side of version 2. 36

3.15 The 3D printed alignment tools that fit a 25mm by 75mm ITO microscope slide. (a) shows version 1. (b) shows version 2. 37

3.16 The first iteration of the optical setup design. The light originates from the LED and is collimated by lens L1. After the DMD partly reflects it, it passes through lens L2, two mirrors M1 and M2, a beamsplitter BS, and through the objective on the OET chip. After illumination, it returns inside the objective and the beamsplitter to enter lens L3 to image in the sensor of the camera. 37

3.17 The second iteration of the optical setup design. The light originates from the LED and is collimated by lens L1. After the DMD partly reflects it, it passes through lens L2, a beamsplitter BS, and through the objective on the OET chip. After illumination, it returns inside the objective, and the beamsplitter is reflected by mirror M1 to enter lens L3 to image in the sensor of the camera. 38

3.18 The third iteration of the optical setup design. The light originates from the LED and is collimated by lens L1. After the DMD partly reflects it, it passes through lens L2, a mirror M1, a beamsplitter BS, and through the objective on the OET chip. After illumination, it returns inside the objective together with light from the lamp to pass the beamsplitter and be reflected by mirror M2 to enter lens L3 to image in the sensor of the camera after being filtered by neutral density filter F. 38

3.19 The fourth iteration of the optical setup design. The light originates from the LED and is collimated by lens L1. After the DMD partly reflects it, it passes through lens L2, a mirror M1, a beamsplitter BS, and the objective on the OET chip. After illumination, it returns inside the objective together with the red light from the lamp to pass the beamsplitter and be reflected by mirror M2 to enter lens L3 to image in the sensor of the camera. 39

3.20 The final iteration of the optical setup design. The light originates from the LED and is collimated by lens L1. The lens L1 and the DMD are aligned by mirrors M1 and M2. After the DMD partly reflects it, it passes through lens L2, a mirror M1, a beamsplitter BS, and the objective on the OET chip. After illumination, it returns inside the objective together with the red light from the lamp to pass the beamsplitter and be reflected by mirror M2 to enter lens L3 to image in the sensor of the camera. 39

3.21 The realization of the first iteration of the optical setup. (1) shows the LED with the collimation lens L1, and (2) shows the DMD. (3) shows lens L2. (4) and (5) are the mirrors M1 and M2. (6) is the beamsplitter. (7) shows the objective and the OET chip holder. (8) and (9) are the lens L3 and the camera. (a) shows the side view of the microscope. The camera on top is opposite to the chip, which is imaged using the objective pointing down. (b) shows a top view of the microscope where the DMD is well visible. 40

3.22 The realization of the second iteration of the optical setup. (1) shows the LED with the collimation lens L1, and (2) shows the DMD. (3) shows lens L2. (4) is the beamsplitter. (5) shows the objective and the OET chip holder. (6) shows the mirror M1 and the lens L3. (7) shows the camera. (a) shows a back view of the microscope. The microscope has two stages. The top stage has a platform on which the chip holder can be placed. The chip is illuminated from below. (b) shows a front view of the microscope. 40

3.23 The realization of the third and fourth iterations of the optical setup. In terms of looks, the third and fourth iterations only differ by the filters. (1) shows the LED with the collimation lens L1, and (2) shows the DMD. (3) shows lens L2. (4) is the beamsplitter. (5) shows the objective and the OET chip holder, and (6) shows the lamp. (7) shows the mirror M1 and the lens L3, and (8) shows the camera with the neutral density filter. (a) shows a back view of the microscope. The lamp illuminates the microfluidic chip from above. The black aluminum foil is to block the stray light from the DMD. (b) shows the front view of the microscope. 41

3.24 The realization of the final iteration of the optical setup. (1) shows the LED with the collimation lens L1, and (2) shows the alignment mirrors M1 and M2. (3) shows the DMD, which reflects the unwanted illumination on a black aluminum plate. (4) shows the beamsplitter BS, of which the stray light is blocked using tape. (5) shows the objective, the stage, and the microfluidic chip. (6) shows the lamp that illuminates the chip using red filtered light. (7) shows the mirror M4 with the lens L3 that focuses the light on the camera sensor. This camera is shown in (8). To store the dielectric media and the dielectric particles safely, a 3D-printed tube holder was designed, which is shown in (9). (a) shows a front view of the microscope, (b) shows the top view of the microscope, and (c) shows the back view of the microscope. 41

3.25 The spectra of the fluorescent beads in the TetraSpeck Fluorescent Microspheres Size Kit. The data is retrieved from the manufacturer [83]. 43

3.26 The fluorescence microscope setup to measure the resolution using the TestraSpeck Fluorescent Microspheres Size Kit and white light source. 43

3.27 An example of using reslice in Fiji. (a) shows a 1 μm diameter bead around 0.14 mm out of focus. In the lower plot, we can see that this matches the intensity at the top of this lower plot. In the small plot to the right, this matches the left. (b) shows the same bead but now in focus. The intensities in both smaller plots are now also at maximum. (c) shows the same bead but 0.13 mm out of focus. This matches the lower part of the small plot below and the right part of the small plot on the right. 44

3.28 The blue LED focused on the optical power sensor such that the full sensor is illuminated. 45

3.29 The power sensor after the alignment mirrors. (a) shows the blue light focused on the sensor so that the full sensor is illuminated. (b) shows the sensor at the same location without the focusing lens. 45

3.30 The power sensor placed on the optical path after the DMD and after a lens that focuses the light on the full sensor. 46

3.31 The optical power meter on the last part of the optical path. (a) shows the sensor placed between the objective lens and a lens that focuses the blue light such that the full sensor is illuminated. (b) shows the optical sensor placed at the place where the microfluidic chip would be set. 46

3.32 The alignment tool using the red CPS635R laser and two SM1D12D irises. The irises make sure that the laser light passes straight through the center of the cage system. Two movable translation stages and a single tilt stage can be used to align the laser. . . 47

3.33 The design of the microgear robots. (a) shows the initial design of the microgear with all the dimensions denoted. (b) shows the microgear design with the ”mouth”. 49

3.34 The STL files of the second iteration of the microbot design. (a) shows the new microbot with a thickness of 50 μm. The small dots are semispheres with a diameter of 10 μm. (b) shows the same microbot but with a thickness of 10 μm. (c) shows a preview of the Nanoscribe where 144 microbots are to be printed in a matrix. 72 microbots with a thickness of 50 μm and 72 microbots with a thickness of 10 μm. 49

3.35 Images made of 3 different types of microbots using a microscope in the chemical laboratory of the faculty ME of the Delft University of Technology. (a) shows the initial design from Figure 3.33.a. (b) shows the same initial design with added 15 μm diameter semispheres. (c) shows the four-legged microbot. 50

3.36 The setup used for separating the PDMS microbots from their substrate. (a) shows the printed robots still attached to the substrate. (b) shows the equipment used to detach the microbots. (1) is the sonicator, (2) is the centrifuge. (3) shows the hot plate with two filled beakers. (4) are the tubes in which the PDMS microbots are deposited using the Eppendorf pipettes shown in (5). 50

3.37 An image of 2 microbots with polystyrene beads inside a microfluidic OET chip created using the OET optical setup. 51

3.38 The expected real parts of the CM factors of PDMS, in blue, and polystyrene, in red, in deionized water. For the PDMS we have $\mathrm{Re}[K(0)] = -0.5$ and $\mathrm{Re}[K(\infty)] = -0.476$. For the polystyrene we have $\mathrm{Re}[K(0)] = 1$ and $\mathrm{Re}[K(\infty)] = -0.475$. For the polystyrene, we find an expected cross-over frequency of 328.9 kHz. 52

4.1 The measured reflection percentages of ITO covered microscope slides with resistances 8-12 Ω, 15-30 Ω, and 70-100 Ω for photons with wavelengths of 470 nm, 635 nm, and 715 nm. The black line denotes the measured reflection percentages of a-Si:H at the same photon wavelengths. 59

4.2 The measured absorption coefficient of the used a-Si:H shown in red with its standard deviation. The blue line shows the absorption coefficient of a-Si:H as found by H. Kang [99]. The green line shows the absorption coefficient of a-Si:H as found by W. Liang [36]. The black dashed line shows the maximum absorption coefficient that we are able to measure using the experimental setup. 60

4.3 The full OET setup. (1) shows the blue LED, which provides light for the illumination of the photoconductive layer. (2) shows the DMD, which determines which pattern gets deflected. This created the control in the OET. (3) shows the microfluidic chip on the movable stage. In the microfluidic chip, the dielectric particles are imaged and manipulated by the DEP force. (4) shows the signal generator, which provides the electrical signal to the microfluidic chip with a particular shape and frequency. (5) shows the waveform amplifier, which increases the voltage, and thus also increases the strength of the electrical field inside the microfluidic chip. (6) shows the oscilloscope, which shows the electrical input signal of the OET. (8) shows the 3D-printed tube holder to safely store the dielectric media and the dielectric particle. (9) shows the computer used for control, imaging, and analysis of the DEP force. 61

4.4 The optical setup used for the OET, denoting three clusters of optical elements by the red dashed rectangles. The efficiency of these three clusters is measured using two different wavelengths of light. 63

4.5 A view of Fiji where we measured the PSF of a single 3 by 3 pixel DMD square projection on the chip. The left screen shows the image of the DMD spot. The yellow line determines the cross-section at which the PSF on the right side is measured. A Gaussian fit is put on the PSF, shown as the blue line. 65

4.6 The lateral resolution and its standard deviation of a single DMD square. The horizontal axis shows the side length in the number of DMD pixels of this DMD square. The vertical axis shows the lateral resolution in µm. The blue dashed line shows a linear fit $y = ax+b$ with $a = 1.6487$ µm and $b = 0.4282$ µm. 66

4.7 The increase in measured maximum intensity depending on the side length of the squares in the grid pattern. The horizontal axis shows the side length in the number of DMD pixels of this DMD square. The vertical axis shows the grey value $\times 10^4$. 66

4.8 A view of Fiji where we show the PSF of nine 7 by 7 pixel DMD square projections on the chip. The left screen shows the image of the DMD spot. The yellow line determines the cross-section at which the PSF on the right side is measured. 67

4.9 A plot showing the maximum intensity distribution of a DMD projection on the microfluidic chip using a 7 by 7 pixel grid as shown in Figure 4.8. The axes denote the positions of the projected dots in the grid. The values inside shown are the relative measured maximum intensities in percentage of the biggest measured intensity. 67

4.10 The measured DEP force exerted on the microbot using a sweep animation with a sweep time of 7 seconds and a thickness of 120 DMD pixels. The microbots are submerged in deionized water with 0.05% Tween-20. The electrical signal is a square wave with a Vpp of 30 V. The blue line shows the measured averaged DEP forces. The red patch shows the measured standard deviation. The green dashed line is an exponential fitted line of the form $y = ae^{-bx} + c$ with $a = 650$, $b = 0.0817$ and $c = 15$. The left vertical axis shows the DEP force magnitude in pN when calculated using the Stokes drag force. The right vertical axis shows the DEP force magnitude in pN when using the conversion rate from literature [8]. 68
4.11 The measured DEP force exerted on the 15 μm polystyrene beads using a sweep animation with a sweep time of 7 seconds and a thickness of 120 DMD pixels. The beads are submerged in deionized water with 0.05% Tween-20. The electrical signal is a square wave with a Vpp of 30 V. The blue line shows the measured averaged DEP forces. The red patch shows the measured standard deviation. The green dashed line is an exponential fitted line of the form $y = ae^{-bx} + c$ with $a = 15$, $b = 0.0817$, and $c = 7$. The left vertical axis shows the DEP force magnitude in pN when calculated using the Stokes drag force. 69
4.12 The effect of light intensity on the DEP force on the microbot and a 15 μm polystyrene bead. The measurements were done using a sweep animation with a sweep time of 15 seconds and a sweep thickness of 90 DMD pixels. All dielectric particles were submerged in deionized water with 0.05% Tween-20. The electrical signal was a square wave with a Vpp of 30 V and a frequency of 5 kHz. The relative current on the LED is given as a percentage of the current at full power. The relative power/force is given as a percentage of the power/force at full optical power. 69
4.13 The effect of sweep thickness on the DEP force on the microbot and a 15 μm polystyrene bead. The measurements were done using a sweep animation with a sweep time of 15 seconds. All dielectric particles were submerged in deionized water with 0.05% Tween-20. The electrical signal was a square wave with a Vpp of 30 V and a frequency of 5 kHz. The optical power of the 455 nm LED was set to maximum output. The relative force is given as a percentage of the force at the sweep thickness of 120 pixels. 70
4.14 The real part of the Clausius-Mossotti factor of both the polystyrene beads and the PDMS microbots in both pure deionized water and deionized water containing 0.05% Tween-20, shown as dashed lines. The values of the CM-factor of the beads are shown on the right vertical axis in orange. The values of the CM-factor of the microbots are shown in blue on the left vertical axis. The red patches show the frequency regions where the chips started to deteriorate due to electrolysis. 72

A.1 The light spectrum of the background in the lab where the OET setup is located. This measurement was done with the main lights of the lab turned on. 127
A.2 The light spectrum of the initial blue LED used for patterning in the OET setup. This LED has a wavelength of 470 nm. 128
A.3 The light spectrum of the second blue LED used for patterning in the OET setup. This LED has a wavelength of 455 nm. 128
A.4 The light spectrum of the lamp used for imaging the full chip in the OET setup. 129
A.5 The light spectrum of the lamp with the red plastic filter, used for imaging the full chip in the OET setup. 129
A.6 The light spectrum of the laser used for experiments and collimation. 130
A.7 The emission spectrum of the blue FluoSphere color. The blue line shows the emission spectrum. The orange line shows the Riemann sum. The dotted blue line is located at half of the total area under the emission spectrum, calculate using the Riemann sum. This dotted blue line is located at the center of mass which is at 420 nm. 131
A.8 The emission spectrum of the yellow-green FluoSphere color. The blue line shows the emission spectrum. The orange line shows the Riemann sum. The dotted blue line is located at half of the total area under the emission spectrum, calculate using the Riemann sum. This dotted blue line is located at the center of mass which is at 532 nm. 131

A.9 The emission spectrum of the orange FluoSphere color. The blue line shows the emission spectrum. The orange line shows the Riemann sum. The dotted blue line is located at half of the total area under the emission spectrum, calculate using the Riemann sum. This dotted blue line is located at the center of mass which is at 566 nm. 131

A.10 The emission spectrum of the dark red FluoSphere color. The blue line shows the emission spectrum. The orange line shows the Riemann sum. The dotted blue line is located at half of the total area under the emission spectrum, calculate using the Riemann sum. This dotted blue line is located at the center of mass which is at 692 nm. 131

C.1 A view of Fiji were we measured the PSF of a single 1 by 1 pixel DMD square projection on the chip. The left screen shows the image of the DMD spot. The yellow line determines the cross-section at which the PSF on the right side is measured. A Gaussian fit is put on the PSF, shown as the blue line. 180

C.2 A view of Fiji were we measured the PSF of a single 2 by 2 pixel DMD square projection on the chip. The left screen shows the image of the DMD spot. The yellow line determines the cross-section at which the PSF on the right side is measured. A Gaussian fit is put on the PSF, shown as the blue line. 180

C.3 A view of Fiji were we measured the PSF of a single 4 by 4 pixel DMD square projection on the chip. The left screen shows the image of the DMD spot. The yellow line determines the cross-section at which the PSF on the right side is measured. A Gaussian fit is put on the PSF, shown as the blue line. 180

C.4 A view of Fiji were we measured the PSF of a single 5 by 5 pixel DMD square projection on the chip. The left screen shows the image of the DMD spot. The yellow line determines the cross-section at which the PSF on the right side is measured. A Gaussian fit is put on the PSF, shown as the blue line. 181

C.5 A view of Fiji were we measured the PSF of a single 6 by 6 pixel DMD square projection on the chip. The left screen shows the image of the DMD spot. The yellow line determines the cross-section at which the PSF on the right side is measured. A Gaussian fit is put on the PSF, shown as the blue line. 181

C.6 A view of Fiji were we measured the PSF of a single 7 by 7 pixel DMD square projection on the chip. The left screen shows the image of the DMD spot. The yellow line determines the cross-section at which the PSF on the right side is measured. A Gaussian fit is put on the PSF, shown as the blue line. 182

C.7 A view of Fiji were we measured the PSF of a single 8 by 8 pixel DMD square projection on the chip. The left screen shows the image of the DMD spot. The yellow line determines the cross-section at which the PSF on the right side is measured. A Gaussian fit is put on the PSF, shown as the blue line. 182

C.8 A view of Fiji were we measured the PSF of a single 9 by 9 pixel DMD square projection on the chip. The left screen shows the image of the DMD spot. The yellow line determines the cross-section at which the PSF on the right side is measured. A Gaussian fit is put on the PSF, shown as the blue line. 183

C.9 A view of Fiji were we measured the PSF of a single 10 by 10 pixel DMD square projection on the chip. The left screen shows the image of the DMD spot. The yellow line determines the cross-section at which the PSF on the right side is measured. A Gaussian fit is put on the PSF, shown as the blue line. 183

D.1 The measured velocities and accelerations of the 15 µm polystyrene beads in the OET with a medium of deionized water with 0.05% Tween-20. The used sweep animation had a sweep time of 3 seconds and a thickness of 120 pixels. The voltage on the chip was 30 V with a frequency of 1 kHz. 208

D.2 The measured velocities and accelerations of the 15 µm polystyrene beads in the OET with a medium of deionized water with 0.05% Tween-20. The used sweep animation had a sweep time of 5 seconds and a thickness of 30 pixels. The voltage on the chip was 30 V with a frequency of 5 kHz. 208

D.3 The measured velocities and accelerations of the 15 µm polystyrene beads in the OET with a medium of deionized water with 0.05% Tween-20. The used sweep animation had a sweep time of 7 seconds and a thickness of 120 pixels. The voltage on the chip was 30 V with a frequency of 1 kHz. 209
D.4 The measured velocities and accelerations of the 15 µm polystyrene beads in the OET with a medium of deionized water with 0.05% Tween-20. The used sweep animation had a sweep time of 7 seconds and a thickness of 120 pixels. The voltage on the chip was 30 V with a frequency of 2 kHz. 209
D.5 The measured velocities and accelerations of the 15 µm polystyrene beads in the OET with a medium of deionized water with 0.05% Tween-20. The used sweep animation had a sweep time of 7 seconds and a thickness of 120 pixels. The voltage on the chip was 30 V with a frequency of 3 kHz. 210
D.6 The measured velocities and accelerations of the 15 µm polystyrene beads in the OET with a medium of deionized water with 0.05% Tween-20. The used sweep animation had a sweep time of 7 seconds and a thickness of 120 pixels. The voltage on the chip was 30 V with a frequency of 4 kHz. 210
D.7 The measured velocities and accelerations of the 15 µm polystyrene beads in the OET with a medium of deionized water with 0.05% Tween-20. The used sweep animation had a sweep time of 7 seconds and a thickness of 120 pixels. The voltage on the chip was 30 V with a frequency of 5 kHz. 211
D.8 The measured velocities and accelerations of the 15 µm polystyrene beads in the OET with a medium of deionized water with 0.05% Tween-20. The used sweep animation had a sweep time of 7 seconds and a thickness of 120 pixels. The voltage on the chip was 30 V with a frequency of 6 kHz. 211
D.9 The measured velocities and accelerations of the 15 µm polystyrene beads in the OET with a medium of deionized water with 0.05% Tween-20. The used sweep animation had a sweep time of 7 seconds and a thickness of 120 pixels. The voltage on the chip was 30 V with a frequency of 7 kHz. 212
D.10 The measured velocities and accelerations of the 15 µm polystyrene beads in the OET with a medium of deionized water with 0.05% Tween-20. The used sweep animation had a sweep time of 7 seconds and a thickness of 120 pixels. The voltage on the chip was 30 V with a frequency of 8 kHz. 212
D.11 The measured velocities and accelerations of the 15 µm polystyrene beads in the OET with a medium of deionized water with 0.05% Tween-20. The used sweep animation had a sweep time of 7 seconds and a thickness of 120 pixels. The voltage on the chip was 30 V with a frequency of 9 kHz. 213
D.12 The measured velocities and accelerations of the 15 µm polystyrene beads in the OET with a medium of deionized water with 0.05% Tween-20. The used sweep animation had a sweep time of 7 seconds and a thickness of 120 pixels. The voltage on the chip was 30 V with a frequency of 10 kHz. 213
D.13 The measured velocities and accelerations of the 15 µm polystyrene beads in the OET with a medium of deionized water with 0.05% Tween-20. The used sweep animation had a sweep time of 7 seconds and a thickness of 120 pixels. The voltage on the chip was 30 V with a frequency of 11 kHz. 214
D.14 The measured velocities and accelerations of the 15 µm polystyrene beads in the OET with a medium of deionized water with 0.05% Tween-20. The used sweep animation had a sweep time of 7 seconds and a thickness of 120 pixels. The voltage on the chip was 30 V with a frequency of 12 kHz. 214
D.15 The measured velocities and accelerations of the 15 µm polystyrene beads in the OET with a medium of deionized water with 0.05% Tween-20. The used sweep animation had a sweep time of 7 seconds and a thickness of 120 pixels. The voltage on the chip was 30 V with a frequency of 13 kHz. 215
D.16 The measured velocities and accelerations of the 15 µm polystyrene beads in the OET with a medium of deionized water with 0.05% Tween-20. The used sweep animation had a sweep time of 7 seconds and a thickness of 120 pixels. The voltage on the chip was 30 V with a frequency of 14 kHz. 215

D.17 The measured velocities and accelerations of the 15 µm polystyrene beads in the OET with a medium of deionized water with 0.05% Tween-20. The used sweep animation had a sweep time of 7 seconds and a thickness of 120 pixels. The voltage on the chip was 30 V with a frequency of 15 kHz. 216
D.18 The measured velocities and accelerations of the 15 µm polystyrene beads in the OET with a medium of deionized water with 0.05% Tween-20. The used sweep animation had a sweep time of 7 seconds and a thickness of 120 pixels. The voltage on the chip was 30 V with a frequency of 16 kHz. 216
D.19 The measured velocities and accelerations of the 15 µm polystyrene beads in the OET with a medium of deionized water with 0.05% Tween-20. The used sweep animation had a sweep time of 7 seconds and a thickness of 120 pixels. The voltage on the chip was 30 V with a frequency of 17 kHz. 217
D.20 The measured velocities and accelerations of the 15 µm polystyrene beads in the OET with a medium of deionized water with 0.05% Tween-20. The used sweep animation had a sweep time of 7 seconds and a thickness of 120 pixels. The voltage on the chip was 30 V with a frequency of 18 kHz. 217
D.21 The measured velocities and accelerations of the 15 µm polystyrene beads in the OET with a medium of deionized water with 0.05% Tween-20. The used sweep animation had a sweep time of 7 seconds and a thickness of 120 pixels. The voltage on the chip was 30 V with a frequency of 19 kHz. 218
D.22 The measured velocities and accelerations of the 15 µm polystyrene beads in the OET with a medium of deionized water with 0.05% Tween-20. The used sweep animation had a sweep time of 7 seconds and a thickness of 120 pixels. The voltage on the chip was 30 V with a frequency of 20 kHz. 218
D.23 The measured velocities and accelerations of the 15 µm polystyrene beads in the OET with a medium of deionized water with 0.05% Tween-20. The used sweep animation had a sweep time of 7 seconds and a thickness of 120 pixels. The voltage on the chip was 30 V with a frequency of 50 kHz. 219
D.24 The measured velocities and accelerations of the 15 µm polystyrene beads in the OET with a medium of deionized water with 0.05% Tween-20. The used sweep animation had a sweep time of 7 seconds and a thickness of 120 pixels. The voltage on the chip was 30 V with a frequency of 100 kHz. 219
D.25 The measured velocities and accelerations of the 15 µm polystyrene beads in the OET with a medium of deionized water with 0.05% Tween-20. The used sweep animation had a sweep time of 15 seconds and a thickness of 60 pixels. The voltage on the chip was 30 V with a frequency of 1 kHz. 220
D.26 The measured velocities and accelerations of the 15 µm polystyrene beads in the OET with a medium of deionized water with 0.05% Tween-20. The used sweep animation had a sweep time of 15 seconds and a thickness of 90 pixels. The voltage on the chip was 30 V with a frequency of 1 kHz. 220
D.27 The measured velocities and accelerations of the 15 µm polystyrene beads in the OET with a medium of deionized water with 0.05% Tween-20. The used sweep animation had a sweep time of 15 seconds and a thickness of 120 pixels. The voltage on the chip was 30 V with a frequency of 1 kHz. 221
D.28 The measured velocities and accelerations of the 15 µm polystyrene beads in the OET with a medium of deionized water with 0.05% Tween-20. The used sweep animation had a sweep time of 15 seconds and a thickness of 30 pixels. The voltage on the chip was 30 V with a frequency of 5 kHz. 221
D.29 The measured velocities and accelerations of the 15 µm polystyrene beads in the OET with a medium of deionized water with 0.05% Tween-20. The used sweep animation had a sweep time of 15 seconds and a thickness of 60 pixels. The voltage on the chip was 30 V with a frequency of 5 kHz. 222
D.30 The measured velocities and accelerations of the 15 µm polystyrene beads in the OET with a medium of deionized water with 0.05% Tween-20. The used sweep animation had a sweep time of 15 seconds and a thickness of 90 pixels. The voltage on the chip was 30 V with a frequency of 5 kHz. 222

D.31 The measured velocities and accelerations of the 15 µm polystyrene beads in the OET with a medium of deionized water with 0.05% Tween-20. The used sweep animation had a sweep time of 15 seconds and a thickness of 90 pixels. The voltage on the chip was 30 V with a frequency of 5 kHz. The illumination was set to 1/3 of full power. 223
D.32 The measured velocities and accelerations of the 15 µm polystyrene beads in the OET with a medium of deionized water with 0.05% Tween-20. The used sweep animation had a sweep time of 15 seconds and a thickness of 90 pixels. The voltage on the chip was 30 V with a frequency of 5 kHz. The illumination was set to 1/2 of full power. 223
D.33 The measured velocities and accelerations of the 15 µm polystyrene beads in the OET with a medium of deionized water with 0.05% Tween-20. The used sweep animation had a sweep time of 15 seconds and a thickness of 90 pixels. The voltage on the chip was 30 V with a frequency of 5 kHz. The illumination was set to 2/3 of full power. 224
D.34 The measured velocities and accelerations of the 15 µm polystyrene beads in the OET with a medium of deionized water with 0.05% Tween-20. The used sweep animation had a sweep time of 15 seconds and a thickness of 90 pixels. The voltage on the chip was 30 V with a frequency of 5 kHz. The illumination was set to 5/6 of full power. 224
D.35 The measured velocities and accelerations of the 15 µm polystyrene beads in the OET with a medium of deionized water with 0.05% Tween-20. The used sweep animation had a sweep time of 15 seconds and a thickness of 120 pixels. The voltage on the chip was 30 V with a frequency of 5 kHz. 225
D.36 The measured velocities and accelerations of the 15 µm polystyrene beads in the OET with a medium of deionized water with 0.05% Tween-20. The used sweep animation had a sweep time of 15 seconds and a thickness of 30 pixels. The voltage on the chip was 30 V with a frequency of 10 kHz. 225
D.37 The measured velocities and accelerations of the 15 µm polystyrene beads in the OET with a medium of deionized water with 0.05% Tween-20. The used sweep animation had a sweep time of 15 seconds and a thickness of 90 pixels. The voltage on the chip was 30 V with a frequency of 10 kHz. 226
D.38 The measured velocities and accelerations of the 15 µm polystyrene beads in the OET with a medium of deionized water with 0.05% Tween-20. The used sweep animation had a sweep time of 15 seconds and a thickness of 30 pixels. The voltage on the chip was 30 V with a frequency of 13 kHz. 226
D.39 The measured velocities and accelerations of the 15 µm polystyrene beads in the OET with a medium of deionized water with 0.05% Tween-20. The used sweep animation had a sweep time of 15 seconds and a thickness of 30 pixels. The voltage on the chip was 30 V with a frequency of 15 kHz. 227
D.40 The measured velocities and accelerations of the 15 µm polystyrene beads in the OET with a medium of deionized water with 0.05% Tween-20. The used sweep animation had a sweep time of 15 seconds and a thickness of 90 pixels. The voltage on the chip was 30 V with a frequency of 15 kHz. 227
D.41 The measured velocities and accelerations of the 15 µm polystyrene beads in the OET with a medium of deionized water with 0.05% Tween-20. The used sweep animation had a sweep time of 15 seconds and a thickness of 30 pixels. The voltage on the chip was 30 V with a frequency of 18 kHz. 228
D.42 The measured positions, velocities, and accelerations of the center position of the microbot in the OET with a medium of deionized water with 0.05% Tween-20. The used sweep animation had a sweep time of 3 seconds and a thickness of 120 pixels. The voltage on the chip was 30 V with a frequency of 18 kHz. 228
D.43 The measured positions, velocities, and accelerations of the center position of the microbot in the OET with a medium of deionized water with 0.05% Tween-20. The used sweep animation had a sweep time of 5 seconds and a thickness of 30 pixels. The voltage on the chip was 30 V with a frequency of 5 kHz. 229
D.44 The measured positions, velocities, and accelerations of the center position of the microbot in the OET with a medium of deionized water with 0.05% Tween-20. The used sweep animation had a sweep time of 7 seconds and a thickness of 120 pixels. The voltage on the chip was 30 V with a frequency of 1 kHz. 229

D.45 The measured positions, velocities, and accelerations of the center position of the microbot in the OET with a medium of deionized water with 0.05% Tween-20. The used sweep animation had a sweep time of 7 seconds and a thickness of 120 pixels. The voltage on the chip was 30 V with a frequency of 2 kHz. 230
D.46 The measured positions, velocities, and accelerations of the center position of the microbot in the OET with a medium of deionized water with 0.05% Tween-20. The used sweep animation had a sweep time of 7 seconds and a thickness of 120 pixels. The voltage on the chip was 30 V with a frequency of 3 kHz. 230
D.47 The measured positions, velocities, and accelerations of the center position of the microbot in the OET with a medium of deionized water with 0.05% Tween-20. The used sweep animation had a sweep time of 7 seconds and a thickness of 120 pixels. The voltage on the chip was 30 V with a frequency of 4 kHz. 231
D.48 The measured positions, velocities, and accelerations of the center position of the microbot in the OET with a medium of deionized water with 0.05% Tween-20. The used sweep animation had a sweep time of 7 seconds and a thickness of 120 pixels. The voltage on the chip was 30 V with a frequency of 5 kHz. 231
D.49 The measured positions, velocities, and accelerations of the center position of the microbot in the OET with a medium of deionized water with 0.05% Tween-20. The used sweep animation had a sweep time of 7 seconds and a thickness of 120 pixels. The voltage on the chip was 30 V with a frequency of 6 kHz. 232
D.50 The measured positions, velocities, and accelerations of the center position of the microbot in the OET with a medium of deionized water with 0.05% Tween-20. The used sweep animation had a sweep time of 7 seconds and a thickness of 120 pixels. The voltage on the chip was 30 V with a frequency of 7 kHz. 232
D.51 The measured positions, velocities, and accelerations of the center position of the microbot in the OET with a medium of deionized water with 0.05% Tween-20. The used sweep animation had a sweep time of 7 seconds and a thickness of 120 pixels. The voltage on the chip was 30 V with a frequency of 8 kHz. 233
D.52 The measured positions, velocities, and accelerations of the center position of the microbot in the OET with a medium of deionized water with 0.05% Tween-20. The used sweep animation had a sweep time of 7 seconds and a thickness of 120 pixels. The voltage on the chip was 30 V with a frequency of 9 kHz. 233
D.53 The measured positions, velocities, and accelerations of the center position of the microbot in the OET with a medium of deionized water with 0.05% Tween-20. The used sweep animation had a sweep time of 7 seconds and a thickness of 120 pixels. The voltage on the chip was 30 V with a frequency of 10 kHz. 234
D.54 The measured positions, velocities, and accelerations of the center position of the microbot in the OET with a medium of deionized water with 0.05% Tween-20. The used sweep animation had a sweep time of 7 seconds and a thickness of 120 pixels. The voltage on the chip was 30 V with a frequency of 11 kHz. 234
D.55 The measured positions, velocities, and accelerations of the center position of the microbot in the OET with a medium of deionized water with 0.05% Tween-20. The used sweep animation had a sweep time of 7 seconds and a thickness of 120 pixels. The voltage on the chip was 30 V with a frequency of 12 kHz. 235
D.56 The measured positions, velocities, and accelerations of the center position of the microbot in the OET with a medium of deionized water with 0.05% Tween-20. The used sweep animation had a sweep time of 7 seconds and a thickness of 120 pixels. The voltage on the chip was 30 V with a frequency of 13 kHz. 235
D.57 The measured positions, velocities, and accelerations of the center position of the microbot in the OET with a medium of deionized water with 0.05% Tween-20. The used sweep animation had a sweep time of 7 seconds and a thickness of 120 pixels. The voltage on the chip was 30 V with a frequency of 14 kHz. 236
D.58 The measured positions, velocities, and accelerations of the center position of the microbot in the OET with a medium of deionized water with 0.05% Tween-20. The used sweep animation had a sweep time of 7 seconds and a thickness of 120 pixels. The voltage on the chip was 30 V with a frequency of 15 kHz. 236

D.59 The measured positions, velocities, and accelerations of the center position of the microbot in the OET with a medium of deionized water with 0.05% Tween-20. The used sweep animation had a sweep time of 7 seconds and a thickness of 120 pixels. The voltage on the chip was 30 V with a frequency of 16 kHz. 237

D.60 The measured positions, velocities, and accelerations of the center position of the microbot in the OET with a medium of deionized water with 0.05% Tween-20. The used sweep animation had a sweep time of 7 seconds and a thickness of 120 pixels. The voltage on the chip was 30 V with a frequency of 17 kHz. 237

D.61 The measured positions, velocities, and accelerations of the center position of the microbot in the OET with a medium of deionized water with 0.05% Tween-20. The used sweep animation had a sweep time of 7 seconds and a thickness of 120 pixels. The voltage on the chip was 30 V with a frequency of 18 kHz. 238

D.62 The measured positions, velocities, and accelerations of the center position of the microbot in the OET with a medium of deionized water with 0.05% Tween-20. The used sweep animation had a sweep time of 7 seconds and a thickness of 120 pixels. The voltage on the chip was 30 V with a frequency of 19 kHz. 238

D.63 The measured positions, velocities, and accelerations of the center position of the microbot in the OET with a medium of deionized water with 0.05% Tween-20. The used sweep animation had a sweep time of 7 seconds and a thickness of 120 pixels. The voltage on the chip was 30 V with a frequency of 20 kHz. 239

D.64 The measured positions, velocities, and accelerations of the center position of the microbot in the OET with a medium of deionized water with 0.05% Tween-20. The used sweep animation had a sweep time of 7 seconds and a thickness of 120 pixels. The voltage on the chip was 30 V with a frequency of 50 kHz. 239

D.65 The measured positions, velocities, and accelerations of the center position of the microbot in the OET with a medium of deionized water with 0.05% Tween-20. The used sweep animation had a sweep time of 7 seconds and a thickness of 120 pixels. The voltage on the chip was 30 V with a frequency of 100 kHz. 240

D.66 The measured positions, velocities, and accelerations of the center position of the microbot in the OET with a medium of deionized water with 0.05% Tween-20. The used sweep animation had a sweep time of 15 seconds and a thickness of 60 pixels. The voltage on the chip was 30 V with a frequency of 1 kHz. 240

D.67 The measured positions, velocities, and accelerations of the center position of the microbot in the OET with a medium of deionized water with 0.05% Tween-20. The used sweep animation had a sweep time of 15 seconds and a thickness of 90 pixels. The voltage on the chip was 30 V with a frequency of 1 kHz. 241

D.68 The measured positions, velocities, and accelerations of the center position of the microbot in the OET with a medium of deionized water with 0.05% Tween-20. The used sweep animation had a sweep time of 15 seconds and a thickness of 120 pixels. The voltage on the chip was 30 V with a frequency of 1 kHz. 241

D.69 The measured positions, velocities, and accelerations of the center position of the microbot in the OET with a medium of deionized water with 0.05% Tween-20. The used sweep animation had a sweep time of 15 seconds and a thickness of 30 pixels. The voltage on the chip was 30 V with a frequency of 5 kHz. 242

D.70 The measured positions, velocities, and accelerations of the center position of the microbot in the OET with a medium of deionized water with 0.05% Tween-20. The used sweep animation had a sweep time of 15 seconds and a thickness of 60 pixels. The voltage on the chip was 30 V with a frequency of 5 kHz. 242

D.71 The measured positions, velocities, and accelerations of the center position of the microbot in the OET with a medium of deionized water with 0.05% Tween-20. The used sweep animation had a sweep time of 15 seconds and a thickness of 90 pixels. The voltage on the chip was 30 V with a frequency of 5 kHz. 243

D.72 The measured positions, velocities, and accelerations of the center position of the microbot in the OET with a medium of deionized water with 0.05% Tween-20. The used sweep animation had a sweep time of 15 seconds and a thickness of 90 pixels. The voltage on the chip was 30 V with a frequency of 5 kHz. The illumination was set to 1/3 of full power. 243
D.73 The measured positions, velocities, and accelerations of the center position of the microbot in the OET with a medium of deionized water with 0.05% Tween-20. The used sweep animation had a sweep time of 15 seconds and a thickness of 90 pixels. The voltage on the chip was 30 V with a frequency of 5 kHz. The illumination was set to 1/2 of full power. 244
D.74 The measured positions, velocities, and accelerations of the center position of the microbot in the OET with a medium of deionized water with 0.05% Tween-20. The used sweep animation had a sweep time of 15 seconds and a thickness of 90 pixels. The voltage on the chip was 30 V with a frequency of 5 kHz. The illumination was set to 2/3 of full power. 244
D.75 The measured positions, velocities, and accelerations of the center position of the microbot in the OET with a medium of deionized water with 0.05% Tween-20. The used sweep animation had a sweep time of 15 seconds and a thickness of 90 pixels. The voltage on the chip was 30 V with a frequency of 5 kHz. The illumination was set to 5/6 of full power. 245
D.76 The measured positions, velocities, and accelerations of the center position of the microbot in the OET with a medium of deionized water with 0.05% Tween-20. The used sweep animation had a sweep time of 15 seconds and a thickness of 120 pixels. The voltage on the chip was 30 V with a frequency of 5 kHz. 245
D.77 The measured positions, velocities, and accelerations of the center position of the microbot in the OET with a medium of deionized water with 0.05% Tween-20. The used sweep animation had a sweep time of 15 seconds and a thickness of 30 pixels. The voltage on the chip was 30 V with a frequency of 10 kHz. 246
D.78 The measured positions, velocities, and accelerations of the center position of the microbot in the OET with a medium of deionized water with 0.05% Tween-20. The used sweep animation had a sweep time of 15 seconds and a thickness of 90 pixels. The voltage on the chip was 30 V with a frequency of 10 kHz. 246
D.79 The measured positions, velocities, and accelerations of the center position of the microbot in the OET with a medium of deionized water with 0.05% Tween-20. The used sweep animation had a sweep time of 15 seconds and a thickness of 30 pixels. The voltage on the chip was 30 V with a frequency of 13 kHz. 247
D.80 The measured positions, velocities, and accelerations of the center position of the microbot in the OET with a medium of deionized water with 0.05% Tween-20. The used sweep animation had a sweep time of 15 seconds and a thickness of 30 pixels. The voltage on the chip was 30 V with a frequency of 15 kHz. 247
D.81 The measured positions, velocities, and accelerations of the center position of the microbot in the OET with a medium of deionized water with 0.05% Tween-20. The used sweep animation had a sweep time of 15 seconds and a thickness of 90 pixels. The voltage on the chip was 30 V with a frequency of 15 kHz. 248
D.82 The measured positions, velocities, and accelerations of the center position of the microbot in the OET with a medium of deionized water with 0.05% Tween-20. The used sweep animation had a sweep time of 15 seconds and a thickness of 30 pixels. The voltage on the chip was 30 V with a frequency of 18 kHz. 248
D.83 The dynamics of the sweep pattern with the fitted linear function in orange. The sweep has a sweep time of 3 second and has a sweep thickness of 120 pixels. The input voltage of the experiment is 30 V with a frequency of 1 kHz. The sweep has a delay of 20 frames and has a peak at 44 frames. 249
D.84 The dynamics of the sweep pattern with the fitted linear function in orange. The sweep has a sweep time of 5 second and has a sweep thickness of 30 pixels. The input voltage of the experiment is 30 V with a frequency of 5 kHz. The sweep has a delay of 9 frames and has a peak at 21 frames. 249

D.85 The dynamics of the sweep pattern with the fitted linear function in orange. The sweep has a sweep time of 7 second and has a sweep thickness of 120 pixels. The input voltage of the experiment is 30 V with a frequency of 1 kHz. The sweep has a delay of 15 frames and has a peak at 32 frames. 249
D.86 The dynamics of the sweep pattern with the fitted linear function in orange. The sweep has a sweep time of 7 second and has a sweep thickness of 120 pixels. The input voltage of the experiment is 30 V with a frequency of 2 kHz. The sweep has a delay of 53 frames and has a peak at 113 frames. 249
D.87 The dynamics of the sweep pattern with the fitted linear function in orange. The sweep has a sweep time of 7 second and has a sweep thickness of 120 pixels. The input voltage of the experiment is 30 V with a frequency of 3 kHz. The sweep has a delay of 32 frames and has a peak at 93 frames. 250
D.88 The dynamics of the sweep pattern with the fitted linear function in orange. The sweep has a sweep time of 7 second and has a sweep thickness of 120 pixels. The input voltage of the experiment is 30 V with a frequency of 4 kHz. The sweep has a delay of 44 frames and has a peak at 104 frames. 250
D.89 The dynamics of the sweep pattern with the fitted linear function in orange. The sweep has a sweep time of 7 second and has a sweep thickness of 120 pixels. The input voltage of the experiment is 30 V with a frequency of 5 kHz. The sweep has a delay of 12 frames and has a peak at 72 frames. 250
D.90 The dynamics of the sweep pattern with the fitted linear function in orange. The sweep has a sweep time of 7 second and has a sweep thickness of 120 pixels. The input voltage of the experiment is 30 V with a frequency of 6 kHz. The sweep has a delay of 26 frames and has a peak at 86 frames. 250
D.91 The dynamics of the sweep pattern with the fitted linear function in orange. The sweep has a sweep time of 7 second and has a sweep thickness of 120 pixels. The input voltage of the experiment is 30 V with a frequency of 7 kHz. The sweep has a delay of 25 frames and has a peak at 86 frames. 251
D.92 The dynamics of the sweep pattern with the fitted linear function in orange. The sweep has a sweep time of 7 second and has a sweep thickness of 120 pixels. The input voltage of the experiment is 30 V with a frequency of 8 kHz. The sweep has a delay of 27 frames and has a peak at 86 frames. 251
D.93 The dynamics of the sweep pattern with the fitted linear function in orange. The sweep has a sweep time of 7 second and has a sweep thickness of 120 pixels. The input voltage of the experiment is 30 V with a frequency of 9 kHz. The sweep has a delay of 18 frames and has a peak at 78 frames. 251
D.94 The dynamics of the sweep pattern with the fitted linear function in orange. The sweep has a sweep time of 7 second and has a sweep thickness of 120 pixels. The input voltage of the experiment is 30 V with a frequency of 10 kHz. The sweep has a delay of 18 frames and has a peak at 77 frames. 251
D.95 The dynamics of the sweep pattern with the fitted linear function in orange. The sweep has a sweep time of 7 second and has a sweep thickness of 120 pixels. The input voltage of the experiment is 30 V with a frequency of 11 kHz. The sweep has a delay of 15 frames and has a peak at 76 frames. 252
D.96 The dynamics of the sweep pattern with the fitted linear function in orange. The sweep has a sweep time of 7 second and has a sweep thickness of 120 pixels. The input voltage of the experiment is 30 V with a frequency of 12 kHz. The sweep has a delay of 22 frames and has a peak at 83 frames. 252
D.97 The dynamics of the sweep pattern with the fitted linear function in orange. The sweep has a sweep time of 7 second and has a sweep thickness of 120 pixels. The input voltage of the experiment is 30 V with a frequency of 13 kHz. The sweep has a delay of 20 frames and has a peak at 81 frames. 252
D.98 The dynamics of the sweep pattern with the fitted linear function in orange. The sweep has a sweep time of 7 second and has a sweep thickness of 120 pixels. The input voltage of the experiment is 30 V with a frequency of 14 kHz. The sweep has a delay of 23 frames and has a peak at 84 frames. 252

D.99 The dynamics of the sweep pattern with the fitted linear function in orange. The sweep has a sweep time of 7 second and has a sweep thickness of 120 pixels. The input voltage of the experiment is 30 V with a frequency of 15 kHz. The sweep has a delay of 15 frames and has a peak at 75 frames. 253
D.100 The dynamics of the sweep pattern with the fitted linear function in orange. The sweep has a sweep time of 7 second and has a sweep thickness of 120 pixels. The input voltage of the experiment is 30 V with a frequency of 16 kHz. The sweep has a delay of 24 frames and has a peak at 84 frames. 253
D.101 The dynamics of the sweep pattern with the fitted linear function in orange. The sweep has a sweep time of 7 second and has a sweep thickness of 120 pixels. The input voltage of the experiment is 30 V with a frequency of 17 kHz. The sweep has a delay of 25 frames and has a peak at 86 frames. 253
D.102 The dynamics of the sweep pattern with the fitted linear function in orange. The sweep has a sweep time of 7 second and has a sweep thickness of 120 pixels. The input voltage of the experiment is 30 V with a frequency of 18 kHz. The sweep has a delay of 17 frames and has a peak at 77 frames. 253
D.103 The dynamics of the sweep pattern with the fitted linear function in orange. The sweep has a sweep time of 7 second and has a sweep thickness of 120 pixels. The input voltage of the experiment is 30 V with a frequency of 19 kHz. The sweep has a delay of 8 frames and has a peak at 69 frames. 254
D.104 The dynamics of the sweep pattern with the fitted linear function in orange. The sweep has a sweep time of 7 second and has a sweep thickness of 120 pixels. The input voltage of the experiment is 30 V with a frequency of 20 kHz. The sweep has a delay of 19 frames and has a peak at 79 frames. 254
D.105 The dynamics of the sweep pattern with the fitted linear function in orange. The sweep has a sweep time of 7 second and has a sweep thickness of 120 pixels. The input voltage of the experiment is 30 V with a frequency of 50 kHz. The sweep has a delay of 11 frames and has a peak at 71 frames. 254
D.106 The dynamics of the sweep pattern with the fitted linear function in orange. The sweep has a sweep time of 7 second and has a sweep thickness of 120 pixels. The input voltage of the experiment is 30 V with a frequency of 100 kHz. The sweep has a delay of 16 frames and has a peak at 77 frames. 254
D.107 The dynamics of the sweep pattern with the fitted linear function in orange. The sweep has a sweep time of 15 second and has a sweep thickness of 60 pixels. The input voltage of the experiment is 30 V with a frequency of 1 kHz. The sweep has a delay of 4 frames and has a peak at 19 frames. 255
D.108 The dynamics of the sweep pattern with the fitted linear function in orange. The sweep has a sweep time of 15 second and has a sweep thickness of 90 pixels. The input voltage of the experiment is 30 V with a frequency of 1 kHz. The sweep has a delay of 2 frames and has a peak at 18 frames. 255
D.109 The dynamics of the sweep pattern with the fitted linear function in orange. The sweep has a sweep time of 15 second and has a sweep thickness of 120 pixels. The input voltage of the experiment is 30 V with a frequency of 1 kHz. The sweep has a delay of 31 frames and has a peak at 141 frames. 255
D.110 The dynamics of the sweep pattern with the fitted linear function in orange. The sweep has a sweep time of 15 second and has a sweep thickness of 90 pixels. The input voltage of the experiment is 30 V with a frequency of 5 kHz. The sweep has a delay of 4 frames and has a peak at 20 frames. 255
D.111 The dynamics of the sweep pattern with the fitted linear function in orange. The sweep has a sweep time of 15 second and has a sweep thickness of 90 pixels. The input voltage of the experiment is 30 V with a frequency of 5 kHz. The illumination power was set to 1/3 of full power. The sweep has a delay of 5 frames and has a peak at 20 frames. . . . 256
D.112 The dynamics of the sweep pattern with the fitted linear function in orange. The sweep has a sweep time of 15 second and has a sweep thickness of 90 pixels. The input voltage of the experiment is 30 V with a frequency of 5 kHz. The illumination power was set to 1/2 of full power. The sweep has a delay of 4 frames and has a peak at 19 frames. . . . 256

D.113 The dynamics of the sweep pattern with the fitted linear function in orange. The sweep has a sweep time of 15 second and has a sweep thickness of 90 pixels. The input voltage of the experiment is 30 V with a frequency of 5 kHz. The illumination power was set to 2/3 of full power. The sweep has a delay of 4 frames and has a peak at 19 frames. . . . 256

D.114 The dynamics of the sweep pattern with the fitted linear function in orange. The sweep has a sweep time of 15 second and has a sweep thickness of 90 pixels. The input voltage of the experiment is 30 V with a frequency of 5 kHz. The illumination power was set to 5/6 of full power. The sweep has a delay of 3 frames and has a peak at 19 frames. . . . 256

D.115 The dynamics of the sweep pattern with the fitted linear function in orange. The sweep has a sweep time of 15 second and has a sweep thickness of 30 pixels. The input voltage of the experiment is 30 V with a frequency of 5 kHz. The sweep has a delay of 13 frames and has a peak at 49 frames. 257

D.116 The dynamics of the sweep pattern with the fitted linear function in orange. The sweep has a sweep time of 15 second and has a sweep thickness of 60 pixels. The input voltage of the experiment is 30 V with a frequency of 5 kHz. The sweep has a delay of 5 frames and has a peak at 20 frames. 257

D.117 The dynamics of the sweep pattern with the fitted linear function in orange. The sweep has a sweep time of 15 second and has a sweep thickness of 120 pixels. The input voltage of the experiment is 30 V with a frequency of 5 kHz. The sweep has a delay of 4 frames and has a peak at 20 frames. 257

D.118 The dynamics of the sweep pattern with the fitted linear function in orange. The sweep has a sweep time of 15 second and has a sweep thickness of 30 pixels. The input voltage of the experiment is 30 V with a frequency of 10 kHz. The sweep has a delay of 11 frames and has a peak at 63 frames. 257

D.119 The dynamics of the sweep pattern with the fitted linear function in orange. The sweep has a sweep time of 15 second and has a sweep thickness of 90 pixels. The input voltage of the experiment is 30 V with a frequency of 10 kHz. The sweep has a delay of 2 frames and has a peak at 17 frames. 258

D.120 The dynamics of the sweep pattern with the fitted linear function in orange. The sweep has a sweep time of 15 second and has a sweep thickness of 30 pixels. The input voltage of the experiment is 30 V with a frequency of 13 kHz. The sweep has a delay of 7 frames and has a peak at 34 frames. 258

D.121 The dynamics of the sweep pattern with the fitted linear function in orange. The sweep has a sweep time of 15 second and has a sweep thickness of 30 pixels. The input voltage of the experiment is 30 V with a frequency of 15 kHz. The sweep has a delay of 6 frames and has a peak at 54 frames. 258

D.122 The dynamics of the sweep pattern with the fitted linear function in orange. The sweep has a sweep time of 15 second and has a sweep thickness of 90 pixels. The input voltage of the experiment is 30 V with a frequency of 15 kHz. The sweep has a delay of 3 frames and has a peak at 18 frames. 258

D.123 The dynamics of the sweep pattern with the fitted linear function in orange. The sweep has a sweep time of 15 second and has a sweep thickness of 30 pixels. The input voltage of the experiment is 30 V with a frequency of 18 kHz. The sweep has a delay of 7 frames and has a peak at 38 frames. 259

D.124 The calculated DEP force on the microbot over time. The separate lines denote the partial forces in x and y directions, and the total force. The error bars denote the standard deviation of the measurement. The sweep used for creating the DEP force had a sweep time of 3 seconds and a sweep thickness of 120 pixels. The input voltage of the experiment is 30 V with a frequency of 1 kHz. 260

D.125 The calculated DEP force on the microbot over time. The separate lines denote the partial forces in x and y directions, and the total force. The error bars denote the standard deviation of the measurement. The sweep used for creating the DEP force had a sweep time of 5 seconds and a sweep thickness of 90 pixels. The input voltage of the experiment is 30 V with a frequency of 5 kHz. 260

D.126 The calculated DEP force on the microbot over time. The separate lines denote the partial forces in x and y directions, and the total force. The error bars denote the standard deviation of the measurement. The sweep used for creating the DEP force had a sweep time of 7 seconds and a sweep thickness of 120 pixels. The input voltage of the experiment is 30 V with a frequency of 1 kHz. 261
D.127 The calculated DEP force on the microbot over time. The separate lines denote the partial forces in x and y directions, and the total force. The error bars denote the standard deviation of the measurement. The sweep used for creating the DEP force had a sweep time of 7 seconds and a sweep thickness of 120 pixels. The input voltage of the experiment is 30 V with a frequency of 2 kHz. 261
D.128 The calculated DEP force on the microbot over time. The separate lines denote the partial forces in x and y directions, and the total force. The error bars denote the standard deviation of the measurement. The sweep used for creating the DEP force had a sweep time of 7 seconds and a sweep thickness of 120 pixels. The input voltage of the experiment is 30 V with a frequency of 3 kHz. 262
D.129 The calculated DEP force on the microbot over time. The separate lines denote the partial forces in x and y directions, and the total force. The error bars denote the standard deviation of the measurement. The sweep used for creating the DEP force had a sweep time of 7 seconds and a sweep thickness of 120 pixels. The input voltage of the experiment is 30 V with a frequency of 4 kHz. 262
D.130 The calculated DEP force on the microbot over time. The separate lines denote the partial forces in x and y directions, and the total force. The error bars denote the standard deviation of the measurement. The sweep used for creating the DEP force had a sweep time of 7 seconds and a sweep thickness of 120 pixels. The input voltage of the experiment is 30 V with a frequency of 5 kHz. 263
D.131 The calculated DEP force on the microbot over time. The separate lines denote the partial forces in x and y directions, and the total force. The error bars denote the standard deviation of the measurement. The sweep used for creating the DEP force had a sweep time of 7 seconds and a sweep thickness of 120 pixels. The input voltage of the experiment is 30 V with a frequency of 6 kHz. 263
D.132 The calculated DEP force on the microbot over time. The separate lines denote the partial forces in x and y directions, and the total force. The error bars denote the standard deviation of the measurement. The sweep used for creating the DEP force had a sweep time of 7 seconds and a sweep thickness of 120 pixels. The input voltage of the experiment is 30 V with a frequency of 7 kHz. 264
D.133 The calculated DEP force on the microbot over time. The separate lines denote the partial forces in x and y directions, and the total force. The error bars denote the standard deviation of the measurement. The sweep used for creating the DEP force had a sweep time of 7 seconds and a sweep thickness of 120 pixels. The input voltage of the experiment is 30 V with a frequency of 8 kHz. 264
D.134 The calculated DEP force on the microbot over time. The separate lines denote the partial forces in x and y directions, and the total force. The error bars denote the standard deviation of the measurement. The sweep used for creating the DEP force had a sweep time of 7 seconds and a sweep thickness of 120 pixels. The input voltage of the experiment is 30 V with a frequency of 9 kHz. 265
D.135 The calculated DEP force on the microbot over time. The separate lines denote the partial forces in x and y directions, and the total force. The error bars denote the standard deviation of the measurement. The sweep used for creating the DEP force had a sweep time of 7 seconds and a sweep thickness of 120 pixels. The input voltage of the experiment is 30 V with a frequency of 10 kHz. 265
D.136 The calculated DEP force on the microbot over time. The separate lines denote the partial forces in x and y directions, and the total force. The error bars denote the standard deviation of the measurement. The sweep used for creating the DEP force had a sweep time of 7 seconds and a sweep thickness of 120 pixels. The input voltage of the experiment is 30 V with a frequency of 11 kHz. 266

D.137 The calculated DEP force on the microbot over time. The separate lines denote the partial forces in x and y directions, and the total force. The error bars denote the standard deviation of the measurement. The sweep used for creating the DEP force had a sweep time of 7 seconds and a sweep thickness of 120 pixels. The input voltage of the experiment is 30 V with a frequency of 12 kHz. 266
D.138 The calculated DEP force on the microbot over time. The separate lines denote the partial forces in x and y directions, and the total force. The error bars denote the standard deviation of the measurement. The sweep used for creating the DEP force had a sweep time of 7 seconds and a sweep thickness of 120 pixels. The input voltage of the experiment is 30 V with a frequency of 13 kHz. 267
D.139 The calculated DEP force on the microbot over time. The separate lines denote the partial forces in x and y directions, and the total force. The error bars denote the standard deviation of the measurement. The sweep used for creating the DEP force had a sweep time of 7 seconds and a sweep thickness of 120 pixels. The input voltage of the experiment is 30 V with a frequency of 14 kHz. 267
D.140 The calculated DEP force on the microbot over time. The separate lines denote the partial forces in x and y directions, and the total force. The error bars denote the standard deviation of the measurement. The sweep used for creating the DEP force had a sweep time of 7 seconds and a sweep thickness of 120 pixels. The input voltage of the experiment is 30 V with a frequency of 15 kHz. 268
D.141 The calculated DEP force on the microbot over time. The separate lines denote the partial forces in x and y directions, and the total force. The error bars denote the standard deviation of the measurement. The sweep used for creating the DEP force had a sweep time of 7 seconds and a sweep thickness of 120 pixels. The input voltage of the experiment is 30 V with a frequency of 16 kHz. 268
D.142 The calculated DEP force on the microbot over time. The separate lines denote the partial forces in x and y directions, and the total force. The error bars denote the standard deviation of the measurement. The sweep used for creating the DEP force had a sweep time of 7 seconds and a sweep thickness of 120 pixels. The input voltage of the experiment is 30 V with a frequency of 17 kHz. 269
D.143 The calculated DEP force on the microbot over time. The separate lines denote the partial forces in x and y directions, and the total force. The error bars denote the standard deviation of the measurement. The sweep used for creating the DEP force had a sweep time of 7 seconds and a sweep thickness of 120 pixels. The input voltage of the experiment is 30 V with a frequency of 18 kHz. 269
D.144 The calculated DEP force on the microbot over time. The separate lines denote the partial forces in x and y directions, and the total force. The error bars denote the standard deviation of the measurement. The sweep used for creating the DEP force had a sweep time of 7 seconds and a sweep thickness of 120 pixels. The input voltage of the experiment is 30 V with a frequency of 19 kHz. 270
D.145 The calculated DEP force on the microbot over time. The separate lines denote the partial forces in x and y directions, and the total force. The error bars denote the standard deviation of the measurement. The sweep used for creating the DEP force had a sweep time of 7 seconds and a sweep thickness of 120 pixels. The input voltage of the experiment is 30 V with a frequency of 20 kHz. 270
D.146 The calculated DEP force on the microbot over time. The separate lines denote the partial forces in x and y directions, and the total force. The error bars denote the standard deviation of the measurement. The sweep used for creating the DEP force had a sweep time of 7 seconds and a sweep thickness of 120 pixels. The input voltage of the experiment is 30 V with a frequency of 50 kHz. 271
D.147 The calculated DEP force on the microbot over time. The separate lines denote the partial forces in x and y directions, and the total force. The error bars denote the standard deviation of the measurement. The sweep used for creating the DEP force had a sweep time of 7 seconds and a sweep thickness of 120 pixels. The input voltage of the experiment is 30 V with a frequency of 100 kHz. 271

D.148 The calculated DEP force on the microbot over time. The separate lines denote the partial forces in x and y directions, and the total force. The error bars denote the standard deviation of the measurement. The sweep used for creating the DEP force had a sweep time of 15 seconds and a sweep thickness of 60 pixels. The input voltage of the experiment is 30 V with a frequency of 1 kHz. 272

D.149 The calculated DEP force on the microbot over time. The separate lines denote the partial forces in x and y directions, and the total force. The error bars denote the standard deviation of the measurement. The sweep used for creating the DEP force had a sweep time of 15 seconds and a sweep thickness of 90 pixels. The input voltage of the experiment is 30 V with a frequency of 1 kHz. 272

D.150 The calculated DEP force on the microbot over time. The separate lines denote the partial forces in x and y directions, and the total force. The error bars denote the standard deviation of the measurement. The sweep used for creating the DEP force had a sweep time of 15 seconds and a sweep thickness of 120 pixels. The input voltage of the experiment is 30 V with a frequency of 1 kHz. 273

D.151 The calculated DEP force on the microbot over time. The separate lines denote the partial forces in x and y directions, and the total force. The error bars denote the standard deviation of the measurement. The sweep used for creating the DEP force had a sweep time of 15 seconds and a sweep thickness of 30 pixels. The input voltage of the experiment is 30 V with a frequency of 5 kHz. 273

D.152 The calculated DEP force on the microbot over time. The separate lines denote the partial forces in x and y directions, and the total force. The error bars denote the standard deviation of the measurement. The sweep used for creating the DEP force had a sweep time of 15 seconds and a sweep thickness of 60 pixels. The input voltage of the experiment is 30 V with a frequency of 5 kHz. 274

D.153 The calculated DEP force on the microbot over time. The separate lines denote the partial forces in x and y directions, and the total force. The error bars denote the standard deviation of the measurement. The sweep used for creating the DEP force had a sweep time of 15 seconds and a sweep thickness of 90 pixels. The input voltage of the experiment is 30 V with a frequency of 5 kHz. 274

D.154 The calculated DEP force on the microbot over time. The separate lines denote the partial forces in x and y directions, and the total force. The error bars denote the standard deviation of the measurement. The sweep used for creating the DEP force had a sweep time of 15 seconds and a sweep thickness of 90 pixels. The input voltage of the experiment is 30 V with a frequency of 5 kHz. The illumination power is set to 1/3 of the full power. 275

D.155 The calculated DEP force on the microbot over time. The separate lines denote the partial forces in x and y directions, and the total force. The error bars denote the standard deviation of the measurement. The sweep used for creating the DEP force had a sweep time of 15 seconds and a sweep thickness of 90 pixels. The input voltage of the experiment is 30 V with a frequency of 5 kHz. The illumination power is set to 1/2 of the full power. 275

D.156 The calculated DEP force on the microbot over time. The separate lines denote the partial forces in x and y directions, and the total force. The error bars denote the standard deviation of the measurement. The sweep used for creating the DEP force had a sweep time of 15 seconds and a sweep thickness of 90 pixels. The input voltage of the experiment is 30 V with a frequency of 5 kHz. The illumination power is set to 2/3 of the full power. 276

D.157 The calculated DEP force on the microbot over time. The separate lines denote the partial forces in x and y directions, and the total force. The error bars denote the standard deviation of the measurement. The sweep used for creating the DEP force had a sweep time of 15 seconds and a sweep thickness of 90 pixels. The input voltage of the experiment is 30 V with a frequency of 5 kHz. The illumination power is set to 5/6 of the full power. 276

D.158 The calculated DEP force on the microbot over time. The separate lines denote the partial forces in x and y directions, and the total force. The error bars denote the standard deviation of the measurement. The sweep used for creating the DEP force had a sweep time of 15 seconds and a sweep thickness of 120 pixels. The input voltage of the experiment is 30 V with a frequency of 5 kHz. 277

D.159 The calculated DEP force on the microbot over time. The separate lines denote the partial forces in x and y directions, and the total force. The error bars denote the standard deviation of the measurement. The sweep used for creating the DEP force had a sweep time of 15 seconds and a sweep thickness of 30 pixels. The input voltage of the experiment is 30 V with a frequency of 10 kHz. 277

D.160 The calculated DEP force on the microbot over time. The separate lines denote the partial forces in x and y directions, and the total force. The error bars denote the standard deviation of the measurement. The sweep used for creating the DEP force had a sweep time of 15 seconds and a sweep thickness of 90 pixels. The input voltage of the experiment is 30 V with a frequency of 10 kHz. 278

D.161 The calculated DEP force on the microbot over time. The separate lines denote the partial forces in x and y directions, and the total force. The error bars denote the standard deviation of the measurement. The sweep used for creating the DEP force had a sweep time of 15 seconds and a sweep thickness of 30 pixels. The input voltage of the experiment is 30 V with a frequency of 13 kHz. 278

D.162 The calculated DEP force on the microbot over time. The separate lines denote the partial forces in x and y directions, and the total force. The error bars denote the standard deviation of the measurement. The sweep used for creating the DEP force had a sweep time of 15 seconds and a sweep thickness of 30 pixels. The input voltage of the experiment is 30 V with a frequency of 15 kHz. 279

D.163 The calculated DEP force on the microbot over time. The separate lines denote the partial forces in x and y directions, and the total force. The error bars denote the standard deviation of the measurement. The sweep used for creating the DEP force had a sweep time of 15 seconds and a sweep thickness of 90 pixels. The input voltage of the experiment is 30 V with a frequency of 15 kHz. 279

D.164 The calculated DEP force on the microbot over time. The separate lines denote the partial forces in x and y directions, and the total force. The error bars denote the standard deviation of the measurement. The sweep used for creating the DEP force had a sweep time of 15 seconds and a sweep thickness of 30 pixels. The input voltage of the experiment is 30 V with a frequency of 18 kHz. 280

D.165 A comparison of the forces on the microbot calculated using Stokes's law and the conversion coefficient from literature [8]. The relative difference is shown as a dashed orange line. When this dashed orange line is not present, it means that the calculated force is 0 pN. The error bars denote the standard deviation of the measurement. The sweep used for creating the DEP force had a sweep time of 3 seconds and a sweep thickness of 120 pixels. The input voltage of the experiment is 30 V with a frequency of 1 kHz. 280

D.166 A comparison of the forces on the microbot calculated using Stokes's law and the conversion coefficient from literature [8]. The relative difference is shown as a dashed orange line. When this dashed orange line is not present, it means that the calculated force is 0 pN. The error bars denote the standard deviation of the measurement. The sweep used for creating the DEP force had a sweep time of 5 seconds and a sweep thickness of 30 pixels. The input voltage of the experiment is 30 V with a frequency of 5 kHz. 281

D.167 A comparison of the forces on the microbot calculated using Stokes's law and the conversion coefficient from literature [8]. The relative difference is shown as a dashed orange line. When this dashed orange line is not present, it means that the calculated force is 0 pN. The error bars denote the standard deviation of the measurement. The sweep used for creating the DEP force had a sweep time of 7 seconds and a sweep thickness of 120 pixels. The input voltage of the experiment is 30 V with a frequency of 1 kHz. 281

D.168 A comparison of the forces on the microbot calculated using Stokes's law and the conversion coefficient from literature [8]. The relative difference is shown as a dashed orange line. When this dashed orange line is not present, it means that the calculated force is 0 pN. The error bars denote the standard deviation of the measurement. The sweep used for creating the DEP force had a sweep time of 7 seconds and a sweep thickness of 120 pixels. The input voltage of the experiment is 30 V with a frequency of 2 kHz. 282

D.169 A comparison of the forces on the microbot calculated using Stokes's law and the conversion coefficient from literature [8]. The relative difference is shown as a dashed orange line. When this dashed orange line is not present, it means that the calculated force is 0 pN. The error bars denote the standard deviation of the measurement. The sweep used for creating the DEP force had a sweep time of 7 seconds and a sweep thickness of 120 pixels. The input voltage of the experiment is 30 V with a frequency of 3 kHz. 282

D.170 A comparison of the forces on the microbot calculated using Stokes's law and the conversion coefficient from literature [8]. The relative difference is shown as a dashed orange line. When this dashed orange line is not present, it means that the calculated force is 0 pN. The error bars denote the standard deviation of the measurement. The sweep used for creating the DEP force had a sweep time of 7 seconds and a sweep thickness of 120 pixels. The input voltage of the experiment is 30 V with a frequency of 4 kHz. 283

D.171 A comparison of the forces on the microbot calculated using Stokes's law and the conversion coefficient from literature [8]. The relative difference is shown as a dashed orange line. When this dashed orange line is not present, it means that the calculated force is 0 pN. The error bars denote the standard deviation of the measurement. The sweep used for creating the DEP force had a sweep time of 7 seconds and a sweep thickness of 120 pixels. The input voltage of the experiment is 30 V with a frequency of 5 kHz. 283

D.172 A comparison of the forces on the microbot calculated using Stokes's law and the conversion coefficient from literature [8]. The relative difference is shown as a dashed orange line. When this dashed orange line is not present, it means that the calculated force is 0 pN. The error bars denote the standard deviation of the measurement. The sweep used for creating the DEP force had a sweep time of 7 seconds and a sweep thickness of 120 pixels. The input voltage of the experiment is 30 V with a frequency of 6 kHz. 284

D.173 A comparison of the forces on the microbot calculated using Stokes's law and the conversion coefficient from literature [8]. The relative difference is shown as a dashed orange line. When this dashed orange line is not present, it means that the calculated force is 0 pN. The error bars denote the standard deviation of the measurement. The sweep used for creating the DEP force had a sweep time of 7 seconds and a sweep thickness of 120 pixels. The input voltage of the experiment is 30 V with a frequency of 7 kHz. 284

D.174 A comparison of the forces on the microbot calculated using Stokes's law and the conversion coefficient from literature [8]. The relative difference is shown as a dashed orange line. When this dashed orange line is not present, it means that the calculated force is 0 pN. The error bars denote the standard deviation of the measurement. The sweep used for creating the DEP force had a sweep time of 7 seconds and a sweep thickness of 120 pixels. The input voltage of the experiment is 30 V with a frequency of 8 kHz. 285

D.175 A comparison of the forces on the microbot calculated using Stokes's law and the conversion coefficient from literature [8]. The relative difference is shown as a dashed orange line. When this dashed orange line is not present, it means that the calculated force is 0 pN. The error bars denote the standard deviation of the measurement. The sweep used for creating the DEP force had a sweep time of 7 seconds and a sweep thickness of 120 pixels. The input voltage of the experiment is 30 V with a frequency of 9 kHz. 285

D.176 A comparison of the forces on the microbot calculated using Stokes's law and the conversion coefficient from literature [8]. The relative difference is shown as a dashed orange line. When this dashed orange line is not present, it means that the calculated force is 0 pN. The error bars denote the standard deviation of the measurement. The sweep used for creating the DEP force had a sweep time of 7 seconds and a sweep thickness of 120 pixels. The input voltage of the experiment is 30 V with a frequency of 10 kHz. 286

D.177 A comparison of the forces on the microbot calculated using Stokes's law and the conversion coefficient from literature [8]. The relative difference is shown as a dashed orange line. When this dashed orange line is not present, it means that the calculated force is 0 pN. The error bars denote the standard deviation of the measurement. The sweep used for creating the DEP force had a sweep time of 7 seconds and a sweep thickness of 120 pixels. The input voltage of the experiment is 30 V with a frequency of 11 kHz. 286

D.178 A comparison of the forces on the microbot calculated using Stokes's law and the conversion coefficient from literature [8]. The relative difference is shown as a dashed orange line. When this dashed orange line is not present, it means that the calculated force is 0 pN. The error bars denote the standard deviation of the measurement. The sweep used for creating the DEP force had a sweep time of 7 seconds and a sweep thickness of 120 pixels. The input voltage of the experiment is 30 V with a frequency of 12 kHz. 287

D.179 A comparison of the forces on the microbot calculated using Stokes's law and the conversion coefficient from literature [8]. The relative difference is shown as a dashed orange line. When this dashed orange line is not present, it means that the calculated force is 0 pN. The error bars denote the standard deviation of the measurement. The sweep used for creating the DEP force had a sweep time of 7 seconds and a sweep thickness of 120 pixels. The input voltage of the experiment is 30 V with a frequency of 13 kHz. 287

D.180 A comparison of the forces on the microbot calculated using Stokes's law and the conversion coefficient from literature [8]. The relative difference is shown as a dashed orange line. When this dashed orange line is not present, it means that the calculated force is 0 pN. The error bars denote the standard deviation of the measurement. The sweep used for creating the DEP force had a sweep time of 7 seconds and a sweep thickness of 120 pixels. The input voltage of the experiment is 30 V with a frequency of 14 kHz. 288

D.181 A comparison of the forces on the microbot calculated using Stokes's law and the conversion coefficient from literature [8]. The relative difference is shown as a dashed orange line. When this dashed orange line is not present, it means that the calculated force is 0 pN. The error bars denote the standard deviation of the measurement. The sweep used for creating the DEP force had a sweep time of 7 seconds and a sweep thickness of 120 pixels. The input voltage of the experiment is 30 V with a frequency of 15 kHz. 288

D.182 A comparison of the forces on the microbot calculated using Stokes's law and the conversion coefficient from literature [8]. The relative difference is shown as a dashed orange line. When this dashed orange line is not present, it means that the calculated force is 0 pN. The error bars denote the standard deviation of the measurement. The sweep used for creating the DEP force had a sweep time of 7 seconds and a sweep thickness of 120 pixels. The input voltage of the experiment is 30 V with a frequency of 16 kHz. 289

D.183 A comparison of the forces on the microbot calculated using Stokes's law and the conversion coefficient from literature [8]. The relative difference is shown as a dashed orange line. When this dashed orange line is not present, it means that the calculated force is 0 pN. The error bars denote the standard deviation of the measurement. The sweep used for creating the DEP force had a sweep time of 7 seconds and a sweep thickness of 120 pixels. The input voltage of the experiment is 30 V with a frequency of 17 kHz. 289

D.184 A comparison of the forces on the microbot calculated using Stokes's law and the conversion coefficient from literature [8]. The relative difference is shown as a dashed orange line. When this dashed orange line is not present, it means that the calculated force is 0 pN. The error bars denote the standard deviation of the measurement. The sweep used for creating the DEP force had a sweep time of 7 seconds and a sweep thickness of 120 pixels. The input voltage of the experiment is 30 V with a frequency of 18 kHz. 290

D.185 A comparison of the forces on the microbot calculated using Stokes's law and the conversion coefficient from literature [8]. The relative difference is shown as a dashed orange line. When this dashed orange line is not present, it means that the calculated force is 0 pN. The error bars denote the standard deviation of the measurement. The sweep used for creating the DEP force had a sweep time of 7 seconds and a sweep thickness of 120 pixels. The input voltage of the experiment is 30 V with a frequency of 19 kHz. 290

D.186 A comparison of the forces on the microbot calculated using Stokes's law and the conversion coefficient from literature [8]. The relative difference is shown as a dashed orange line. When this dashed orange line is not present, it means that the calculated force is 0 pN. The error bars denote the standard deviation of the measurement. The sweep used for creating the DEP force had a sweep time of 7 seconds and a sweep thickness of 120 pixels. The input voltage of the experiment is 30 V with a frequency of 20 kHz. 291

D.187 A comparison of the forces on the microbot calculated using Stokes's law and the conversion coefficient from literature [8]. The relative difference is shown as a dashed orange line. When this dashed orange line is not present, it means that the calculated force is 0 pN. The error bars denote the standard deviation of the measurement. The sweep used for creating the DEP force had a sweep time of 7 seconds and a sweep thickness of 120 pixels. The input voltage of the experiment is 30 V with a frequency of 50 kHz. 291

D.188 A comparison of the forces on the microbot calculated using Stokes's law and the conversion coefficient from literature [8]. The relative difference is shown as a dashed orange line. When this dashed orange line is not present, it means that the calculated force is 0 pN. The error bars denote the standard deviation of the measurement. The sweep used for creating the DEP force had a sweep time of 7 seconds and a sweep thickness of 120 pixels. The input voltage of the experiment is 30 V with a frequency of 100 kHz. 292

D.189 A comparison of the forces on the microbot calculated using Stokes's law and the conversion coefficient from literature [8]. The relative difference is shown as a dashed orange line. When this dashed orange line is not present, it means that the calculated force is 0 pN. The error bars denote the standard deviation of the measurement. The sweep used for creating the DEP force had a sweep time of 15 seconds and a sweep thickness of 60 pixels. The input voltage of the experiment is 30 V with a frequency of 1 kHz. 292

D.190 A comparison of the forces on the microbot calculated using Stokes's law and the conversion coefficient from literature [8]. The relative difference is shown as a dashed orange line. When this dashed orange line is not present, it means that the calculated force is 0 pN. The error bars denote the standard deviation of the measurement. The sweep used for creating the DEP force had a sweep time of 15 seconds and a sweep thickness of 90 pixels. The input voltage of the experiment is 30 V with a frequency of 1 kHz. 293

D.191 A comparison of the forces on the microbot calculated using Stokes's law and the conversion coefficient from literature [8]. The relative difference is shown as a dashed orange line. When this dashed orange line is not present, it means that the calculated force is 0 pN. The error bars denote the standard deviation of the measurement. The sweep used for creating the DEP force had a sweep time of 15 seconds and a sweep thickness of 120 pixels. The input voltage of the experiment is 30 V with a frequency of 1 kHz. . . . 293

D.192 A comparison of the forces on the microbot calculated using Stokes's law and the conversion coefficient from literature [8]. The relative difference is shown as a dashed orange line. When this dashed orange line is not present, it means that the calculated force is 0 pN. The error bars denote the standard deviation of the measurement. The sweep used for creating the DEP force had a sweep time of 15 seconds and a sweep thickness of 30 pixels. The input voltage of the experiment is 30 V with a frequency of 5 kHz. 294

D.193 A comparison of the forces on the microbot calculated using Stokes's law and the conversion coefficient from literature [8]. The relative difference is shown as a dashed orange line. When this dashed orange line is not present, it means that the calculated force is 0 pN. The error bars denote the standard deviation of the measurement. The sweep used for creating the DEP force had a sweep time of 15 seconds and a sweep thickness of 60 pixels. The input voltage of the experiment is 30 V with a frequency of 5 kHz. 294

D.194 A comparison of the forces on the microbot calculated using Stokes's law and the conversion coefficient from literature [8]. The relative difference is shown as a dashed orange line. When this dashed orange line is not present, it means that the calculated force is 0 pN. The error bars denote the standard deviation of the measurement. The sweep used for creating the DEP force had a sweep time of 15 seconds and a sweep thickness of 90 pixels. The input voltage of the experiment is 30 V with a frequency of 5 kHz. 295

D.195 A comparison of the forces on the microbot calculated using Stokes's law and the conversion coefficient from literature [8]. The relative difference is shown as a dashed orange line. When this dashed orange line is not present, it means that the calculated force is 0 pN. The error bars denote the standard deviation of the measurement. The sweep used for creating the DEP force had a sweep time of 15 seconds and a sweep thickness of 90 pixels. The input voltage of the experiment is 30 V with a frequency of 5 kHz. The illumination power used is 1/3 of the full power. 295

D.196 A comparison of the forces on the microbot calculated using Stokes's law and the conversion coefficient from literature [8]. The relative difference is shown as a dashed orange line. When this dashed orange line is not present, it means that the calculated force is 0 pN. The error bars denote the standard deviation of the measurement. The sweep used for creating the DEP force had a sweep time of 15 seconds and a sweep thickness of 90 pixels. The input voltage of the experiment is 30 V with a frequency of 5 kHz. The illumination power used is 1/2 of the full power. 296

D.197 A comparison of the forces on the microbot calculated using Stokes's law and the conversion coefficient from literature [8]. The relative difference is shown as a dashed orange line. When this dashed orange line is not present, it means that the calculated force is 0 pN. The error bars denote the standard deviation of the measurement. The sweep used for creating the DEP force had a sweep time of 15 seconds and a sweep thickness of 90 pixels. The input voltage of the experiment is 30 V with a frequency of 5 kHz. The illumination power used is 2/3 of the full power. 296

D.198 A comparison of the forces on the microbot calculated using Stokes's law and the conversion coefficient from literature [8]. The relative difference is shown as a dashed orange line. When this dashed orange line is not present, it means that the calculated force is 0 pN. The error bars denote the standard deviation of the measurement. The sweep used for creating the DEP force had a sweep time of 15 seconds and a sweep thickness of 90 pixels. The input voltage of the experiment is 30 V with a frequency of 5 kHz. The illumination power used is 5/6 of the full power. 297

D.199 A comparison of the forces on the microbot calculated using Stokes's law and the conversion coefficient from literature [8]. The relative difference is shown as a dashed orange line. When this dashed orange line is not present, it means that the calculated force is 0 pN. The error bars denote the standard deviation of the measurement. The sweep used for creating the DEP force had a sweep time of 15 seconds and a sweep thickness of 120 pixels. The input voltage of the experiment is 30 V with a frequency of 5 kHz. . . . 297

D.200 A comparison of the forces on the microbot calculated using Stokes's law and the conversion coefficient from literature [8]. The relative difference is shown as a dashed orange line. When this dashed orange line is not present, it means that the calculated force is 0 pN. The error bars denote the standard deviation of the measurement. The sweep used for creating the DEP force had a sweep time of 15 seconds and a sweep thickness of 30 pixels. The input voltage of the experiment is 30 V with a frequency of 10 kHz. 298

D.201 A comparison of the forces on the microbot calculated using Stokes's law and the conversion coefficient from literature [8]. The relative difference is shown as a dashed orange line. When this dashed orange line is not present, it means that the calculated force is 0 pN. The error bars denote the standard deviation of the measurement. The sweep used for creating the DEP force had a sweep time of 15 seconds and a sweep thickness of 90 pixels. The input voltage of the experiment is 30 V with a frequency of 10 kHz. 298

D.202 A comparison of the forces on the microbot calculated using Stokes's law and the conversion coefficient from literature [8]. The relative difference is shown as a dashed orange line. When this dashed orange line is not present, it means that the calculated force is 0 pN. The error bars denote the standard deviation of the measurement. The sweep used for creating the DEP force had a sweep time of 15 seconds and a sweep thickness of 30 pixels. The input voltage of the experiment is 30 V with a frequency of 13 kHz. 299

D.203 A comparison of the forces on the microbot calculated using Stokes's law and the conversion coefficient from literature [8]. The relative difference is shown as a dashed orange line. When this dashed orange line is not present, it means that the calculated force is 0 pN. The error bars denote the standard deviation of the measurement. The sweep used for creating the DEP force had a sweep time of 15 seconds and a sweep thickness of 30 pixels. The input voltage of the experiment is 30 V with a frequency of 15 kHz. 299
D.204 A comparison of the forces on the microbot calculated using Stokes's law and the conversion coefficient from literature [8]. The relative difference is shown as a dashed orange line. When this dashed orange line is not present, it means that the calculated force is 0 pN. The error bars denote the standard deviation of the measurement. The sweep used for creating the DEP force had a sweep time of 15 seconds and a sweep thickness of 90 pixels. The input voltage of the experiment is 30 V with a frequency of 15 kHz. 300
D.205 A comparison of the forces on the microbot calculated using Stokes's law and the conversion coefficient from literature [8]. The relative difference is shown as a dashed orange line. When this dashed orange line is not present, it means that the calculated force is 0 pN. The error bars denote the standard deviation of the measurement. The sweep used for creating the DEP force had a sweep time of 15 seconds and a sweep thickness of 30 pixels. The input voltage of the experiment is 30 V with a frequency of 18 kHz. 300

List of Tables

2.1 The photoconductivity of a-Si:H depends on the wavelength of the photons. For this data, an optical power of $S = 0.2$ mW/cm^2 was used [36]. 15

3.1 The lenses used in the five optical setup iterations. 40
3.2 The theoretical magnifications of each optical setup iteration. 42

4.1 Measured resistance per meter, correction factors, and conductivity for different concentrations of Tween-20 in deionized water. 58
4.2 Capacitance measurements and dielectric constant calculations for Tape, a-Si:H, and Air. 59
4.3 Capacitance measurements and dielectric constant calculations for different Tween-20 concentrations. 59
4.4 Reflected intensity measurements at different wavelengths for ITO-covered microscope slides with different resistances. All values are in nanowatts (nW) except for reflection percentages. 60
4.5 The measured absorption coefficient α of a-Si:H at different photon wavelengths with its standard deviation. The resulting reflection percentages with their standard deviations are calculated using this absorption coefficient and are also shown in Figure 4.1. 61
4.6 The measured distances in camera sensor pixels of objects in the microfluidic chip. Using the known ground truths of the lengths, the conversion and consequently, the magnification from the chip to the camera could be retrieved. 62
4.7 The measured distances in camera sensor pixels of projected DMD sweep animations in the microfluidic chip with different thicknesses. Using the known ground truths of the lengths, the conversion and consequently, the magnification from the DMD to the camera could be retrieved. The last two columns give the ratio between a DMD pixel size and a camera sensor pixel size. 62
4.8 Efficiency measurements for the Thorlabs M455D3 at different stages in the optical setup. FW = full white screen pattern on the DMD. 64p = checker pattern with blocks with a side length of 64 pixels. SP = only a single pixel in the center of the DMD switched on. 64
4.9 Efficiency measurements for the Roschwege HighPower LED Koningsblauw at different stages in the optical setup. FW = full white screen pattern on the DMD. 64p = checker pattern with blocks with a side length of 64 pixels. SP = only a single pixel in the center of the DMD switched on. 64
4.10 Measured values for the lateral resolution ρ and DoF $2\Delta Z$ with their corresponding derived wavelength values using three differently sized TetraSpeck Fluorescent beads. . . 65
4.11 Highest DEP forces found for the microbot under different experimental conditions. The DEP force is expressed in picoNewtons (pN). 71
4.12 Lowest DEP forces found for the microbot under different experimental conditions. The DEP force is expressed in picoNewtons (pN). 71

B.1 Measurements of the thickness of a single strip of double-sided tape. The first 5 measurements were done on the tape with the protective foil attached. The second measurement was done on only the sticky tape and the third measurement was done on only the protective foil. The calculated foil thickness was done by subtracting the measured the tape thickness from the measured tape+foil thickness. 137

B.2 Measurements of the thickness of a 2 pieces of tape stuck together with their sticky sides together. The first 5 measurements were done on the 2 tapes with the protective foils attached. The second measurement was done with one piece of foil removed and the third measurement was done without any protective foil. The calculated foil thickness was done by subtracting the measured the ”1 foil + 2 tape” thickness from the measured ”2 foil + 2 tape” thickness. 137
B.3 Measurements of the thickness of a 2 pieces of tape stuck together with the sticky side of 1 piece of tape on to foil of the tape. The first 5 measurements were done on the 2 tapes with the protective foils attached. The second measurement was done with one piece of foil removed. The calculated foil thickness was done by subtracting the measured the ”1 foil + 2 tape” thickness from the measured ”2 foil + 2 tape” thickness. 138
B.4 Resistance measurements for different 8-12 Ω ITO glass samples and noise levels. . . 139
B.5 Resistance measurements of the wires and conductive tape used for supplying electricity to the microfluidic chip, with all values in Ohms (Ω). 139
B.6 Resistance measurements in deionized water at different distances. All values are in Ohms (Ω), except the last two rows in Ohms per meter (Ω/m). 140
B.7 Resistance measurements in deionized water with 0.05% Tween-20 at different distances. All values are in Ohms (Ω), except the last two rows in Ohms per meter (Ω/m). 140
B.8 Resistance measurements in deionized water with 5% Tween-20 at different distances. All values are in Ohms (Ω), except the last two rows in Ohms per meter (Ω/m). 140
B.9 Capacitance measurements for 2 small ITO covered microscope coverslips sandwiching a small single layer of double-sided tape. The relative permittivity is calculated using the formula of the capacitance from equation 3.3. 141
B.10 Capacitance measurements for a ITO covered microscope slide and a ITO covered coverslip, sandwiching a small single layer of double-sided tape and a 1μm layer of a-Si:H. The relative permittivity is calculated using the formula of the capacitance from equation 3.3. 142
B.11 Capacitance measurements of functional OET microfluidic chip number 2. The capacitance measurements were done using deionized water, deionized water with 5% Tween-20, and with air present in the microfluidic chip. The relative permittivity is calculated using the formula of the capacitance from equation 3.3. 143
B.12 Capacitance measurements of functional OET microfluidic chip number 3. The capacitance measurements were done using deionized water, and with air present in the microfluidic chip. The relative permittivity is calculated using the formula of the capacitance from equation 3.3. 144
B.13 Capacitance measurements of functional OET microfluidic chip number 10. The capacitance measurements were done using deionized water with 0.05% Tween-20, and with air present in the microfluidic chip. The relative permittivity is calculated using the formula of the capacitance from equation 3.3. 145
B.14 Capacitance measurements of functional OET microfluidic chip number 11. The capacitance measurements were done using deionized water with 0.05% Tween-20, and with air present in the microfluidic chip. The relative permittivity is calculated using the formula of the capacitance from equation 3.3. 146
B.15 Intensity measurements of the incoming light I_0 and noise in nanowatts for Thorlabs MC470L3-C1 with a wavelength of 470 nm. 147
B.16 Intensity measurements to measure the transmitted intensity I_t and reflected intensity I_r in nanowatts for different 8-12 Ω glass samples at 470 nm. 147
B.17 Intensity measurements to measure the transmitted intensity I_t and reflected intensity I_r in nanowatts for different 15-30 Ω glass samples at 470 nm. 148
B.18 Intensity measurements to measure the transmitted intensity I_t and reflected intensity I_r in nanowatts for different 70-100 Ω glass samples at 470 nm. 148
B.19 Intensity measurements of the incoming intensity I_0 in nanowatts for the Thorlabs CPS635R with a wavelength of 635 nm. 149
B.20 Intensity measurements to measure the transmitted intensity I_t and reflected intensity I_r in nanowatts for different 8-12 Ω glass samples at 635 nm. 149

B.21 Intensity measurements to measure the transmitted intensity I_t and reflected intensity I_r in nanowatts for different 15-30 Ω glass samples at 635 nm. 150
B.22 Intensity measurements to measure the transmitted intensity I_t and reflected intensity I_r in nanowatts for different 70-100 Ω glass samples at 635 nm. 150
B.23 Intensity measurements of the initial intensity I_0 and noise levels in nanowatts for the Thorlabs QTH10/M with Red Plastic Filter with a wavelength of 715 nm. 151
B.24 Intensity measurements to measure the transmitted intensity I_t and reflected intensity I_r in nanowatts for different 8-12 Ω glass samples at 715 nm. 151
B.25 Intensity measurements to measure the transmitted intensity I_t and reflected intensity I_r in nanowatts for different 15-30 Ω glass samples at 715 nm. 152
B.26 Intensity measurements to measure the transmitted intensity I_t and reflected intensity I_r in nanowatts for different 70-100 Ω glass samples at 715 nm. 152
B.27 Measurements of the initial light power and the noise before and after the beam splitter for Thorlabs MC470L3-C1. 153
B.28 Measured and calculated reflection intensity for 8-12 Ω ITO glass at 470 nm in the setup containing the beamsplitter. This information is used for calculation the absorption coefficient of the a-Si:H. 153
B.29 Measured and calculated reflection intensity for 15-30 Ω ITO glass at 470 nm in the setup containing the beamsplitter. This information is used for calculation the absorption coefficient of the a-Si:H. 154
B.30 Measured and calculated reflection intensity for 70-100 Ω ITO glass at 470 nm in the setup containing the beamsplitter. This information is used for calculation the absorption coefficient of the a-Si:H. 154
B.31 Measurements of the initial light power and the noise before and after the beam splitter for Thorlabs CPS635R. 155
B.32 Measured and calculated reflection intensity for 8-12 Ω ITO glass at 635 nm in the setup containing the beamsplitter. This information is used for calculation the absorption coefficient of the a-Si:H. 155
B.33 Measured and calculated reflection intensity for 15-30 Ω ITO glass at 635 nm in the setup containing the beamsplitter. This information is used for calculation the absorption coefficient of the a-Si:H. 156
B.34 Measured and calculated reflection intensity for 70-100 Ω ITO glass at 635 nm in the setup containing the beamsplitter. This information is used for calculation the absorption coefficient of the a-Si:H. 156
B.35 Measurements of the initial light power and the noise before and after the beam splitter for Thorlabs QTH10/M+ red plastic filter. 157
B.36 Measured and calculated reflection intensity for 8-12 Ω ITO glass at 715 nm in the setup containing the beamsplitter. This information is used for calculation the absorption coefficient of the a-Si:H. 157
B.37 Measured and calculated reflection intensity for 15-30 Ω ITO glass at 715 nm in the setup containing the beamsplitter. This information is used for calculation the absorption coefficient of the a-Si:H. 158
B.38 Measured and calculated reflection intensity for 70-100 Ω ITO glass at 715 nm in the setup containing the beamsplitter. This information is used for calculation the absorption coefficient of the a-Si:H. 158
B.39 The upper table gives the initial light beam power with the calculated reflected power due to the ITO glass. The lower table shows the measurements of the transmitted light power, resulting in an absorption coefficient using equation 2.20. The ITO microscope slide has a resistance of 8-12 Ω and the photon wavelength used is 470 nm. 159
B.40 The upper table gives the initial light beam power with the calculated reflected power due to the ITO glass. The lower table shows the measurements of the transmitted light power, resulting in an absorption coefficient using equation 2.20. The ITO microscope slide has a resistance of 15-30 Ω and the photon wavelength used is 470 nm. 159

B.41 The upper table gives the initial light beam power with the calculated reflected power due to the ITO glass. The lower table shows the measurements of the transmitted light power, resulting in an absorption coefficient using equation 2.20. The ITO microscope slide has a resistance of 70-100 Ω and the photon wavelength used is 470 nm. 160
B.42 The upper table gives the initial light beam power with the calculated reflected power due to the ITO glass. The lower table shows the measurements of the transmitted light power, resulting in an absorption coefficient using equation 2.20. The ITO microscope slide has a resistance of 8-12 Ω and the photon wavelength used is 635 nm. 160
B.43 The upper table gives the initial light beam power with the calculated reflected power due to the ITO glass. The lower table shows the measurements of the transmitted light power, resulting in an absorption coefficient using equation 2.20. The ITO microscope slide has a resistance of 15-30 Ω and the photon wavelength used is 635 nm. 161
B.44 The upper table gives the initial light beam power with the calculated reflected power due to the ITO glass. The lower table shows the measurements of the transmitted light power, resulting in an absorption coefficient using equation 2.20. The ITO microscope slide has a resistance of 70-100 Ω and the photon wavelength used is 635 nm. 161
B.45 The upper table gives the initial light beam power with the calculated reflected power due to the ITO glass. The lower table shows the measurements of the transmitted light power, resulting in an absorption coefficient using equation 2.20. The ITO microscope slide has a resistance of 8-12 Ω and the photon wavelength used is 715 nm. 162
B.46 The upper table gives the initial light beam power with the calculated reflected power due to the ITO glass. The lower table shows the measurements of the transmitted light power, resulting in an absorption coefficient using equation 2.20. The ITO microscope slide has a resistance of 15-30 Ω and the photon wavelength used is 715 nm. 162
B.47 The upper table gives the initial light beam power with the calculated reflected power due to the ITO glass. The lower table shows the measurements of the transmitted light power, resulting in an absorption coefficient using equation 2.20. The ITO microscope slide has a resistance of 70-100 Ω and the photon wavelength used is 715 nm. 163

C.1 Multiple measurements done on beads with a diameter of 15 µm in the microfluidic chip using the optical setup. The measured size, in terms of camera pixels, gives the conversion using the ground truth of 15 µm. This conversion gives the magnification from the chip to the camera. 165
C.2 Multiple measurements done on the microbot with a diameter of 200 µm in the microfluidic chip using the optical setup. The measured size, in terms of camera pixels, gives the conversion using the ground truth of 200 µm. This conversion gives the magnification from the chip to the camera. 166
C.3 Multiple measurements done on the outer radius of the microbot, i.e. the microbot without the teeth, with a diameter of 125 µm in the microfluidic chip using the optical setup. The measured size, in terms of camera pixels, gives the conversion using the ground truth of 125 µm. This conversion gives the magnification from the chip to the camera. 166
C.4 Multiple measurements done on the width of the teeth of the microbot with a length of 25 µm in the microfluidic chip using the optical setup. The measured size, in terms of camera pixels, gives the conversion using the ground truth of 25 µm. This conversion gives the magnification from the chip to the camera. 166
C.5 Multiple measurements done on the width of the sweep animation created by the DMD and projected on the microfluidic chip. The sweep has a thickness of 30 pixels which is equal to 324 µm on the DMD. The measured size, in terms of camera pixels, gives the conversion from pixel to µm. This conversion gives the magnification from the DMD to the camera. 167
C.6 Multiple measurements done on the width of the sweep animation created by the DMD and projected on the microfluidic chip. The sweep has a thickness of 60 pixels which is equal to 648 µm on the DMD. The measured size, in terms of camera pixels, gives the conversion from pixel to µm. This conversion gives the magnification from the DMD to the camera. 167

C.7 Multiple measurements done on the width of the sweep animation created by the DMD and projected on the microfluidic chip. The sweep has a thickness of 90 pixels which is equal to 972 µm on the DMD. The measured size, in terms of camera pixels, gives the conversion from pixel to µm. This conversion gives the magnification from the DMD to the camera. 167

C.8 Multiple measurements done on the width of the sweep animation created by the DMD and projected on the microfluidic chip. The sweep has a thickness of 120 pixels which is equal to 1296 µm on the DMD. The measured size, in terms of camera pixels, gives the conversion from pixel to µm. This conversion gives the magnification from the DMD to the camera. 168

C.9 Measured optical power with different relative amounts of electrical power. When the power switch if fully on, the power is 1, while when half on, the power is 0.5. The LED used is the Thorlabs M455D3 and is measured by directly focusing the LED light on the power meter. 168

C.10 Measured optical power with different relative amounts of electrical power. When the power switch if fully on, the power is 1, while when half on, the power is 0.5. The LED used is the Roschwege HighPower LED Koningsblauw and is measured by directly focusing the LED light on the power meter. 168

C.11 Measured optical power after the allignment mirrors with different relative amounts of electrical power. When the power switch if fully on, the power is 1, while when half on, the power is 0.5. The LED used is the Thorlabs M455D3 and is measured by directly focusing the LED light on the power meter in the upper table. 169

C.12 Measured optical power after the DMD with different relative amounts of electrical power. When the power switch if fully on, the power is 1, while when half on, the power is 0.5. The DMD shows three different patterns: a full white screen, a 64 pixel sided checker, and a single mirror flipped on in the center. The LED used is the Thorlabs M455D3 and is measured by directly focusing the LED light on the power meter in the upper table. . . 169

C.13 Measured optical power after the DMD with different relative amounts of electrical power. When the power switch if fully on, the power is 1, while when half on, the power is 0.5. The DMD shows three different patterns: a full white screen, a 64 pixel sided checker, and a single mirror flipped on in the center. The LED used is the Thorlabs M455D3. . . 170

C.14 Measured optical power after the final objective lens with different relative amounts of electrical power. When the power switch if fully on, the power is 1, while when half on, the power is 0.5. The DMD shows three different patterns: a full white screen, a 64 pixel sided checker, and a single mirror flipped on in the center. The LED used is the Thorlabs M455D3. 170

C.15 Measured optical power before the final objective lens with different relative amounts of electrical power. When the power switch if fully on, the power is 1, while when half on, the power is 0.5. The DMD shows three different patterns: a full white screen, a 64 pixel sided checker, and a single mirror flipped on in the center. The LED used is the Thorlabs M455D3 and is measured by directly focusing the LED light on the power meter in the upper table. 171

C.16 Noise measurements taken at different positions in the setup for the Thorlabs M455D3. 171

C.17 Noise measurements taken at different positions in the setup for the Roschwege HighPower LED Koningsblauw. 172

C.18 Measured optical power after the allignment mirrors with different relative amounts of electrical power. When the power switch if fully on, the power is 1, while when half on, the power is 0.5. The LED used is the Roschwege HighPower LED Koningsblauw and is measured by directly focusing the LED light on the power meter in the upper table. . . 172

C.19 Measured optical power after the DMD with different relative amounts of electrical power. When the power switch if fully on, the power is 1, while when half on, the power is 0.5. The DMD shows three different patterns: a full white screen, a 64 pixel sided checker, and a single mirror flipped on in the center. The LED used is the Roschwege HighPower LED Koningsblauw and is measured by directly focusing the LED light on the power meter in the upper table. 173

C.20 Measured optical power after the DMD with different relative amounts of electrical power. When the power switch if fully on, the power is 1, while when half on, the power is 0.5. The DMD shows three different patterns: a full white screen, a 64 pixel sided checker, and a single mirror flipped on in the center. The LED used is the Roschwege HighPower LED Koningsblauw. 174
C.21 Measured optical power after the final objective lens with different relative amounts of electrical power. When the power switch if fully on, the power is 1, while when half on, the power is 0.5. The DMD shows three different patterns: a full white screen, a 64 pixel sided checker, and a single mirror flipped on in the center. The LED used is the Roschwege HighPower LED Koningsblauw. 175
C.22 Measured optical power before the final objective lens with different relative amounts of electrical power. When the power switch if fully on, the power is 1, while when half on, the power is 0.5. The DMD shows three different patterns: a full white screen, a 64 pixel sided checker, and a single mirror flipped on in the center. The LED used is the Roschwege HighPower LED Koningsblauw and is measured by directly focusing the LED light on the power meter in the upper table. 176
C.23 Spatial resolution measurements for a 4 µm TetraSpeck Fluorescent bead. The standard deviation of the Gaussian fit on the PSF and its full-width at half-maximum (FWHM) values are shown in micrometers (µm). 177
C.24 Depth of Focus (DoF) measurements for a TetraSpeck Fluorescent 4 µm bead. The standard deviation of the Gaussian fit on the PSF and its full-width at half-maximum (FWHM) values are shown in micrometers (µm). 177
C.25 Spatial resolution measurements for a 1 µm TetraSpeck Fluorescent bead. The standard deviation of the Gaussian fit on the PSF and its full-width at half-maximum (FWHM) values are shown in micrometers (µm). 178
C.26 Depth of Focus (DoF) measurements for a 1 µm TetraSpeck Fluorescent bead. The standard deviation of the Gaussian fit on the PSF and its full-width at half-maximum (FWHM) values are shown in micrometers (µm). 178
C.27 Spatial resolution measurements for a 0.5 µm TetraSpeck Fluorescent bead. The standard deviation of the Gaussian fit on the PSF and its full-width at half-maximum (FWHM) values are shown in micrometers (µm). 179
C.28 Depth of focus (DoF) measurements for a 0.5 µm TetraSpeck Fluorescent bead. The standard deviation of the Gaussian fit on the PSF and its full-width at half-maximum (FWHM) values are shown in micrometers (µm). 179
C.29 The standard deviation of a Gaussian fit on the PSF, its FWHM, and maximum intensity for different positions in a grid of 1 by 1 pixel tiles. Std. Gaussian Fit and FWHM are in micrometers (µm), while intensity is greyvalues. The light source used was a 455 nm LED. 184
C.30 The standard deviation of a Gaussian fit on the PSF, its FWHM, and maximum intensity for different positions in a grid of 2 by 2 pixel tiles. Std. Gaussian Fit and FWHM are in micrometers (µm), while intensity is greyvalues. The light source used was a 455 nm LED. 184
C.31 The standard deviation of a Gaussian fit on the PSF, its FWHM, and maximum intensity for different positions in a grid of 3 by 3 pixel tiles. Std. Gaussian Fit and FWHM are in micrometers (µm), while intensity is greyvalues. The light source used was a 455 nm LED. 185
C.32 The standard deviation of a Gaussian fit on the PSF, its FWHM, and maximum intensity for different positions in a grid of 4 by 4 pixel tiles. Std. Gaussian Fit and FWHM are in micrometers (µm), while intensity is greyvalues. The light source used was a 455 nm LED. 185
C.33 The standard deviation of a Gaussian fit on the PSF, its FWHM, and maximum intensity for different positions in a grid of 5 by 5 pixel tiles. Std. Gaussian Fit and FWHM are in micrometers (µm), while intensity is greyvalues. The light source used was a 455 nm LED. 186
C.34 The standard deviation of a Gaussian fit on the PSF, its FWHM, and maximum intensity for different positions in a grid of 6 by 6 pixel tiles. Std. Gaussian Fit and FWHM are in micrometers (µm), while intensity is greyvalues. The light source used was a 455 nm LED. 186
C.35 The standard deviation of a Gaussian fit on the PSF, its FWHM, and maximum intensity for different positions in a grid of 7 by 7 pixel tiles. Std. Gaussian Fit and FWHM are in micrometers (µm), while intensity is greyvalues. The light source used was a 455 nm LED. 187

C.36 The standard deviation of a Gaussian fit on the PSF, its FWHM, and maximum intensity for different positions in a grid of 8 by 8 pixel tiles. Std. Gaussian Fit and FWHM are in micrometers (μm), while intensity is greyvalues. The light source used was a 455 nm LED. 187
C.37 The standard deviation of a Gaussian fit on the PSF, its FWHM, and maximum intensity for different positions in a grid of 9 by 9 pixel tiles. Std. Gaussian Fit and FWHM are in micrometers (μm), while intensity is greyvalues. The light source used was a 455 nm LED. 188
C.38 The standard deviation of a Gaussian fit on the PSF, its FWHM, and maximum intensity for different positions in a grid of 10 by 10 pixel tiles. Std. Gaussian Fit and FWHM are in micrometers (μm), while intensity is greyvalues. The light source used was a 455 nm LED. 188
C.39 Increase of the spatial resolution with increase square sizes in the projected grid. The light source used was a 455 nm LED. 189
C.40 Increase of maximum intensity as a function of grid size. All values are measured in grey value. 189
C.41 Intensity values of the pixel center positions of a grid of 7 by 7 pixel squares. The X an Y positions denote the position of the grid pixels. The intensities are given in grey values. 190

D.1 Limits of the applied electrical signal frequency before electrolysis occurs for different chips in deionized water at varying voltage levels. 301
D.2 Limits of the applied electrical signal frequency before electrolysis occurs for different chips in deionized water with 0.05% Tween-20 at varying voltage levels. 301
D.3 Limits of the applied electrical signal frequency before electrolysis occurs for different chips in deionized water with 5% Tween-20 at varying voltage levels. 301

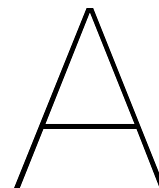

Experimental

A.1. Intensity Spectra

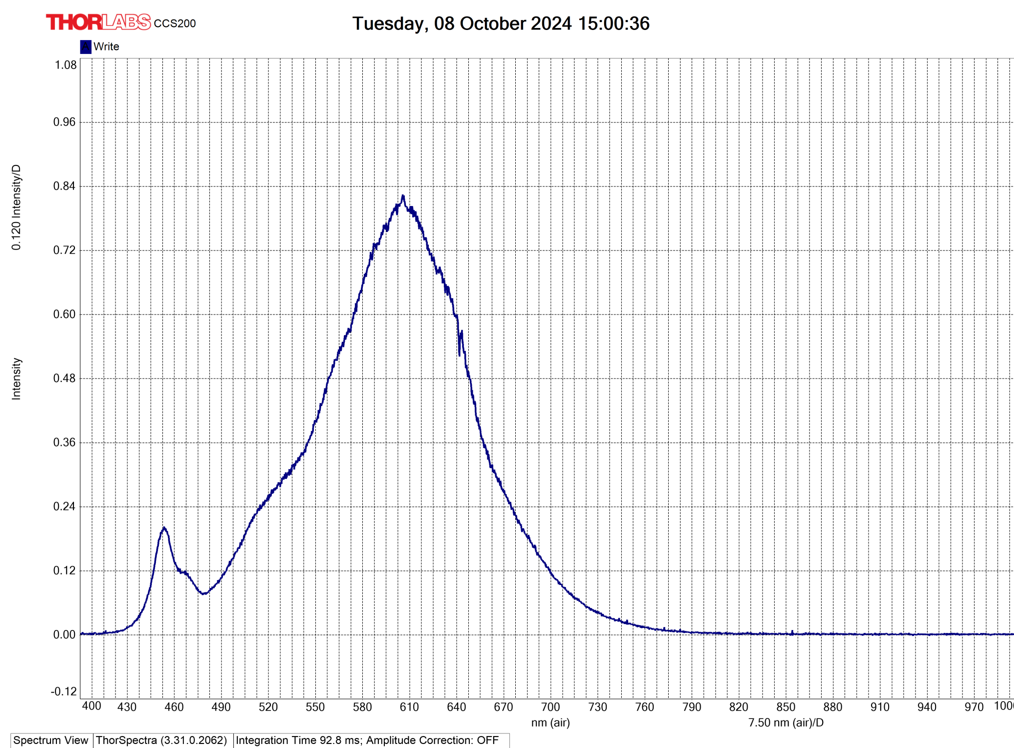

Figure A.1: The light spectrum of the background in the lab where the OET setup is located. This measurement was done with the main lights of the lab turned on.

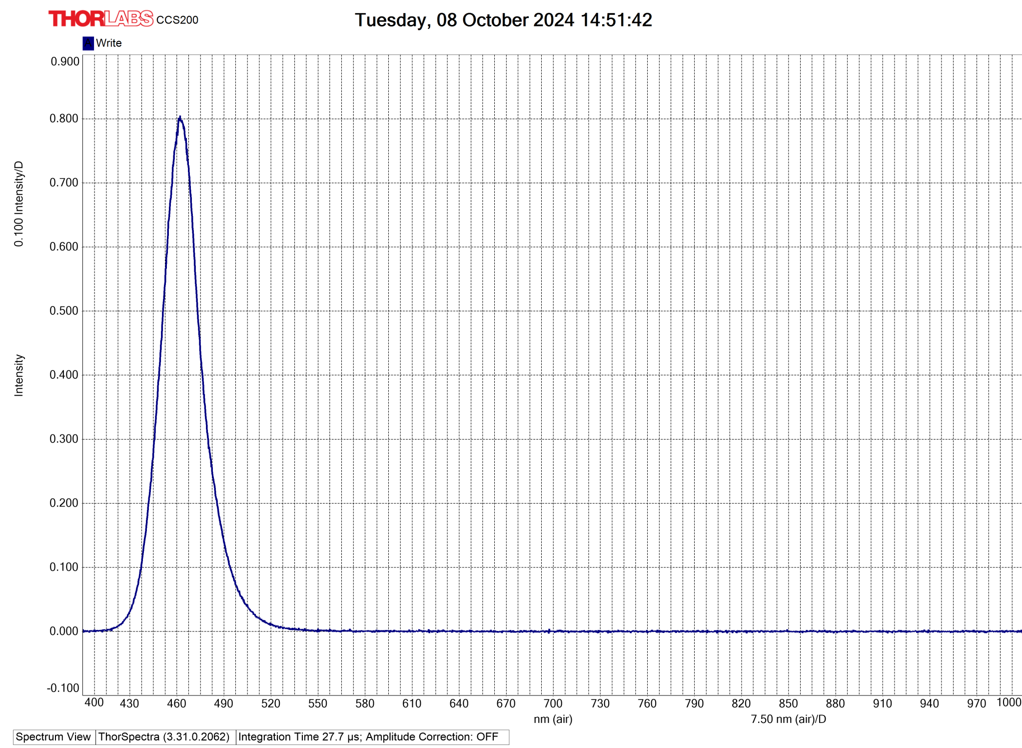

Figure A.2: The light spectrum of the initial blue LED used for patterning in the OET setup. This LED has a wavelength of 470 nm.

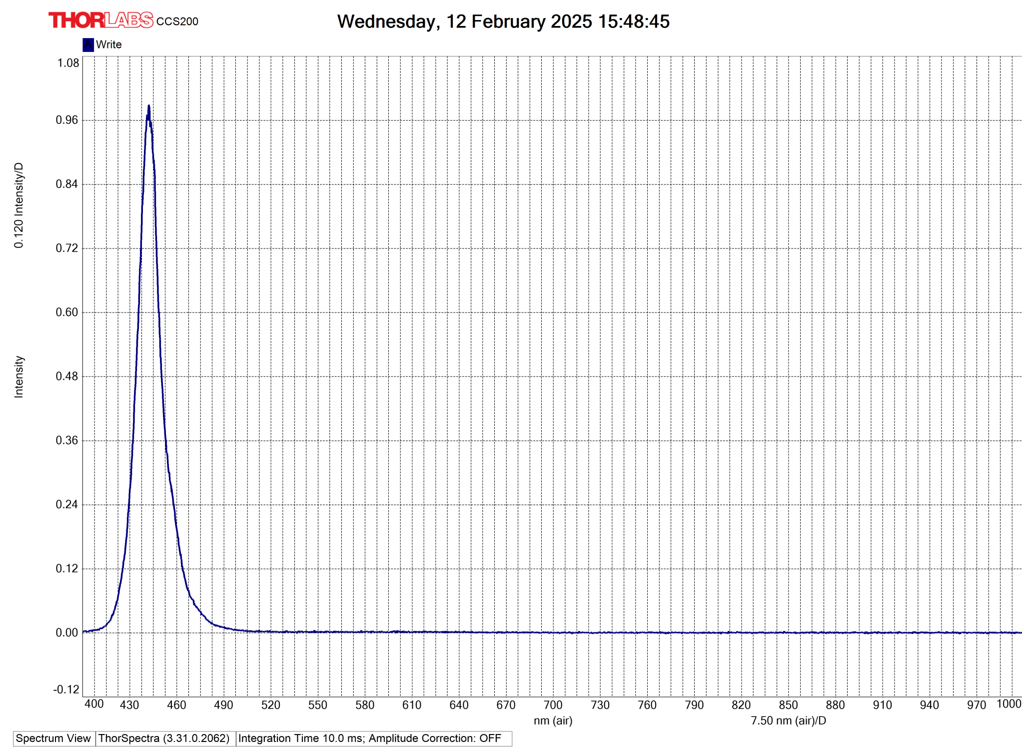

Figure A.3: The light spectrum of the second blue LED used for patterning in the OET setup. This LED has a wavelength of 455 nm.

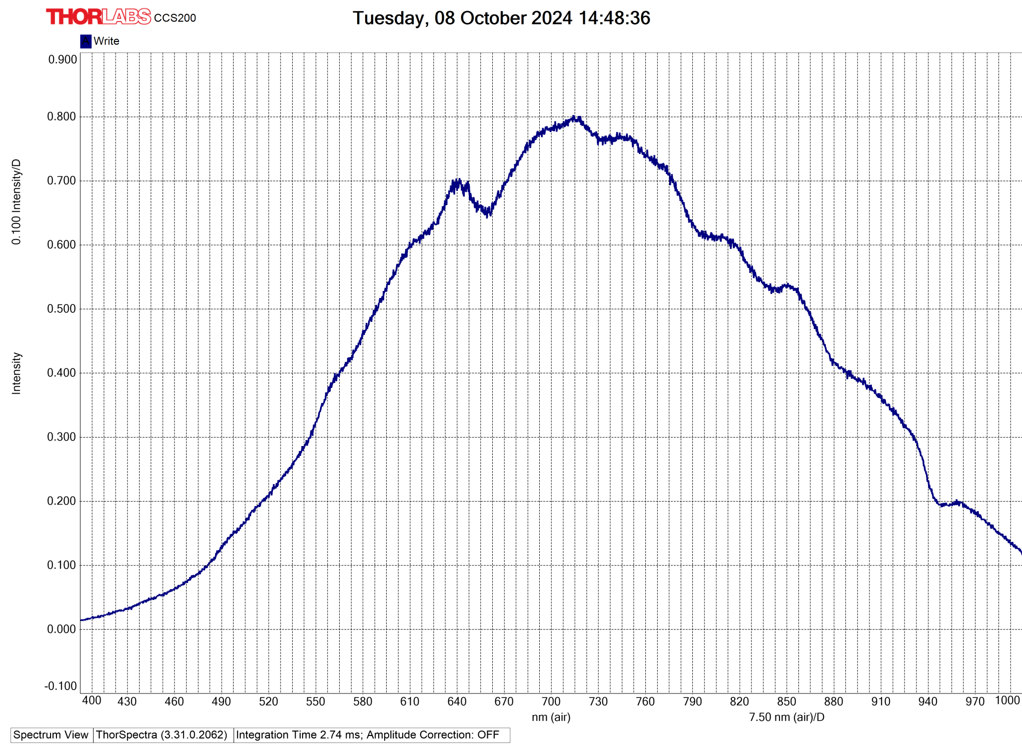

Figure A.4: The light spectrum of the lamp used for imaging the full chip in the OET setup.

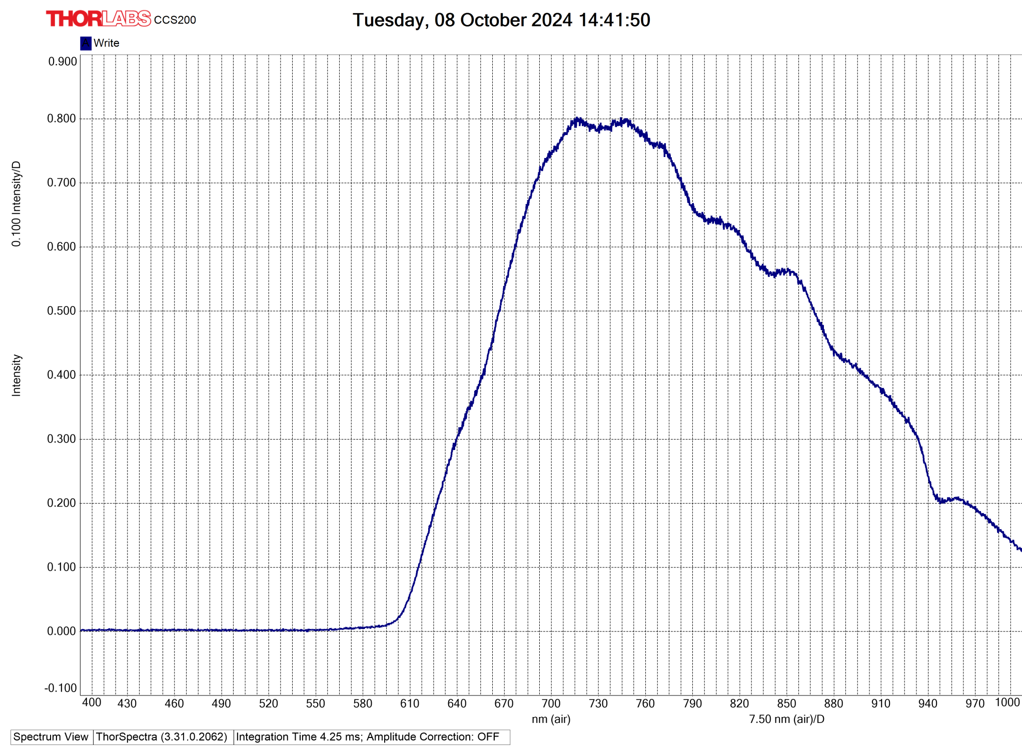

Figure A.5: The light spectrum of the lamp with the red plastic filter, used for imaging the full chip in the OET setup.

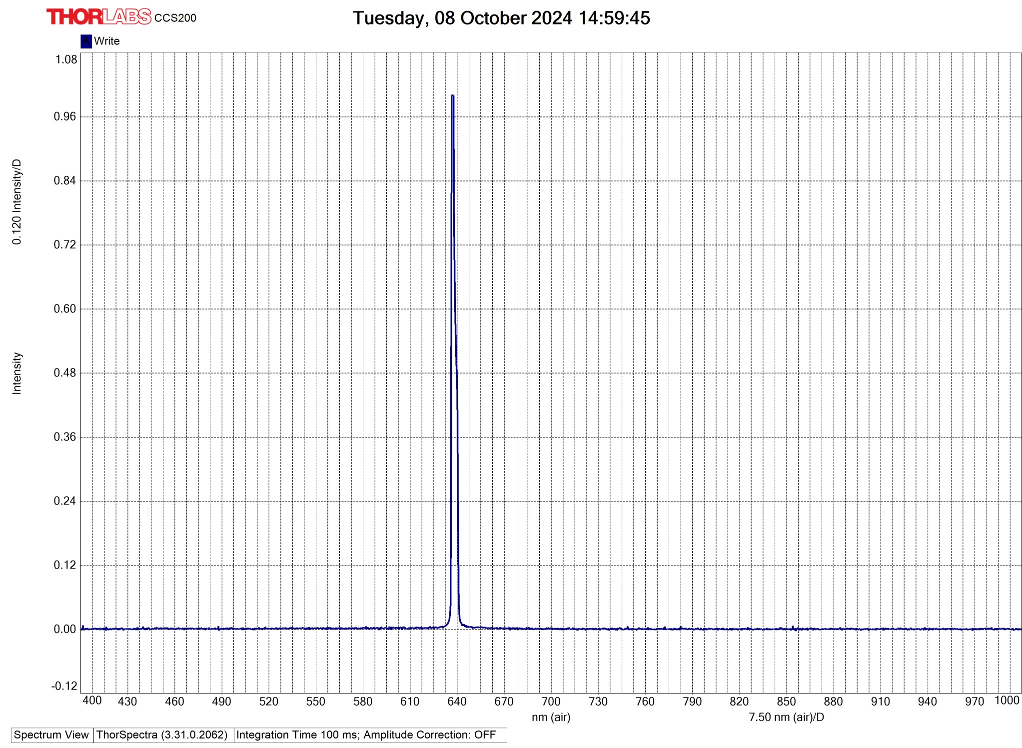

Figure A.6: The light spectrum of the laser used for experiments and collimation.

A.2. Fluorescent Spectra

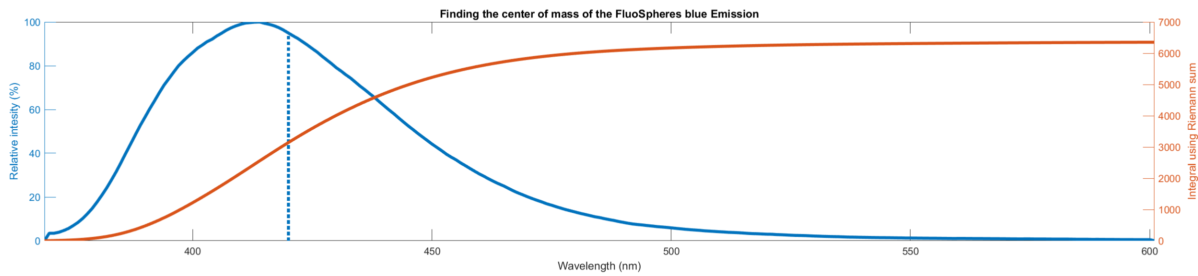

Figure A.7: The emission spectrum of the blue FluoSphere color. The blue line shows the emission spectrum. The orange line shows the Riemann sum. The dotted blue line is located at half of the total area under the emission spectrum, calculate using the Riemann sum. This dotted blue line is located at the center of mass which is at 420 nm.

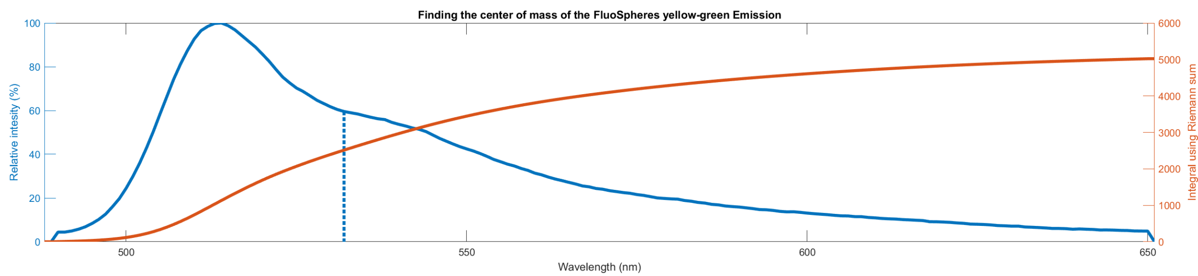

Figure A.8: The emission spectrum of the yellow-green FluoSphere color. The blue line shows the emission spectrum. The orange line shows the Riemann sum. The dotted blue line is located at half of the total area under the emission spectrum, calculate using the Riemann sum. This dotted blue line is located at the center of mass which is at 532 nm.

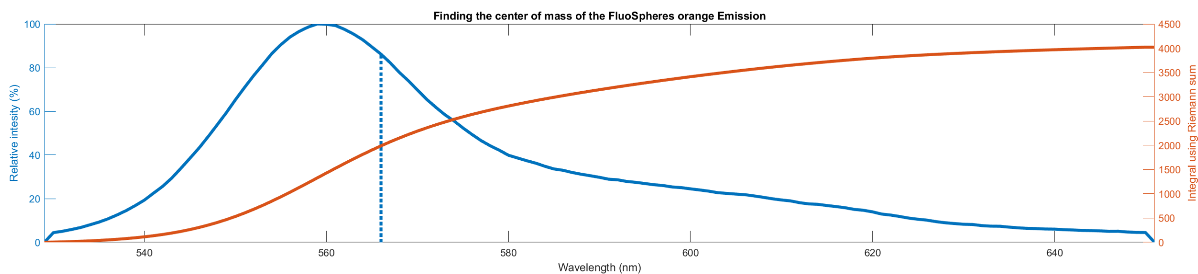

Figure A.9: The emission spectrum of the orange FluoSphere color. The blue line shows the emission spectrum. The orange line shows the Riemann sum. The dotted blue line is located at half of the total area under the emission spectrum, calculate using the Riemann sum. This dotted blue line is located at the center of mass which is at 566 nm.

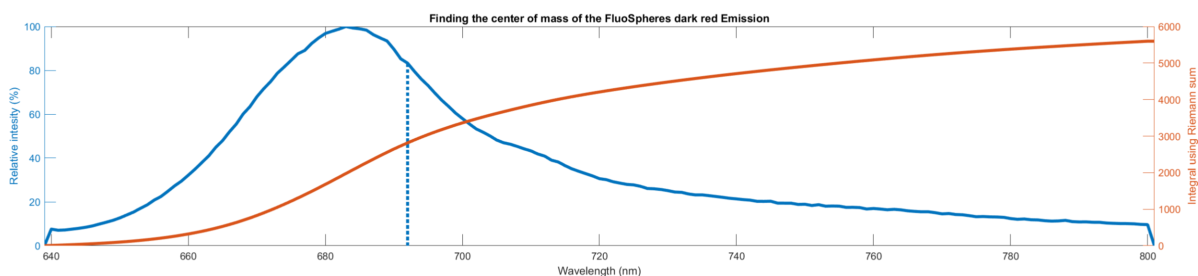

Figure A.10: The emission spectrum of the dark red FluoSphere color. The blue line shows the emission spectrum. The orange line shows the Riemann sum. The dotted blue line is located at half of the total area under the emission spectrum, calculate using the Riemann sum. This dotted blue line is located at the center of mass which is at 692 nm.

A.3. Code for controlling the DMD

A.3.1. Creating the sweep animation

```
# import needed libraries for the code
    import numpy as np
    import time

# Set the DMD resolution/output size
    width = 1920
    height = 1200

# Set expected framerate of the DMD and thickness of the border
    framerate = 72
    d = 2

# Set the time it takes for a sweep to one direction
    sweeptime = 7

# Calculate the needed length of the image stack
    frames = int(2*sweeptime*framerate)

# Set the FoV and the initial rectangular ring image
    x, y = width // 2, height // 2
    rangew, rangeh = 978, 736
    block_width, block_height = rangew // 2, rangeh // 2
    border = 30*d

    img = np.zeros([height, width], dtype=np.uint8)
    img[y - block_height:y + block_height, x - block_width:x + block_width] = 255
    img[y - block_height + border:y + block_height - border, x - block_width + border:x +
    block_width - border] = 0

# Create each frame of the sweep animation
    rangex = 2*block_width - 2*border
    stepsize = rangex/(frames/2)
    sweepthick = 30*d

    imgstack = np.zeros([frames, height, width], dtype=np.uint8)

# Create the animation from left to right
    for i in range(int(frames/2)):
        imgloop = img.copy()  # Copy the initial image
            imgloop[y - block_height:y + block_height, x - block_width + int(i*stepsize):x -
    block_width + int(stepsize*i) + sweepthick] = 255 # Add the sweep to the initial image
        imgstack[i] = imgloop # Fill the imgstack with each sweep animation

# Create the animation from right to left
    for i in range(int(frames/2)):
        imgloop = img.copy()  # Copy the initial image
            imgloop[y - block_height:y + block_height, x + block_width - int(i*stepsize):x +
    block_width - int(stepsize*i) + sweepthick] = 255 # Add the sweep to the initial image
        imgstack[int(i+frames/2)] = imgloop # Fill the imgstack with each sweep animation

# Save as numpy array. This sweep has a single sweeptime of 7s and a border of 2d thick
    np.save("sweepstack_back_7s_2d.npy", imgstack)
```

Listing A.1: Python code for creating the sweep animation.

A.3.2. Showing the sweep animation on the DMD

```
# import needed libraries for the code
    import numpy as np
    import time
    from ALP4 import ALP4  # Zorg ervoor dat deze import werkt

# Start a timer to verify the framerate of the sweep animation
    start = time.time()

# Laad the numpy array containing the sweep animation
    imgstack = np.load("sweepstack_back_7s_2d.npy")

# Settings of the sweep animation
    framerate = 72  # set framerate of the sweepanimation
    bitDepth = 1  # bitDepth is 1 because the DMD only has on/off states

# Convert the framerate to microseconds per frame
    microsecond_framerate = int(1e6 / framerate)
    sweepamount = 2 # Set how many times the sweepanimation needs to be repeated
    timecalc = sweepamount*len(imgstack)/framerate # Calculate the needed runtime of full
    animation

# Connect and intialise the DMD at version 4.3
    DMD = ALP4(version='4.3')
    DMD.Initialize()

# Go through each frame in the imported stack and show them after each other at the selected
    framerate
    j = 1 # start the counter of how many repetitions of the animation has been showed
    startloop = time.time() # start the timer to check the duration of the animation
    try:
        while j <= sweepamount: # If there are repetitions of the animation to go
            for i in range(len(imgstack)):
                frame = imgstack[i] # Set the frame of the DMD to be a frame from the
    imported numpy array

                imgSeq = frame.ravel()  # Change the image to a 1D array for the DMD

                # Allocated memory on the DMD with the set bit depth
                DMD.SeqAlloc(nbImg=1, bitDepth=bitDepth)

                # Send the frame to the DMD and run it
                DMD.SeqPut(imgData=imgSeq)
                DMD.Run()

                # After the frame has been showed long enough, stop the frame and free the
    memory
                DMD.Halt()
                DMD.FreeSeq()
            j += 1 # If a full animation of the sweep has been showed, add 1 to the
    repetition counter
        print("All frames of the animation has been showed on the DMD")

    finally:
        # Disconnect the DMD from python
        DMD.Free()

# Check if the output framerate has been similar to the set framerate
    endloop = time.time()
    print("----------------------------")
    print(f"Execution time: {endloop - startloop} seconds")
    print(f"The time should be: {timecalc} seconds")
    error = abs(endloop-start-timecalc)
    calcframerate = sweepamount*len(imgstack)/(endloop-start)
    print(f"The error is: {error} seconds")
    print(f"The calculated framerate is: {calcframerate} frames per second")
```

Listing A.2: Python code for showing the sweep animation on the DMD.

A.3.3. Dynamically creat a ring animation on the DMD

```
1 # import needed libraries for the code
2     import numpy as np
3     import time
4     import tkinter as tk
5     from ALP4 import ALP4
6 
7 # Connect and intialise the DMD at version 4.3
8     DMD = ALP4(version='4.3')
9     DMD.Initialize()
10 
11 # Set the resolution of the control using the sizes of the DMD
12     width, height = DMD.nSizeX, DMD.nSizeY
13 
14 # Set the starting positions of the ring in the center of the DMD
15     x, y = width // 2, height // 2  # Start at the center
16     radius = 1  # Initial outer radius of the ring
17     border_thickness = 1  # Initial thickness of the ring
18 
19 # Set the movement degrees of freedom
20     direction = {'Left': False, 'Right': False, 'Up': False, 'Down': False}
21 
22 # Set the initial speed of the ring. This is in pixels per refresh
23     speed_factor = 10
24 
25 # Function to create a ring with the set position, outer radius and border thickness
26     def plot_circle_on_dmd(x, y, radius, border_thickness):
27         # Create an initial black and white image
28         img = np.zeros([height, width], dtype=np.uint8)
29 
30         # Draw the circle on the DMD. The lower left corner is the origin
31         for i in range(x - radius, x + radius):
32             for j in range(y - radius, y + radius):
33                 # Calculate the distance of each point to the center of the ring
34                 distance = np.sqrt((i - x) ** 2 + (j - y) ** 2)
35 
36                 # Only make the point in the matrix white if is part of the ring
37                 # So the distance must be greater than the inner radius and smaller than the
    outer radius
38                 if distance <= radius and (distance >= radius - border_thickness):
39                     # Only make parts of the image white if the are part of the DMD size
40                     if 0 <= i < width and 0 <= j < height:
41                         img[j, i] = 255
42 
43         # Ensure the DMD is ready to recieve and image
44         if hasattr(plot_circle_on_dmd, "has_run"):
45             DMD.Halt()
46             DMD.FreeSeq()
47         plot_circle_on_dmd.has_run = True
48 
49         # Send the image to the DMD
50         DMD.SeqAlloc(nbImg=1, bitDepth=1)  # Allocated memory on the DMD with the set bit
    depth
51         DMD.SeqPut(imgData=img.ravel())   # Change the image to a 1D array for the DMD and
    send it to the DMD
52         DMD.SetTiming(pictureTime = 100000) # Select how many microseconds each image needs
    to be showed
53         DMD.Run()  # Start the DMD
54 
55 # This function creates the circle and moves it using the set radii
56     def move_circle():
57         # Import global variables
58         global x, y, last_move_time
59 
60         # Calculate how much time has passed to known when a new input can be assigned.
61         # This prevents overflow of input after a keypress
62         current_time = time.perf_counter()
63         time_diff = current_time - last_move_time
64 
65         # Change the speed dynamically of the ring depending on its size
```

```
66         time_per_pixel = (speed_factor / (1000.0 * radius))
67         # Ensure the movement of the ring keeps the same speed independent of the ring size
68         time_per_pixel = max(time_per_pixel, 0.005)
69 
70         # If enough time has passed, register a key as pressed
71         if time_diff >= time_per_pixel:
72             # If the left arrow key has been pressed on the keyboard, move the ring left
73             if direction['Left']:
74                 x -= 1
75             # If the right arrow key has been pressed on the keyboard, move the ring right
76             elif direction['Right']:
77                 x += 1
78             # If the up arrow key has been pressed on the keyboard, move the ring up
79             elif direction['Up']:
80                 y -= 1
81             # If the down arrow key has been pressed on the keyboard, move the ring down
82             elif direction['Down']:
83                 y += 1
84 
85             # Update the circle with the new center coordinates and radii
86             plot_circle_on_dmd(x, y, radius, border_thickness)
87 
88             # Update the timer for registering keypresses
89             last_move_time = current_time
90 
91             # Print the status of the parameters on the GUI
92             position_label.config(text=f"Position: ({x}, {y})")
93             radius_label.config(text=f"Radius: {radius}")
94             border_label.config(text=f"Border Thickness: {border_thickness}")
95             speed_label.config(text=f"Speed Factor: {speed_factor}")
96 
97 # Function to register key presses and assign what happens if specific keys are pressed
98     def on_key_press(event):
99         global direction, radius, border_thickness, speed_factor
100        if event.keysym == 'Left':
101            direction['Left'] = True
102            direction['Right'] = False
103            direction['Up'] = False
104            direction['Down'] = False
105        elif event.keysym == 'Right':
106            direction['Left'] = False
107            direction['Right'] = True
108            direction['Up'] = False
109            direction['Down'] = False
110        elif event.keysym == 'Up':
111            direction['Left'] = False
112            direction['Right'] = False
113            direction['Up'] = True
114            direction['Down'] = False
115        elif event.keysym == 'Down':
116            direction['Left'] = False
117            direction['Right'] = False
118            direction['Up'] = False
119            direction['Down'] = True
120        elif event.keysym == 'p':  # Increase the outer radius if p is pressed
121            radius += 1
122        elif event.keysym == 'o':  # Decrease the outer radius if o is pressed
123            radius -= 1
124        elif event.keysym == 'm':  # Decrease the inner radius if m is pressed
125            border_thickness += 1
126        elif event.keysym == 'n':  # Increase the inner radius if n is pressed
127            border_thickness -= 1
128        elif event.keysym == 'u':  # Increase the speed with 1 pixel per step if u is pressed
129            speed_factor += 1
130        elif event.keysym == 'y':  # Decrease the speed with 1 pixel per step if y is pressed
131            speed_factor = max(1, speed_factor - 1)  # The minimal speed is 1 pixel per step
132 
133 # Function to release the key presses
134     def on_key_release(event):
135         global direction
136         if event.keysym == 'Left':
```

```
137             direction['Left'] = False
138         elif event.keysym == 'Right':
139             direction['Right'] = False
140         elif event.keysym == 'Up':
141             direction['Up'] = False
142         elif event.keysym == 'Down':
143             direction['Down'] = False
144 
145 # Create a GUI for moving the circle.
146 # The GUI shows the parameters of the circle movement
147 # If the GUI is closed, the DMD disconnects automatically
148     root = tk.Tk()
149     root.bind("<KeyPress>", on_key_press)
150     root.bind("<KeyRelease>", on_key_release)
151 
152     # Print the labels of the parameters and update them
153     position_label = tk.Label(root, text=f"Position: ({x}, {y})")
154     position_label.pack()
155 
156     radius_label = tk.Label(root, text=f"Radius: {radius}")
157     radius_label.pack()
158 
159     border_label = tk.Label(root, text=f"Border Thickness: {border_thickness}")
160     border_label.pack()
161 
162     speed_label = tk.Label(root, text=f"Speed Factor: {speed_factor}")
163     speed_label.pack()
164 
165 # Start the key press for the move_circle function
166     last_move_time = time.perf_counter()
167 
168 # Update the circle every 5 ms
169     def update():
170         move_circle()
171         root.after(5, update)
172 
173     update()
174 
175 # Start the GUI and the circle animation
176     root.mainloop()
177 
178 # Free and close the DMD when closing the GUI
179     DMD.Halt()
180     DMD.FreeSeq()
181     DMD.Free()
```

Listing A.3: Python code for creating a ring on the DMD that can be dynamically controlled using key presses.

B

Results

B.1. Microfluidic chip

B.1.1. The thickness of the double-sided tape

	1 foil + 1 tape	Foil	Tape
1	0.17 mm	0.09 mm	0.08 mm
2	0.17 mm	0.09 mm	0.08 mm
3	0.16 mm	0.09 mm	0.07 mm
4	0.17 mm	0.08 mm	0.08 mm
5	0.17 mm	0.10 mm	0.08 mm
Average	0.1680 mm	0.0900 mm	0.0780 mm
Std	0.0045 mm	0.0071 mm	0.0045 mm
Calculated foil thickness: 0.0780 mm			
Calculated tape thickness: 0.0900 mm			

Table B.1: Measurements of the thickness of a single strip of double-sided tape. The first 5 measurements were done on the tape with the protective foil attached. The second measurement was done on only the sticky tape and the third measurement was done on only the protective foil. The calculated foil thickness was done by subtracting the measured the tape thickness from the measured tape+foil thickness.

	2 foil + 2 tape	1 foil + 2 tape	2 tape
1	0.36 mm	0.27 mm	0.20 mm
2	0.35 mm	0.28 mm	0.20 mm
3	0.36 mm	0.28 mm	0.20 mm
4	0.35 mm	0.28 mm	0.20 mm
5	0.36 mm	0.28 mm	0.20 mm
Average	0.3560 mm	0.2780 mm	0.2000 mm
Std	0.0055 mm	0.0045 mm	0.0000 mm
Calculated foil thickness: 0.0780 mm			
Calculated tape thickness: 0.1000 mm			

Table B.2: Measurements of the thickness of a 2 pieces of tape stuck together with their sticky sides together. The first 5 measurements were done on the 2 tapes with the protective foils attached. The second measurement was done with one piece of foil removed and the third measurement was done without any protective foil. The calculated foil thickness was done by subtracting the measured the ”1 foil + 2 tape” thickness from the measured ”2 foil + 2 tape” thickness.

	2 foil + 2 tape	1 foil + 2 tape
1	0.35 mm	0.27 mm
2	0.36 mm	0.27 mm
3	0.34 mm	0.27 mm
4	0.33 mm	0.28 mm
5	0.35 mm	0.26 mm
Average	0.3460 mm	0.2700 mm
Std	0.0114 mm	0.0071 mm
Calculated foil thickness: 0.0760 mm		
Calculated tape thickness: 0.0970 mm		

Table B.3: Measurements of the thickness of a 2 pieces of tape stuck together with the sticky side of 1 piece of tape on to foil of the tape. The first 5 measurements were done on the 2 tapes with the protective foils attached. The second measurement was done with one piece of foil removed. The calculated foil thickness was done by subtracting the measured the ”1 foil + 2 tape” thickness from the measured ”2 foil + 2 tape” thickness.

B.1.2. The electrical resistances of the microfluidic chip components

Measurement	Glass 1	Glass 2	Glass 3	Glass 4	Noise
1	14.634 Ω	13.787 Ω	13.664 Ω	13.975 Ω	0.204 Ω
2	14.927 Ω	15.682 Ω	13.420 Ω	13.123 Ω	0.192 Ω
3	13.492 Ω	13.924 Ω	14.214 Ω	12.971 Ω	0.190 Ω
4	14.682 Ω	13.964 Ω	13.907 Ω	13.036 Ω	0.191 Ω
5	-	-	16.096 Ω	13.112 Ω	0.192 Ω
Average	14.434 Ω	14.339 Ω	14.260 Ω	13.243 Ω	0.194 Ω
Std	0.641 Ω	0.898 Ω	1.068 Ω	0.414 Ω	0.006 Ω

Table B.4: Resistance measurements for different 8-12 Ω ITO glass samples and noise levels.

Measurement	Wire 1	Wire 2	Wires + Strip
1	2.635 Ω	1.832 Ω	6.294 Ω
2	2.813 Ω	1.489 Ω	5.834 Ω
3	2.784 Ω	1.480 Ω	2.884 Ω
4	3.065 Ω	1.423 Ω	4.784 Ω
5	3.003 Ω	1.273 Ω	4.532 Ω
6	2.127 Ω	-	8.562 Ω
7	2.492 Ω	-	-
Average	2.703 Ω	1.499 Ω	5.482 Ω
Std	0.322 Ω	0.205 Ω	1.919 Ω

Table B.5: Resistance measurements of the wires and conductive tape used for supplying electricity to the microfluidic chip, with all values in Ohms (Ω).

Deionized water			
Measurement	**29 mm**	**23 mm**	**3 mm**
1	$2.19 \times 10^6\ \Omega$	$1.82 \times 10^6\ \Omega$	$1.07 \times 10^6\ \Omega$
2	$2.09 \times 10^6\ \Omega$	$1.77 \times 10^6\ \Omega$	$1.07 \times 10^6\ \Omega$
3	$2.11 \times 10^6\ \Omega$	$1.72 \times 10^6\ \Omega$	$1.06 \times 10^6\ \Omega$
4	$2.00 \times 10^6\ \Omega$	$1.71 \times 10^6\ \Omega$	$1.06 \times 10^6\ \Omega$
5	$2.27 \times 10^6\ \Omega$	$1.71 \times 10^6\ \Omega$	$1.06 \times 10^6\ \Omega$
6	$2.12 \times 10^6\ \Omega$	-	-
Average	$2.13 \times 10^6\ \Omega$	$1.75 \times 10^6\ \Omega$	$1.06 \times 10^6\ \Omega$
Std	$9.06 \times 10^4\ \Omega$	$5.07 \times 10^4\ \Omega$	$6.98 \times 10^3\ \Omega$
Average (Ω/m)	$7.34 \times 10^7\ \Omega$/m	$7.94 \times 10^7\ \Omega$/m	$3.55 \times 10^8\ \Omega$/m
Std (Ω/m)	$3.12 \times 10^6\ \Omega$/m	$1.75 \times 10^6\ \Omega$/m	$2.41 \times 10^5\ \Omega$/m

Table B.6: Resistance measurements in deionized water at different distances. All values are in Ohms (Ω), except the last two rows in Ohms per meter (Ω/m).

Deionized water + 0.05% Tween-20			
Measurement	**29 mm**	**23 mm**	**3 mm**
1	$2.97 \times 10^5\ \Omega$	$2.90 \times 10^5\ \Omega$	$2.03 \times 10^5\ \Omega$
2	$3.00 \times 10^5\ \Omega$	$2.84 \times 10^5\ \Omega$	$2.06 \times 10^5\ \Omega$
3	$3.05 \times 10^5\ \Omega$	$2.44 \times 10^5\ \Omega$	$2.22 \times 10^5\ \Omega$
4	$2.97 \times 10^5\ \Omega$	$2.37 \times 10^5\ \Omega$	$2.14 \times 10^5\ \Omega$
5	$3.04 \times 10^5\ \Omega$	$2.42 \times 10^5\ \Omega$	$2.09 \times 10^5\ \Omega$
6	$3.06 \times 10^5\ \Omega$	$2.47 \times 10^5\ \Omega$	$2.08 \times 10^5\ \Omega$
7	$3.05 \times 10^5\ \Omega$	$2.35 \times 10^5\ \Omega$	$2.16 \times 10^5\ \Omega$
Average	$3.02 \times 10^5\ \Omega$	$2.54 \times 10^5\ \Omega$	$2.11 \times 10^5\ \Omega$
Std	$3.86 \times 10^3\ \Omega$	$2.30 \times 10^4\ \Omega$	$6.58 \times 10^3\ \Omega$
Average (Ω/m)	$1.04 \times 10^7\ \Omega$/m	$1.15 \times 10^7\ \Omega$/m	$7.04 \times 10^7\ \Omega$/m
Std (Ω/m)	$1.33 \times 10^5\ \Omega$/m	$7.93 \times 10^5\ \Omega$/m	$2.27 \times 10^5\ \Omega$/m

Table B.7: Resistance measurements in deionized water with 0.05% Tween-20 at different distances. All values are in Ohms (Ω), except the last two rows in Ohms per meter (Ω/m).

Deionized water + 5% Tween-20			
Measurement	**29 mm**	**23 mm**	**3 mm**
1	$1.31 \times 10^5\ \Omega$	$1.00 \times 10^5\ \Omega$	$7.20 \times 10^4\ \Omega$
2	$1.31 \times 10^5\ \Omega$	$1.01 \times 10^5\ \Omega$	$7.21 \times 10^4\ \Omega$
3	$1.31 \times 10^5\ \Omega$	$1.07 \times 10^5\ \Omega$	$7.21 \times 10^4\ \Omega$
4	$1.30 \times 10^5\ \Omega$	$1.07 \times 10^5\ \Omega$	$7.21 \times 10^4\ \Omega$
5	$1.30 \times 10^5\ \Omega$	-	$7.22 \times 10^4\ \Omega$
6	-	-	-
7	-	-	-
Average	$1.30 \times 10^5\ \Omega$	$1.04 \times 10^5\ \Omega$	$7.21 \times 10^4\ \Omega$
Std	$4.33 \times 10^2\ \Omega$	$3.80 \times 10^3\ \Omega$	$5.95 \times 10^1\ \Omega$
Average (Ω/m)	$4.50 \times 10^6\ \Omega$/m	$4.72 \times 10^6\ \Omega$/m	$2.40 \times 10^7\ \Omega$/m
Std (Ω/m)	$1.49 \times 10^4\ \Omega$/m	$1.31 \times 10^5\ \Omega$/m	$2.05 \times 10^3\ \Omega$/m

Table B.8: Resistance measurements in deionized water with 5% Tween-20 at different distances. All values are in Ohms (Ω), except the last two rows in Ohms per meter (Ω/m).

B.1.3. Capacitance of tape

	Chip 1	**Chip 2**	
A	4.68×10^{-4} m^2	4.92×10^{-4} m^2	
d	9.57×10^{-5} m	9.57×10^{-5} m	
ϵ_0	8.85×10^{-12} F/m	8.85×10^{-12} F/m	
Measurement	**Capacitance**	**Capacitance**	**Noise**
1	1.43×10^{-10} F	1.74×10^{-10} F	1.90×10^{-11} F
2	1.38×10^{-10} F	1.73×10^{-10} F	1.30×10^{-11} F
3	1.40×10^{-10} F	1.69×10^{-10} F	1.20×10^{-11} F
4	1.43×10^{-10} F	1.68×10^{-10} F	4.31×10^{-11} F
5	1.39×10^{-10} F	1.68×10^{-10} F	2.14×10^{-11} F
Average	1.41×10^{-10} F	1.70×10^{-10} F	2.17×10^{-11} F
Std	2.30×10^{-12} F	2.88×10^{-12} F	1.26×10^{-11} F
Derived ϵ	2.87×10^{-11} F/m	3.31×10^{-11} F/m	
Derived ϵ_r	3.24	3.74	

Table B.9: Capacitance measurements for 2 small ITO covered microscope coverslips sandwiching a small single layer of double-sided tape. The relative permittivity is calculated using the formula of the capacitance from equation 3.3.

B.1.4. Capacitance photoconductive layer

	Chip 1	**Chip 2**
A	7.27×10^{-4} m^2	7.33×10^{-4} m^2
d_{sil}	1.00×10^{-6} m	1.00×10^{-6} m
d_{tape}	9.57×10^{-5} m	9.57×10^{-5} m
ϵ_0	8.85×10^{-12} F/m	8.85×10^{-12} F/m
Measurement	**Capacitance**	**Capacitance**
1	1.71×10^{-10} F	1.76×10^{-10} F
2	1.72×10^{-10} F	1.75×10^{-10} F
3	1.70×10^{-10} F	1.77×10^{-10} F
4	1.70×10^{-10} F	1.75×10^{-10} F
5	1.71×10^{-10} F	1.74×10^{-10} F
6	1.72×10^{-10} F	1.75×10^{-10} F
7	1.69×10^{-10} F	1.77×10^{-10} F
Mean	1.71×10^{-10} F	1.76×10^{-10} F
Std	1.11×10^{-12} F	1.13×10^{-12} F
ϵ_{tape}	3.49	3.49
C_{tape}	2.35×10^{-10} F	2.37×10^{-10} F
$\frac{1}{C_{\text{PL}}} = \frac{1}{C} - \frac{1}{C_T}$	1.60×10^{9} F^{-1}	1.48×10^{9} F^{-1}
C_{PL}	6.26×10^{-10} F	6.78×10^{-10} F
Derived ϵ	8.61×10^{-13} F/m	9.24×10^{-13} F/m
Derived ϵ_r	0.097	0.104

Table B.10: Capacitance measurements for a ITO covered microscope slide and a ITO covered coverslip, sandwiching a small single layer of double-sided tape and a 1μm layer of a-Si:H. The relative permittivity is calculated using the formula of the capacitance from equation 3.3.

B.1.5. Capacitance medium

Chip 2	Empty	Deionized water	Deionized water + 5% Tween-20
ϵ_0	8.85×10^{-12} F/m	8.85×10^{-12} F/m	8.85×10^{-12} F/m
d_{tape}	9.57×10^{-5} m	9.57×10^{-5} m	9.57×10^{-5} m
A_{total}	8.00×10^{-4} m^2	8.00×10^{-4} m^2	8.00×10^{-4} m^2
A_{channel}	2.70×10^{-4} m^2	2.70×10^{-4} m^2	2.70×10^{-4} m^2
A_{tape}	5.30×10^{-4} m^2	5.30×10^{-4} m^2	5.30×10^{-4} m^2
ϵ_{tape}	3.5	3.5	3.5
C_{tape}	1.72×10^{-10} F	1.72×10^{-10} F	1.72×10^{-10} F
d_{PL}	1.00×10^{-6} m	1.00×10^{-6} m	1.00×10^{-6} m
A_{hole}	7.07×10^{-6} m^2	7.07×10^{-6} m^2	7.07×10^{-6} m^2
$A_{\text{PL, effective}}$	7.86×10^{-4} m^2	7.86×10^{-4} m^2	7.86×10^{-4} m^2
$\epsilon_{\text{silicon}}$	11	11	11
C_{silicon}	7.65×10^{-8} F	7.65×10^{-8} F	7.65×10^{-8} F
$A_{\text{channel, effective}}$	2.56×10^{-4} m^2	2.56×10^{-4} m^2	2.56×10^{-4} m^2
Measurement	**Capacitance**	**Capacitance**	**Capacitance**
1	4.19×10^{-6} F	5.44×10^{-6} F	4.62×10^{-6} F
2	4.19×10^{-6} F	5.36×10^{-6} F	4.71×10^{-6} F
3	4.22×10^{-6} F	5.80×10^{-6} F	4.96×10^{-6} F
4	4.38×10^{-6} F	5.42×10^{-6} F	4.82×10^{-6} F
5	4.28×10^{-6} F	5.46×10^{-6} F	5.00×10^{-6} F
6	4.35×10^{-6} F	5.61×10^{-6} F	5.08×10^{-6} F
Average	4.27×10^{-6} F	5.51×10^{-6} F	4.86×10^{-6} F
Std	8.36×10^{-8} F	1.62×10^{-7} F	1.80×10^{-7} F
$(C_{\text{tape}} + C_{\text{medium}})^{-1}$	-1.28×10^{7} F^{-1}	-1.29×10^{7} F^{-1}	-1.29×10^{7} F^{-1}
C_{medium}	-7.81×10^{-8} F	-7.78×10^{-8} F	-7.79×10^{-8} F
Derived ϵ	-2.92×10^{-8} F/m	-2.91×10^{-8} F/m	-2.91×10^{-8} F/m
Derived ϵ_r	-3299.50	-3286.00	-3292.17

Table B.11: Capacitance measurements of functional OET microfluidic chip number 2. The capacitance measurements were done using deionized water, deionized water with 5% Tween-20, and with air present in the microfluidic chip. The relative permittivity is calculated using the formula of the capacitance from equation 3.3.

Chip 3	Empty	Deionized water
ϵ_0	8.85×10^{-12} F/m	8.85×10^{-12} F/m
d_{tape}	9.57×10^{-5} m	9.57×10^{-5} m
A_{total}	8.00×10^{-4} m^2	8.00×10^{-4} m^2
A_{channel}	2.70×10^{-4} m^2	2.70×10^{-4} m^2
A_{tape}	5.30×10^{-4} m^2	5.30×10^{-4} m^2
ϵ_{tape}	3.5	3.5
C_{tape}	1.72×10^{-10} F	1.72×10^{-10} F
d_{PL}	1.00×10^{-6} m	1.00×10^{-6} m
A_{hole}	7.07×10^{-6} m^2	7.07×10^{-6} m^2
$A_{\text{PL, effective}}$	7.86×10^{-4} m^2	7.86×10^{-4} m^2
$\epsilon_{\text{silicon}}$	11	11
C_{silicon}	7.65×10^{-8} F	7.65×10^{-8} F
$A_{\text{channel, effective}}$	2.56×10^{-4} m^2	2.56×10^{-4} m^2
Measurement	**Capacitance**	**Capacitance**
1	1.72×10^{-10} F	2.23×10^{-6} F
2	1.73×10^{-10} F	2.82×10^{-6} F
3	1.73×10^{-10} F	2.66×10^{-6} F
4	1.73×10^{-10} F	2.84×10^{-6} F
5	1.69×10^{-10} F	1.18×10^{-6} F
6	1.69×10^{-10} F	2.13×10^{-6} F
Average	1.72×10^{-10} F	2.31×10^{-6} F
Std	1.97×10^{-12} F	6.30×10^{-7} F
$(C_{\text{tape}} + C_{\text{medium}})^{-1}$	5.82×10^{9} F^{-1}	-1.26×10^{7} F^{-1}
C_{medium}	2.64×10^{-13} F	-7.93×10^{-8} F
Derived ϵ	9.86×10^{-14} F/m	-2.97×10^{-8} F/m
Derived ϵ_r	0.01	-3351.27

Table B.12: Capacitance measurements of functional OET microfluidic chip number 3. The capacitance measurements were done using deionized water, and with air present in the microfluidic chip. The relative permittivity is calculated using the formula of the capacitance from equation 3.3.

Chip 10	**Empty**	**Deionized water + 0.05% Tween-20**
ϵ_0	8.85×10^{-12} F/m	8.85×10^{-12} F/m
d_{tape}	9.57×10^{-5} m	9.57×10^{-5} m
A_{total}	8.00×10^{-4} m^2	8.00×10^{-4} m^2
A_{channel}	2.70×10^{-4} m^2	2.70×10^{-4} m^2
A_{tape}	5.30×10^{-4} m^2	5.30×10^{-4} m^2
ϵ_{tape}	3.5	3.5
C_{tape}	1.72×10^{-10} F	1.72×10^{-10} F
d_{PL}	1.00×10^{-6} m	1.00×10^{-6} m
A_{hole}	7.07×10^{-6} m^2	7.07×10^{-6} m^2
$A_{\text{PL, effective}}$	7.86×10^{-4} m^2	7.86×10^{-4} m^2
$\epsilon_{\text{silicon}}$	11	11
C_{silicon}	7.65×10^{-8} F	7.65×10^{-8} F
$A_{\text{channel, effective}}$	2.56×10^{-4} m^2	2.56×10^{-4} m^2
Measurement	**Capacitance**	**Capacitance**
1	1.50×10^{-10} F	1.73×10^{-6} F
2	1.51×10^{-10} F	2.15×10^{-6} F
3	1.48×10^{-10} F	1.99×10^{-6} F
4	1.51×10^{-10} F	1.88×10^{-6} F
5	1.51×10^{-10} F	1.91×10^{-6} F
6	1.51×10^{-10} F	1.91×10^{-6} F
Average	1.50×10^{-10} F	1.93×10^{-6} F
Std	1.24×10^{-12} F	1.38×10^{-7} F
$(C_{\text{tape}} + C_{\text{medium}})^{-1}$	6.63×10^{9} F^{-1}	-1.25×10^{7} F^{-1}
C_{medium}	-2.09×10^{-11} F	-7.99×10^{-8} F
Derived ϵ	-7.80×10^{-12} F/m	-2.99×10^{-8} F/m
Derived ϵ_r	-0.88	-3374.15

Table B.13: Capacitance measurements of functional OET microfluidic chip number 10. The capacitance measurements were done using deionized water with 0.05% Tween-20, and with air present in the microfluidic chip. The relative permittivity is calculated using the formula of the capacitance from equation 3.3.

Chip 11	Empty	Deionized water + 0.05% Tween-20
ϵ_0	8.85×10^{-12} F/m	8.85×10^{-12} F/m
d_{tape}	9.57×10^{-5} m	9.57×10^{-5} m
A_{total}	8.00×10^{-4} m^2	8.00×10^{-4} m^2
A_{channel}	2.70×10^{-4} m^2	2.70×10^{-4} m^2
A_{tape}	5.30×10^{-4} m^2	5.30×10^{-4} m^2
ϵ_{tape}	3.5	3.5
C_{tape}	1.72×10^{-10} F	1.72×10^{-10} F
d_{PL}	1.00×10^{-6} m	1.00×10^{-6} m
A_{hole}	7.07×10^{-6} m^2	7.07×10^{-6} m^2
$A_{\text{PL, effective}}$	7.86×10^{-4} m^2	7.86×10^{-4} m^2
$\epsilon_{\text{silicon}}$	11	11
C_{silicon}	7.65×10^{-8} F	7.65×10^{-8} F
$A_{\text{channel, effective}}$	2.56×10^{-4} m^2	2.56×10^{-4} m^2
Measurement	**Capacitance**	**Capacitance**
1	1.01×10^{-10} F	1.74×10^{-6} F
2	9.84×10^{-11} F	1.75×10^{-6} F
3	1.01×10^{-10} F	1.76×10^{-6} F
4	1.00×10^{-10} F	1.78×10^{-6} F
5	1.00×10^{-10} F	1.81×10^{-6} F
6	9.74×10^{-11} F	1.85×10^{-6} F
Average	9.96×10^{-11} F	1.78×10^{-6} F
Std	1.41×10^{-12} F	4.11×10^{-8} F
$(C_{\text{tape}} + C_{\text{medium}})^{-1}$	1.00×10^{10} F^{-1}	-1.25×10^{7} F^{-1}
C_{medium}	-7.19×10^{-11} F	-8.01×10^{-8} F
Derived ϵ	-2.69×10^{-11} F/m	-3.00×10^{-8} F/m
Derived ϵ_r	-3.04	-3385.48

Table B.14: Capacitance measurements of functional OET microfluidic chip number 11. The capacitance measurements were done using deionized water with 0.05% Tween-20, and with air present in the microfluidic chip. The relative permittivity is calculated using the formula of the capacitance from equation 3.3.

B.2. Reflection

B.2.1. Reflection of ITO glass using 470 nm LED

Thorlabs MC470L3-C1		
Measurement	I_0 (nW)	Noise (nW)
1	6.68×10^6 nW	8.30×10^1 nW
2	6.70×10^6 nW	8.20×10^1 nW
3	6.69×10^6 nW	8.10×10^1 nW
4	6.68×10^6 nW	8.10×10^1 nW
5	6.68×10^6 nW	8.00×10^1 nW
6	6.68×10^6 nW	8.00×10^1 nW
7	6.68×10^6 nW	8.50×10^1 nW
8	6.68×10^6 nW	8.40×10^1 nW
9	6.70×10^6 nW	8.40×10^1 nW
10	6.69×10^6 nW	8.50×10^1 nW
Average	6.69×10^6 nW	8.25×10^1 nW
Std	8.43×10^3 nW	1.96×10^0 nW

Table B.15: Intensity measurements of the incoming light I_0 and noise in nanowatts for Thorlabs MC470L3-C1 with a wavelength of 470 nm.

ITO 8-12 Ω (470 nm)						
	Glass 1		**Glass 2**		**Glass 3**	
Meas.	I_t	I_r	I_t	I_r	I_t	I_r
1	5.76×10^6 nW	9.26×10^5 nW	5.66×10^6 nW	1.03×10^6 nW	5.65×10^6 nW	1.04×10^6 nW
2	5.76×10^6 nW	9.26×10^5 nW	5.66×10^6 nW	1.03×10^6 nW	5.65×10^6 nW	1.04×10^6 nW
3	5.78×10^6 nW	9.06×10^5 nW	5.67×10^6 nW	1.02×10^6 nW	5.65×10^6 nW	1.04×10^6 nW
4	5.77×10^6 nW	9.16×10^5 nW	5.69×10^6 nW	9.96×10^5 nW	5.71×10^6 nW	9.76×10^5 nW
5	5.76×10^6 nW	9.26×10^5 nW	5.67×10^6 nW	1.02×10^6 nW	5.69×10^6 nW	9.96×10^5 nW
6	5.76×10^6 nW	9.26×10^5 nW	5.66×10^6 nW	1.03×10^6 nW	5.66×10^6 nW	1.03×10^6 nW
7	5.76×10^6 nW	9.26×10^5 nW	5.66×10^6 nW	1.03×10^6 nW	5.65×10^6 nW	1.04×10^6 nW
8	5.76×10^6 nW	9.26×10^5 nW	5.66×10^6 nW	1.03×10^6 nW	5.65×10^6 nW	1.04×10^6 nW
9	5.76×10^6 nW	9.26×10^5 nW	5.66×10^6 nW	1.03×10^6 nW	5.65×10^6 nW	1.04×10^6 nW
10	5.76×10^6 nW	9.26×10^5 nW	5.65×10^6 nW	1.04×10^6 nW	5.65×10^6 nW	1.04×10^6 nW
Avg.	5.76×10^6 nW	9.23×10^5 nW	5.66×10^6 nW	1.02×10^6 nW	5.66×10^6 nW	1.03×10^6 nW
Std	6.75×10^3 nW	6.75×10^3 nW	1.07×10^4 nW	1.07×10^4 nW	2.13×10^4 nW	2.13×10^4 nW

Table B.16: Intensity measurements to measure the transmitted intensity I_t and reflected intensity I_r in nanowatts for different 8-12 Ω glass samples at 470 nm.

ITO 15-30 Ω (470 nm)						
	Glass 1		**Glass 2**		**Glass 3**	
Meas.	I_t (nW)	I_r (nW)	I_t (nW)	I_r (nW)	I_t (nW)	I_r (nW)
1	5.30×10^6 nW	1.39×10^6 nW	5.36×10^6 nW	1.33×10^6 nW	5.36×10^6 nW	1.33×10^6 nW
2	5.30×10^6 nW	1.39×10^6 nW	5.36×10^6 nW	1.33×10^6 nW	5.37×10^6 nW	1.32×10^6 nW
3	5.30×10^6 nW	1.39×10^6 nW	5.36×10^6 nW	1.33×10^6 nW	5.37×10^6 nW	1.32×10^6 nW
4	5.36×10^6 nW	1.33×10^6 nW	5.36×10^6 nW	1.33×10^6 nW	5.37×10^6 nW	1.32×10^6 nW
5	5.32×10^6 nW	1.37×10^6 nW	5.42×10^6 nW	1.27×10^6 nW	5.37×10^6 nW	1.32×10^6 nW
6	5.31×10^6 nW	1.38×10^6 nW	5.39×10^6 nW	1.30×10^6 nW	5.45×10^6 nW	1.24×10^6 nW
7	5.31×10^6 nW	1.38×10^6 nW	5.37×10^6 nW	1.32×10^6 nW	5.41×10^6 nW	1.28×10^6 nW
8	5.30×10^6 nW	1.39×10^6 nW	5.36×10^6 nW	1.33×10^6 nW	5.38×10^6 nW	1.31×10^6 nW
9	5.30×10^6 nW	1.39×10^6 nW	5.36×10^6 nW	1.33×10^6 nW	5.37×10^6 nW	1.32×10^6 nW
10	5.30×10^6 nW	1.39×10^6 nW	5.36×10^6 nW	1.33×10^6 nW	5.37×10^6 nW	1.32×10^6 nW
Avg.	5.31×10^6 nW	1.38×10^6 nW	5.37×10^6 nW	1.32×10^6 nW	5.38×10^6 nW	1.30×10^6 nW
Std.	1.89×10^4 nW	1.89×10^4 nW	2.00×10^4 nW	2.00×10^4 nW	2.74×10^4 nW	2.74×10^4 nW

Table B.17: Intensity measurements to measure the transmitted intensity I_t and reflected intensity I_r in nanowatts for different 15-30 Ω glass samples at 470 nm.

ITO 70-100 Ω (470 nm)						
	Glass 1		**Glass 2**		**Glass 3**	
Meas.	I_t (nW)	I_r (nW)	I_t (nW)	I_r (nW)	I_t (nW)	I_r (nW)
1	5.80×10^6 nW	8.86×10^5 nW	5.76×10^6 nW	9.26×10^5 nW	5.77×10^6 nW	9.16×10^5 nW
2	5.79×10^6 nW	8.96×10^5 nW	5.76×10^6 nW	9.26×10^5 nW	5.77×10^6 nW	9.16×10^5 nW
3	5.79×10^6 nW	8.96×10^5 nW	5.76×10^6 nW	9.26×10^5 nW	5.77×10^6 nW	9.16×10^5 nW
4	5.80×10^6 nW	8.86×10^5 nW	5.76×10^6 nW	9.26×10^5 nW	5.83×10^6 nW	8.56×10^5 nW
5	5.82×10^6 nW	8.66×10^5 nW	5.76×10^6 nW	9.26×10^5 nW	5.80×10^6 nW	8.86×10^5 nW
6	5.81×10^6 nW	8.76×10^5 nW	5.76×10^6 nW	9.26×10^5 nW	5.78×10^6 nW	9.06×10^5 nW
7	5.81×10^6 nW	8.76×10^5 nW	5.84×10^6 nW	8.46×10^5 nW	5.78×10^6 nW	9.06×10^5 nW
8	5.80×10^6 nW	8.86×10^5 nW	5.78×10^6 nW	9.06×10^5 nW	5.77×10^6 nW	9.16×10^5 nW
9	5.80×10^6 nW	8.86×10^5 nW	5.76×10^6 nW	9.26×10^5 nW	5.77×10^6 nW	9.16×10^5 nW
10	5.80×10^6 nW	8.86×10^5 nW	5.76×10^6 nW	9.26×10^5 nW	5.77×10^6 nW	9.16×10^5 nW
Avg.	5.80×10^6 nW	8.84×10^5 nW	5.77×10^6 nW	9.16×10^5 nW	5.78×10^6 nW	9.05×10^5 nW
Std.	9.19×10^3 nW	9.19×10^3 nW	2.54×10^4 nW	2.54×10^4 nW	1.97×10^4 nW	1.97×10^4 nW

Table B.18: Intensity measurements to measure the transmitted intensity I_t and reflected intensity I_r in nanowatts for different 70-100 Ω glass samples at 470 nm.

B.2.2. Reflection of ITO glass using 635 nm laser

Thorlabs CPS635R	
Measurement	I_0 (nW)
1	1.16×10^6 nW
2	1.16×10^6 nW
3	1.16×10^6 nW
4	1.16×10^6 nW
5	1.16×10^6 nW
6	1.16×10^6 nW
7	1.16×10^6 nW
8	1.16×10^6 nW
9	1.16×10^6 nW
10	1.16×10^6 nW
Average	1.16×10^6 nW
Std.	9.94×10^2 nW

Table B.19: Intensity measurements of the incoming intensity I_0 in nanowatts for the Thorlabs CPS635R with a wavelength of 635 nm.

ITO 8-12 Ω (635 nm)						
	Glass 1		**Glass 2**		**Glass 3**	
Meas.	I_t (nW)	I_r (nW)	I_t (nW)	I_r (nW)	I_t (nW)	I_r (nW)
1	1.03×10^6 nW	1.28×10^5 nW	9.28×10^5 nW	2.33×10^5 nW	1.11×10^6 nW	4.89×10^4 nW
2	1.03×10^6 nW	1.27×10^5 nW	9.29×10^5 nW	2.32×10^5 nW	1.11×10^6 nW	4.89×10^4 nW
3	1.04×10^6 nW	1.23×10^5 nW	9.30×10^5 nW	2.31×10^5 nW	1.11×10^6 nW	5.29×10^4 nW
4	1.03×10^6 nW	1.28×10^5 nW	9.34×10^5 nW	2.27×10^5 nW	1.11×10^6 nW	5.09×10^4 nW
5	1.04×10^6 nW	1.26×10^5 nW	9.34×10^5 nW	2.27×10^5 nW	1.11×10^6 nW	4.99×10^4 nW
6	1.04×10^6 nW	1.25×10^5 nW	9.25×10^5 nW	2.36×10^5 nW	1.11×10^6 nW	4.99×10^4 nW
7	1.04×10^6 nW	1.21×10^5 nW	9.32×10^5 nW	2.29×10^5 nW	1.11×10^6 nW	4.99×10^4 nW
8	1.04×10^6 nW	1.20×10^5 nW	9.34×10^5 nW	2.27×10^5 nW	1.11×10^6 nW	5.29×10^4 nW
9	1.03×10^6 nW	1.29×10^5 nW	9.26×10^5 nW	2.35×10^5 nW	1.11×10^6 nW	5.19×10^4 nW
10	1.04×10^6 nW	1.25×10^5 nW	9.27×10^5 nW	2.34×10^5 nW	1.11×10^6 nW	5.09×10^4 nW
Avg.	1.04×10^6 nW	1.25×10^5 nW	9.30×10^5 nW	2.31×10^5 nW	1.11×10^6 nW	5.07×10^4 nW
Std.	3.05×10^3 nW	3.05×10^3 nW	3.45×10^3 nW	3.45×10^3 nW	1.48×10^3 nW	1.48×10^3 nW

Table B.20: Intensity measurements to measure the transmitted intensity I_t and reflected intensity I_r in nanowatts for different 8-12 Ω glass samples at 635 nm.

ITO 15-30 Ω (635 nm)						
	Glass 1		**Glass 2**		**Glass 3**	
Meas.	I_t (nW)	I_r (nW)	I_t (nW)	I_r (nW)	I_t (nW)	I_r (nW)
1	9.99×10^5 nW	1.62×10^5 nW	1.09×10^6 nW	6.79×10^4 nW	1.07×10^6 nW	8.79×10^4 nW
2	1.00×10^6 nW	1.61×10^5 nW	1.10×10^6 nW	6.39×10^4 nW	1.07×10^6 nW	8.69×10^4 nW
3	9.99×10^5 nW	1.62×10^5 nW	1.10×10^6 nW	6.39×10^4 nW	1.07×10^6 nW	8.79×10^4 nW
4	9.98×10^5 nW	1.63×10^5 nW	1.10×10^6 nW	6.39×10^4 nW	1.07×10^6 nW	8.89×10^4 nW
5	9.98×10^5 nW	1.63×10^5 nW	1.10×10^6 nW	6.49×10^4 nW	1.07×10^6 nW	8.79×10^4 nW
6	9.99×10^5 nW	1.62×10^5 nW	1.10×10^6 nW	6.49×10^4 nW	1.07×10^6 nW	8.89×10^4 nW
7	1.00×10^6 nW	1.61×10^5 nW	1.09×10^6 nW	6.69×10^4 nW	1.07×10^6 nW	8.99×10^4 nW
8	9.99×10^5 nW	1.62×10^5 nW	1.10×10^6 nW	6.49×10^4 nW	1.07×10^6 nW	9.09×10^4 nW
9	1.00×10^6 nW	1.61×10^5 nW	1.10×10^6 nW	6.49×10^4 nW	1.07×10^6 nW	9.09×10^4 nW
10	9.99×10^5 nW	1.62×10^5 nW	1.10×10^6 nW	6.39×10^4 nW	1.07×10^6 nW	9.09×10^4 nW
Avg.	9.99×10^5 nW	1.62×10^5 nW	1.10×10^6 nW	6.50×10^4 nW	1.07×10^6 nW	8.91×10^4 nW
Std.	7.38×10^2 nW	7.38×10^2 nW	1.37×10^3 nW	1.37×10^3 nW	1.48×10^3 nW	1.48×10^3 nW

Table B.21: Intensity measurements to measure the transmitted intensity I_t and reflected intensity I_r in nanowatts for different 15-30 Ω glass samples at 635 nm.

ITO 70-100 Ω (635 nm)						
	Glass 1		**Glass 2**		**Glass 3**	
Meas.	I_t (nW)	I_r (nW)	I_t (nW)	I_r (nW)	I_t (nW)	I_r (nW)
1	9.09×10^5 nW	2.52×10^5 nW	9.24×10^5 nW	2.37×10^5 nW	9.09×10^5 nW	2.52×10^5 nW
2	9.10×10^5 nW	2.51×10^5 nW	9.23×10^5 nW	2.38×10^5 nW	9.05×10^5 nW	2.56×10^5 nW
3	9.09×10^5 nW	2.52×10^5 nW	9.24×10^5 nW	2.37×10^5 nW	9.06×10^5 nW	2.55×10^5 nW
4	9.11×10^5 nW	2.50×10^5 nW	9.34×10^5 nW	2.27×10^5 nW	9.07×10^5 nW	2.54×10^5 nW
5	9.11×10^5 nW	2.50×10^5 nW	9.32×10^5 nW	2.29×10^5 nW	9.07×10^5 nW	2.54×10^5 nW
6	9.09×10^5 nW	2.52×10^5 nW	9.24×10^5 nW	2.37×10^5 nW	9.08×10^5 nW	2.53×10^5 nW
7	9.12×10^5 nW	2.49×10^5 nW	9.28×10^5 nW	2.33×10^5 nW	9.08×10^5 nW	2.53×10^5 nW
8	8.87×10^5 nW	2.74×10^5 nW	9.20×10^5 nW	2.41×10^5 nW	9.09×10^5 nW	2.52×10^5 nW
9	9.11×10^5 nW	2.50×10^5 nW	9.17×10^5 nW	2.44×10^5 nW	9.09×10^5 nW	2.52×10^5 nW
10	8.82×10^5 nW	2.79×10^5 nW	9.16×10^5 nW	2.45×10^5 nW	9.05×10^5 nW	2.56×10^5 nW
Avg.	9.05×10^5 nW	2.56×10^5 nW	9.24×10^5 nW	2.37×10^5 nW	9.07×10^5 nW	2.54×10^5 nW
Std.	1.10×10^4 nW	1.10×10^4 nW	5.87×10^3 nW	5.87×10^3 nW	1.57×10^3 nW	1.57×10^3 nW

Table B.22: Intensity measurements to measure the transmitted intensity I_t and reflected intensity I_r in nanowatts for different 70-100 Ω glass samples at 635 nm.

B.2.3. Reflection of ITO glass using 715 nm filtered lamp

Thorlabs QTH10/M with Red Plastic Filter		
Measurement	I_0 (nW)	Noise (nW)
1	3.09×10^6 nW	8.70×10^1 nW
2	3.09×10^6 nW	8.20×10^1 nW
3	3.09×10^6 nW	8.20×10^1 nW
4	3.09×10^6 nW	8.20×10^1 nW
5	3.10×10^6 nW	8.20×10^1 nW
6	3.08×10^6 nW	8.20×10^1 nW
7	3.02×10^6 nW	8.50×10^1 nW
8	3.05×10^6 nW	8.40×10^1 nW
9	3.03×10^6 nW	8.10×10^1 nW
10	3.02×10^6 nW	8.20×10^1 nW
Average	3.07×10^6 nW	8.29×10^1 nW
Std.	3.24×10^4 nW	1.85×10^0 nW

Table B.23: Intensity measurements of the initial intensity I_0 and noise levels in nanowatts for the Thorlabs QTH10/M with Red Plastic Filter with a wavelength of 715 nm.

ITO 8-12 Ω (715 nm)						
	Glass 1		**Glass 2**		**Glass 3**	
Meas.	I_t (nW)	I_r (nW)	I_t (nW)	I_r (nW)	I_t (nW)	I_r (nW)
1	2.71×10^6 nW	3.56×10^5 nW	2.70×10^6 nW	3.66×10^5 nW	2.70×10^6 nW	3.66×10^5 nW
2	2.71×10^6 nW	3.56×10^5 nW	2.70×10^6 nW	3.66×10^5 nW	2.70×10^6 nW	3.66×10^5 nW
3	2.70×10^6 nW	3.66×10^5 nW	2.70×10^6 nW	3.66×10^5 nW	2.70×10^6 nW	3.66×10^5 nW
4	2.71×10^6 nW	3.56×10^5 nW	2.70×10^6 nW	3.66×10^5 nW	2.69×10^6 nW	3.76×10^5 nW
5	2.71×10^6 nW	3.56×10^5 nW	2.71×10^6 nW	3.56×10^5 nW	2.71×10^6 nW	3.56×10^5 nW
6	2.71×10^6 nW	3.56×10^5 nW	2.70×10^6 nW	3.66×10^5 nW	2.71×10^6 nW	3.56×10^5 nW
7	2.71×10^6 nW	3.56×10^5 nW	2.70×10^6 nW	3.66×10^5 nW	2.71×10^6 nW	3.56×10^5 nW
8	2.71×10^6 nW	3.56×10^5 nW	2.71×10^6 nW	3.56×10^5 nW	2.71×10^6 nW	3.56×10^5 nW
9	2.71×10^6 nW	3.56×10^5 nW	2.70×10^6 nW	3.66×10^5 nW	2.71×10^6 nW	3.56×10^5 nW
10	2.71×10^6 nW	3.56×10^5 nW	2.70×10^6 nW	3.66×10^5 nW	2.71×10^6 nW	3.56×10^5 nW
Avg.	2.71×10^6 nW	3.57×10^5 nW	2.70×10^6 nW	3.64×10^5 nW	2.71×10^6 nW	3.61×10^5 nW
Std.	3.16×10^3 nW	3.16×10^3 nW	4.22×10^3 nW	4.22×10^3 nW	7.07×10^3 nW	7.07×10^3 nW

Table B.24: Intensity measurements to measure the transmitted intensity I_t and reflected intensity I_r in nanowatts for different 8-12 Ω glass samples at 715 nm.

ITO 15-30 Ω (715 nm)						
	Glass 1		Glass 2		Glass 3	
Meas.	I_t (nW)	I_r (nW)	I_t (nW)	I_r (nW)	I_t (nW)	I_r (nW)
1	2.65×10^6 nW	4.16×10^5 nW	2.65×10^6 nW	4.16×10^5 nW	2.64×10^6 nW	4.26×10^5 nW
2	2.65×10^6 nW	4.16×10^5 nW	2.65×10^6 nW	4.16×10^5 nW	2.64×10^6 nW	4.26×10^5 nW
3	2.65×10^6 nW	4.16×10^5 nW	2.65×10^6 nW	4.16×10^5 nW	2.64×10^6 nW	4.26×10^5 nW
4	2.65×10^6 nW	4.16×10^5 nW	2.65×10^6 nW	4.16×10^5 nW	2.65×10^6 nW	4.16×10^5 nW
5	2.65×10^6 nW	4.16×10^5 nW	2.64×10^6 nW	4.26×10^5 nW	2.64×10^6 nW	4.26×10^5 nW
6	2.66×10^6 nW	4.06×10^5 nW	2.65×10^6 nW	4.16×10^5 nW	2.64×10^6 nW	4.26×10^5 nW
7	2.65×10^6 nW	4.16×10^5 nW	2.65×10^6 nW	4.16×10^5 nW	2.64×10^6 nW	4.26×10^5 nW
8	2.65×10^6 nW	4.16×10^5 nW	2.65×10^6 nW	4.16×10^5 nW	2.64×10^6 nW	4.26×10^5 nW
9	2.65×10^6 nW	4.16×10^5 nW	2.65×10^6 nW	4.16×10^5 nW	2.64×10^6 nW	4.26×10^5 nW
10	2.65×10^6 nW	4.16×10^5 nW	2.65×10^6 nW	4.16×10^5 nW	2.64×10^6 nW	4.26×10^5 nW
Avg.	2.65×10^6 nW	4.15×10^5 nW	2.65×10^6 nW	4.17×10^5 nW	2.64×10^6 nW	4.25×10^5 nW
Std.	3.16×10^3 nW	3.16×10^3 nW	3.16×10^3 nW	3.16×10^3 nW	3.16×10^3 nW	3.16×10^3 nW

Table B.25: Intensity measurements to measure the transmitted intensity I_t and reflected intensity I_r in nanowatts for different 15-30 Ω glass samples at 715 nm.

ITO 70-100 Ω (715 nm)						
	Glass 1		Glass 2		Glass 3	
Meas.	I_t (nW)	I_r (nW)	I_t (nW)	I_r (nW)	I_t (nW)	I_r (nW)
1	2.62×10^6 nW	4.46×10^5 nW	2.60×10^6 nW	4.66×10^5 nW	2.59×10^6 nW	4.76×10^5 nW
2	2.62×10^6 nW	4.46×10^5 nW	2.60×10^6 nW	4.66×10^5 nW	2.59×10^6 nW	4.76×10^5 nW
3	2.63×10^6 nW	4.36×10^5 nW	2.60×10^6 nW	4.66×10^5 nW	2.59×10^6 nW	4.76×10^5 nW
4	2.63×10^6 nW	4.36×10^5 nW	2.60×10^6 nW	4.66×10^5 nW	2.59×10^6 nW	4.76×10^5 nW
5	2.63×10^6 nW	4.36×10^5 nW	2.59×10^6 nW	4.76×10^5 nW	2.59×10^6 nW	4.76×10^5 nW
6	2.63×10^6 nW	4.36×10^5 nW	2.60×10^6 nW	4.66×10^5 nW	2.60×10^6 nW	4.66×10^5 nW
7	2.62×10^6 nW	4.46×10^5 nW	2.60×10^6 nW	4.66×10^5 nW	2.59×10^6 nW	4.76×10^5 nW
8	2.63×10^6 nW	4.36×10^5 nW	2.60×10^6 nW	4.66×10^5 nW	2.59×10^6 nW	4.76×10^5 nW
9	2.63×10^6 nW	4.36×10^5 nW	2.60×10^6 nW	4.66×10^5 nW	2.59×10^6 nW	4.76×10^5 nW
10	2.63×10^6 nW	4.36×10^5 nW	2.60×10^6 nW	4.66×10^5 nW	2.59×10^6 nW	4.76×10^5 nW
Avg.	2.63×10^6 nW	4.39×10^5 nW	2.60×10^6 nW	4.67×10^5 nW	2.59×10^6 nW	4.75×10^5 nW
Std.	4.83×10^3 nW	4.83×10^3 nW	3.16×10^3 nW	3.16×10^3 nW	3.16×10^3 nW	3.16×10^3 nW

Table B.26: Intensity measurements to measure the transmitted intensity I_t and reflected intensity I_r in nanowatts for different 70-100 Ω glass samples at 715 nm.

B.2.4. Reflection of ITO glass using 470 nm LED in the absorption measurement experimental setup with beamsplitter

Thorlabs MC470L3-C1			
Meas.	I_0 (nW)	Noise (nW)	Noise after BS (nW)
1	7.49×10^5 nW	1.00×10^1 nW	1.72×10^3 nW
2	7.49×10^5 nW	1.00×10^1 nW	1.72×10^3 nW
3	7.49×10^5 nW	1.00×10^1 nW	1.72×10^3 nW
4	7.52×10^5 nW	2.00×10^1 nW	1.72×10^3 nW
5	7.51×10^5 nW	1.00×10^1 nW	1.73×10^3 nW
6	7.50×10^5 nW	1.00×10^1 nW	1.72×10^3 nW
7	7.49×10^5 nW	1.00×10^1 nW	1.73×10^3 nW
8	7.48×10^5 nW	1.00×10^1 nW	1.73×10^3 nW
9	7.48×10^5 nW	1.00×10^1 nW	1.73×10^3 nW
10	7.48×10^5 nW	1.00×10^1 nW	1.72×10^3 nW
Avg.	7.49×10^5 nW	1.10×10^1 nW	1.72×10^3 nW
Std.	1.34×10^3 nW	3.16×10^0 nW	4.55×10^0 nW

Table B.27: Measurements of the initial light power and the noise before and after the beam splitter for Thorlabs MC470L3-C1.

ITO glass 8-12 Ohm, 470 nm			
Meas.	I_t	Measured I_r	Calculated I_r
1	2.70×10^1 nW	8.13×10^4 nW	1.63×10^5 nW
2	2.70×10^1 nW	8.13×10^4 nW	1.63×10^5 nW
3	2.70×10^1 nW	8.13×10^4 nW	1.63×10^5 nW
4	2.70×10^1 nW	8.15×10^4 nW	1.63×10^5 nW
5	2.70×10^1 nW	8.15×10^4 nW	1.63×10^5 nW
6	2.70×10^1 nW	8.14×10^4 nW	1.63×10^5 nW
7	2.80×10^1 nW	8.14×10^4 nW	1.63×10^5 nW
8	2.60×10^1 nW	8.13×10^4 nW	1.63×10^5 nW
9	2.70×10^1 nW	8.13×10^4 nW	1.63×10^5 nW
10	2.80×10^1 nW	8.13×10^4 nW	1.63×10^5 nW
Avg.	2.71×10^1 nW	8.14×10^4 nW	1.63×10^5 nW
Std.	5.68×10^{-1} nW	8.43×10^1 nW	1.69×10^2 nW

Table B.28: Measured and calculated reflection intensity for 8-12 Ω ITO glass at 470 nm in the setup containing the beamsplitter. This information is used for calculation the absorption coefficient of the a-Si:H.

ITO glass 15-30 Ohm, 470 nm			
Meas.	I_t (nW)	Measured I_r (nW)	Calculated I_r (nW)
1	2.60×10^1 nW	5.07×10^4 nW	1.01×10^5 nW
2	2.60×10^1 nW	5.07×10^4 nW	1.01×10^5 nW
3	2.60×10^1 nW	5.07×10^4 nW	1.01×10^5 nW
4	2.70×10^1 nW	5.07×10^4 nW	1.01×10^5 nW
5	2.60×10^1 nW	5.07×10^4 nW	1.01×10^5 nW
6	2.80×10^1 nW	5.11×10^4 nW	1.02×10^5 nW
7	2.60×10^1 nW	5.09×10^4 nW	1.02×10^5 nW
8	2.60×10^1 nW	5.08×10^4 nW	1.02×10^5 nW
9	2.60×10^1 nW	5.07×10^4 nW	1.01×10^5 nW
10	2.60×10^1 nW	5.07×10^4 nW	1.01×10^5 nW
Avg.	2.63×10^1 nW	5.08×10^4 nW	1.02×10^5 nW
Std.	6.75×10^{-1} nW	1.34×10^2 nW	2.67×10^2 nW

Table B.29: Measured and calculated reflection intensity for 15-30 Ω ITO glass at 470 nm in the setup containing the beamsplitter. This information is used for calculation the absorption coefficient of the a-Si:H.

ITO glass 70-100 Ohm, 470 nm			
Meas.	I_t (nW)	Measured I_r (nW)	Calculated I_r (nW)
1	2.70×10^1 nW	4.65×10^4 nW	9.30×10^4 nW
2	2.90×10^1 nW	4.65×10^4 nW	9.30×10^4 nW
3	2.70×10^1 nW	4.65×10^4 nW	9.30×10^4 nW
4	2.70×10^1 nW	4.69×10^4 nW	9.38×10^4 nW
5	2.70×10^1 nW	4.68×10^4 nW	9.36×10^4 nW
6	2.80×10^1 nW	4.66×10^4 nW	9.32×10^4 nW
7	2.80×10^1 nW	4.66×10^4 nW	9.32×10^4 nW
8	2.80×10^1 nW	4.65×10^4 nW	9.30×10^4 nW
9	2.70×10^1 nW	4.65×10^4 nW	9.30×10^4 nW
10	2.80×10^1 nW	4.65×10^4 nW	9.30×10^4 nW
Avg.	2.76×10^1 nW	4.66×10^4 nW	9.32×10^4 nW
Std.	6.99×10^{-1} nW	1.45×10^2 nW	2.90×10^2 nW

Table B.30: Measured and calculated reflection intensity for 70-100 Ω ITO glass at 470 nm in the setup containing the beam-splitter. This information is used for calculation the absorption coefficient of the a-Si:H.

B.2.5. Reflection of ITO glass using 635 nm laser in the absorption measurement experimental setup with beamsplitter

Thorlabs CPS635R			
Meas.	I_0 (nW)	Noise (nW)	Noise after BS (nW)
1	5.45×10^5 nW	1.00×10^1 nW	2.24×10^3 nW
2	5.45×10^5 nW	1.00×10^1 nW	2.24×10^3 nW
3	5.45×10^5 nW	1.00×10^1 nW	2.24×10^3 nW
4	5.46×10^5 nW	1.00×10^1 nW	2.24×10^3 nW
5	5.46×10^5 nW	1.00×10^1 nW	2.24×10^3 nW
6	5.46×10^5 nW	1.00×10^1 nW	2.23×10^3 nW
7	5.44×10^5 nW	1.00×10^1 nW	2.24×10^3 nW
8	5.44×10^5 nW	2.00×10^1 nW	2.24×10^3 nW
9	5.45×10^5 nW	2.00×10^1 nW	2.23×10^3 nW
10	5.45×10^5 nW	1.00×10^1 nW	2.24×10^3 nW
Avg.	5.45×10^5 nW	1.20×10^1 nW	2.24×10^3 nW
Std.	7.38×10^2 nW	4.22×10^0 nW	4.22×10^0 nW

Table B.31: Measurements of the initial light power and the noise before and after the beam splitter for Thorlabs CPS635R.

ITO glass 8-12 Ohm, 635 nm			
Meas.	I_t (nW)	Measured I_r (nW)	Calculated I_r (nW)
1	4.32×10^4 nW	4.75×10^4 nW	9.50×10^4 nW
2	4.33×10^4 nW	4.74×10^4 nW	9.48×10^4 nW
3	4.33×10^4 nW	4.74×10^4 nW	9.48×10^4 nW
4	4.34×10^4 nW	4.74×10^4 nW	9.48×10^4 nW
5	4.34×10^4 nW	4.74×10^4 nW	9.48×10^4 nW
6	4.35×10^4 nW	4.74×10^4 nW	9.48×10^4 nW
7	4.36×10^4 nW	4.74×10^4 nW	9.48×10^4 nW
8	4.37×10^4 nW	4.73×10^4 nW	9.46×10^4 nW
9	4.38×10^4 nW	4.75×10^4 nW	9.50×10^4 nW
10	4.39×10^4 nW	4.73×10^4 nW	9.46×10^4 nW
Avg.	4.35×10^4 nW	4.74×10^4 nW	9.48×10^4 nW
Std.	2.33×10^2 nW	6.67×10^1 nW	1.33×10^2 nW

Table B.32: Measured and calculated reflection intensity for 8-12 Ω ITO glass at 635 nm in the setup containing the beamsplitter. This information is used for calculation the absorption coefficient of the a-Si:H.

ITO glass 15-30 Ohm, 635 nm			
Meas.	I_t (nW)	Measured I_r (nW)	Calculated I_r (nW)
1	3.94×10^4 nW	6.21×10^4 nW	1.24×10^5 nW
2	3.96×10^4 nW	6.20×10^4 nW	1.24×10^5 nW
3	3.95×10^4 nW	6.19×10^4 nW	1.24×10^5 nW
4	3.98×10^4 nW	6.20×10^4 nW	1.24×10^5 nW
5	3.95×10^4 nW	6.22×10^4 nW	1.24×10^5 nW
6	3.99×10^4 nW	6.25×10^4 nW	1.25×10^5 nW
7	3.96×10^4 nW	6.28×10^4 nW	1.26×10^5 nW
8	3.97×10^4 nW	6.30×10^4 nW	1.26×10^5 nW
9	4.00×10^4 nW	6.31×10^4 nW	1.26×10^5 nW
10	3.97×10^4 nW	6.25×10^4 nW	1.25×10^5 nW
Avg.	3.97×10^4 nW	6.24×10^4 nW	1.25×10^5 nW
Std.	1.89×10^2 nW	4.38×10^2 nW	8.77×10^2 nW

Table B.33: Measured and calculated reflection intensity for 15-30 Ω ITO glass at 635 nm in the setup containing the beamsplitter. This information is used for calculation the absorption coefficient of the a-Si:H.

ITO glass 70-100 Ohm, 635 nm			
Meas.	I_t (nW)	Measured I_r (nW)	Calculated I_r (nW)
1	4.40×10^4 nW	6.30×10^4 nW	1.26×10^5 nW
2	4.39×10^4 nW	6.30×10^4 nW	1.26×10^5 nW
3	4.39×10^4 nW	6.29×10^4 nW	1.26×10^5 nW
4	4.39×10^4 nW	6.28×10^4 nW	1.26×10^5 nW
5	4.38×10^4 nW	6.29×10^4 nW	1.26×10^5 nW
6	4.38×10^4 nW	6.31×10^4 nW	1.26×10^5 nW
7	4.37×10^4 nW	6.32×10^4 nW	1.26×10^5 nW
8	4.37×10^4 nW	6.33×10^4 nW	1.27×10^5 nW
9	4.36×10^4 nW	6.34×10^4 nW	1.27×10^5 nW
10	4.35×10^4 nW	6.35×10^4 nW	1.27×10^5 nW
Avg.	4.38×10^4 nW	6.31×10^4 nW	1.26×10^5 nW
Std.	1.55×10^2 nW	2.33×10^2 nW	4.66×10^2 nW

Table B.34: Measured and calculated reflection intensity for 70-100 Ω ITO glass at 635 nm in the setup containing the beam-splitter. This information is used for calculation the absorption coefficient of the a-Si:H.

B.2.6. Reflection of ITO glass using 715 nm filtered lamp in the absorption measurement experimental setup with beamsplitter

Thorlabs QTH10/M+ red plastic filter			
Meas.	I_0 (nW)	Noise (nW)	Noise after BS (nW)
1	9.81×10^5 nW	6.00×10^3 nW	2.40×10^5 nW
2	9.82×10^5 nW	6.00×10^3 nW	2.44×10^5 nW
3	9.81×10^5 nW	7.00×10^3 nW	2.45×10^5 nW
4	9.82×10^5 nW	6.00×10^3 nW	2.46×10^5 nW
5	9.82×10^5 nW	6.00×10^3 nW	2.64×10^5 nW
6	9.82×10^5 nW	6.00×10^3 nW	2.66×10^5 nW
7	9.81×10^5 nW	7.00×10^3 nW	2.67×10^5 nW
8	9.79×10^5 nW	6.00×10^3 nW	2.66×10^5 nW
9	9.79×10^5 nW	6.00×10^3 nW	2.66×10^5 nW
10	9.79×10^5 nW	6.00×10^3 nW	2.65×10^5 nW
Avg.	9.81×10^5 nW	6.20×10^3 nW	2.57×10^5 nW
Std.	1.32×10^3 nW	4.22×10^2 nW	1.14×10^4 nW

Table B.35: Measurements of the initial light power and the noise before and after the beam splitter for Thorlabs QTH10/M+ red plastic filter.

ITO glass 8-12 Ohm, 715 nm			
Meas.	I_t (nW)	Measured I_r (nW)	Calculated I_r (nW)
1	5.22×10^5 nW	3.48×10^5 nW	6.96×10^5 nW
2	5.22×10^5 nW	3.38×10^5 nW	6.76×10^5 nW
3	5.21×10^5 nW	3.37×10^5 nW	6.74×10^5 nW
4	5.20×10^5 nW	3.38×10^5 nW	6.76×10^5 nW
5	5.18×10^5 nW	3.40×10^5 nW	6.80×10^5 nW
6	5.19×10^5 nW	3.42×10^5 nW	6.84×10^5 nW
7	5.18×10^5 nW	3.41×10^5 nW	6.82×10^5 nW
8	5.18×10^5 nW	3.40×10^5 nW	6.80×10^5 nW
9	5.17×10^5 nW	3.41×10^5 nW	6.82×10^5 nW
10	5.18×10^5 nW	3.45×10^5 nW	6.90×10^5 nW
Avg.	5.19×10^5 nW	3.41×10^5 nW	6.82×10^5 nW
Std.	1.83×10^3 nW	3.37×10^3 nW	6.73×10^3 nW

Table B.36: Measured and calculated reflection intensity for 8-12 Ω ITO glass at 715 nm in the setup containing the beamsplitter. This information is used for calculation the absorption coefficient of the a-Si:H.

ITO glass 15-30 Ohm, 715 nm			
Meas.	I_t (nW)	Measured I_r (nW)	Calculated I_r (nW)
1	4.98×10^5 nW	3.58×10^5 nW	7.16×10^5 nW
2	4.86×10^5 nW	3.60×10^5 nW	7.20×10^5 nW
3	4.92×10^5 nW	3.61×10^5 nW	7.22×10^5 nW
4	4.97×10^5 nW	3.59×10^5 nW	7.18×10^5 nW
5	5.03×10^5 nW	3.60×10^5 nW	7.20×10^5 nW
6	5.05×10^5 nW	3.61×10^5 nW	7.22×10^5 nW
7	5.12×10^5 nW	3.59×10^5 nW	7.18×10^5 nW
8	5.10×10^5 nW	3.57×10^5 nW	7.14×10^5 nW
9	5.10×10^5 nW	3.61×10^5 nW	7.22×10^5 nW
10	5.10×10^5 nW	3.63×10^5 nW	7.26×10^5 nW
Avg.	5.02×10^5 nW	3.60×10^5 nW	7.20×10^5 nW
Std.	8.81×10^3 nW	1.73×10^3 nW	3.46×10^3 nW

Table B.37: Measured and calculated reflection intensity for 15-30 Ω ITO glass at 715 nm in the setup containing the beamsplitter. This information is used for calculation the absorption coefficient of the a-Si:H.

ITO glass 70-100 Ohm, 715 nm			
Meas.	I_t (nW)	Measured I_r (nW)	Calculated I_r (nW)
1	5.66×10^5 nW	3.62×10^5 nW	7.24×10^5 nW
2	5.65×10^5 nW	3.60×10^5 nW	7.20×10^5 nW
3	5.64×10^5 nW	3.59×10^5 nW	7.18×10^5 nW
4	5.66×10^5 nW	3.56×10^5 nW	7.12×10^5 nW
5	5.67×10^5 nW	3.38×10^5 nW	6.76×10^5 nW
6	5.68×10^5 nW	3.46×10^5 nW	6.92×10^5 nW
7	5.64×10^5 nW	3.45×10^5 nW	6.90×10^5 nW
8	5.68×10^5 nW	3.54×10^5 nW	7.08×10^5 nW
9	5.67×10^5 nW	3.50×10^5 nW	7.00×10^5 nW
10	5.57×10^5 nW	3.56×10^5 nW	7.12×10^5 nW
Avg.	5.65×10^5 nW	3.53×10^5 nW	7.05×10^5 nW
Std.	3.22×10^3 nW	7.68×10^3 nW	1.54×10^4 nW

Table B.38: Measured and calculated reflection intensity for 70-100 Ω ITO glass at 715 nm in the setup containing the beam-splitter. This information is used for calculation the absorption coefficient of the a-Si:H.

B.3. Absorption coefficient

B.3.1. Absorption by a-Si:H on ITO covered microscope slides with different resistances using 470 nm LED

ITO glass 8-12 Ohm, 470 nm	
I_0 (nW)	7.49×10^5 nW
Refl. %	14.81%
I_t ITO (nW)	6.38×10^5 nW

Meas.	Measured I_t (nW)	Calculated I_r (nW)	I_r a-Si:H (nW)	ln(I_t/I_0)	α (m^{-1})
1	2.70×10^1	1.63×10^5	5.17×10^4	-10.07	1.01×10^7
2	2.70×10^1	1.63×10^5	5.17×10^4	-10.07	1.01×10^7
3	2.70×10^1	1.63×10^5	5.17×10^4	-10.07	1.01×10^7
4	2.70×10^1	1.63×10^5	5.21×10^4	-10.07	1.01×10^7
5	2.70×10^1	1.63×10^5	5.21×10^4	-10.07	1.01×10^7
6	2.70×10^1	1.63×10^5	5.19×10^4	-10.07	1.01×10^7
7	2.80×10^1	1.63×10^5	5.19×10^4	-10.03	1.00×10^7
8	2.60×10^1	1.63×10^5	5.17×10^4	-10.11	1.01×10^7
9	2.70×10^1	1.63×10^5	5.17×10^4	-10.07	1.01×10^7
10	2.80×10^1	1.63×10^5	5.17×10^4	-10.03	1.00×10^7
Avg.	2.71×10^1	1.63×10^5	5.18×10^4	-10.07	1.01×10^7
Std.	5.68×10^{-1}	1.69×10^2	1.69×10^2	0.02	2.09×10^4

Table B.39: The upper table gives the initial light beam power with the calculated reflected power due to the ITO glass. The lower table shows the measurements of the transmitted light power, resulting in an absorption coefficient using equation 2.20. The ITO microscope slide has a resistance of 8-12 Ω and the photon wavelength used is 470 nm.

ITO glass 15-30 Ohm, 470 nm	
I_0 (nW)	7.49×10^5 nW
Refl. %	19.92%
I_t ITO (nW)	6.00×10^5 nW

Meas.	Measured I_t (nW)	Calculated I_r (nW)	I_r a-Si:H (nW)	ln(I_t/I_0)	α (m^{-1})
1	2.60×10^1	1.01×10^5	-4.79×10^4	-10.05	1.00×10^7
2	2.60×10^1	1.01×10^5	-4.79×10^4	-10.05	1.00×10^7
3	2.60×10^1	1.01×10^5	-4.79×10^4	-10.05	1.00×10^7
4	2.70×10^1	1.01×10^5	-4.79×10^4	-10.01	1.00×10^7
5	2.60×10^1	1.01×10^5	-4.79×10^4	-10.05	1.00×10^7
6	2.80×10^1	1.02×10^5	-4.71×10^4	-9.97	9.97×10^6
7	2.60×10^1	1.02×10^5	-4.75×10^4	-10.05	1.00×10^7
8	2.60×10^1	1.02×10^5	-4.77×10^4	-10.05	1.00×10^7
9	2.60×10^1	1.01×10^5	-4.79×10^4	-10.05	1.00×10^7
10	2.60×10^1	1.01×10^5	-4.79×10^4	-10.05	1.00×10^7
Avg.	2.63×10^1	1.02×10^5	-4.77×10^4	-10.04	1.00×10^7
Std.	6.75×10^{-1}	2.67×10^2	2.67×10^2	0.03	2.51×10^4

Table B.40: The upper table gives the initial light beam power with the calculated reflected power due to the ITO glass. The lower table shows the measurements of the transmitted light power, resulting in an absorption coefficient using equation 2.20. The ITO microscope slide has a resistance of 15-30 Ω and the photon wavelength used is 470 nm.

ITO glass 70-100 Ohm, 470 nm	
I_0 (nW)	7.49×10^5 nW
Refl. %	13.49%
I_t ITO (nW)	6.48×10^5 nW

Meas.	Measured I_t (nW)	Calculated I_r (nW)	I_r a-Si:H (nW)	$\ln(I_t/I_0)$	$\alpha\ (m^{-1})$
1	2.70×10^1	9.30×10^4	-8.05×10^3	-10.09	1.01×10^7
2	2.90×10^1	9.30×10^4	-8.05×10^3	-10.01	1.00×10^7
3	2.70×10^1	9.30×10^4	-8.05×10^3	-10.09	1.01×10^7
4	2.70×10^1	9.38×10^4	-7.25×10^3	-10.09	1.01×10^7
5	2.70×10^1	9.36×10^4	-7.45×10^3	-10.09	1.01×10^7
6	2.80×10^1	9.32×10^4	-7.85×10^3	-10.05	1.00×10^7
7	2.80×10^1	9.32×10^4	-7.85×10^3	-10.05	1.00×10^7
8	2.80×10^1	9.30×10^4	-8.05×10^3	-10.05	1.00×10^7
9	2.70×10^1	9.30×10^4	-8.05×10^3	-10.09	1.01×10^7
10	2.80×10^1	9.30×10^4	-8.05×10^3	-10.05	1.00×10^7
Avg.	2.76×10^1	9.32×10^4	-7.87×10^3	-10.06	1.01×10^7
Std.	6.99×10^{-1}	2.90×10^2	2.90×10^2	0.03	2.51×10^4

Table B.41: The upper table gives the initial light beam power with the calculated reflected power due to the ITO glass. The lower table shows the measurements of the transmitted light power, resulting in an absorption coefficient using equation 2.20. The ITO microscope slide has a resistance of 70-100 Ω and the photon wavelength used is 470 nm.

B.3.2. Absorption by a-Si:H on ITO covered microscope slides with different resistances using 635 nm laser

ITO glass 8-12 Ohm, 635 nm	
I_0 (nW)	5.45×10^5 nW
Refl. %	11.68%
I_t ITO (nW)	4.81×10^5 nW

Meas.	Measured I_t (nW)	Calculated I_r (nW)	I_r a-Si:H (nW)	$\ln(I_t/I_0)$	$\alpha\ (m^{-1})$
1	4.32×10^4	9.50×10^4	3.13×10^4	-2.41	2.41×10^6
2	4.33×10^4	9.48×10^4	3.11×10^4	-2.41	2.41×10^6
3	4.33×10^4	9.48×10^4	3.11×10^4	-2.41	2.41×10^6
4	4.34×10^4	9.48×10^4	3.11×10^4	-2.41	2.41×10^6
5	4.34×10^4	9.48×10^4	3.11×10^4	-2.41	2.41×10^6
6	4.35×10^4	9.48×10^4	3.11×10^4	-2.40	2.40×10^6
7	4.36×10^4	9.48×10^4	3.11×10^4	-2.40	2.40×10^6
8	4.37×10^4	9.46×10^4	3.09×10^4	-2.40	2.40×10^6
9	4.38×10^4	9.50×10^4	3.13×10^4	-2.40	2.40×10^6
10	4.39×10^4	9.46×10^4	3.09×10^4	-2.39	2.39×10^6
Avg.	4.35×10^4	9.48×10^4	3.11×10^4	-2.40	2.40×10^6
Std.	2.33×10^2	1.33×10^2	1.33×10^2	0.01	5.35×10^3

Table B.42: The upper table gives the initial light beam power with the calculated reflected power due to the ITO glass. The lower table shows the measurements of the transmitted light power, resulting in an absorption coefficient using equation 2.20. The ITO microscope slide has a resistance of 8-12 Ω and the photon wavelength used is 635 nm.

ITO glass 15-30 Ohm, 635 nm	
I_0 (nW)	5.45×10^5 nW
Refl. %	9.07%
I_t ITO (nW)	4.96×10^5 nW

Meas.	Measured I_t (nW)	Calculated I_r (nW)	I_r a-Si:H (nW)	ln(I_t/I_0)	α (m^{-1})
1	3.94×10^4	6.21×10^4	1.27×10^4	-2.53	2.53×10^6
2	3.96×10^4	6.20×10^4	1.26×10^4	-2.53	2.53×10^6
3	3.95×10^4	6.19×10^4	1.25×10^4	-2.53	2.53×10^6
4	3.98×10^4	6.20×10^4	1.26×10^4	-2.52	2.52×10^6
5	3.95×10^4	6.22×10^4	1.28×10^4	-2.53	2.53×10^6
6	3.99×10^4	6.25×10^4	1.31×10^4	-2.52	2.52×10^6
7	3.96×10^4	6.28×10^4	1.34×10^4	-2.53	2.53×10^6
8	3.97×10^4	6.30×10^4	1.36×10^4	-2.52	2.52×10^6
9	4.00×10^4	6.31×10^4	1.37×10^4	-2.52	2.52×10^6
10	3.97×10^4	6.25×10^4	1.31×10^4	-2.52	2.52×10^6
Avg.	3.97×10^4	6.24×10^4	1.30×10^4	-2.53	2.53×10^6
Std.	1.89×10^2	4.38×10^2	4.38×10^2	0.00	4.76×10^3

Table B.43: The upper table gives the initial light beam power with the calculated reflected power due to the ITO glass. The lower table shows the measurements of the transmitted light power, resulting in an absorption coefficient using equation 2.20. The ITO microscope slide has a resistance of 15-30 Ω and the photon wavelength used is 635 nm.

ITO glass 70-100 Ohm, 635 nm	
I_0 (nW)	5.45×10^5 nW
Refl. %	21.42%
I_t ITO (nW)	4.28×10^5 nW

Meas.	Measured I_t (nW)	Calculated I_r (nW)	I_r a-Si:H (nW)	ln(I_t/I_0)	α (m^{-1})
1	4.40×10^4	1.26×10^5	9.22×10^3	-2.28	2.28×10^6
2	4.39×10^4	1.26×10^5	9.22×10^3	-2.28	2.28×10^6
3	4.39×10^4	1.26×10^5	9.02×10^3	-2.28	2.28×10^6
4	4.39×10^4	1.26×10^5	8.82×10^3	-2.28	2.28×10^6
5	4.38×10^4	1.26×10^5	9.02×10^3	-2.28	2.28×10^6
6	4.38×10^4	1.26×10^5	9.42×10^3	-2.28	2.28×10^6
7	4.37×10^4	1.26×10^5	9.62×10^3	-2.28	2.28×10^6
8	4.37×10^4	1.27×10^5	9.82×10^3	-2.28	2.28×10^6
9	4.36×10^4	1.27×10^5	1.00×10^4	-2.28	2.28×10^6
10	4.35×10^4	1.27×10^5	1.02×10^4	-2.29	2.29×10^6
Avg.	4.38×10^4	1.26×10^5	9.44×10^3	-2.28	2.28×10^6
Std.	1.55×10^2	4.66×10^2	4.66×10^2	0.00	3.54×10^3

Table B.44: The upper table gives the initial light beam power with the calculated reflected power due to the ITO glass. The lower table shows the measurements of the transmitted light power, resulting in an absorption coefficient using equation 2.20. The ITO microscope slide has a resistance of 70-100 Ω and the photon wavelength used is 635 nm.

B.3.3. Absorption by a-Si:H on ITO covered microscope slides with different resistances using 715 nm filtered lamp

ITO glass 8-12 Ohm, 715 nm	
I_0 (nW)	9.81×10^5 nW
Refl. %	11.76%
I_t ITO (nW)	8.65×10^5 nW

Meas.	Measured I_t (nW)	Calculated I_r (nW)	I_r a-Si:H (nW)	ln(I_t/I_0)	α (m^{-1})
1	5.22×10^5	6.96×10^5	5.81×10^5	-0.51	5.06×10^5
2	5.22×10^5	6.76×10^5	5.61×10^5	-0.51	5.06×10^5
3	5.21×10^5	6.74×10^5	5.59×10^5	-0.51	5.07×10^5
4	5.20×10^5	6.76×10^5	5.61×10^5	-0.51	5.09×10^5
5	5.18×10^5	6.80×10^5	5.65×10^5	-0.51	5.13×10^5
6	5.19×10^5	6.84×10^5	5.69×10^5	-0.51	5.11×10^5
7	5.18×10^5	6.82×10^5	5.67×10^5	-0.51	5.13×10^5
8	5.18×10^5	6.80×10^5	5.65×10^5	-0.51	5.13×10^5
9	5.17×10^5	6.82×10^5	5.67×10^5	-0.52	5.15×10^5
10	5.18×10^5	6.90×10^5	5.75×10^5	-0.51	5.13×10^5
Avg.	5.19×10^5	6.82×10^5	5.67×10^5	-0.51	5.11×10^5
Std.	1.83×10^3	6.73×10^3	6.73×10^3	0.00	3.52×10^3

Table B.45: The upper table gives the initial light beam power with the calculated reflected power due to the ITO glass. The lower table shows the measurements of the transmitted light power, resulting in an absorption coefficient using equation 2.20. The ITO microscope slide has a resistance of 8-12 Ω and the photon wavelength used is 715 nm.

ITO glass 15-30 Ohm, 715 nm	
I_0 (nW)	9.81×10^5 nW
Refl. %	13.67%
I_t ITO (nW)	8.47×10^5 nW

Meas.	Measured I_t (nW)	Calculated I_r (nW)	I_r a-Si:H (nW)	ln(I_t/I_0)	α (m^{-1})
1	4.98×10^5	7.16×10^5	5.82×10^5	-0.53	5.31×10^5
2	4.86×10^5	7.20×10^5	5.86×10^5	-0.56	5.55×10^5
3	4.92×10^5	7.22×10^5	5.88×10^5	-0.54	5.43×10^5
4	4.97×10^5	7.18×10^5	5.84×10^5	-0.53	5.33×10^5
5	5.03×10^5	7.20×10^5	5.86×10^5	-0.52	5.21×10^5
6	5.05×10^5	7.22×10^5	5.88×10^5	-0.52	5.17×10^5
7	5.12×10^5	7.18×10^5	5.84×10^5	-0.50	5.03×10^5
8	5.10×10^5	7.14×10^5	5.80×10^5	-0.51	5.07×10^5
9	5.10×10^5	7.22×10^5	5.88×10^5	-0.51	5.07×10^5
10	5.10×10^5	7.26×10^5	5.92×10^5	-0.51	5.07×10^5
Avg.	5.02×10^5	7.20×10^5	5.86×10^5	-0.52	5.22×10^5
Std.	8.81×10^3	3.46×10^3	3.46×10^3	0.02	1.76×10^4

Table B.46: The upper table gives the initial light beam power with the calculated reflected power due to the ITO glass. The lower table shows the measurements of the transmitted light power, resulting in an absorption coefficient using equation 2.20. The ITO microscope slide has a resistance of 15-30 Ω and the photon wavelength used is 715 nm.

ITO glass 70-100 Ohm, 715 nm	
I_0 (nW)	9.81×10^5 nW
Refl. %	15.01%
I_t ITO (nW)	8.34×10^5 nW

Meas.	Measured I_t (nW)	Calculated I_r (nW)	I_r a-Si:H (nW)	$\ln(I_t/I_0)$	α (m^{-1})
1	5.66×10^5	7.24×10^5	5.77×10^5	-0.39	3.87×10^5
2	5.65×10^5	7.20×10^5	5.73×10^5	-0.39	3.89×10^5
3	5.64×10^5	7.18×10^5	5.71×10^5	-0.39	3.91×10^5
4	5.66×10^5	7.12×10^5	5.65×10^5	-0.39	3.87×10^5
5	5.67×10^5	6.76×10^5	5.29×10^5	-0.39	3.85×10^5
6	5.68×10^5	6.92×10^5	5.45×10^5	-0.38	3.84×10^5
7	5.64×10^5	6.90×10^5	5.43×10^5	-0.39	3.91×10^5
8	5.68×10^5	7.08×10^5	5.61×10^5	-0.38	3.84×10^5
9	5.67×10^5	7.00×10^5	5.53×10^5	-0.39	3.85×10^5
10	5.57×10^5	7.12×10^5	5.65×10^5	-0.40	4.03×10^5
Avg.	5.65×10^5	7.05×10^5	5.58×10^5	-0.39	3.89×10^5
Std.	3.22×10^3	1.54×10^4	1.54×10^4	0.01	5.73×10^3

Table B.47: The upper table gives the initial light beam power with the calculated reflected power due to the ITO glass. The lower table shows the measurements of the transmitted light power, resulting in an absorption coefficient using equation 2.20. The ITO microscope slide has a resistance of 70-100 Ω and the photon wavelength used is 715 nm.

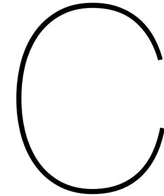

Results: Optical setup

C.1. Magnification

C.1.1. Magnification Chip to Camera

Bead with a diameter of 15 µm				
Bead	Pixels (px)	Conversion (m/pix)	Conversion (µm/pix)	Magnification $M_{\text{Chip}\rightarrow\text{Cam}}$
1	19.334 px	7.76×10^{-7} m/pix	0.776 µm/pix	4.45
2	18.314 px	8.19×10^{-7} m/pix	0.819 µm/pix	4.21
3	18.305 px	8.19×10^{-7} m/pix	0.819 µm/pix	4.21
4	17.451 px	8.60×10^{-7} m/pix	0.860 µm/pix	4.01
5	17.187 px	8.73×10^{-7} m/pix	0.873 µm/pix	3.95
6	18.085 px	8.29×10^{-7} m/pix	0.829 µm/pix	4.16
7	16.882 px	8.89×10^{-7} m/pix	0.889 µm/pix	3.88
8	17.575 px	8.53×10^{-7} m/pix	0.853 µm/pix	4.04
9	18.038 px	8.32×10^{-7} m/pix	0.832 µm/pix	4.15
10	16.378 px	9.16×10^{-7} m/pix	0.916 µm/pix	3.77
11	18.842 px	7.96×10^{-7} m/pix	0.796 µm/pix	4.33
12	17.649 px	8.50×10^{-7} m/pix	0.850 µm/pix	4.06
Average	17.837 px	8.43×10^{-7} m/pix	0.843 µm/pix	4.10
Std.	0.827 px	3.91×10^{-8} m/pix	0.039 µm/pix	0.19

Table C.1: Multiple measurements done on beads with a diameter of 15 µm in the microfluidic chip using the optical setup. The measured size, in terms of camera pixels, gives the conversion using the ground truth of 15 µm. This conversion gives the magnification from the chip to the camera.

Robot full length: 200 μm				
Measurement	Pixels (px)	Conversion (m/pix)	Conversion (μm/pix)	Magnification $M_{\text{Chip}\rightarrow\text{Cam}}$
1	260.427 px	7.68×10^{-7} m/pix	0.768 μm/pix	4.49
2	249.802 px	8.01×10^{-7} m/pix	0.801 μm/pix	4.31
3	245.726 px	8.14×10^{-7} m/pix	0.814 μm/pix	4.24
4	259.939 px	7.69×10^{-7} m/pix	0.769 μm/pix	4.48
5	257.004 px	7.78×10^{-7} m/pix	0.778 μm/pix	4.43
6	253.283 px	7.90×10^{-7} m/pix	0.790 μm/pix	4.37
Average	254.364 px	7.87×10^{-7} m/pix	0.787 μm/pix	4.388
Std.	5.855 px	1.83×10^{-8} m/pix	0.018 μm/pix	0.101

Table C.2: Multiple measurements done on the microbot with a diameter of 200 μm in the microfluidic chip using the optical setup. The measured size, in terms of camera pixels, gives the conversion using the ground truth of 200 μm. This conversion gives the magnification from the chip to the camera.

Robot circle diameter: 125 μm				
Measurement	Pixels (px)	Conversion (m/pix)	Conversion (μm/pix)	Magnification $M_{\text{Chip}\rightarrow\text{Cam}}$
1	153.48 px	8.14×10^{-7} m/pix	0.814 μm/pix	4.24
2	154.225 px	8.11×10^{-7} m/pix	0.811 μm/pix	4.26
3	147.98 px	8.45×10^{-7} m/pix	0.845 μm/pix	4.08
4	155.732 px	8.03×10^{-7} m/pix	0.803 μm/pix	4.30
5	144.462 px	8.65×10^{-7} m/pix	0.865 μm/pix	3.99
6	148.106 px	8.44×10^{-7} m/pix	0.844 μm/pix	4.09
Average	150.664 px	8.30×10^{-7} m/pix	0.830 μm/pix	4.158
Std.	4.439 px	2.46×10^{-8} m/pix	0.025 μm/pix	0.123

Table C.3: Multiple measurements done on the outer radius of the microbot, i.e. the microbot without the teeth, with a diameter of 125 μm in the microfluidic chip using the optical setup. The measured size, in terms of camera pixels, gives the conversion using the ground truth of 125 μm. This conversion gives the magnification from the chip to the camera.

Robot leg width: 25 μm				
Measurement	Pixels (px)	Conversion (m/pix)	Conversion (μm/pix)	Magnification $M_{\text{Chip}\rightarrow\text{Cam}}$
1	32.867 px	7.61×10^{-7} m/pix	0.761 μm/pix	4.54
2	29.77 px	8.40×10^{-7} m/pix	0.840 μm/pix	4.11
3	34.47 px	7.25×10^{-7} m/pix	0.725 μm/pix	4.76
4	33.215 px	7.53×10^{-7} m/pix	0.753 μm/pix	4.58
5	31.314 px	7.98×10^{-7} m/pix	0.798 μm/pix	4.32
6	32.069 px	7.80×10^{-7} m/pix	0.780 μm/pix	4.43
7	31.064 px	8.05×10^{-7} m/pix	0.805 μm/pix	4.29
Average	32.110 px	7.80×10^{-7} m/pix	0.780 μm/pix	4.431
Std.	1.558 px	3.80×10^{-8} m/pix	0.038 μm/pix	0.215

Table C.4: Multiple measurements done on the width of the teeth of the microbot with a length of 25 μm in the microfluidic chip using the optical setup. The measured size, in terms of camera pixels, gives the conversion using the ground truth of 25 μm. This conversion gives the magnification from the chip to the camera.

C.1.2. Magnification DMD to camera

Sweep 30 pixels: 3.24E-04 m				
Measurement	**Camera Pixels (px)**	**Conversion (m/pix)**	**Conversion (µm/pix)**	**Magnification M**
1	62.000 px	5.23×10^{-6} m/pix	5.23 µm/pix	0.660
2	60.500 px	5.36×10^{-6} m/pix	5.36 µm/pix	0.644
3	60.167 px	5.39×10^{-6} m/pix	5.39 µm/pix	0.641
4	60.667 px	5.34×10^{-6} m/pix	5.34 µm/pix	0.646
5	60.500 px	5.36×10^{-6} m/pix	5.36 µm/pix	0.644
6	58.875 px	5.50×10^{-6} m/pix	5.50 µm/pix	0.627
Average	60.451 px	5.36×10^{-6} m/pix	5.361 µm/pix	0.644
Std.	1.002 px	8.89×10^{-8} m/pix	0.089 µm/pix	0.011

Table C.5: Multiple measurements done on the width of the sweep animation created by the DMD and projected on the microfluidic chip. The sweep has a thickness of 30 pixels which is equal to 324 µm on the DMD. The measured size, in terms of camera pixels, gives the conversion from pixel to µm. This conversion gives the magnification from the DMD to the camera.

Sweep 60 pixels: 6.48E-04 m				
Measurement	**Camera Pixels (px)**	**Conversion (m/pix)**	**Conversion (µm/pix)**	**Magnification M**
1	124.667 px	5.20×10^{-6} m/pix	5.20 µm/pix	0.664
2	125.667 px	5.16×10^{-6} m/pix	5.16 µm/pix	0.669
3	126.667 px	5.12×10^{-6} m/pix	5.12 µm/pix	0.674
4	127.667 px	5.08×10^{-6} m/pix	5.08 µm/pix	0.680
5	128.667 px	5.04×10^{-6} m/pix	5.04 µm/pix	0.685
6	129.667 px	5.00×10^{-6} m/pix	5.00 µm/pix	0.690
Average	127.167 px	5.10×10^{-6} m/pix	5.097 µm/pix	0.677
Std.	1.871 px	7.50×10^{-8} m/pix	0.075 µm/pix	0.010

Table C.6: Multiple measurements done on the width of the sweep animation created by the DMD and projected on the microfluidic chip. The sweep has a thickness of 60 pixels which is equal to 648 µm on the DMD. The measured size, in terms of camera pixels, gives the conversion from pixel to µm. This conversion gives the magnification from the DMD to the camera.

Sweep 90 pixels: 9.72×10^{-4} m				
Measurement	**Camera Pixels (px)**	**Conversion (m/pix)**	**Conversion (µm/pix)**	**Magnification M**
1	187.500 px	5.18×10^{-6} m/pix	5.18 µm/pix	0.666
2	188.500 px	5.16×10^{-6} m/pix	5.16 µm/pix	0.669
3	189.500 px	5.13×10^{-6} m/pix	5.13 µm/pix	0.673
4	190.500 px	5.10×10^{-6} m/pix	5.10 µm/pix	0.676
5	191.500 px	5.08×10^{-6} m/pix	5.08 µm/pix	0.680
6	192.500 px	5.05×10^{-6} m/pix	5.05 µm/pix	0.683
Average	190.000 px	5.12×10^{-6} m/pix	5.116 µm/pix	0.674
Std.	1.871 px	5.04×10^{-8} m/pix	0.050 µm/pix	0.007

Table C.7: Multiple measurements done on the width of the sweep animation created by the DMD and projected on the microfluidic chip. The sweep has a thickness of 90 pixels which is equal to 972 µm on the DMD. The measured size, in terms of camera pixels, gives the conversion from pixel to µm. This conversion gives the magnification from the DMD to the camera.

Sweep 120 pixels: 1.30×10^{-3} m				
Measurement	**Pixels (px)**	**Conversion (m/pix)**	**Conversion (µm/pix)**	**Magnification M**
1	252.000 px	5.14×10^{-6} m/pix	5.14 µm/pix	0.671
2	253.000 px	5.12×10^{-6} m/pix	5.12 µm/pix	0.673
3	254.000 px	5.10×10^{-6} m/pix	5.10 µm/pix	0.676
4	255.000 px	5.08×10^{-6} m/pix	5.08 µm/pix	0.679
5	256.000 px	5.06×10^{-6} m/pix	5.06 µm/pix	0.681
6	257.000 px	5.04×10^{-6} m/pix	5.04 µm/pix	0.684
Average	254.500 px	5.09×10^{-6} m/pix	5.093 µm/pix	0.677
Std.	1.871 px	3.74×10^{-8} m/pix	0.037 µm/pix	0.005

Table C.8: Multiple measurements done on the width of the sweep animation created by the DMD and projected on the microfluidic chip. The sweep has a thickness of 120 pixels which is equal to 1296 µm on the DMD. The measured size, in terms of camera pixels, gives the conversion from pixel to µm. This conversion gives the magnification from the DMD to the camera.

C.2. Optical efficiency

C.2.1. Optical power

Direct Focused LED Light - Thorlabs M455D3					
Power	**Meas. 1**	**Meas. 2**	**Meas. 3**	**Mean**	**Std.**
1.00	1.18×10^{8} nW	1.26×10^{8} nW	1.34×10^{8} nW	1.26×10^{8} nW	7.85×10^{6} nW
0.83	9.53×10^{7} nW	9.84×10^{7} nW	1.05×10^{8} nW	9.94×10^{7} nW	4.69×10^{6} nW
0.75	6.44×10^{7} nW	7.53×10^{7} nW	7.64×10^{7} nW	7.20×10^{7} nW	6.63×10^{6} nW
0.67	4.47×10^{7} nW	4.78×10^{7} nW	4.97×10^{7} nW	4.74×10^{7} nW	2.52×10^{6} nW
0.50	1.53×10^{7} nW	1.59×10^{7} nW	1.74×10^{7} nW	1.62×10^{7} nW	1.08×10^{6} nW
0.33	9.21×10^{6} nW	1.01×10^{7} nW	1.07×10^{7} nW	9.99×10^{6} nW	7.57×10^{5} nW
0.25	6.80×10^{6} nW	6.93×10^{6} nW	7.31×10^{6} nW	7.01×10^{6} nW	2.65×10^{5} nW
0.17	3.60×10^{6} nW	3.95×10^{6} nW	4.19×10^{6} nW	3.91×10^{6} nW	2.97×10^{5} nW

Table C.9: Measured optical power with different relative amounts of electrical power. When the power switch if fully on, the power is 1, while when half on, the power is 0.5. The LED used is the Thorlabs M455D3 and is measured by directly focusing the LED light on the power meter.

Direct Focused LED Light - Roschwege HighPower LED Koningsblauw					
Power	**Meas. 1**	**Meas. 2**	**Meas. 3**	**Mean**	**Std.**
1.00	4.62×10^{7} nW	4.75×10^{7} nW	4.79×10^{7} nW	4.72×10^{7} nW	7.26×10^{5} nW
0.75	3.02×10^{7} nW	3.06×10^{7} nW	3.02×10^{7} nW	3.03×10^{7} nW	1.89×10^{5} nW
0.50	7.97×10^{6} nW	8.28×10^{6} nW	8.28×10^{6} nW	8.18×10^{6} nW	1.46×10^{5} nW
0.25	3.54×10^{6} nW	3.64×10^{6} nW	3.85×10^{6} nW	3.68×10^{6} nW	1.29×10^{5} nW

Table C.10: Measured optical power with different relative amounts of electrical power. When the power switch if fully on, the power is 1, while when half on, the power is 0.5. The LED used is the Roschwege HighPower LED Koningsblauw and is measured by directly focusing the LED light on the power meter.

C.2.2. Intensity measurements 445 nm

Focussed after alignment mirrors - Thorlabs M455D3					
Power	**Meas. 1**	**Meas. 2**	**Meas. 3**	**Mean**	**Std.**
1.00	9.74E+07 nW	9.70E+07 nW	9.81E+07 nW	9.75E+07 nW	5.57E+05 nW
0.75	5.81E+07 nW	5.85E+07 nW	5.76E+07 nW	5.81E+07 nW	4.51E+05 nW
0.50	1.25E+07 nW	1.28E+07 nW	1.28E+07 nW	1.27E+07 nW	1.93E+05 nW
0.25	5.68E+06 nW	5.66E+06 nW	5.69E+06 nW	5.68E+06 nW	1.53E+04 nW

Not focussed after alignment mirrors - Thorlabs M455D3					
Power	**Meas. 1**	**Meas. 2**	**Meas. 3**	**Mean**	**Std.**
1.00	3.31E+07 nW	3.31E+07 nW	3.31E+07 nW	3.31E+07 nW	3.06E+04 nW
0.75	1.92E+07 nW	1.93E+07 nW	1.93E+07 nW	1.93E+07 nW	5.51E+04 nW
0.50	4.24E+06 nW	4.25E+06 nW	4.23E+06 nW	4.24E+06 nW	1.00E+04 nW
0.25	2.03E+06 nW	2.03E+06 nW	2.04E+06 nW	2.03E+06 nW	5.77E+02 nW

Table C.11: Measured optical power after the allignment mirrors with different relative amounts of electrical power. When the power switch if fully on, the power is 1, while when half on, the power is 0.5. The LED used is the Thorlabs M455D3 and is measured by directly focusing the LED light on the power meter in the upper table.

Focussed after DMD with full white screen - Thorlabs M455D3					
Power	**Meas. 1**	**Meas. 2**	**Meas. 3**	**Mean**	**Std.**
1.00	4.25E+07 nW	4.22E+07 nW	4.23E+07 nW	4.23E+07 nW	1.53E+05 nW
0.75	2.39E+07 nW	2.40E+07 nW	2.38E+07 nW	2.39E+07 nW	8.96E+04 nW
0.50	5.43E+06 nW	5.44E+06 nW	5.61E+06 nW	5.49E+06 nW	1.01E+05 nW
0.25	2.35E+06 nW	2.40E+06 nW	2.40E+06 nW	2.38E+06 nW	2.92E+04 nW

Focussed after DMD with a 64 pixel checker pattern - Thorlabs M455D3					
Power	**Meas. 1**	**Meas. 2**	**Meas. 3**	**Mean**	**Std.**
1.00	2.11E+07 nW	2.10E+07 nW	2.09E+07 nW	2.10E+07 nW	8.02E+04 nW
0.75	1.24E+07 nW	1.23E+07 nW	1.20E+07 nW	1.22E+07 nW	1.73E+05 nW
0.50	2.71E+06 nW	2.76E+06 nW	2.73E+06 nW	2.73E+06 nW	2.72E+04 nW
0.25	1.19E+06 nW	1.13E+06 nW	1.16E+06 nW	1.16E+06 nW	2.97E+04 nW

Focussed after DMD with only the single center mirror - Thorlabs M455D3					
Power	**Meas. 1**	**Meas. 2**	**Meas. 3**	**Mean**	**Std.**
1.00	4.61E+03 nW	4.63E+03 nW	4.59E+03 nW	4.61E+03 nW	2.00E+01 nW
0.75	2.78E+03 nW	2.67E+03 nW	2.69E+03 nW	2.71E+03 nW	5.86E+01 nW
0.50	6.80E+02 nW	8.40E+02 nW	7.00E+02 nW	7.40E+02 nW	8.72E+01 nW
0.25	4.20E+02 nW	3.20E+02 nW	4.30E+02 nW	3.90E+02 nW	6.08E+01 nW

Table C.12: Measured optical power after the DMD with different relative amounts of electrical power. When the power switch if fully on, the power is 1, while when half on, the power is 0.5. The DMD shows three different patterns: a full white screen, a 64 pixel sided checker, and a single mirror flipped on in the center. The LED used is the Thorlabs M455D3 and is measured by directly focusing the LED light on the power meter in the upper table.

Not focussed after DMD with full white screen - Thorlabs M455D3					
Power	**Meas. 1**	**Meas. 2**	**Meas. 3**	**Mean**	**Std.**
1.00	1.37E+07 nW	1.37E+07 nW	1.35E+07 nW	1.36E+07 nW	1.47E+05 nW
0.75	7.75E+06 nW	8.04E+06 nW	7.70E+06 nW	7.83E+06 nW	1.84E+05 nW
0.50	1.79E+06 nW	1.79E+06 nW	1.80E+06 nW	1.80E+06 nW	7.57E+03 nW
0.25	8.03E+05 nW	7.68E+05 nW	7.85E+05 nW	7.85E+05 nW	1.75E+04 nW

Not focussed after DMD with a 64 pixel checker pattern - Thorlabs M455D3					
Power	**Meas. 1**	**Meas. 2**	**Meas. 3**	**Mean**	**Std.**
1.00	6.69E+06 nW	6.74E+06 nW	6.73E+06 nW	6.72E+06 nW	2.65E+04 nW
0.75	3.96E+06 nW	3.98E+06 nW	3.84E+06 nW	3.92E+06 nW	7.49E+04 nW
0.50	8.90E+05 nW	8.72E+05 nW	8.85E+05 nW	8.82E+05 nW	9.29E+03 nW
0.25	3.85E+05 nW	3.63E+05 nW	3.75E+05 nW	3.74E+05 nW	1.10E+04 nW

Not focussed after DMD with only the single center mirror - Thorlabs M455D3					
Power	**Meas. 1**	**Meas. 2**	**Meas. 3**	**Mean**	**Std.**
1.00	1.51E+03 nW	1.62E+03 nW	1.19E+03 nW	1.44E+03 nW	2.21E+02 nW
0.75	6.94E+02 nW	6.99E+02 nW	7.52E+02 nW	7.15E+02 nW	3.21E+01 nW
0.50	2.07E+02 nW	2.09E+02 nW	2.06E+02 nW	2.07E+02 nW	1.35E+00 nW
0.25	1.17E+02 nW	1.19E+02 nW	1.20E+02 nW	1.19E+02 nW	1.40E+00 nW

Table C.13: Measured optical power after the DMD with different relative amounts of electrical power. When the power switch if fully on, the power is 1, while when half on, the power is 0.5. The DMD shows three different patterns: a full white screen, a 64 pixel sided checker, and a single mirror flipped on in the center. The LED used is the Thorlabs M455D3.

After the objective with DMD with full white screen - Thorlabs M455D3					
Power	**Meas. 1**	**Meas. 2**	**Meas. 3**	**Mean**	**Std.**
1.00	6.60E+06 nW	6.57E+06 nW	6.58E+06 nW	6.58E+06 nW	1.53E+04 nW
0.75	3.62E+06 nW	3.65E+06 nW	3.77E+06 nW	3.68E+06 nW	8.11E+04 nW
0.50	9.02E+05 nW	8.85E+05 nW	8.88E+05 nW	8.92E+05 nW	9.07E+03 nW
0.25	3.65E+05 nW	3.70E+05 nW	3.75E+05 nW	3.70E+05 nW	4.92E+03 nW

After the objective with DMD with a 64 pixel checker pattern - Thorlabs M455D3					
Power	**Meas. 1**	**Meas. 2**	**Meas. 3**	**Mean**	**Std.**
1.00	3.31E+06 nW	3.29E+06 nW	3.29E+06 nW	3.30E+06 nW	1.49E+04 nW
0.75	1.86E+06 nW	1.87E+06 nW	1.86E+06 nW	1.86E+06 nW	6.08E+03 nW
0.50	4.40E+05 nW	4.45E+05 nW	4.34E+05 nW	4.40E+05 nW	5.77E+03 nW
0.25	1.86E+05 nW	1.82E+05 nW	1.86E+05 nW	1.85E+05 nW	2.08E+03 nW

After the objective with DMD with only the single center mirror - Thorlabs M455D3					
Power	**Meas. 1**	**Meas. 2**	**Meas. 3**	**Mean**	**Std.**
1.00	1.13E+02 nW	1.15E+02 nW	1.14E+02 nW	1.14E+02 nW	8.14E-01 nW
0.75	7.16E+01 nW	7.15E+01 nW	7.42E+01 nW	7.24E+01 nW	1.53E+00 nW
0.50	3.05E+01 nW	3.12E+01 nW	3.74E+01 nW	3.30E+01 nW	3.80E+00 nW
0.25	2.36E+01 nW	2.37E+01 nW	2.36E+01 nW	2.36E+01 nW	5.77E-02 nW

Table C.14: Measured optical power after the final objective lens with different relative amounts of electrical power. When the power switch if fully on, the power is 1, while when half on, the power is 0.5. The DMD shows three different patterns: a full white screen, a 64 pixel sided checker, and a single mirror flipped on in the center. The LED used is the Thorlabs M455D3.

Focussed before the objective with DMD with full white screen - Thorlabs M455D3					
Power	**Meas. 1**	**Meas. 2**	**Meas. 3**	**Mean**	**Std.**
1.00	1.46E+07 nW	1.48E+07 nW	1.47E+07 nW	1.47E+07 nW	8.39E+04 nW
0.75	8.31E+06 nW	8.33E+06 nW	8.35E+06 nW	8.33E+06 nW	2.00E+04 nW
0.50	1.94E+06 nW	1.93E+06 nW	1.93E+06 nW	1.93E+06 nW	6.66E+03 nW
0.25	8.48E+05 nW	8.15E+05 nW	8.22E+05 nW	8.28E+05 nW	1.74E+04 nW

Focussed before the objective with DMD with a 64 pixel checker pattern - Thorlabs M455D3					
Power	**Meas. 1**	**Meas. 2**	**Meas. 3**	**Mean**	**Std.**
1.00	7.44E+06 nW	7.41E+06 nW	7.39E+06 nW	7.41E+06 nW	2.52E+04 nW
0.75	4.38E+06 nW	4.15E+06 nW	4.20E+06 nW	4.24E+06 nW	1.22E+05 nW
0.50	9.63E+05 nW	9.63E+05 nW	9.57E+05 nW	9.61E+05 nW	3.46E+03 nW
0.25	4.10E+05 nW	4.16E+05 nW	4.13E+05 nW	4.13E+05 nW	3.10E+03 nW

Focussed before the objective with DMD with only the single center mirror - Thorlabs M455D3					
Power	**Meas. 1**	**Meas. 2**	**Meas. 3**	**Mean**	**Std.**
1.00	4.16E+02 nW	4.18E+02 nW	4.15E+02 nW	4.16E+02 nW	1.53E+00 nW
0.75	2.39E+02 nW	2.29E+02 nW	2.40E+02 nW	2.36E+02 nW	5.66E+00 nW
0.50	6.10E+01 nW	6.02E+01 nW	6.07E+01 nW	6.06E+01 nW	4.04E-01 nW
0.25	2.78E+01 nW	2.62E+01 nW	2.85E+01 nW	2.75E+01 nW	1.18E+00 nW

Table C.15: Measured optical power before the final objective lens with different relative amounts of electrical power. When the power switch if fully on, the power is 1, while when half on, the power is 0.5. The DMD shows three different patterns: a full white screen, a 64 pixel sided checker, and a single mirror flipped on in the center. The LED used is the Thorlabs M455D3 and is measured by directly focusing the LED light on the power meter in the upper table.

Noise Measurements - Thorlabs M455D3			
Measurement	**After DMD**	**Before Objective**	**After Objective**
1	71.1 nW	4.70 nW	17.4 nW
2	69.9 nW	4.70 nW	19.5 nW
3	62.4 nW	5.00 nW	18.6 nW
4	63.4 nW	3.60 nW	18.5 nW
5	69.8 nW	5.20 nW	18.7 nW
6	64.2 nW	5.00 nW	18.6 nW
7	70.9 nW	4.90 nW	18.6 nW
8	68.8 nW	4.80 nW	18.6 nW
Mean	67.6 nW	4.74 nW	18.6 nW
Std.	3.60 nW	0.49 nW	0.57 nW

Table C.16: Noise measurements taken at different positions in the setup for the Thorlabs M455D3.

C.2.3. Intensity measurements 480 nm

Noise Measurements - Roschwege HighPower LED Koningsblauw			
Measurement	**After DMD**	**Before Objective**	**After Objective**
1	15.2 nW	1.40 nW	25.4 nW
2	14.6 nW	1.90 nW	25.5 nW
3	14.2 nW	1.80 nW	25.3 nW
4	14.5 nW	1.70 nW	25.3 nW
5	13.9 nW	1.40 nW	25.2 nW
6	14.4 nW	1.90 nW	25.1 nW
7	14.4 nW	1.60 nW	24.6 nW
8	13.8 nW	1.70 nW	25.0 nW
Mean	14.4 nW	1.68 nW	25.2 nW
Std.	0.409 nW	0.185 nW	0.263 nW

Table C.17: Noise measurements taken at different positions in the setup for the Roschwege HighPower LED Koningsblauw.

Focussed after alignment mirrors - Roschwege HighPower LED Koningsblauw					
Power	**Meas. 1**	**Meas. 2**	**Meas. 3**	**Mean**	**Std.**
1.00	3.35E+07 nW	3.29E+07 nW	3.31E+07 nW	3.32E+07 nW	2.49E+05 nW
0.75	2.24E+07 nW	2.22E+07 nW	2.12E+07 nW	2.19E+07 nW	5.08E+05 nW
0.50	5.79E+06 nW	5.72E+06 nW	5.50E+06 nW	5.67E+06 nW	1.24E+05 nW
0.25	2.47E+06 nW	2.51E+06 nW	2.35E+06 nW	2.44E+06 nW	6.75E+04 nW

Not focussed after alignment mirrors - Roschwege HighPower LED Koningsblauw					
Power	**Meas. 1**	**Meas. 2**	**Meas. 3**	**Mean**	**Std.**
1.00	1.03E+07 nW	1.02E+07 nW	1.02E+07 nW	1.02E+07 nW	2.05E+04 nW
0.75	6.81E+06 nW	6.97E+06 nW	6.62E+06 nW	6.80E+06 nW	1.43E+05 nW
0.50	1.81E+06 nW	1.77E+06 nW	1.77E+06 nW	1.78E+06 nW	1.99E+04 nW
0.25	7.78E+05 nW	7.84E+05 nW	7.80E+05 nW	7.81E+05 nW	2.49E+03 nW

Table C.18: Measured optical power after the allignment mirrors with different relative amounts of electrical power. When the power switch if fully on, the power is `1`, while when half on, the power is `0.5`. The LED used is the Roschwege HighPower LED Koningsblauw and is measured by directly focusing the LED light on the power meter in the upper table.

Roschwege HighPower LED Koningsblauw Focussed after DMD with full white screen					
Power	**Meas. 1**	**Meas. 2**	**Meas. 3**	**Mean**	**Std.**
1.00	1.28E+07 nW	1.27E+07 nW	1.30E+07 nW	1.29E+07 nW	1.22E+05 nW
0.75	8.06E+06 nW	7.86E+06 nW	8.35E+06 nW	8.09E+06 nW	2.01E+05 nW
0.50	2.20E+06 nW	2.33E+06 nW	2.29E+06 nW	2.27E+06 nW	5.38E+04 nW
0.25	9.82E+05 nW	9.84E+05 nW	9.88E+05 nW	9.85E+05 nW	2.49E+03 nW

Roschwege HighPower LED Koningsblauw Focussed after DMD with a 64 pixel checker pattern					
Power	**Meas. 1**	**Meas. 2**	**Meas. 3**	**Mean**	**Std.**
1.00	6.46E+06 nW	6.46E+06 nW	6.47E+06 nW	6.46E+06 nW	4.71E+03 nW
0.75	4.40E+06 nW	4.00E+06 nW	4.13E+06 nW	4.18E+06 nW	1.67E+05 nW
0.50	1.16E+06 nW	1.14E+06 nW	1.14E+06 nW	1.14E+06 nW	8.26E+03 nW
0.25	5.88E+05 nW	5.86E+05 nW	5.36E+05 nW	5.70E+05 nW	2.41E+04 nW

Roschwege HighPower LED Koningsblauw Focussed after DMD with only the single center mirror					
Power	**Meas. 1**	**Meas. 2**	**Meas. 3**	**Mean**	**Std.**
1.00	7.83E+02 nW	8.85E+02 nW	7.48E+02 nW	8.05E+02 nW	5.81E+01 nW
0.75	5.20E+02 nW	5.86E+02 nW	5.18E+02 nW	5.41E+02 nW	3.16E+01 nW
0.50	1.55E+02 nW	1.69E+02 nW	1.49E+02 nW	1.58E+02 nW	8.10E+00 nW
0.25	8.36E+01 nW	9.28E+01 nW	8.65E+01 nW	8.76E+01 nW	3.84E+00 nW

Table C.19: Measured optical power after the DMD with different relative amounts of electrical power. When the power switch if fully on, the power is 1, while when half on, the power is 0.5. The DMD shows three different patterns: a full white screen, a 64 pixel sided checker, and a single mirror flipped on in the center. The LED used is the Roschwege HighPower LED Koningsblauw and is measured by directly focusing the LED light on the power meter in the upper table.

Roschwege HighPower LED Koningsblauw Not Focussed after DMD with Full White Screen					
Power	**Meas. 1**	**Meas. 2**	**Meas. 3**	**Mean**	**Std.**
1.00	3.21E+06 nW	3.19E+06 nW	3.23E+06 nW	3.21E+06 nW	1.63E+04 nW
0.75	2.16E+06 nW	2.17E+06 nW	2.10E+06 nW	2.14E+06 nW	3.04E+04 nW
0.50	6.20E+05 nW	5.94E+05 nW	6.08E+05 nW	6.07E+05 nW	1.06E+04 nW
0.25	2.68E+05 nW	2.86E+05 nW	2.88E+05 nW	2.81E+05 nW	8.99E+03 nW

Roschwege HighPower LED Koningsblauw Not Focussed after DMD with a 64 Pixel Checker Pattern					
Power	**Meas. 1**	**Meas. 2**	**Meas. 3**	**Mean**	**Std.**
1.00	1.61E+06 nW	1.62E+06 nW	1.52E+06 nW	1.58E+06 nW	4.30E+04 nW
0.75	1.04E+06 nW	1.05E+06 nW	1.01E+06 nW	1.03E+06 nW	1.53E+04 nW
0.50	3.04E+05 nW	3.05E+05 nW	2.70E+05 nW	2.93E+05 nW	1.63E+04 nW
0.25	1.49E+05 nW	1.48E+05 nW	1.24E+05 nW	1.40E+05 nW	1.16E+04 nW

Roschwege HighPower LED Koningsblauw Not Focussed after DMD with Only the Single Center Mirror					
Power	**Meas. 1**	**Meas. 2**	**Meas. 3**	**Mean**	**Std.**
1.00	2.11E+02 nW	1.90E+02 nW	1.93E+02 nW	1.98E+02 nW	8.85E+00 nW
0.75	1.43E+02 nW	1.36E+02 nW	1.27E+02 nW	1.35E+02 nW	6.46E+00 nW
0.50	5.01E+01 nW	4.67E+01 nW	4.51E+01 nW	4.73E+01 nW	2.08E+00 nW
0.25	3.15E+01 nW	3.04E+01 nW	2.98E+01 nW	3.06E+01 nW	7.04E-01 nW

Table C.20: Measured optical power after the DMD with different relative amounts of electrical power. When the power switch if fully on, the power is 1, while when half on, the power is 0.5. The DMD shows three different patterns: a full white screen, a 64 pixel sided checker, and a single mirror flipped on in the center. The LED used is the Roschwege HighPower LED Koningsblauw.

Roschwege HighPower LED Koningsblauw After the Objective with DMD with Full White Screen					
Power	**Meas. 1**	**Meas. 2**	**Meas. 3**	**Mean**	**Std.**
1.00	1.03E+06 nW	1.03E+06 nW	1.03E+06 nW	1.03E+06 nW	2.16E+03 nW
0.75	6.47E+05 nW	6.68E+05 nW	6.65E+05 nW	6.60E+05 nW	9.27E+03 nW
0.50	1.96E+05 nW	1.95E+05 nW	1.95E+05 nW	1.95E+05 nW	4.19E+02 nW
0.25	9.50E+04 nW	9.78E+04 nW	9.80E+04 nW	9.69E+04 nW	1.37E+03 nW

Roschwege HighPower LED Koningsblauw After the Objective with DMD with a 64 Pixel Checker Pattern					
Power	**Meas. 1**	**Meas. 2**	**Meas. 3**	**Mean**	**Std.**
1.00	5.18E+05 nW	5.19E+05 nW	5.17E+05 nW	5.18E+05 nW	8.16E+02 nW
0.75	3.31E+05 nW	3.22E+05 nW	3.35E+05 nW	3.29E+05 nW	5.44E+03 nW
0.50	9.69E+04 nW	9.84E+04 nW	9.76E+04 nW	9.76E+04 nW	6.13E+02 nW
0.25	5.22E+04 nW	5.22E+04 nW	4.60E+04 nW	5.01E+04 nW	2.92E+03 nW

Roschwege HighPower LED Koningsblauw After the Objective with DMD with Only the Single Center Mirror					
Power	**Meas. 1**	**Meas. 2**	**Meas. 3**	**Mean**	**Std.**
1.00	4.05E+01 nW	4.00E+01 nW	3.91E+01 nW	3.99E+01 nW	5.79E-01 nW
0.75	3.24E+01 nW	3.45E+01 nW	3.33E+01 nW	3.34E+01 nW	8.60E-01 nW
0.50	2.75E+01 nW	2.71E+01 nW	2.71E+01 nW	2.72E+01 nW	1.89E-01 nW
0.25	2.68E+01 nW	2.68E+01 nW	2.48E+01 nW	2.61E+01 nW	9.43E-01 nW

Table C.21: Measured optical power after the final objective lens with different relative amounts of electrical power. When the power switch if fully on, the power is 1, while when half on, the power is 0.5. The DMD shows three different patterns: a full white screen, a 64 pixel sided checker, and a single mirror flipped on in the center. The LED used is the Roschwege HighPower LED Koningsblauw.

Roschwege HighPower LED Koningsblauw Focussed Before the Objective with Full White Screen					
Power	**Meas. 1**	**Meas. 2**	**Meas. 3**	**Mean**	**Std.**
1.00	3.82E+06 nW	3.95E+06 nW	3.92E+06 nW	3.90E+06 nW	5.56E+04 nW
0.75	2.49E+06 nW	2.39E+06 nW	2.53E+06 nW	2.47E+06 nW	6.00E+04 nW
0.50	6.86E+05 nW	6.75E+05 nW	7.10E+05 nW	6.90E+05 nW	1.46E+04 nW
0.25	3.12E+05 nW	3.20E+05 nW	3.26E+05 nW	3.19E+05 nW	5.80E+03 nW

Roschwege HighPower LED Koningsblauw Focussed Before the Objective with a 64 Pixel Checker Pattern					
Power	**Meas. 1**	**Meas. 2**	**Meas. 3**	**Mean**	**Std.**
1.00	1.98E+06 nW	1.97E+06 nW	1.93E+06 nW	1.96E+06 nW	2.16E+04 nW
0.75	1.29E+06 nW	1.19E+06 nW	1.22E+06 nW	1.23E+06 nW	4.25E+04 nW
0.50	3.35E+05 nW	3.47E+05 nW	3.40E+05 nW	3.41E+05 nW	4.92E+03 nW
0.25	1.66E+05 nW	1.55E+05 nW	1.52E+05 nW	1.58E+05 nW	5.65E+03 nW

Roschwege HighPower LED Koningsblauw Focussed Before the Objective with Only the Single Center Mirror					
Power	**Meas. 1**	**Meas. 2**	**Meas. 3**	**Mean**	**Std.**
1.00	9.53E+01 nW	9.10E+01 nW	9.74E+01 nW	9.46E+01 nW	2.66E+00 nW
0.75	5.93E+01 nW	5.92E+01 nW	5.88E+01 nW	5.91E+01 nW	2.16E-01 nW
0.50	1.77E+01 nW	1.63E+01 nW	1.88E+01 nW	1.76E+01 nW	1.02E+00 nW
0.25	8.90E+00 nW	8.40E+00 nW	9.30E+00 nW	8.87E+00 nW	3.68E-01 nW

Table C.22: Measured optical power before the final objective lens with different relative amounts of electrical power. When the power switch if fully on, the power is 1, while when half on, the power is 0.5. The DMD shows three different patterns: a full white screen, a 64 pixel sided checker, and a single mirror flipped on in the center. The LED used is the Roschwege HighPower LED Koningsblauw and is measured by directly focusing the LED light on the power meter in the upper table.

C.3. Resolution

C.3.1. 4 μm TetraSpeck Fluorescent bead

Spatial Resolution - 4 μm Bead		
Bead	**Gaussian Fit Std. (μm)**	**FWHM (μm)**
1	1.4906 μm	3.5100 μm
2	1.4310 μm	3.3697 μm
3	1.4955 μm	3.5216 μm
4	1.5719 μm	3.7014 μm
5	1.4018 μm	3.3009 μm
6	1.4009 μm	3.2988 μm
7	1.4595 μm	3.4368 μm
8	1.4706 μm	3.4631 μm
9	1.6166 μm	3.8068 μm
10	1.5278 μm	3.5977 μm
Mean	1.4866 μm	3.5007 μm
Std.	0.0704 μm	0.1657 μm

Table C.23: Spatial resolution measurements for a 4 μm TetraSpeck Fluorescent bead. The standard deviation of the Gaussian fit on the PSF and its full-width at half-maximum (FWHM) values are shown in micrometers (μm).

Depth of Focus (DoF) - 4 μm Bead		
Bead	**Gaussian Fit Std. (μm)**	**FWHM (μm)**
1	41.3558 μm	97.3855 μm
2	37.5107 μm	88.3308 μm
3	37.1393 μm	87.4564 μm
4	36.8303 μm	86.7287 μm
5	35.2463 μm	82.9987 μm
6	38.1198 μm	89.7652 μm
7	36.9220 μm	86.9446 μm
8	33.9053 μm	79.8409 μm
9	38.4870 μm	90.6300 μm
10	40.4785 μm	95.3195 μm
Mean	37.5995 μm	88.5400 μm
Std.	2.2089 μm	5.2015 μm

Table C.24: Depth of Focus (DoF) measurements for a TetraSpeck Fluorescent 4 μm bead. The standard deviation of the Gaussian fit on the PSF and its full-width at half-maximum (FWHM) values are shown in micrometers (μm).

C.3.2. 1 µm TetraSpeck Fluorescent bead

Spatial Resolution - 1 µm Bead		
Bead	**Gaussian Fit Std. (µm)**	**FWHM (µm)**
1	1.3926 µm	3.2793 µm
2	1.4494 µm	3.4130 µm
3	1.3194 µm	3.1068 µm
4	1.4653 µm	3.4504 µm
5	1.3934 µm	3.2812 µm
6	1.4572 µm	3.4314 µm
7	1.4419 µm	3.3954 µm
8	1.4850 µm	3.4968 µm
9	1.4053 µm	3.3093 µm
10	1.3960 µm	3.2872 µm
Mean	1.4205 µm	3.3451 µm
Std.	0.0487 µm	0.1147 µm

Table C.25: Spatial resolution measurements for a 1 µm TetraSpeck Fluorescent bead. The standard deviation of the Gaussian fit on the PSF and its full-width at half-maximum (FWHM) values are shown in micrometers (µm).

Depth of Focus (DoF) - 1 µm Bead		
Bead	**Gaussian Fit Std. (µm)**	**FWHM (µm)**
1	34.15 µm	80.43 µm
2	40.97 µm	96.47 µm
3	37.28 µm	87.79 µm
4	30.11 µm	70.90 µm
5	45.55 µm	107.26 µm
6	38.11 µm	89.74 µm
7	34.14 µm	80.39 µm
8	39.30 µm	92.55 µm
9	38.91 µm	91.63 µm
10	42.36 µm	99.75 µm
Mean	38.09 µm	89.69 µm
Std.	4.47 µm	10.52 µm

Table C.26: Depth of Focus (DoF) measurements for a 1 µm TetraSpeck Fluorescent bead. The standard deviation of the Gaussian fit on the PSF and its full-width at half-maximum (FWHM) values are shown in micrometers (µm).

C.3.3. 0.5 µm TetraSpeck Fluorescent bead

Spatial Resolution - 0.5 µm Bead		
Bead	**Gaussian Fit Std. (µm)**	**FWHM (µm)**
1	1.367 µm	3.220 µm
2	1.312 µm	3.088 µm
3	1.516 µm	3.570 µm
4	1.473 µm	3.468 µm
5	1.421 µm	3.346 µm
6	1.398 µm	3.292 µm
7	1.397 µm	3.289 µm
8	1.392 µm	3.277 µm
9	1.341 µm	3.159 µm
10	1.391 µm	3.276 µm
Mean	1.401 µm	3.299 µm
Std.	0.059 µm	0.140 µm

Table C.27: Spatial resolution measurements for a 0.5 µm TetraSpeck Fluorescent bead. The standard deviation of the Gaussian fit on the PSF and its full-width at half-maximum (FWHM) values are shown in micrometers (µm).

Depth of Focus - 0.5 µm Bead		
Bead	**Gaussian Fit Std. (µm)**	**FWHM (µm)**
1	40.76 µm	95.99 µm
2	40.81 µm	96.11 µm
3	40.14 µm	94.52 µm
4	42.89 µm	100.99 µm
5	40.79 µm	96.06 µm
6	43.32 µm	102.02 µm
7	43.28 µm	101.93 µm
8	42.69 µm	100.54 µm
9	41.34 µm	97.36 µm
10	40.72 µm	95.89 µm
Mean	41.68 µm	98.14 µm
Std.	1.23 µm	2.89 µm

Table C.28: Depth of focus (DoF) measurements for a 0.5 µm TetraSpeck Fluorescent bead. The standard deviation of the Gaussian fit on the PSF and its full-width at half-maximum (FWHM) values are shown in micrometers (µm).

C.4. DMD measurements

C.4.1. DMD PSF measurements

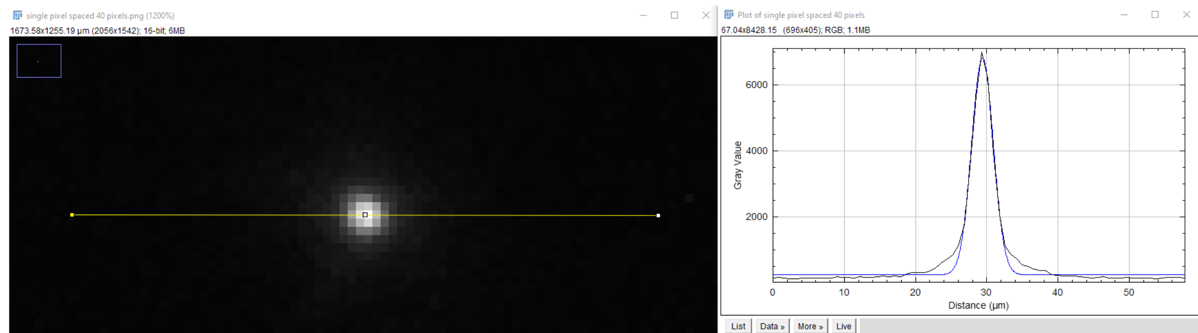

Figure C.1: A view of Fiji were we measured the PSF of a single 1 by 1 pixel DMD square projection on the chip. The left screen shows the image of the DMD spot. The yellow line determines the cross-section at which the PSF on the right side is measured. A Gaussian fit is put on the PSF, shown as the blue line.

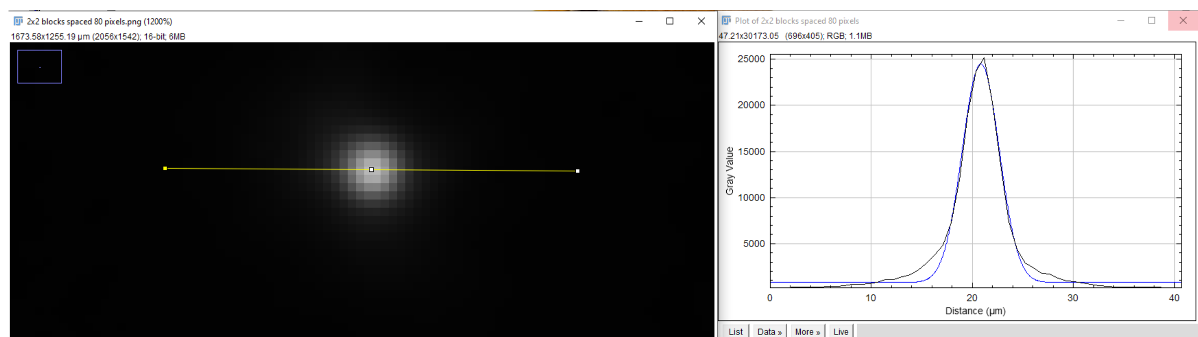

Figure C.2: A view of Fiji were we measured the PSF of a single 2 by 2 pixel DMD square projection on the chip. The left screen shows the image of the DMD spot. The yellow line determines the cross-section at which the PSF on the right side is measured. A Gaussian fit is put on the PSF, shown as the blue line.

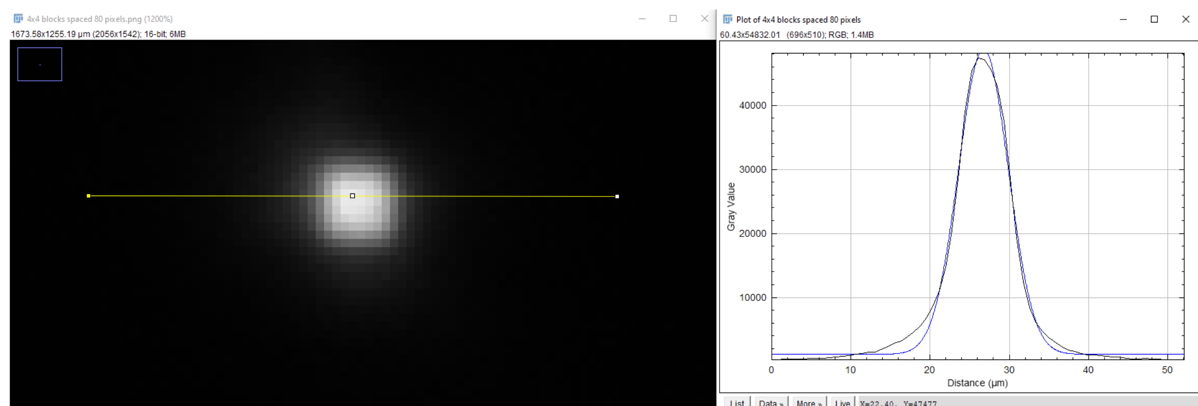

Figure C.3: A view of Fiji were we measured the PSF of a single 4 by 4 pixel DMD square projection on the chip. The left screen shows the image of the DMD spot. The yellow line determines the cross-section at which the PSF on the right side is measured. A Gaussian fit is put on the PSF, shown as the blue line.

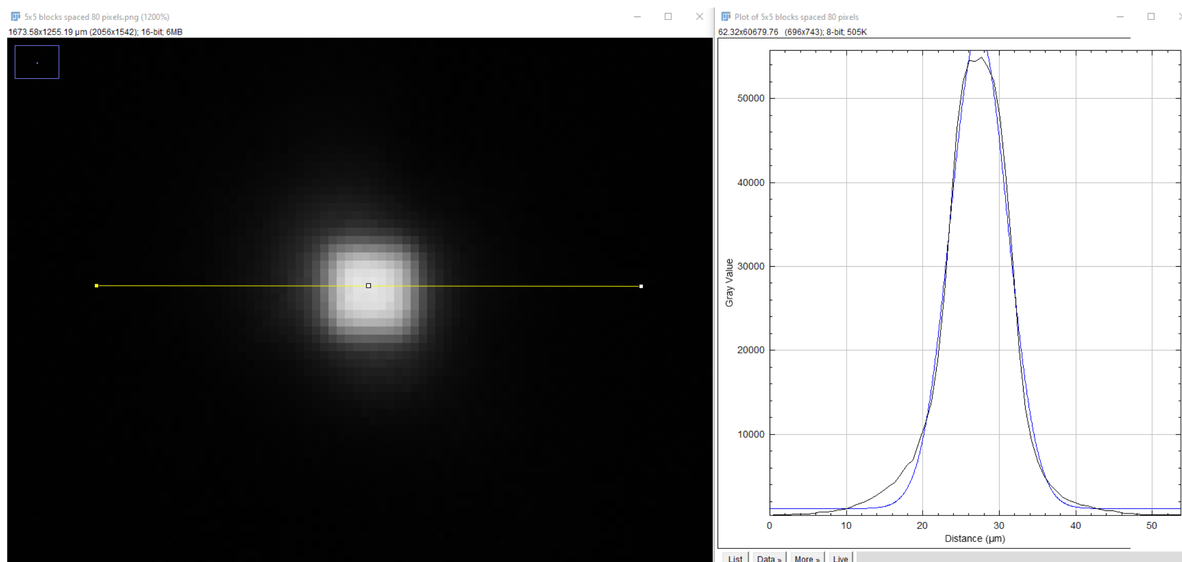

Figure C.4: A view of Fiji were we measured the PSF of a single 5 by 5 pixel DMD square projection on the chip. The left screen shows the image of the DMD spot. The yellow line determines the cross-section at which the PSF on the right side is measured. A Gaussian fit is put on the PSF, shown as the blue line.

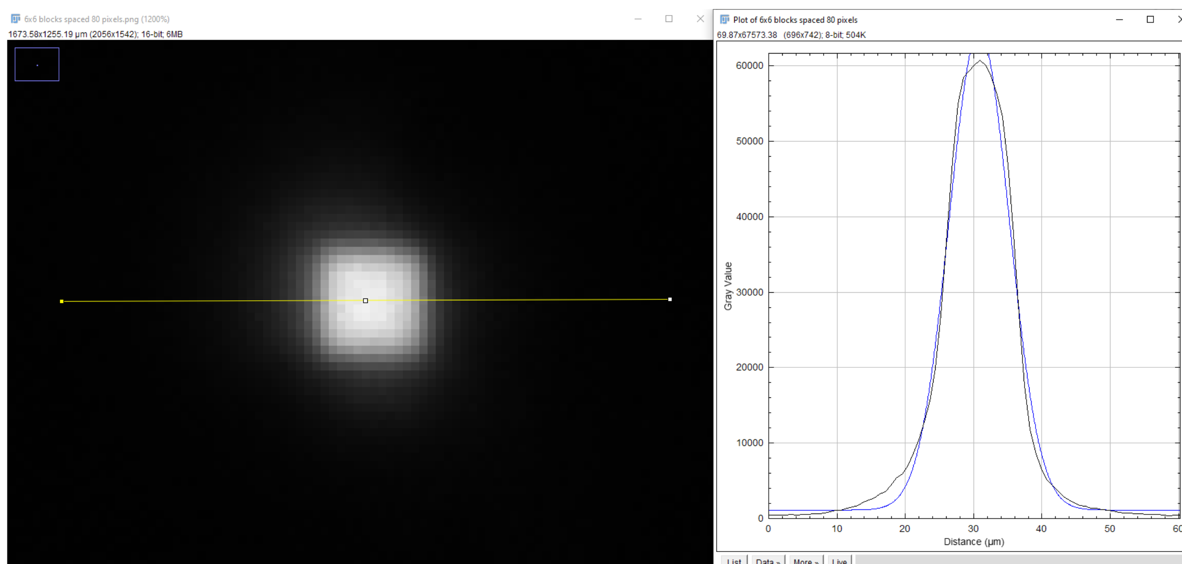

Figure C.5: A view of Fiji were we measured the PSF of a single 6 by 6 pixel DMD square projection on the chip. The left screen shows the image of the DMD spot. The yellow line determines the cross-section at which the PSF on the right side is measured. A Gaussian fit is put on the PSF, shown as the blue line.

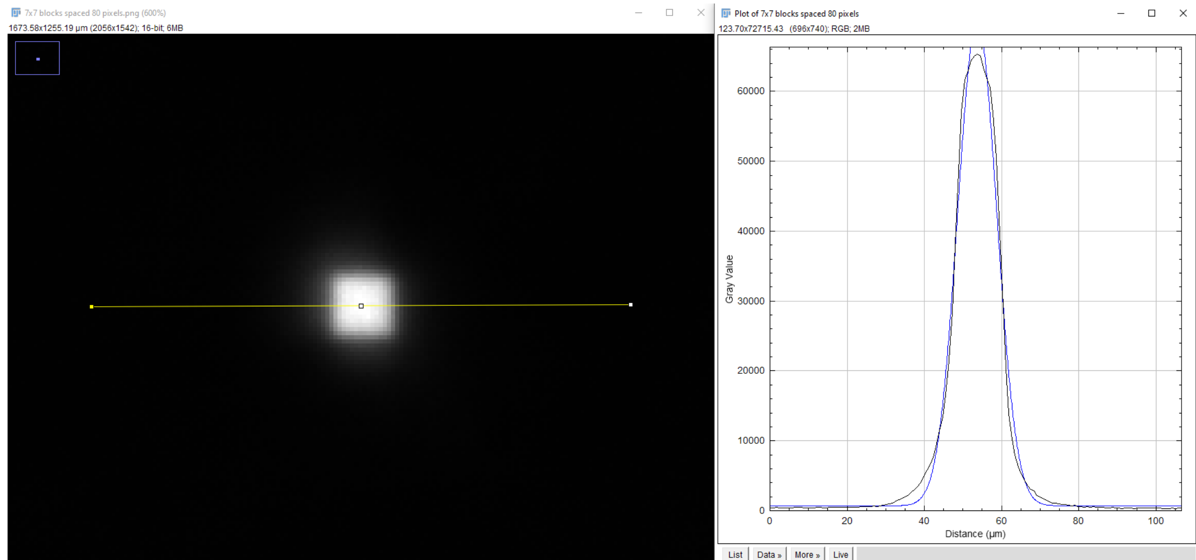

Figure C.6: A view of Fiji were we measured the PSF of a single 7 by 7 pixel DMD square projection on the chip. The left screen shows the image of the DMD spot. The yellow line determines the cross-section at which the PSF on the right side is measured. A Gaussian fit is put on the PSF, shown as the blue line.

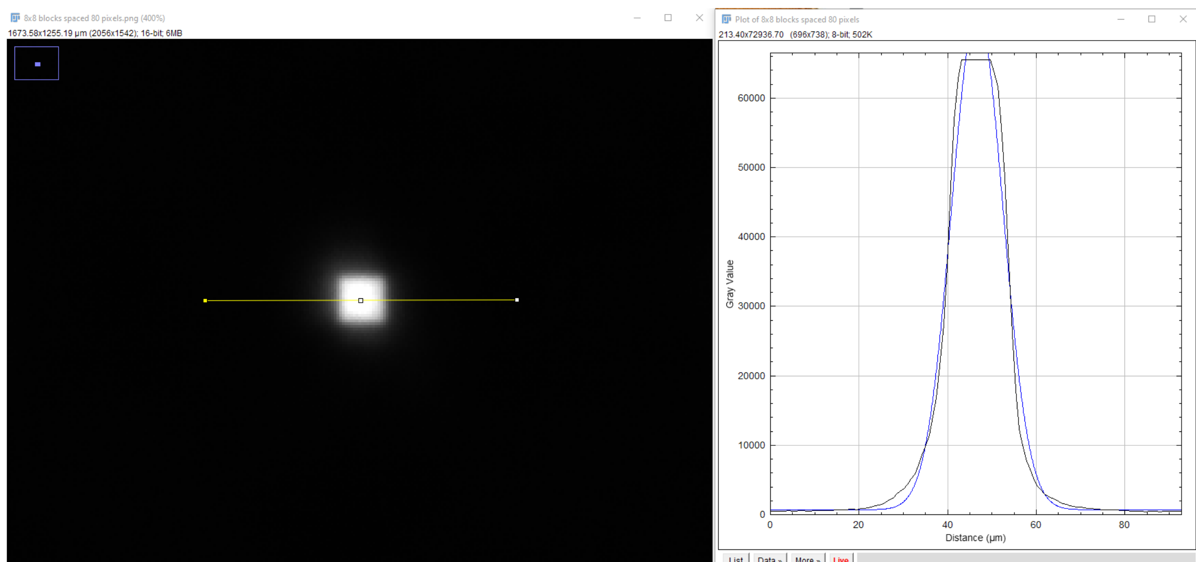

Figure C.7: A view of Fiji were we measured the PSF of a single 8 by 8 pixel DMD square projection on the chip. The left screen shows the image of the DMD spot. The yellow line determines the cross-section at which the PSF on the right side is measured. A Gaussian fit is put on the PSF, shown as the blue line.

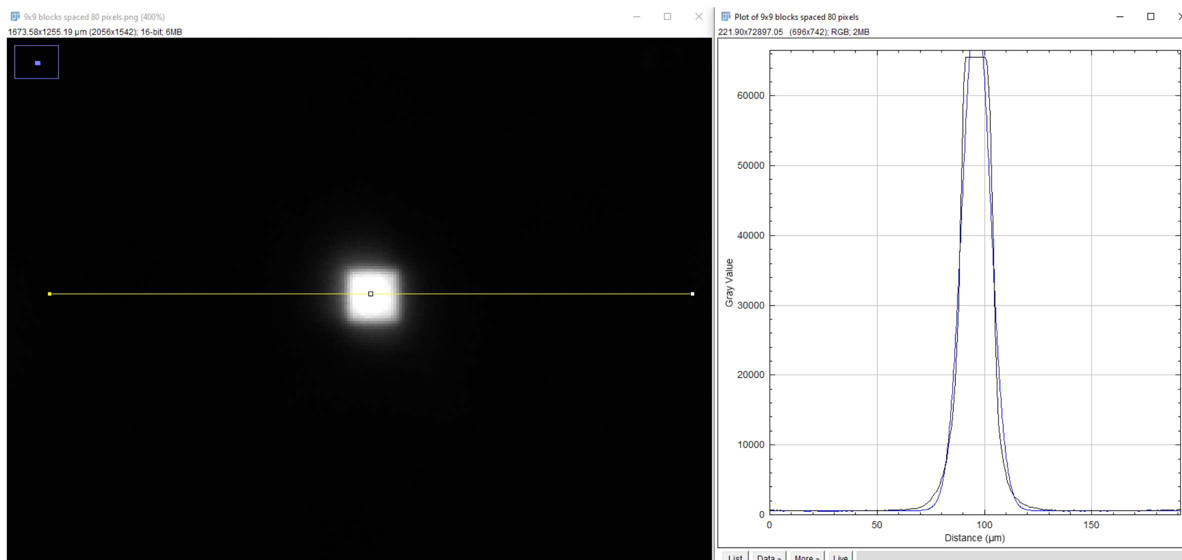

Figure C.8: A view of Fiji were we measured the PSF of a single 9 by 9 pixel DMD square projection on the chip. The left screen shows the image of the DMD spot. The yellow line determines the cross-section at which the PSF on the right side is measured. A Gaussian fit is put on the PSF, shown as the blue line.

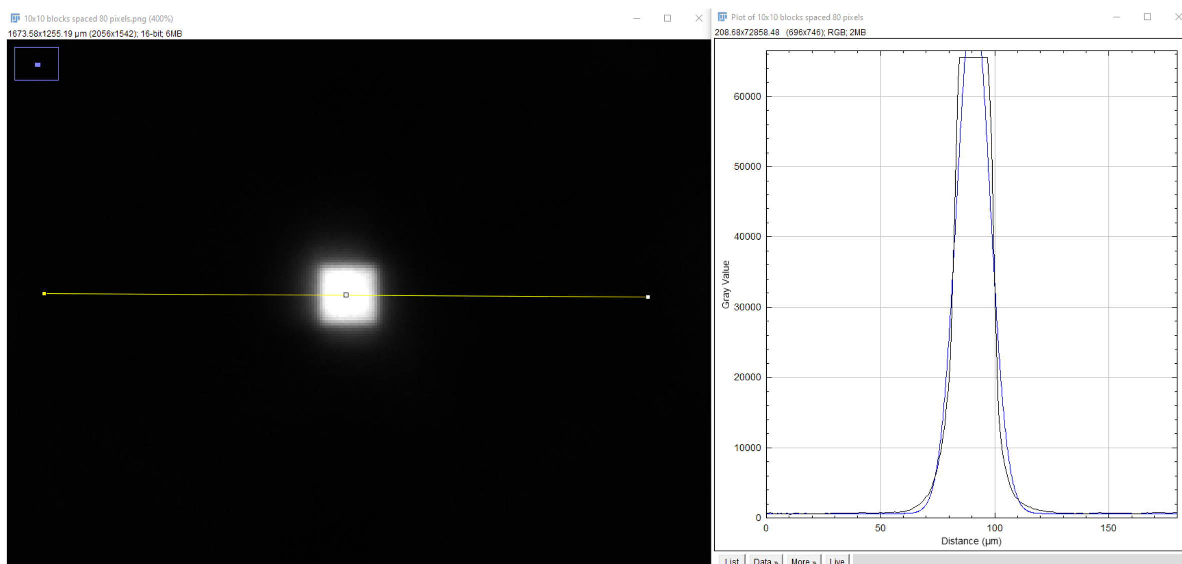

Figure C.9: A view of Fiji were we measured the PSF of a single 10 by 10 pixel DMD square projection on the chip. The left screen shows the image of the DMD spot. The yellow line determines the cross-section at which the PSF on the right side is measured. A Gaussian fit is put on the PSF, shown as the blue line.

C.4.2. Measurements on differently sized pixel grids

Grid of 1 by 1 Pixel Tiles			
Position in Grid	**Std. Gaussian Fit (µm)**	**FWHM (µm)**	**Max Intensity**
Upper left	1.75544 µm	4.13375 µm	3698
Upper right	1.65841 µm	3.90526 µm	2323
Lower right	1.18359 µm	2.78714 µm	3223
Lower left	1.69781 µm	3.99804 µm	3439
Left middle	1.72277 µm	4.05681 µm	3343
Upper middle	1.48888 µm	3.50604 µm	2163
Right middle	1.51763 µm	3.57375 µm	4469
Lower middle	1.49136 µm	3.51188 µm	5451
Center	1.51485 µm	3.56720 µm	6958

Table C.29: The standard deviation of a Gaussian fit on the PSF, its FWHM, and maximum intensity for different positions in a grid of 1 by 1 pixel tiles. Std. Gaussian Fit and FWHM are in micrometers (µm), while intensity is greyvalues. The light source used was a 455 nm LED.

Grid of 2 by 2 Pixel Tiles			
Position in Grid	**Std. Gaussian Fit (µm)**	**FWHM (µm)**	**Max Intensity**
Upper left	2.17093 µm	5.11215 µm	15055
Upper right	1.76168 µm	4.14844 µm	8164
Lower right	1.66720 µm	3.92596 µm	15113
Lower left	2.08512 µm	4.91008 µm	14421
Left middle	1.90986 µm	4.49738 µm	18440
Upper middle	1.83324 µm	4.31695 µm	15244
Right middle	1.79790 µm	4.23373 µm	17326
Lower middle	1.82672 µm	4.30160 µm	22317
Center	1.83311 µm	4.31664 µm	25249

Table C.30: The standard deviation of a Gaussian fit on the PSF, its FWHM, and maximum intensity for different positions in a grid of 2 by 2 pixel tiles. Std. Gaussian Fit and FWHM are in micrometers (µm), while intensity is greyvalues. The light source used was a 455 nm LED.

Grid of 3 by 3 Pixel Tiles			
Position in Grid	**Std. Gaussian Fit (μm)**	**FWHM (μm)**	**Max Intensity**
Upper left	2.62612 μm	6.18404 μm	25706
Upper right	2.34151 μm	5.51383 μm	13670
Lower right	2.38099 μm	5.60680 μm	21680
Lower left	2.58285 μm	6.08215 μm	24773
Left middle	2.44853 μm	5.76585 μm	30912
Upper middle	2.31901 μm	5.46085 μm	26075
Right middle	2.29901 μm	5.41375 μm	28905
Lower middle	2.38242 μm	5.61017 μm	36666
Center	2.45981 μm	5.79241 μm	38727

Table C.31: The standard deviation of a Gaussian fit on the PSF, its FWHM, and maximum intensity for different positions in a grid of 3 by 3 pixel tiles. Std. Gaussian Fit and FWHM are in micrometers (μm), while intensity is greyvalues. The light source used was a 455 nm LED.

Grid of 4 by 4 Pixel Tiles			
Position in Grid	**Std. Gaussian Fit (μm)**	**FWHM (μm)**	**Max Intensity**
Upper left	3.4083 μm	8.0259 μm	35537
Upper right	3.1173 μm	7.3407 μm	18369
Lower right	3.0979 μm	7.2949 μm	27280
Lower left	3.2256 μm	7.5956 μm	33509
Left middle	3.0675 μm	7.2234 μm	41412
Upper middle	2.9572 μm	6.9637 μm	34417
Right middle	2.9058 μm	6.8427 μm	35673
Lower middle	2.9635 μm	6.9784 μm	44600
Center	3.1413 μm	7.3971 μm	47477

Table C.32: The standard deviation of a Gaussian fit on the PSF, its FWHM, and maximum intensity for different positions in a grid of 4 by 4 pixel tiles. Std. Gaussian Fit and FWHM are in micrometers (μm), while intensity is greyvalues. The light source used was a 455 nm LED.

Grid of 5 by 5 Pixel Tiles			
Position in Grid	**Std. Gaussian Fit (μm)**	**FWHM (μm)**	**Max Intensity**
Upper left	4.036 μm	9.5040 μm	42430
Upper right	3.693 μm	8.6973 μm	20584
Lower right	3.895 μm	9.1720 μm	32970
Lower left	3.829 μm	9.0156 μm	40264
Left middle	3.697 μm	8.7068 μm	48532
Upper middle	3.650 μm	8.5961 μm	40807
Right middle	3.470 μm	8.1711 μm	41414
Lower middle	3.647 μm	8.5891 μm	53090
Center	3.737 μm	8.8003 μm	54506

Table C.33: The standard deviation of a Gaussian fit on the PSF, its FWHM, and maximum intensity for different positions in a grid of 5 by 5 pixel tiles. Std. Gaussian Fit and FWHM are in micrometers (μm), while intensity is greyvalues. The light source used was a 455 nm LED.

Grid of 6 by 6 Pixel Tiles			
Position in Grid	**Std. Gaussian Fit (μm)**	**FWHM (μm)**	**Max Intensity**
Upper left	4.670 μm	10.997 μm	50336
Upper right	4.468 μm	10.521 μm	22728
Lower right	4.552 μm	10.718 μm	37014
Lower left	4.648 μm	10.945 μm	45551
Left middle	4.608 μm	10.851 μm	54840
Upper middle	4.424 μm	10.417 μm	46303
Right middle	4.132 μm	9.730 μm	46506
Lower middle	4.292 μm	10.108 μm	58986
Center	4.405 μm	10.372 μm	60561

Table C.34: The standard deviation of a Gaussian fit on the PSF, its FWHM, and maximum intensity for different positions in a grid of 6 by 6 pixel tiles. Std. Gaussian Fit and FWHM are in micrometers (μm), while intensity is greyvalues. The light source used was a 455 nm LED.

Grid of 7 by 7 Pixel Tiles			
Position in Grid	**Std. Gaussian Fit (μm)**	**FWHM (μm)**	**Max Intensity**
Upper left	5.474 μm	12.890 μm	56156
Upper right	5.085 μm	11.975 μm	25859
Lower right	5.261 μm	12.389 μm	41049
Lower left	5.455 μm	12.846 μm	51379
Left middle	5.311 μm	12.506 μm	60607
Upper middle	5.103 μm	12.018 μm	50364
Right middle	4.706 μm	11.081 μm	50687
Lower middle	4.949 μm	11.654 μm	64558
Center	5.063 μm	11.922 μm	65535

Table C.35: The standard deviation of a Gaussian fit on the PSF, its FWHM, and maximum intensity for different positions in a grid of 7 by 7 pixel tiles. Std. Gaussian Fit and FWHM are in micrometers (μm), while intensity is greyvalues. The light source used was a 455 nm LED.

Grid of 8 by 8 Pixel Tiles			
Position in Grid	**Std. Gaussian Fit (μm)**	**FWHM (μm)**	**Max Intensity**
Upper left	6.159 μm	14.504 μm	60041
Upper right	5.868 μm	13.818 μm	27449
Lower right	5.919 μm	13.939 μm	43797
Lower left	5.964 μm	14.044 μm	56566
Left middle	6.046 μm	14.238 μm	64706
Upper middle	5.692 μm	13.403 μm	55375
Right middle	5.293 μm	12.463 μm	53747
Lower middle	5.664 μm	13.338 μm	65535
Center	5.780 μm	13.611 μm	65535

Table C.36: The standard deviation of a Gaussian fit on the PSF, its FWHM, and maximum intensity for different positions in a grid of 8 by 8 pixel tiles. Std. Gaussian Fit and FWHM are in micrometers (μm), while intensity is greyvalues. The light source used was a 455 nm LED.

Grid of 9 by 9 Pixel Tiles			
Position in Grid	**Std. Gaussian Fit (μm)**	**FWHM (μm)**	**Max Intensity**
Upper left	6.851 μm	16.132 μm	65535
Upper right	6.407 μm	15.088 μm	29441
Lower right	6.504 μm	15.316 μm	47678
Lower left	6.446 μm	15.179 μm	59114
Left middle	6.839 μm	16.104 μm	65535
Upper middle	6.342 μm	14.933 μm	58049
Right middle	5.940 μm	13.988 μm	55973
Lower middle	6.477 μm	15.253 μm	65535
Center	6.544 μm	15.410 μm	65535

Table C.37: The standard deviation of a Gaussian fit on the PSF, its FWHM, and maximum intensity for different positions in a grid of 9 by 9 pixel tiles. Std. Gaussian Fit and FWHM are in micrometers (μm), while intensity is greyvalues. The light source used was a 455 nm LED.

Grid of 10 by 10 Pixel Tiles			
Position in Grid	**Std. Gaussian Fit (μm)**	**FWHM (μm)**	**Max Intensity**
Upper left	7.623 μm	17.950 μm	65535
Upper right	7.027 μm	16.547 μm	31281
Lower right	7.139 μm	16.810 μm	50637
Lower left	7.184 μm	16.916 μm	63053
Left middle	7.697 μm	18.125 μm	65535
Upper middle	7.000 μm	16.483 μm	60263
Right middle	6.550 μm	15.424 μm	58300
Lower middle	7.132 μm	16.794 μm	65535
Center	7.300 μm	17.191 μm	65535

Table C.38: The standard deviation of a Gaussian fit on the PSF, its FWHM, and maximum intensity for different positions in a grid of 10 by 10 pixel tiles. Std. Gaussian Fit and FWHM are in micrometers (μm), while intensity is greyvalues. The light source used was a 455 nm LED.

Increase of ρ with Grid Size				
Grid Size	ρ (µm)	Std. ρ (µm)	ρ Increase (µm)	Std. ρ Increase (µm)
Grid 1x1	3.671 µm	0.415 µm	-	-
Grid 2x2	4.418 µm	0.373 µm	0.747 µm	0.105 µm
Grid 3x3	5.714 µm	0.270 µm	1.296 µm	0.125 µm
Grid 4x4	7.296 µm	0.363 µm	1.581 µm	0.109 µm
Grid 5x5	8.806 µm	0.384 µm	1.510 µm	0.100 µm
Grid 6x6	10.518 µm	0.416 µm	1.712 µm	0.101 µm
Grid 7x7	12.142 µm	0.581 µm	1.625 µm	0.101 µm
Grid 8x8	13.707 µm	0.600 µm	1.564 µm	0.101 µm
Grid 9x9	15.267 µm	0.638 µm	1.560 µm	0.094 µm
Grid 10x10	16.916 µm	0.805 µm	1.649 µm	0.104 µm

Table C.39: Increase of the spatial resolution with increase square sizes in the projected grid. The light source used was a 455 nm LED.

Increase of Maximum Intensity with Grid Size				
Grid Size	**Mean Max Intensity**	**Std. Max Intensity**	**Max Int. Increase**	**Std. Max Int. Increase**
Grid 1x1	3896	1525	-	-
Grid 2x2	16814	4916	12918	6311
Grid 3x3	27457	7595	10643	4284
Grid 4x4	35364	8855	7907	2950
Grid 5x5	41622	10404	6258	2214
Grid 6x6	46981	11682	5359	1889
Grid 7x7	51799	12450	4819	1666
Grid 8x8	54750	12398	2951	974
Grid 9x9	56933	11960	2183	674
Grid 10x10	58408	11316	1475	422

Table C.40: Increase of maximum intensity as a function of grid size. All values are measured in grey value.

C.4.3. Intensity map

X ↓ Y →	1	2	3	4	5	6	7	8	9
1	55754	64753	44799	65535	61232	64949	65535	65145	48907
2	36976	35411	58497	54584	57323	51454	55562	65344	55171
3	52625	51060	41083	65535	48125	35018	53799	65535	53799
4	55168	55168	58298	43822	61428	42061	65341	65145	65535
5	44019	58497	65149	57323	60453	65535	27781	65535	52628
6	41867	65344	65535	38541	61627	60258	65344	53997	55953
7	50668	60449	64753	29736	65535	49690	64949	60058	63384
8	50532	57366	45137	55747	55567	43339	49813	45677	60423
9	54421	46434	39191	47549	61479	50706	45691	61851	61479
10	23049	49658	28858	47784	54342	52656	62400	38602	48908
11	45947	24918	57964	50365	44003	59378	47891	41353	48421
12	25401	32703	47150	53183	50325	35878	49531	30481	39689

Table C.41: Intensity values of the pixel center positions of a grid of 7 by 7 pixel squares. The X an Y positions denote the position of the grid pixels. The intensities are given in grey values.

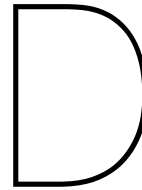

Results: Dielectric particle

D.1. MATLAB code to calculate the DEP motion

```
1
2 % Clean up the workspace
3     close all; clear all; clc;
4
5 % Load in the measurement data from Fiji.
6     % Column 1 contains the data number. For example, the data for the
    beads
7     % contains 4 data numbers. A set of data for each bead.
8     % Column 3 contains the measured X position
9     % Column 4 contains the measured Y position
10
11    data_gear_NaN = readmatrix("Tracking gear 15s 19kHz quadruple 10 fps.
    csv");
12    data_beads_NaN = readmatrix("Tracking beads 15s 19kHz quadruple 10 fps
    .csv");
13    data_pattern_NaN = readmatrix("Tracking pattern 15s 19kHz quadruple 10
     fps.csv");
14
15 % Set up the system parameters to provide the correct plots and data
16
17    % coordinates(d) returns the DMD pattern sizes that correspond to the
18    % thickness used. In this case, because the filename has the word
19    % "quadruple" in it, we know that the used pattern thickness is 4
    times 30
20    % pixels. Therefore, the thickness d input is 4.
21    coord = coordinates(4);
22
23    % The fps should correspond to the fps used in the name of the data
24    % files. The title_name is used for the plots and should correspond to
25    % the data file names.
26    fps = 10;
27    title_name = "T = 7s, f = 19kHz, d = 4d, fr = 10fps";
28
29    % Before we can calculate the fit on the pattern motion, we need to
30    % give an estimate on which frame the pattern has its peak and delay.
31    % This can be done by looking at the data itself. The code will
32    % find an optimal around the given estimates.
33    tpeak = 69;
```

```
34      delay = 8;
35
36      % These are some predefined values to calculate the correct distances
37      % and forces
38      robotdia = 254.775; % This is the diameter of the robot in µm
39      umpix = 0.814; % This is the measured conversion from camera pixel to
        µm
40      dt = 1/fps; % This is the time between each frame
41
42      % Ag and Bg give the force on the gear using the acceleration and
        velocity of the gear
43      % F = Ag*a_gear+Bg*v_gear
44      Ag = 6.588*1e-10;
45      Bg = 1.885*1e-6;
46
47      % C gives the force on the gear using a conversion factor. F = C*
        v_gear
48      C = 3.88*1e-7;
49
50      % Ab and Bb give the force on the beads using the acceleration and
        velocity of the bead
51      % F = Ag*a_bead+Bg*v_bead
52      Ab = 1.856e-12;
53      Bb = 1.414e-7;
54
55  % Clean up the data and show the number of frames for one measurement
56
57      data_gear = datacleanup(data_gear_NaN);
58      data_beads = datacleanup(data_beads_NaN);
59      data_pattern = datacleanup_pattern(data_pattern_NaN);
60      disp(["Length of data = ",length(data_pattern(:,3,1))])
61
62      % Find the fitted x position of the pattern. The steps define how many
63      % neighboring point will be search. The percent determines how big the
64      % search area is around the given tpeak and delay.
65      steps = 300;
66      percent = 45;
67      [x_fitted_opt, opt, tpeak_opt,a1] = optimizepatternfit(tpeak,delay,
        steps,percent,data_pattern,coord,title_name);
68
69      % Separate the data for each point in the gear, for each bead and for
        the
70      % pattern.
71      data1 = data_gear(:,:,1);
72      data2 = data_gear(:,:,2);
73      data3 = data_gear(:,:,3);
74      data4 = data_gear(:,:,4);
75
76      bead1 = data_beads(:,:,1);
77      bead2 = data_beads(:,:,2);
78      bead3 = data_beads(:,:,3);
79      bead4 = data_beads(:,:,4);
80      datax_pix = [bead1(:,3),bead2(:,3),bead3(:,3),bead4(:,3)];
81      datay_pix = [bead1(:,4),bead2(:,4),bead3(:,4),bead4(:,4)];
82
83      datapattern = x_fitted_opt;
```

```
84
85      % Rewrite the data to µm
86      data1um = data1*umpix;
87      data2um = data2*umpix;
88      data3um = data3*umpix;
89      data4um = data4*umpix;
90
91      datax = umpix*datax_pix;
92      datay = umpix*datay_pix;
93
94  % Create the resulting analysis
95      results_table = plot_avg_center_velocity_acceleration(data1um, data2um
    , data3um, data4um, dt, title_name);
96      force_table_motion = compute_force_from_motion(results_table, Ag, Bg,
    title_name);
97      force_table_velocity = compute_force_with_velocity(results_table, C,
    title_name);
98      compare_force_methods(force_table_motion, force_table_velocity,
    title_name);
99      [max_force_motion, max_force_velocity] = find_max_force(
    force_table_motion, force_table_velocity);
100     analyze_bead_motion(datax, datay, dt, Ab, Bb, title_name);
101
102 %%% FUNCTIONS %%%
103
104 % This function cleans up the data from the gear and the beads
105 function dataclean = datacleanup(data)
106
107     % Find the different measurement numbers, e.g. the data from bead 3
108     meas = unique(data(:,1));
109     num_meas = numel(meas); % Outputs the amount of data, in our case
    always 4
110
111     % Create struct to save data temporary
112     dataPerMeas = cell(num_meas, 1);
113
114     % Delete double time steps if this mistake is occuring in the data
115     for i = 1:num_meas
116         idx = data(:,1) == meas(i);  % Find the data with measurement
    number
117         temp = data(idx, :);  % Use the data with this number
118
119         % Sort time steps of measurements
120         temp = sortrows(temp, 2);
121
122         % Delete double time steps and save last
123         [~, uniqueIdx] = unique(temp(:,2), 'last');
124         temp = temp(uniqueIdx, :);
125
126         % Save in temporary cell
127         dataPerMeas{i} = temp;
128     end
129
130     % Determine shortest measurement length
131     shortest_length = min(cellfun(@(x) size(x,1), dataPerMeas));
132
```

```
133     % Create new 3D matrix to seperate the data with all the same length
134     dataclean = NaN(shortest_length, size(data,2), num_meas);
135 
136     % Seperate the data and interpolate the NaNs
137     for i = 1:num_meas
138         temp = dataPerMeas{i};
139         temp = temp(1:shortest_length, :);
140 
141         % Clean up bad data. When a measurement could not be done in Fiji,
142         % a corner is selected of the frame. So when the Y-value is close
143         % to the upper or lower border, the values need to be replaced by
144         % NaNs for they are faulty data.
145         idx = (temp(:,4) < 15) | (temp(:,4) > 1400);
146         temp(idx,3) = NaN;
147         temp(idx,4) = NaN;
148 
149         % Fill in NaNs for X and Y data
150         temp(:,3) = fillmissing(temp(:,3), 'linear'); % Interpolate
151         temp(:,3) = fillmissing(temp(:,3), 'nearest'); % Fill in
    boundaries if NaN
152 
153         temp(:,4) = fillmissing(temp(:,4), 'linear');
154         temp(:,4) = fillmissing(temp(:,4), 'nearest');
155 
156         % remove negative values and cap them at zero.
157         idx = (temp(:,3) < 0);
158         temp(idx,3) = 0;
159 
160         % save the cleaned data
161         dataclean(:,:,i) = temp;
162     end
163 end
164 
165 % This function cleans up the data from the pattern
166 function dataclean = datacleanup_pattern(data_pattern_NaN)
167     data = data_pattern_NaN;
168     % Find measurements numbers
169     meas = unique(data(:,1));
170     num_meas = numel(meas);
171 
172     % Create struct to save data temporary
173     dataPerMeas = cell(num_meas, 1);
174 
175     % Delete double time steps
176     for i = 1:num_meas
177         idx = data(:,1) == meas(i);  % Find the data with measurement
    number
178         temp = data(idx, :);  % The data with this number
179 
180         % Sort time step of measurements
181         temp = sortrows(temp, 2);
182 
183         % Delete double steps and save last
184         [~, uniqueIdx] = unique(temp(:,2), 'last');
185         temp = temp(uniqueIdx, :);
186 
```

```
187         % Save in temporary cell
188         dataPerMeas{i} = temp;
189     end
190 
191     % Determine shortest measurement length
192     shortest_length = min(cellfun(@(x) size(x,1), dataPerMeas));
193 
194     % Create new 3D matrix to seperate the data with all the same length
195     dataclean = NaN(shortest_length, size(data,2), num_meas);
196 
197     % Seperate the data and interpolate the NaNs
198     for i = 1:num_meas
199         temp = dataPerMeas{i};
200         temp = temp(1:shortest_length, :);
201 
202         % Clean up bad data. When a measurement could not be done in Fiji,
203         % a corner is selected of the frame. So when the Y-value is close
204         % to the upper or lower border, the values need to be replaced by
205         % NaNs for they are faulty data.
206         idx = (temp(:,4) < 100) | (temp(:,4) > 1170);
207         temp(idx,3) = NaN;
208         temp(idx,4) = NaN;
209 
210         % remove negative values and cap them at zero.
211         idx = (temp(:,3) < 0);
212         temp(idx,3) = 0;
213 
214         % save the clean data
215         dataclean(:,:,i) = temp;
216     end
217 end
218 
219 % Return the pattern dimensions given the predefined relative thickness.
220 % The values are experimentally found.
221 function coord = coordinates(thickness)
222     if thickness == 1
223         border_thickness = 60.45;
224         left_thickness = 51.24;
225         left_pos = 51.57;
226         top_thickness = 56.04;
227         top_pos = 74.81;
228         right_thickness = 49.69;
229         right_pos = 1979.36;
230         bottom_thickness = 44.38;
231         bottom_pos = 1496.74;
232     elseif thickness == 2
233         border_thickness = 125.5596;
234         left_thickness = 125.3546;
235         left_pos = 126;
236         top_thickness = 126.381;
237         top_pos = 129.2857;
238         right_thickness = 126.8555;
239         right_pos = 1922.286;
240         bottom_thickness = 117.5713;
241         bottom_pos = 1421;
242     elseif thickness == 3
```

```
243             border_thickness = 189.571649;
244             left_thickness = 188.9260023;
245             left_pos = 195.5;
246             top_thickness = 188.2849202;
247             top_pos = 201.1905714;
248             right_thickness = 196.9759342;
249             right_pos = 1859.523857;
250             bottom_thickness = 188.5726627;
251             bottom_pos = 1358.571429;
252         elseif thickness == 4
253             border_thickness = 251.7142888;
254             left_thickness = 237.9505003;
255             left_pos = 237.9505003;
256             top_thickness = 240.500738;
257             top_pos = 240.500738;
258             right_thickness = 249.7143292;
259             right_pos = 2056-229.1788;
260             bottom_thickness = 249.4278307;
261             bottom_pos = 1542-249.4278307-9.976128622;
262         end
263         coord = [border_thickness; left_thickness;left_pos; top_thickness;
        top_pos; right_thickness;right_pos; bottom_thickness;bottom_pos];
264     end
265 
266     % This functions creates the fitted x positions of the projected pattern.
267     function [x_fitted,opt] = patternfit(coord,data_pattern,tpeak,delay)
268         % Set up the parameters
269         border_thickness = coord(1);
270         left_pos = coord(3);
271         right_thickness = coord(6);
272         right_pos = coord(7);
273 
274         x1 = left_pos; % The left border of the projection
275         x2 = left_pos+border_thickness; % The right side of the left border of
         the projection
276         x3 = right_pos-border_thickness; % The left side of the right border
        of the projection
277         x4 = right_pos; % The right border of the projection
278         z1 = (x2+x1)/2; % The center position of the left border
279         z2 = (x4+x3)/2; % The center position of the right border
280 
281         y1 = right_pos+right_thickness;
282         y2 = right_pos+right_thickness+border_thickness;
283         w1 = (y2+y1)/2;
284 
285         dataclean = data_pattern;
286 
287         % derive the average x position from the data by averaging the right
        and left side x positions of the pattern.
288         datamid = (dataclean(:,3,1)+dataclean(:,3,2))/2;
289 
290         % Creating the animation fit
291         b1 = z1; % Startposition of the sweep
292         a1 = (z2-z1)/(tpeak-delay); % The number of frames it takes to go from
         left to right
293         xp1 = delay:1:tpeak; % Used time steps for the animation from left to
```

```
    right
294     yp1 = (xp1-delay)*a1+b1; % The animation from left to right
295 
296     b2 = w1; % Startposition of the sweep from right to left
297     a2 = -a1;
298     xp2 = tpeak:1:length(dataclean);
299     yp2 = (xp2-tpeak)*a2+b2; % The animation from right to left
300     yp2(yp2<=b1) = b1; % ensure that the animation stops at b1
301 
302     zeropadlen = length(dataclean)-length(yp1)-length(yp2);
303     x_fitted = [ones(1,zeropadlen)*b1,yp1,yp2];
304 
305     nanloc = find(~isnan(datamid)); % Select the points in the fit where
    we have real data
306     opt = norm((x_fitted(nanloc)-datamid(nanloc)')); % Calculate the norm
    of the fit. The lower, the better the fit is
307 end
308 
309 % This functions searches for the optimal fitted x positions of the
    projected pattern.
310 function [x_fitted_opt, opt, tpeak_opt, a1] = optimizepatternfit(tpeak,
    delay, steps, percent, data_pattern, coord, title_name)
311     % Define search ranges
312     tpeakrange = linspace((100-percent)/100*tpeak, (100+percent)/100*tpeak
    , steps);
313     delayrange = linspace((100-percent)/100*delay, (100+percent)/100*delay
    , steps);
314 
315     % Set up the parameters
316     border_thickness = coord(1);
317     left_pos = coord(3);
318     right_pos = coord(7);
319 
320     % Calculate middle position of the sweep
321     datamid = (data_pattern(:,3,1) + data_pattern(:,3,2)) / 2;
322 
323     % Define pattern fit parameters
324     x1 = left_pos;
325     x2 = left_pos + border_thickness;
326     x3 = right_pos - border_thickness;
327     x4 = right_pos;
328     z1 = (x2 + x1) / 2; % Start position on the left
329     z2 = (x4 + x3) / 2; % Start position on the right
330     a1 = (z2 - z1) / (tpeak - delay); % The speed of the sweep
331 
332     % Initialize optimization matrix
333     opt = zeros(steps, steps);
334 
335     % Find the fit in the full search space
336     for i = 1:length(tpeakrange)
337         for j = 1:length(delayrange)
338             [~, opt(i, j)] = patternfit(coord, data_pattern, tpeakrange(i)
    , delayrange(j));
339         end
340     end
341 
```

```
342     % Find the optimal fit
343     [tpeakind, delayind] = find(opt == min(opt(:)));
344     tpeakopt = tpeakrange(tpeakind);
345     delayopt = delayrange(delayind);
346
347     % Save the optimal fit
348     [x_fitted, opt] = patternfit(coord, data_pattern, tpeakopt, delayopt);
349
350     % Display the optimal fit parameter
351     disp(["Optimal T_peak =", tpeakopt]);
352     disp(["Optimal delay =", delayopt]);
353     disp(["Optimal norm of error =", opt]);
354
355     % Plot results
356     figure;
357         hold on; grid on; box on;
358         set(gca, 'FontSize', 14, 'LineWidth', 1.5);
359
360         plot(datamid, 'LineWidth', 3, 'DisplayName', 'True data');
361         plot(x_fitted, ':', 'LineWidth', 1.5, 'DisplayName', 'Fitted
    pattern');
362
363         xlabel('Time step [frames]');
364         ylabel('X Position [pixels]');
365         title(['Optimized Linear Fit of Pattern position - ', title_name])
    ;
366         legend('Location', 'best');
367
368         hold off;
369
370     % Output optimized values
371     x_fitted_opt = x_fitted;
372     tpeak_opt = tpeakopt;
373 end
374
375 % Function to create a circle using three points and return the center
376 % position and radius. It makes use of the solution of the linear system
377 % and uses the determinant d.
378 function [xc, yc, r] = circumcircle(x, y)
379     % Calculate the denominator and ensure that it is not (almost) zero.
    If
380     % so, the points are overlapping and we cannot create a circle. The
381     % output is then NaN.
382     d = 2*( x(1)*(y(2)-y(3)) + x(2)*(y(3)-y(1)) + x(3)*(y(1)-y(2)) );
383     if abs(d) < 1e-10
384         xc = NaN; yc = NaN; r = NaN;
385         return;
386     end
387
388     % Calculate the center positions and radius using the determinant
389     xc = ((x(1)^2+y(1)^2)*(y(2)-y(3)) + (x(2)^2+y(2)^2)*(y(3)-y(1)) + (x
    (3)^2+y(3)^2)*(y(1)-y(2)))/d;
390     yc = ((x(1)^2+y(1)^2)*(x(3)-x(2)) + (x(2)^2+y(2)^2)*(x(1)-x(3)) + (x
    (3)^2+y(3)^2)*(x(2)-x(1)))/d;
391     r = sqrt((x(1)-xc)^2+(y(1)-yc)^2);
392 end
```

```
393
394 % This function creates a table with the position, velocity and
395 % acceleration of the microgear microbot and their standard deviations.
396 function results_table = plot_avg_center_velocity_acceleration(data1,
    data2, data3, data4, dt, title_name)
397     % Find the smallest array to make sure we work with arrays of the same
398     % length
399     num_steps = min([size(data1,1), size(data2,1), size(data3,1), size(
    data4,1)]);
400
401     % Compute the circumcenter for 4 different triangle combinations
402     centers_x = NaN(num_steps, 4);
403     centers_y = NaN(num_steps, 4);
404
405     for t = 1:num_steps
406         x1 = data1(t,3); y1 = data1(t,4);
407         x2 = data2(t,3); y2 = data2(t,4);
408         x3 = data3(t,3); y3 = data3(t,4);
409         x4 = data4(t,3); y4 = data4(t,4);
410
411         % Compute a circle for the 4 combinations of 3 points
412         [xc1, yc1, ~] = circumcircle([x1, x2, x3], [y1, y2, y3]);
413         [xc2, yc2, ~] = circumcircle([x2, x3, x4], [y2, y3, y4]);
414         [xc3, yc3, ~] = circumcircle([x3, x4, x1], [y3, y4, y1]);
415         [xc4, yc4, ~] = circumcircle([x4, x1, x2], [y4, y1, y2]);
416
417         centers_x(t,:) = [xc1, xc2, xc3, xc4];
418         centers_y(t,:) = [yc1, yc2, yc3, yc4];
419     end
420
421     % Compute mean and std of circle center position without regarding the
     NaN
422     % values
423     avg_center_x = nanmean(centers_x, 2);
424     avg_center_y = nanmean(centers_y, 2);
425     std_center_x = nanstd(centers_x, 0, 2);
426     std_center_y = nanstd(centers_y, 0, 2);
427
428     % Create a time vector
429     time = (0:num_steps-1)' * dt;
430
431     % Compute velocity in µm/s
432     vxi_all = diff(centers_x) / dt;
433     vyi_all = diff(centers_y) / dt;
434
435     % Compute mean and std of circle center velocity without regarding the
     NaN
436     % values
437     vx_avg = nanmean(vxi_all, 2);
438     vx_std = nanstd(vxi_all, 0, 2);
439     vy_avg = nanmean(vyi_all, 2);
440     vy_std = nanstd(vyi_all, 0, 2);
441
442     % Calculate the total velocity of the center point
443     vtotal_all = sqrt(vxi_all.^2 + vyi_all.^2);
444     vtotal_avg = nanmean(vtotal_all, 2);
```

```
445     vtotal_std = nanstd(vtotal_all, 0, 2);
446
447     % reduce the time vector to be the same length as the velocity vector
448     time_v = time(2:end);
449
450     % Compute acceleration in µm/s^2
451     axi_all = diff(vxi_all) / dt;
452     ayi_all = diff(vyi_all) / dt;
453
454     % Compute mean and std of circle center acceleration without regarding
         the NaN
455     % values
456     ax_avg = nanmean(axi_all, 2);
457     ax_std = nanstd(axi_all, 0, 2);
458     ay_avg = nanmean(ayi_all, 2);
459     ay_std = nanstd(ayi_all, 0, 2);
460
461     % Calculate the total acceleration of the center point
462     atotal_all = sqrt(axi_all.^2 + ayi_all.^2);
463     atotal_avg = nanmean(atotal_all, 2);
464     atotal_std = nanstd(atotal_all, 0, 2);
465
466     % reduce the time vector to be the same length as the acceleration
        vector
467     time_a = time_v(2:end);
468
469     % Create Figure plotting the positions, the velocities and the
470     % accelerations
471     figure;
472
473         % Plot 1: Position
474         subplot(3,1,1);
475         hold on; grid on; box on;
476         set(gca, 'FontSize', 14, 'LineWidth', 1.5);
477
478         patch([time; flipud(time)], [avg_center_x - std_center_x; flipud(
        avg_center_x + std_center_x)], [1 0.7 0.7], 'EdgeColor','none','
        FaceAlpha',0.3);
479         h_avg_x = plot(time, avg_center_x, 'r-', 'LineWidth', 2);
480
481         patch([time; flipud(time)], [avg_center_y - std_center_y; flipud(
        avg_center_y + std_center_y)], [0.7 0.7 1], 'EdgeColor','none','
        FaceAlpha',0.3);
482         h_avg_y = plot(time, avg_center_y, 'b-', 'LineWidth', 2);
483
484         xlabel('Time (s)');
485         ylabel('Position (\mum)');
486         title(['Average Microbot Center Position - ', title_name]);
487         legend([h_avg_x, h_avg_y], {'X Position','Y Position'}, 'Location'
        ,'best');
488
489         % Plot 2: Velocity
490         subplot(3,1,2);
491         hold on; grid on; box on;
492         set(gca, 'FontSize', 14, 'LineWidth', 1.5);
493
```

```
494         patch([time_v; flipud(time_v)], [vx_avg - vx_std; flipud(vx_avg +
        vx_std)], [1 0.7 0.7], 'EdgeColor','none','FaceAlpha',0.3);
495         h_vx = plot(time_v, vx_avg, 'r-', 'LineWidth', 2);
496
497         patch([time_v; flipud(time_v)], [vy_avg - vy_std; flipud(vy_avg +
        vy_std)], [0.7 0.7 1], 'EdgeColor','none','FaceAlpha',0.3);
498         h_vy = plot(time_v, vy_avg, 'b-', 'LineWidth', 2);
499
500         patch([time_v; flipud(time_v)], [vtotal_avg - vtotal_std; flipud(
        vtotal_avg + vtotal_std)], [0.5 0.5 0.5], 'EdgeColor','none','FaceAlpha
        ',0.3);
501         h_vtotal = plot(time_v, vtotal_avg, 'k-', 'LineWidth', 2);
502
503         xlabel('Time (s)');
504         ylabel('Velocity (\mum/s)');
505         title(['Average Microbot Velocity - ', title_name]);
506         legend([h_vx, h_vy, h_vtotal], {'v_x','v_y','v_{total}'}, '
        Location','best');
507
508         % Plot 3: Acceleration
509         subplot(3,1,3);
510         hold on; grid on; box on;
511         set(gca, 'FontSize', 14, 'LineWidth', 1.5);
512
513         patch([time_a; flipud(time_a)], [ax_avg - ax_std; flipud(ax_avg +
        ax_std)], [1 0.7 0.7], 'EdgeColor','none','FaceAlpha',0.3);
514         h_ax = plot(time_a, ax_avg, 'r-', 'LineWidth', 2);
515
516         patch([time_a; flipud(time_a)], [ay_avg - ay_std; flipud(ay_avg +
        ay_std)], [0.7 0.7 1], 'EdgeColor','none','FaceAlpha',0.3);
517         h_ay = plot(time_a, ay_avg, 'b-', 'LineWidth', 2);
518
519         patch([time_a; flipud(time_a)], [atotal_avg - atotal_std; flipud(
        atotal_avg + atotal_std)], [0.5 0.5 0.5], 'EdgeColor','none','FaceAlpha
        ',0.3);
520         h_atotal = plot(time_a, atotal_avg, 'k-', 'LineWidth', 2);
521
522         xlabel('Time (s)');
523         ylabel('Acceleration (\mum/s^2)');
524         title(['Average Microbot Acceleration - ', title_name]);
525         legend([h_ax, h_ay, h_atotal], {'a_x','a_y','a_{total}'}, '
        Location','best');
526
527     % Create Results Table containing all derived information
528     results_table = table(time, avg_center_x, std_center_x, avg_center_y,
        std_center_y, ...
529                            [NaN; vx_avg], [NaN; vx_std], [NaN; vy_avg], [
        NaN; vy_std], [NaN; vtotal_avg], [NaN; vtotal_std], ...
530                            [NaN; NaN; ax_avg], [NaN; NaN; ax_std], [NaN;
        NaN; ay_avg], [NaN; NaN; ay_std], [NaN; NaN; atotal_avg], [NaN; NaN;
        atotal_std], ...
531                            'VariableNames', {'Time', 'X_Pos', 'X_Std', '
        Y_Pos', 'Y_Std', ...
532                                                 'Vx', 'Vx_Std', 'Vy', 'Vy_Std'
        , 'Vtotal', 'Vtotal_Std', ...
533                                                 'Ax', 'Ax_Std', 'Ay', 'Ay_Std'
```

```
    , 'Atotal', 'Atotal_Std'});
534 end
535
536 % This function calculates the force on the microbot using the EoM used
537 % from Stokes's law.
538 function force_table = compute_force_from_motion(data_table, A, B,
    title_name)
539     % Convert acceleration and velocity from µm/s² and µm/s to m/s² and m/
    s
540     um_to_m = 1e-6;
541
542     ax_m = data_table.Ax * um_to_m;
543     ax_std_m = data_table.Ax_Std * um_to_m;
544     ay_m = data_table.Ay * um_to_m;
545     ay_std_m = data_table.Ay_Std * um_to_m;
546
547     vx_m = data_table.Vx * um_to_m;
548     vx_std_m = data_table.Vx_Std * um_to_m;
549     vy_m = data_table.Vy * um_to_m;
550     vy_std_m = data_table.Vy_Std * um_to_m;
551
552     vtotal_m = data_table.Vtotal * um_to_m;
553     vtotal_std_m = data_table.Vtotal_Std * um_to_m;
554
555     atotal_m = data_table.Atotal * um_to_m;
556     atotal_std_m = data_table.Atotal_Std * um_to_m;
557
558     % Compute forces (in Newtons)
559     Fx_N = A * ax_m + B * vx_m;
560     Fx_std_N = sqrt((A * ax_std_m).^2 + (B * vx_std_m).^2);
561
562     Fy_N = A * ay_m + B * vy_m;
563     Fy_std_N = sqrt((A * ay_std_m).^2 + (B * vy_std_m).^2);
564
565     Ftotal_N = A * atotal_m + B * vtotal_m;
566     Ftotal_std_N = sqrt((A * atotal_std_m).^2 + (B * vtotal_std_m).^2);
567
568     % Convert forces to pN
569     N_to_pN = 1e12;
570     Fx_pN = Fx_N * N_to_pN;
571     Fx_std_pN = Fx_std_N * N_to_pN;
572
573     Fy_pN = Fy_N * N_to_pN;
574     Fy_std_pN = Fy_std_N * N_to_pN;
575
576     Ftotal_pN = Ftotal_N * N_to_pN;
577     Ftotal_std_pN = Ftotal_std_N * N_to_pN;
578
579     % Create output table
580     force_table = table(data_table.Time, Fx_pN, Fx_std_pN, Fy_pN,
    Fy_std_pN, Ftotal_pN, Ftotal_std_pN, ...
581                          'VariableNames', {'Time', 'Fx_pN', 'Fx_Std_pN', '
    Fy_pN', 'Fy_Std_pN', 'Ftotal_pN', 'Ftotal_Std_pN'});
582
583     % Plot results
584     figure;
```

```
585         hold on; grid on; box on;
586         set(gca, 'FontSize', 14, 'LineWidth', 1.5);
587 
588         time_f = data_table.Time;
589 
590         % Plot F_x met error bars
591         h_fx = errorbar(time_f, Fx_pN, Fx_std_pN, 'r-', 'LineWidth', 2, '
    CapSize', 5);
592 
593         % Plot F_y met error bars
594         h_fy = errorbar(time_f, Fy_pN, Fy_std_pN, 'b-', 'LineWidth', 2, '
    CapSize', 5);
595 
596         % Plot F_total met error bars
597         h_ftotal = errorbar(time_f, Ftotal_pN, Ftotal_std_pN, 'k-', '
    LineWidth', 2, 'CapSize', 5);
598 
599         xlabel('Time (s)');
600         ylabel('Force (pN)');
601         title(['Computed DEP force on microbots using the EoM - ',
    title_name]); % Gebruik datasetnaam in titel
602         legend([h_fx, h_fy, h_ftotal], {'F_x','F_y','F_{total}'}, '
    Location','best');
603 
604         hold off;
605 end
606 
607 % This function calculates the force on the microbot using the EoM used
608 % from the conversion rate from the paper from Zhang et al. 2019 on the
    microbots.
609 function force_table = compute_force_with_velocity(data_table, C,
    title_name)
610     % Convert velocity from µm/s to m/s
611     um_to_m = 1e-6;
612 
613     vx_m = data_table.Vx * um_to_m;
614     vx_std_m = data_table.Vx_Std * um_to_m;
615     vy_m = data_table.Vy * um_to_m;
616     vy_std_m = data_table.Vy_Std * um_to_m;
617     vtotal_m = data_table.Vtotal * um_to_m;
618     vtotal_std_m = data_table.Vtotal_Std * um_to_m;
619 
620     % Compute forces (in Newtons)
621     Fx_N = C * vx_m;
622     Fx_std_N = abs(C * vx_std_m);
623 
624     Fy_N = C * vy_m;
625     Fy_std_N = abs(C * vy_std_m);
626 
627     Ftotal_N = C * vtotal_m;
628     Ftotal_std_N = abs(C * vtotal_std_m);
629 
630     % Convert forces to pN
631     N_to_pN = 1e12;
632     Fx_pN = Fx_N * N_to_pN;
633     Fx_std_pN = Fx_std_N * N_to_pN;
```

```
634
635     Fy_pN = Fy_N * N_to_pN;
636     Fy_std_pN = Fy_std_N * N_to_pN;
637
638     Ftotal_pN = Ftotal_N * N_to_pN;
639     Ftotal_std_pN = Ftotal_std_N * N_to_pN;
640
641     % Create output table
642     force_table = table(data_table.Time, Fx_pN, Fx_std_pN, Fy_pN,
        Fy_std_pN, Ftotal_pN, Ftotal_std_pN, ...
643                          'VariableNames', {'Time', 'Fx_pN', 'Fx_Std_pN', '
        Fy_pN', 'Fy_Std_pN', 'Ftotal_pN', 'Ftotal_Std_pN'});
644
645     % Plot results
646     figure('Visible','off');
647         hold on; grid on; box on;
648         set(gca, 'FontSize', 14, 'LineWidth', 1.5);
649
650         time_f = data_table.Time;
651
652         % Plot F_x met error bars
653         h_fx = errorbar(time_f, Fx_pN, Fx_std_pN, 'r-', 'LineWidth', 2, '
        CapSize', 5);
654
655         % Plot F_y met error bars
656         h_fy = errorbar(time_f, Fy_pN, Fy_std_pN, 'b-', 'LineWidth', 2, '
        CapSize', 5);
657
658         % Plot F_total met error bars
659         h_ftotal = errorbar(time_f, Ftotal_pN, Ftotal_std_pN, 'k-', '
        LineWidth', 2, 'CapSize', 5);
660
661         xlabel('Time (s)');
662         ylabel('Force (pN)');
663         title(['Computed DEP forces on microbot using conversion factor -
        ', title_name]); % Gebruik datasetnaam in titel
664         legend([h_fx, h_fy, h_ftotal], {'F_x','F_y','F_{total}'}, '
        Location','best');
665
666         hold off;
667 end
668
669 % This function creates a figure showing the differnce between the force
        on
670 % the microbot calculated using Stokes's law and the conversion from Zhang
671 % et al.
672 function compare_force_methods(force_table_motion, force_table_velocity,
        title_name)
673     % Extract data
674     time = force_table_motion.Time;
675
676     % Force computed from Stokes's law (F = A*a + B*V)
677     Fmotion_pN = force_table_motion.Ftotal_pN;
678     Fmotion_std_pN = force_table_motion.Ftotal_Std_pN;
679
680     % Force computed from conversion from literature (F = C*V)
```

```
681     Fvelocity_pN = force_table_velocity.Ftotal_pN;
682     Fvelocity_std_pN = force_table_velocity.Ftotal_Std_pN;
683 
684     % Compute percentage difference (relative to Fmotion)
685     Fdiff_pN = Fmotion_pN - Fvelocity_pN;
686 
687     percentage_diff = (Fdiff_pN ./ abs(Fmotion_pN)) * 100; % Difference in
        %
688 
689     % Create margins in the plot on the y-axis for visibility
690     margin = 0.2 * (max(percentage_diff) - min(percentage_diff)); % 20%
       margin
691     ymin = min(percentage_diff) - margin;
692     ymax = max(percentage_diff) + margin;
693 
694     % Create figure with dual y-axis
695     figure;
696     hold on; grid on; box on;
697     set(gca, 'FontSize', 14, 'LineWidth', 1.5);
698 
699     % Create first y-axis denoting the DEP force
700     yyaxis left;
701     ylabel('Force (pN)');
702 
703     % Plot F from motion with whiskers
704     h_fmotion = errorbar(time, Fmotion_pN, Fmotion_std_pN, 'r-', '
       LineWidth', 2, 'CapSize', 5);
705 
706     % Plot F from velocity with whiskers
707     h_fvelocity = errorbar(time, Fvelocity_pN, Fvelocity_std_pN, 'b-', '
       LineWidth', 2, 'CapSize', 5);
708 
709     % Create second y-axis showing the percentage difference with zoomed
       scale
710     yyaxis right;
711     ylabel('Difference (%)');
712     ylim([ymin, ymax]);
713 
714     % Get color of right y-axis
715     right_color = get(gca, 'YColor');
716 
717     % Plot percentage difference as a dashed line
718     h_fdiff = plot(time, percentage_diff, '--', 'Color', right_color, '
       LineWidth', 2);
719 
720     xlabel('Time (s)');
721     title(['Comparison of Forces - ', title_name]);
722     legend([h_fmotion, h_fvelocity, h_fdiff], ...
723            {'F_{EoM}', 'F_{Conversion}', 'Relative Difference (%)'}, ...
724            'Location', 'best');
725 
726     hold off;
727 end
728 
729 % This function calculates the maximum force on the microbot using the two
730 % methods.
```

```
731 function [max_force_motion, max_force_velocity] = find_max_force(
    force_table_motion, force_table_velocity)
732     % Extract data
733     Fmotion_pN = force_table_motion.Ftotal_pN;
734     Fmotion_std_pN = force_table_motion.Ftotal_Std_pN;
735
736     Fvelocity_pN = force_table_velocity.Ftotal_pN;
737     Fvelocity_std_pN = force_table_velocity.Ftotal_Std_pN;
738
739     % Find maximum values and corresponding standard deviations
740     [max_force_motion, idx_motion] = max(Fmotion_pN);
741     max_force_motion_std = Fmotion_std_pN(idx_motion);
742
743     [max_force_velocity, idx_velocity] = max(Fvelocity_pN);
744     max_force_velocity_std = Fvelocity_std_pN(idx_velocity);
745
746     % Print results
747     fprintf('Maximum Force (EoM Method): %.2f ± %.2f pN\n',
    max_force_motion, max_force_motion_std);
748     fprintf('Maximum Force (Coversion Method): %.2f ± %.2f pN\n',
    max_force_velocity, max_force_velocity_std);
749 end
750
751 % This function calculates the dynamics of the beads and plots them. From
752 % this, using Stokes's law, the DEP force has been calculated and plotted
753 % as well.
754 function analyze_bead_motion(datax, datay, dt, A, B, title_name)
755     % Determine the time vector
756     [num_steps, num_beads] = size(datax);
757     time = (0:num_steps-1)' * dt;
758
759     % Determine the velocities and accelerations of the bead
760     velocities_x = diff(datax) / dt; % (num_steps-1) × num_beads
761     velocities_y = diff(datay) / dt;
762
763     accelerations_x = diff(velocities_x) / dt; % (num_steps-2) × num_beads
764     accelerations_y = diff(velocities_y) / dt;
765
766     % Calculate the total velocity and acceleration of the beads
767     velocities_total = sqrt(velocities_x.^2 + velocities_y.^2);
768     accelerations_total = sqrt(accelerations_x.^2 + accelerations_y.^2);
769
770     % Plot the dynamics of the beads
771     figure;
772     subplot(2,1,1); hold on; grid on;
773     for i = 1:num_beads
774         plot(time(2:end), velocities_total(:, i), '-', 'LineWidth', 1.2);
775     end
776     xlabel('Time (s)'); ylabel('Total Velocity (µm/s)');
777     title(['Total Velocity per Bead - ', title_name]);
778
779     subplot(2,1,2); hold on; grid on;
780     for i = 1:num_beads
781         plot(time(3:end), accelerations_total(:, i), '-', 'LineWidth',
    1.2);
782     end
```

```
783     xlabel('Time (s)'); ylabel('Total Acceleration (µm/s²)');
784     title(['Total Acceleration per Bead - ', title_name]);
785     legend(arrayfun(@(i) sprintf('Bead %d', i), 1:num_beads, '
        UniformOutput', false));
786
787     % Calculate the DEP force on the beads
788     um_to_m = 1e-6;
789
790     velocities_x_cut = velocities_x(1:end-1, :);
791     velocities_y_cut = velocities_y(1:end-1, :);
792
793     Fx_pN = (A * accelerations_x * um_to_m + B * velocities_x_cut *
        um_to_m) * 1e12;
794     Fy_pN = (A * accelerations_y * um_to_m + B * velocities_y_cut *
        um_to_m) * 1e12;
795     Ftotal_pN = sqrt(Fx_pN.^2 + Fy_pN.^2);
796
797     % Max F per bead
798     max_F_per_bead = max(Ftotal_pN, [], 1);
799
800     % Calculate the average max DEP force on the beads in the experiments
801     % with standard deviation
802     mean_Fmax = mean(max_F_per_bead);
803     std_Fmax = std(max_F_per_bead);
804
805     % Print the results for all the beads
806     fprintf('\n===== Maximum Forces per Bead =====\n');
807     for i = 1:num_beads
808         fprintf('Bead %d: %.2f pN\n', i, max_F_per_bead(i));
809     end
810
811     % Print the mean DEP force for the beads
812     fprintf('\n===== Mean Maximum Force =====\n');
813     fprintf('Mean Fmax: %.2f ± %.2f pN\n', mean_Fmax, std_Fmax);
814 end
```

D.2. DEP motion

D.2.1. Bead motion

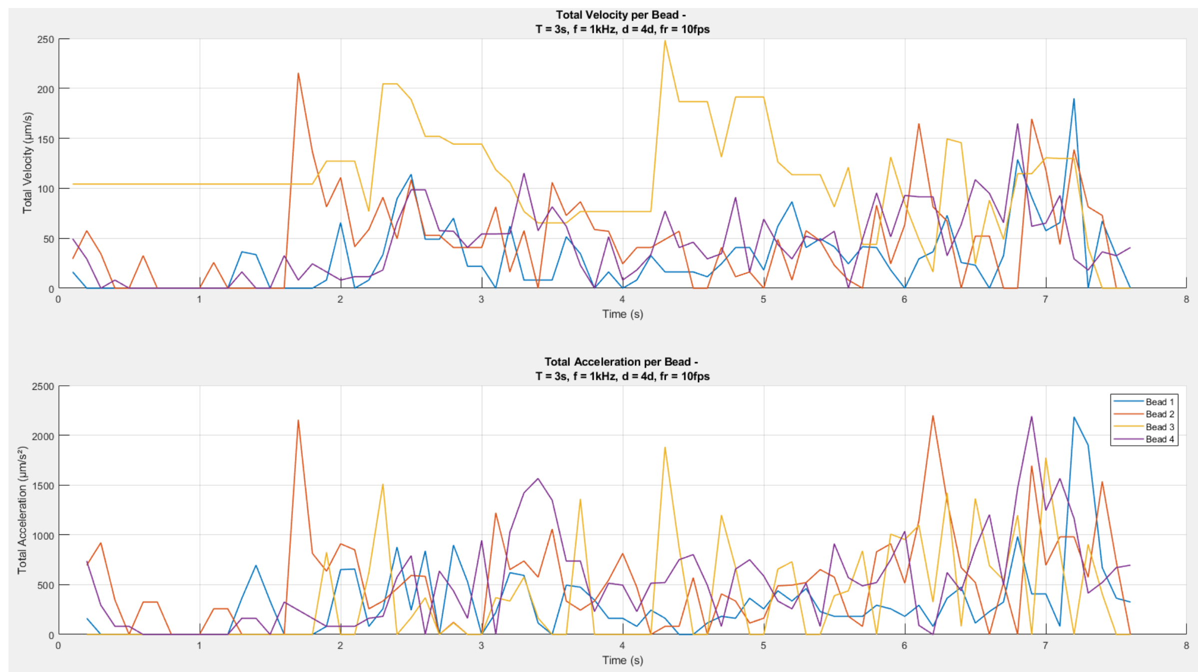

Figure D.1: The measured velocities and accelerations of the 15 µm polystyrene beads in the OET with a medium of deionized water with 0.05% Tween-20. The used sweep animation had a sweep time of 3 seconds and a thickness of 120 pixels. The voltage on the chip was 30 V with a frequency of 1 kHz.

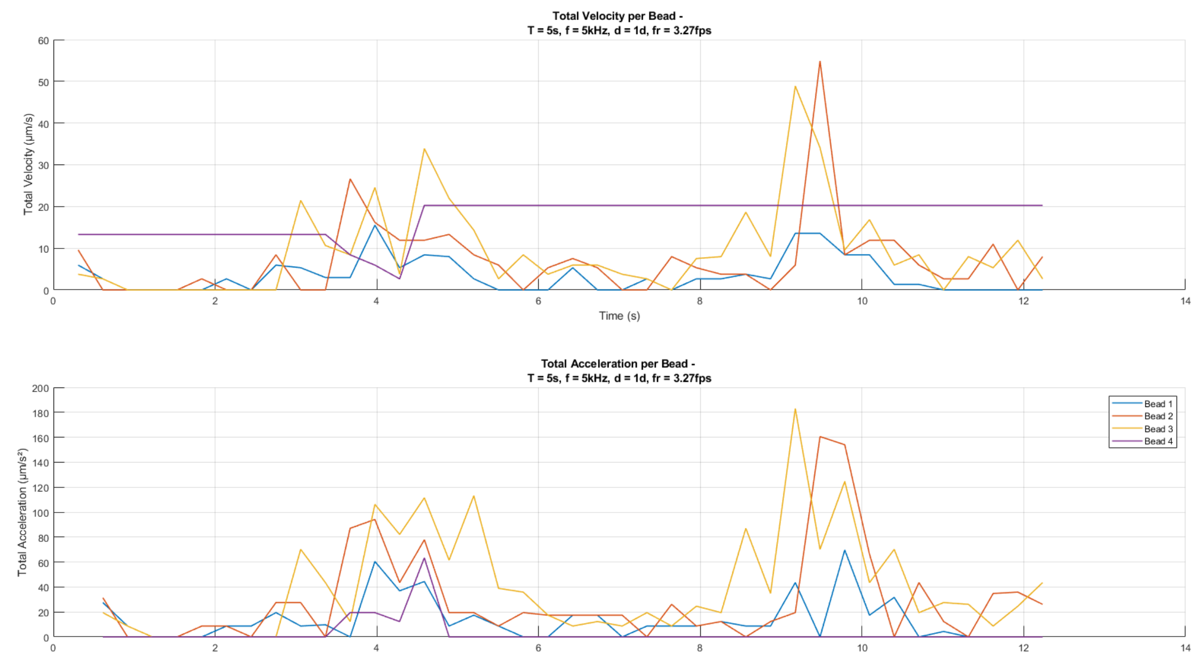

Figure D.2: The measured velocities and accelerations of the 15 µm polystyrene beads in the OET with a medium of deionized water with 0.05% Tween-20. The used sweep animation had a sweep time of 5 seconds and a thickness of 30 pixels. The voltage on the chip was 30 V with a frequency of 5 kHz.

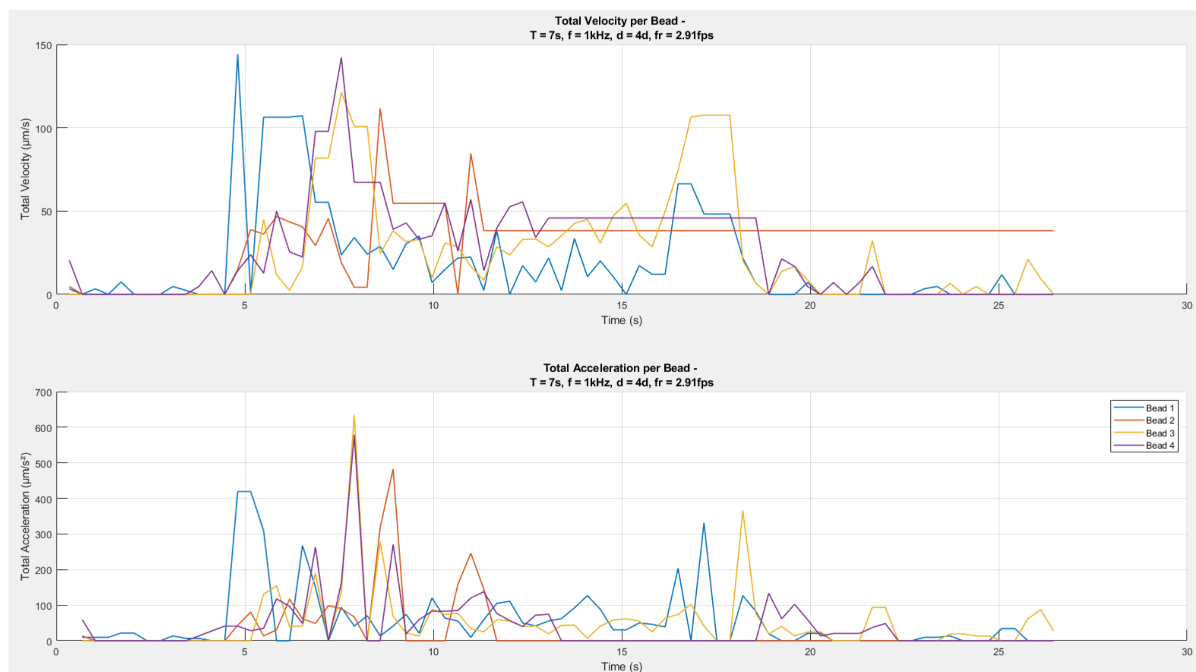

Figure D.3: The measured velocities and accelerations of the 15 μm polystyrene beads in the OET with a medium of deionized water with 0.05% Tween-20. The used sweep animation had a sweep time of 7 seconds and a thickness of 120 pixels. The voltage on the chip was 30 V with a frequency of 1 kHz.

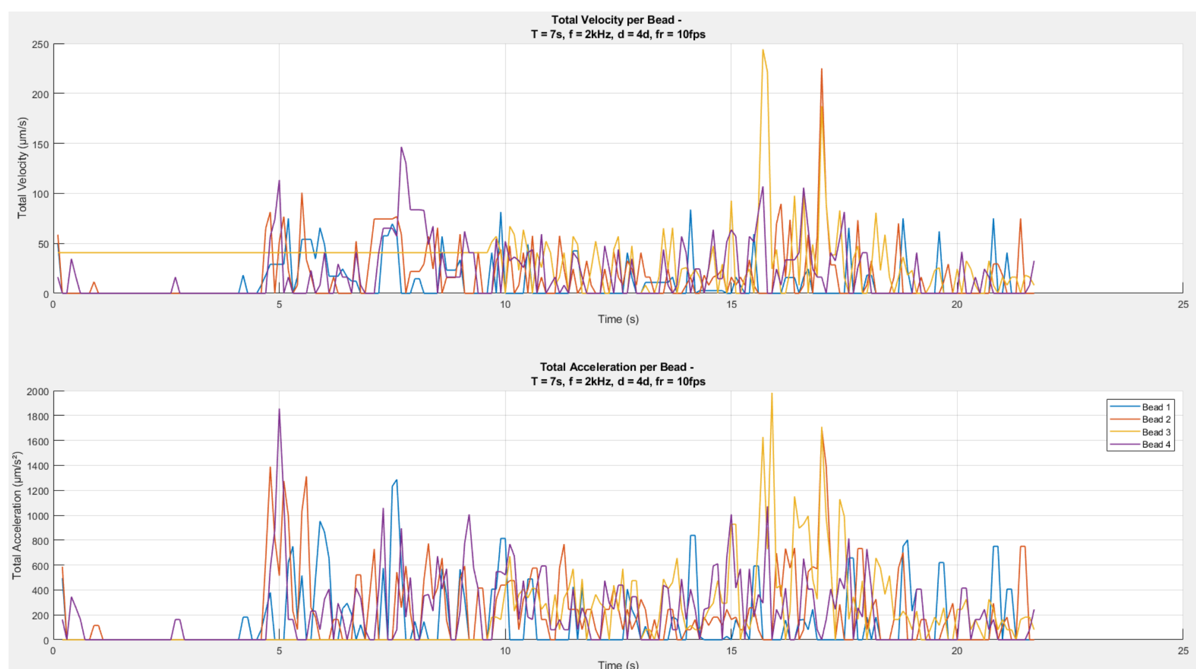

Figure D.4: The measured velocities and accelerations of the 15 μm polystyrene beads in the OET with a medium of deionized water with 0.05% Tween-20. The used sweep animation had a sweep time of 7 seconds and a thickness of 120 pixels. The voltage on the chip was 30 V with a frequency of 2 kHz.

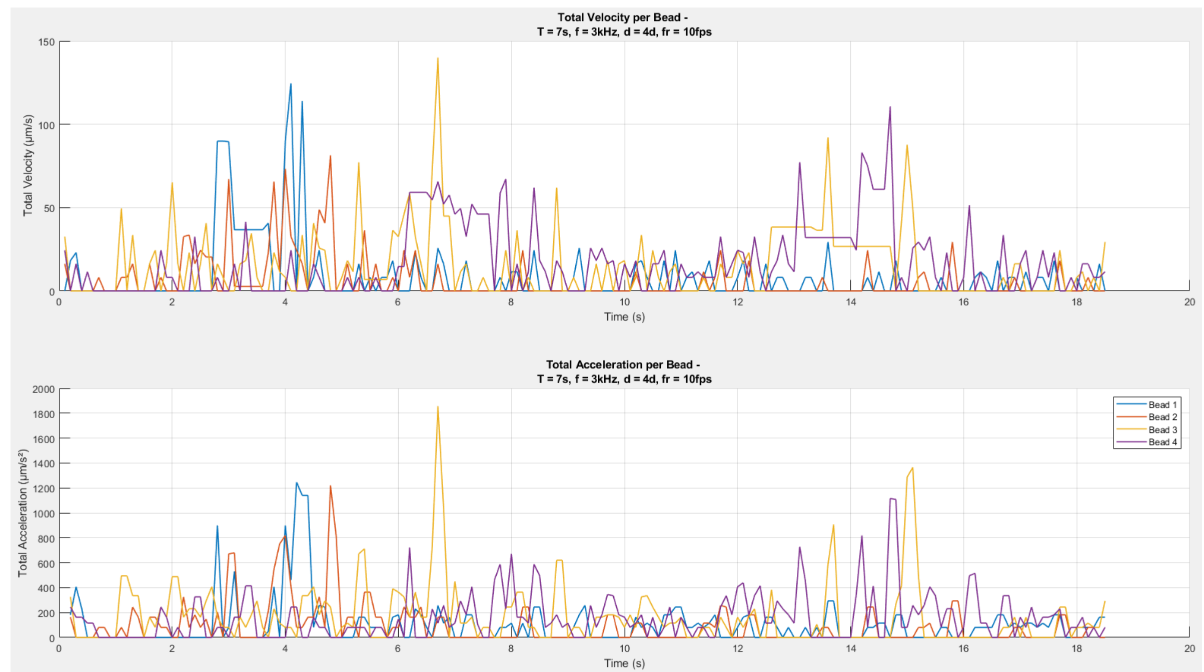

Figure D.5: The measured velocities and accelerations of the 15 µm polystyrene beads in the OET with a medium of deionized water with 0.05% Tween-20. The used sweep animation had a sweep time of 7 seconds and a thickness of 120 pixels. The voltage on the chip was 30 V with a frequency of 3 kHz.

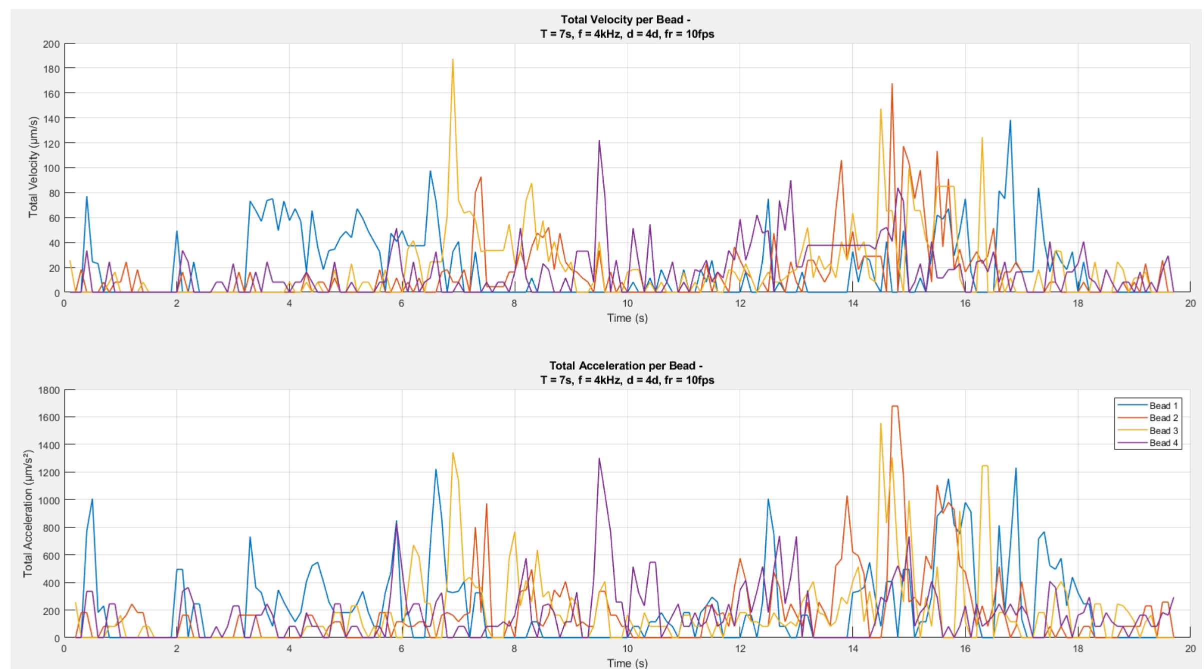

Figure D.6: The measured velocities and accelerations of the 15 µm polystyrene beads in the OET with a medium of deionized water with 0.05% Tween-20. The used sweep animation had a sweep time of 7 seconds and a thickness of 120 pixels. The voltage on the chip was 30 V with a frequency of 4 kHz.

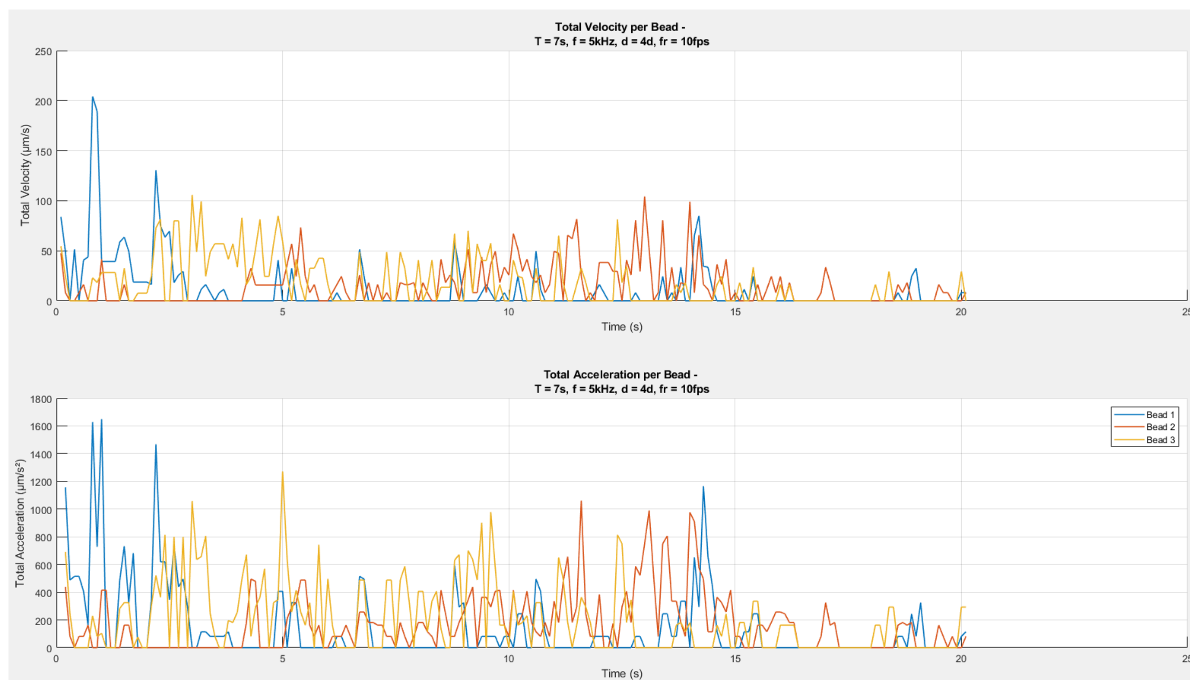

Figure D.7: The measured velocities and accelerations of the 15 μm polystyrene beads in the OET with a medium of deionized water with 0.05% Tween-20. The used sweep animation had a sweep time of 7 seconds and a thickness of 120 pixels. The voltage on the chip was 30 V with a frequency of 5 kHz.

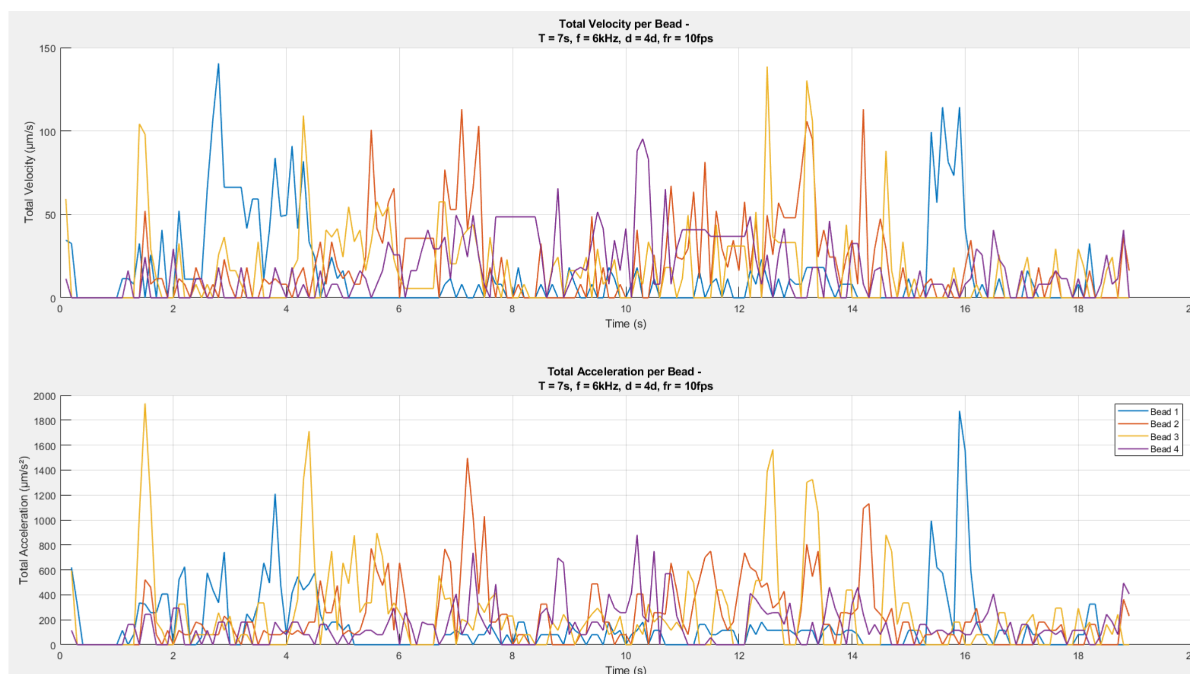

Figure D.8: The measured velocities and accelerations of the 15 μm polystyrene beads in the OET with a medium of deionized water with 0.05% Tween-20. The used sweep animation had a sweep time of 7 seconds and a thickness of 120 pixels. The voltage on the chip was 30 V with a frequency of 6 kHz.

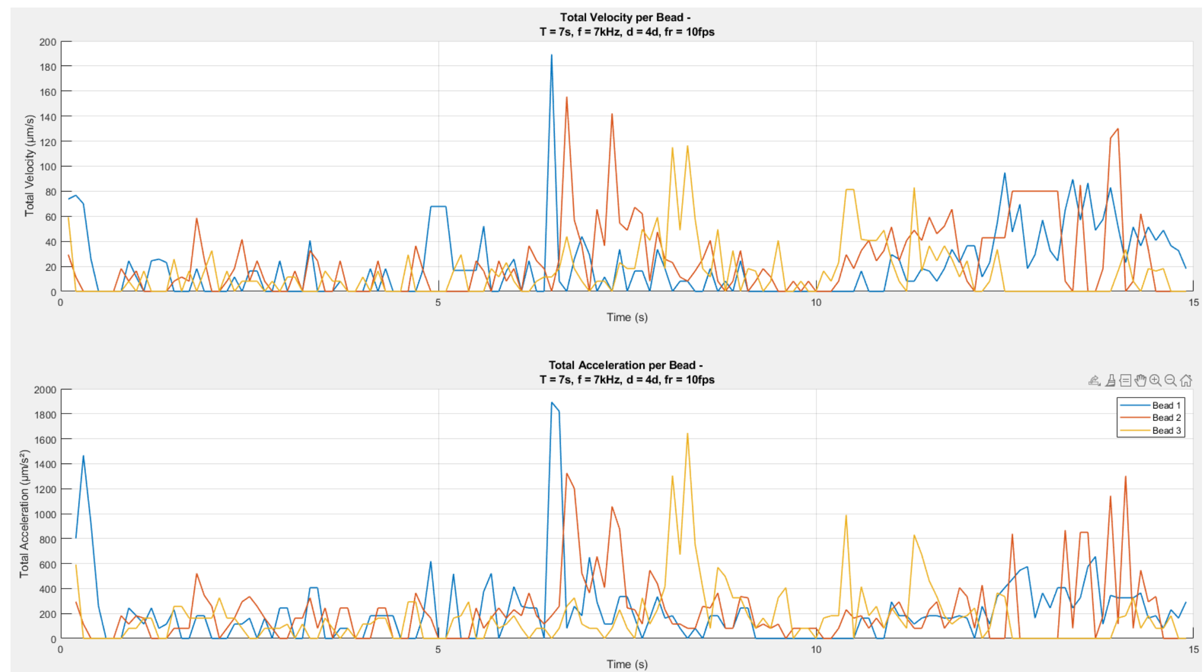

Figure D.9: The measured velocities and accelerations of the 15 μm polystyrene beads in the OET with a medium of deionized water with 0.05% Tween-20. The used sweep animation had a sweep time of 7 seconds and a thickness of 120 pixels. The voltage on the chip was 30 V with a frequency of 7 kHz.

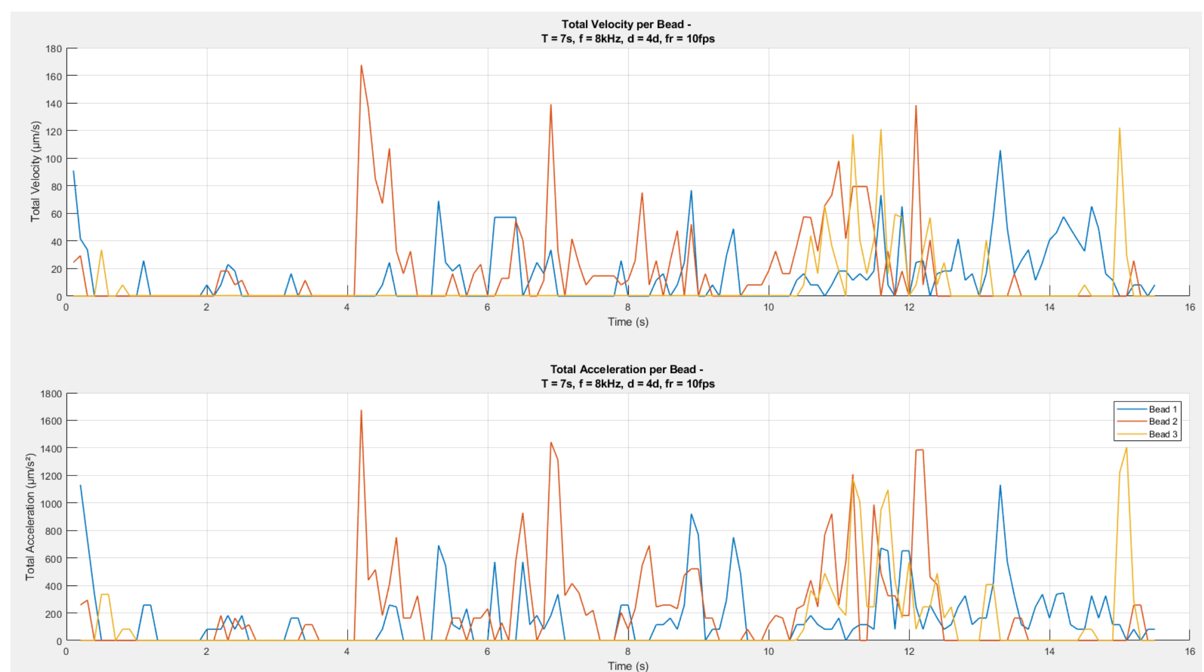

Figure D.10: The measured velocities and accelerations of the 15 μm polystyrene beads in the OET with a medium of deionized water with 0.05% Tween-20. The used sweep animation had a sweep time of 7 seconds and a thickness of 120 pixels. The voltage on the chip was 30 V with a frequency of 8 kHz.

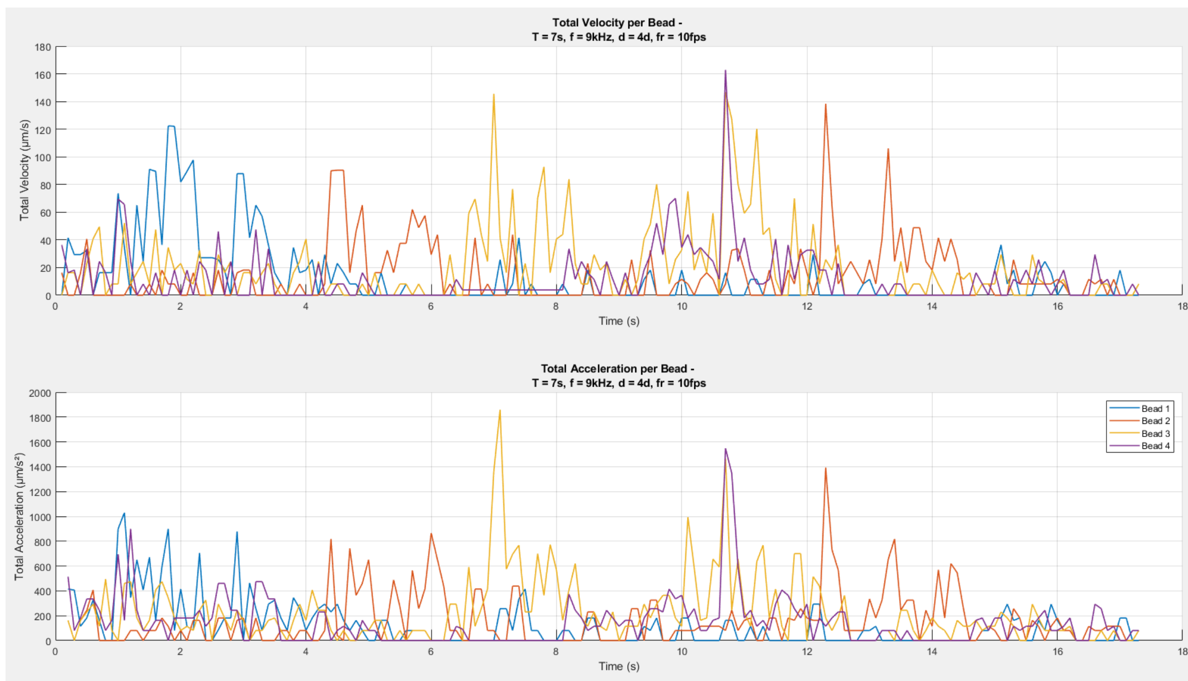

Figure D.11: The measured velocities and accelerations of the 15 µm polystyrene beads in the OET with a medium of deionized water with 0.05% Tween-20. The used sweep animation had a sweep time of 7 seconds and a thickness of 120 pixels. The voltage on the chip was 30 V with a frequency of 9 kHz.

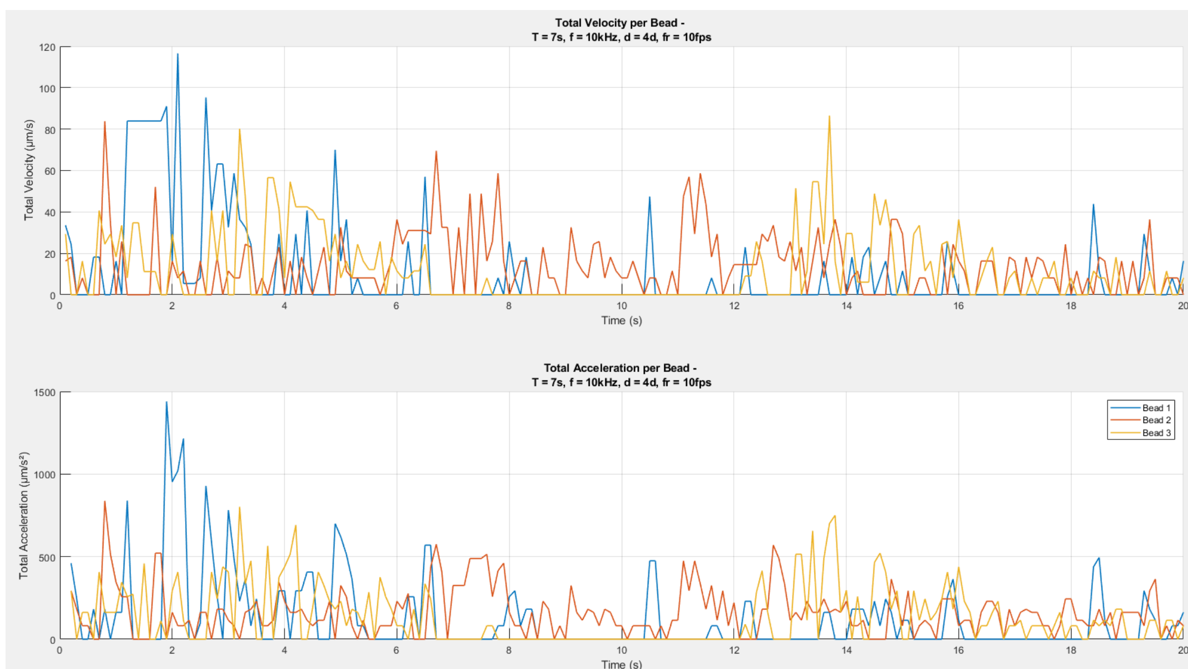

Figure D.12: The measured velocities and accelerations of the 15 µm polystyrene beads in the OET with a medium of deionized water with 0.05% Tween-20. The used sweep animation had a sweep time of 7 seconds and a thickness of 120 pixels. The voltage on the chip was 30 V with a frequency of 10 kHz.

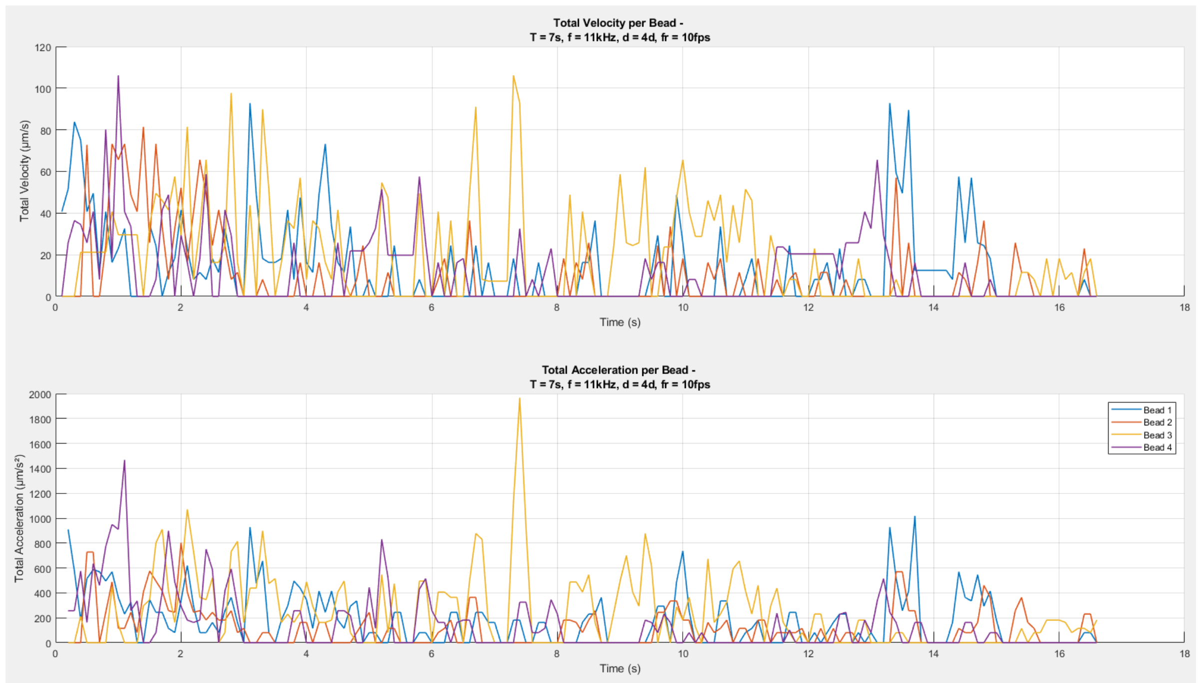

Figure D.13: The measured velocities and accelerations of the 15 µm polystyrene beads in the OET with a medium of deionized water with 0.05% Tween-20. The used sweep animation had a sweep time of 7 seconds and a thickness of 120 pixels. The voltage on the chip was 30 V with a frequency of 11 kHz.

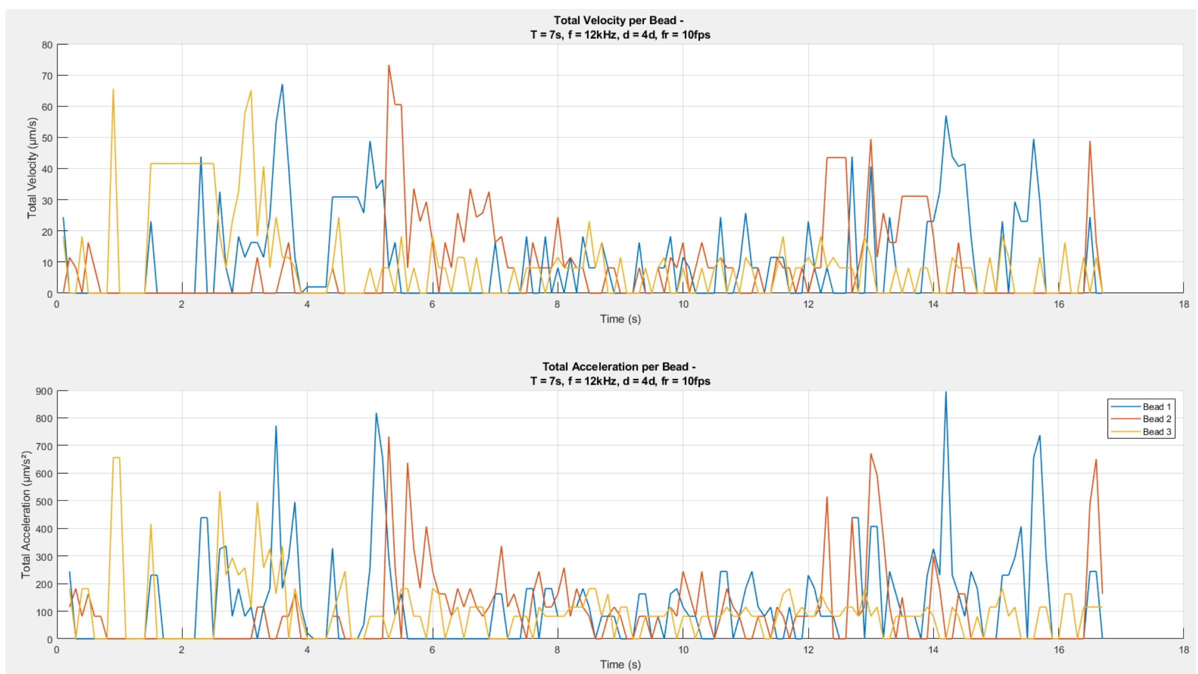

Figure D.14: The measured velocities and accelerations of the 15 µm polystyrene beads in the OET with a medium of deionized water with 0.05% Tween-20. The used sweep animation had a sweep time of 7 seconds and a thickness of 120 pixels. The voltage on the chip was 30 V with a frequency of 12 kHz.

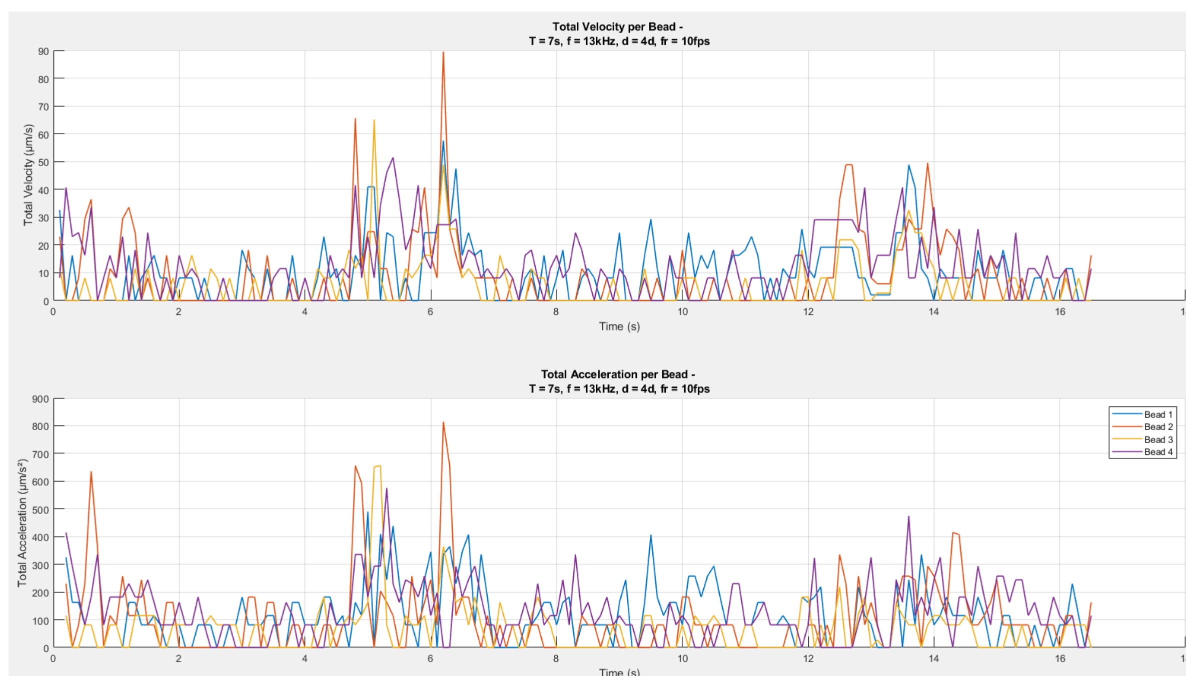

Figure D.15: The measured velocities and accelerations of the 15 µm polystyrene beads in the OET with a medium of deionized water with 0.05% Tween-20. The used sweep animation had a sweep time of 7 seconds and a thickness of 120 pixels. The voltage on the chip was 30 V with a frequency of 13 kHz.

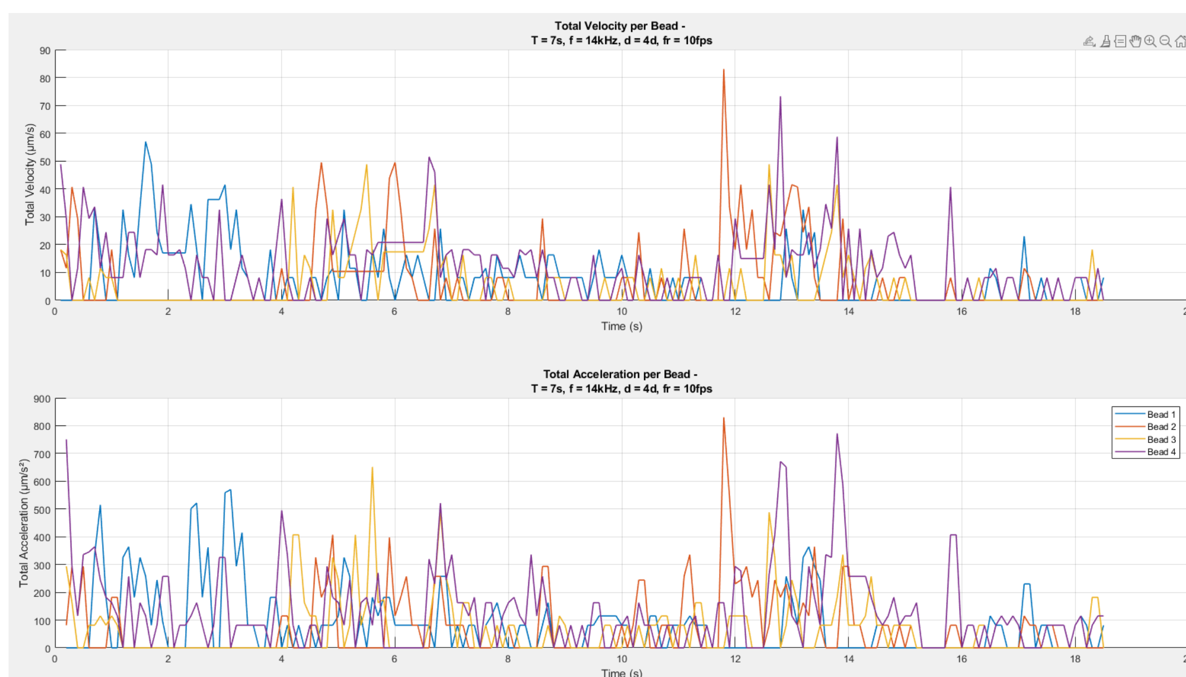

Figure D.16: The measured velocities and accelerations of the 15 µm polystyrene beads in the OET with a medium of deionized water with 0.05% Tween-20. The used sweep animation had a sweep time of 7 seconds and a thickness of 120 pixels. The voltage on the chip was 30 V with a frequency of 14 kHz.

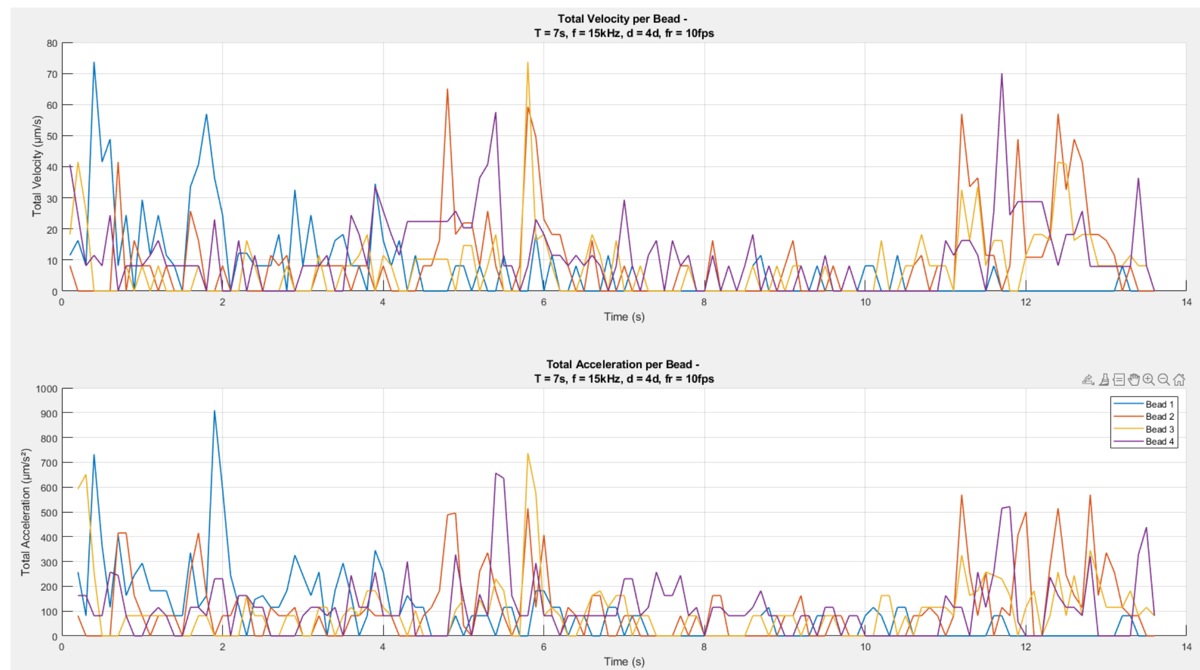

Figure D.17: The measured velocities and accelerations of the 15 µm polystyrene beads in the OET with a medium of deionized water with 0.05% Tween-20. The used sweep animation had a sweep time of 7 seconds and a thickness of 120 pixels. The voltage on the chip was 30 V with a frequency of 15 kHz.

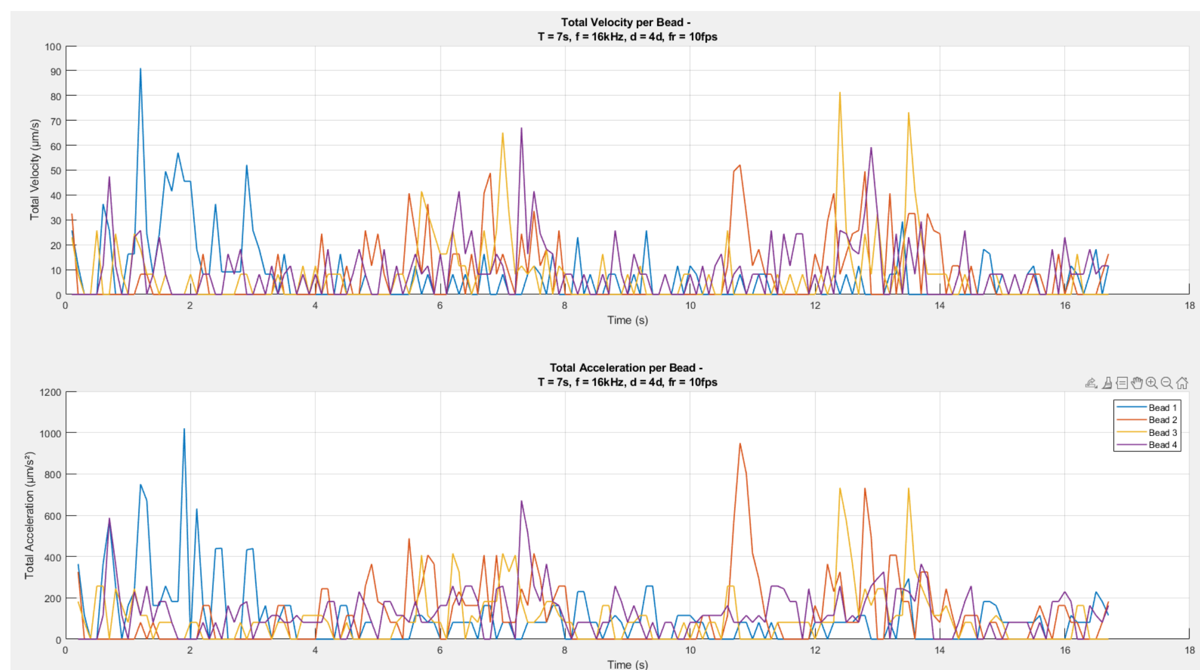

Figure D.18: The measured velocities and accelerations of the 15 µm polystyrene beads in the OET with a medium of deionized water with 0.05% Tween-20. The used sweep animation had a sweep time of 7 seconds and a thickness of 120 pixels. The voltage on the chip was 30 V with a frequency of 16 kHz.

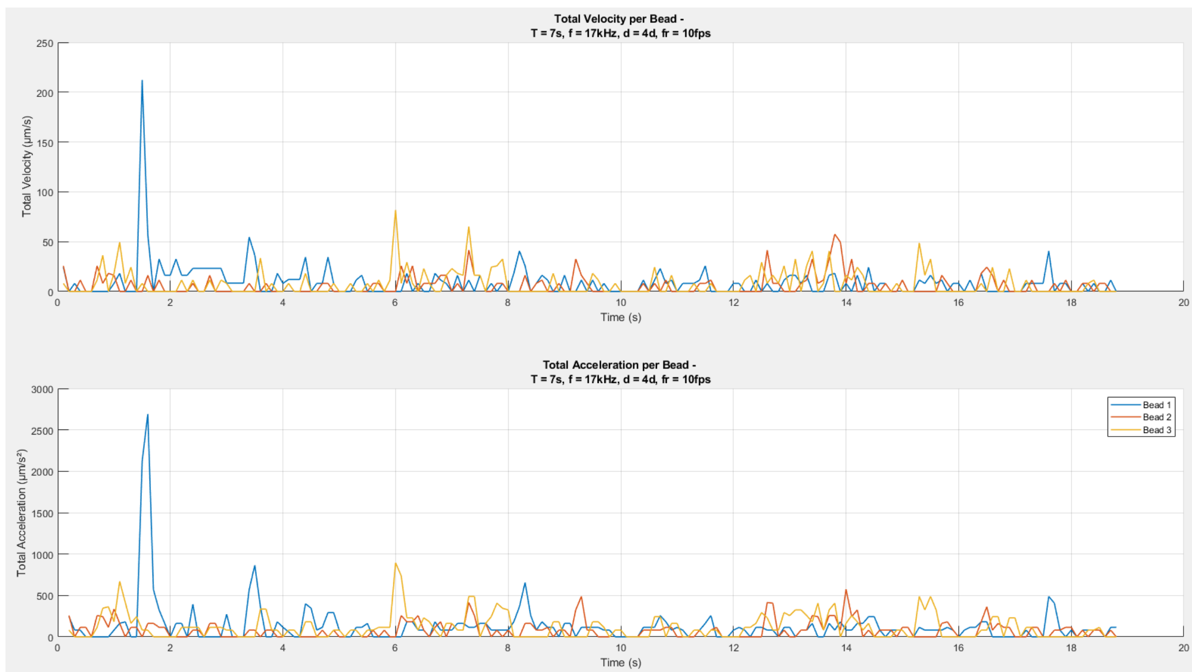

Figure D.19: The measured velocities and accelerations of the 15 µm polystyrene beads in the OET with a medium of deionized water with 0.05% Tween-20. The used sweep animation had a sweep time of 7 seconds and a thickness of 120 pixels. The voltage on the chip was 30 V with a frequency of 17 kHz.

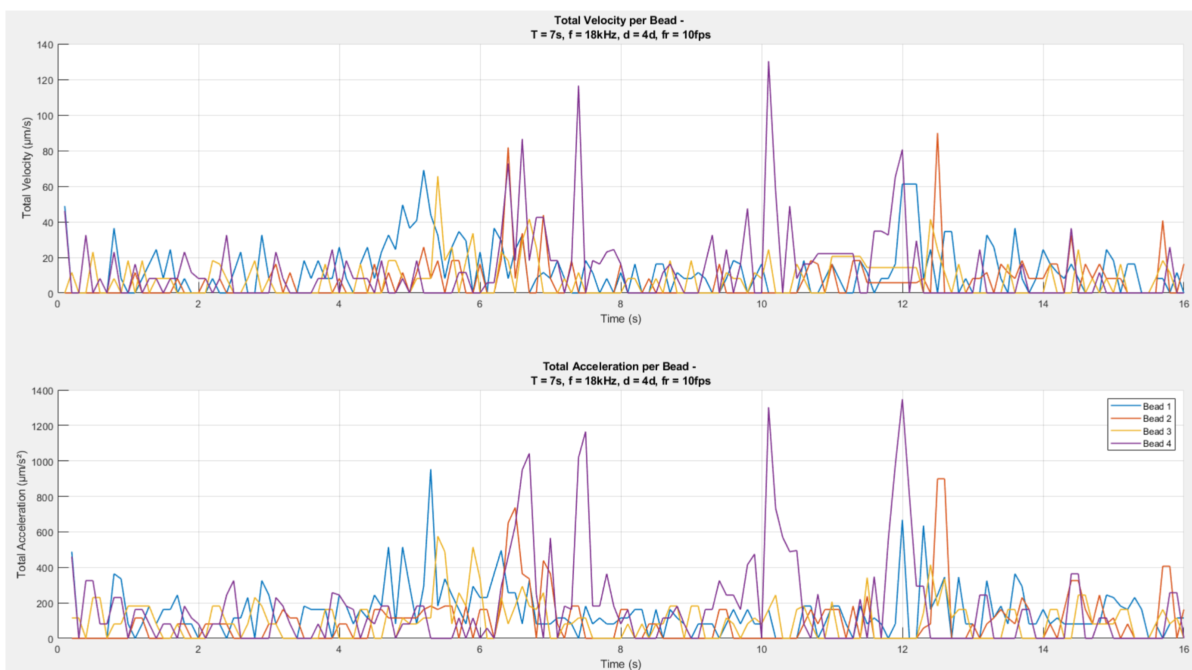

Figure D.20: The measured velocities and accelerations of the 15 µm polystyrene beads in the OET with a medium of deionized water with 0.05% Tween-20. The used sweep animation had a sweep time of 7 seconds and a thickness of 120 pixels. The voltage on the chip was 30 V with a frequency of 18 kHz.

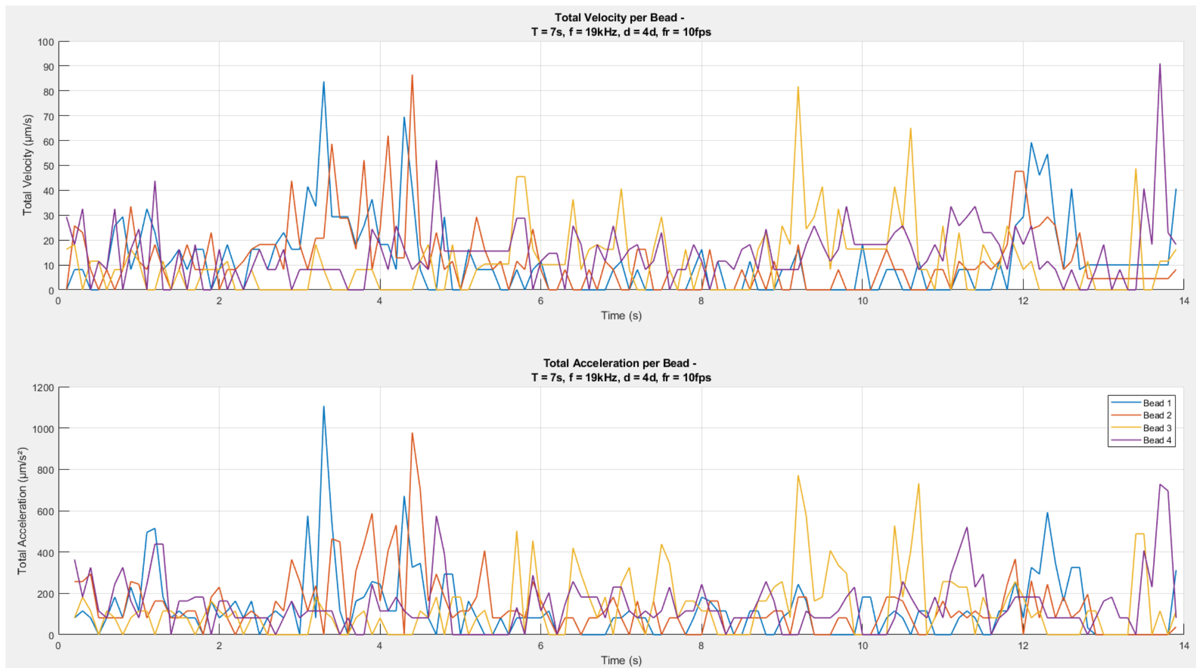

Figure D.21: The measured velocities and accelerations of the 15 µm polystyrene beads in the OET with a medium of deionized water with 0.05% Tween-20. The used sweep animation had a sweep time of 7 seconds and a thickness of 120 pixels. The voltage on the chip was 30 V with a frequency of 19 kHz.

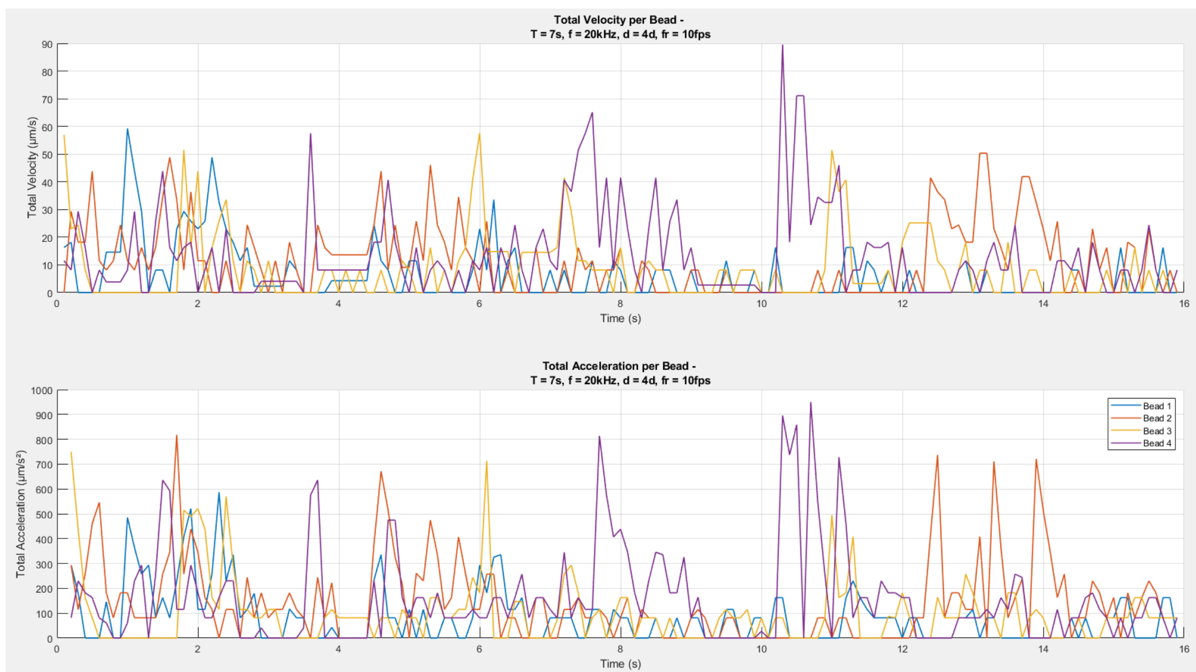

Figure D.22: The measured velocities and accelerations of the 15 µm polystyrene beads in the OET with a medium of deionized water with 0.05% Tween-20. The used sweep animation had a sweep time of 7 seconds and a thickness of 120 pixels. The voltage on the chip was 30 V with a frequency of 20 kHz.

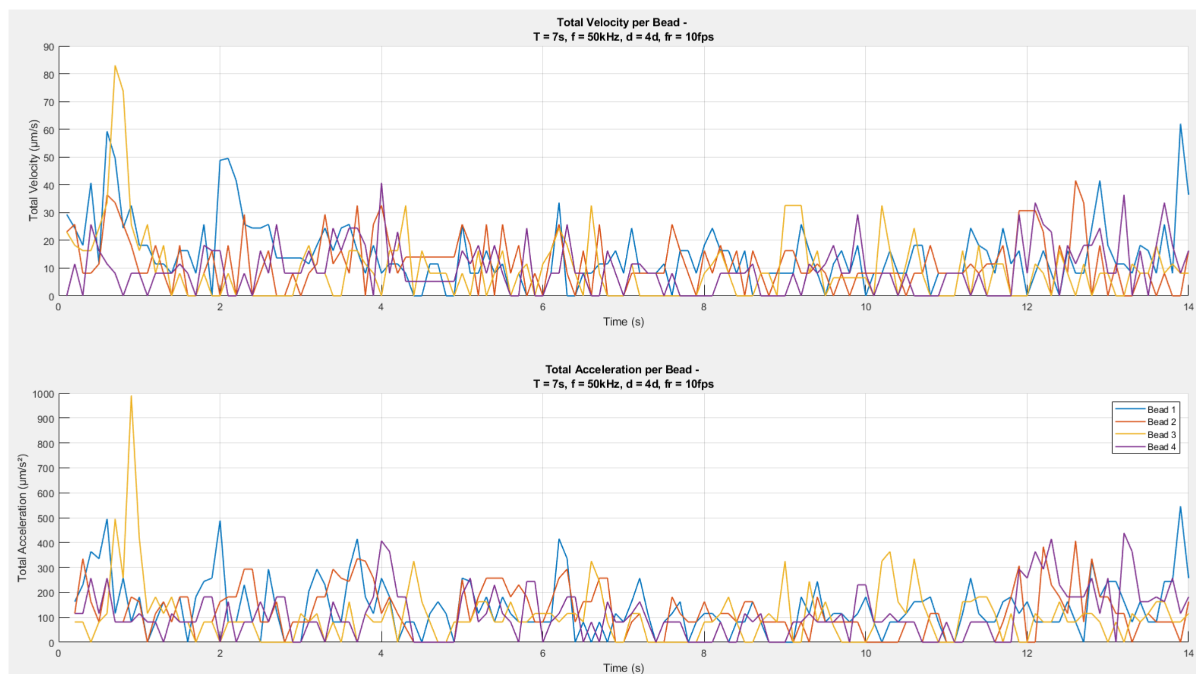

Figure D.23: The measured velocities and accelerations of the 15 μm polystyrene beads in the OET with a medium of deionized water with 0.05% Tween-20. The used sweep animation had a sweep time of 7 seconds and a thickness of 120 pixels. The voltage on the chip was 30 V with a frequency of 50 kHz.

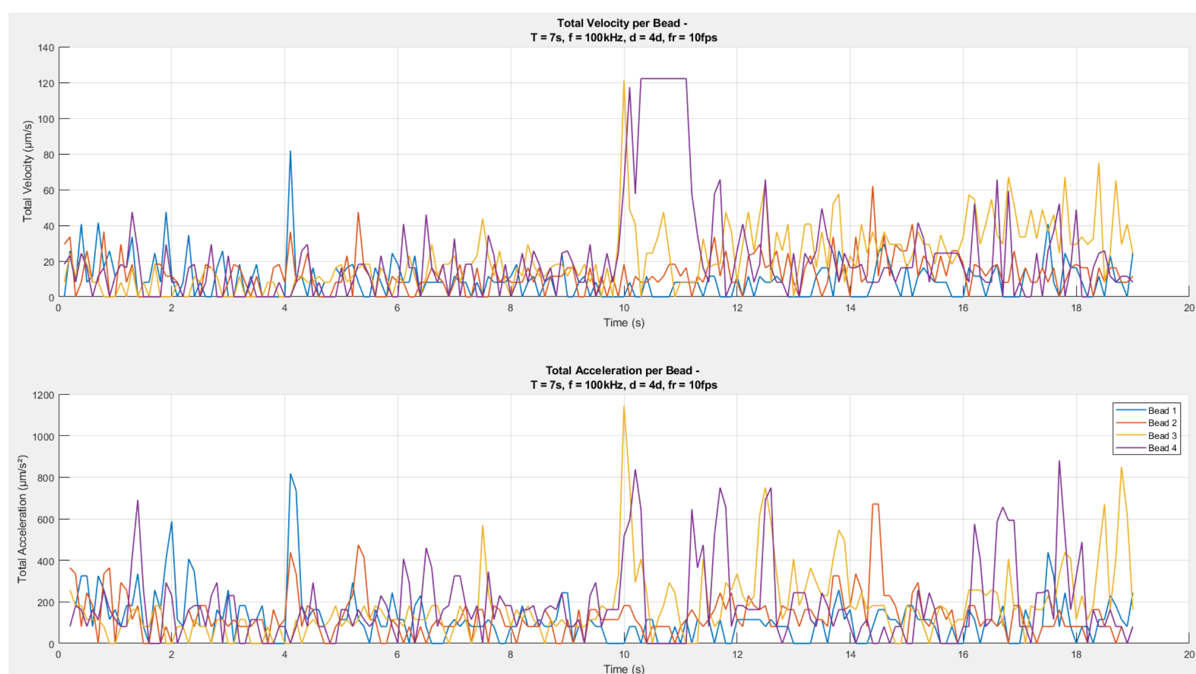

Figure D.24: The measured velocities and accelerations of the 15 μm polystyrene beads in the OET with a medium of deionized water with 0.05% Tween-20. The used sweep animation had a sweep time of 7 seconds and a thickness of 120 pixels. The voltage on the chip was 30 V with a frequency of 100 kHz.

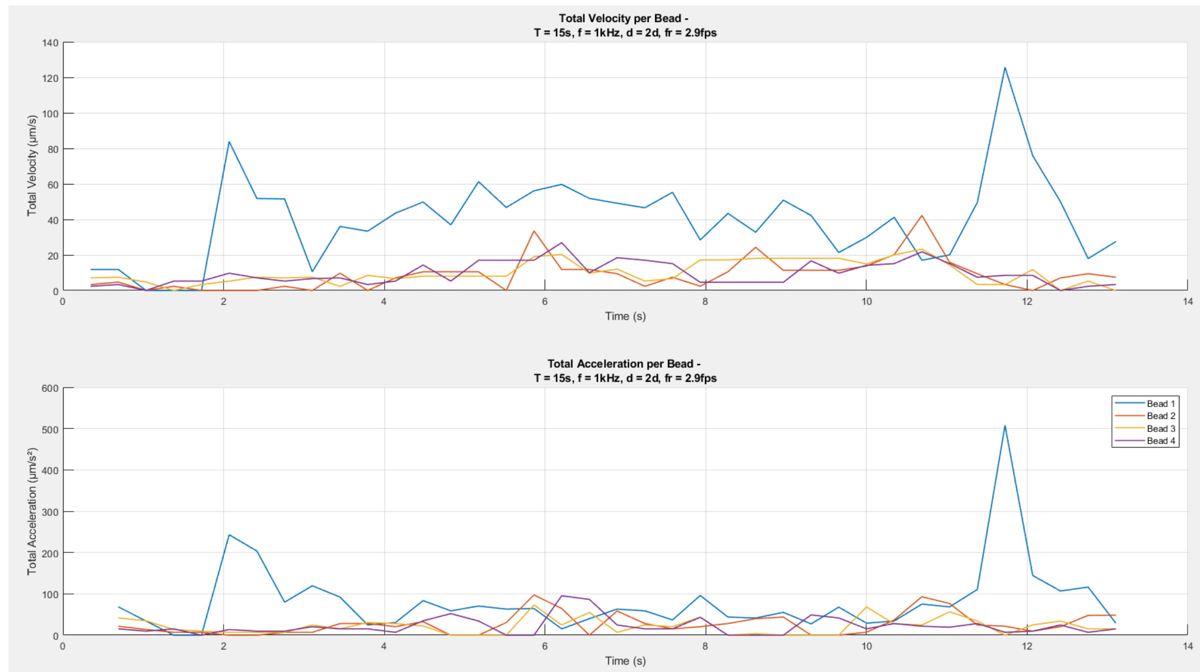

Figure D.25: The measured velocities and accelerations of the 15 µm polystyrene beads in the OET with a medium of deionized water with 0.05% Tween-20. The used sweep animation had a sweep time of 15 seconds and a thickness of 60 pixels. The voltage on the chip was 30 V with a frequency of 1 kHz.

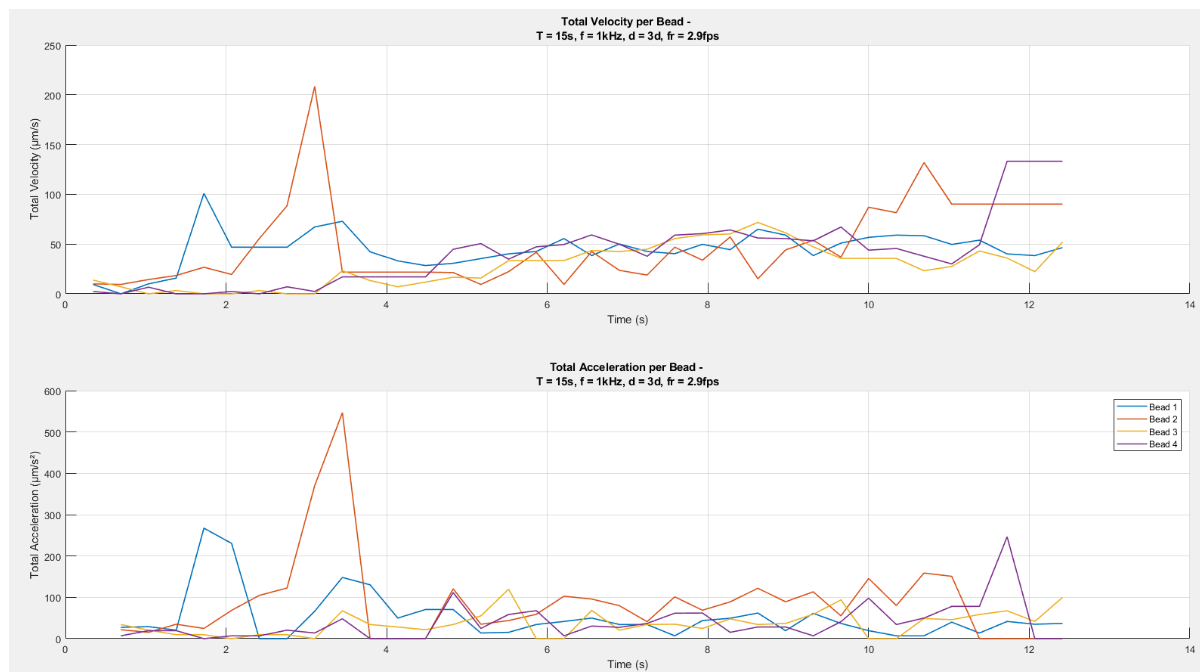

Figure D.26: The measured velocities and accelerations of the 15 µm polystyrene beads in the OET with a medium of deionized water with 0.05% Tween-20. The used sweep animation had a sweep time of 15 seconds and a thickness of 90 pixels. The voltage on the chip was 30 V with a frequency of 1 kHz.

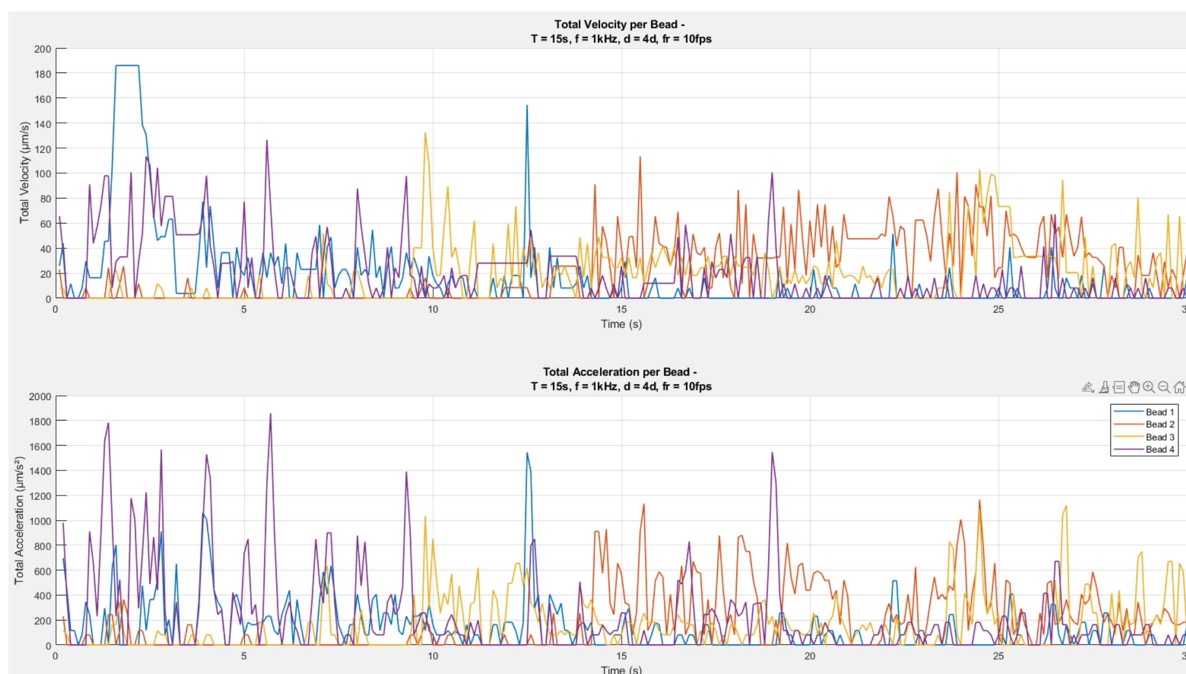

Figure D.27: The measured velocities and accelerations of the 15 µm polystyrene beads in the OET with a medium of deionized water with 0.05% Tween-20. The used sweep animation had a sweep time of 15 seconds and a thickness of 120 pixels. The voltage on the chip was 30 V with a frequency of 1 kHz.

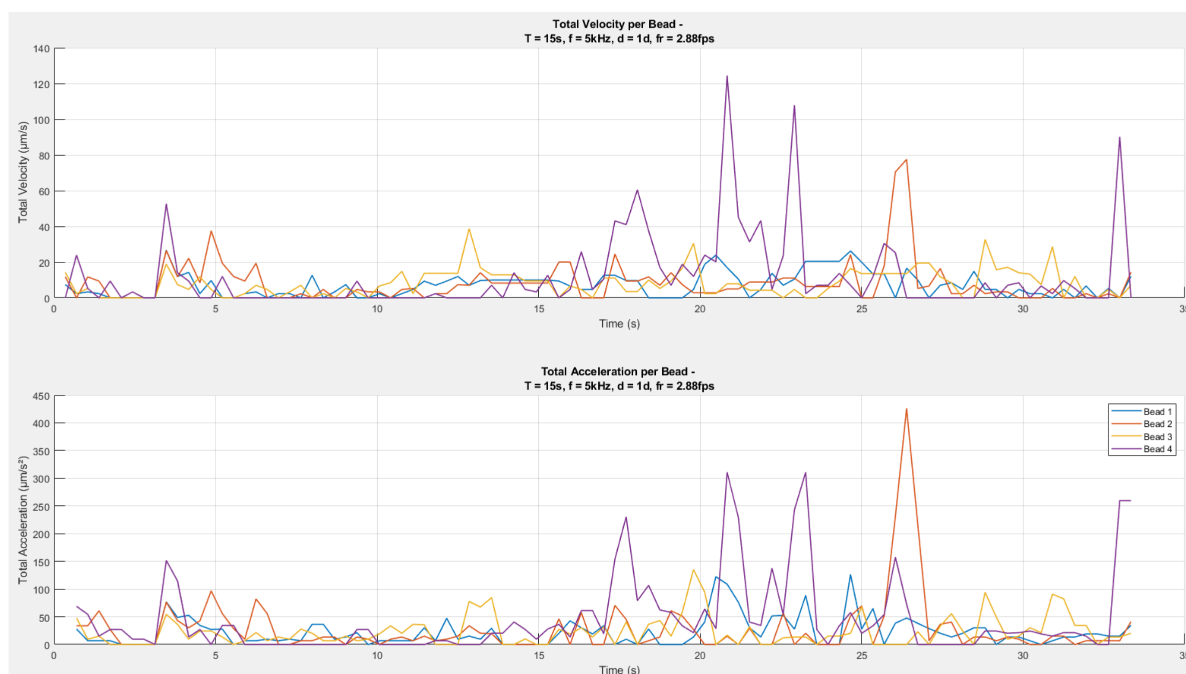

Figure D.28: The measured velocities and accelerations of the 15 µm polystyrene beads in the OET with a medium of deionized water with 0.05% Tween-20. The used sweep animation had a sweep time of 15 seconds and a thickness of 30 pixels. The voltage on the chip was 30 V with a frequency of 5 kHz.

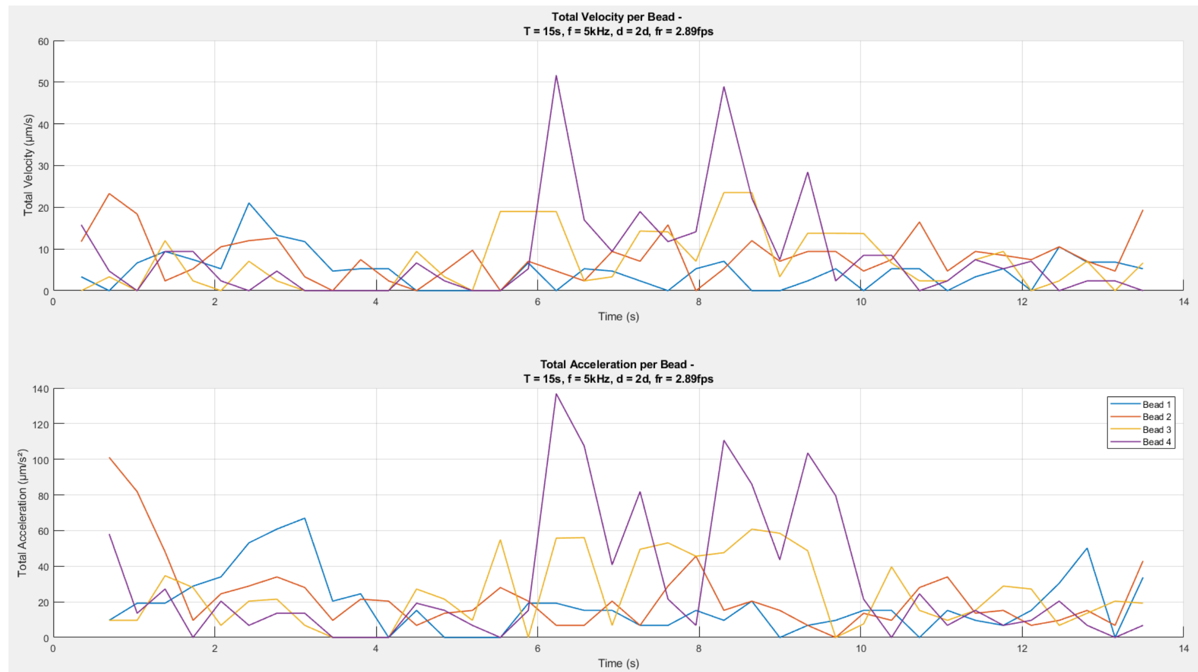

Figure D.29: The measured velocities and accelerations of the 15 µm polystyrene beads in the OET with a medium of deionized water with 0.05% Tween-20. The used sweep animation had a sweep time of 15 seconds and a thickness of 60 pixels. The voltage on the chip was 30 V with a frequency of 5 kHz.

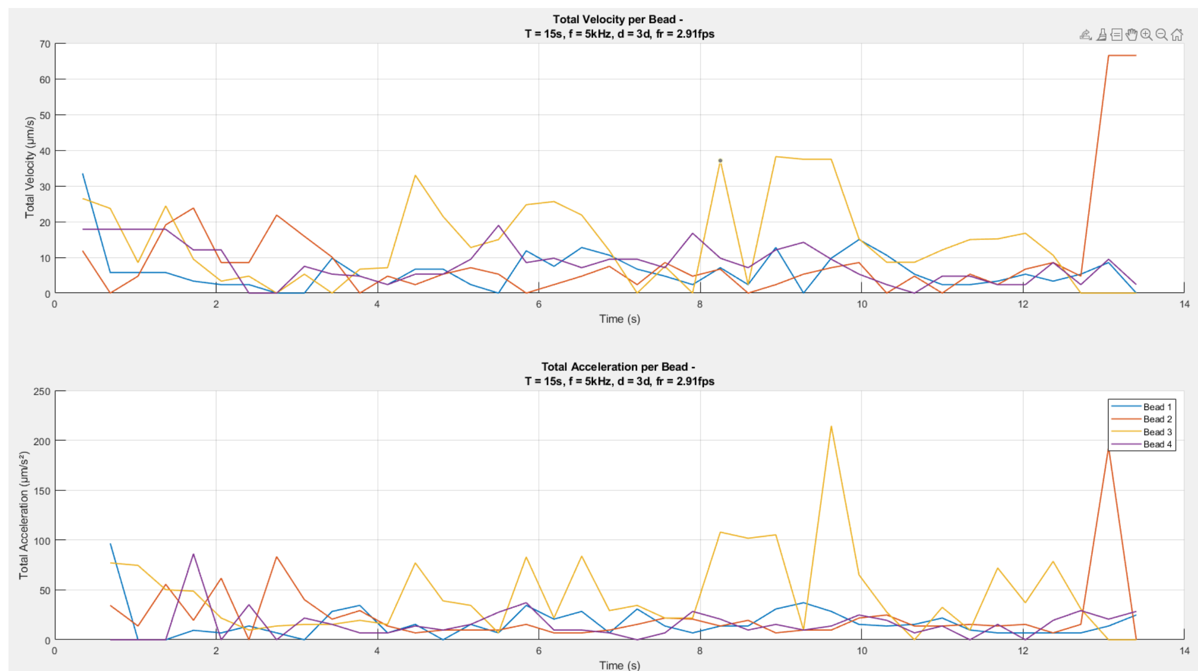

Figure D.30: The measured velocities and accelerations of the 15 µm polystyrene beads in the OET with a medium of deionized water with 0.05% Tween-20. The used sweep animation had a sweep time of 15 seconds and a thickness of 90 pixels. The voltage on the chip was 30 V with a frequency of 5 kHz.

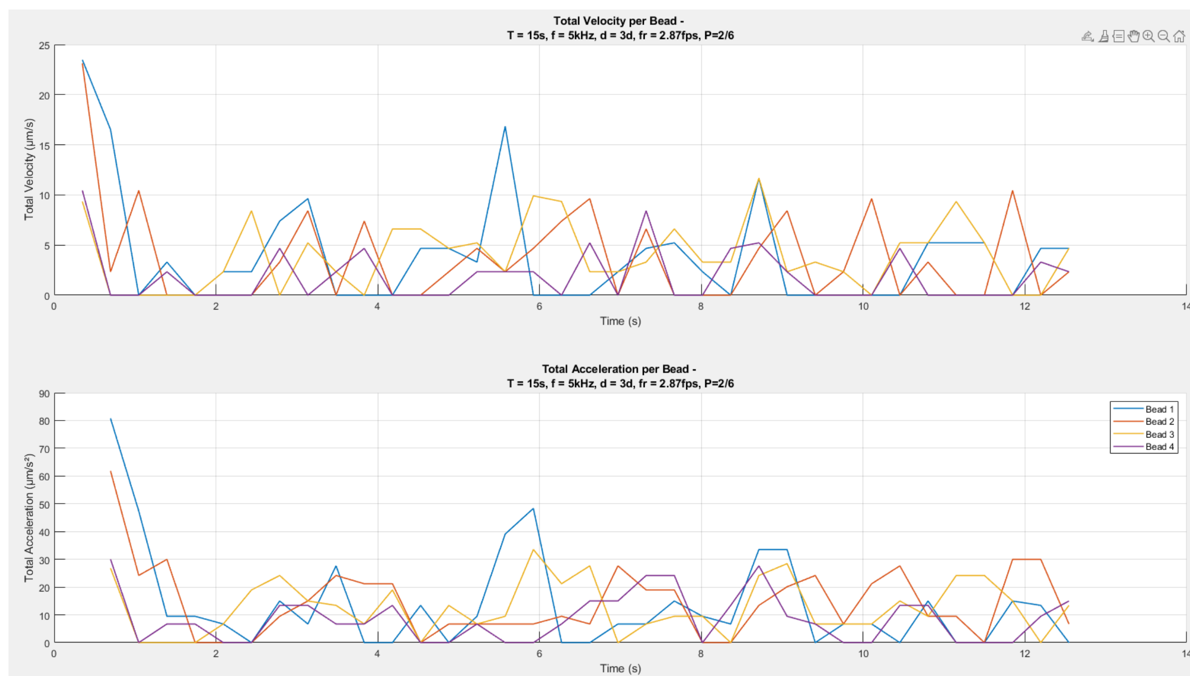

Figure D.31: The measured velocities and accelerations of the 15 µm polystyrene beads in the OET with a medium of deionized water with 0.05% Tween-20. The used sweep animation had a sweep time of 15 seconds and a thickness of 90 pixels. The voltage on the chip was 30 V with a frequency of 5 kHz. The illumination was set to 1/3 of full power.

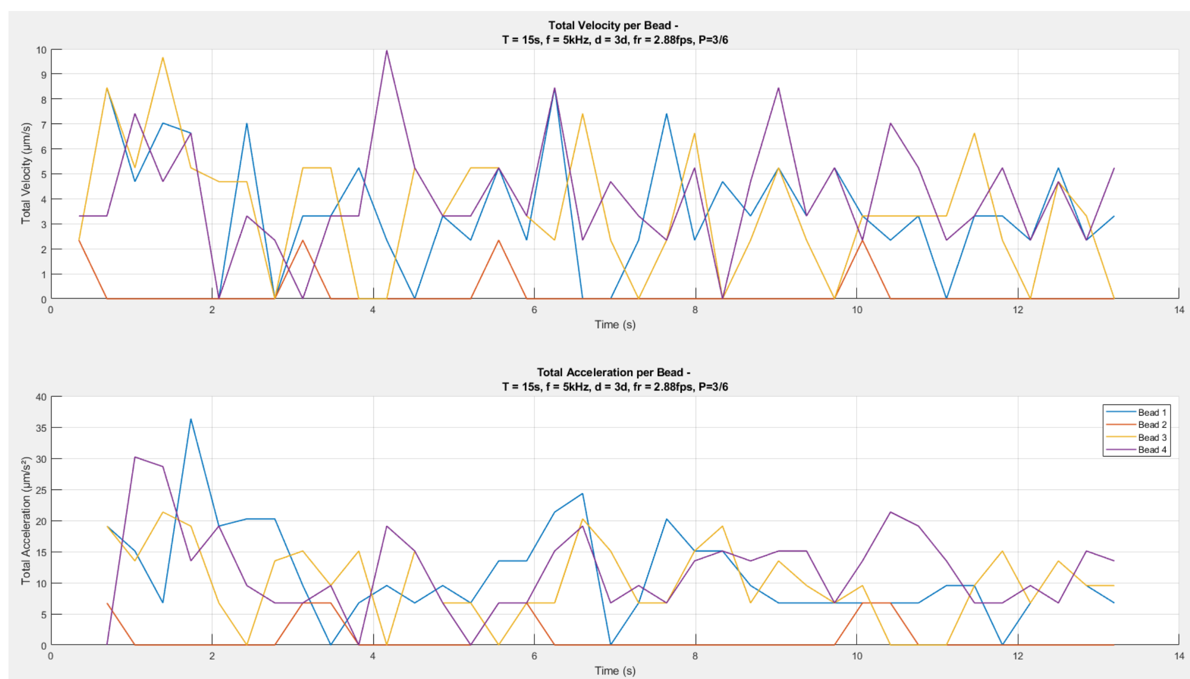

Figure D.32: The measured velocities and accelerations of the 15 µm polystyrene beads in the OET with a medium of deionized water with 0.05% Tween-20. The used sweep animation had a sweep time of 15 seconds and a thickness of 90 pixels. The voltage on the chip was 30 V with a frequency of 5 kHz. The illumination was set to 1/2 of full power.

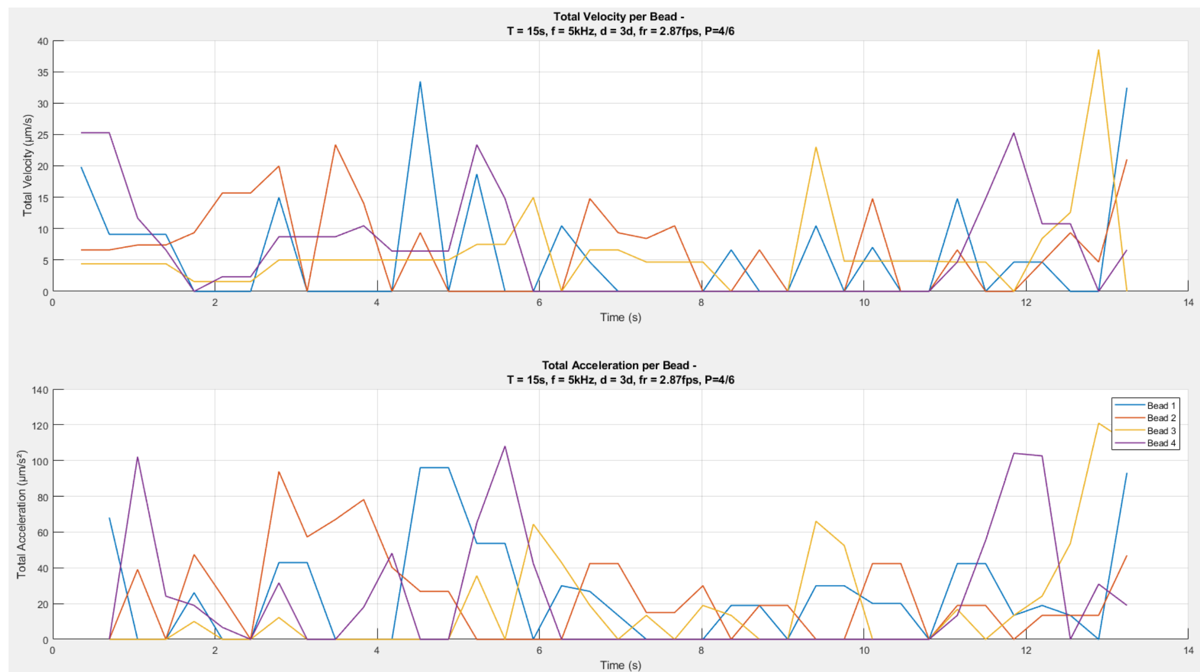

Figure D.33: The measured velocities and accelerations of the 15 µm polystyrene beads in the OET with a medium of deionized water with 0.05% Tween-20. The used sweep animation had a sweep time of 15 seconds and a thickness of 90 pixels. The voltage on the chip was 30 V with a frequency of 5 kHz. The illumination was set to 2/3 of full power.

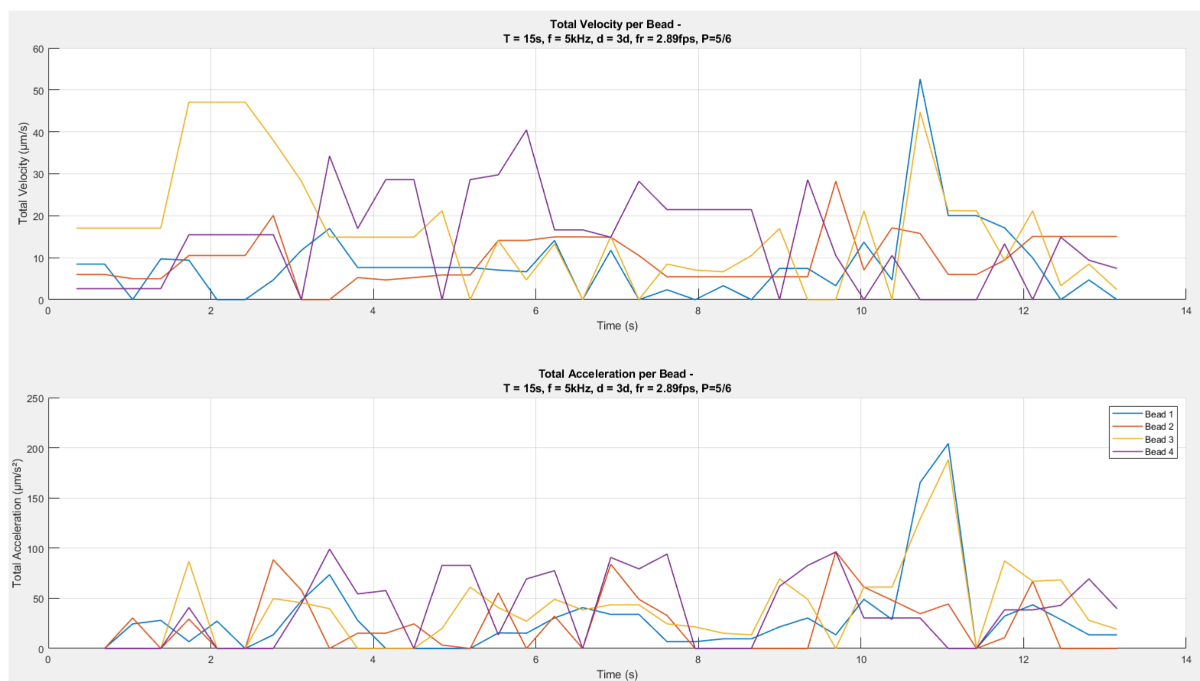

Figure D.34: The measured velocities and accelerations of the 15 µm polystyrene beads in the OET with a medium of deionized water with 0.05% Tween-20. The used sweep animation had a sweep time of 15 seconds and a thickness of 90 pixels. The voltage on the chip was 30 V with a frequency of 5 kHz. The illumination was set to 5/6 of full power.

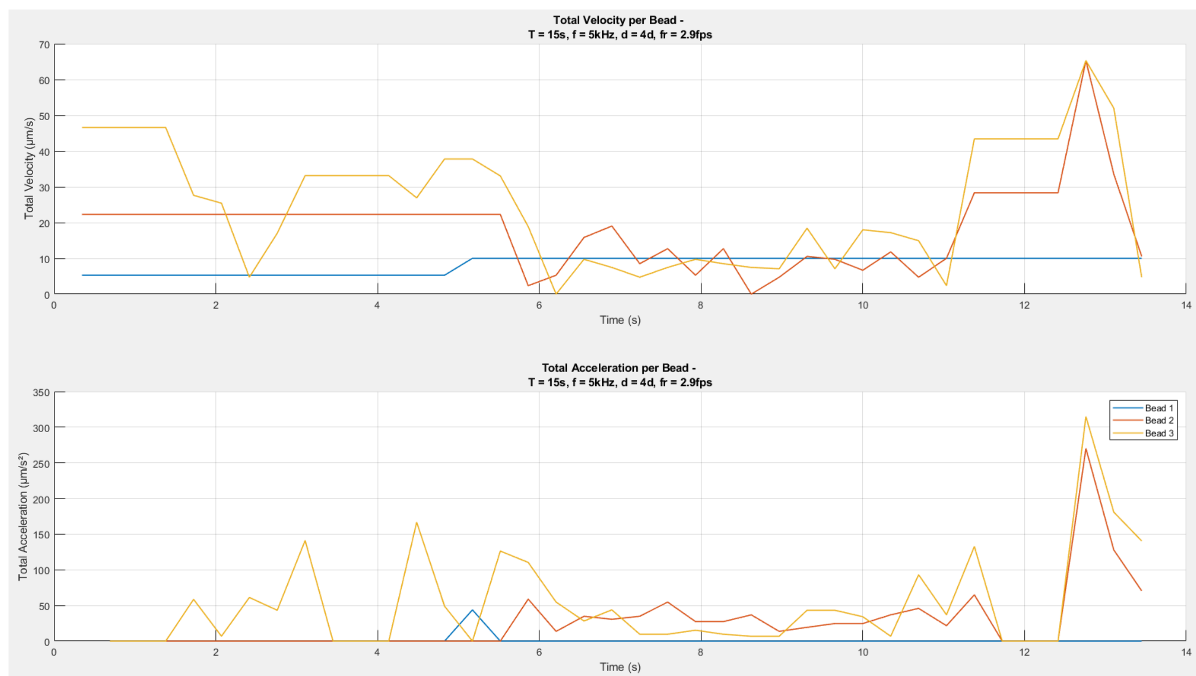

Figure D.35: The measured velocities and accelerations of the 15 µm polystyrene beads in the OET with a medium of deionized water with 0.05% Tween-20. The used sweep animation had a sweep time of 15 seconds and a thickness of 120 pixels. The voltage on the chip was 30 V with a frequency of 5 kHz.

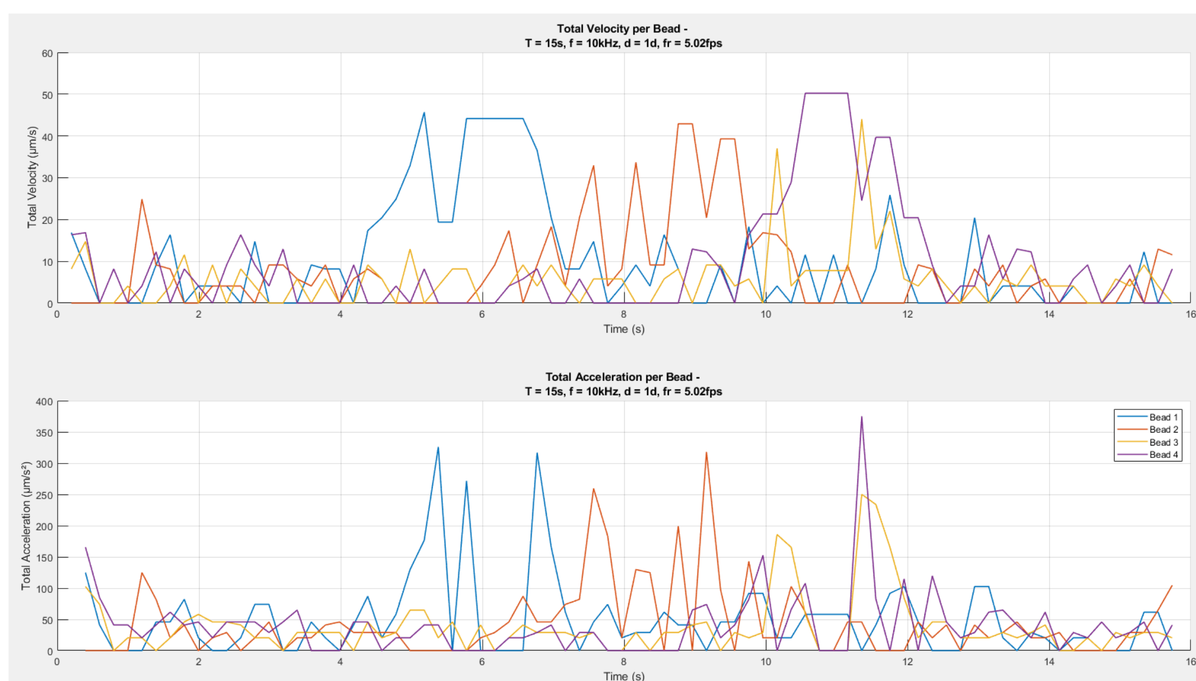

Figure D.36: The measured velocities and accelerations of the 15 µm polystyrene beads in the OET with a medium of deionized water with 0.05% Tween-20. The used sweep animation had a sweep time of 15 seconds and a thickness of 30 pixels. The voltage on the chip was 30 V with a frequency of 10 kHz.

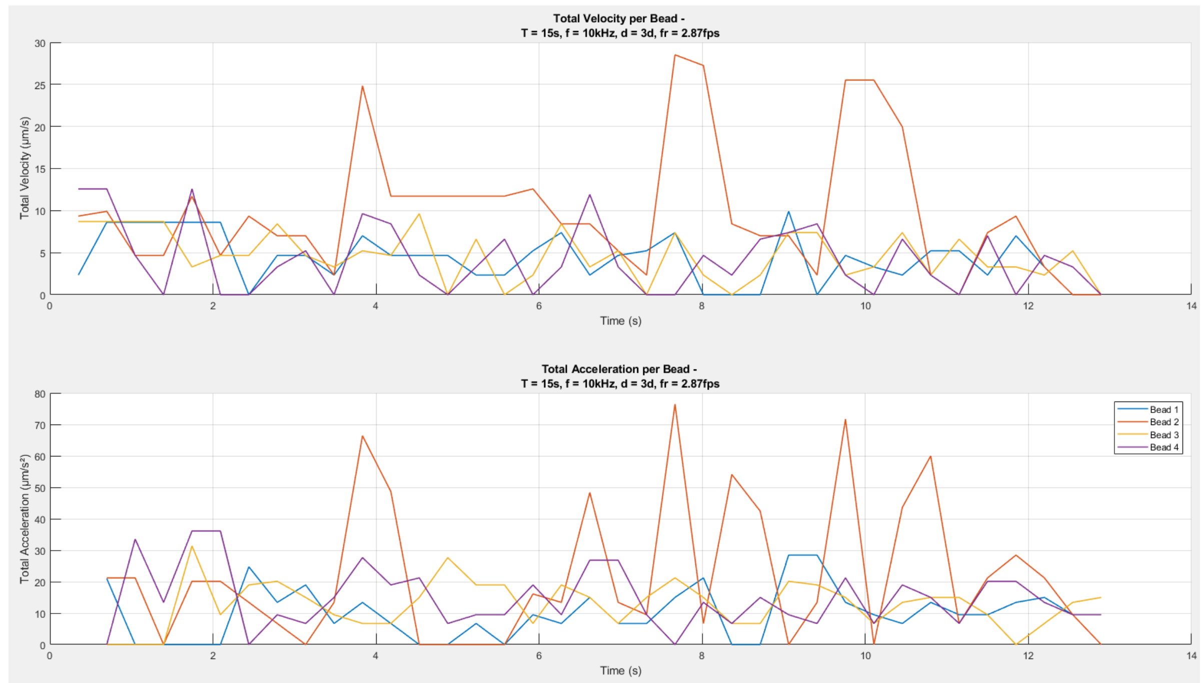

Figure D.37: The measured velocities and accelerations of the 15 µm polystyrene beads in the OET with a medium of deionized water with 0.05% Tween-20. The used sweep animation had a sweep time of 15 seconds and a thickness of 90 pixels. The voltage on the chip was 30 V with a frequency of 10 kHz.

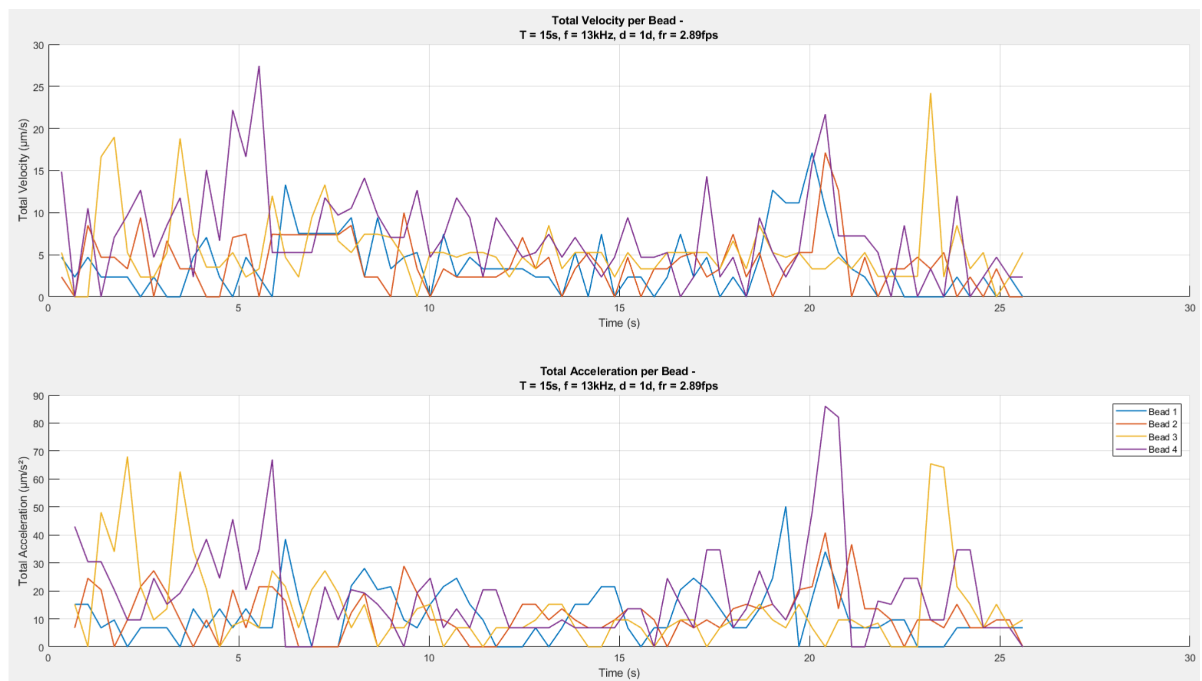

Figure D.38: The measured velocities and accelerations of the 15 µm polystyrene beads in the OET with a medium of deionized water with 0.05% Tween-20. The used sweep animation had a sweep time of 15 seconds and a thickness of 30 pixels. The voltage on the chip was 30 V with a frequency of 13 kHz.

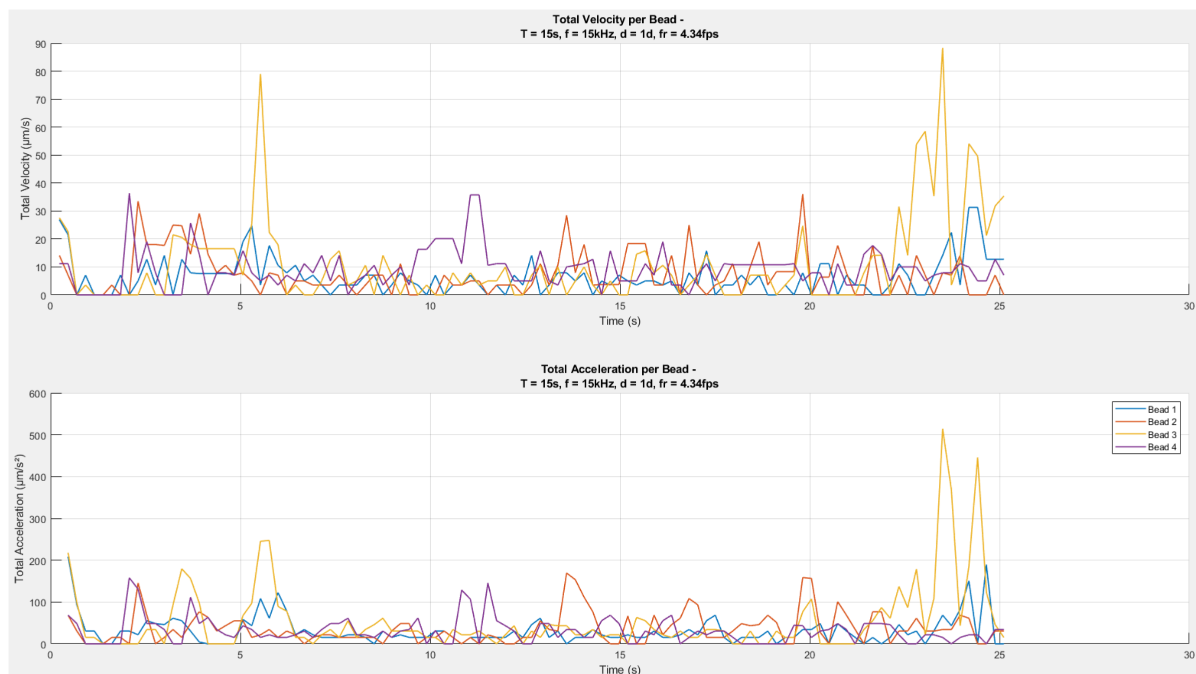

Figure D.39: The measured velocities and accelerations of the 15 µm polystyrene beads in the OET with a medium of deionized water with 0.05% Tween-20. The used sweep animation had a sweep time of 15 seconds and a thickness of 30 pixels. The voltage on the chip was 30 V with a frequency of 15 kHz.

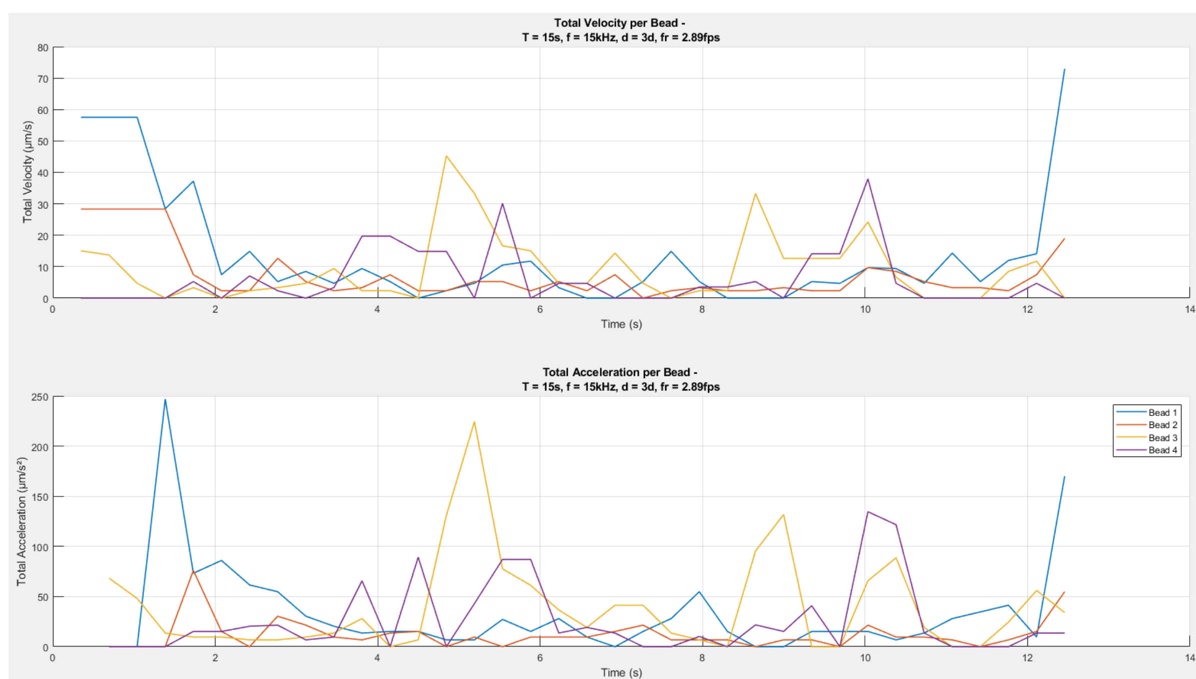

Figure D.40: The measured velocities and accelerations of the 15 µm polystyrene beads in the OET with a medium of deionized water with 0.05% Tween-20. The used sweep animation had a sweep time of 15 seconds and a thickness of 90 pixels. The voltage on the chip was 30 V with a frequency of 15 kHz.

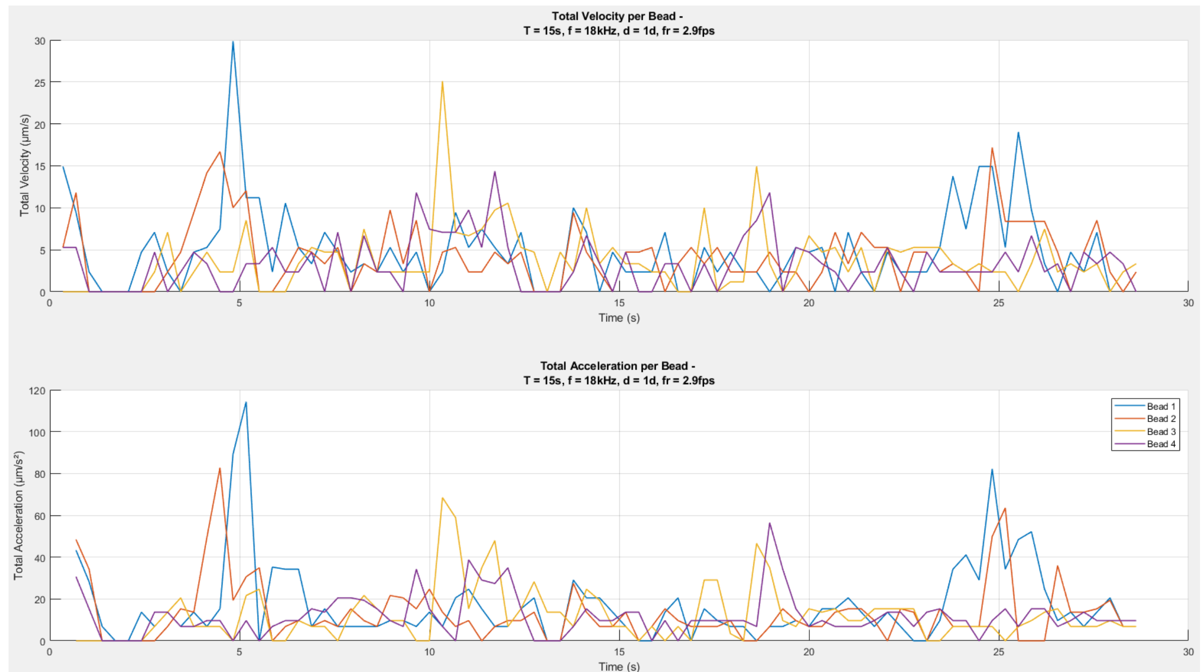

Figure D.41: The measured velocities and accelerations of the 15 µm polystyrene beads in the OET with a medium of deionized water with 0.05% Tween-20. The used sweep animation had a sweep time of 15 seconds and a thickness of 30 pixels. The voltage on the chip was 30 V with a frequency of 18 kHz.

D.2.2. Gear motion

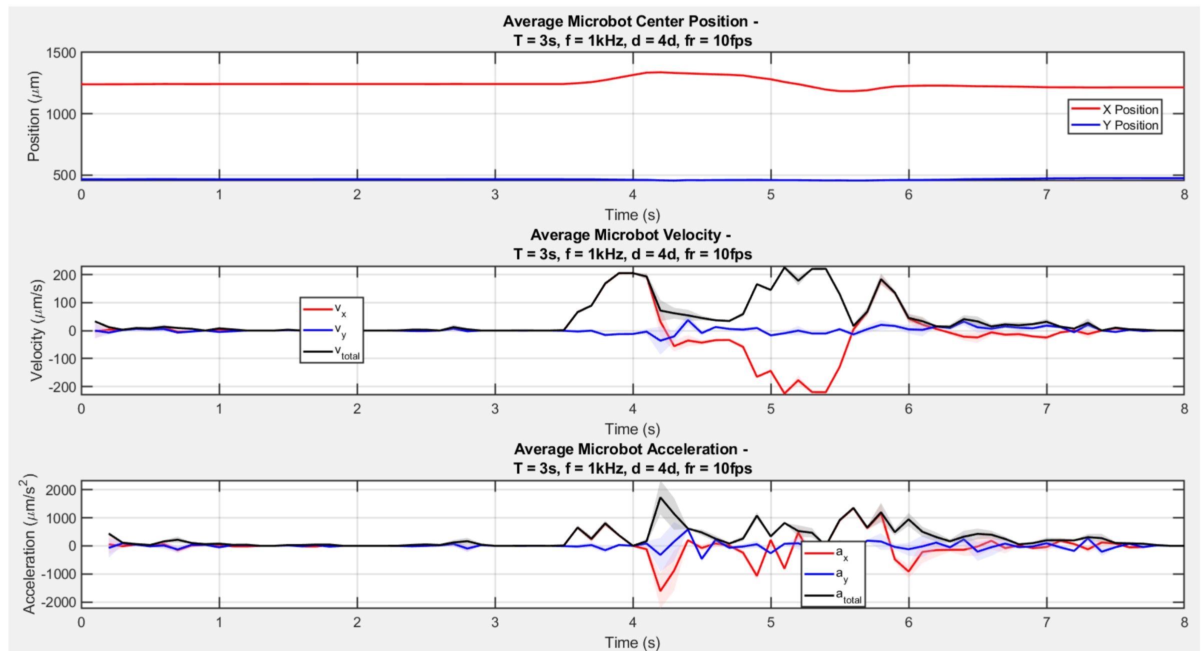

Figure D.42: The measured positions, velocities, and accelerations of the center position of the microbot in the OET with a medium of deionized water with 0.05% Tween-20. The used sweep animation had a sweep time of 3 seconds and a thickness of 120 pixels. The voltage on the chip was 30 V with a frequency of 18 kHz.

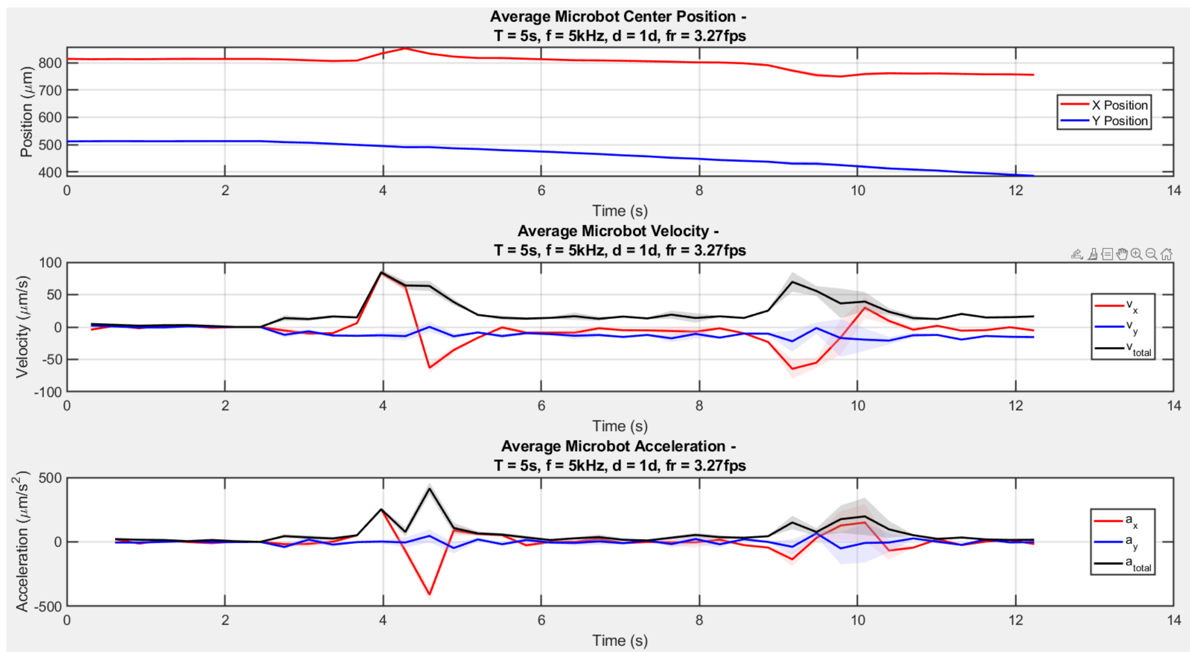

Figure D.43: The measured positions, velocities, and accelerations of the center position of the microbot in the OET with a medium of deionized water with 0.05% Tween-20. The used sweep animation had a sweep time of 5 seconds and a thickness of 30 pixels. The voltage on the chip was 30 V with a frequency of 5 kHz.

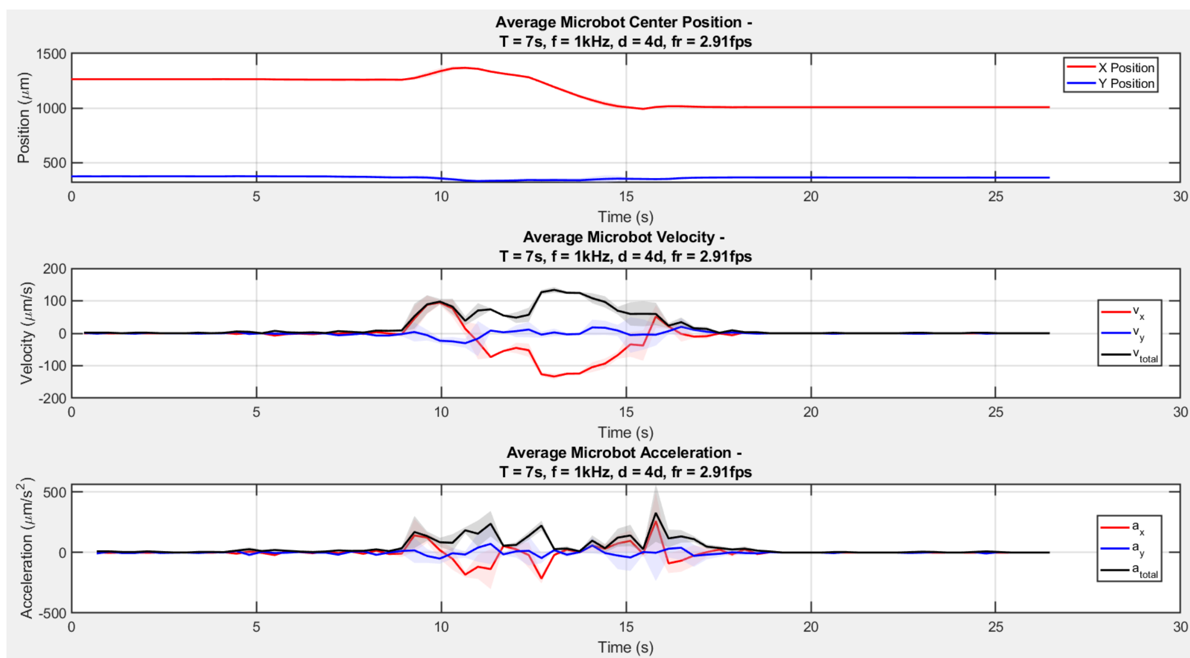

Figure D.44: The measured positions, velocities, and accelerations of the center position of the microbot in the OET with a medium of deionized water with 0.05% Tween-20. The used sweep animation had a sweep time of 7 seconds and a thickness of 120 pixels. The voltage on the chip was 30 V with a frequency of 1 kHz.

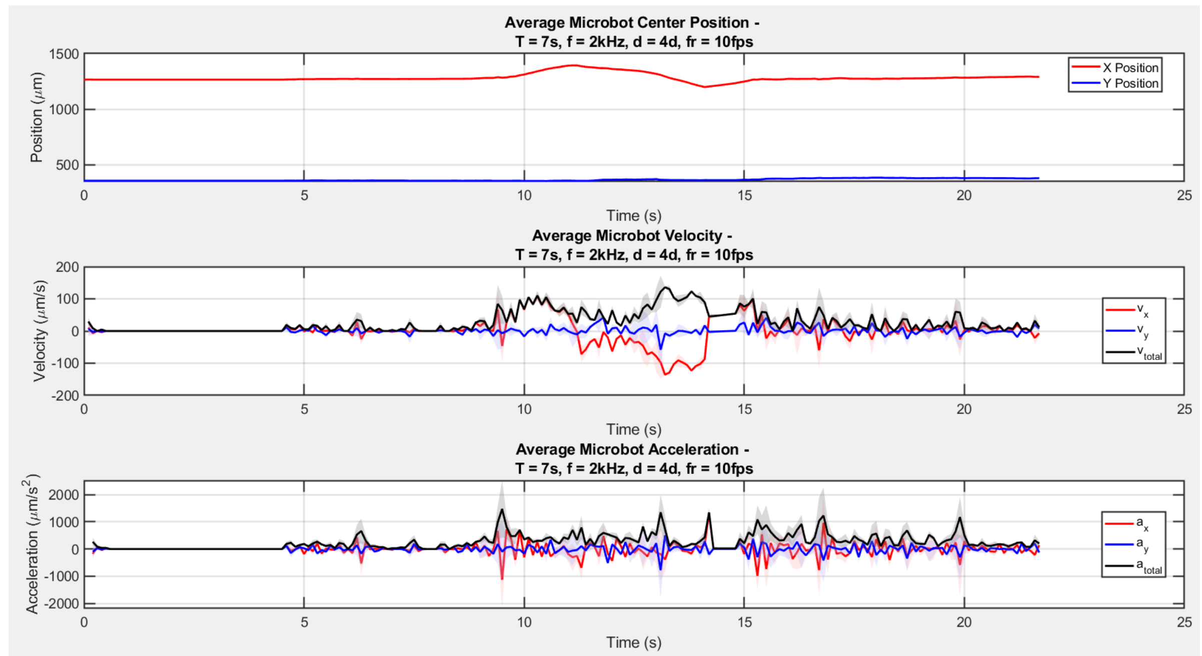

Figure D.45: The measured positions, velocities, and accelerations of the center position of the microbot in the OET with a medium of deionized water with 0.05% Tween-20. The used sweep animation had a sweep time of 7 seconds and a thickness of 120 pixels. The voltage on the chip was 30 V with a frequency of 2 kHz.

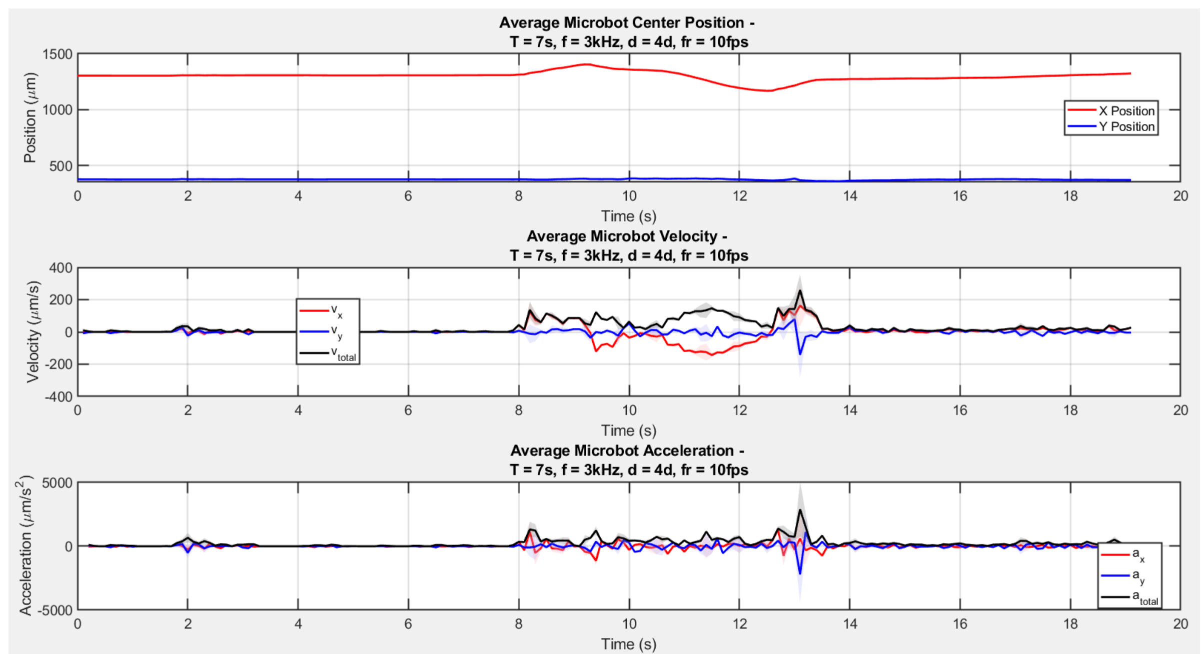

Figure D.46: The measured positions, velocities, and accelerations of the center position of the microbot in the OET with a medium of deionized water with 0.05% Tween-20. The used sweep animation had a sweep time of 7 seconds and a thickness of 120 pixels. The voltage on the chip was 30 V with a frequency of 3 kHz.

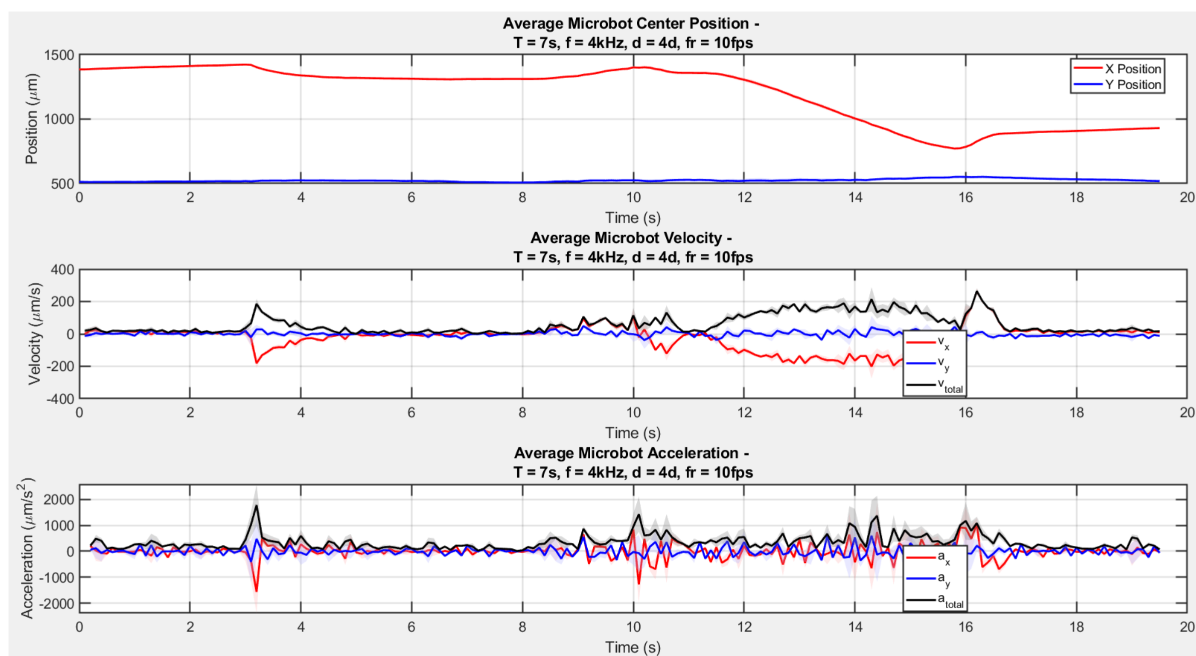

Figure D.47: The measured positions, velocities, and accelerations of the center position of the microbot in the OET with a medium of deionized water with 0.05% Tween-20. The used sweep animation had a sweep time of 7 seconds and a thickness of 120 pixels. The voltage on the chip was 30 V with a frequency of 4 kHz.

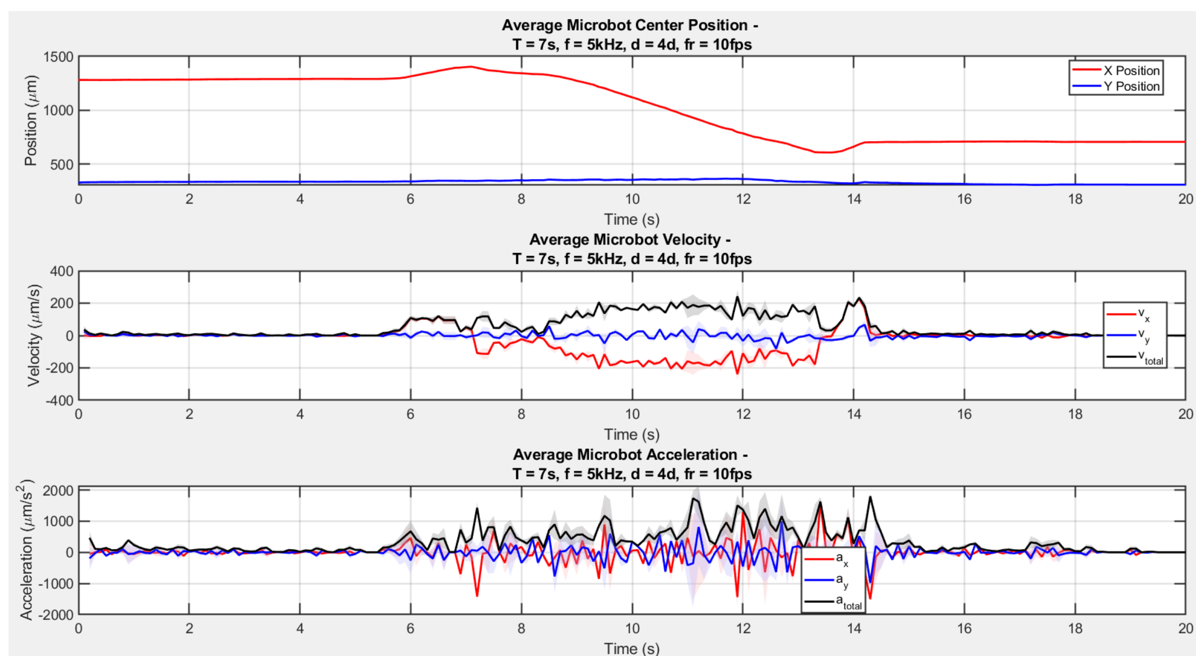

Figure D.48: The measured positions, velocities, and accelerations of the center position of the microbot in the OET with a medium of deionized water with 0.05% Tween-20. The used sweep animation had a sweep time of 7 seconds and a thickness of 120 pixels. The voltage on the chip was 30 V with a frequency of 5 kHz.

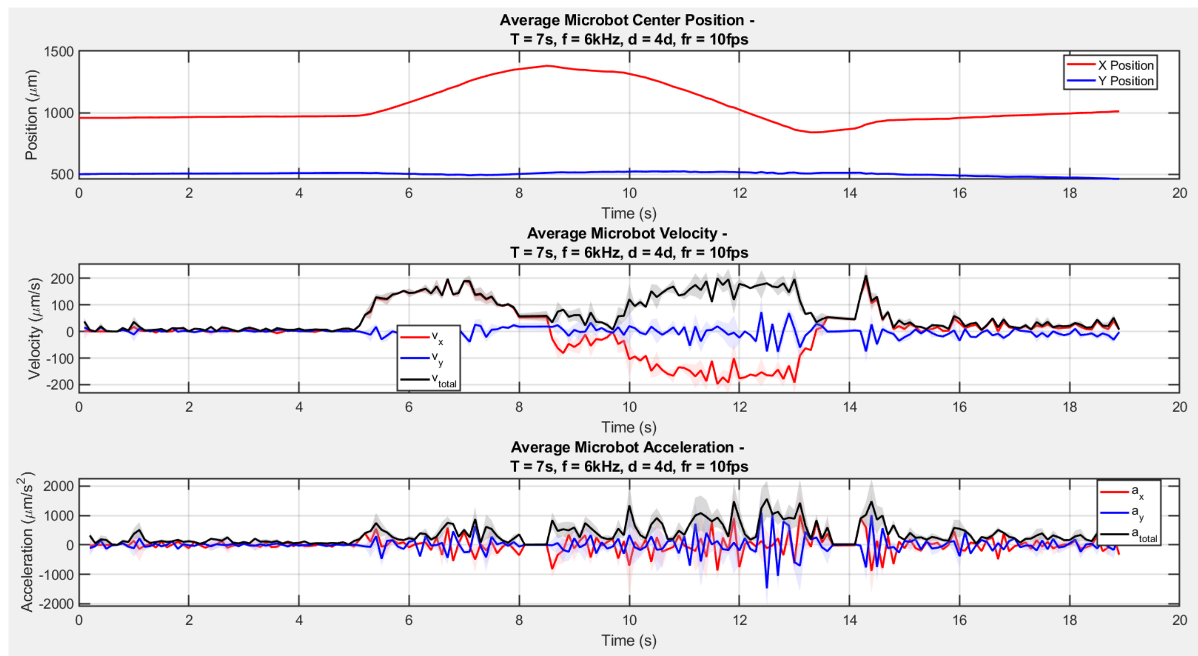

Figure D.49: The measured positions, velocities, and accelerations of the center position of the microbot in the OET with a medium of deionized water with 0.05% Tween-20. The used sweep animation had a sweep time of 7 seconds and a thickness of 120 pixels. The voltage on the chip was 30 V with a frequency of 6 kHz.

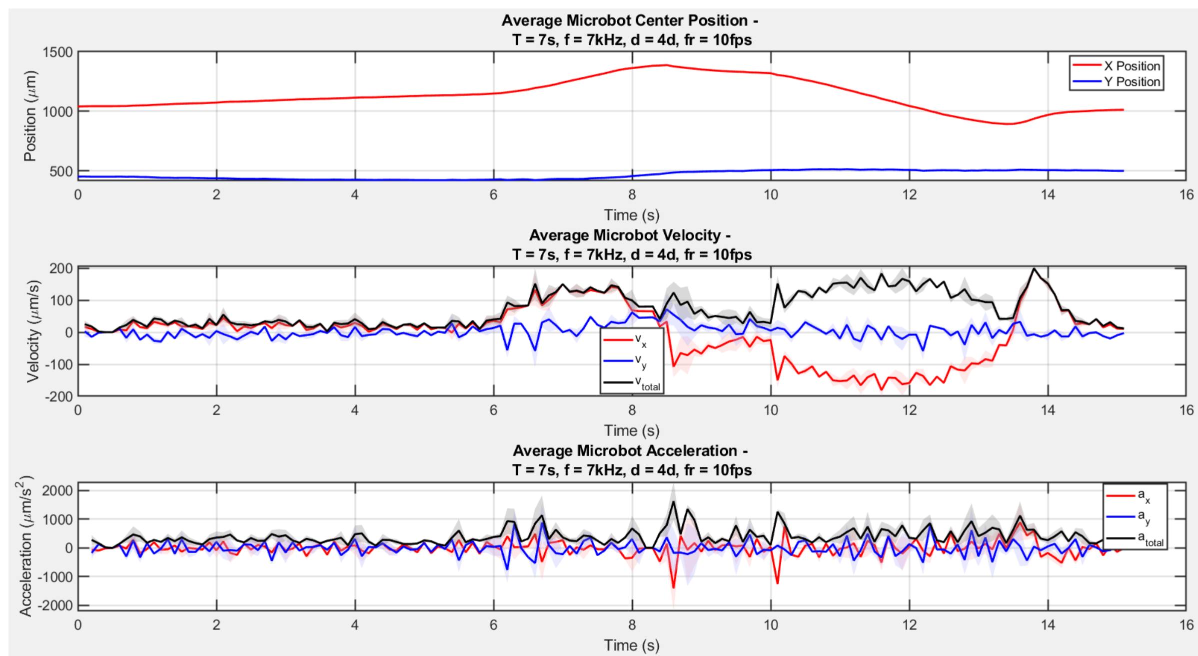

Figure D.50: The measured positions, velocities, and accelerations of the center position of the microbot in the OET with a medium of deionized water with 0.05% Tween-20. The used sweep animation had a sweep time of 7 seconds and a thickness of 120 pixels. The voltage on the chip was 30 V with a frequency of 7 kHz.

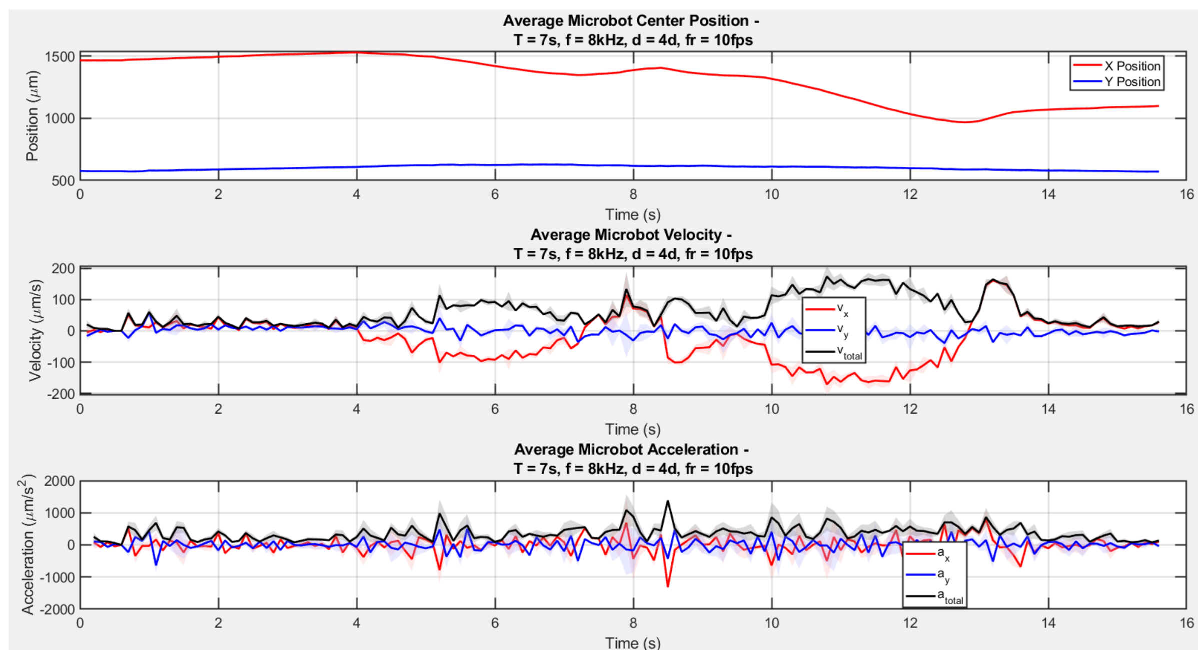

Figure D.51: The measured positions, velocities, and accelerations of the center position of the microbot in the OET with a medium of deionized water with 0.05% Tween-20. The used sweep animation had a sweep time of 7 seconds and a thickness of 120 pixels. The voltage on the chip was 30 V with a frequency of 8 kHz.

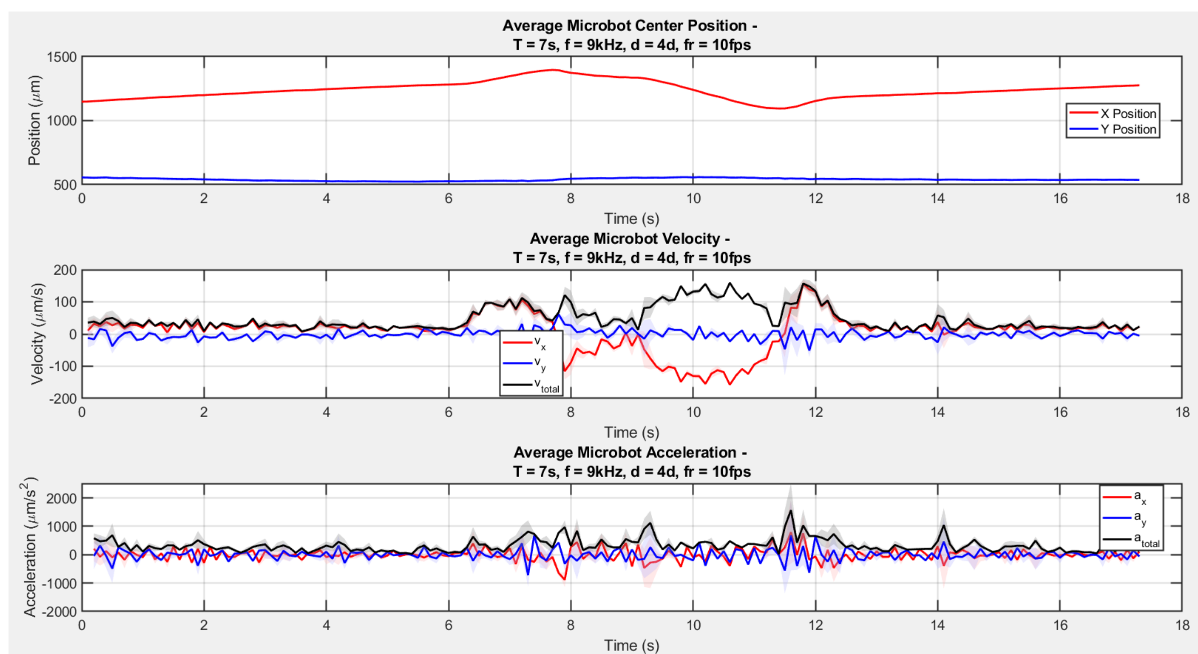

Figure D.52: The measured positions, velocities, and accelerations of the center position of the microbot in the OET with a medium of deionized water with 0.05% Tween-20. The used sweep animation had a sweep time of 7 seconds and a thickness of 120 pixels. The voltage on the chip was 30 V with a frequency of 9 kHz.

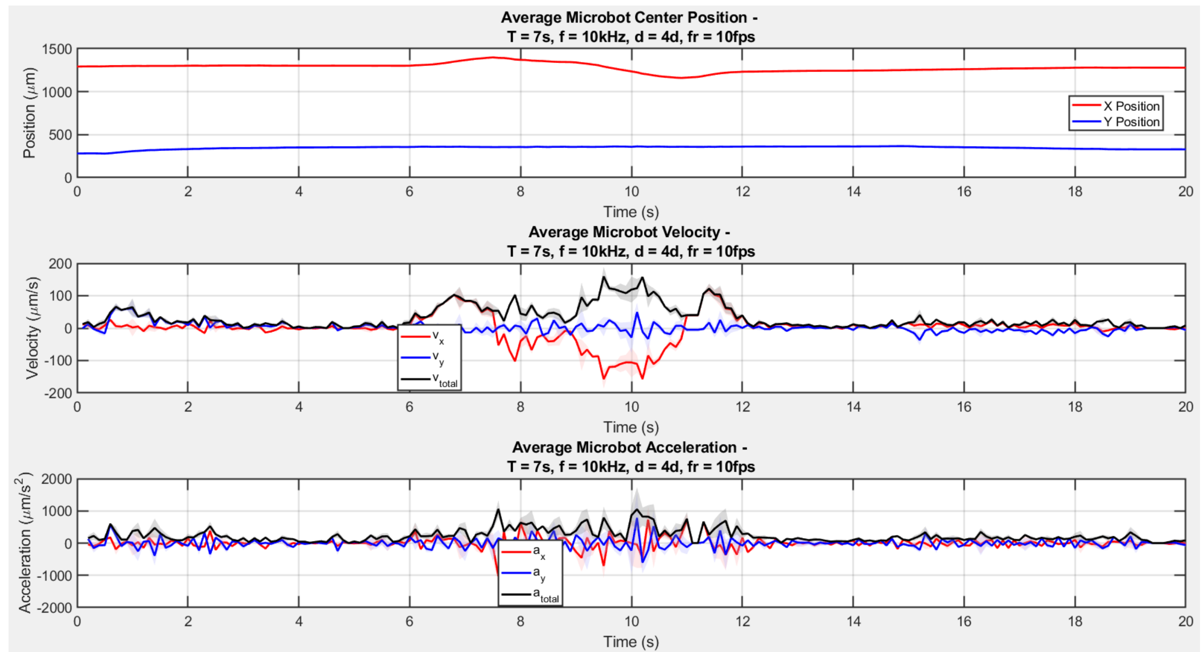

Figure D.53: The measured positions, velocities, and accelerations of the center position of the microbot in the OET with a medium of deionized water with 0.05% Tween-20. The used sweep animation had a sweep time of 7 seconds and a thickness of 120 pixels. The voltage on the chip was 30 V with a frequency of 10 kHz.

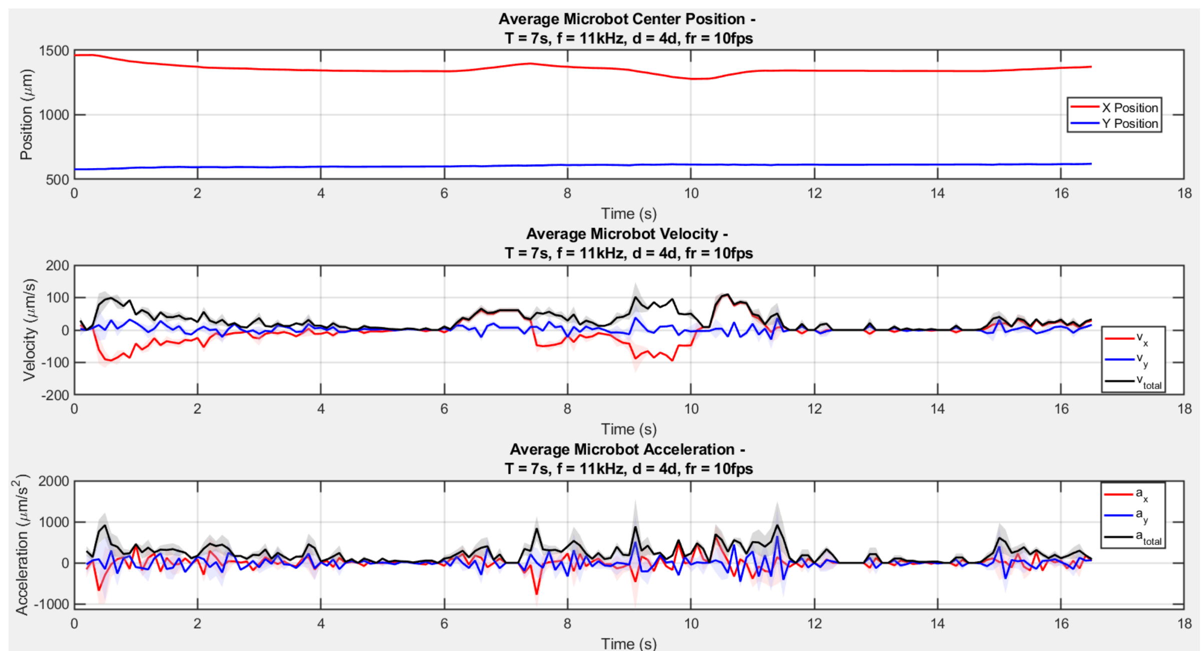

Figure D.54: The measured positions, velocities, and accelerations of the center position of the microbot in the OET with a medium of deionized water with 0.05% Tween-20. The used sweep animation had a sweep time of 7 seconds and a thickness of 120 pixels. The voltage on the chip was 30 V with a frequency of 11 kHz.

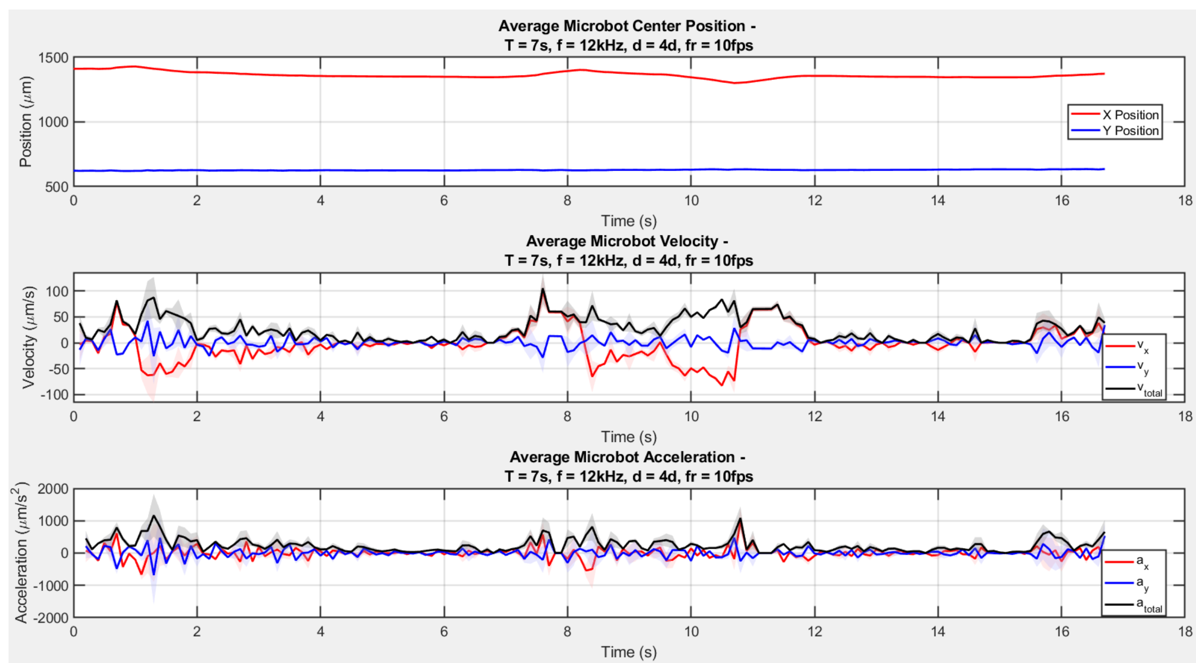

Figure D.55: The measured positions, velocities, and accelerations of the center position of the microbot in the OET with a medium of deionized water with 0.05% Tween-20. The used sweep animation had a sweep time of 7 seconds and a thickness of 120 pixels. The voltage on the chip was 30 V with a frequency of 12 kHz.

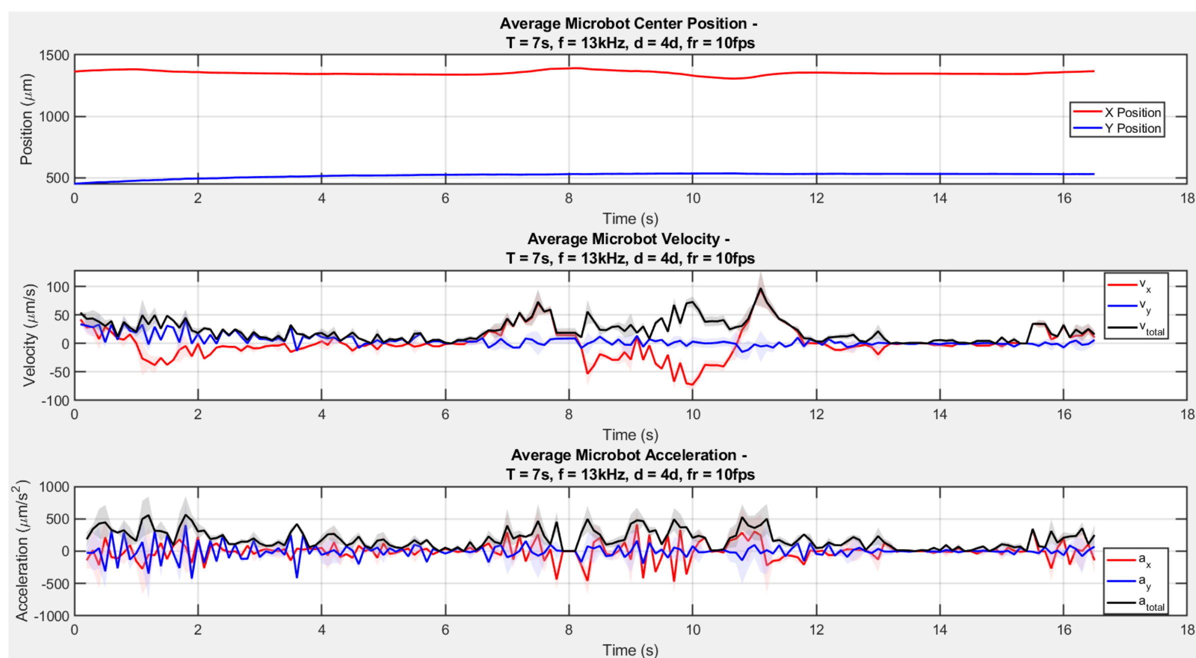

Figure D.56: The measured positions, velocities, and accelerations of the center position of the microbot in the OET with a medium of deionized water with 0.05% Tween-20. The used sweep animation had a sweep time of 7 seconds and a thickness of 120 pixels. The voltage on the chip was 30 V with a frequency of 13 kHz.

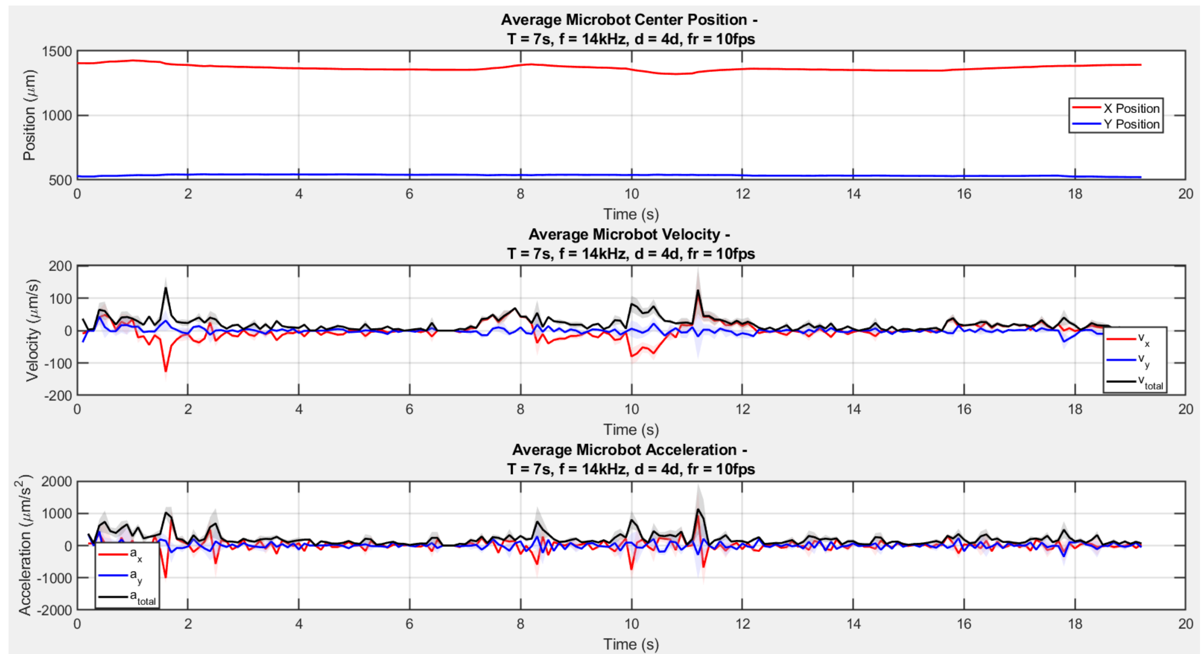

Figure D.57: The measured positions, velocities, and accelerations of the center position of the microbot in the OET with a medium of deionized water with 0.05% Tween-20. The used sweep animation had a sweep time of 7 seconds and a thickness of 120 pixels. The voltage on the chip was 30 V with a frequency of 14 kHz.

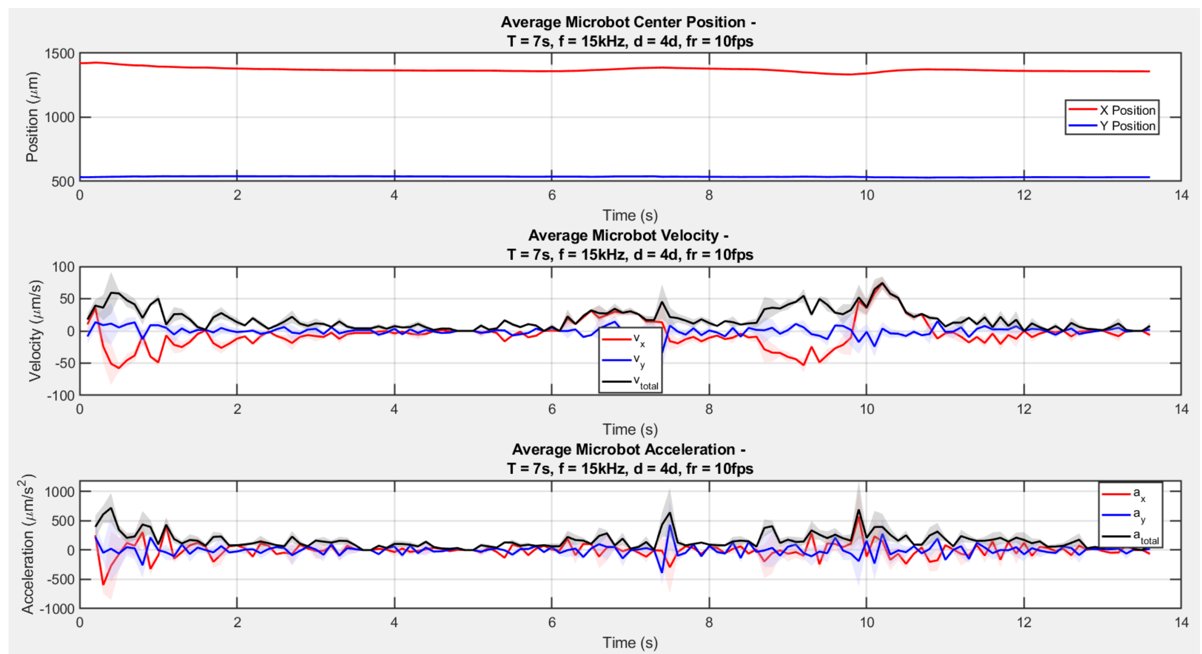

Figure D.58: The measured positions, velocities, and accelerations of the center position of the microbot in the OET with a medium of deionized water with 0.05% Tween-20. The used sweep animation had a sweep time of 7 seconds and a thickness of 120 pixels. The voltage on the chip was 30 V with a frequency of 15 kHz.

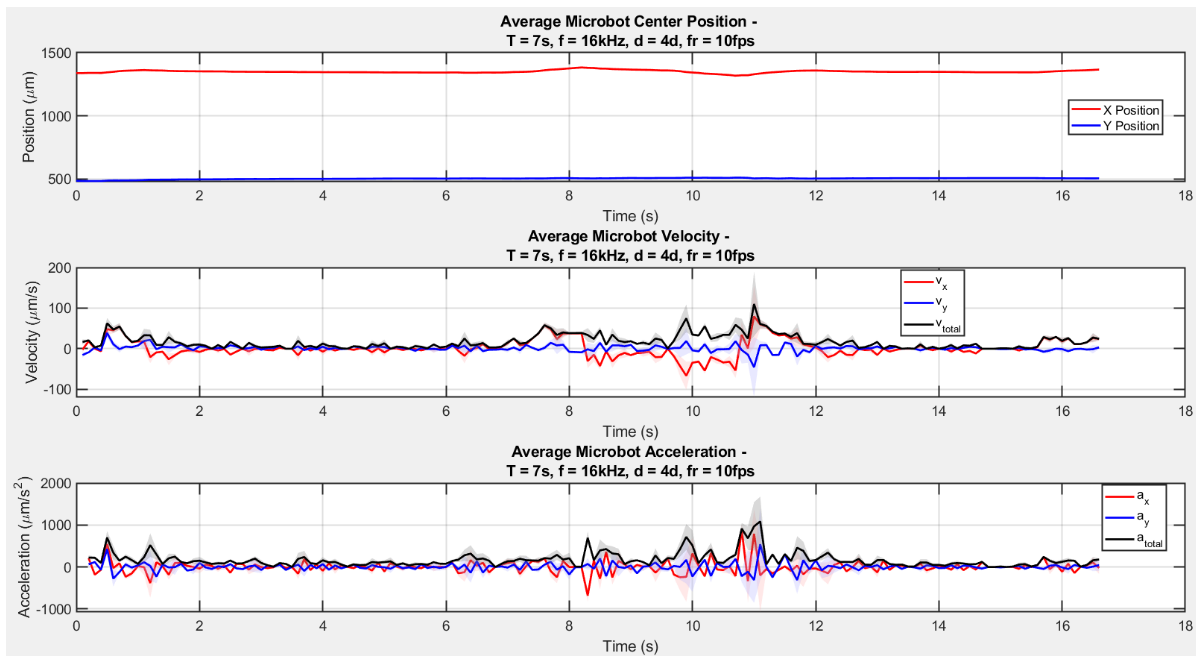

Figure D.59: The measured positions, velocities, and accelerations of the center position of the microbot in the OET with a medium of deionized water with 0.05% Tween-20. The used sweep animation had a sweep time of 7 seconds and a thickness of 120 pixels. The voltage on the chip was 30 V with a frequency of 16 kHz.

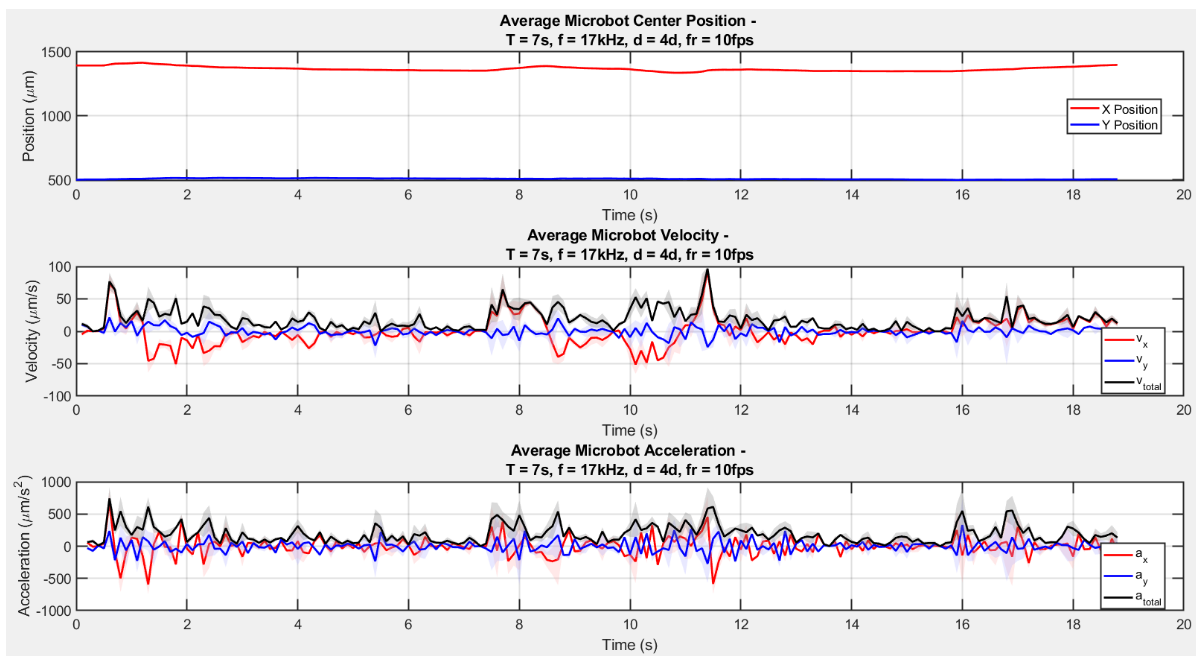

Figure D.60: The measured positions, velocities, and accelerations of the center position of the microbot in the OET with a medium of deionized water with 0.05% Tween-20. The used sweep animation had a sweep time of 7 seconds and a thickness of 120 pixels. The voltage on the chip was 30 V with a frequency of 17 kHz.

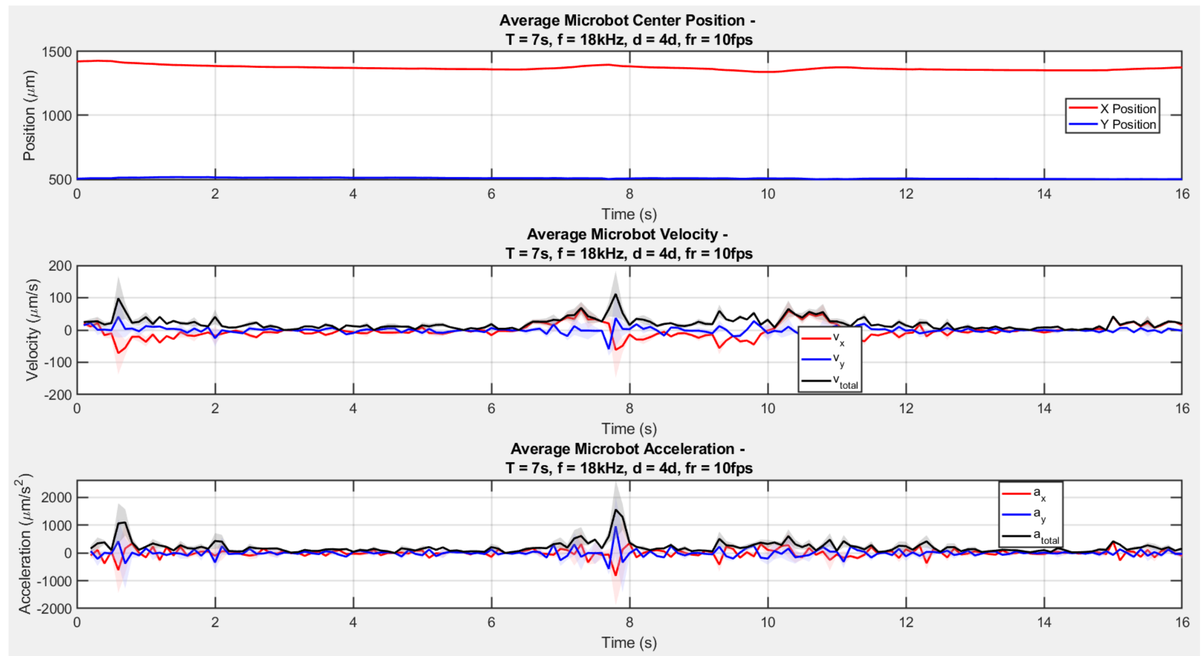

Figure D.61: The measured positions, velocities, and accelerations of the center position of the microbot in the OET with a medium of deionized water with 0.05% Tween-20. The used sweep animation had a sweep time of 7 seconds and a thickness of 120 pixels. The voltage on the chip was 30 V with a frequency of 18 kHz.

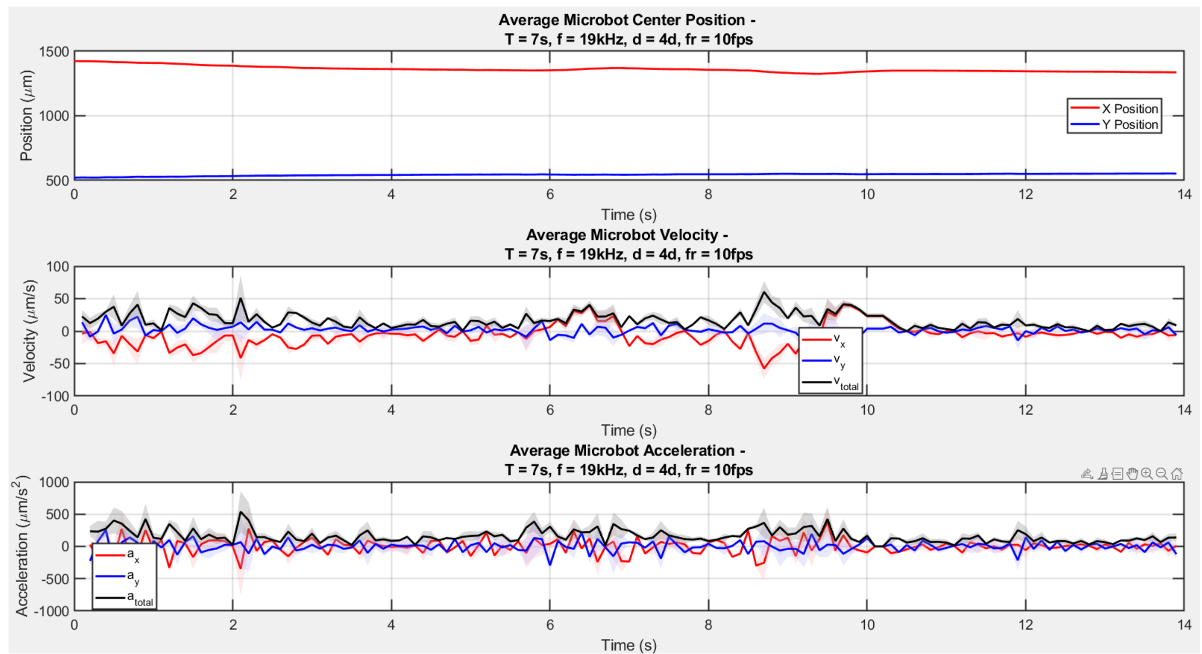

Figure D.62: The measured positions, velocities, and accelerations of the center position of the microbot in the OET with a medium of deionized water with 0.05% Tween-20. The used sweep animation had a sweep time of 7 seconds and a thickness of 120 pixels. The voltage on the chip was 30 V with a frequency of 19 kHz.

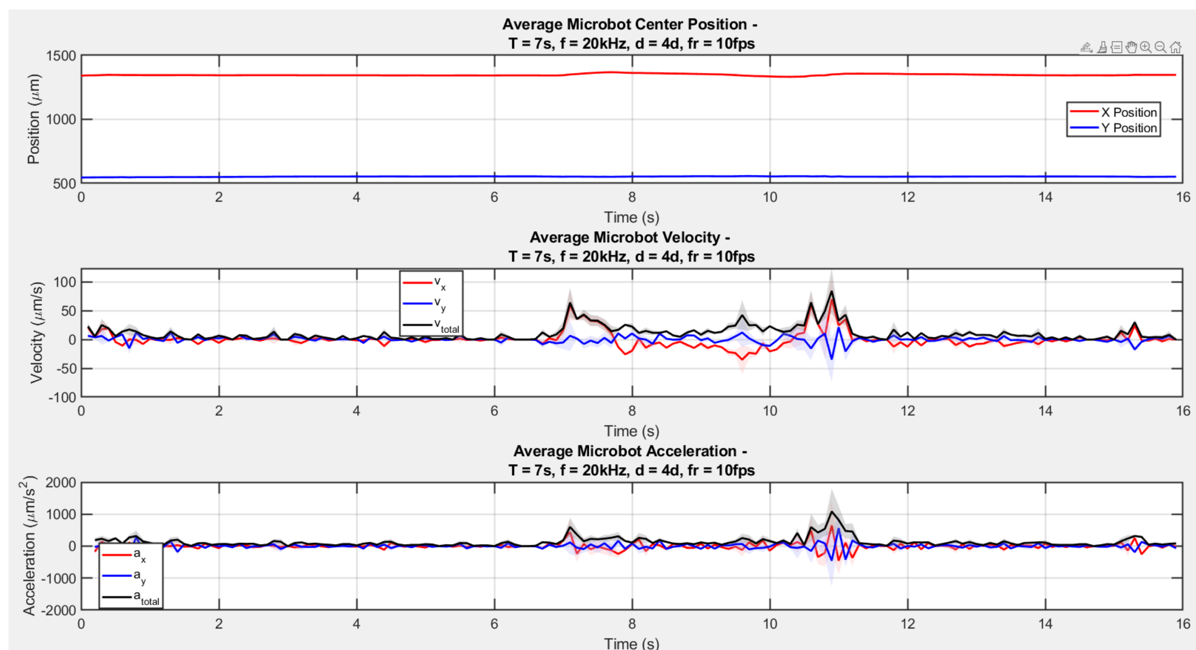

Figure D.63: The measured positions, velocities, and accelerations of the center position of the microbot in the OET with a medium of deionized water with 0.05% Tween-20. The used sweep animation had a sweep time of 7 seconds and a thickness of 120 pixels. The voltage on the chip was 30 V with a frequency of 20 kHz.

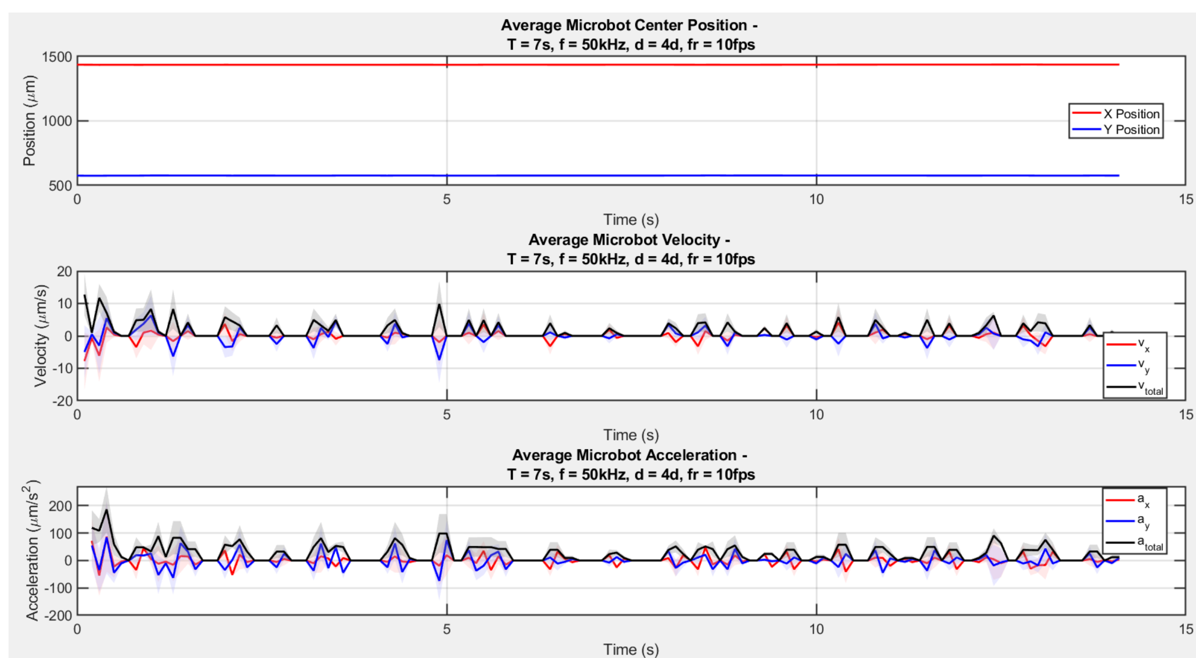

Figure D.64: The measured positions, velocities, and accelerations of the center position of the microbot in the OET with a medium of deionized water with 0.05% Tween-20. The used sweep animation had a sweep time of 7 seconds and a thickness of 120 pixels. The voltage on the chip was 30 V with a frequency of 50 kHz.

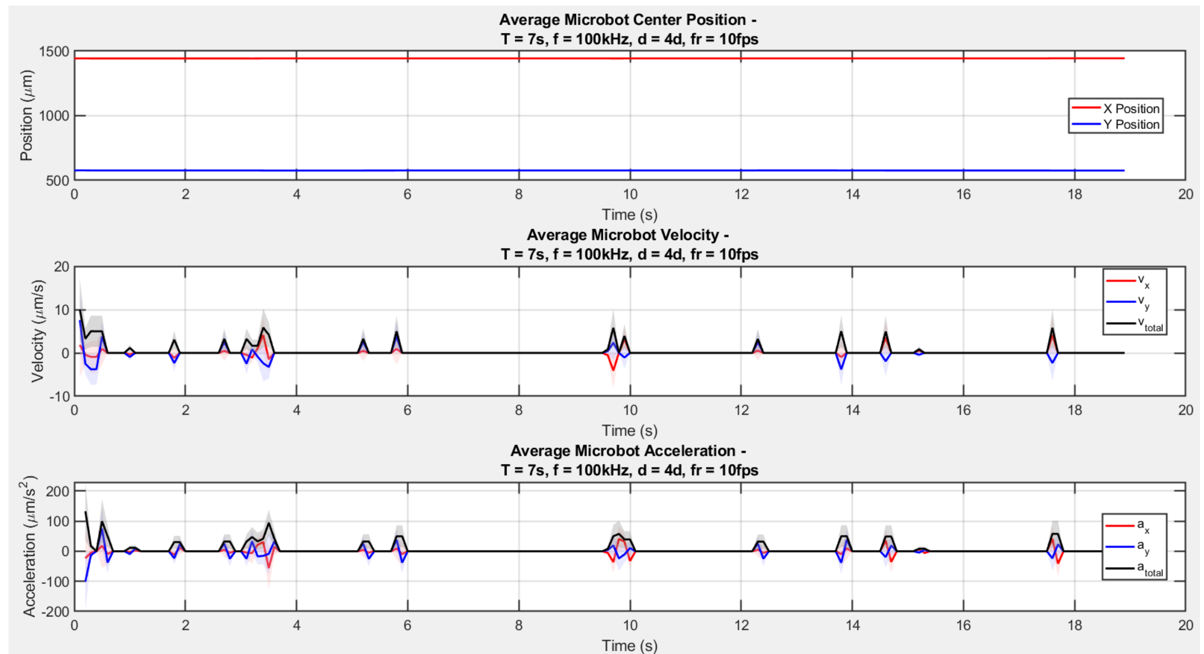

Figure D.65: The measured positions, velocities, and accelerations of the center position of the microbot in the OET with a medium of deionized water with 0.05% Tween-20. The used sweep animation had a sweep time of 7 seconds and a thickness of 120 pixels. The voltage on the chip was 30 V with a frequency of 100 kHz.

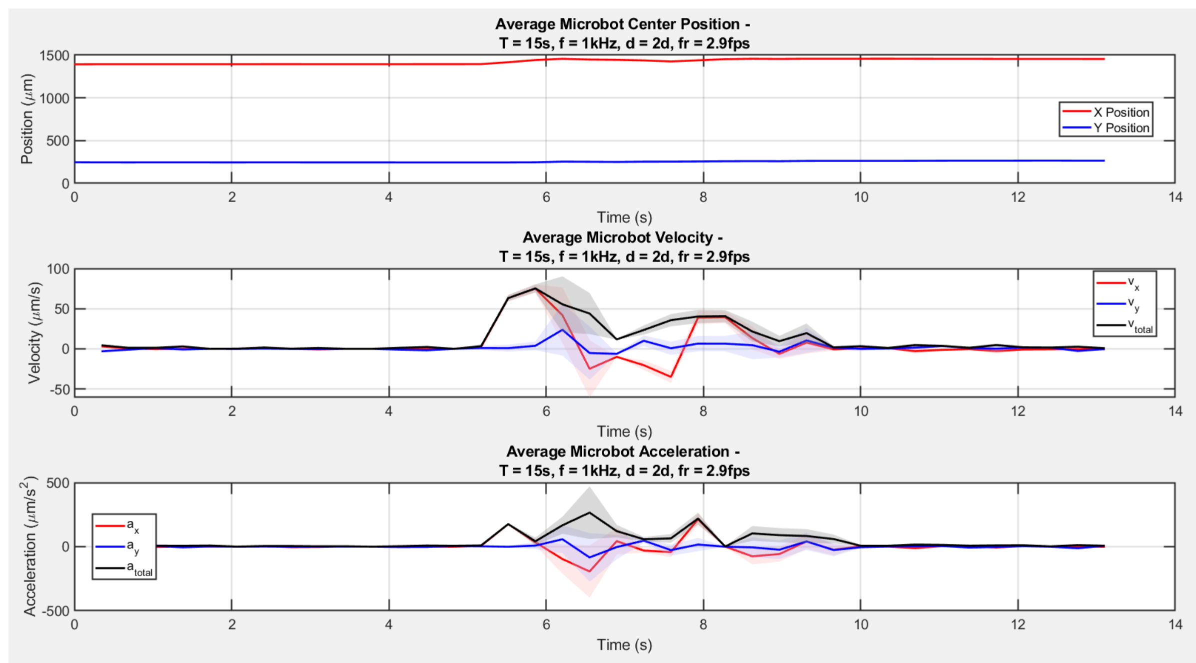

Figure D.66: The measured positions, velocities, and accelerations of the center position of the microbot in the OET with a medium of deionized water with 0.05% Tween-20. The used sweep animation had a sweep time of 15 seconds and a thickness of 60 pixels. The voltage on the chip was 30 V with a frequency of 1 kHz.

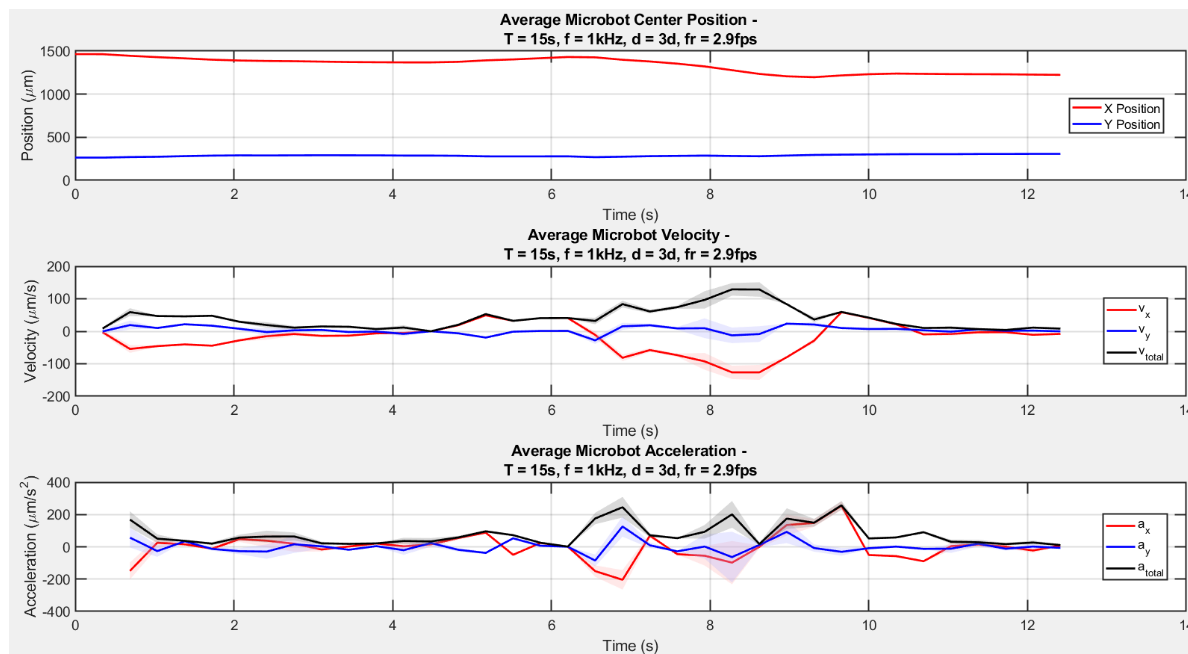

Figure D.67: The measured positions, velocities, and accelerations of the center position of the microbot in the OET with a medium of deionized water with 0.05% Tween-20. The used sweep animation had a sweep time of 15 seconds and a thickness of 90 pixels. The voltage on the chip was 30 V with a frequency of 1 kHz.

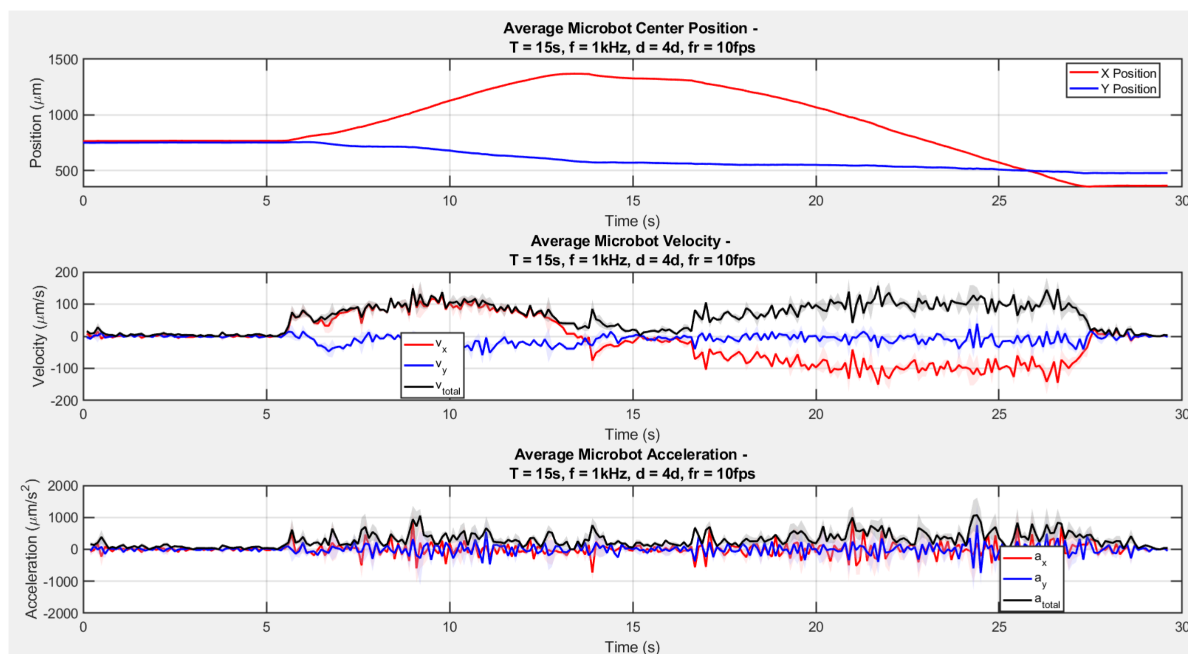

Figure D.68: The measured positions, velocities, and accelerations of the center position of the microbot in the OET with a medium of deionized water with 0.05% Tween-20. The used sweep animation had a sweep time of 15 seconds and a thickness of 120 pixels. The voltage on the chip was 30 V with a frequency of 1 kHz.

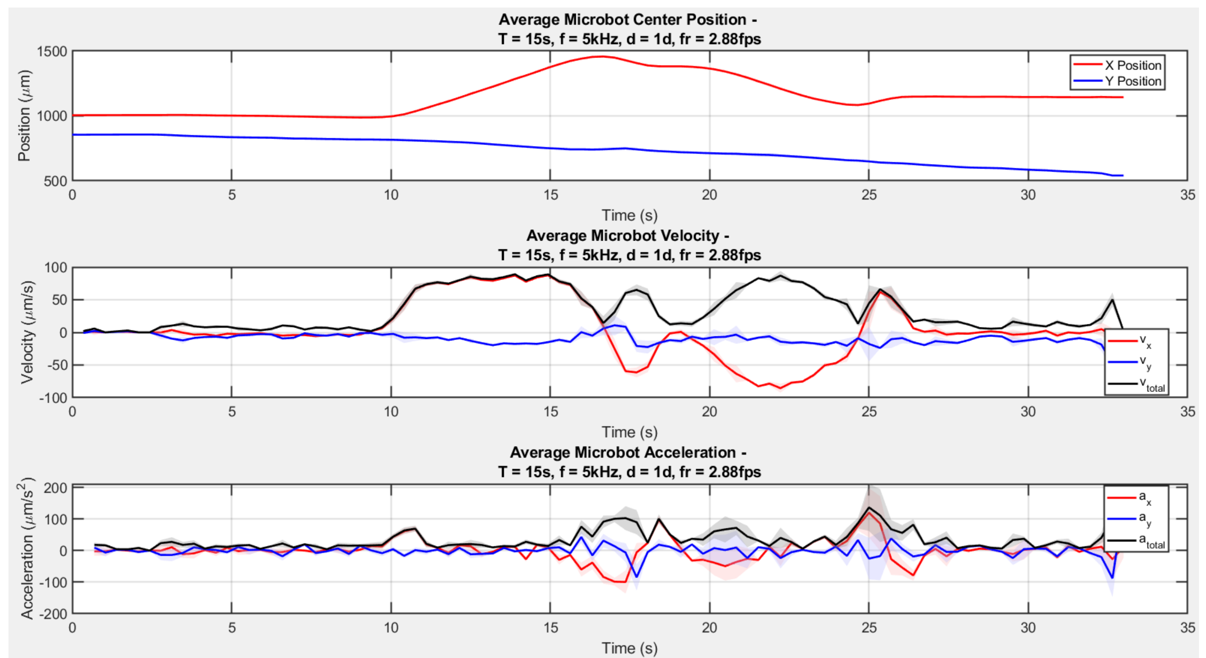

Figure D.69: The measured positions, velocities, and accelerations of the center position of the microbot in the OET with a medium of deionized water with 0.05% Tween-20. The used sweep animation had a sweep time of 15 seconds and a thickness of 30 pixels. The voltage on the chip was 30 V with a frequency of 5 kHz.

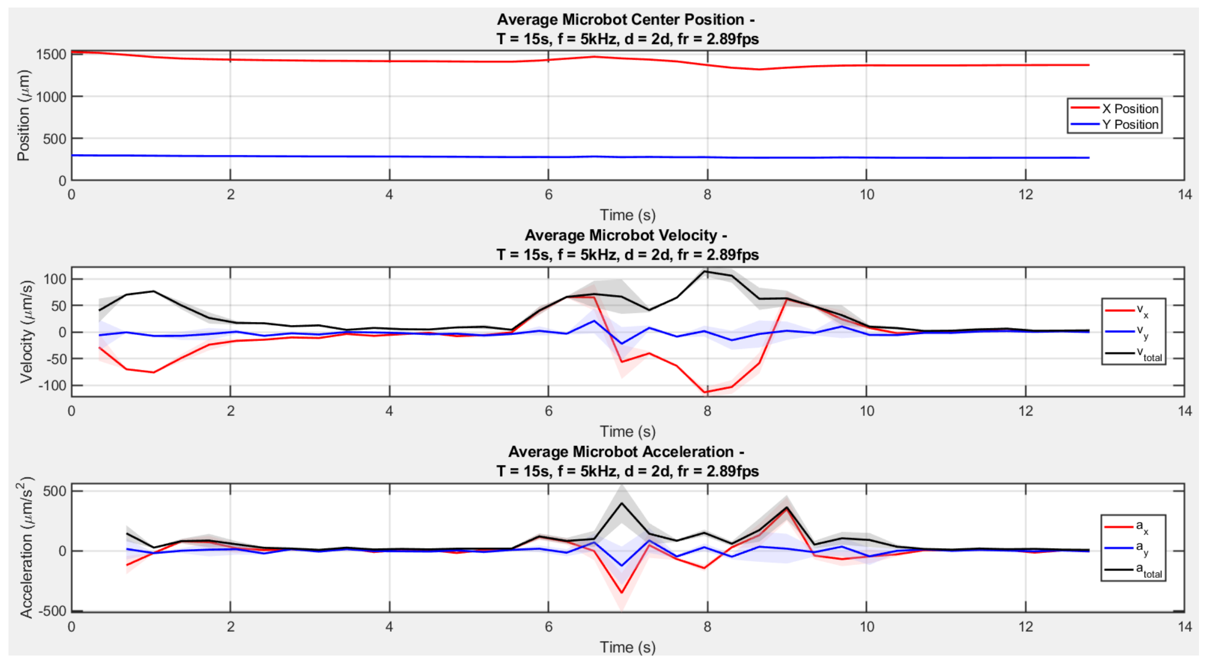

Figure D.70: The measured positions, velocities, and accelerations of the center position of the microbot in the OET with a medium of deionized water with 0.05% Tween-20. The used sweep animation had a sweep time of 15 seconds and a thickness of 60 pixels. The voltage on the chip was 30 V with a frequency of 5 kHz.

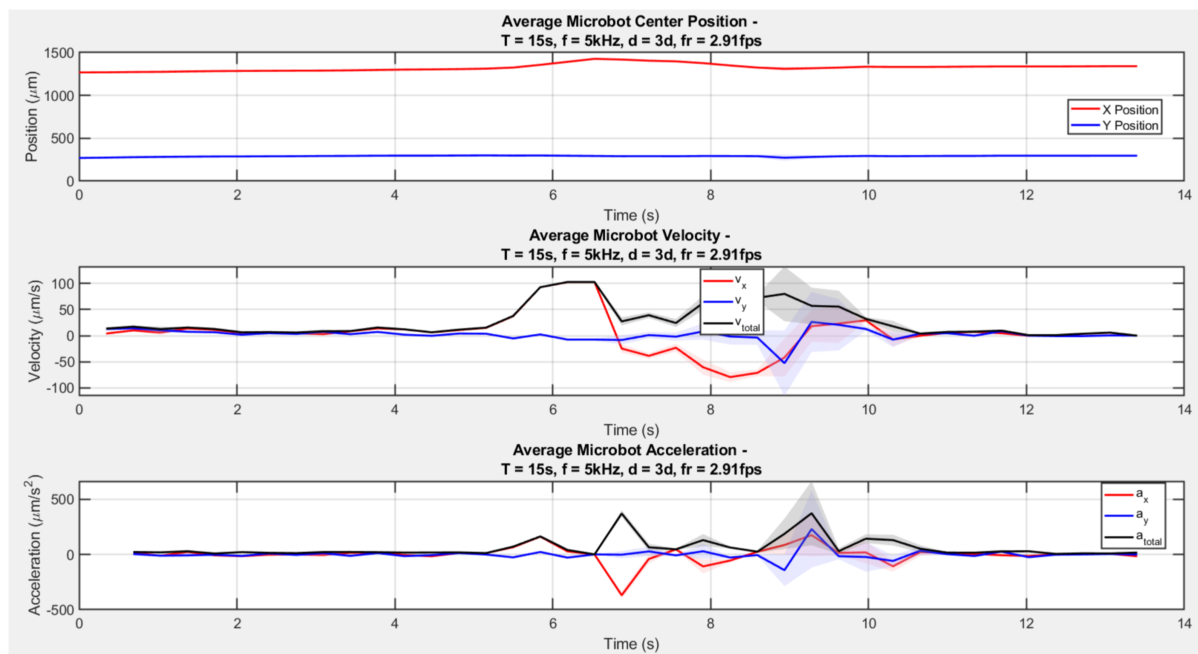

Figure D.71: The measured positions, velocities, and accelerations of the center position of the microbot in the OET with a medium of deionized water with 0.05% Tween-20. The used sweep animation had a sweep time of 15 seconds and a thickness of 90 pixels. The voltage on the chip was 30 V with a frequency of 5 kHz.

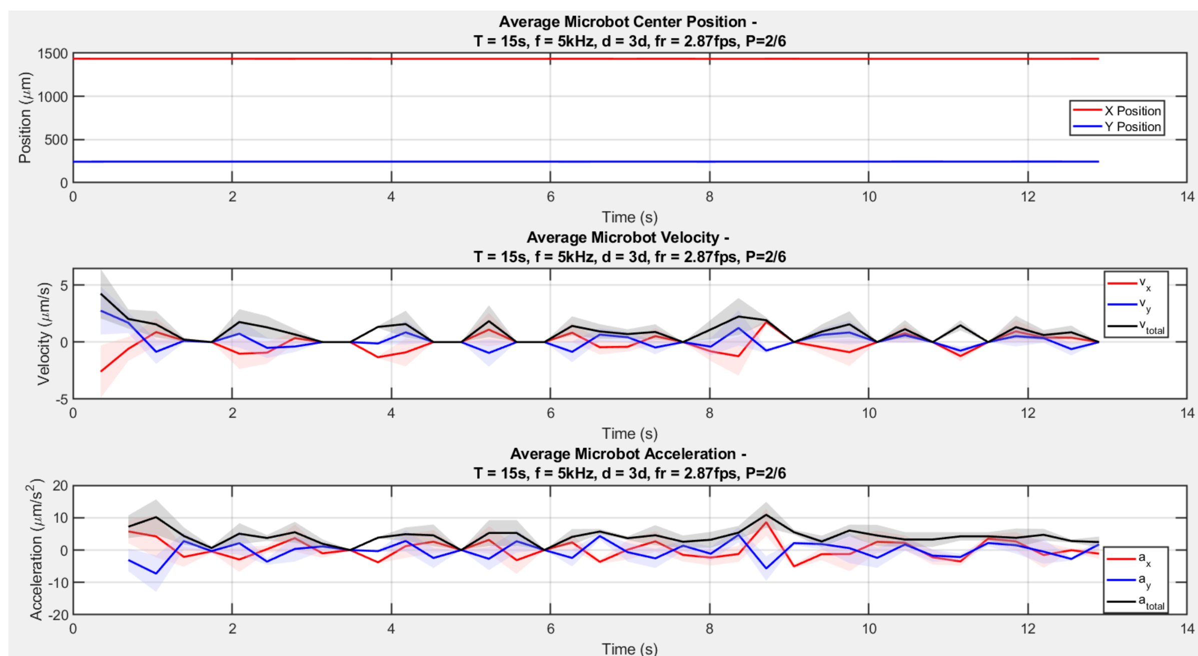

Figure D.72: The measured positions, velocities, and accelerations of the center position of the microbot in the OET with a medium of deionized water with 0.05% Tween-20. The used sweep animation had a sweep time of 15 seconds and a thickness of 90 pixels. The voltage on the chip was 30 V with a frequency of 5 kHz. The illumination was set to 1/3 of full power.

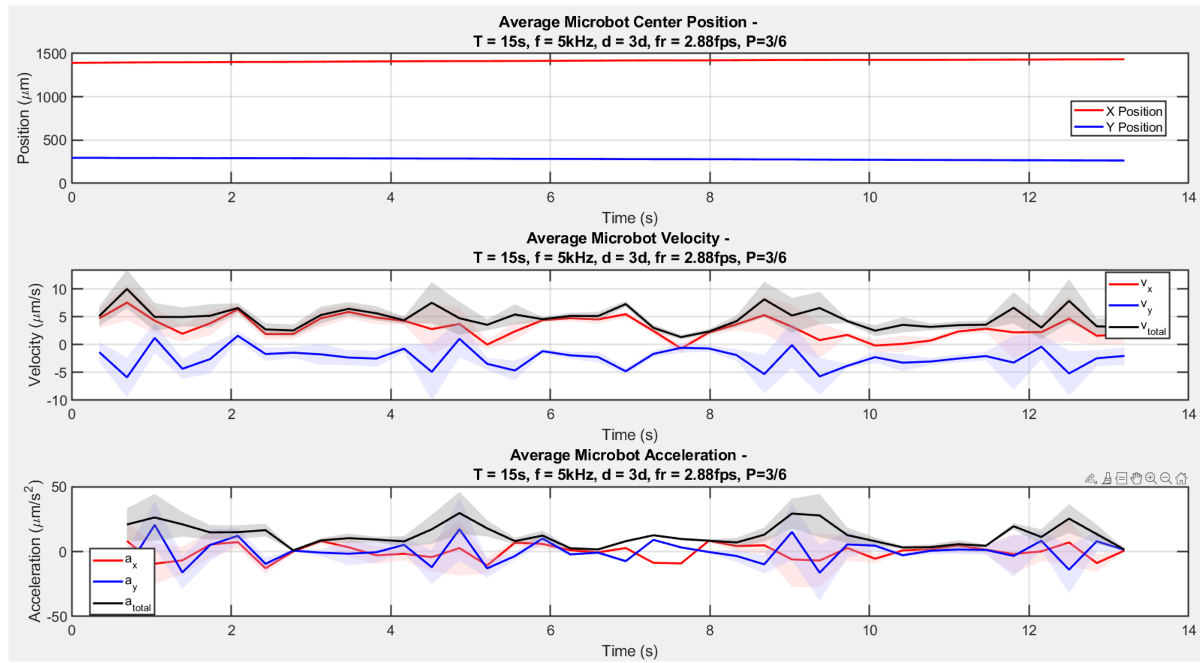

Figure D.73: The measured positions, velocities, and accelerations of the center position of the microbot in the OET with a medium of deionized water with 0.05% Tween-20. The used sweep animation had a sweep time of 15 seconds and a thickness of 90 pixels. The voltage on the chip was 30 V with a frequency of 5 kHz. The illumination was set to 1/2 of full power.

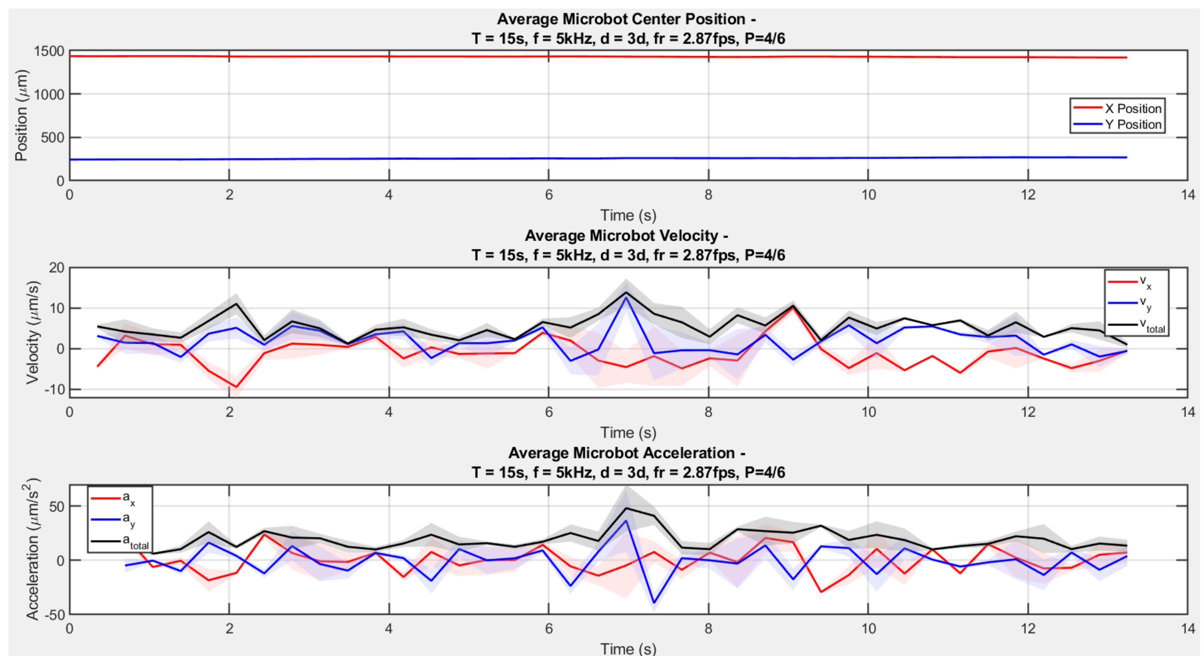

Figure D.74: The measured positions, velocities, and accelerations of the center position of the microbot in the OET with a medium of deionized water with 0.05% Tween-20. The used sweep animation had a sweep time of 15 seconds and a thickness of 90 pixels. The voltage on the chip was 30 V with a frequency of 5 kHz. The illumination was set to 2/3 of full power.

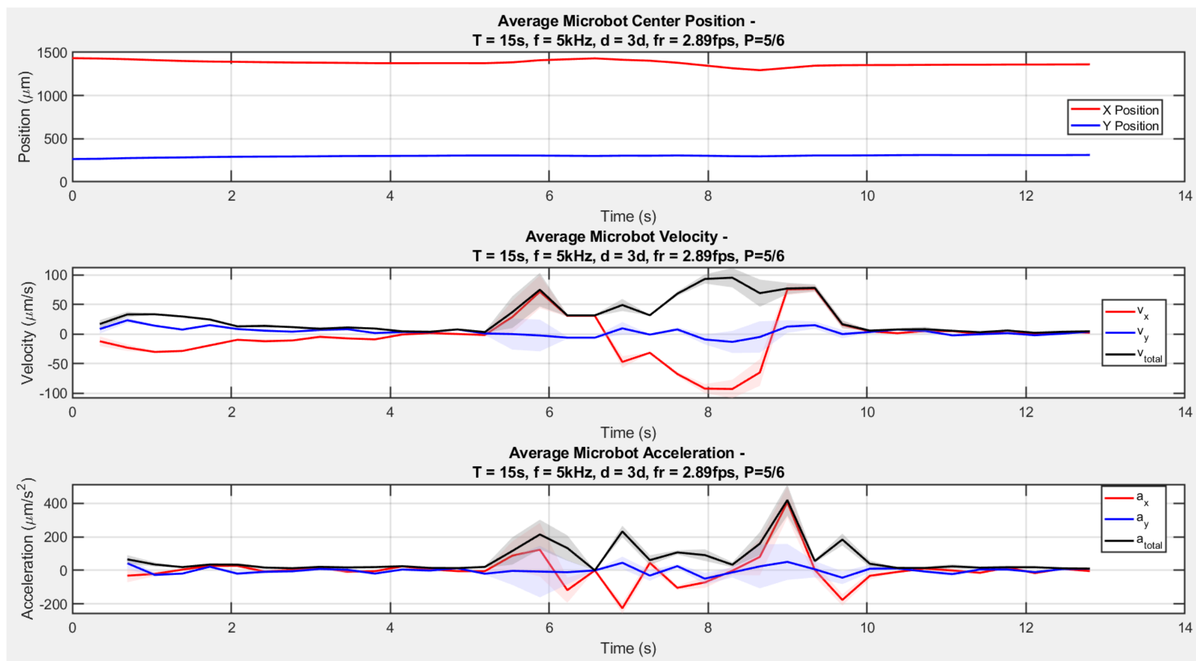

Figure D.75: The measured positions, velocities, and accelerations of the center position of the microbot in the OET with a medium of deionized water with 0.05% Tween-20. The used sweep animation had a sweep time of 15 seconds and a thickness of 90 pixels. The voltage on the chip was 30 V with a frequency of 5 kHz. The illumination was set to 5/6 of full power.

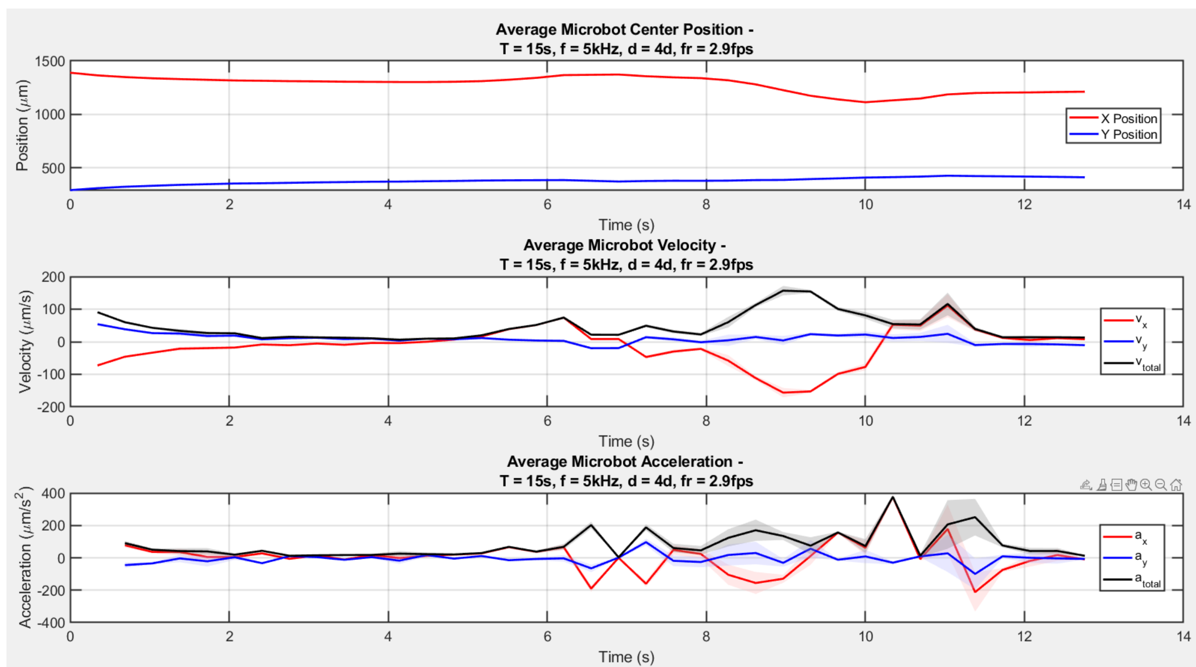

Figure D.76: The measured positions, velocities, and accelerations of the center position of the microbot in the OET with a medium of deionized water with 0.05% Tween-20. The used sweep animation had a sweep time of 15 seconds and a thickness of 120 pixels. The voltage on the chip was 30 V with a frequency of 5 kHz.

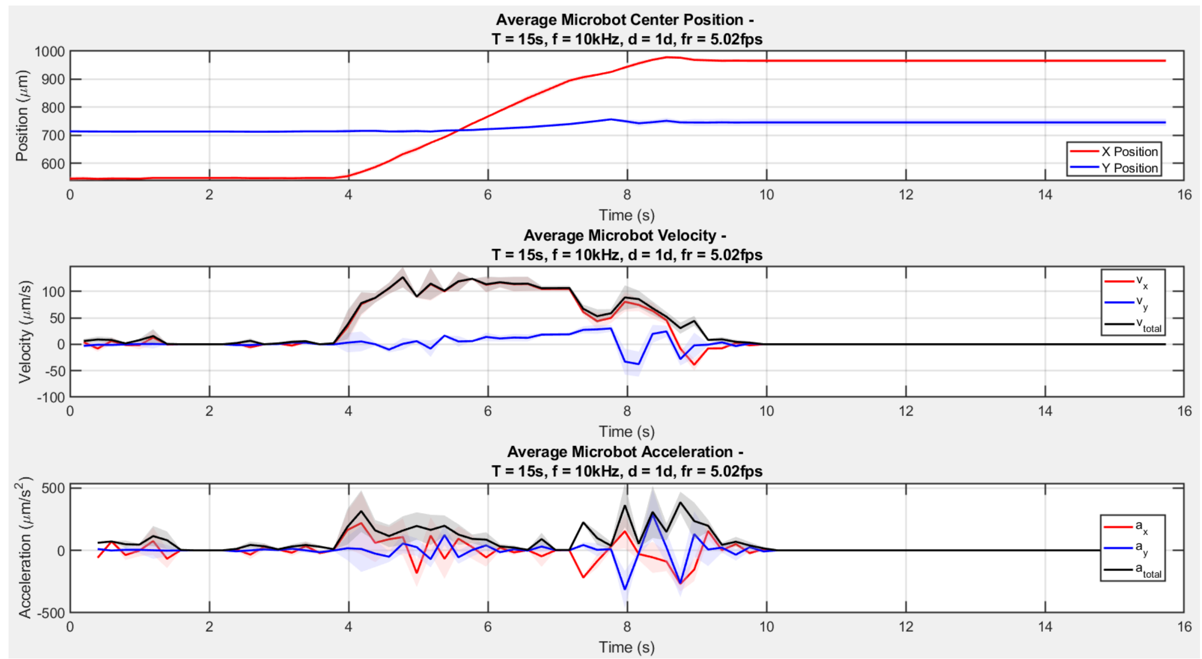

Figure D.77: The measured positions, velocities, and accelerations of the center position of the microbot in the OET with a medium of deionized water with 0.05% Tween-20. The used sweep animation had a sweep time of 15 seconds and a thickness of 30 pixels. The voltage on the chip was 30 V with a frequency of 10 kHz.

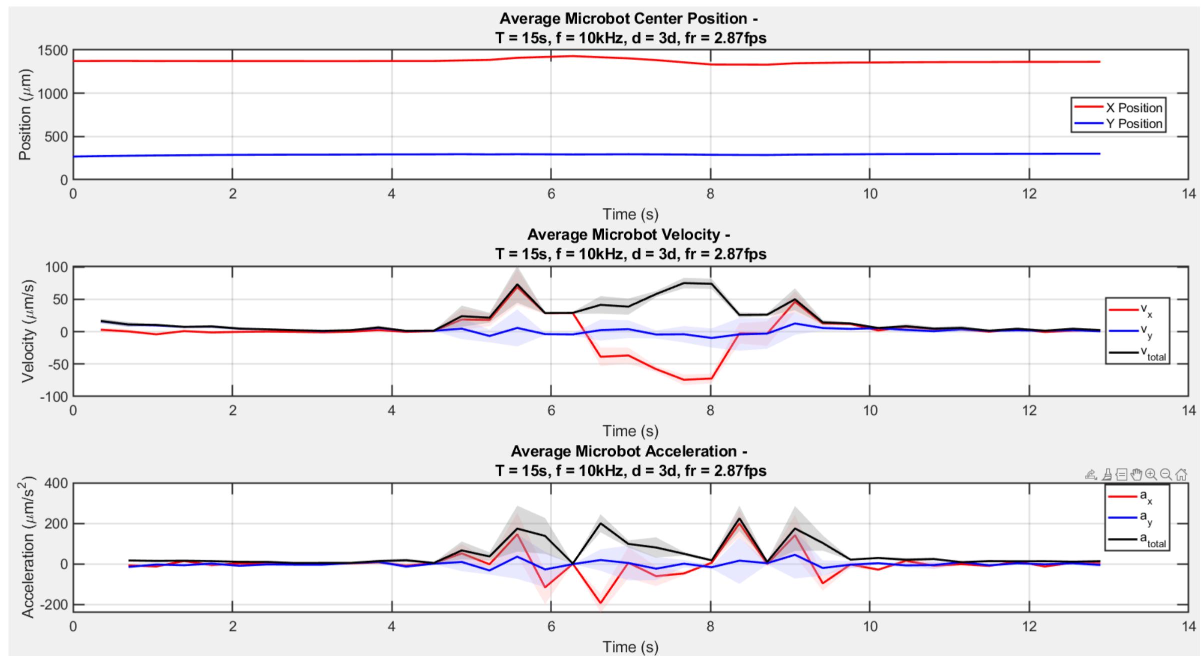

Figure D.78: The measured positions, velocities, and accelerations of the center position of the microbot in the OET with a medium of deionized water with 0.05% Tween-20. The used sweep animation had a sweep time of 15 seconds and a thickness of 90 pixels. The voltage on the chip was 30 V with a frequency of 10 kHz.

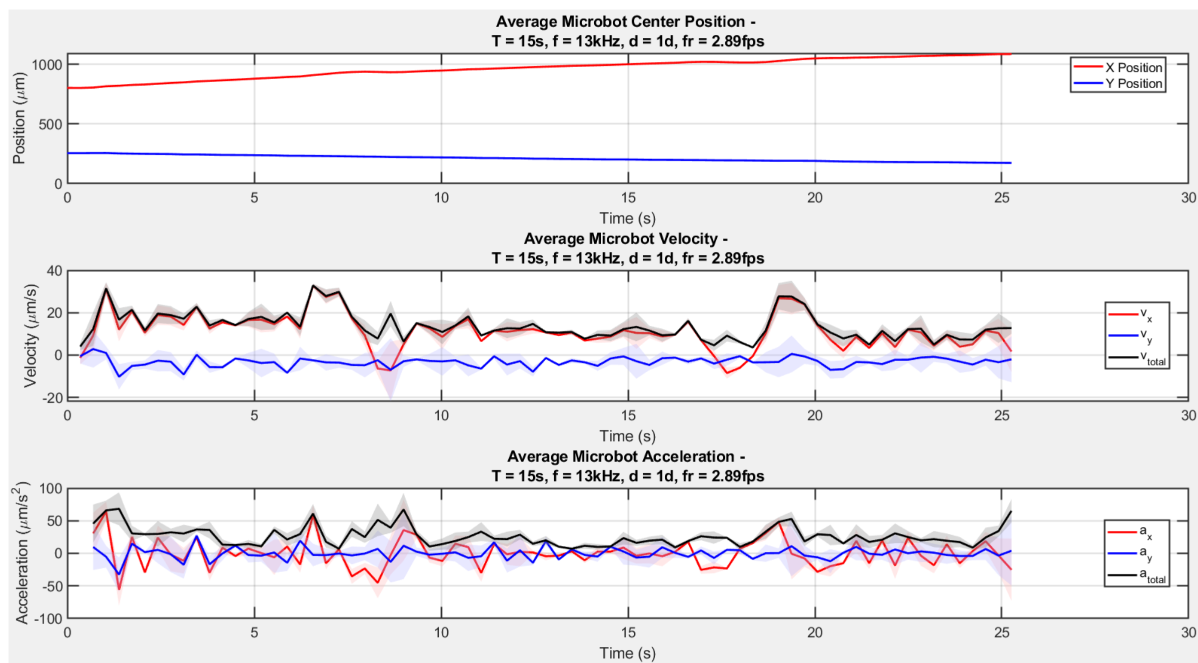

Figure D.79: The measured positions, velocities, and accelerations of the center position of the microbot in the OET with a medium of deionized water with 0.05% Tween-20. The used sweep animation had a sweep time of 15 seconds and a thickness of 30 pixels. The voltage on the chip was 30 V with a frequency of 13 kHz.

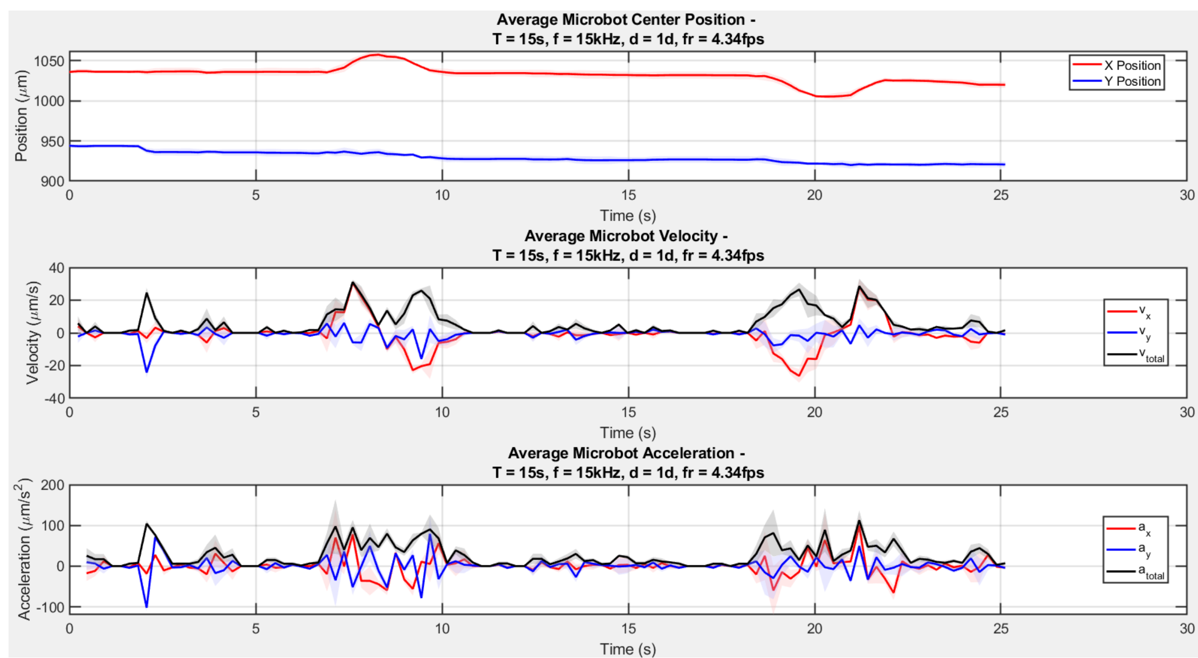

Figure D.80: The measured positions, velocities, and accelerations of the center position of the microbot in the OET with a medium of deionized water with 0.05% Tween-20. The used sweep animation had a sweep time of 15 seconds and a thickness of 30 pixels. The voltage on the chip was 30 V with a frequency of 15 kHz.

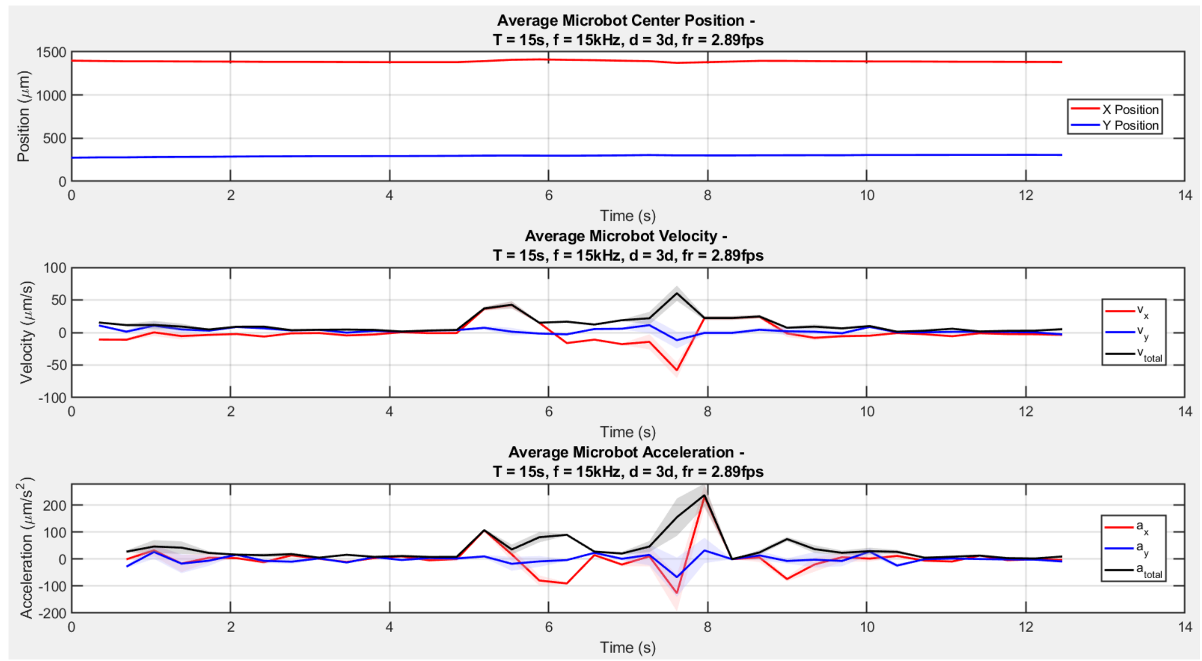

Figure D.81: The measured positions, velocities, and accelerations of the center position of the microbot in the OET with a medium of deionized water with 0.05% Tween-20. The used sweep animation had a sweep time of 15 seconds and a thickness of 90 pixels. The voltage on the chip was 30 V with a frequency of 15 kHz.

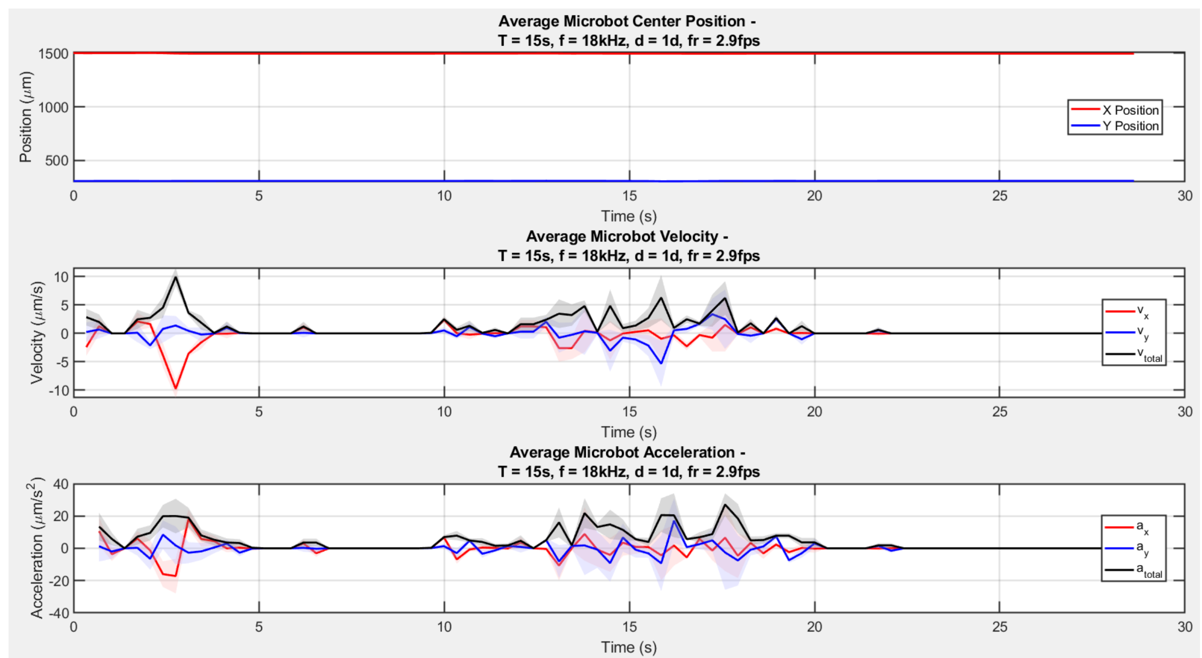

Figure D.82: The measured positions, velocities, and accelerations of the center position of the microbot in the OET with a medium of deionized water with 0.05% Tween-20. The used sweep animation had a sweep time of 15 seconds and a thickness of 30 pixels. The voltage on the chip was 30 V with a frequency of 18 kHz.

D.2.3. Pattern motion

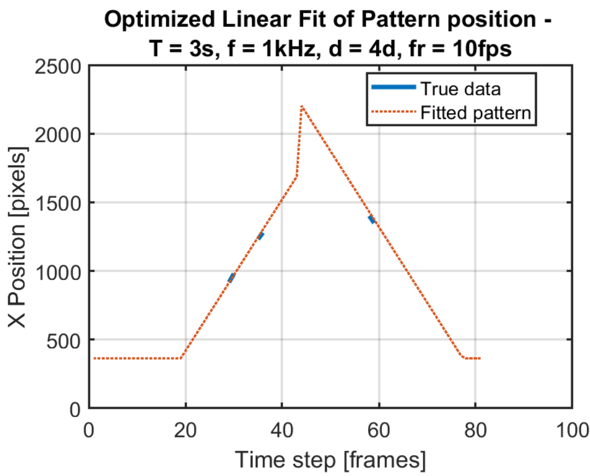

Figure D.83: The dynamics of the sweep pattern with the fitted linear function in orange. The sweep has a sweep time of 3 second and has a sweep thickness of 120 pixels. The input voltage of the experiment is 30 V with a frequency of 1 kHz. The sweep has a delay of 20 frames and has a peak at 44 frames.

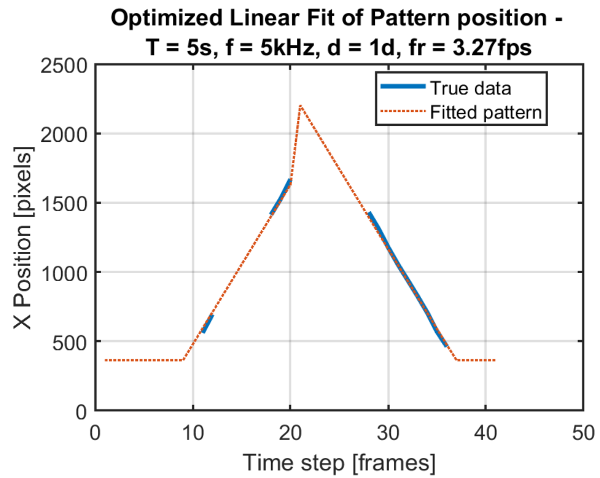

Figure D.84: The dynamics of the sweep pattern with the fitted linear function in orange. The sweep has a sweep time of 5 second and has a sweep thickness of 30 pixels. The input voltage of the experiment is 30 V with a frequency of 5 kHz. The sweep has a delay of 9 frames and has a peak at 21 frames.

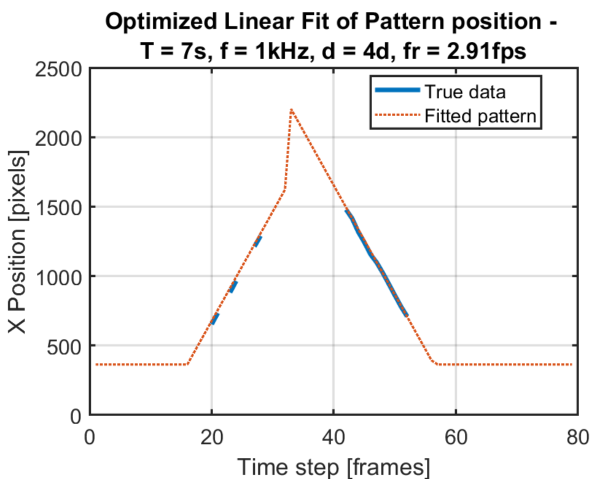

Figure D.85: The dynamics of the sweep pattern with the fitted linear function in orange. The sweep has a sweep time of 7 second and has a sweep thickness of 120 pixels. The input voltage of the experiment is 30 V with a frequency of 1 kHz. The sweep has a delay of 15 frames and has a peak at 32 frames.

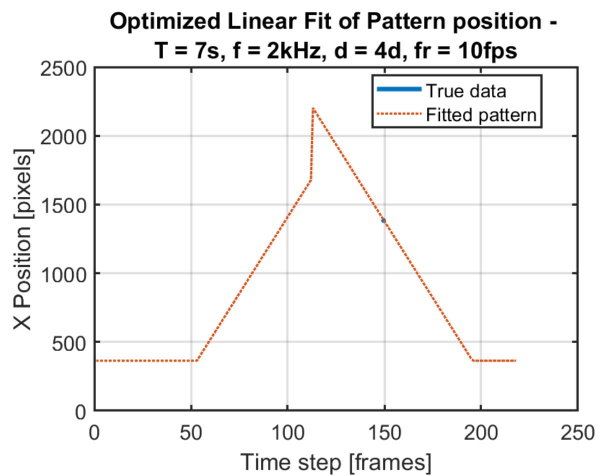

Figure D.86: The dynamics of the sweep pattern with the fitted linear function in orange. The sweep has a sweep time of 7 second and has a sweep thickness of 120 pixels. The input voltage of the experiment is 30 V with a frequency of 2 kHz. The sweep has a delay of 53 frames and has a peak at 113 frames.

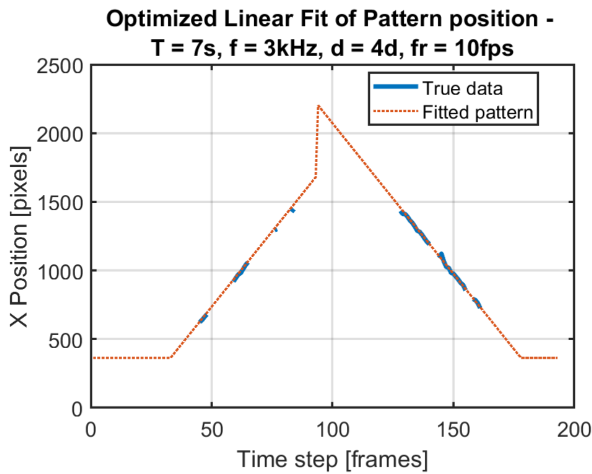

Figure D.87: The dynamics of the sweep pattern with the fitted linear function in orange. The sweep has a sweep time of 7 second and has a sweep thickness of 120 pixels. The input voltage of the experiment is 30 V with a frequency of 3 kHz. The sweep has a delay of 32 frames and has a peak at 93 frames.

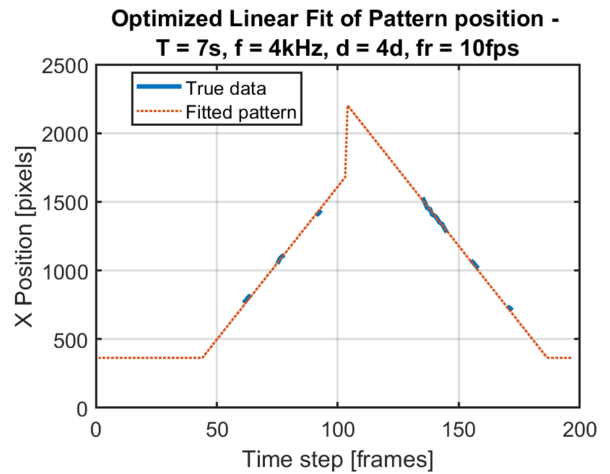

Figure D.88: The dynamics of the sweep pattern with the fitted linear function in orange. The sweep has a sweep time of 7 second and has a sweep thickness of 120 pixels. The input voltage of the experiment is 30 V with a frequency of 4 kHz. The sweep has a delay of 44 frames and has a peak at 104 frames.

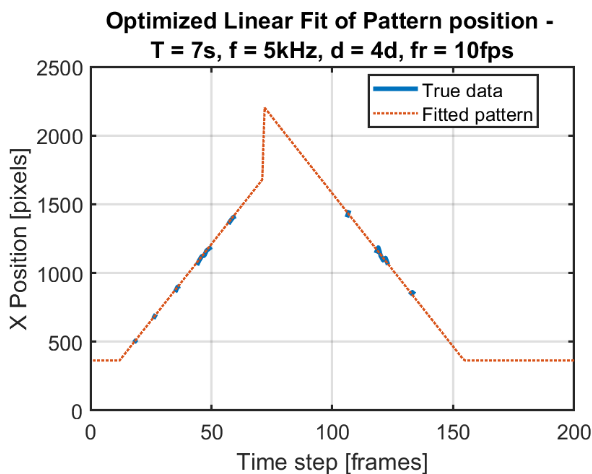

Figure D.89: The dynamics of the sweep pattern with the fitted linear function in orange. The sweep has a sweep time of 7 second and has a sweep thickness of 120 pixels. The input voltage of the experiment is 30 V with a frequency of 5 kHz. The sweep has a delay of 12 frames and has a peak at 72 frames.

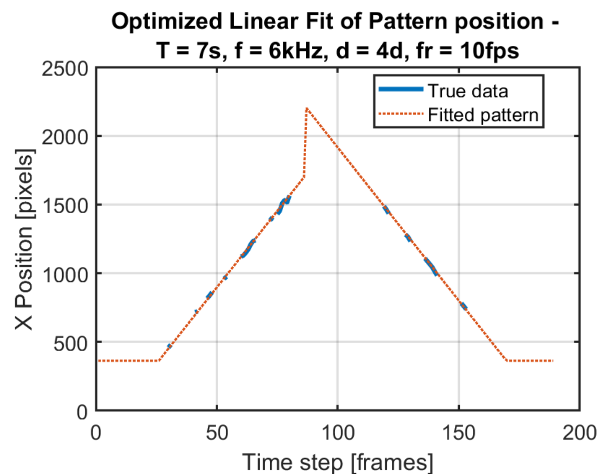

Figure D.90: The dynamics of the sweep pattern with the fitted linear function in orange. The sweep has a sweep time of 7 second and has a sweep thickness of 120 pixels. The input voltage of the experiment is 30 V with a frequency of 6 kHz. The sweep has a delay of 26 frames and has a peak at 86 frames.

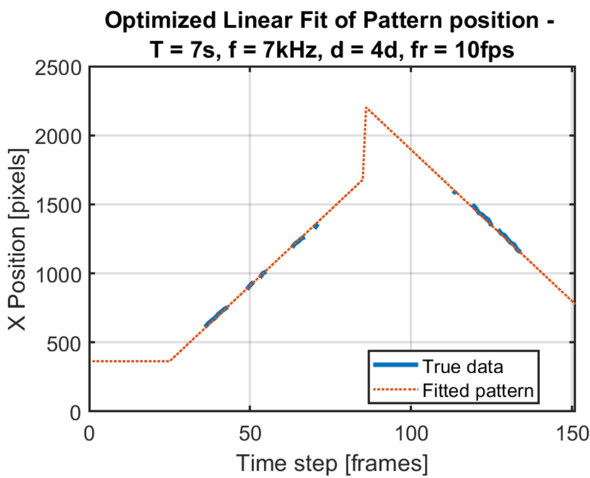

Figure D.91: The dynamics of the sweep pattern with the fitted linear function in orange. The sweep has a sweep time of 7 second and has a sweep thickness of 120 pixels. The input voltage of the experiment is 30 V with a frequency of 7 kHz. The sweep has a delay of 25 frames and has a peak at 86 frames.

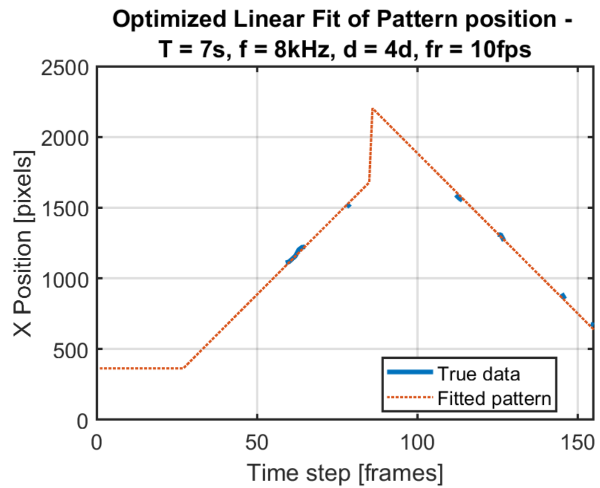

Figure D.92: The dynamics of the sweep pattern with the fitted linear function in orange. The sweep has a sweep time of 7 second and has a sweep thickness of 120 pixels. The input voltage of the experiment is 30 V with a frequency of 8 kHz. The sweep has a delay of 27 frames and has a peak at 86 frames.

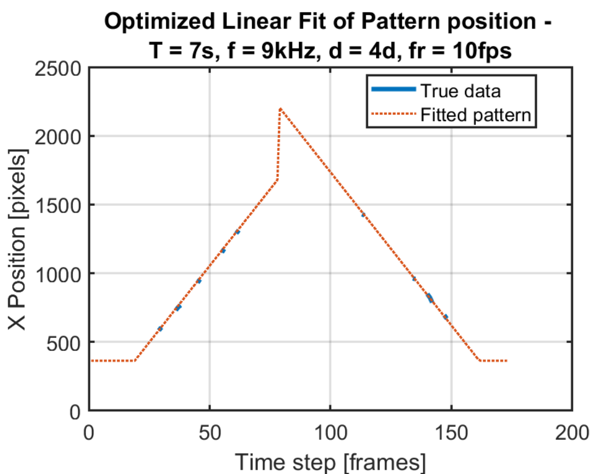

Figure D.93: The dynamics of the sweep pattern with the fitted linear function in orange. The sweep has a sweep time of 7 second and has a sweep thickness of 120 pixels. The input voltage of the experiment is 30 V with a frequency of 9 kHz. The sweep has a delay of 18 frames and has a peak at 78 frames.

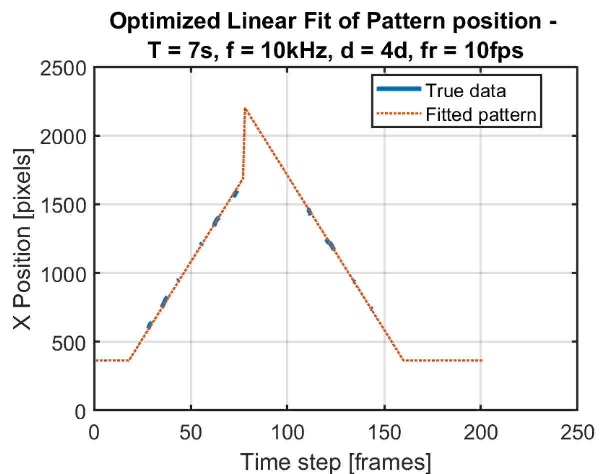

Figure D.94: The dynamics of the sweep pattern with the fitted linear function in orange. The sweep has a sweep time of 7 second and has a sweep thickness of 120 pixels. The input voltage of the experiment is 30 V with a frequency of 10 kHz. The sweep has a delay of 18 frames and has a peak at 77 frames.

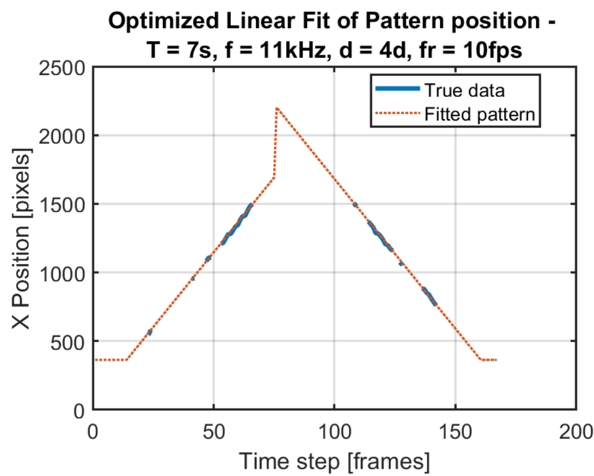

Figure D.95: The dynamics of the sweep pattern with the fitted linear function in orange. The sweep has a sweep time of 7 second and has a sweep thickness of 120 pixels. The input voltage of the experiment is 30 V with a frequency of 11 kHz. The sweep has a delay of 15 frames and has a peak at 76 frames.

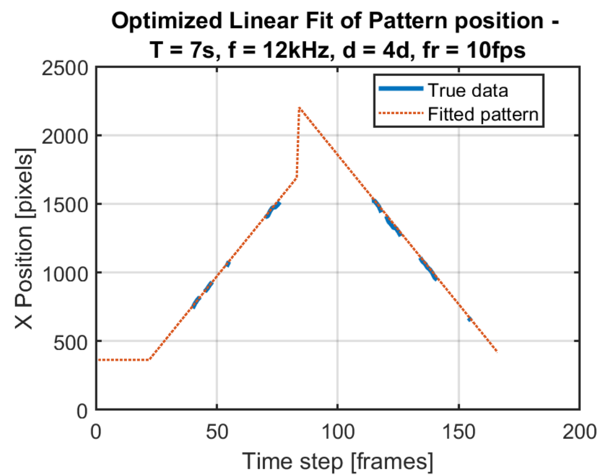

Figure D.96: The dynamics of the sweep pattern with the fitted linear function in orange. The sweep has a sweep time of 7 second and has a sweep thickness of 120 pixels. The input voltage of the experiment is 30 V with a frequency of 12 kHz. The sweep has a delay of 22 frames and has a peak at 83 frames.

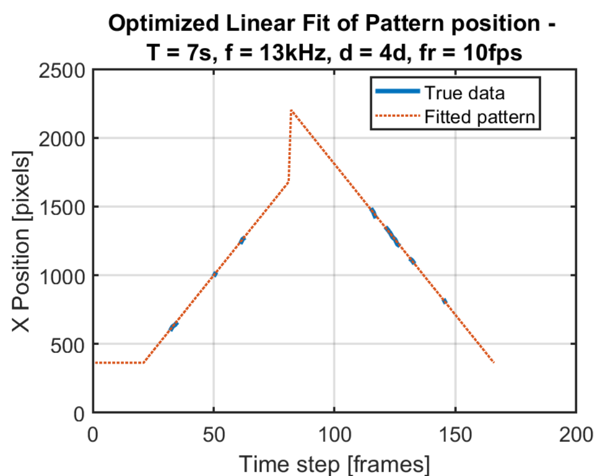

Figure D.97: The dynamics of the sweep pattern with the fitted linear function in orange. The sweep has a sweep time of 7 second and has a sweep thickness of 120 pixels. The input voltage of the experiment is 30 V with a frequency of 13 kHz. The sweep has a delay of 20 frames and has a peak at 81 frames.

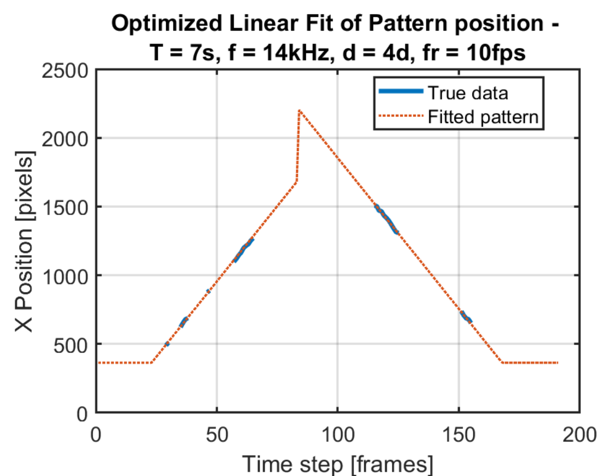

Figure D.98: The dynamics of the sweep pattern with the fitted linear function in orange. The sweep has a sweep time of 7 second and has a sweep thickness of 120 pixels. The input voltage of the experiment is 30 V with a frequency of 14 kHz. The sweep has a delay of 23 frames and has a peak at 84 frames.

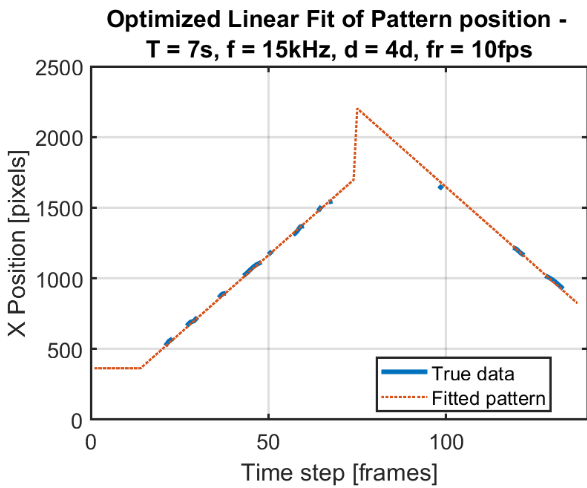

Figure D.99: The dynamics of the sweep pattern with the fitted linear function in orange. The sweep has a sweep time of 7 second and has a sweep thickness of 120 pixels. The input voltage of the experiment is 30 V with a frequency of 15 kHz. The sweep has a delay of 15 frames and has a peak at 75 frames.

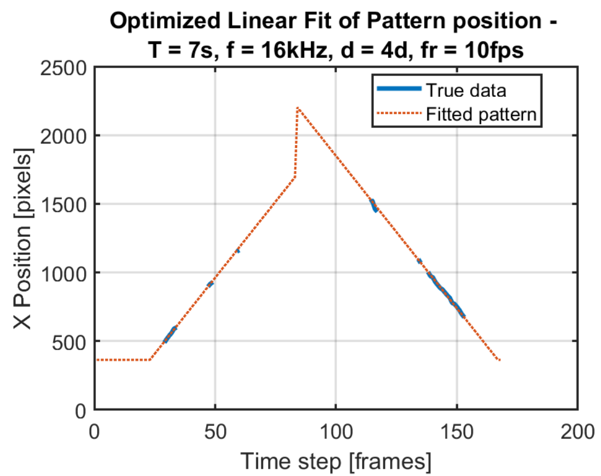

Figure D.100: The dynamics of the sweep pattern with the fitted linear function in orange. The sweep has a sweep time of 7 second and has a sweep thickness of 120 pixels. The input voltage of the experiment is 30 V with a frequency of 16 kHz. The sweep has a delay of 24 frames and has a peak at 84 frames.

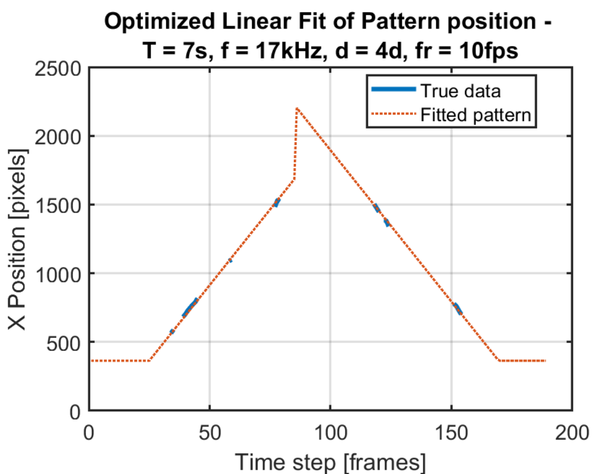

Figure D.101: The dynamics of the sweep pattern with the fitted linear function in orange. The sweep has a sweep time of 7 second and has a sweep thickness of 120 pixels. The input voltage of the experiment is 30 V with a frequency of 17 kHz. The sweep has a delay of 25 frames and has a peak at 86 frames.

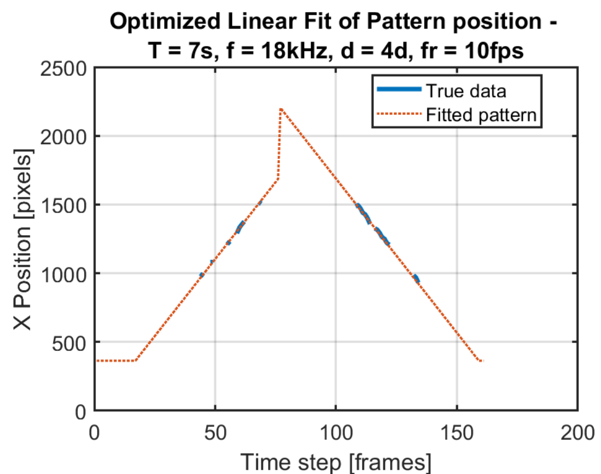

Figure D.102: The dynamics of the sweep pattern with the fitted linear function in orange. The sweep has a sweep time of 7 second and has a sweep thickness of 120 pixels. The input voltage of the experiment is 30 V with a frequency of 18 kHz. The sweep has a delay of 17 frames and has a peak at 77 frames.

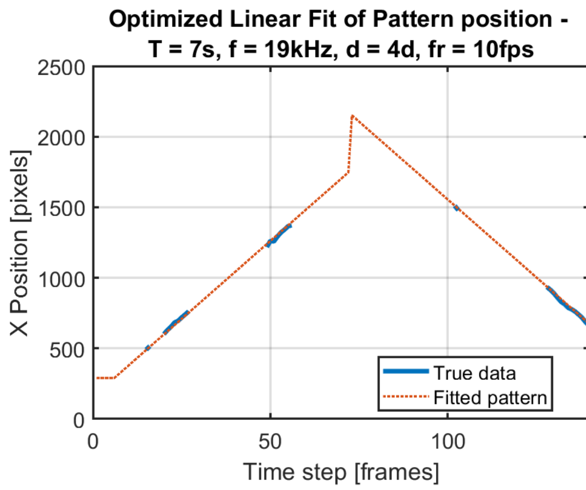

Figure D.103: The dynamics of the sweep pattern with the fitted linear function in orange. The sweep has a sweep time of 7 second and has a sweep thickness of 120 pixels. The input voltage of the experiment is 30 V with a frequency of 19 kHz. The sweep has a delay of 8 frames and has a peak at 69 frames.

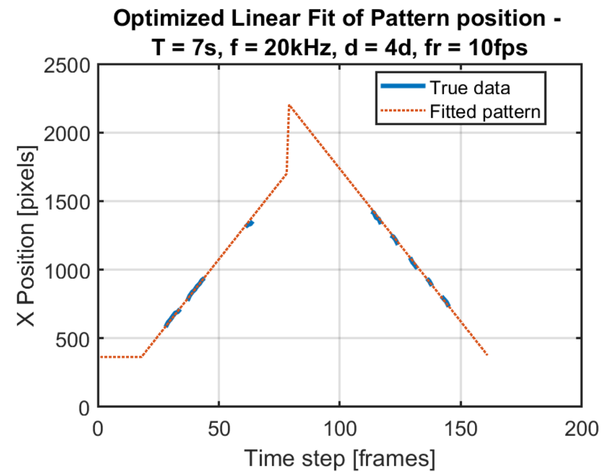

Figure D.104: The dynamics of the sweep pattern with the fitted linear function in orange. The sweep has a sweep time of 7 second and has a sweep thickness of 120 pixels. The input voltage of the experiment is 30 V with a frequency of 20 kHz. The sweep has a delay of 19 frames and has a peak at 79 frames.

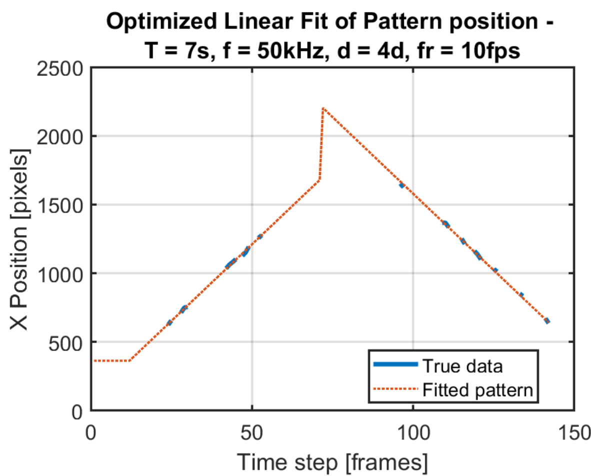

Figure D.105: The dynamics of the sweep pattern with the fitted linear function in orange. The sweep has a sweep time of 7 second and has a sweep thickness of 120 pixels. The input voltage of the experiment is 30 V with a frequency of 50 kHz. The sweep has a delay of 11 frames and has a peak at 71 frames.

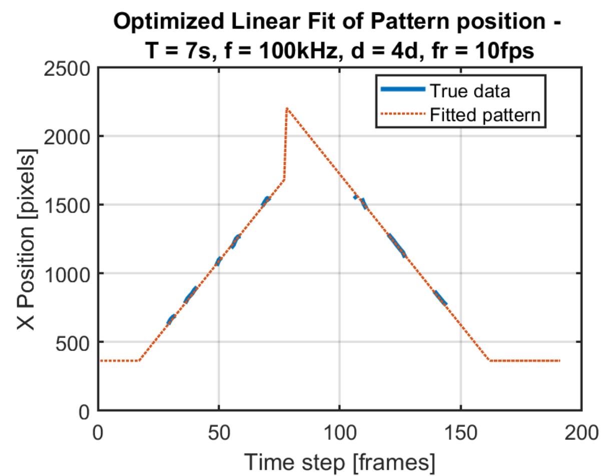

Figure D.106: The dynamics of the sweep pattern with the fitted linear function in orange. The sweep has a sweep time of 7 second and has a sweep thickness of 120 pixels. The input voltage of the experiment is 30 V with a frequency of 100 kHz. The sweep has a delay of 16 frames and has a peak at 77 frames.

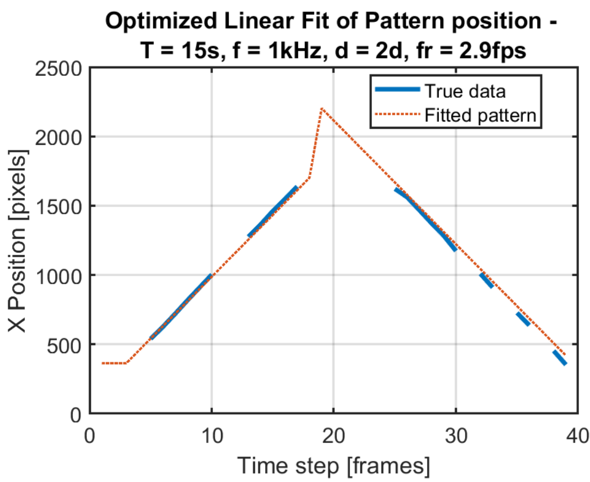

Figure D.107: The dynamics of the sweep pattern with the fitted linear function in orange. The sweep has a sweep time of 15 second and has a sweep thickness of 60 pixels. The input voltage of the experiment is 30 V with a frequency of 1 kHz. The sweep has a delay of 4 frames and has a peak at 19 frames.

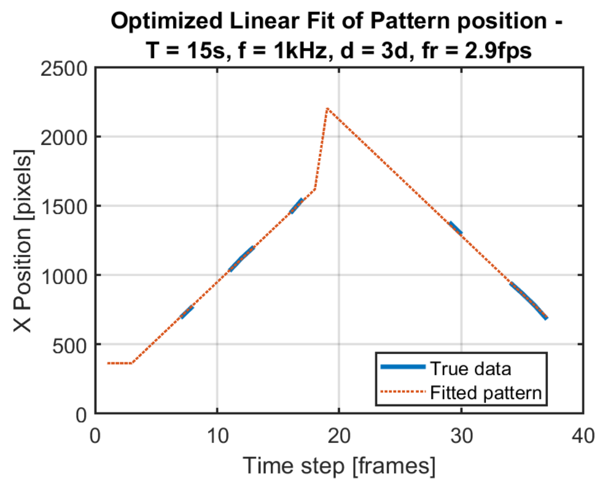

Figure D.108: The dynamics of the sweep pattern with the fitted linear function in orange. The sweep has a sweep time of 15 second and has a sweep thickness of 90 pixels. The input voltage of the experiment is 30 V with a frequency of 1 kHz. The sweep has a delay of 2 frames and has a peak at 18 frames.

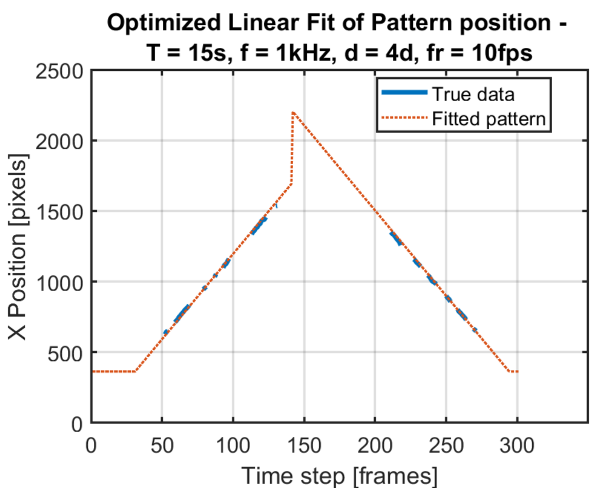

Figure D.109: The dynamics of the sweep pattern with the fitted linear function in orange. The sweep has a sweep time of 15 second and has a sweep thickness of 120 pixels. The input voltage of the experiment is 30 V with a frequency of 1 kHz. The sweep has a delay of 31 frames and has a peak at 141 frames.

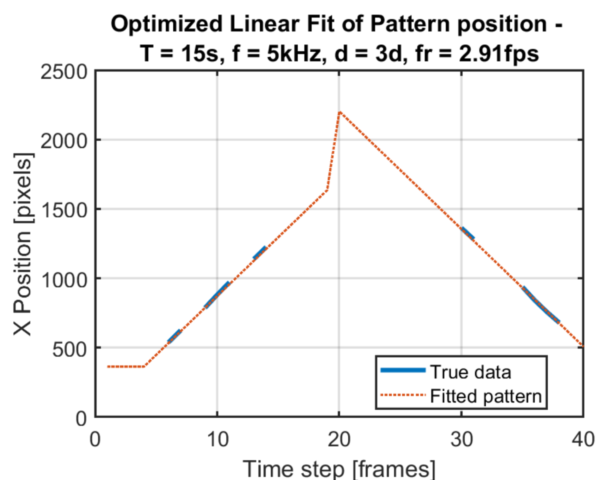

Figure D.110: The dynamics of the sweep pattern with the fitted linear function in orange. The sweep has a sweep time of 15 second and has a sweep thickness of 90 pixels. The input voltage of the experiment is 30 V with a frequency of 5 kHz. The sweep has a delay of 4 frames and has a peak at 20 frames.

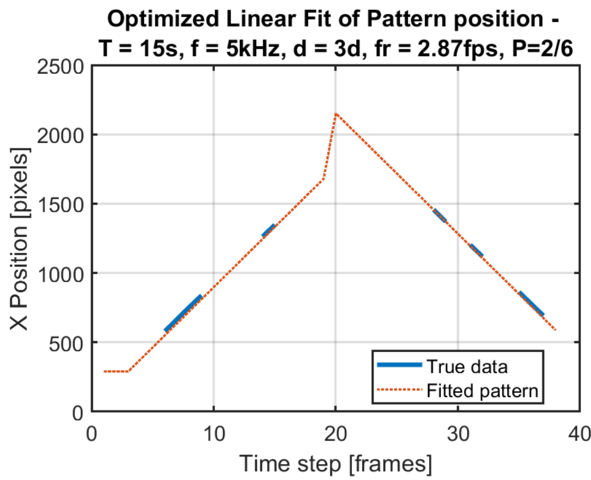

Figure D.111: The dynamics of the sweep pattern with the fitted linear function in orange. The sweep has a sweep time of 15 second and has a sweep thickness of 90 pixels. The input voltage of the experiment is 30 V with a frequency of 5 kHz. The illumination power was set to 1/3 of full power. The sweep has a delay of 5 frames and has a peak at 20 frames.

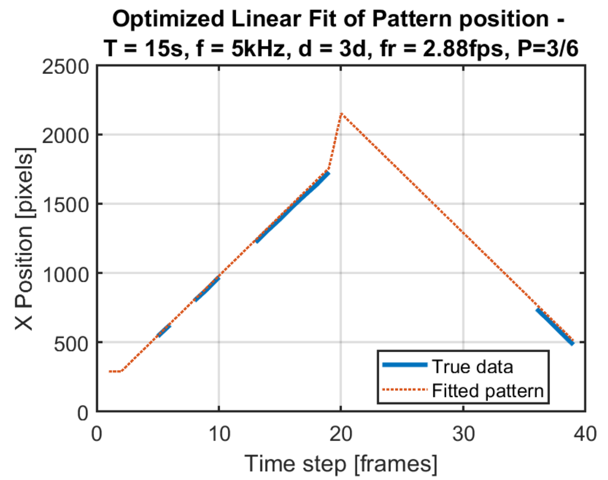

Figure D.112: The dynamics of the sweep pattern with the fitted linear function in orange. The sweep has a sweep time of 15 second and has a sweep thickness of 90 pixels. The input voltage of the experiment is 30 V with a frequency of 5 kHz. The illumination power was set to 1/2 of full power. The sweep has a delay of 4 frames and has a peak at 19 frames.

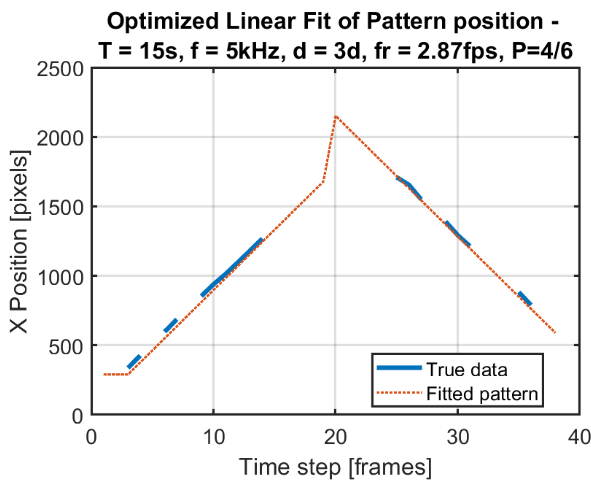

Figure D.113: The dynamics of the sweep pattern with the fitted linear function in orange. The sweep has a sweep time of 15 second and has a sweep thickness of 90 pixels. The input voltage of the experiment is 30 V with a frequency of 5 kHz. The illumination power was set to 2/3 of full power. The sweep has a delay of 4 frames and has a peak at 19 frames.

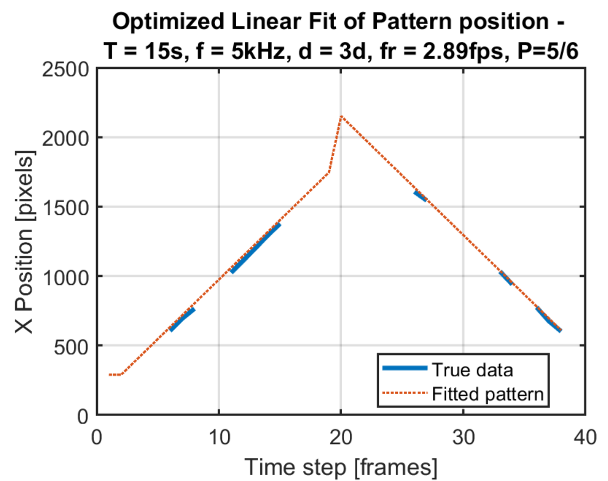

Figure D.114: The dynamics of the sweep pattern with the fitted linear function in orange. The sweep has a sweep time of 15 second and has a sweep thickness of 90 pixels. The input voltage of the experiment is 30 V with a frequency of 5 kHz. The illumination power was set to 5/6 of full power. The sweep has a delay of 3 frames and has a peak at 19 frames.

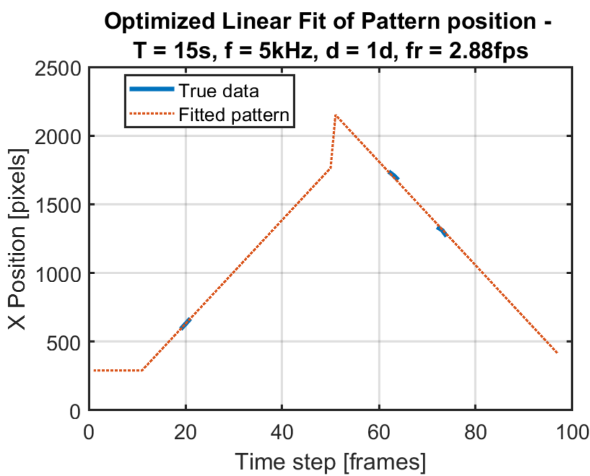

Figure D.115: The dynamics of the sweep pattern with the fitted linear function in orange. The sweep has a sweep time of 15 second and has a sweep thickness of 30 pixels. The input voltage of the experiment is 30 V with a frequency of 5 kHz. The sweep has a delay of 13 frames and has a peak at 49 frames.

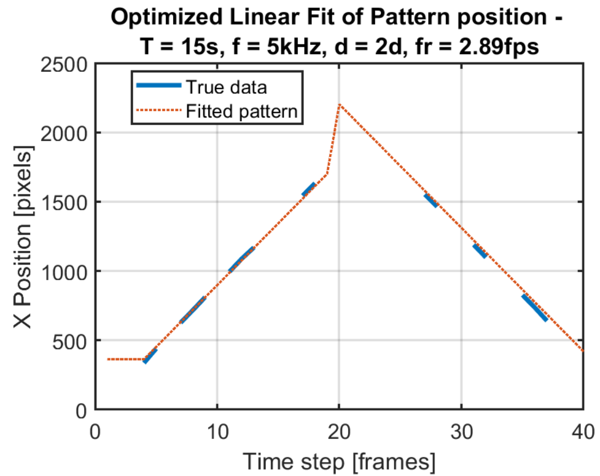

Figure D.116: The dynamics of the sweep pattern with the fitted linear function in orange. The sweep has a sweep time of 15 second and has a sweep thickness of 60 pixels. The input voltage of the experiment is 30 V with a frequency of 5 kHz. The sweep has a delay of 5 frames and has a peak at 20 frames.

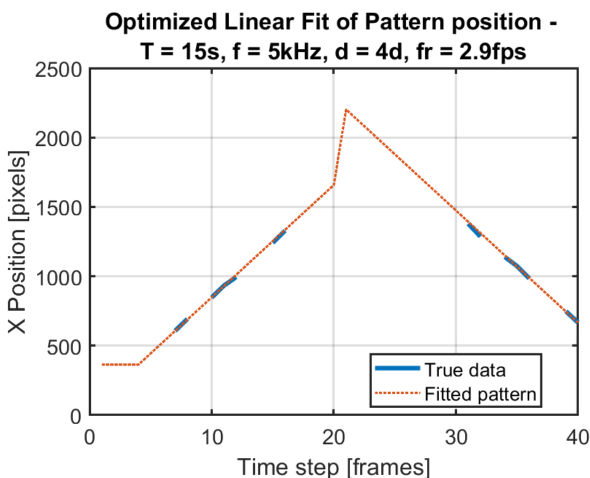

Figure D.117: The dynamics of the sweep pattern with the fitted linear function in orange. The sweep has a sweep time of 15 second and has a sweep thickness of 120 pixels. The input voltage of the experiment is 30 V with a frequency of 5 kHz. The sweep has a delay of 4 frames and has a peak at 20 frames.

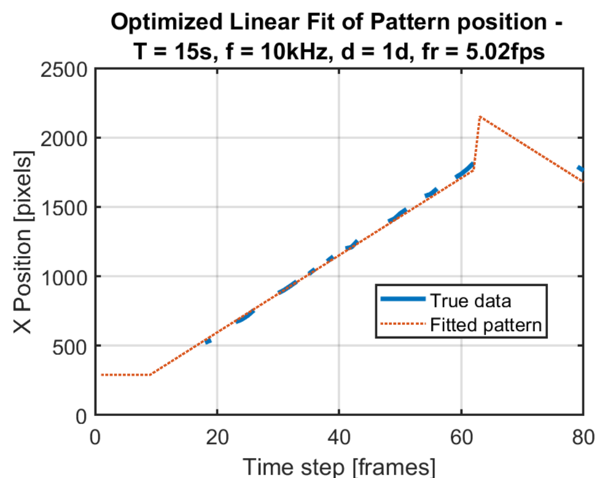

Figure D.118: The dynamics of the sweep pattern with the fitted linear function in orange. The sweep has a sweep time of 15 second and has a sweep thickness of 30 pixels. The input voltage of the experiment is 30 V with a frequency of 10 kHz. The sweep has a delay of 11 frames and has a peak at 63 frames.

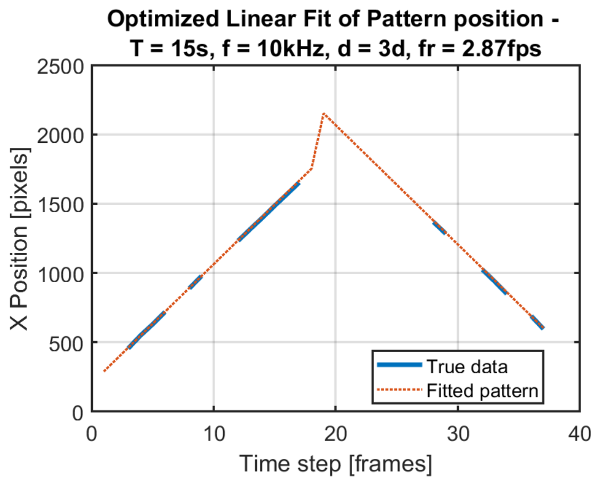

Figure D.119: The dynamics of the sweep pattern with the fitted linear function in orange. The sweep has a sweep time of 15 second and has a sweep thickness of 90 pixels. The input voltage of the experiment is 30 V with a frequency of 10 kHz. The sweep has a delay of 2 frames and has a peak at 17 frames.

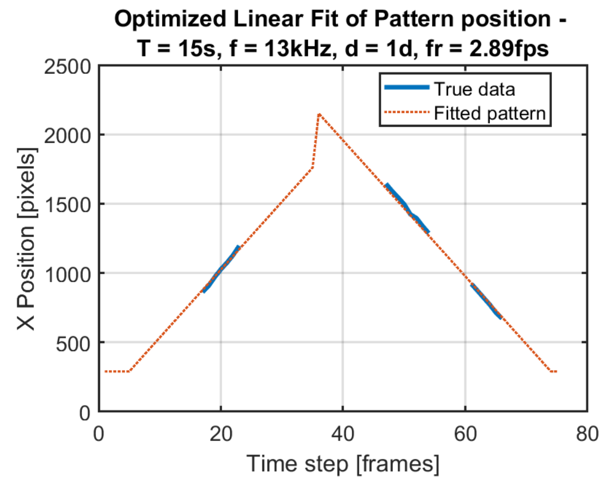

Figure D.120: The dynamics of the sweep pattern with the fitted linear function in orange. The sweep has a sweep time of 15 second and has a sweep thickness of 30 pixels. The input voltage of the experiment is 30 V with a frequency of 13 kHz. The sweep has a delay of 7 frames and has a peak at 34 frames.

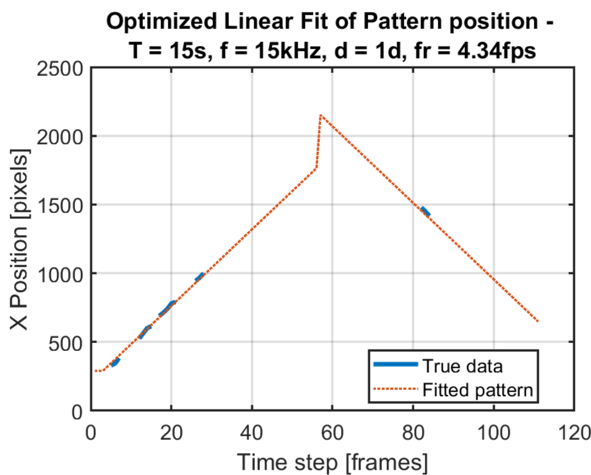

Figure D.121: The dynamics of the sweep pattern with the fitted linear function in orange. The sweep has a sweep time of 15 second and has a sweep thickness of 30 pixels. The input voltage of the experiment is 30 V with a frequency of 15 kHz. The sweep has a delay of 6 frames and has a peak at 54 frames.

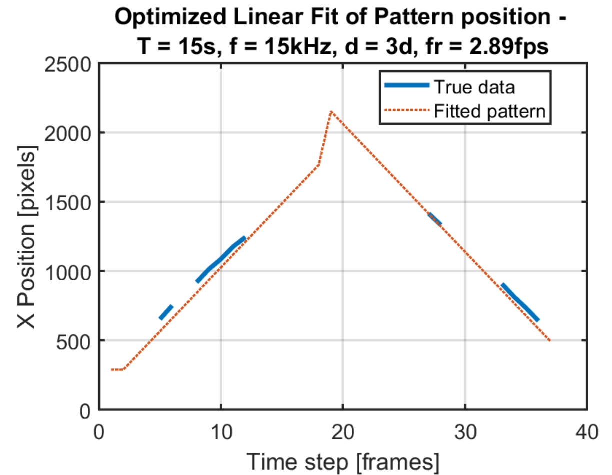

Figure D.122: The dynamics of the sweep pattern with the fitted linear function in orange. The sweep has a sweep time of 15 second and has a sweep thickness of 90 pixels. The input voltage of the experiment is 30 V with a frequency of 15 kHz. The sweep has a delay of 3 frames and has a peak at 18 frames.

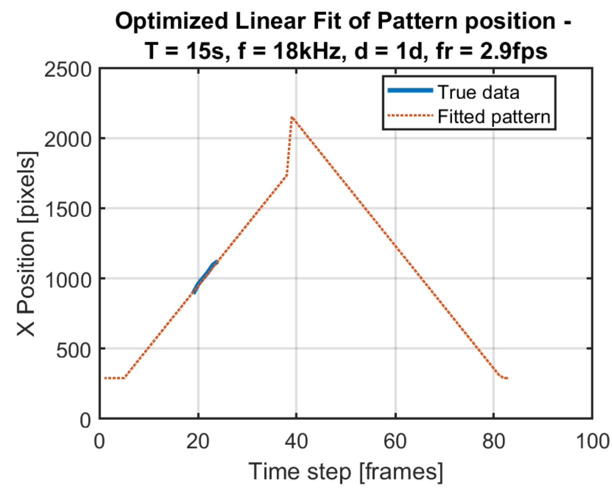

Figure D.123: The dynamics of the sweep pattern with the fitted linear function in orange. The sweep has a sweep time of 15 second and has a sweep thickness of 30 pixels. The input voltage of the experiment is 30 V with a frequency of 18 kHz. The sweep has a delay of 7 frames and has a peak at 38 frames.

D.3. DEP force

D.3.1. DEP force on the microbot, calculated using Stokes's law

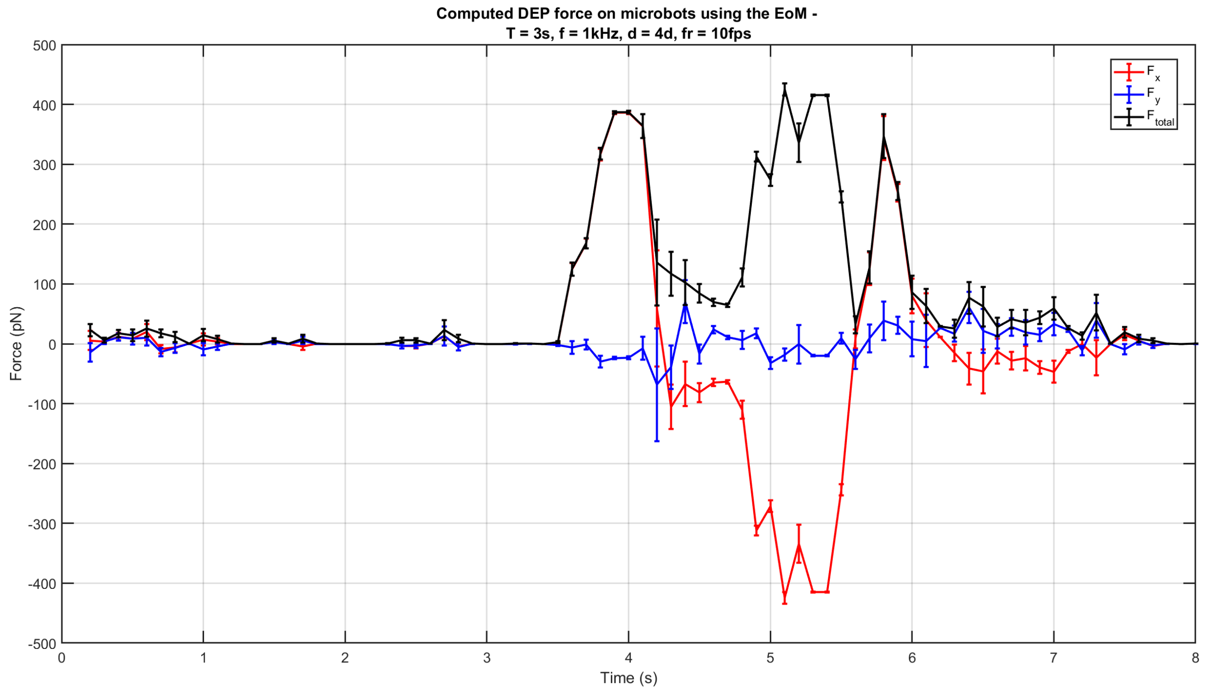

Figure D.124: The calculated DEP force on the microbot over time. The separate lines denote the partial forces in x and y directions, and the total force. The error bars denote the standard deviation of the measurement. The sweep used for creating the DEP force had a sweep time of 3 seconds and a sweep thickness of 120 pixels. The input voltage of the experiment is 30 V with a frequency of 1 kHz.

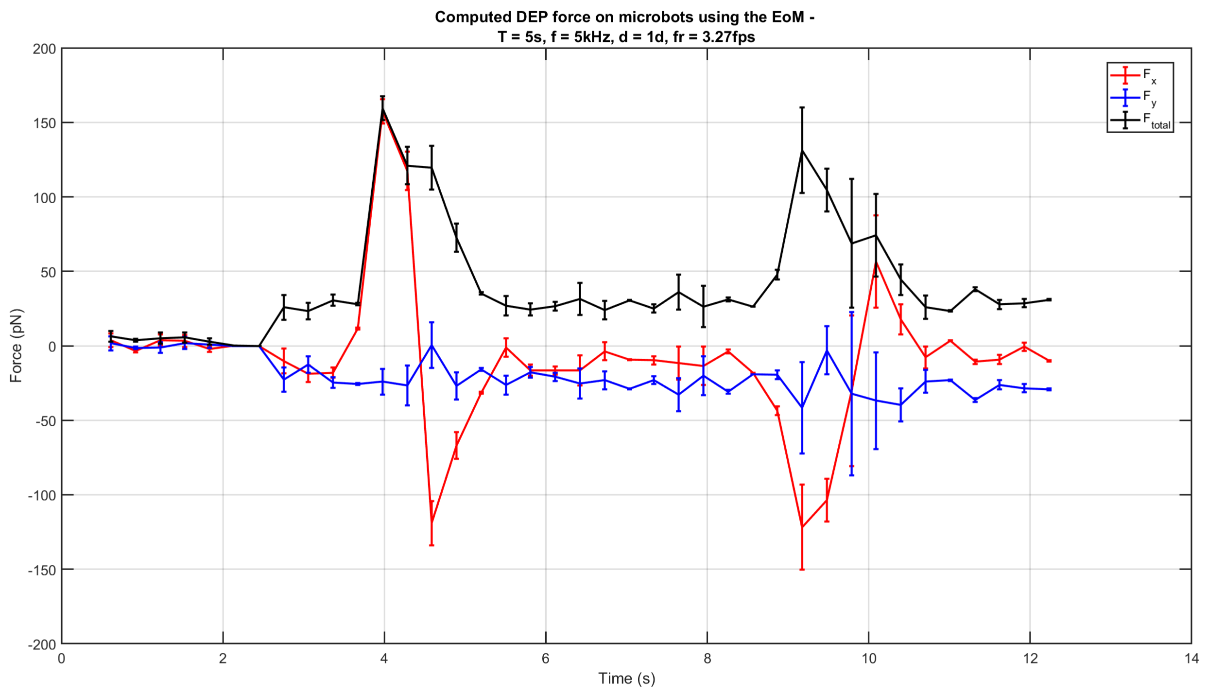

Figure D.125: The calculated DEP force on the microbot over time. The separate lines denote the partial forces in x and y directions, and the total force. The error bars denote the standard deviation of the measurement. The sweep used for creating the DEP force had a sweep time of 5 seconds and a sweep thickness of 90 pixels. The input voltage of the experiment is 30 V with a frequency of 5 kHz.

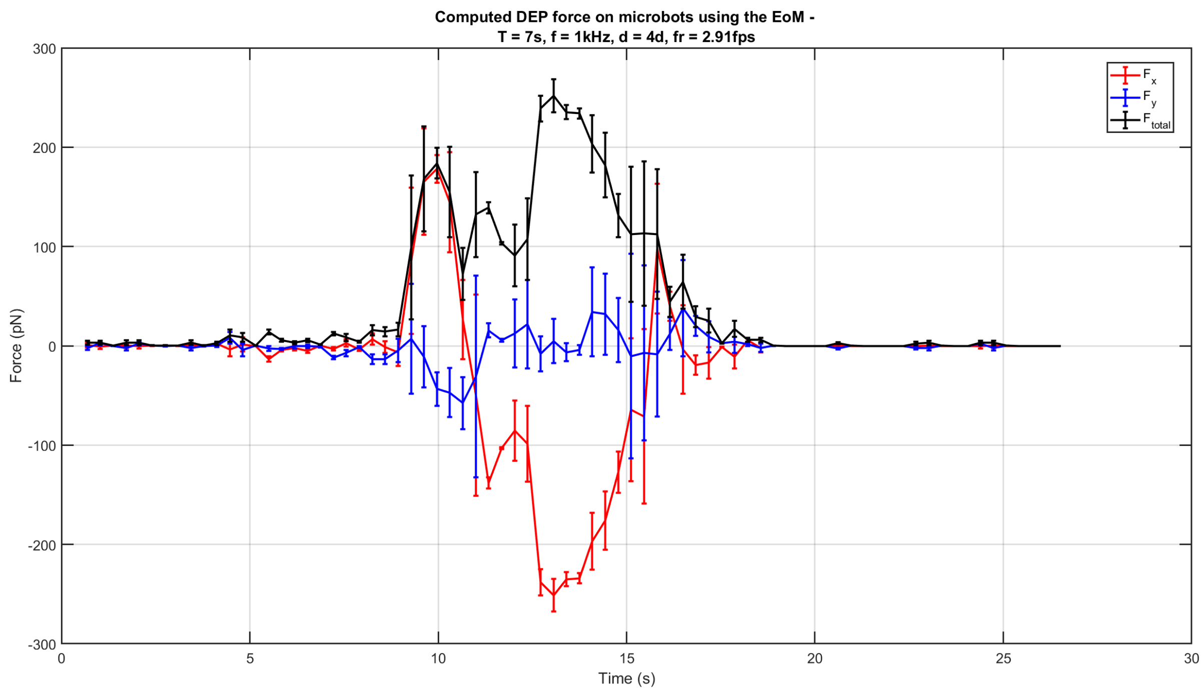

Figure D.126: The calculated DEP force on the microbot over time. The separate lines denote the partial forces in x and y directions, and the total force. The error bars denote the standard deviation of the measurement. The sweep used for creating the DEP force had a sweep time of 7 seconds and a sweep thickness of 120 pixels. The input voltage of the experiment is 30 V with a frequency of 1 kHz.

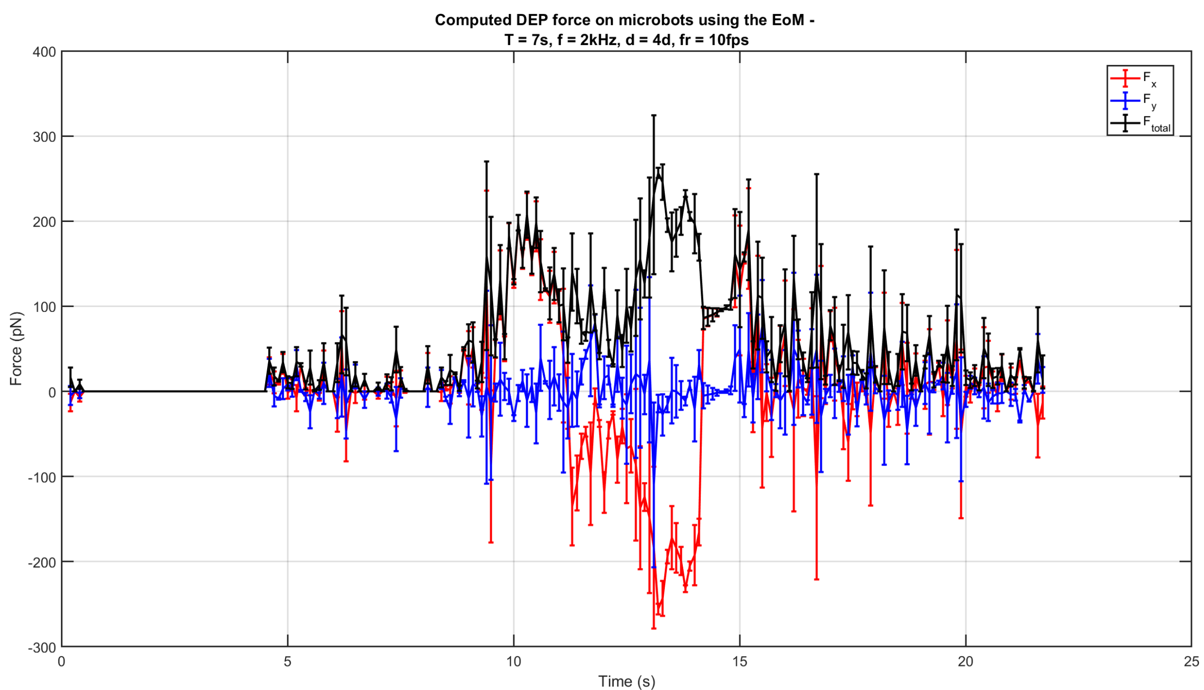

Figure D.127: The calculated DEP force on the microbot over time. The separate lines denote the partial forces in x and y directions, and the total force. The error bars denote the standard deviation of the measurement. The sweep used for creating the DEP force had a sweep time of 7 seconds and a sweep thickness of 120 pixels. The input voltage of the experiment is 30 V with a frequency of 2 kHz.

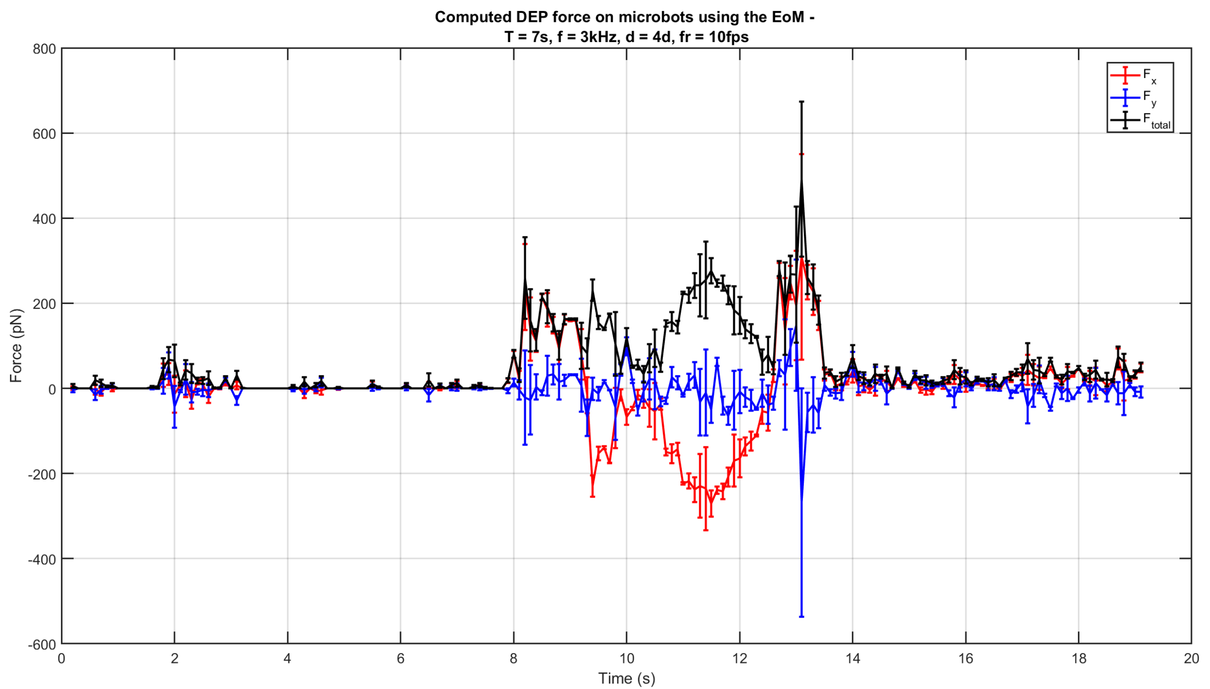

Figure D.128: The calculated DEP force on the microbot over time. The separate lines denote the partial forces in x and y directions, and the total force. The error bars denote the standard deviation of the measurement. The sweep used for creating the DEP force had a sweep time of 7 seconds and a sweep thickness of 120 pixels. The input voltage of the experiment is 30 V with a frequency of 3 kHz.

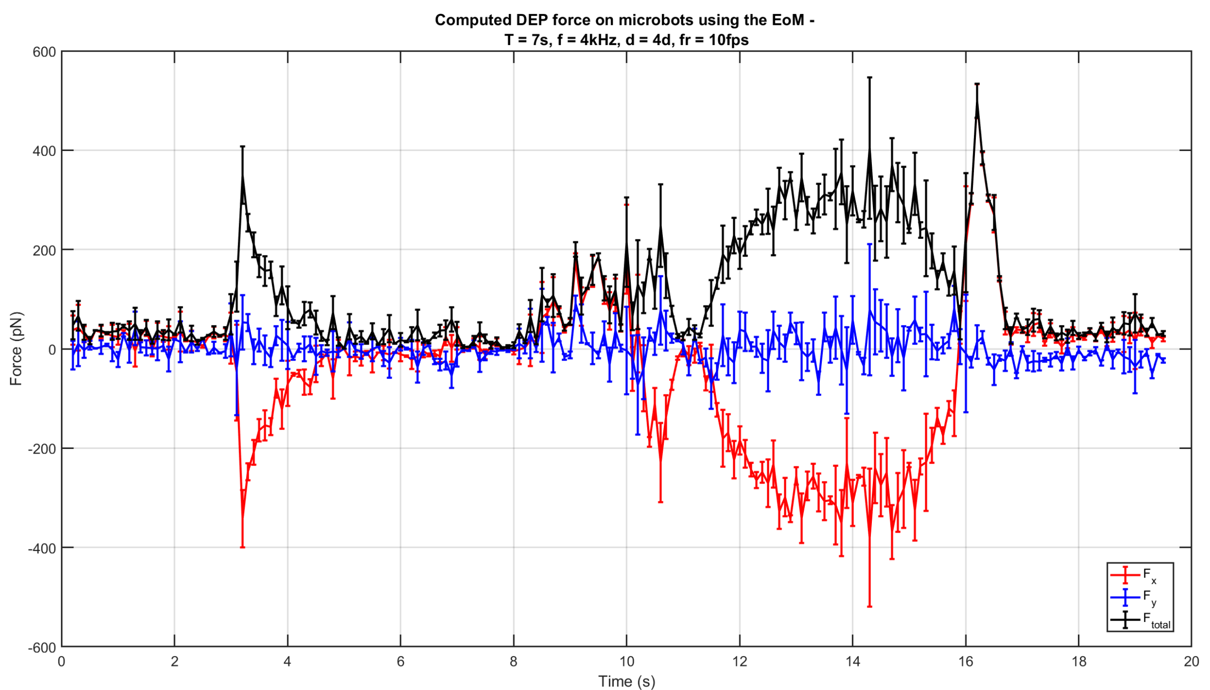

Figure D.129: The calculated DEP force on the microbot over time. The separate lines denote the partial forces in x and y directions, and the total force. The error bars denote the standard deviation of the measurement. The sweep used for creating the DEP force had a sweep time of 7 seconds and a sweep thickness of 120 pixels. The input voltage of the experiment is 30 V with a frequency of 4 kHz.

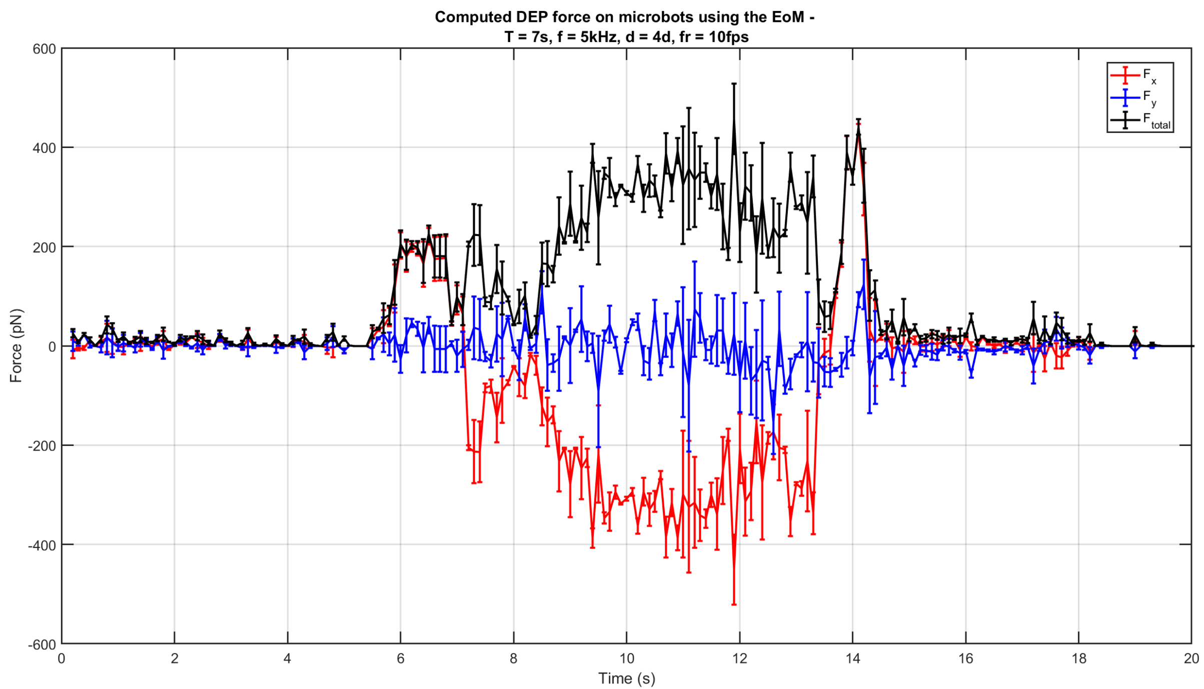

Figure D.130: The calculated DEP force on the microbot over time. The separate lines denote the partial forces in x and y directions, and the total force. The error bars denote the standard deviation of the measurement. The sweep used for creating the DEP force had a sweep time of 7 seconds and a sweep thickness of 120 pixels. The input voltage of the experiment is 30 V with a frequency of 5 kHz.

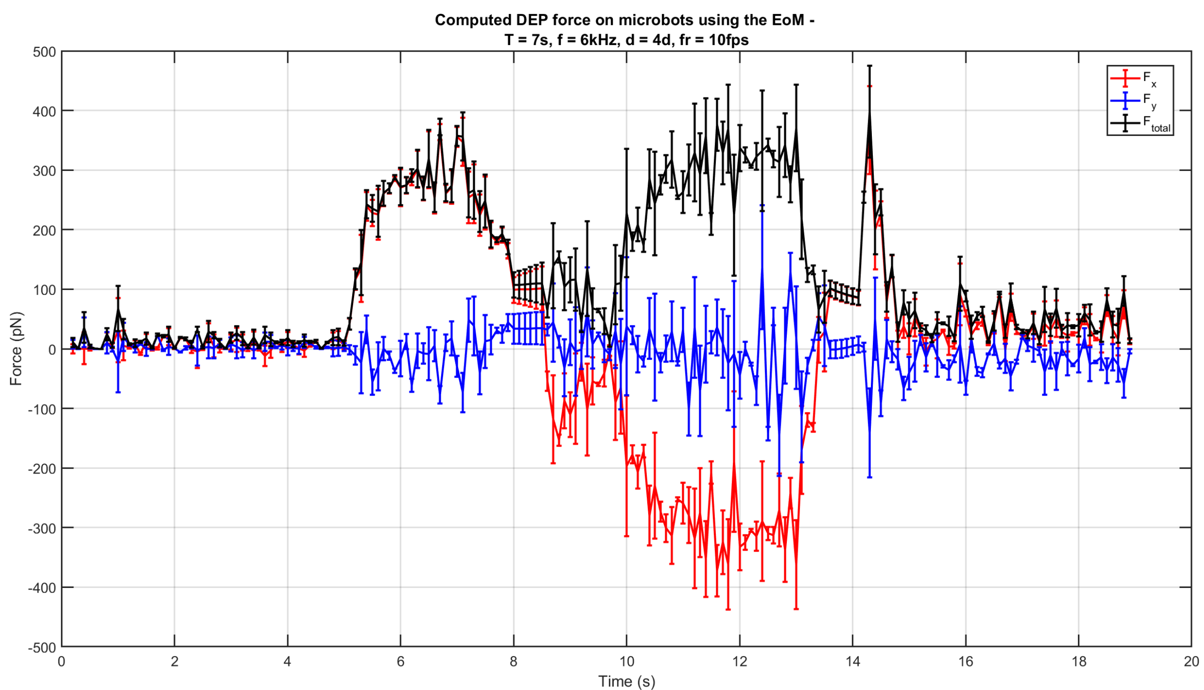

Figure D.131: The calculated DEP force on the microbot over time. The separate lines denote the partial forces in x and y directions, and the total force. The error bars denote the standard deviation of the measurement. The sweep used for creating the DEP force had a sweep time of 7 seconds and a sweep thickness of 120 pixels. The input voltage of the experiment is 30 V with a frequency of 6 kHz.

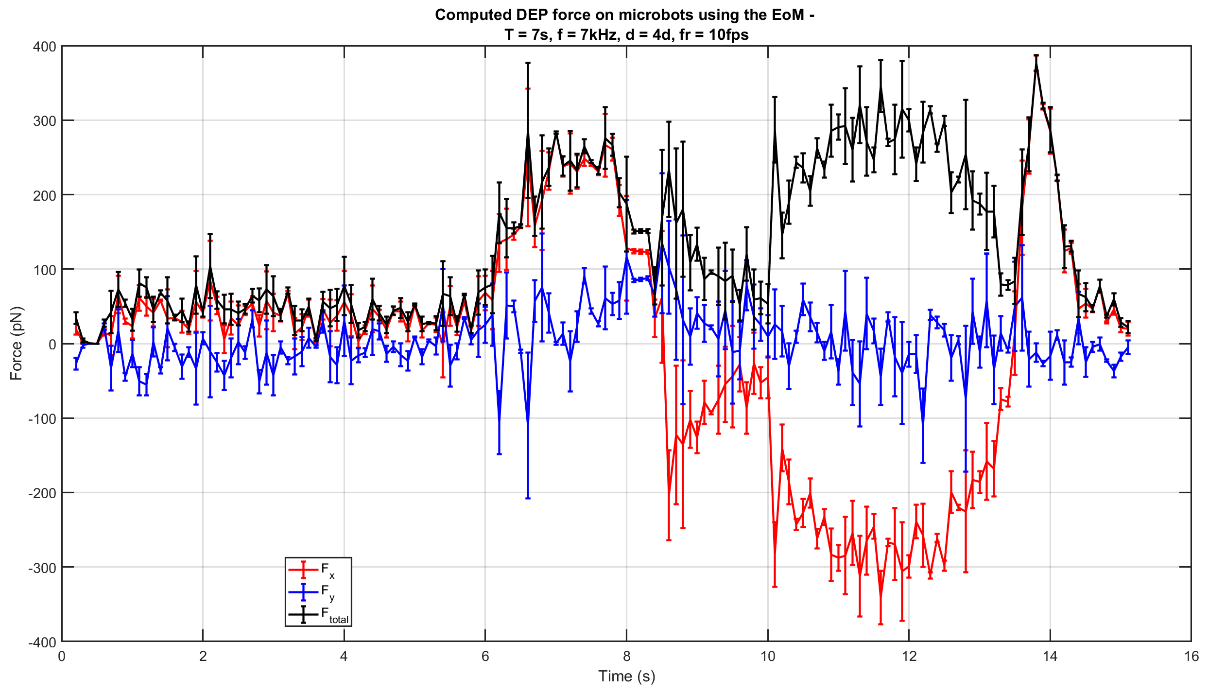

Figure D.132: The calculated DEP force on the microbot over time. The separate lines denote the partial forces in x and y directions, and the total force. The error bars denote the standard deviation of the measurement. The sweep used for creating the DEP force had a sweep time of 7 seconds and a sweep thickness of 120 pixels. The input voltage of the experiment is 30 V with a frequency of 7 kHz.

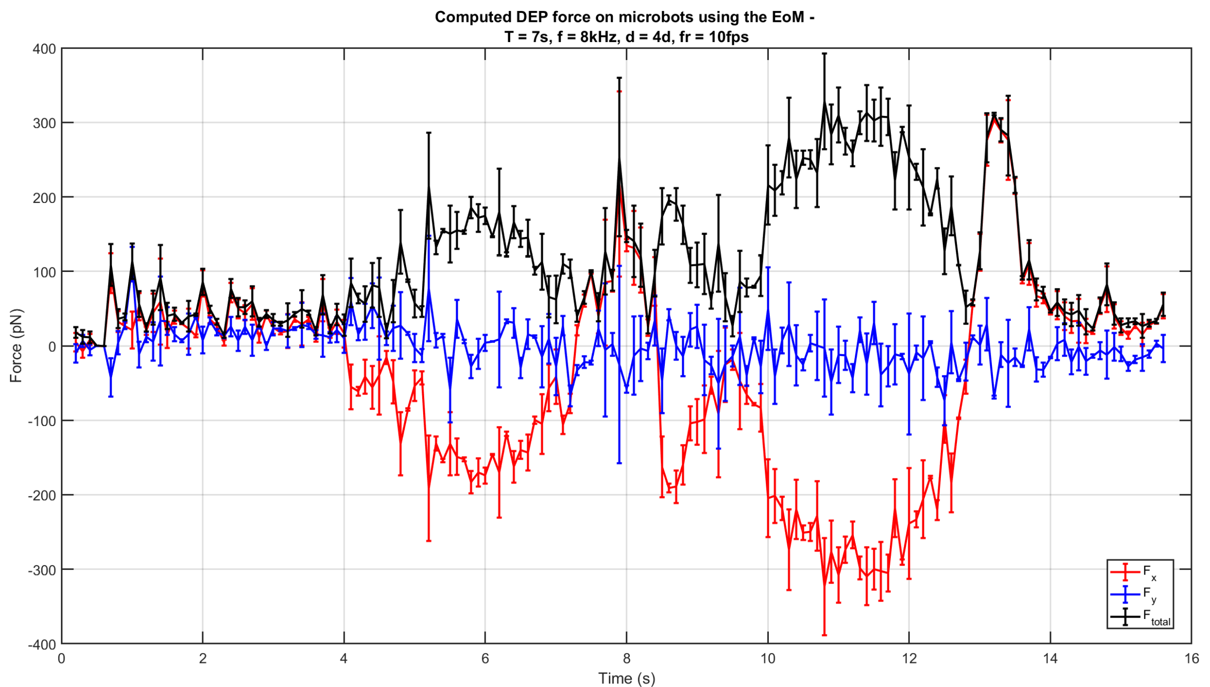

Figure D.133: The calculated DEP force on the microbot over time. The separate lines denote the partial forces in x and y directions, and the total force. The error bars denote the standard deviation of the measurement. The sweep used for creating the DEP force had a sweep time of 7 seconds and a sweep thickness of 120 pixels. The input voltage of the experiment is 30 V with a frequency of 8 kHz.

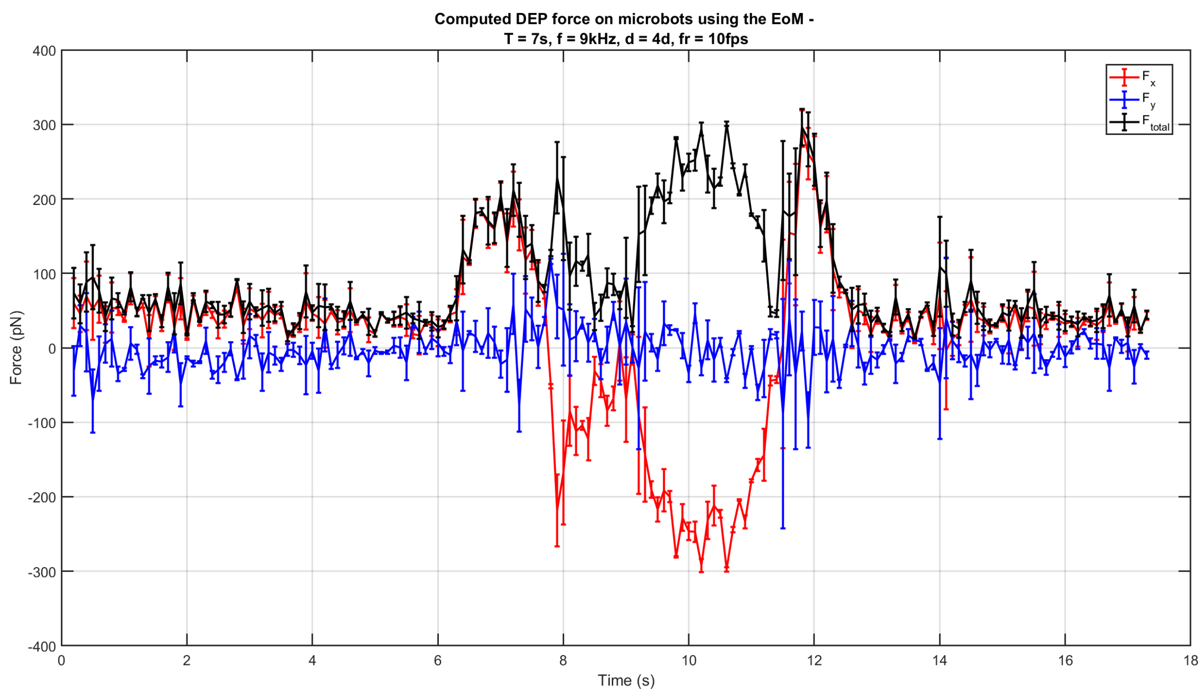

Figure D.134: The calculated DEP force on the microbot over time. The separate lines denote the partial forces in x and y directions, and the total force. The error bars denote the standard deviation of the measurement. The sweep used for creating the DEP force had a sweep time of 7 seconds and a sweep thickness of 120 pixels. The input voltage of the experiment is 30 V with a frequency of 9 kHz.

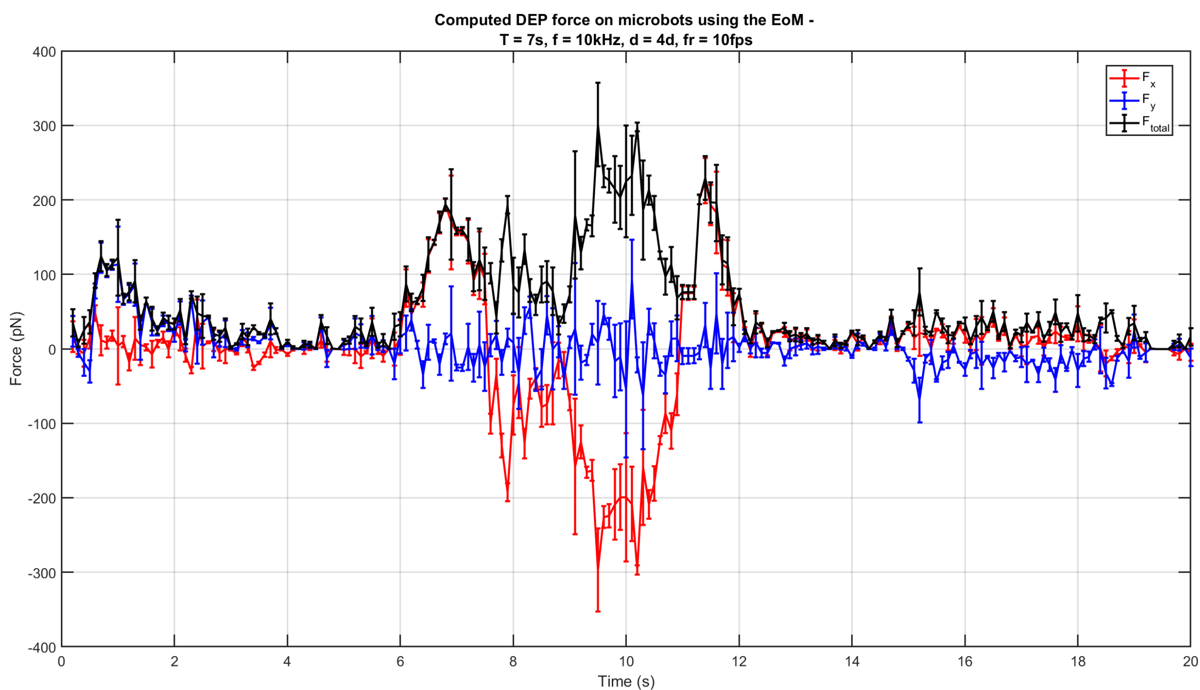

Figure D.135: The calculated DEP force on the microbot over time. The separate lines denote the partial forces in x and y directions, and the total force. The error bars denote the standard deviation of the measurement. The sweep used for creating the DEP force had a sweep time of 7 seconds and a sweep thickness of 120 pixels. The input voltage of the experiment is 30 V with a frequency of 10 kHz.

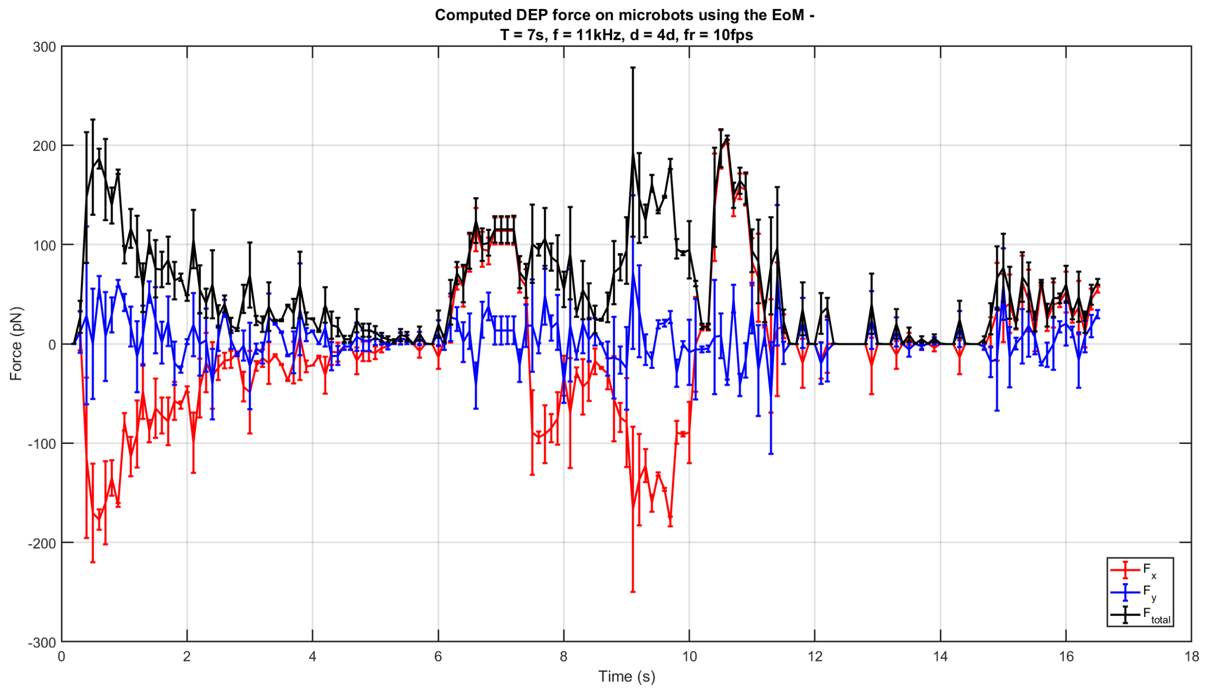

Figure D.136: The calculated DEP force on the microbot over time. The separate lines denote the partial forces in x and y directions, and the total force. The error bars denote the standard deviation of the measurement. The sweep used for creating the DEP force had a sweep time of 7 seconds and a sweep thickness of 120 pixels. The input voltage of the experiment is 30 V with a frequency of 11 kHz.

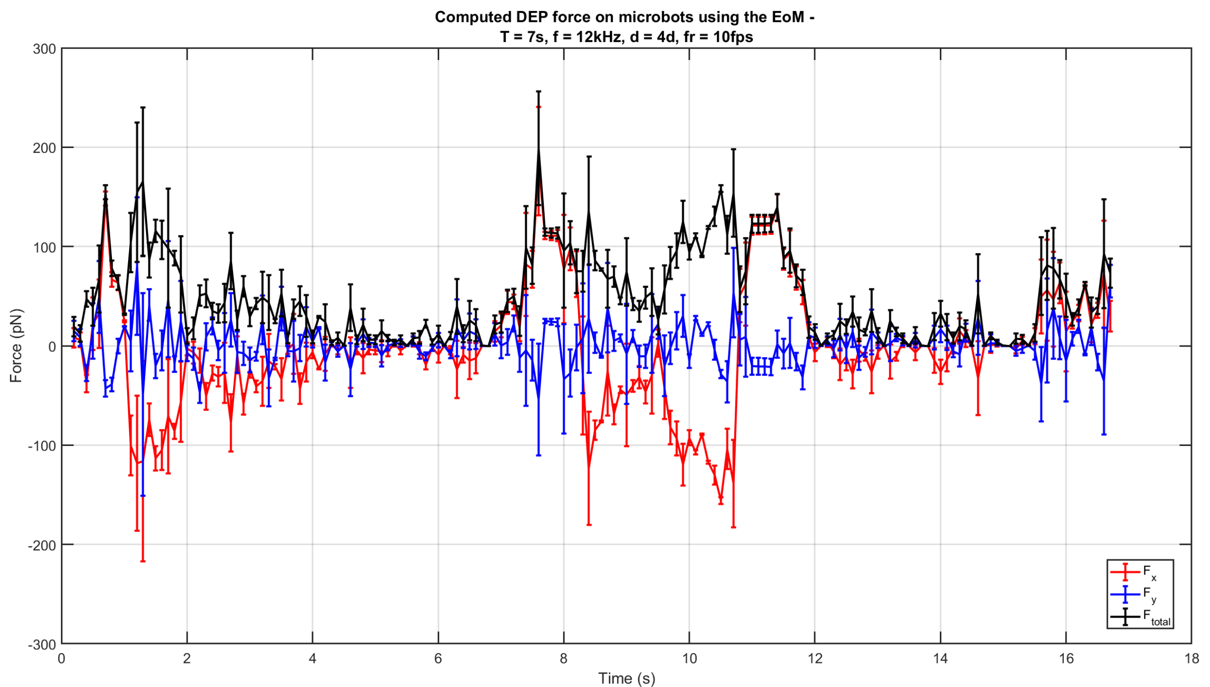

Figure D.137: The calculated DEP force on the microbot over time. The separate lines denote the partial forces in x and y directions, and the total force. The error bars denote the standard deviation of the measurement. The sweep used for creating the DEP force had a sweep time of 7 seconds and a sweep thickness of 120 pixels. The input voltage of the experiment is 30 V with a frequency of 12 kHz.

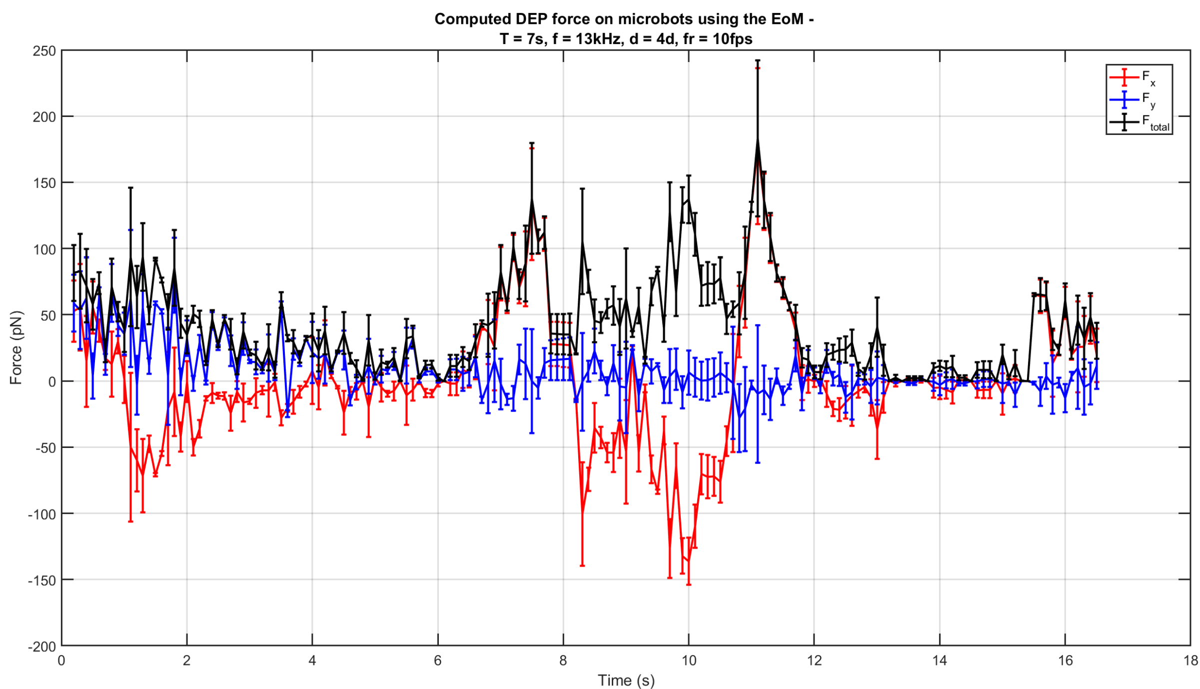

Figure D.138: The calculated DEP force on the microbot over time. The separate lines denote the partial forces in x and y directions, and the total force. The error bars denote the standard deviation of the measurement. The sweep used for creating the DEP force had a sweep time of 7 seconds and a sweep thickness of 120 pixels. The input voltage of the experiment is 30 V with a frequency of 13 kHz.

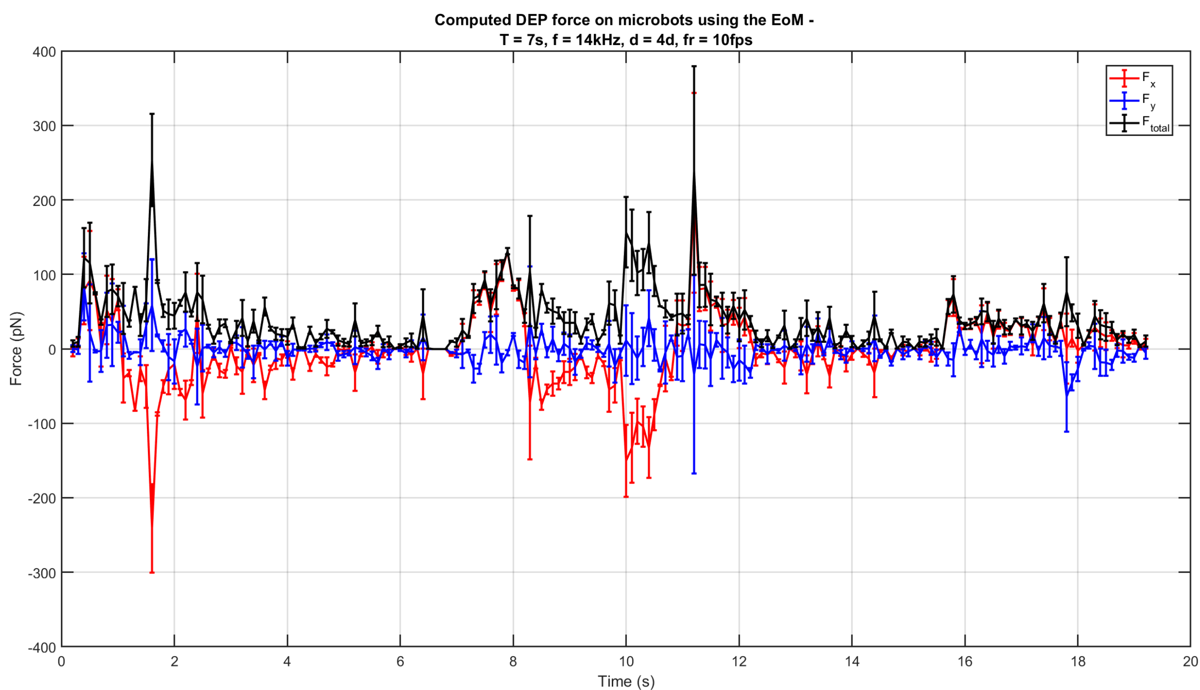

Figure D.139: The calculated DEP force on the microbot over time. The separate lines denote the partial forces in x and y directions, and the total force. The error bars denote the standard deviation of the measurement. The sweep used for creating the DEP force had a sweep time of 7 seconds and a sweep thickness of 120 pixels. The input voltage of the experiment is 30 V with a frequency of 14 kHz.

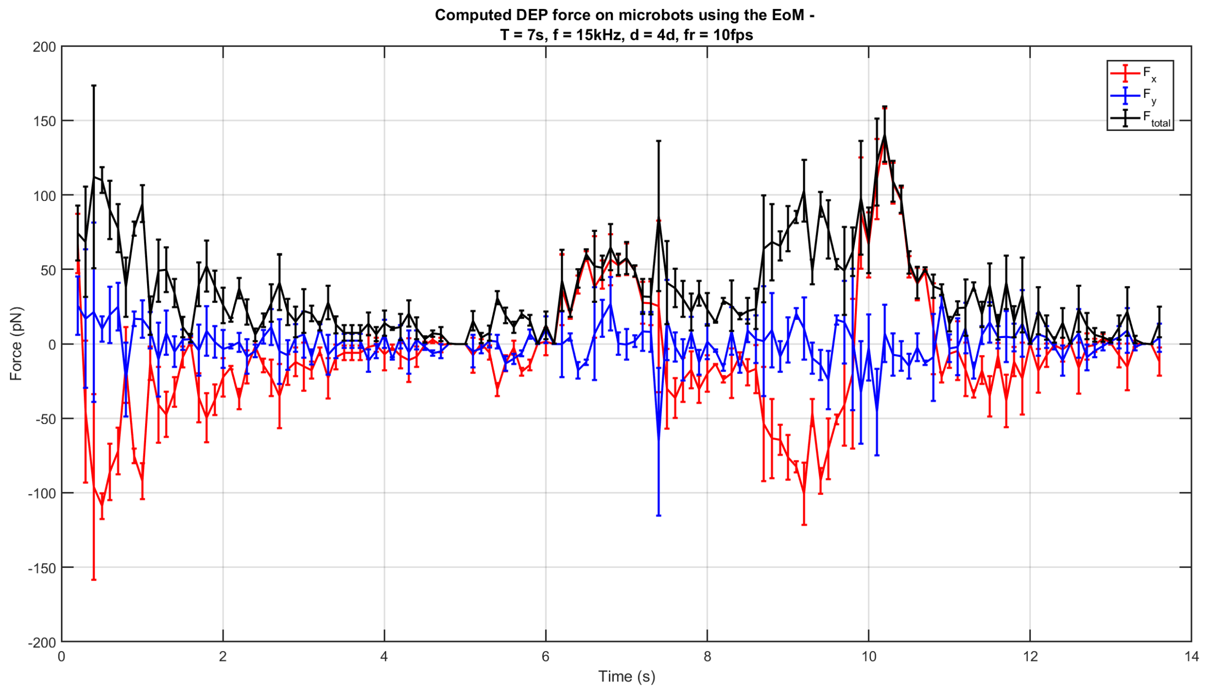

Figure D.140: The calculated DEP force on the microbot over time. The separate lines denote the partial forces in x and y directions, and the total force. The error bars denote the standard deviation of the measurement. The sweep used for creating the DEP force had a sweep time of 7 seconds and a sweep thickness of 120 pixels. The input voltage of the experiment is 30 V with a frequency of 15 kHz.

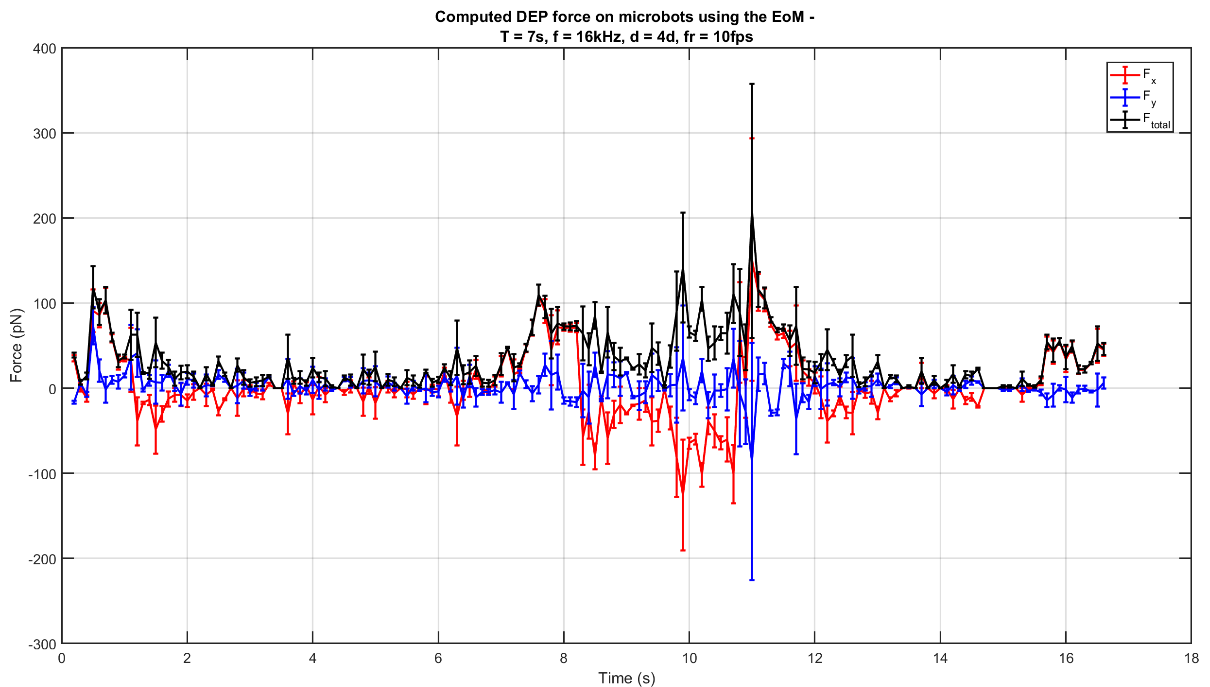

Figure D.141: The calculated DEP force on the microbot over time. The separate lines denote the partial forces in x and y directions, and the total force. The error bars denote the standard deviation of the measurement. The sweep used for creating the DEP force had a sweep time of 7 seconds and a sweep thickness of 120 pixels. The input voltage of the experiment is 30 V with a frequency of 16 kHz.

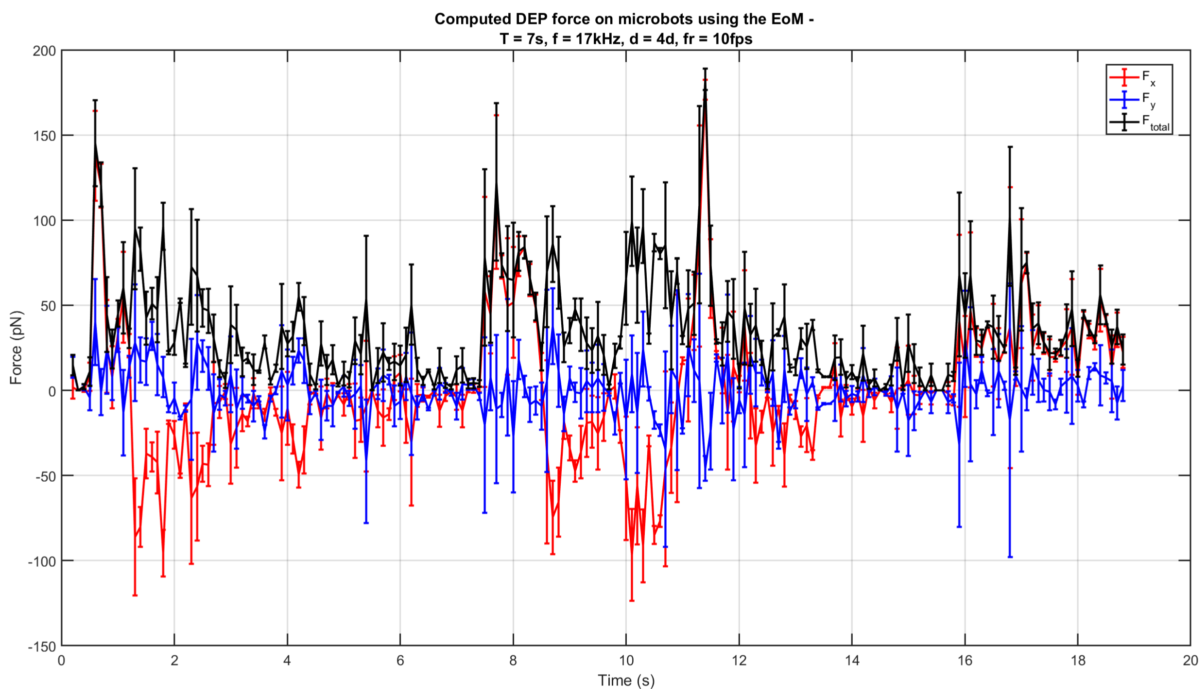

Figure D.142: The calculated DEP force on the microbot over time. The separate lines denote the partial forces in x and y directions, and the total force. The error bars denote the standard deviation of the measurement. The sweep used for creating the DEP force had a sweep time of 7 seconds and a sweep thickness of 120 pixels. The input voltage of the experiment is 30 V with a frequency of 17 kHz.

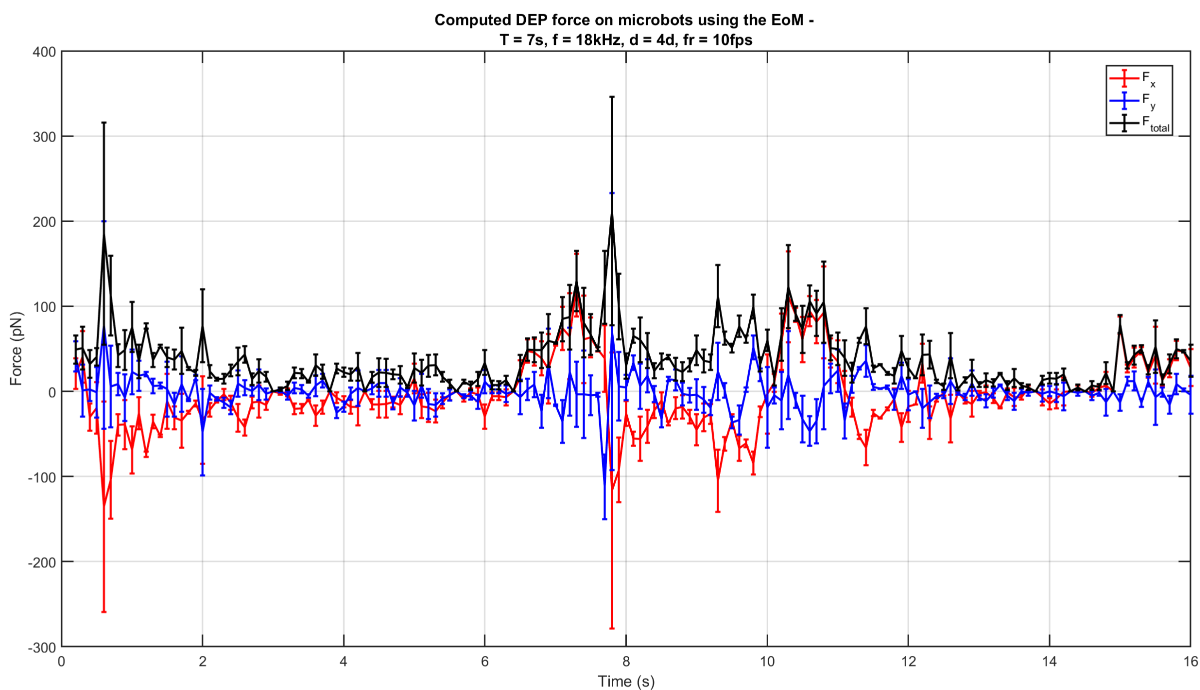

Figure D.143: The calculated DEP force on the microbot over time. The separate lines denote the partial forces in x and y directions, and the total force. The error bars denote the standard deviation of the measurement. The sweep used for creating the DEP force had a sweep time of 7 seconds and a sweep thickness of 120 pixels. The input voltage of the experiment is 30 V with a frequency of 18 kHz.

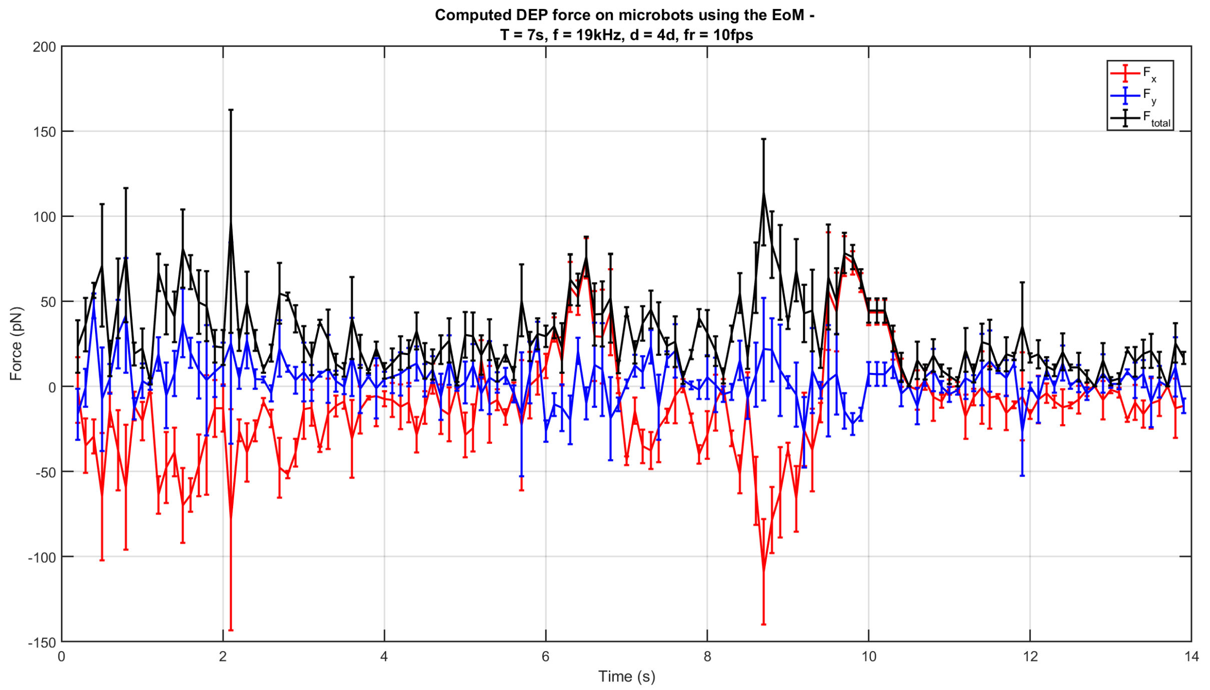

Figure D.144: The calculated DEP force on the microbot over time. The separate lines denote the partial forces in x and y directions, and the total force. The error bars denote the standard deviation of the measurement. The sweep used for creating the DEP force had a sweep time of 7 seconds and a sweep thickness of 120 pixels. The input voltage of the experiment is 30 V with a frequency of 19 kHz.

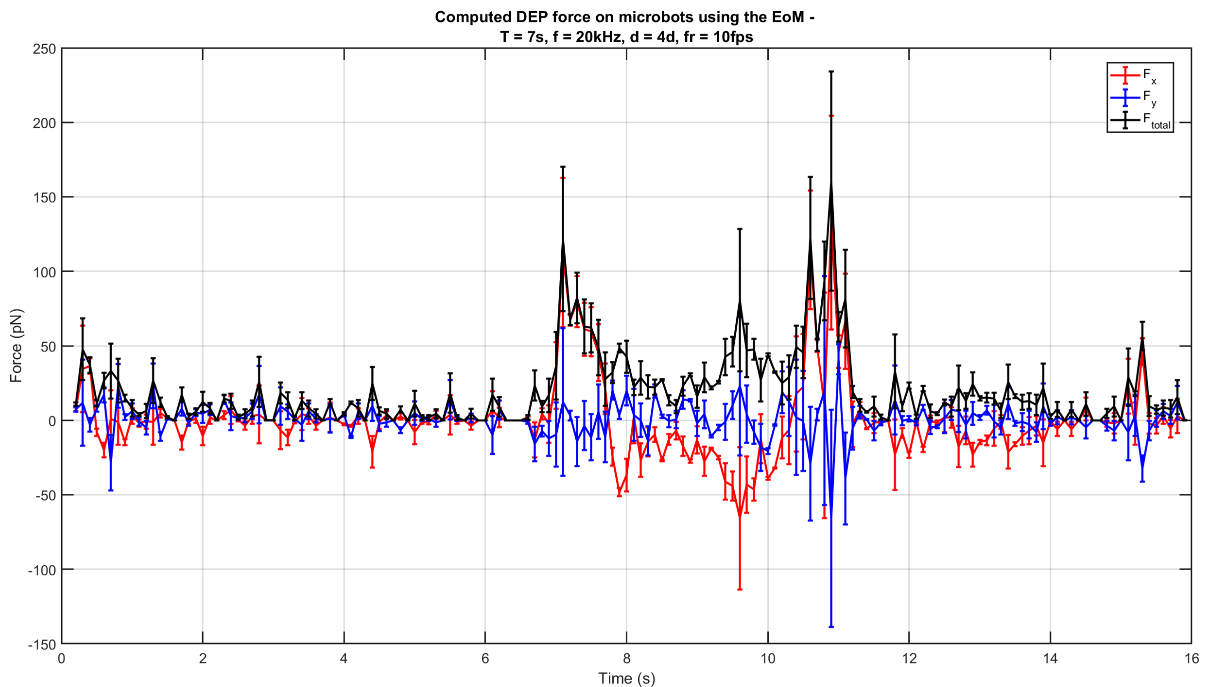

Figure D.145: The calculated DEP force on the microbot over time. The separate lines denote the partial forces in x and y directions, and the total force. The error bars denote the standard deviation of the measurement. The sweep used for creating the DEP force had a sweep time of 7 seconds and a sweep thickness of 120 pixels. The input voltage of the experiment is 30 V with a frequency of 20 kHz.

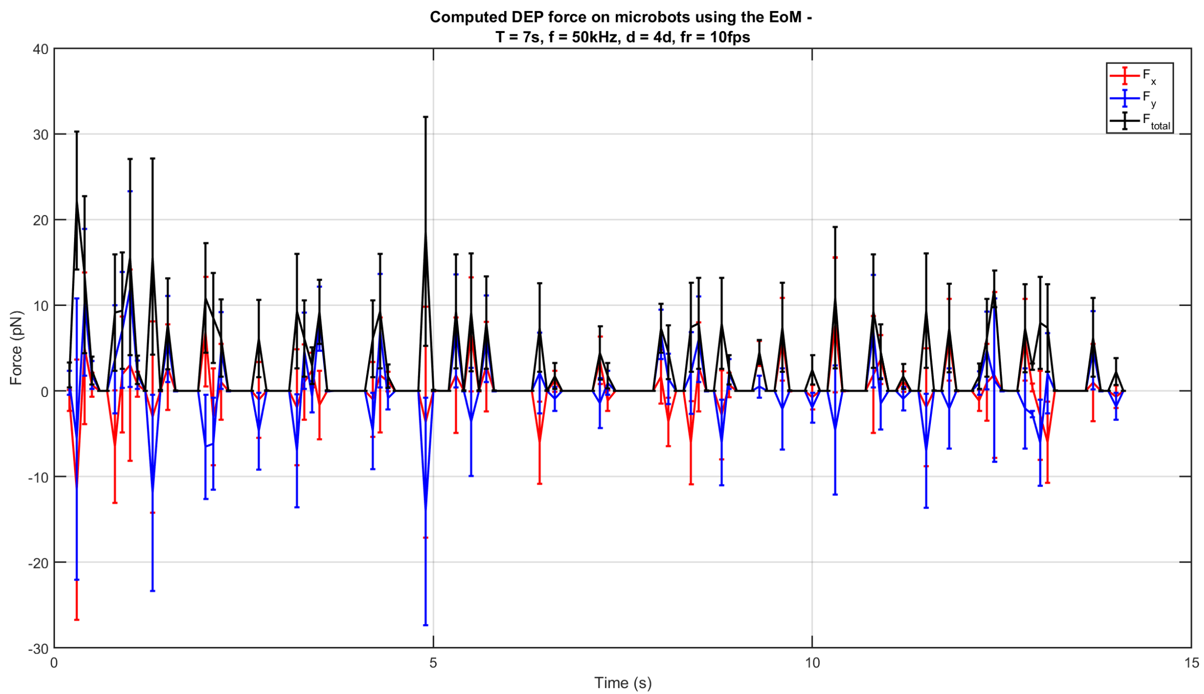

Figure D.146: The calculated DEP force on the microbot over time. The separate lines denote the partial forces in x and y directions, and the total force. The error bars denote the standard deviation of the measurement. The sweep used for creating the DEP force had a sweep time of 7 seconds and a sweep thickness of 120 pixels. The input voltage of the experiment is 30 V with a frequency of 50 kHz.

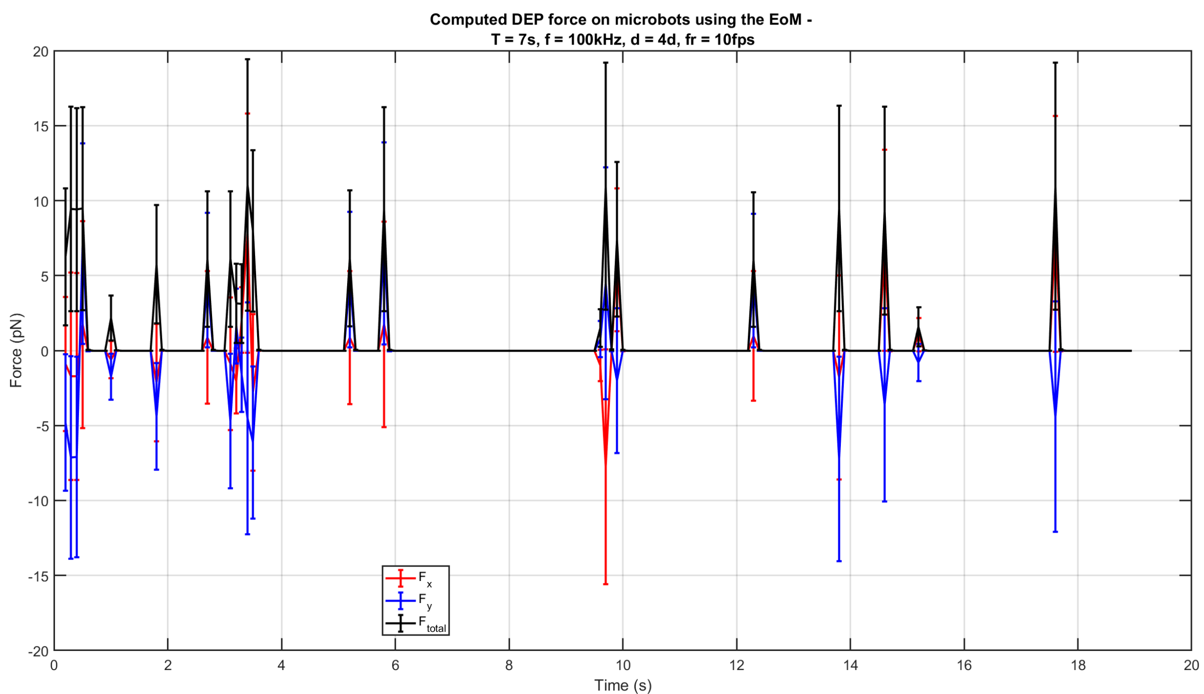

Figure D.147: The calculated DEP force on the microbot over time. The separate lines denote the partial forces in x and y directions, and the total force. The error bars denote the standard deviation of the measurement. The sweep used for creating the DEP force had a sweep time of 7 seconds and a sweep thickness of 120 pixels. The input voltage of the experiment is 30 V with a frequency of 100 kHz.

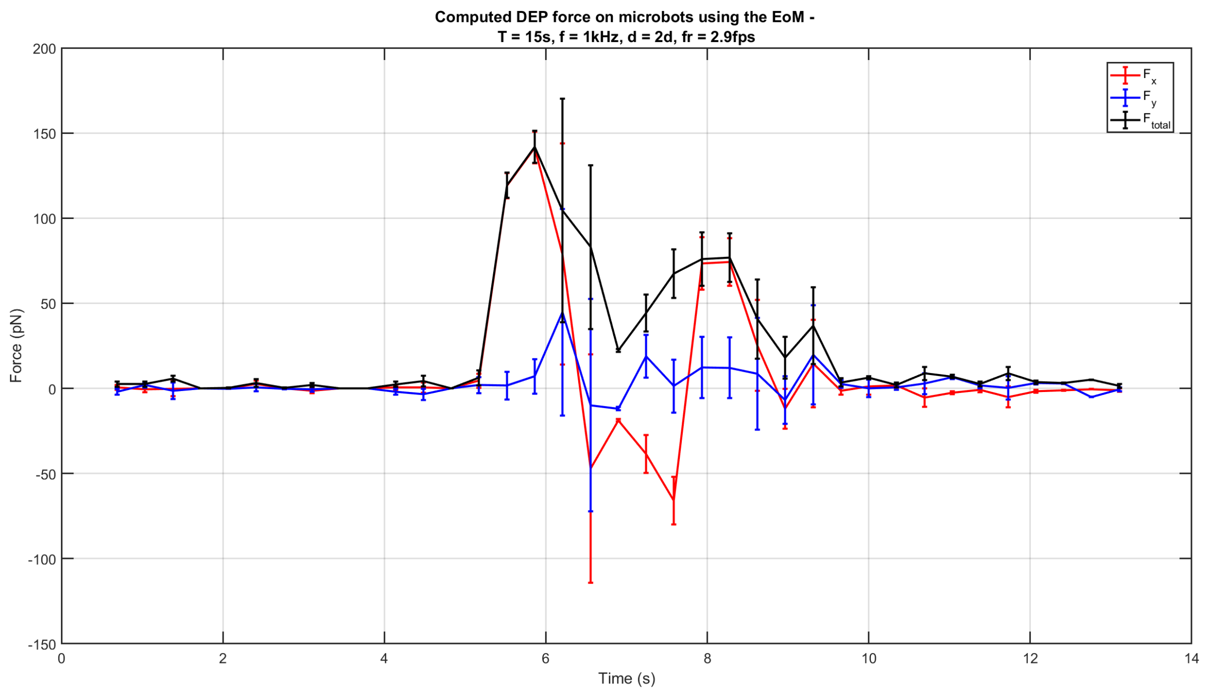

Figure D.148: The calculated DEP force on the microbot over time. The separate lines denote the partial forces in x and y directions, and the total force. The error bars denote the standard deviation of the measurement. The sweep used for creating the DEP force had a sweep time of 15 seconds and a sweep thickness of 60 pixels. The input voltage of the experiment is 30 V with a frequency of 1 kHz.

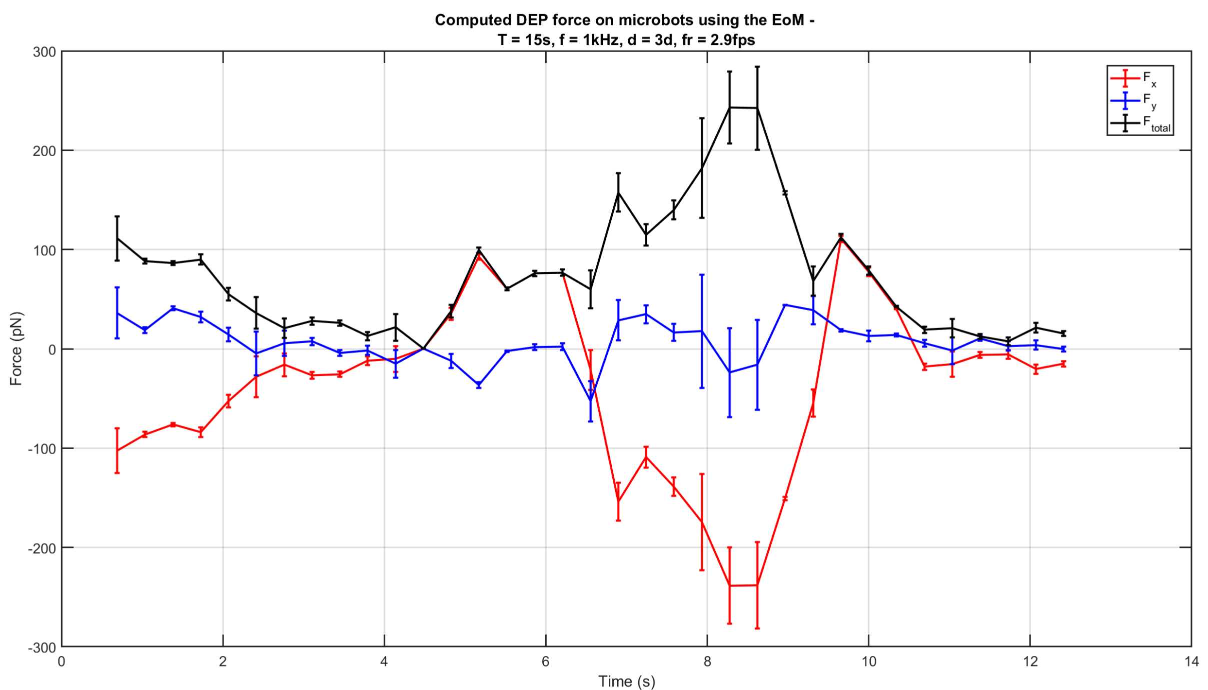

Figure D.149: The calculated DEP force on the microbot over time. The separate lines denote the partial forces in x and y directions, and the total force. The error bars denote the standard deviation of the measurement. The sweep used for creating the DEP force had a sweep time of 15 seconds and a sweep thickness of 90 pixels. The input voltage of the experiment is 30 V with a frequency of 1 kHz.

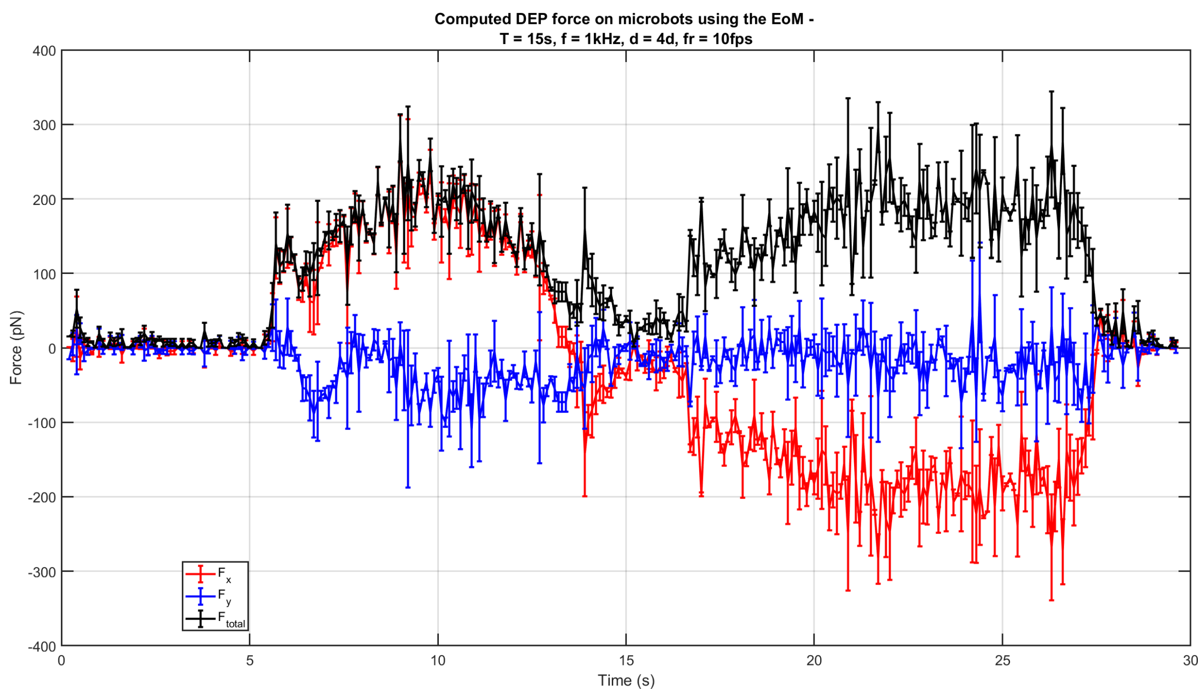

Figure D.150: The calculated DEP force on the microbot over time. The separate lines denote the partial forces in x and y directions, and the total force. The error bars denote the standard deviation of the measurement. The sweep used for creating the DEP force had a sweep time of 15 seconds and a sweep thickness of 120 pixels. The input voltage of the experiment is 30 V with a frequency of 1 kHz.

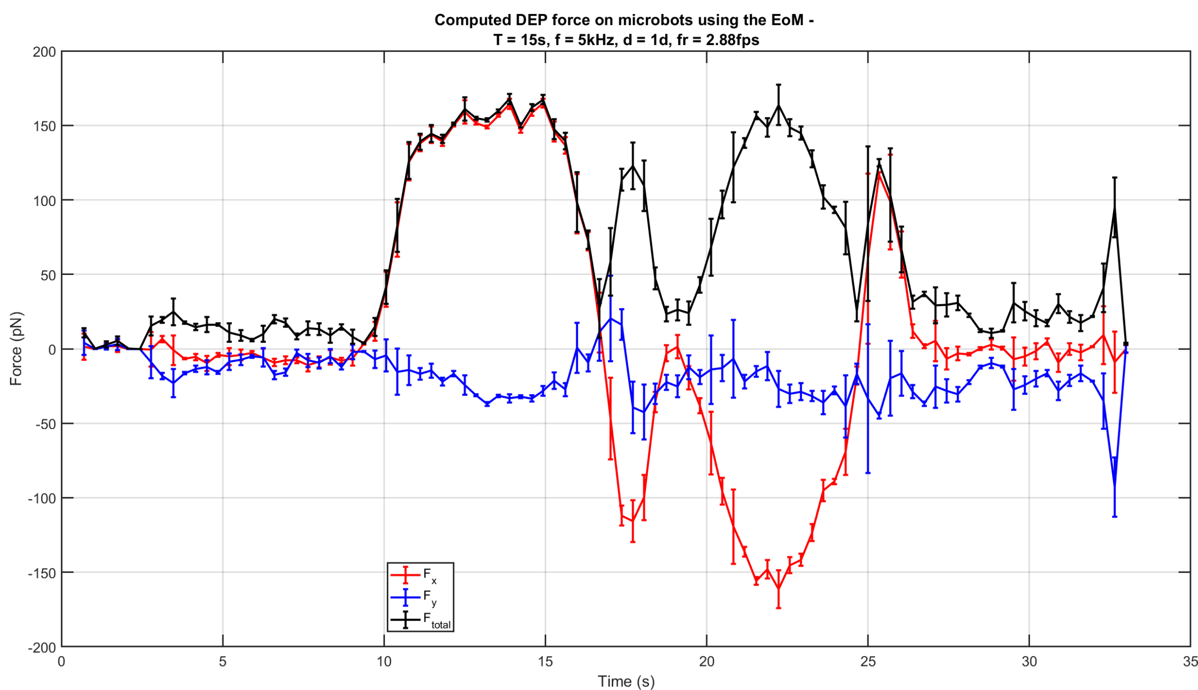

Figure D.151: The calculated DEP force on the microbot over time. The separate lines denote the partial forces in x and y directions, and the total force. The error bars denote the standard deviation of the measurement. The sweep used for creating the DEP force had a sweep time of 15 seconds and a sweep thickness of 30 pixels. The input voltage of the experiment is 30 V with a frequency of 5 kHz.

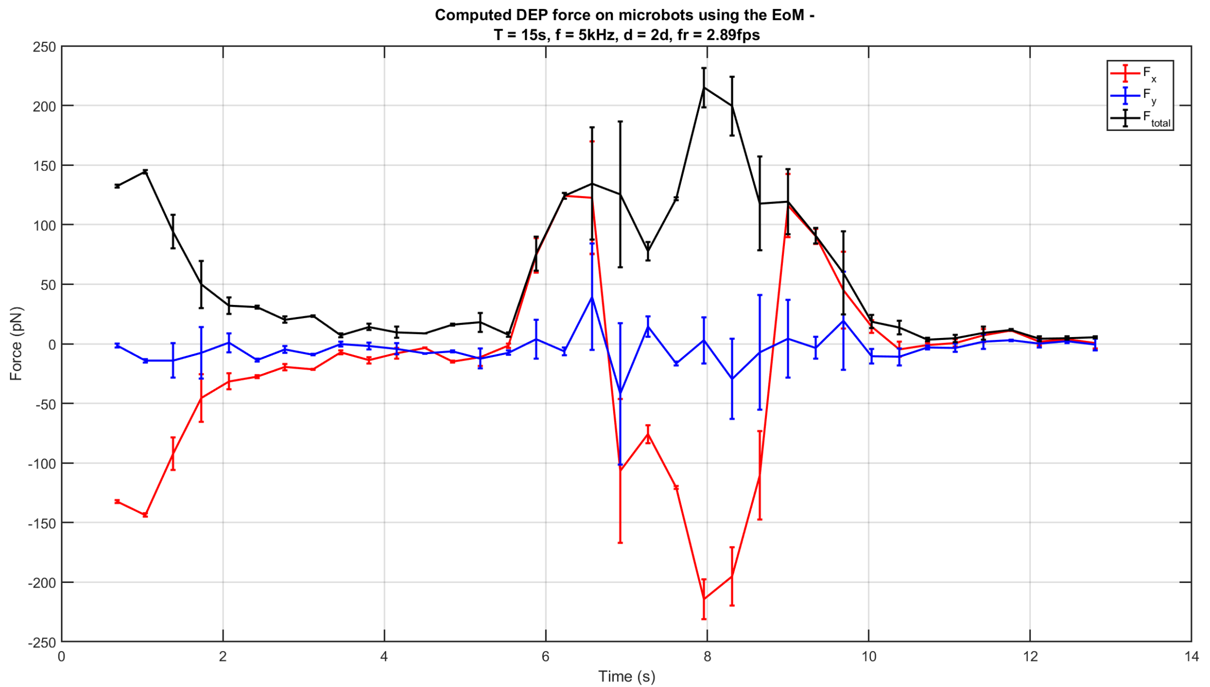

Figure D.152: The calculated DEP force on the microbot over time. The separate lines denote the partial forces in x and y directions, and the total force. The error bars denote the standard deviation of the measurement. The sweep used for creating the DEP force had a sweep time of 15 seconds and a sweep thickness of 60 pixels. The input voltage of the experiment is 30 V with a frequency of 5 kHz.

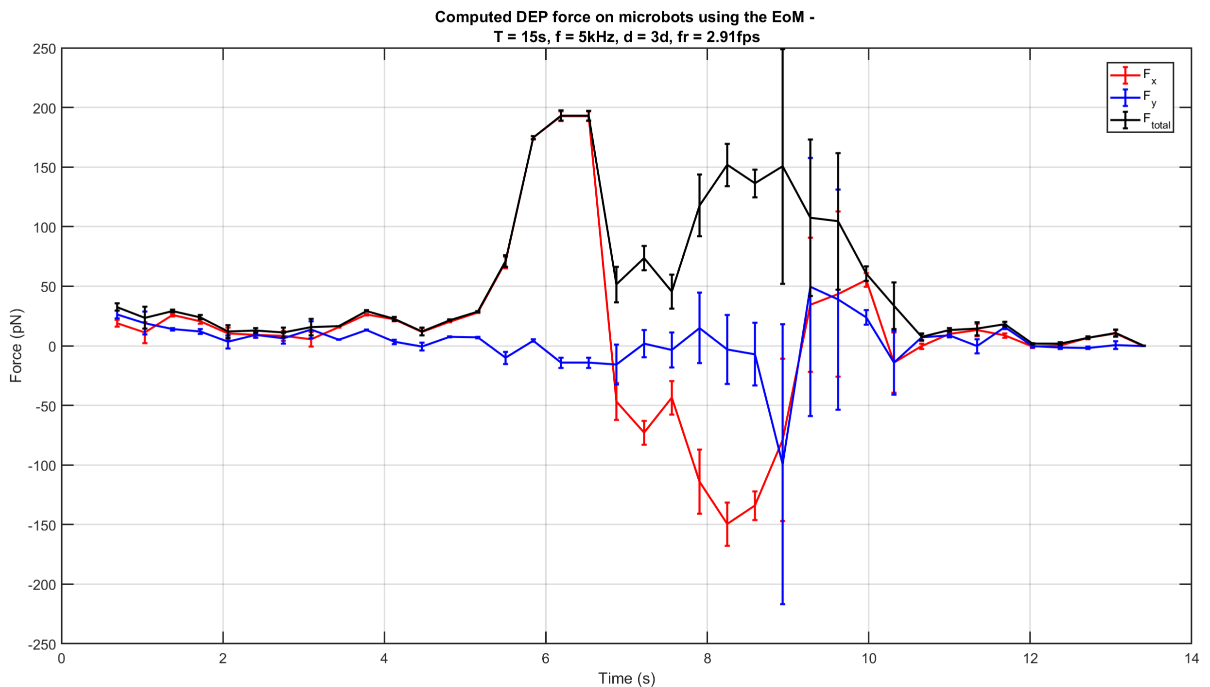

Figure D.153: The calculated DEP force on the microbot over time. The separate lines denote the partial forces in x and y directions, and the total force. The error bars denote the standard deviation of the measurement. The sweep used for creating the DEP force had a sweep time of 15 seconds and a sweep thickness of 90 pixels. The input voltage of the experiment is 30 V with a frequency of 5 kHz.

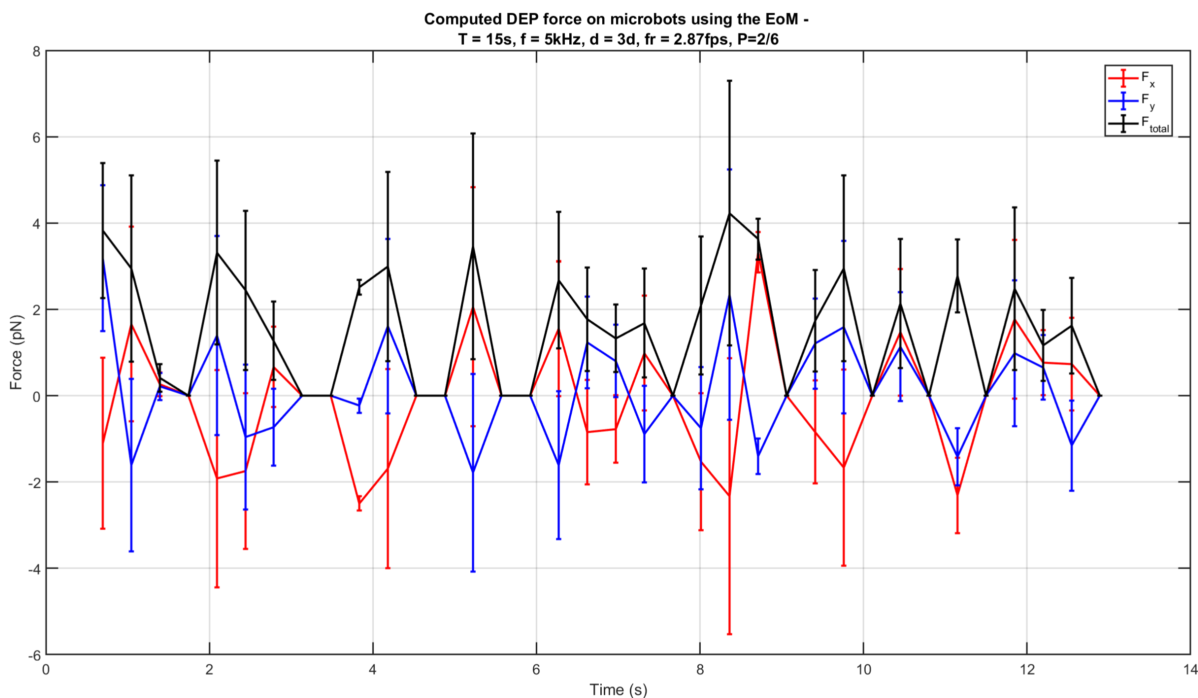

Figure D.154: The calculated DEP force on the microbot over time. The separate lines denote the partial forces in x and y directions, and the total force. The error bars denote the standard deviation of the measurement. The sweep used for creating the DEP force had a sweep time of 15 seconds and a sweep thickness of 90 pixels. The input voltage of the experiment is 30 V with a frequency of 5 kHz. The illumination power is set to 1/3 of the full power.

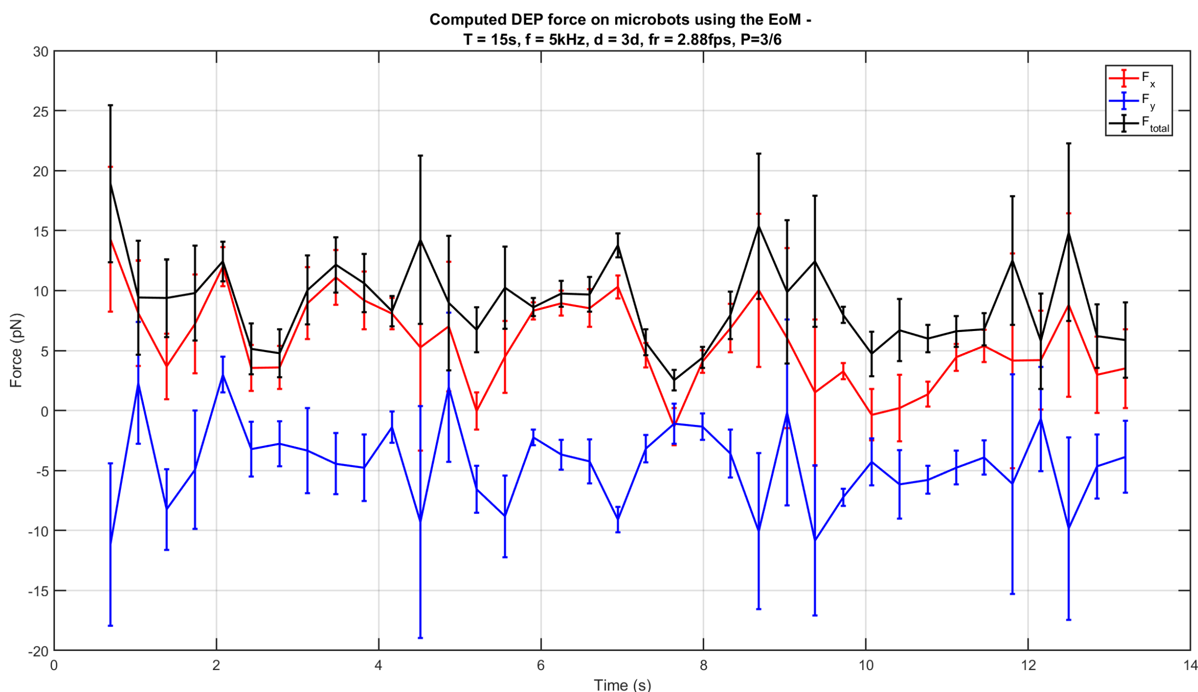

Figure D.155: The calculated DEP force on the microbot over time. The separate lines denote the partial forces in x and y directions, and the total force. The error bars denote the standard deviation of the measurement. The sweep used for creating the DEP force had a sweep time of 15 seconds and a sweep thickness of 90 pixels. The input voltage of the experiment is 30 V with a frequency of 5 kHz. The illumination power is set to 1/2 of the full power.

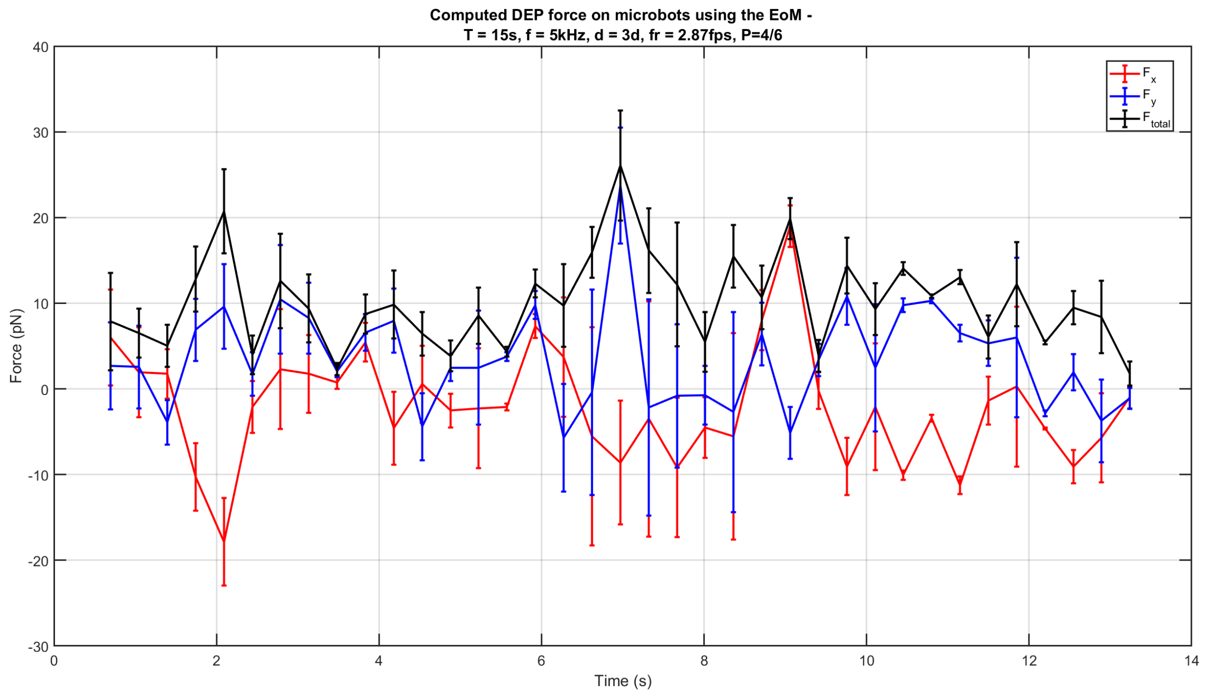

Figure D.156: The calculated DEP force on the microbot over time. The separate lines denote the partial forces in x and y directions, and the total force. The error bars denote the standard deviation of the measurement. The sweep used for creating the DEP force had a sweep time of 15 seconds and a sweep thickness of 90 pixels. The input voltage of the experiment is 30 V with a frequency of 5 kHz. The illumination power is set to 2/3 of the full power.

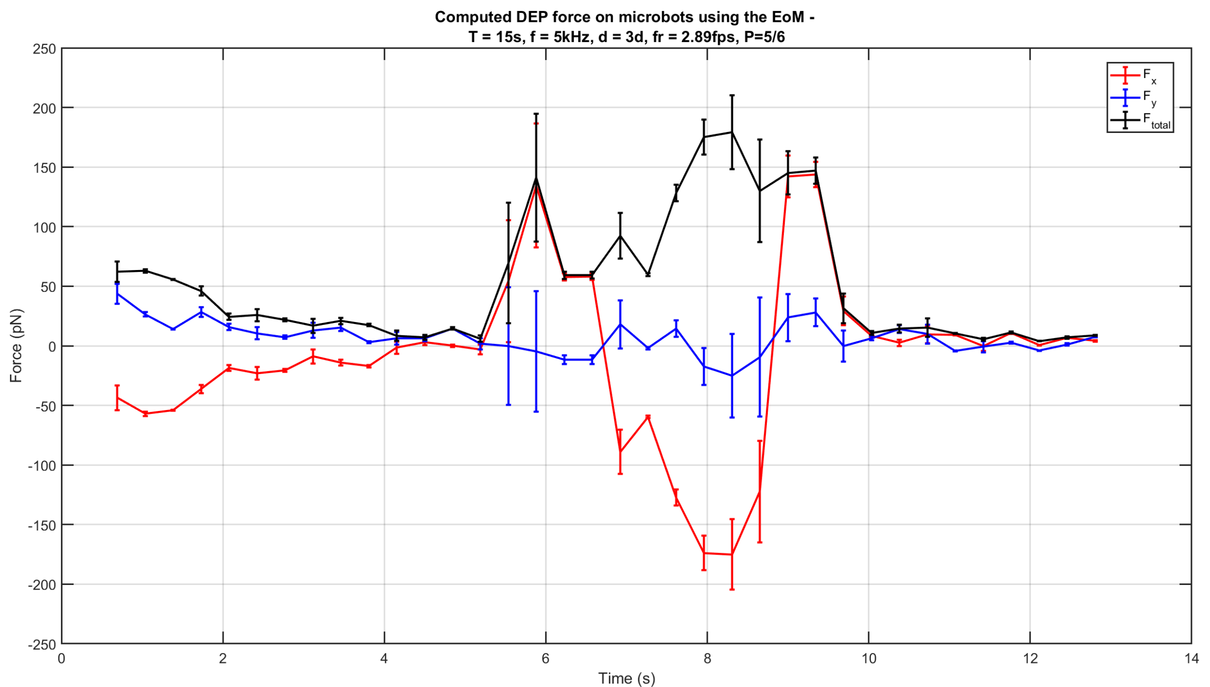

Figure D.157: The calculated DEP force on the microbot over time. The separate lines denote the partial forces in x and y directions, and the total force. The error bars denote the standard deviation of the measurement. The sweep used for creating the DEP force had a sweep time of 15 seconds and a sweep thickness of 90 pixels. The input voltage of the experiment is 30 V with a frequency of 5 kHz. The illumination power is set to 5/6 of the full power.

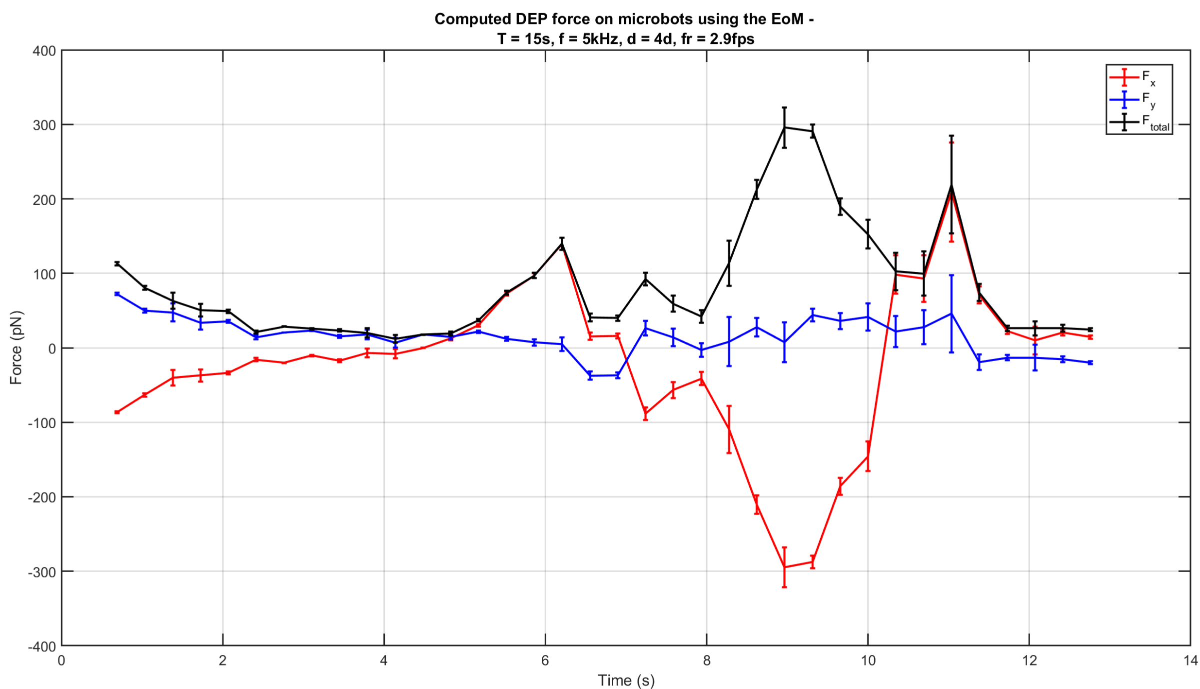

Figure D.158: The calculated DEP force on the microbot over time. The separate lines denote the partial forces in x and y directions, and the total force. The error bars denote the standard deviation of the measurement. The sweep used for creating the DEP force had a sweep time of 15 seconds and a sweep thickness of 120 pixels. The input voltage of the experiment is 30 V with a frequency of 5 kHz.

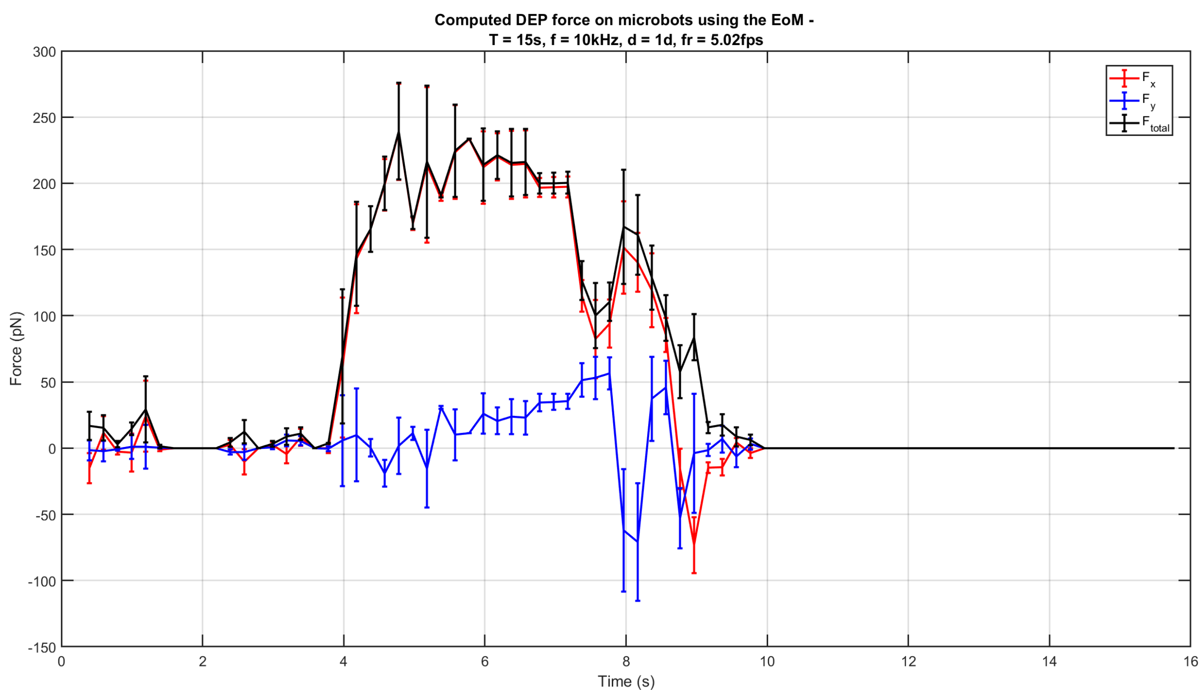

Figure D.159: The calculated DEP force on the microbot over time. The separate lines denote the partial forces in x and y directions, and the total force. The error bars denote the standard deviation of the measurement. The sweep used for creating the DEP force had a sweep time of 15 seconds and a sweep thickness of 30 pixels. The input voltage of the experiment is 30 V with a frequency of 10 kHz.

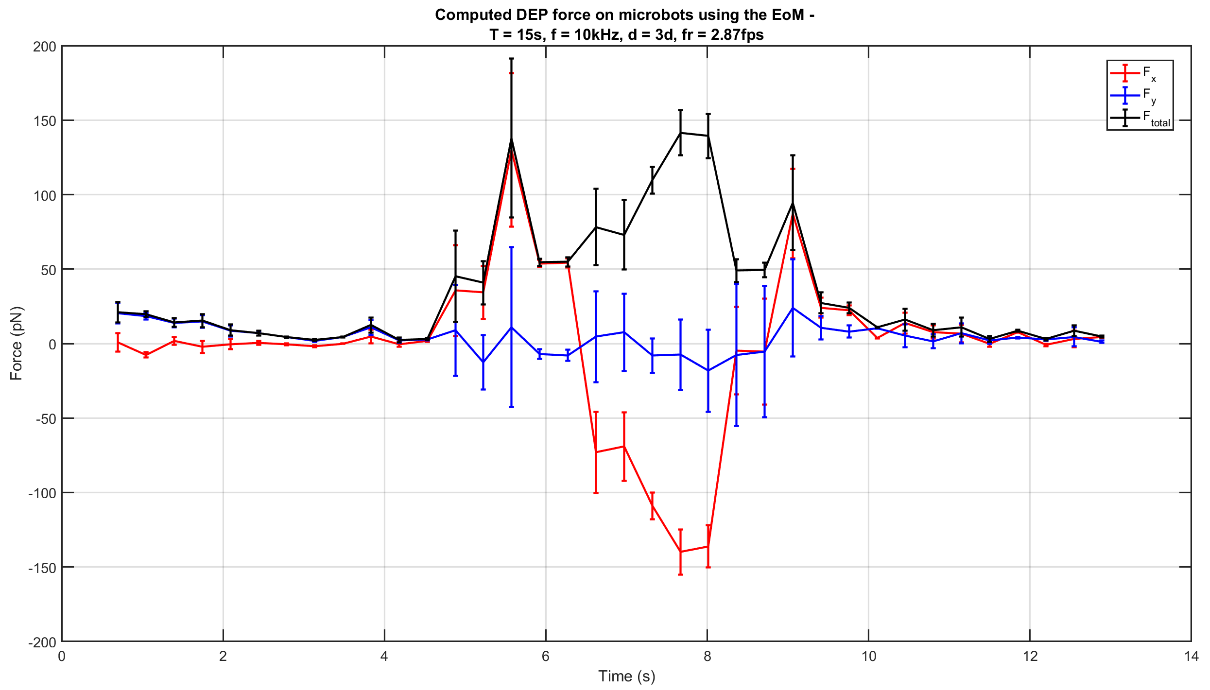

Figure D.160: The calculated DEP force on the microbot over time. The separate lines denote the partial forces in x and y directions, and the total force. The error bars denote the standard deviation of the measurement. The sweep used for creating the DEP force had a sweep time of 15 seconds and a sweep thickness of 90 pixels. The input voltage of the experiment is 30 V with a frequency of 10 kHz.

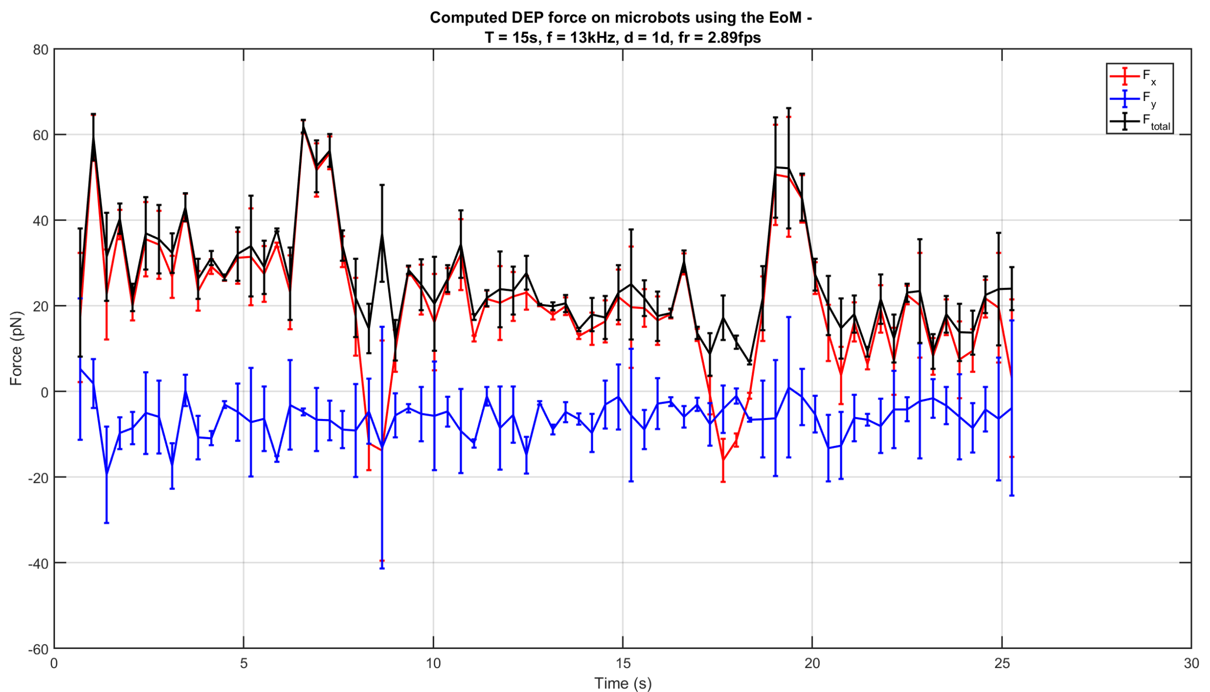

Figure D.161: The calculated DEP force on the microbot over time. The separate lines denote the partial forces in x and y directions, and the total force. The error bars denote the standard deviation of the measurement. The sweep used for creating the DEP force had a sweep time of 15 seconds and a sweep thickness of 30 pixels. The input voltage of the experiment is 30 V with a frequency of 13 kHz.

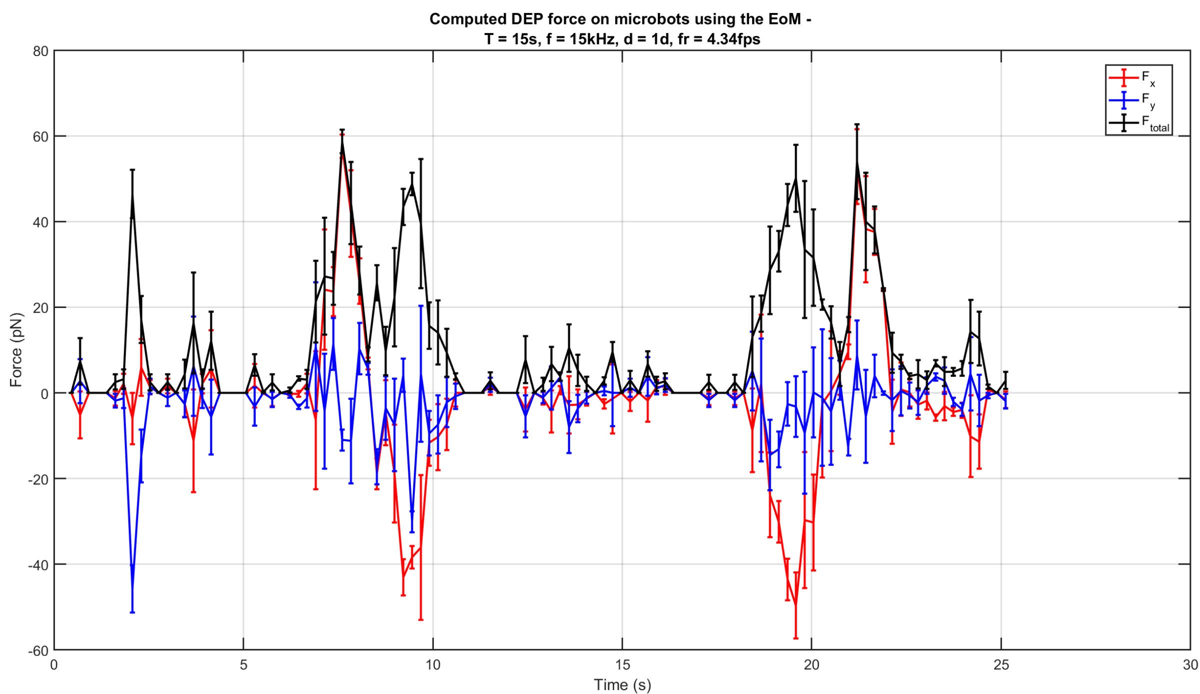

Figure D.162: The calculated DEP force on the microbot over time. The separate lines denote the partial forces in x and y directions, and the total force. The error bars denote the standard deviation of the measurement. The sweep used for creating the DEP force had a sweep time of 15 seconds and a sweep thickness of 30 pixels. The input voltage of the experiment is 30 V with a frequency of 15 kHz.

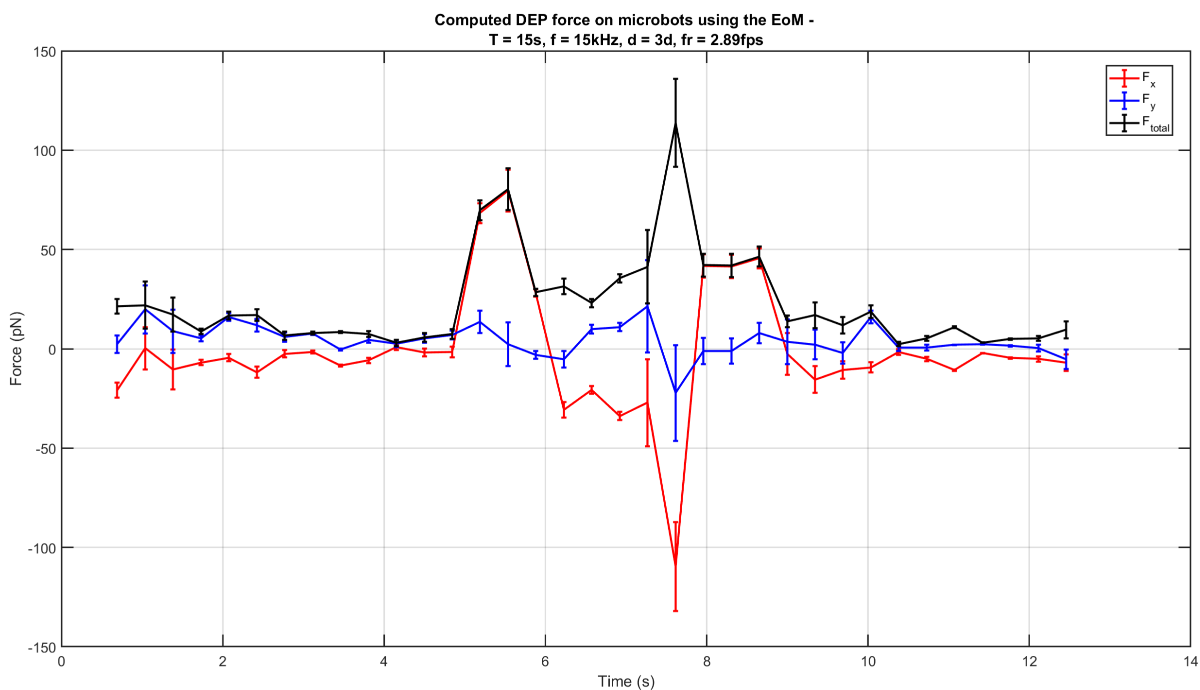

Figure D.163: The calculated DEP force on the microbot over time. The separate lines denote the partial forces in x and y directions, and the total force. The error bars denote the standard deviation of the measurement. The sweep used for creating the DEP force had a sweep time of 15 seconds and a sweep thickness of 90 pixels. The input voltage of the experiment is 30 V with a frequency of 15 kHz.

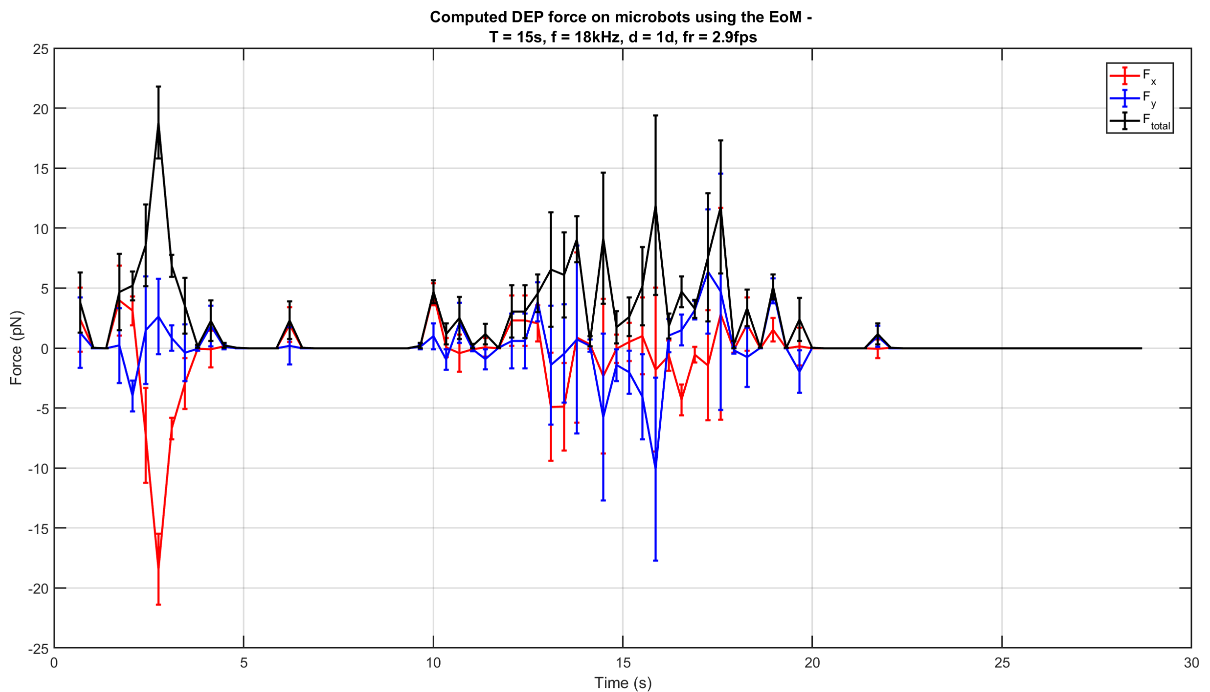

Figure D.164: The calculated DEP force on the microbot over time. The separate lines denote the partial forces in x and y directions, and the total force. The error bars denote the standard deviation of the measurement. The sweep used for creating the DEP force had a sweep time of 15 seconds and a sweep thickness of 30 pixels. The input voltage of the experiment is 30 V with a frequency of 18 kHz.

D.3.2. DEP force on the microbot, compared to literature

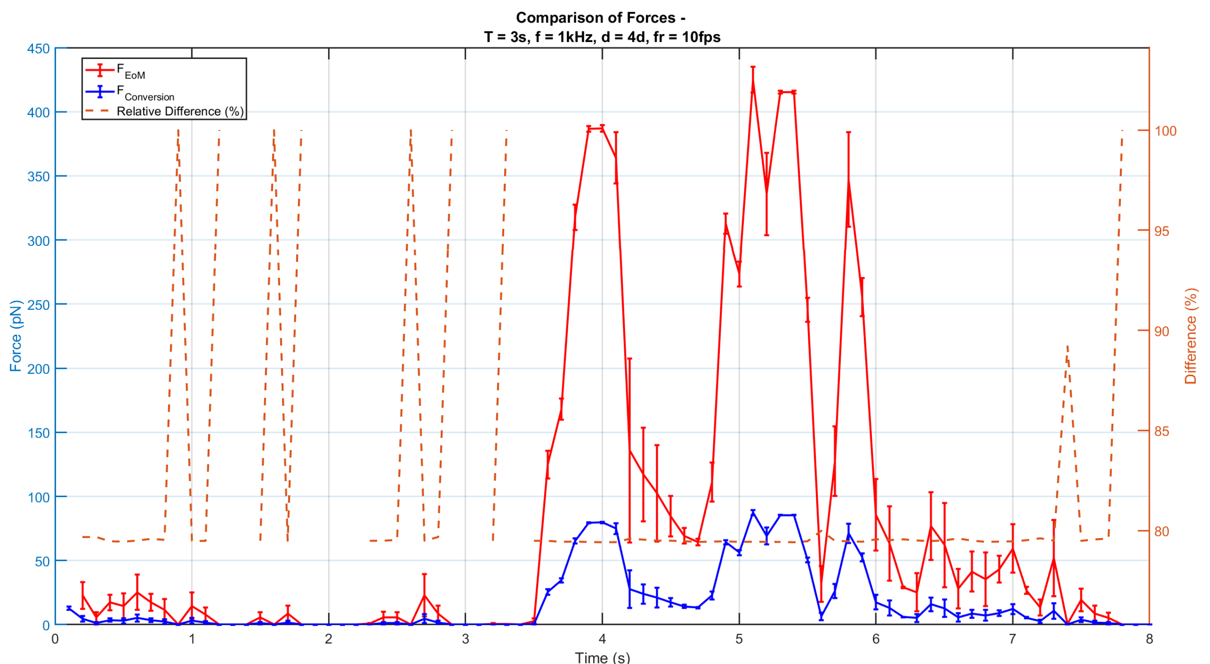

Figure D.165: A comparison of the forces on the microbot calculated using Stokes's law and the conversion coefficient from literature [8]. The relative difference is shown as a dashed orange line. When this dashed orange line is not present, it means that the calculated force is 0 pN. The error bars denote the standard deviation of the measurement. The sweep used for creating the DEP force had a sweep time of 3 seconds and a sweep thickness of 120 pixels. The input voltage of the experiment is 30 V with a frequency of 1 kHz.

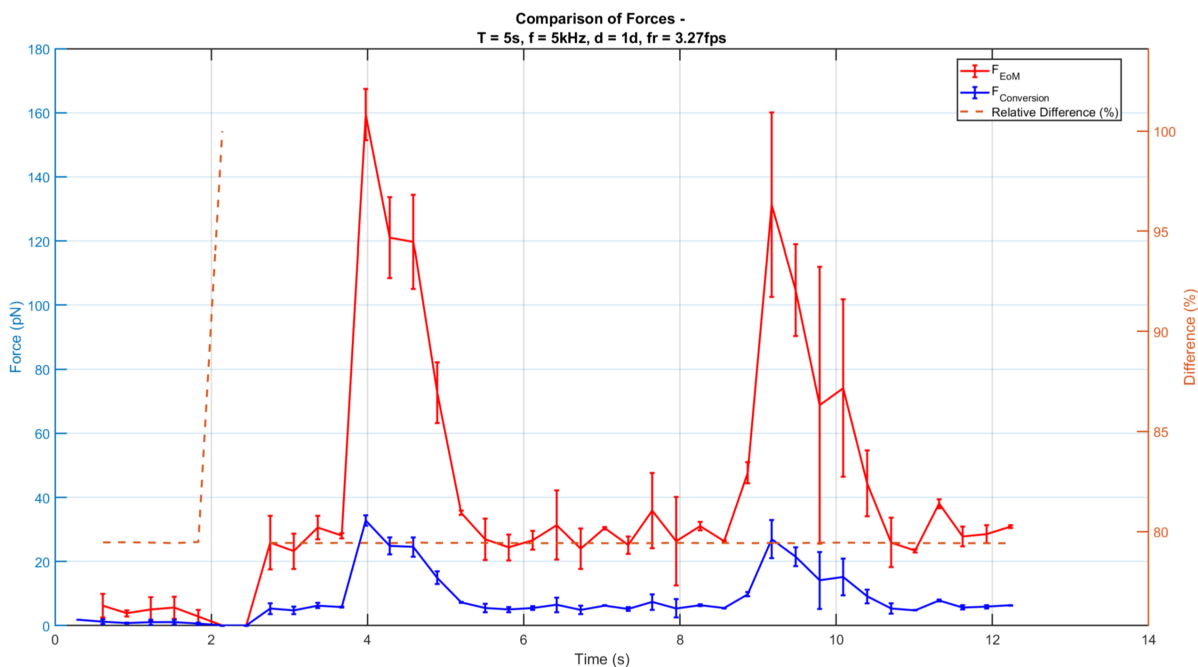

Figure D.166: A comparison of the forces on the microbot calculated using Stokes's law and the conversion coefficient from literature [8]. The relative difference is shown as a dashed orange line. When this dashed orange line is not present, it means that the calculated force is 0 pN. The error bars denote the standard deviation of the measurement. The sweep used for creating the DEP force had a sweep time of 5 seconds and a sweep thickness of 30 pixels. The input voltage of the experiment is 30 V with a frequency of 5 kHz.

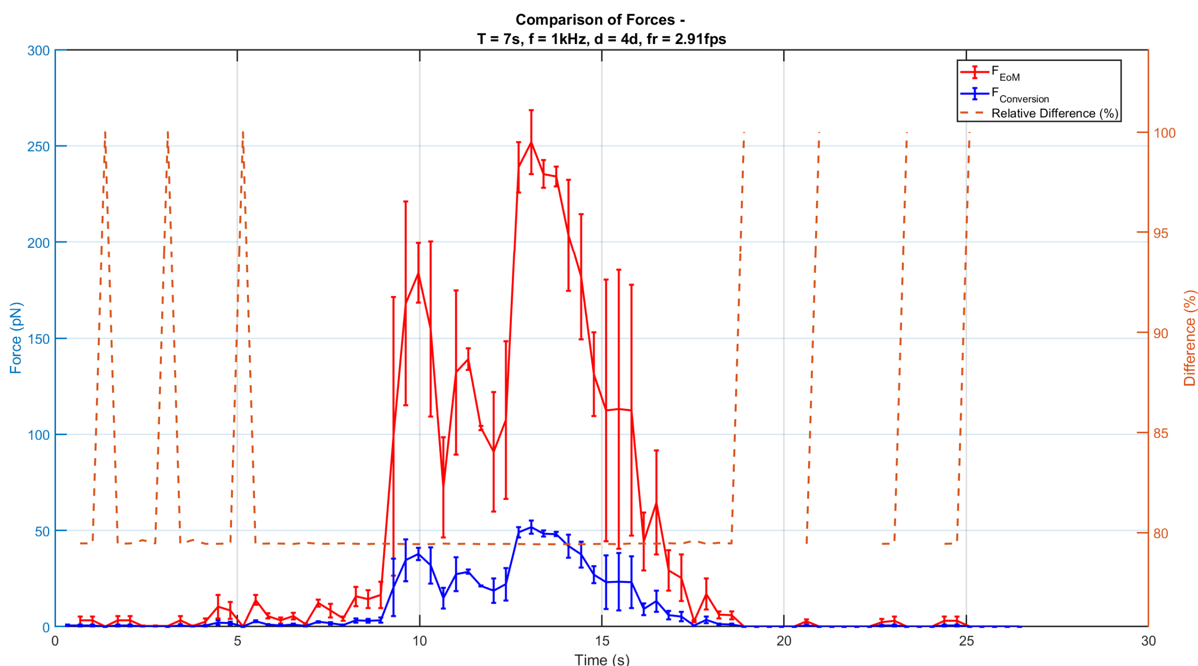

Figure D.167: A comparison of the forces on the microbot calculated using Stokes's law and the conversion coefficient from literature [8]. The relative difference is shown as a dashed orange line. When this dashed orange line is not present, it means that the calculated force is 0 pN. The error bars denote the standard deviation of the measurement. The sweep used for creating the DEP force had a sweep time of 7 seconds and a sweep thickness of 120 pixels. The input voltage of the experiment is 30 V with a frequency of 1 kHz.

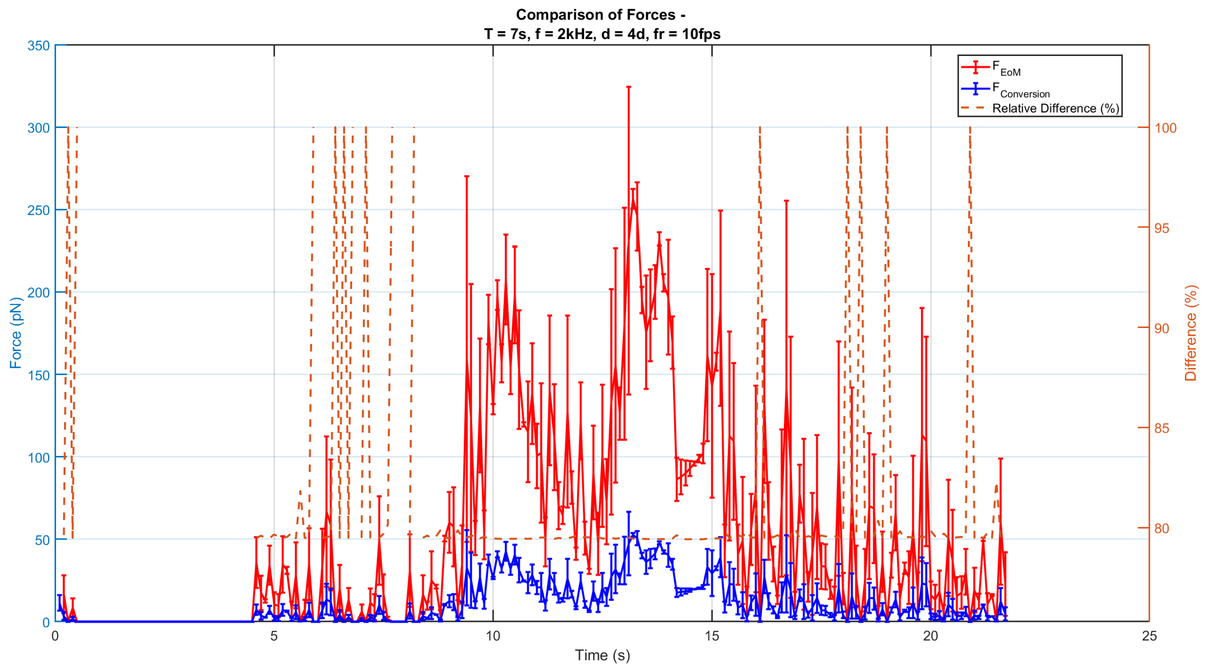

Figure D.168: A comparison of the forces on the microbot calculated using Stokes's law and the conversion coefficient from literature [8]. The relative difference is shown as a dashed orange line. When this dashed orange line is not present, it means that the calculated force is 0 pN. The error bars denote the standard deviation of the measurement. The sweep used for creating the DEP force had a sweep time of 7 seconds and a sweep thickness of 120 pixels. The input voltage of the experiment is 30 V with a frequency of 2 kHz.

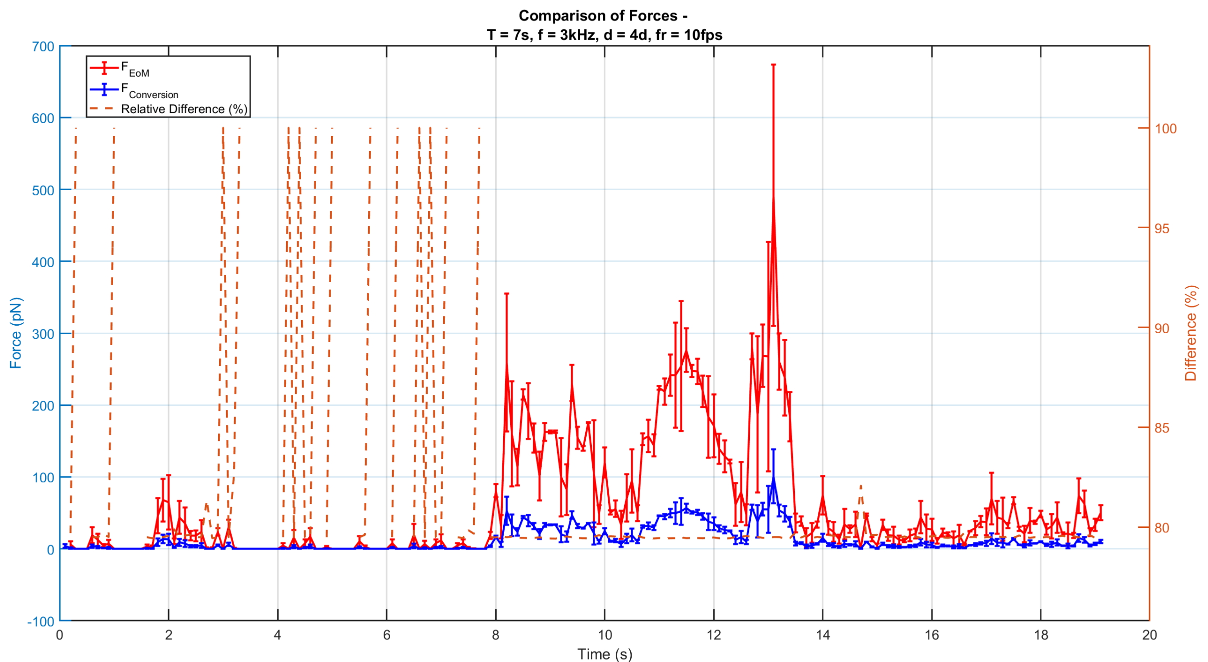

Figure D.169: A comparison of the forces on the microbot calculated using Stokes's law and the conversion coefficient from literature [8]. The relative difference is shown as a dashed orange line. When this dashed orange line is not present, it means that the calculated force is 0 pN. The error bars denote the standard deviation of the measurement. The sweep used for creating the DEP force had a sweep time of 7 seconds and a sweep thickness of 120 pixels. The input voltage of the experiment is 30 V with a frequency of 3 kHz.

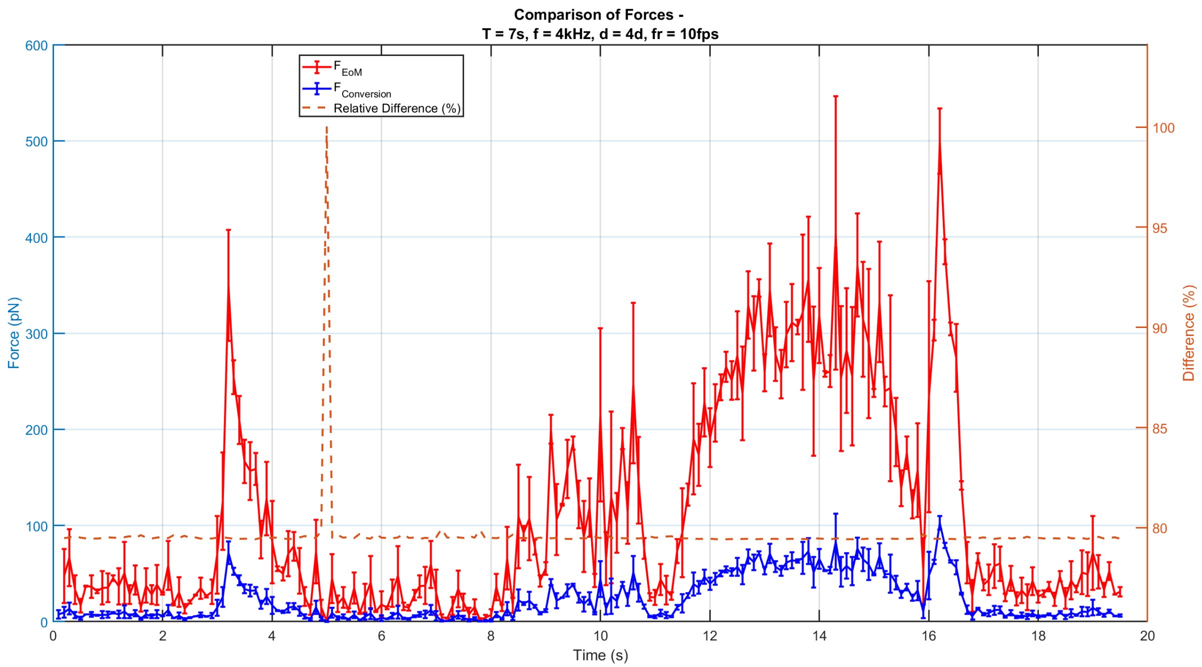

Figure D.170: A comparison of the forces on the microbot calculated using Stokes's law and the conversion coefficient from literature [8]. The relative difference is shown as a dashed orange line. When this dashed orange line is not present, it means that the calculated force is 0 pN. The error bars denote the standard deviation of the measurement. The sweep used for creating the DEP force had a sweep time of 7 seconds and a sweep thickness of 120 pixels. The input voltage of the experiment is 30 V with a frequency of 4 kHz.

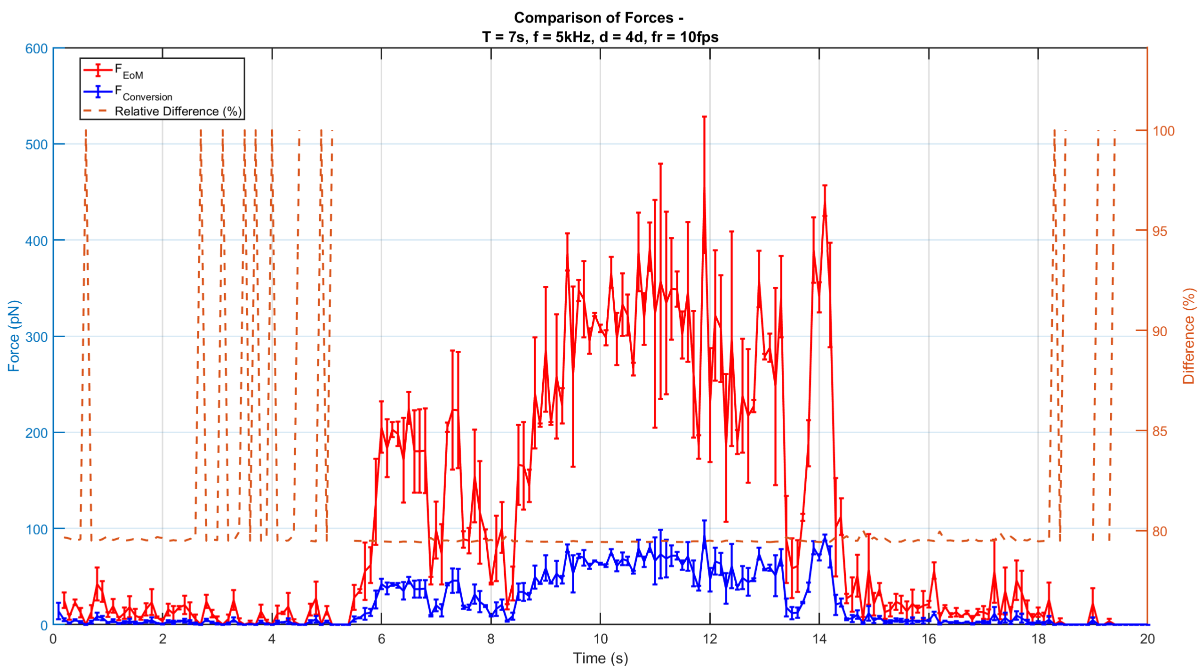

Figure D.171: A comparison of the forces on the microbot calculated using Stokes's law and the conversion coefficient from literature [8]. The relative difference is shown as a dashed orange line. When this dashed orange line is not present, it means that the calculated force is 0 pN. The error bars denote the standard deviation of the measurement. The sweep used for creating the DEP force had a sweep time of 7 seconds and a sweep thickness of 120 pixels. The input voltage of the experiment is 30 V with a frequency of 5 kHz.

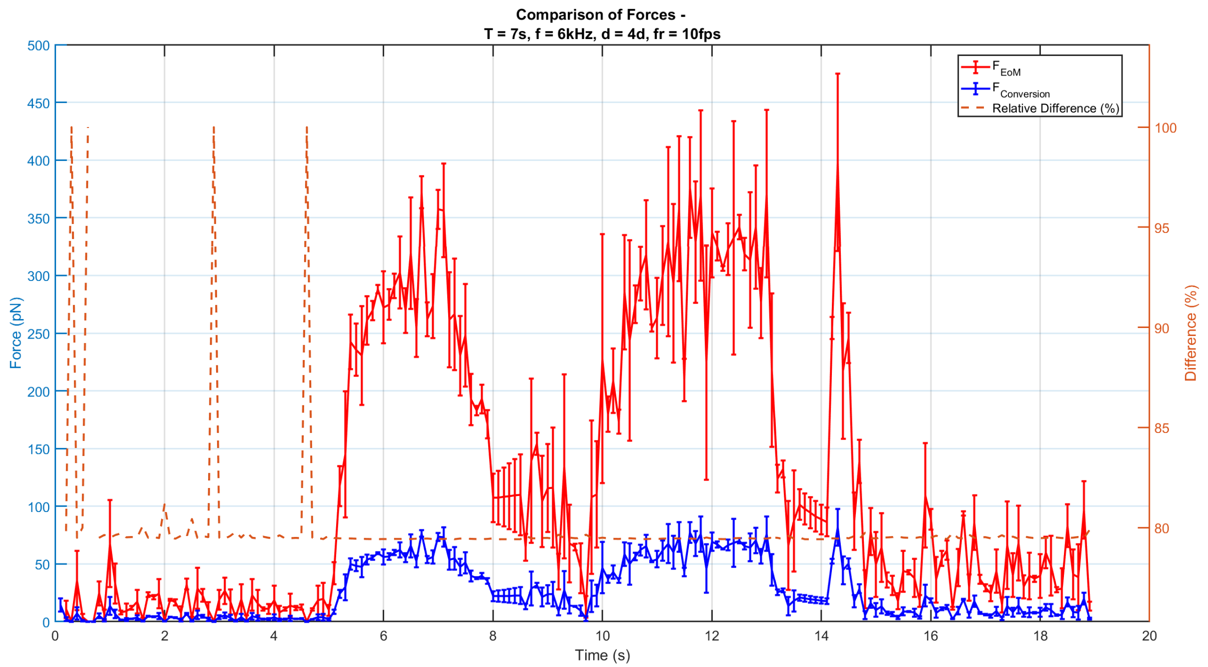

Figure D.172: A comparison of the forces on the microbot calculated using Stokes's law and the conversion coefficient from literature [8]. The relative difference is shown as a dashed orange line. When this dashed orange line is not present, it means that the calculated force is 0 pN. The error bars denote the standard deviation of the measurement. The sweep used for creating the DEP force had a sweep time of 7 seconds and a sweep thickness of 120 pixels. The input voltage of the experiment is 30 V with a frequency of 6 kHz.

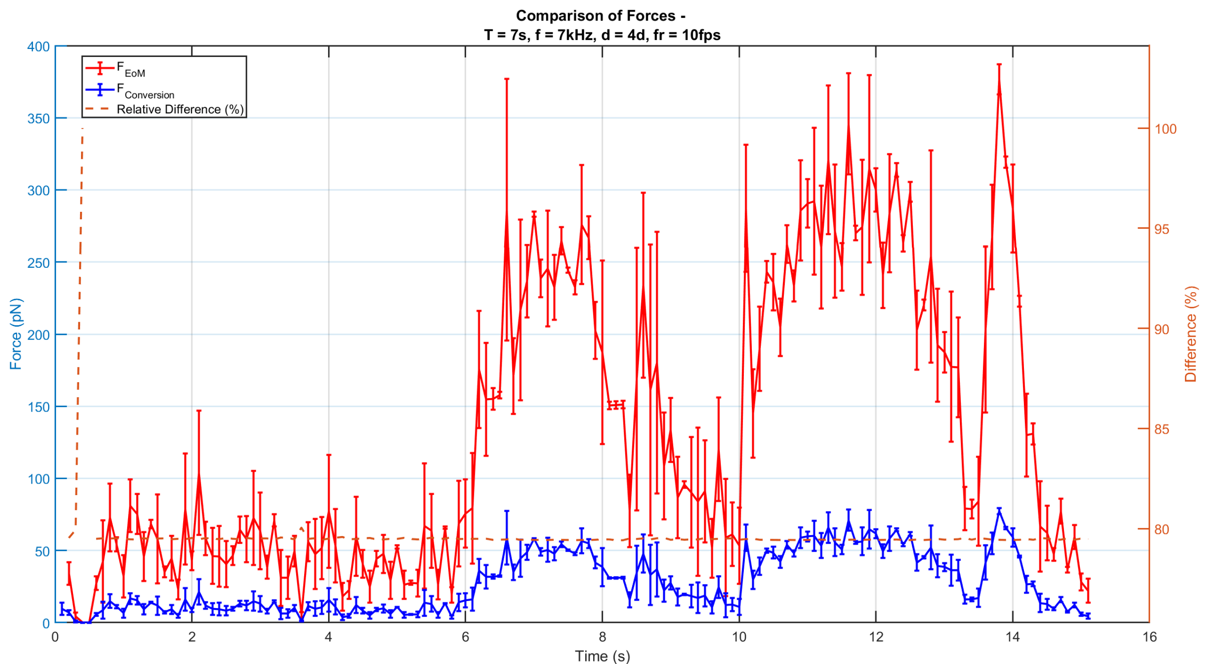

Figure D.173: A comparison of the forces on the microbot calculated using Stokes's law and the conversion coefficient from literature [8]. The relative difference is shown as a dashed orange line. When this dashed orange line is not present, it means that the calculated force is 0 pN. The error bars denote the standard deviation of the measurement. The sweep used for creating the DEP force had a sweep time of 7 seconds and a sweep thickness of 120 pixels. The input voltage of the experiment is 30 V with a frequency of 7 kHz.

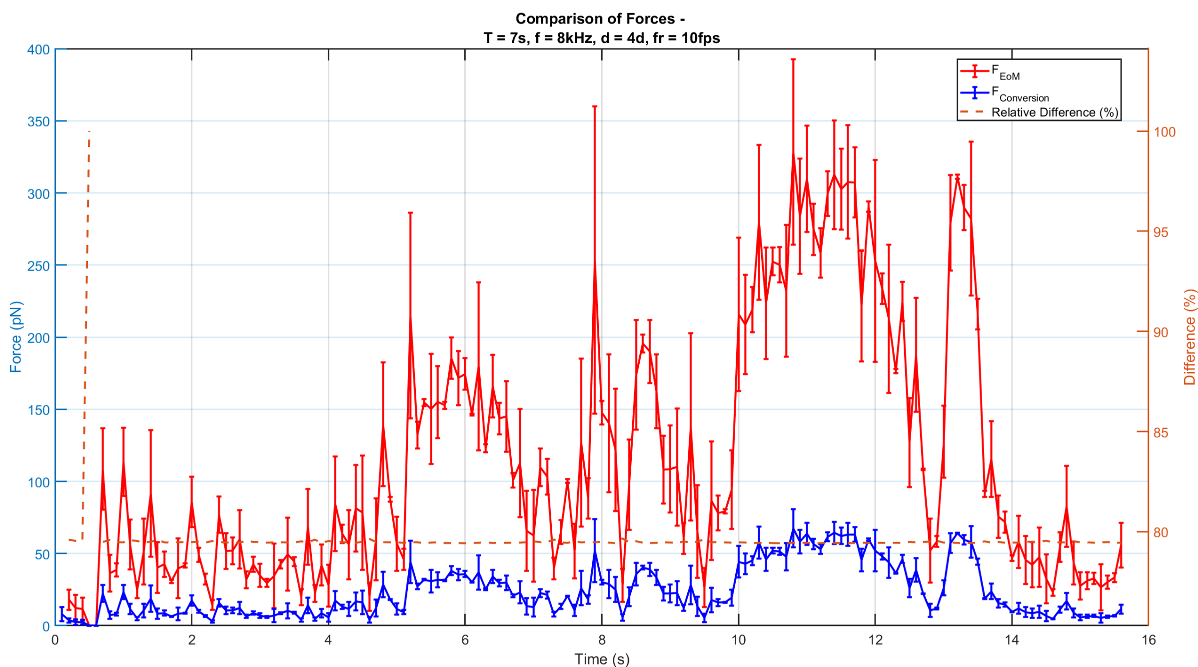

Figure D.174: A comparison of the forces on the microbot calculated using Stokes's law and the conversion coefficient from literature [8]. The relative difference is shown as a dashed orange line. When this dashed orange line is not present, it means that the calculated force is 0 pN. The error bars denote the standard deviation of the measurement. The sweep used for creating the DEP force had a sweep time of 7 seconds and a sweep thickness of 120 pixels. The input voltage of the experiment is 30 V with a frequency of 8 kHz.

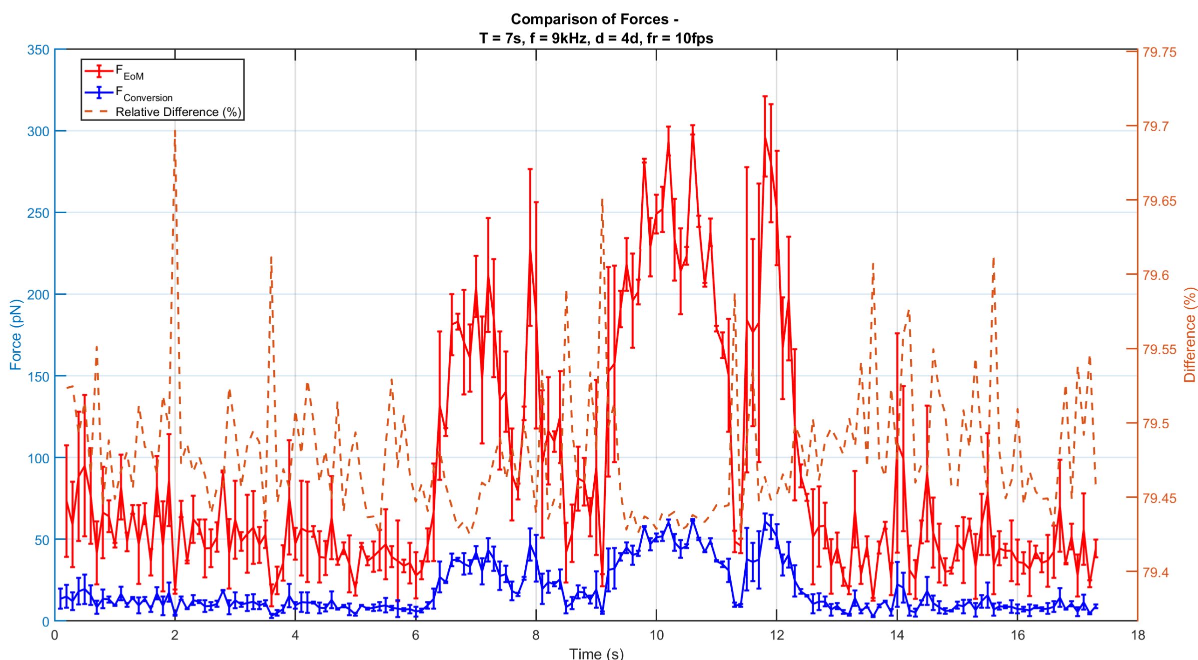

Figure D.175: A comparison of the forces on the microbot calculated using Stokes's law and the conversion coefficient from literature [8]. The relative difference is shown as a dashed orange line. When this dashed orange line is not present, it means that the calculated force is 0 pN. The error bars denote the standard deviation of the measurement. The sweep used for creating the DEP force had a sweep time of 7 seconds and a sweep thickness of 120 pixels. The input voltage of the experiment is 30 V with a frequency of 9 kHz.

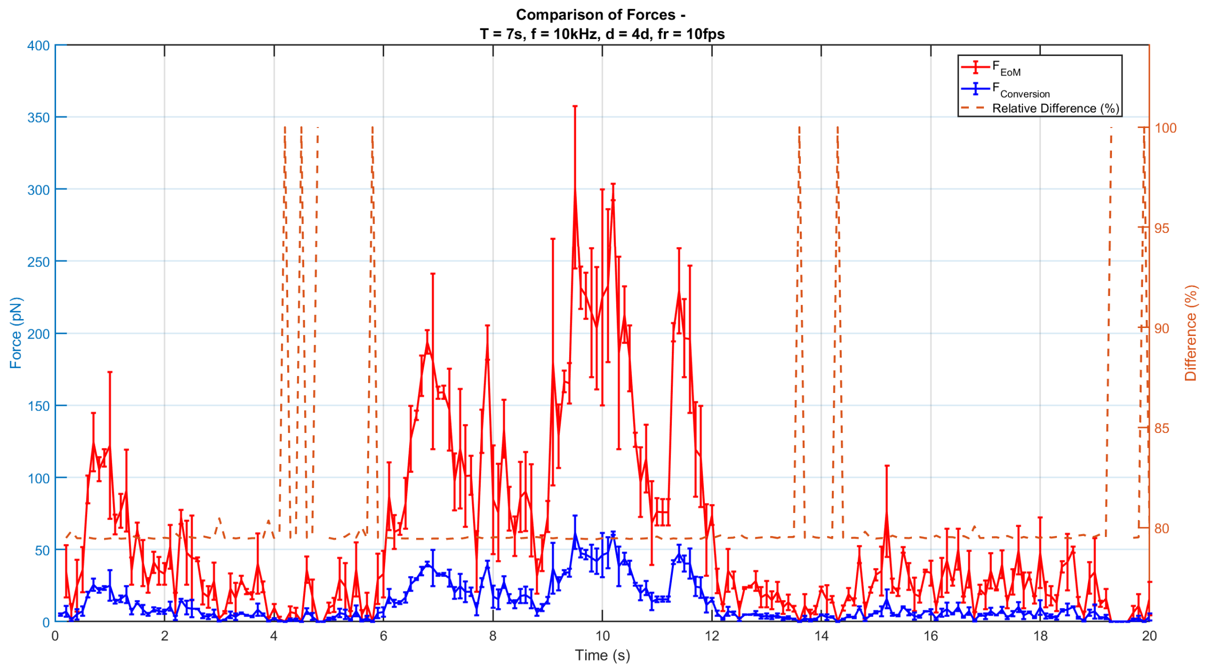

Figure D.176: A comparison of the forces on the microbot calculated using Stokes's law and the conversion coefficient from literature [8]. The relative difference is shown as a dashed orange line. When this dashed orange line is not present, it means that the calculated force is 0 pN. The error bars denote the standard deviation of the measurement. The sweep used for creating the DEP force had a sweep time of 7 seconds and a sweep thickness of 120 pixels. The input voltage of the experiment is 30 V with a frequency of 10 kHz.

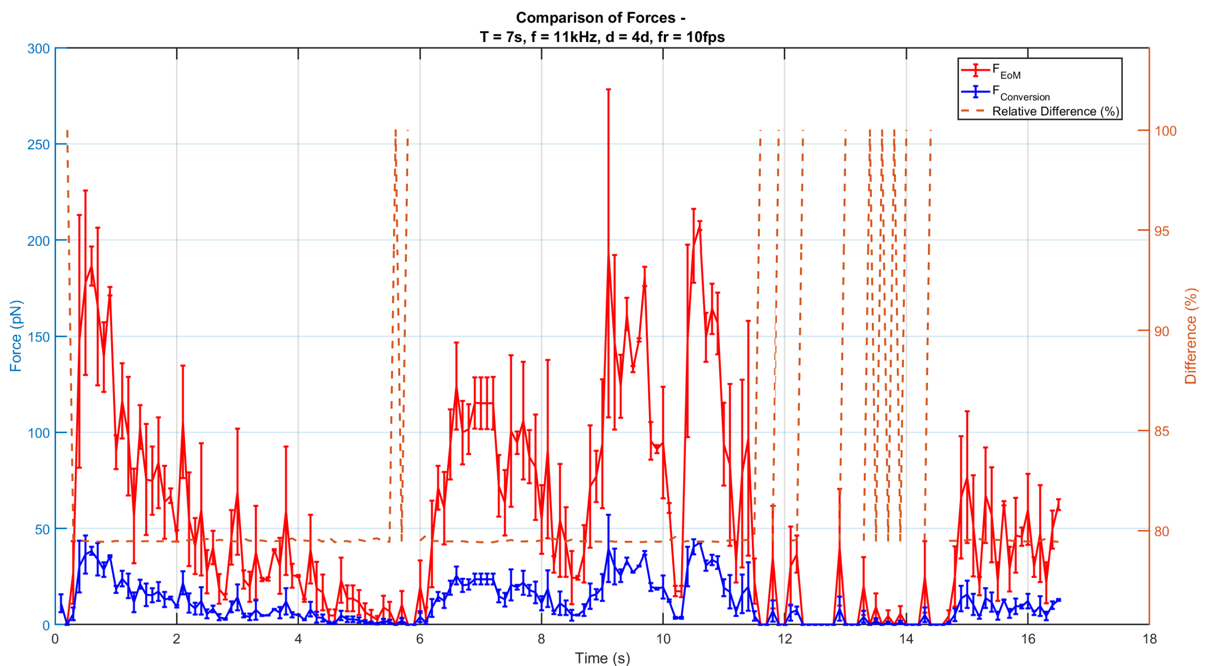

Figure D.177: A comparison of the forces on the microbot calculated using Stokes's law and the conversion coefficient from literature [8]. The relative difference is shown as a dashed orange line. When this dashed orange line is not present, it means that the calculated force is 0 pN. The error bars denote the standard deviation of the measurement. The sweep used for creating the DEP force had a sweep time of 7 seconds and a sweep thickness of 120 pixels. The input voltage of the experiment is 30 V with a frequency of 11 kHz.

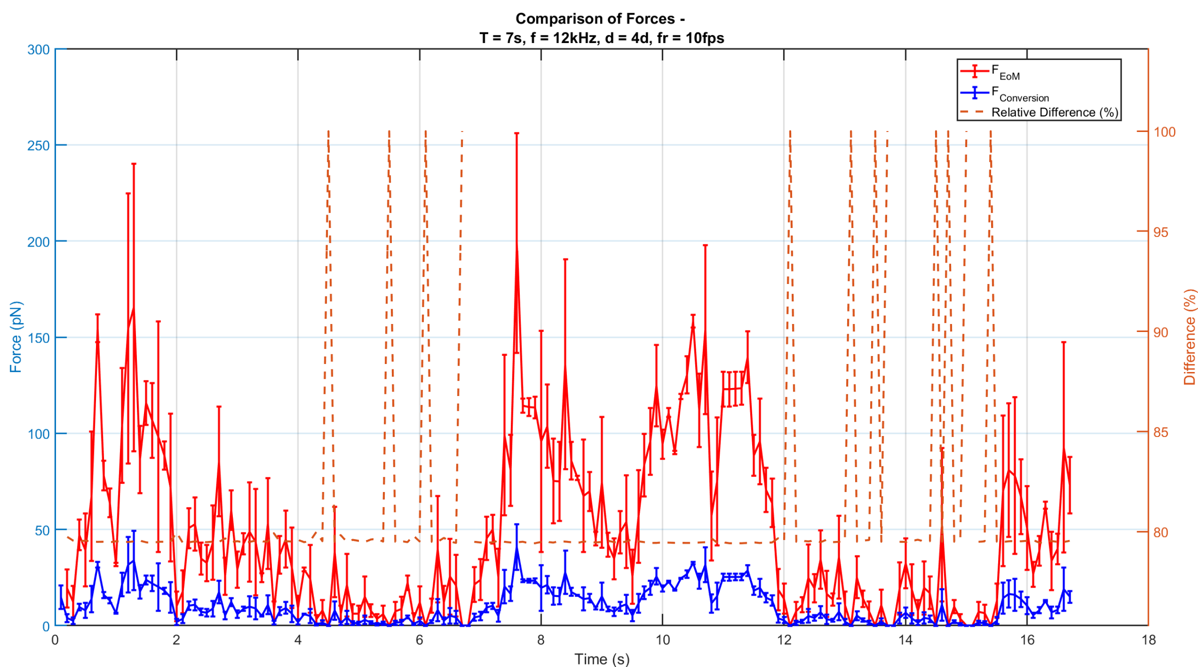

Figure D.178: A comparison of the forces on the microbot calculated using Stokes's law and the conversion coefficient from literature [8]. The relative difference is shown as a dashed orange line. When this dashed orange line is not present, it means that the calculated force is 0 pN. The error bars denote the standard deviation of the measurement. The sweep used for creating the DEP force had a sweep time of 7 seconds and a sweep thickness of 120 pixels. The input voltage of the experiment is 30 V with a frequency of 12 kHz.

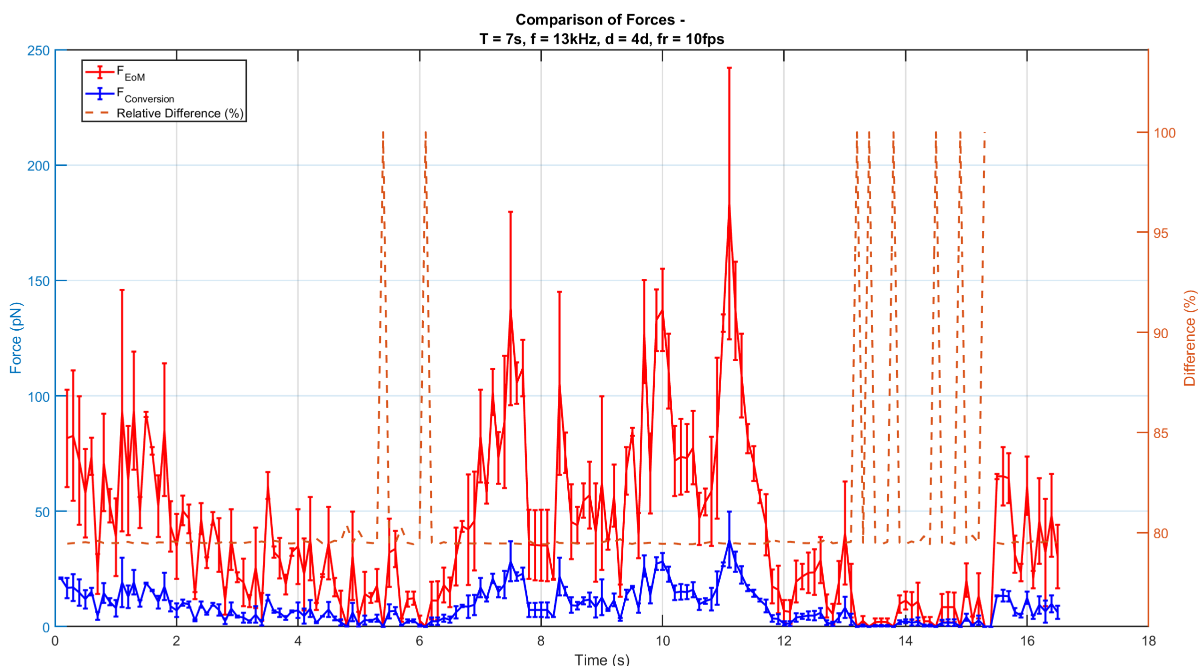

Figure D.179: A comparison of the forces on the microbot calculated using Stokes's law and the conversion coefficient from literature [8]. The relative difference is shown as a dashed orange line. When this dashed orange line is not present, it means that the calculated force is 0 pN. The error bars denote the standard deviation of the measurement. The sweep used for creating the DEP force had a sweep time of 7 seconds and a sweep thickness of 120 pixels. The input voltage of the experiment is 30 V with a frequency of 13 kHz.

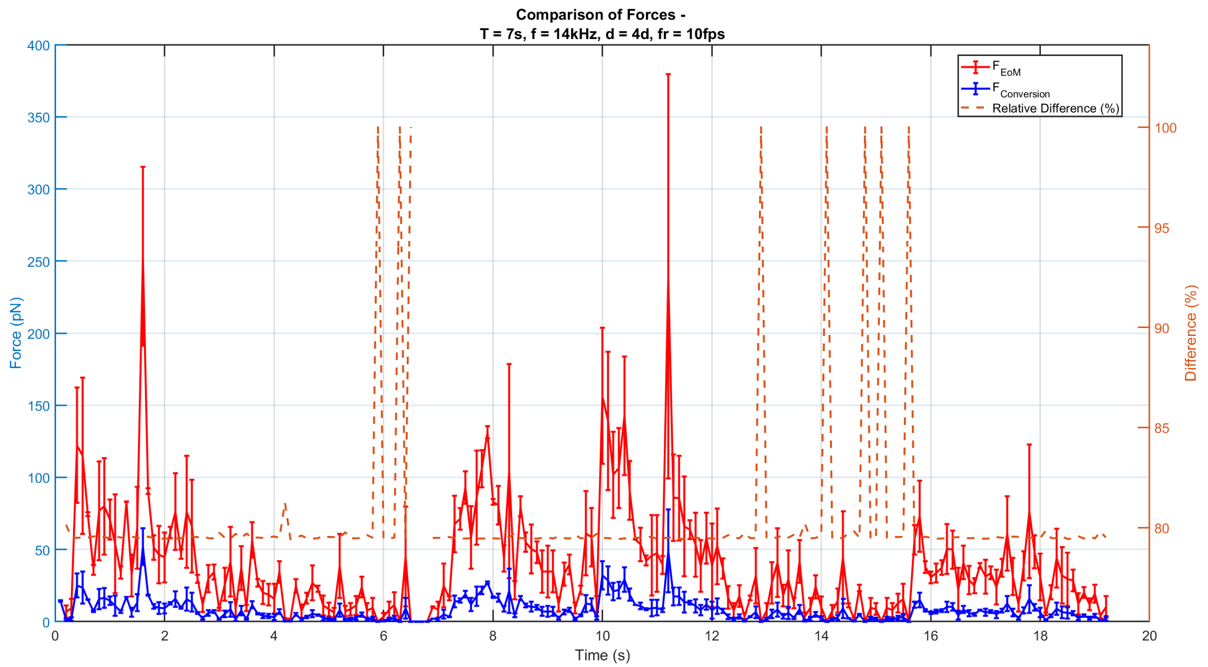

Figure D.180: A comparison of the forces on the microbot calculated using Stokes's law and the conversion coefficient from literature [8]. The relative difference is shown as a dashed orange line. When this dashed orange line is not present, it means that the calculated force is 0 pN. The error bars denote the standard deviation of the measurement. The sweep used for creating the DEP force had a sweep time of 7 seconds and a sweep thickness of 120 pixels. The input voltage of the experiment is 30 V with a frequency of 14 kHz.

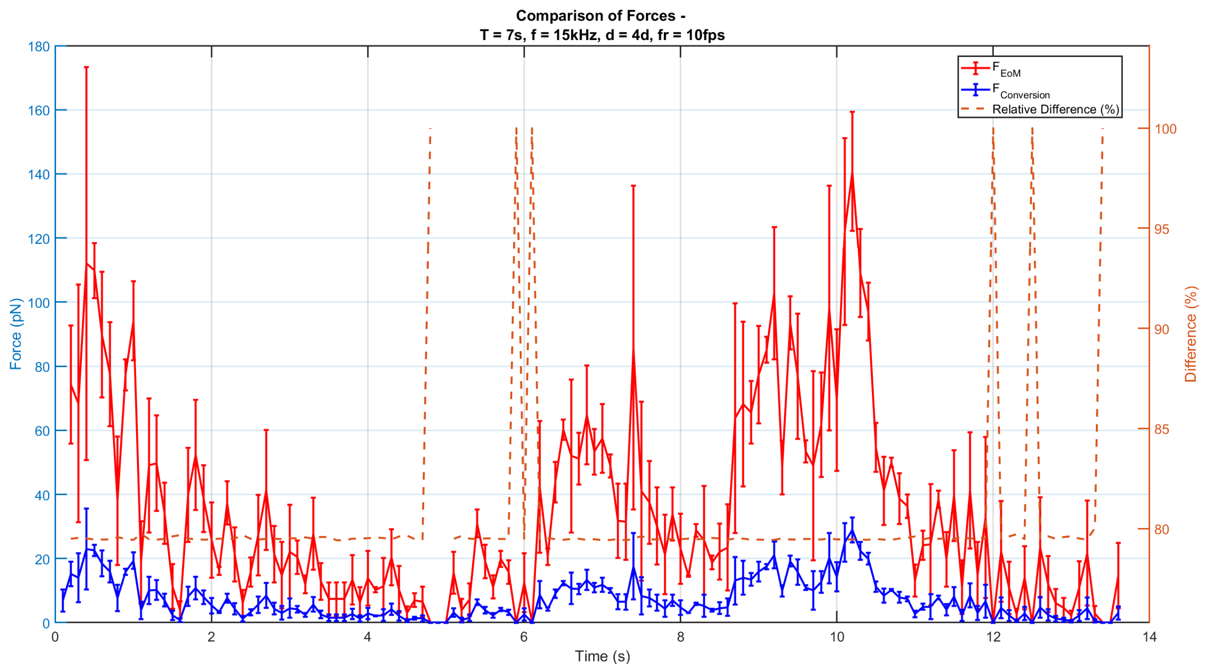

Figure D.181: A comparison of the forces on the microbot calculated using Stokes's law and the conversion coefficient from literature [8]. The relative difference is shown as a dashed orange line. When this dashed orange line is not present, it means that the calculated force is 0 pN. The error bars denote the standard deviation of the measurement. The sweep used for creating the DEP force had a sweep time of 7 seconds and a sweep thickness of 120 pixels. The input voltage of the experiment is 30 V with a frequency of 15 kHz.

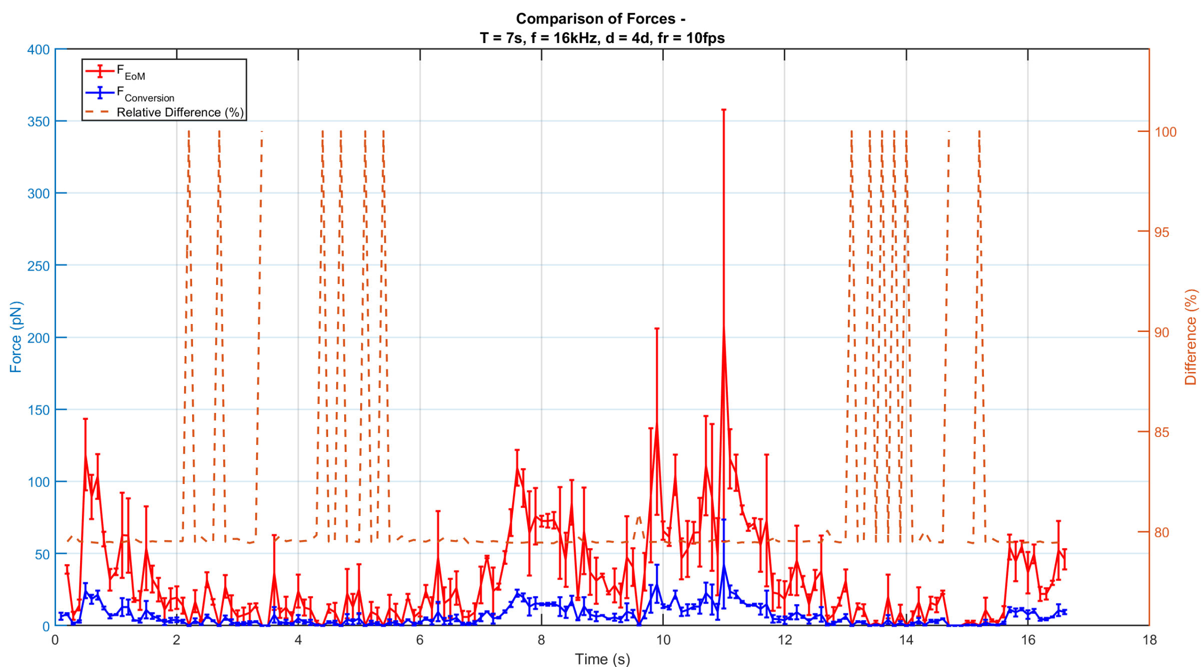

Figure D.182: A comparison of the forces on the microbot calculated using Stokes's law and the conversion coefficient from literature [8]. The relative difference is shown as a dashed orange line. When this dashed orange line is not present, it means that the calculated force is 0 pN. The error bars denote the standard deviation of the measurement. The sweep used for creating the DEP force had a sweep time of 7 seconds and a sweep thickness of 120 pixels. The input voltage of the experiment is 30 V with a frequency of 16 kHz.

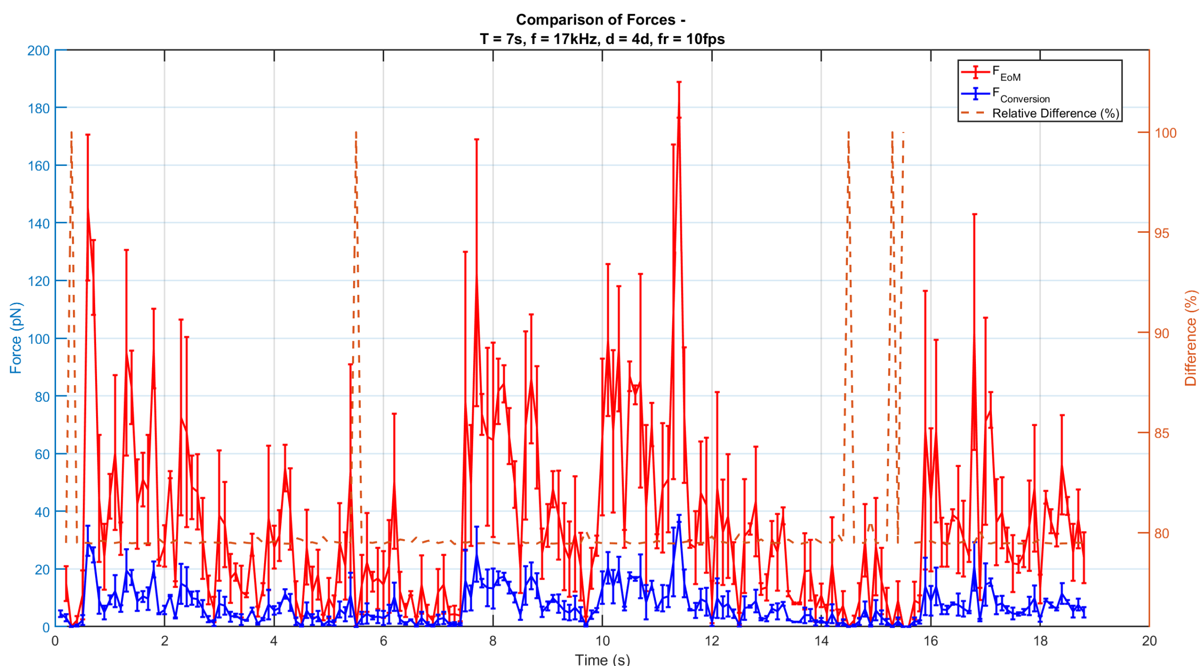

Figure D.183: A comparison of the forces on the microbot calculated using Stokes's law and the conversion coefficient from literature [8]. The relative difference is shown as a dashed orange line. When this dashed orange line is not present, it means that the calculated force is 0 pN. The error bars denote the standard deviation of the measurement. The sweep used for creating the DEP force had a sweep time of 7 seconds and a sweep thickness of 120 pixels. The input voltage of the experiment is 30 V with a frequency of 17 kHz.

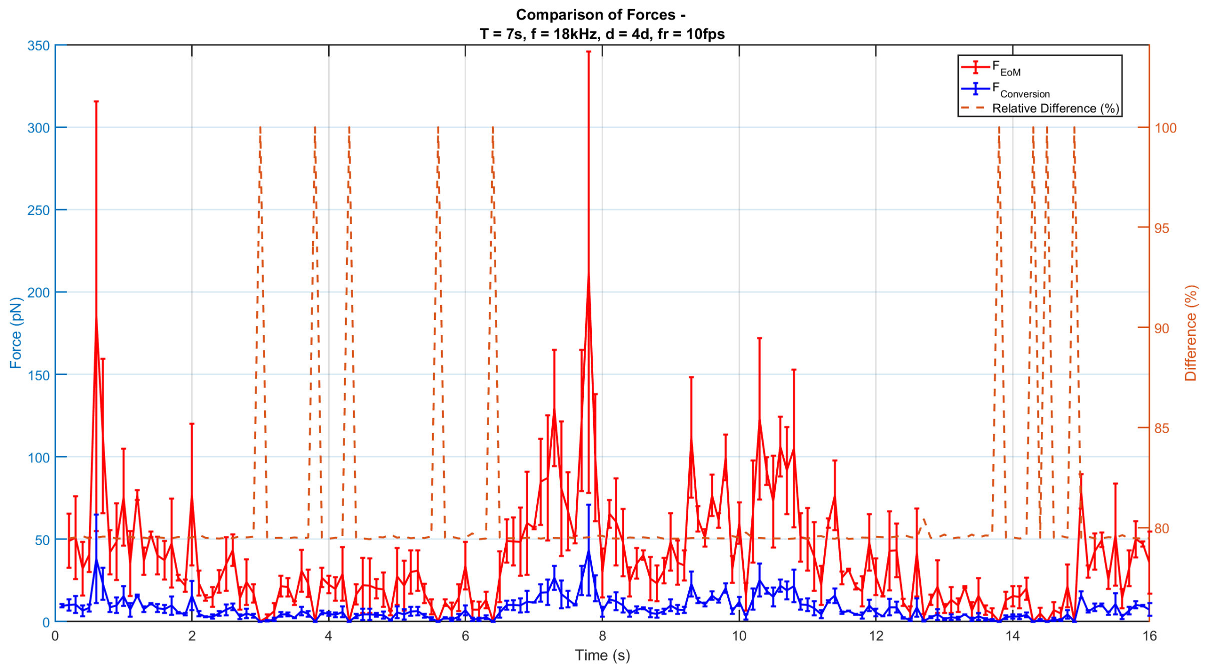

Figure D.184: A comparison of the forces on the microbot calculated using Stokes's law and the conversion coefficient from literature [8]. The relative difference is shown as a dashed orange line. When this dashed orange line is not present, it means that the calculated force is 0 pN. The error bars denote the standard deviation of the measurement. The sweep used for creating the DEP force had a sweep time of 7 seconds and a sweep thickness of 120 pixels. The input voltage of the experiment is 30 V with a frequency of 18 kHz.

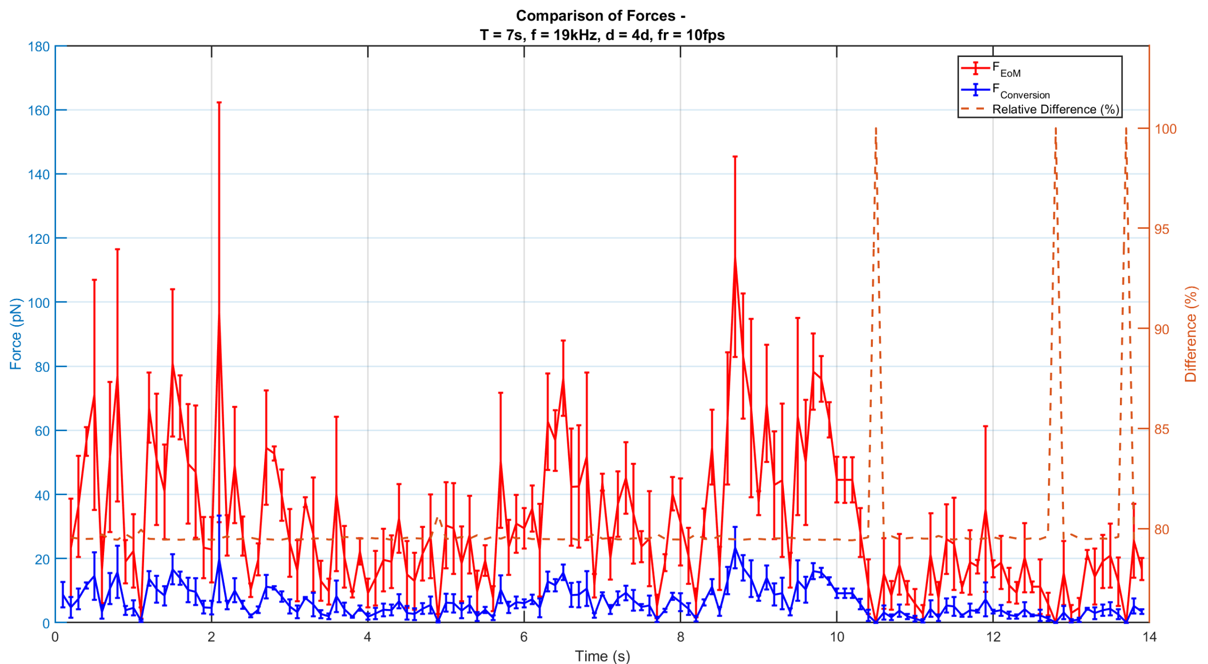

Figure D.185: A comparison of the forces on the microbot calculated using Stokes's law and the conversion coefficient from literature [8]. The relative difference is shown as a dashed orange line. When this dashed orange line is not present, it means that the calculated force is 0 pN. The error bars denote the standard deviation of the measurement. The sweep used for creating the DEP force had a sweep time of 7 seconds and a sweep thickness of 120 pixels. The input voltage of the experiment is 30 V with a frequency of 19 kHz.

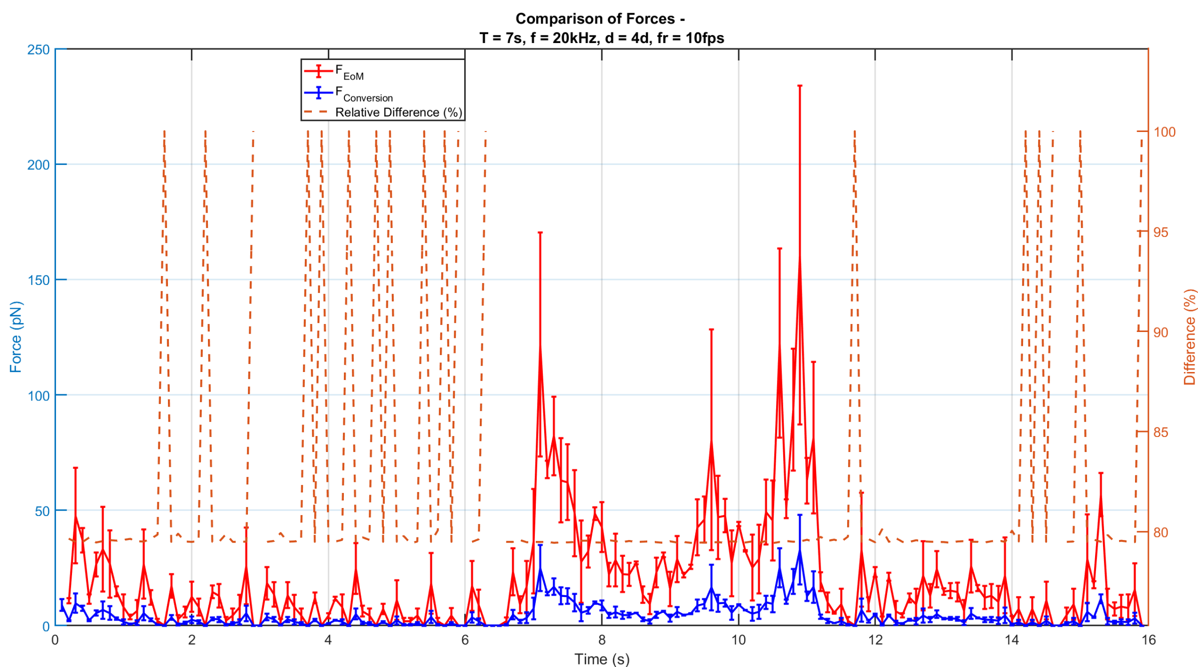

Figure D.186: A comparison of the forces on the microbot calculated using Stokes's law and the conversion coefficient from literature [8]. The relative difference is shown as a dashed orange line. When this dashed orange line is not present, it means that the calculated force is 0 pN. The error bars denote the standard deviation of the measurement. The sweep used for creating the DEP force had a sweep time of 7 seconds and a sweep thickness of 120 pixels. The input voltage of the experiment is 30 V with a frequency of 20 kHz.

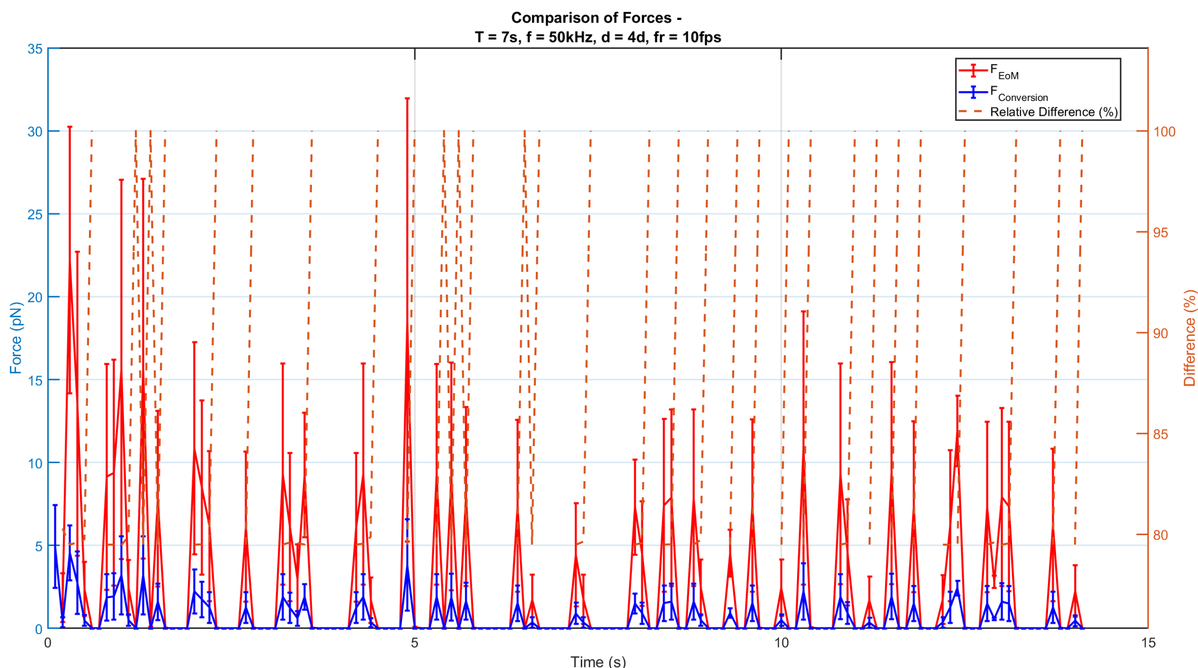

Figure D.187: A comparison of the forces on the microbot calculated using Stokes's law and the conversion coefficient from literature [8]. The relative difference is shown as a dashed orange line. When this dashed orange line is not present, it means that the calculated force is 0 pN. The error bars denote the standard deviation of the measurement. The sweep used for creating the DEP force had a sweep time of 7 seconds and a sweep thickness of 120 pixels. The input voltage of the experiment is 30 V with a frequency of 50 kHz.

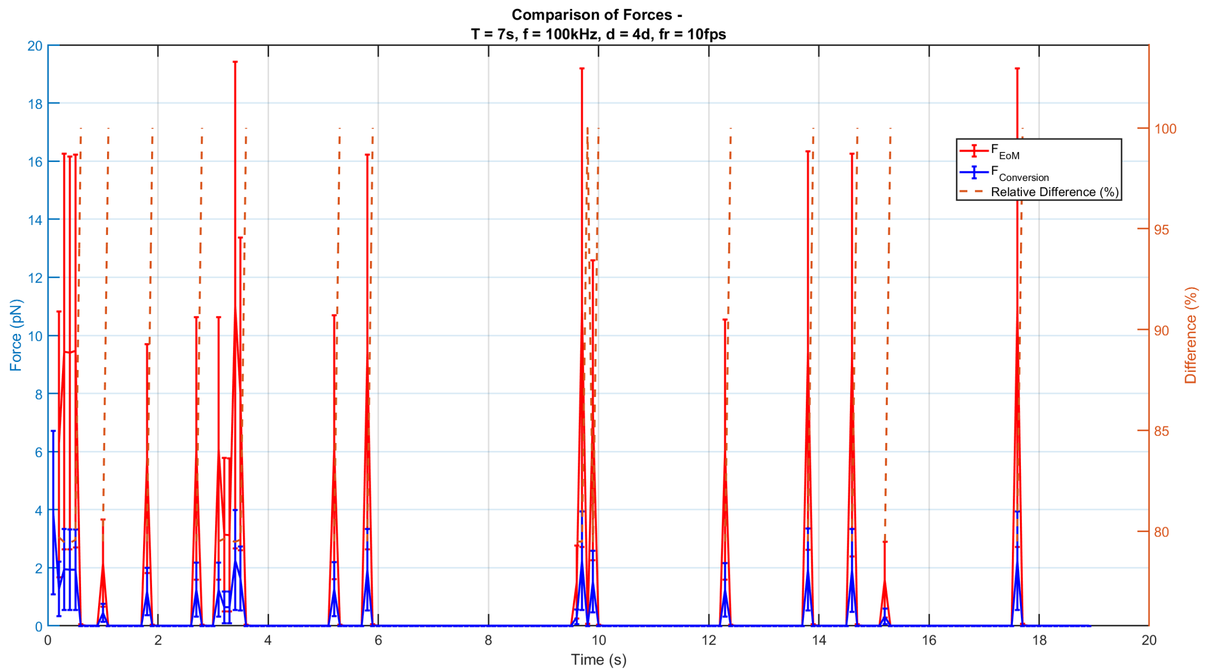

Figure D.188: A comparison of the forces on the microbot calculated using Stokes's law and the conversion coefficient from literature [8]. The relative difference is shown as a dashed orange line. When this dashed orange line is not present, it means that the calculated force is 0 pN. The error bars denote the standard deviation of the measurement. The sweep used for creating the DEP force had a sweep time of 7 seconds and a sweep thickness of 120 pixels. The input voltage of the experiment is 30 V with a frequency of 100 kHz.

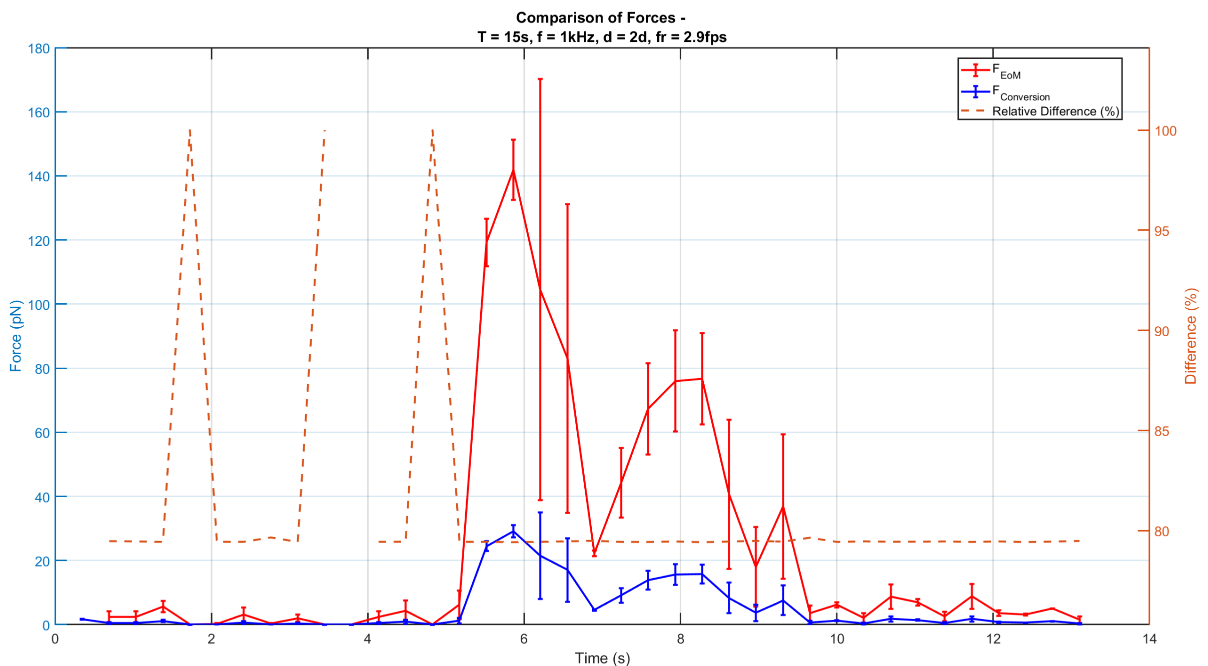

Figure D.189: A comparison of the forces on the microbot calculated using Stokes's law and the conversion coefficient from literature [8]. The relative difference is shown as a dashed orange line. When this dashed orange line is not present, it means that the calculated force is 0 pN. The error bars denote the standard deviation of the measurement. The sweep used for creating the DEP force had a sweep time of 15 seconds and a sweep thickness of 60 pixels. The input voltage of the experiment is 30 V with a frequency of 1 kHz.

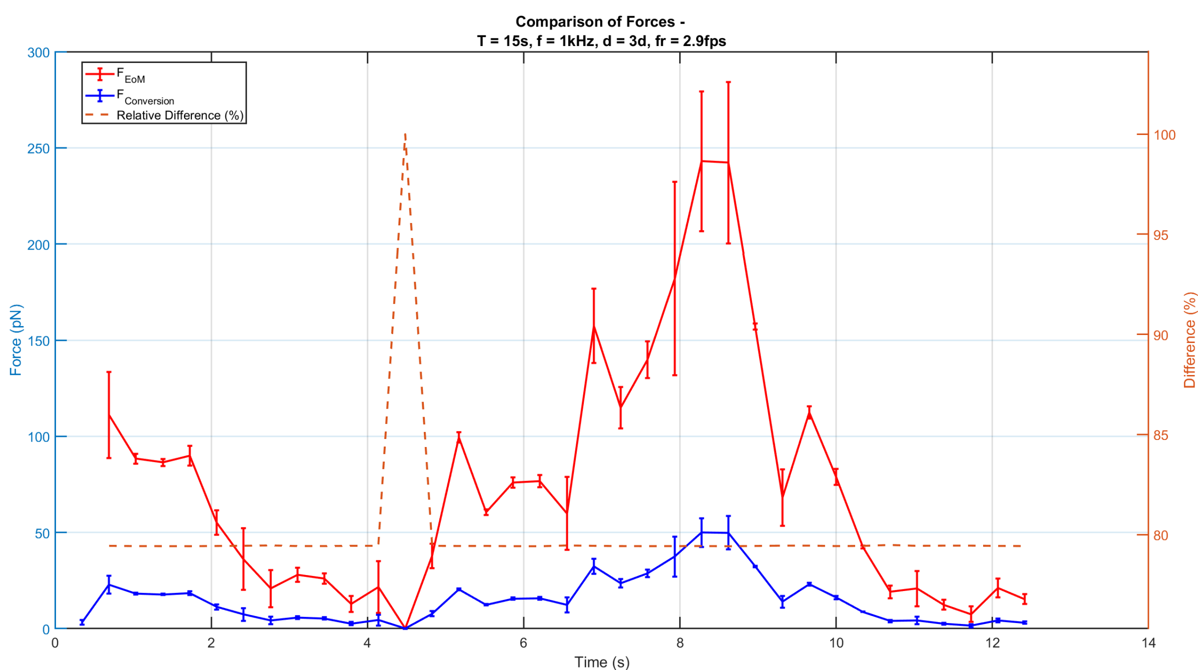

Figure D.190: A comparison of the forces on the microbot calculated using Stokes's law and the conversion coefficient from literature [8]. The relative difference is shown as a dashed orange line. When this dashed orange line is not present, it means that the calculated force is 0 pN. The error bars denote the standard deviation of the measurement. The sweep used for creating the DEP force had a sweep time of 15 seconds and a sweep thickness of 90 pixels. The input voltage of the experiment is 30 V with a frequency of 1 kHz.

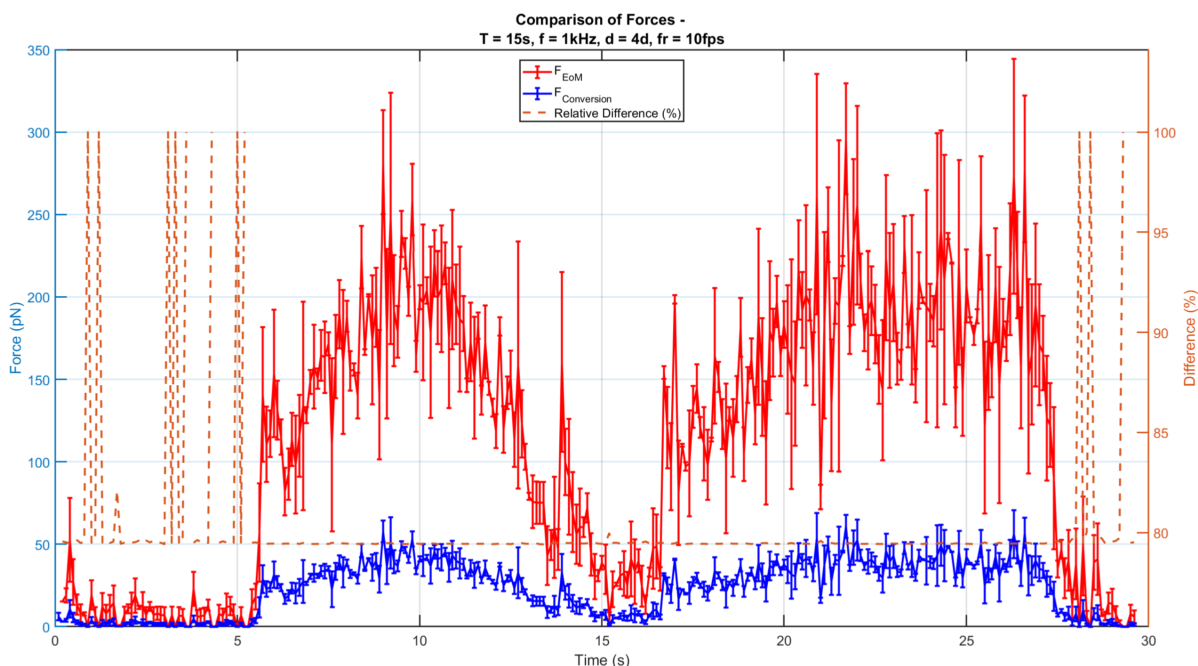

Figure D.191: A comparison of the forces on the microbot calculated using Stokes's law and the conversion coefficient from literature [8]. The relative difference is shown as a dashed orange line. When this dashed orange line is not present, it means that the calculated force is 0 pN. The error bars denote the standard deviation of the measurement. The sweep used for creating the DEP force had a sweep time of 15 seconds and a sweep thickness of 120 pixels. The input voltage of the experiment is 30 V with a frequency of 1 kHz.

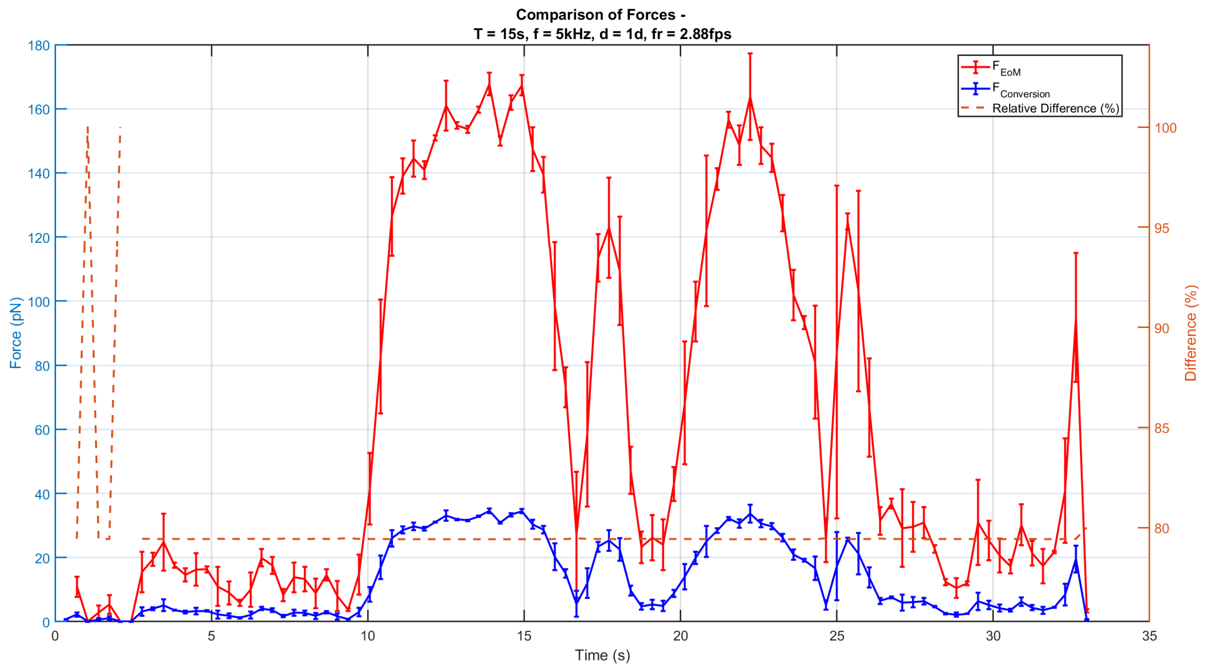

Figure D.192: A comparison of the forces on the microbot calculated using Stokes's law and the conversion coefficient from literature [8]. The relative difference is shown as a dashed orange line. When this dashed orange line is not present, it means that the calculated force is 0 pN. The error bars denote the standard deviation of the measurement. The sweep used for creating the DEP force had a sweep time of 15 seconds and a sweep thickness of 30 pixels. The input voltage of the experiment is 30 V with a frequency of 5 kHz.

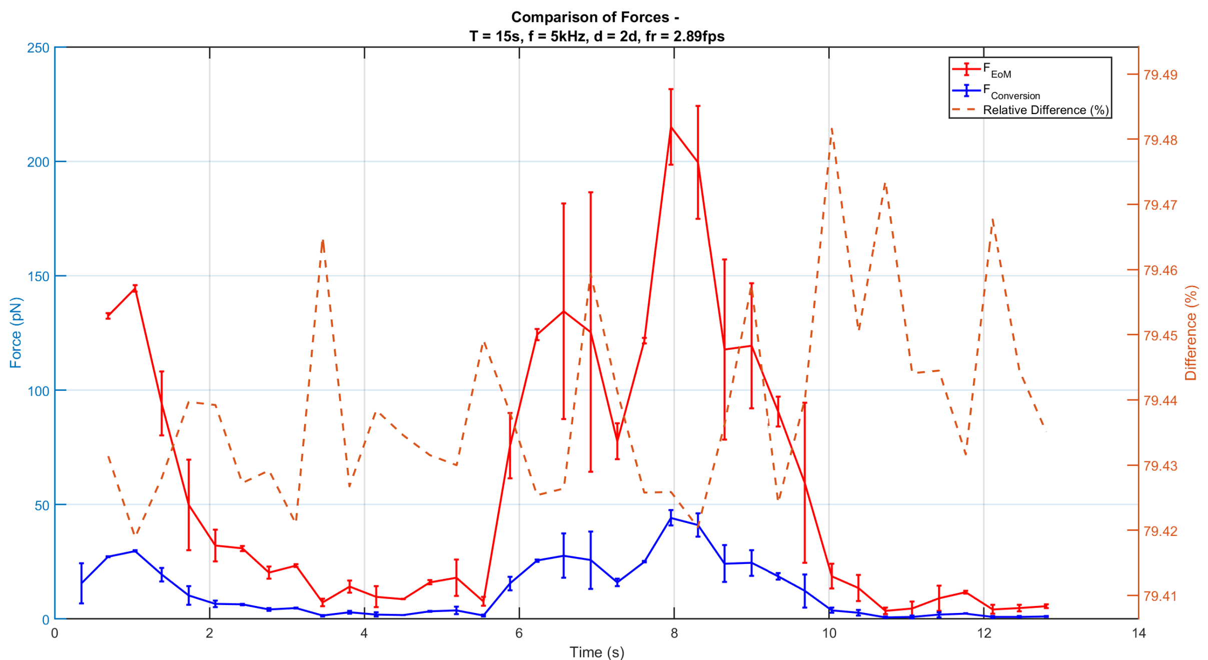

Figure D.193: A comparison of the forces on the microbot calculated using Stokes's law and the conversion coefficient from literature [8]. The relative difference is shown as a dashed orange line. When this dashed orange line is not present, it means that the calculated force is 0 pN. The error bars denote the standard deviation of the measurement. The sweep used for creating the DEP force had a sweep time of 15 seconds and a sweep thickness of 60 pixels. The input voltage of the experiment is 30 V with a frequency of 5 kHz.

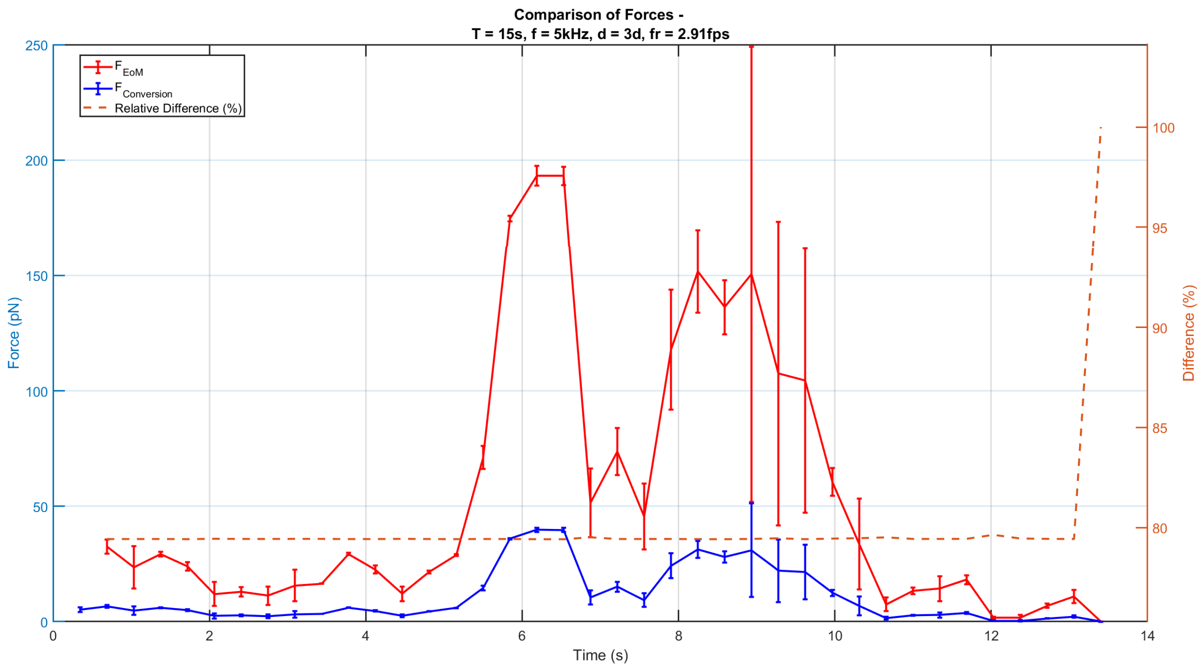

Figure D.194: A comparison of the forces on the microbot calculated using Stokes's law and the conversion coefficient from literature [8]. The relative difference is shown as a dashed orange line. When this dashed orange line is not present, it means that the calculated force is 0 pN. The error bars denote the standard deviation of the measurement. The sweep used for creating the DEP force had a sweep time of 15 seconds and a sweep thickness of 90 pixels. The input voltage of the experiment is 30 V with a frequency of 5 kHz.

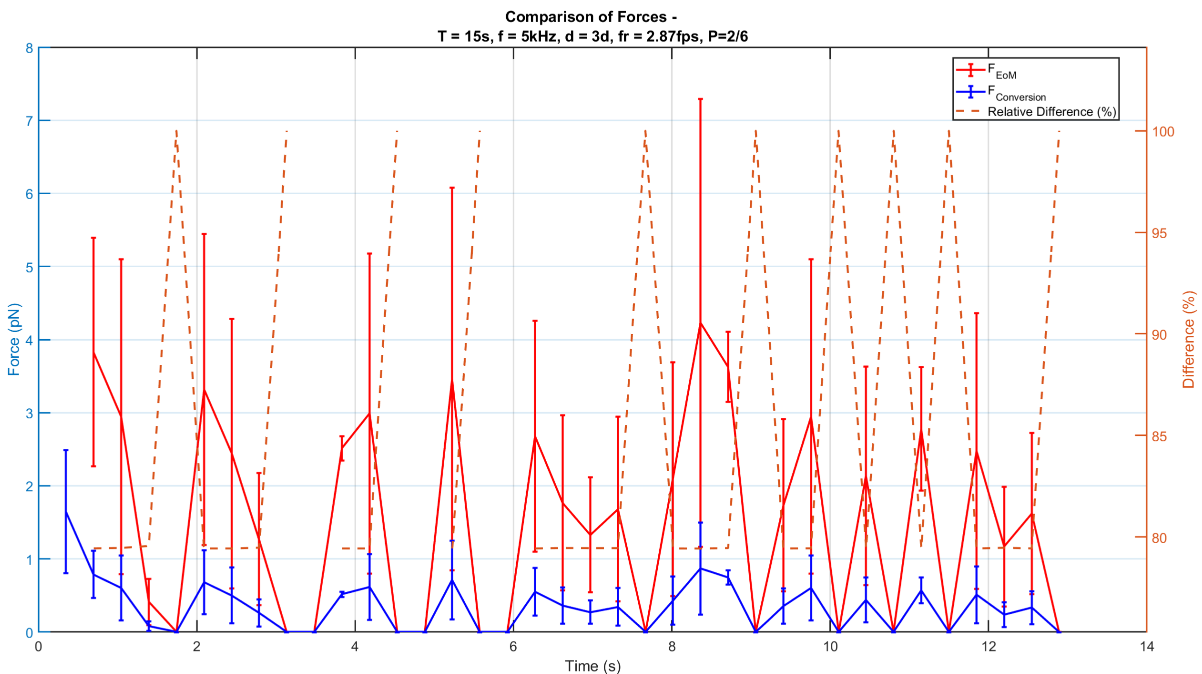

Figure D.195: A comparison of the forces on the microbot calculated using Stokes's law and the conversion coefficient from literature [8]. The relative difference is shown as a dashed orange line. When this dashed orange line is not present, it means that the calculated force is 0 pN. The error bars denote the standard deviation of the measurement. The sweep used for creating the DEP force had a sweep time of 15 seconds and a sweep thickness of 90 pixels. The input voltage of the experiment is 30 V with a frequency of 5 kHz. The illumination power used is 1/3 of the full power.

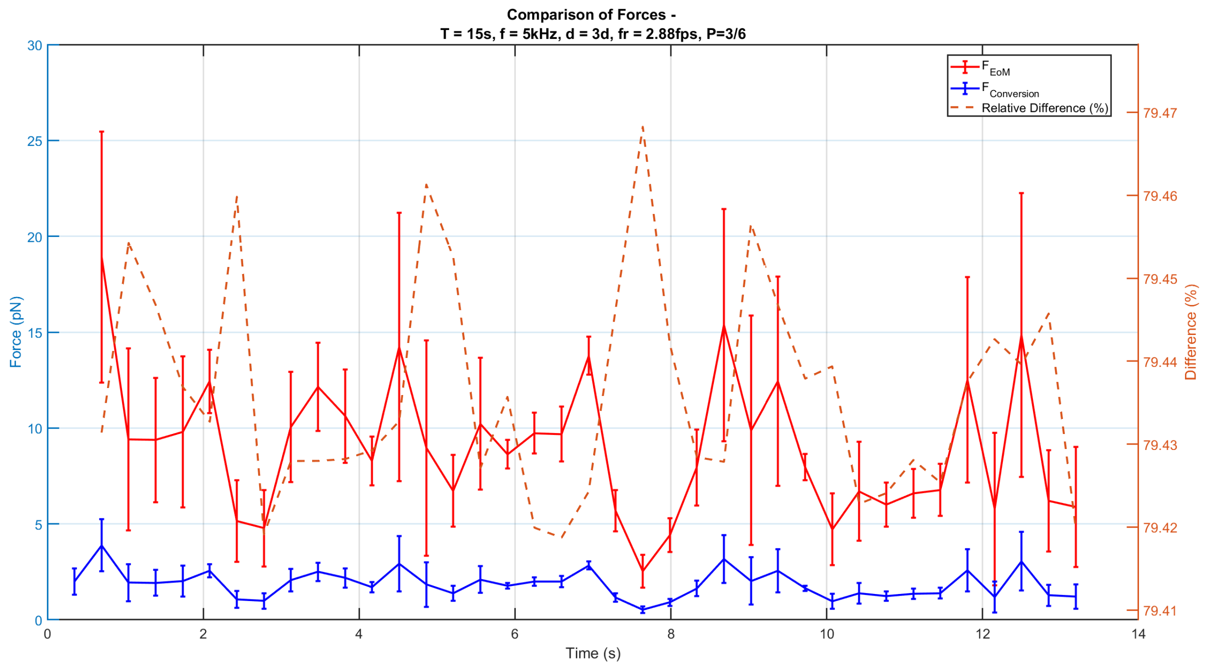

Figure D.196: A comparison of the forces on the microbot calculated using Stokes's law and the conversion coefficient from literature [8]. The relative difference is shown as a dashed orange line. When this dashed orange line is not present, it means that the calculated force is 0 pN. The error bars denote the standard deviation of the measurement. The sweep used for creating the DEP force had a sweep time of 15 seconds and a sweep thickness of 90 pixels. The input voltage of the experiment is 30 V with a frequency of 5 kHz. The illumination power used is 1/2 of the full power.

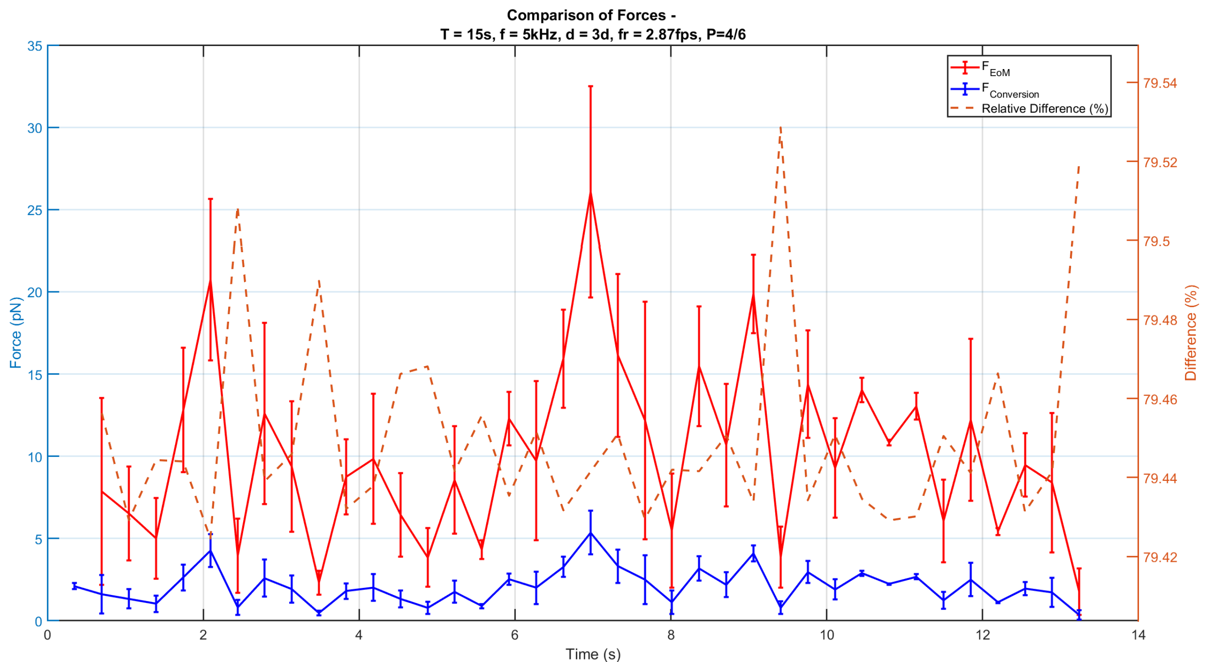

Figure D.197: A comparison of the forces on the microbot calculated using Stokes's law and the conversion coefficient from literature [8]. The relative difference is shown as a dashed orange line. When this dashed orange line is not present, it means that the calculated force is 0 pN. The error bars denote the standard deviation of the measurement. The sweep used for creating the DEP force had a sweep time of 15 seconds and a sweep thickness of 90 pixels. The input voltage of the experiment is 30 V with a frequency of 5 kHz. The illumination power used is 2/3 of the full power.

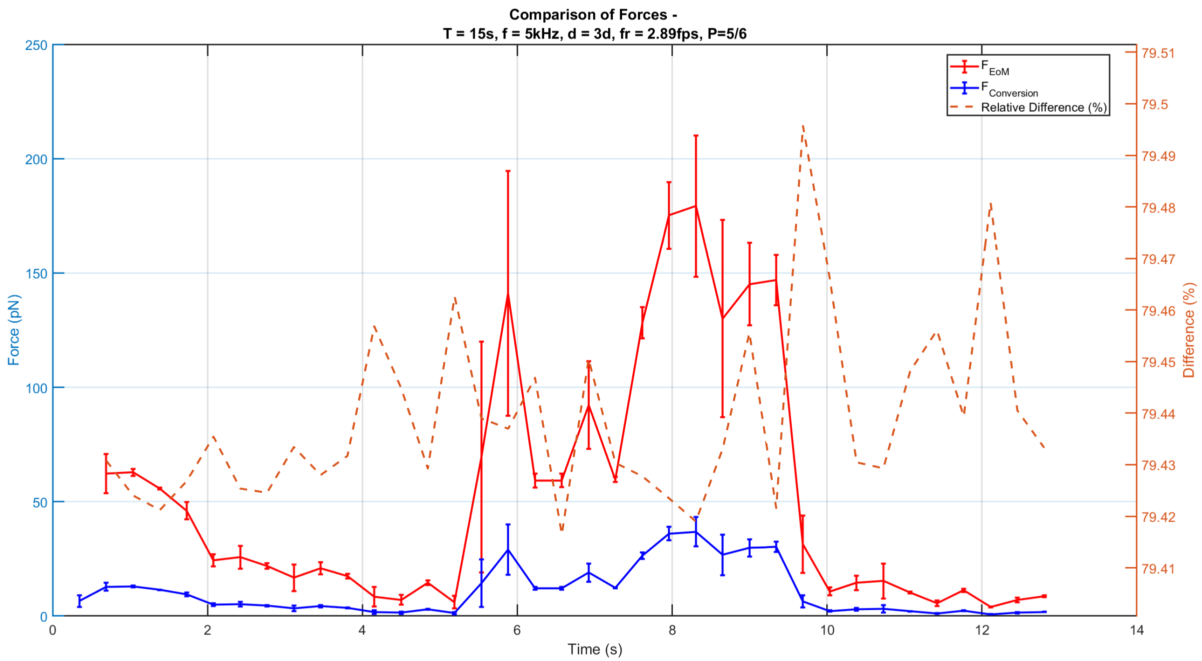

Figure D.198: A comparison of the forces on the microbot calculated using Stokes's law and the conversion coefficient from literature [8]. The relative difference is shown as a dashed orange line. When this dashed orange line is not present, it means that the calculated force is 0 pN. The error bars denote the standard deviation of the measurement. The sweep used for creating the DEP force had a sweep time of 15 seconds and a sweep thickness of 90 pixels. The input voltage of the experiment is 30 V with a frequency of 5 kHz. The illumination power used is 5/6 of the full power.

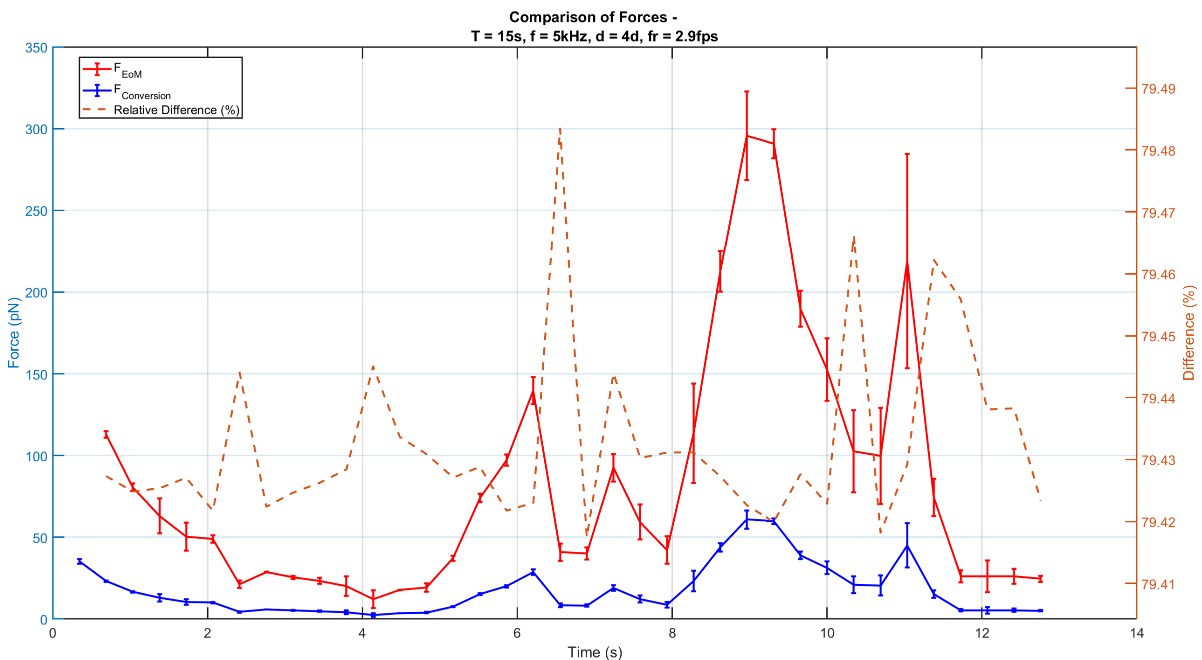

Figure D.199: A comparison of the forces on the microbot calculated using Stokes's law and the conversion coefficient from literature [8]. The relative difference is shown as a dashed orange line. When this dashed orange line is not present, it means that the calculated force is 0 pN. The error bars denote the standard deviation of the measurement. The sweep used for creating the DEP force had a sweep time of 15 seconds and a sweep thickness of 120 pixels. The input voltage of the experiment is 30 V with a frequency of 5 kHz.

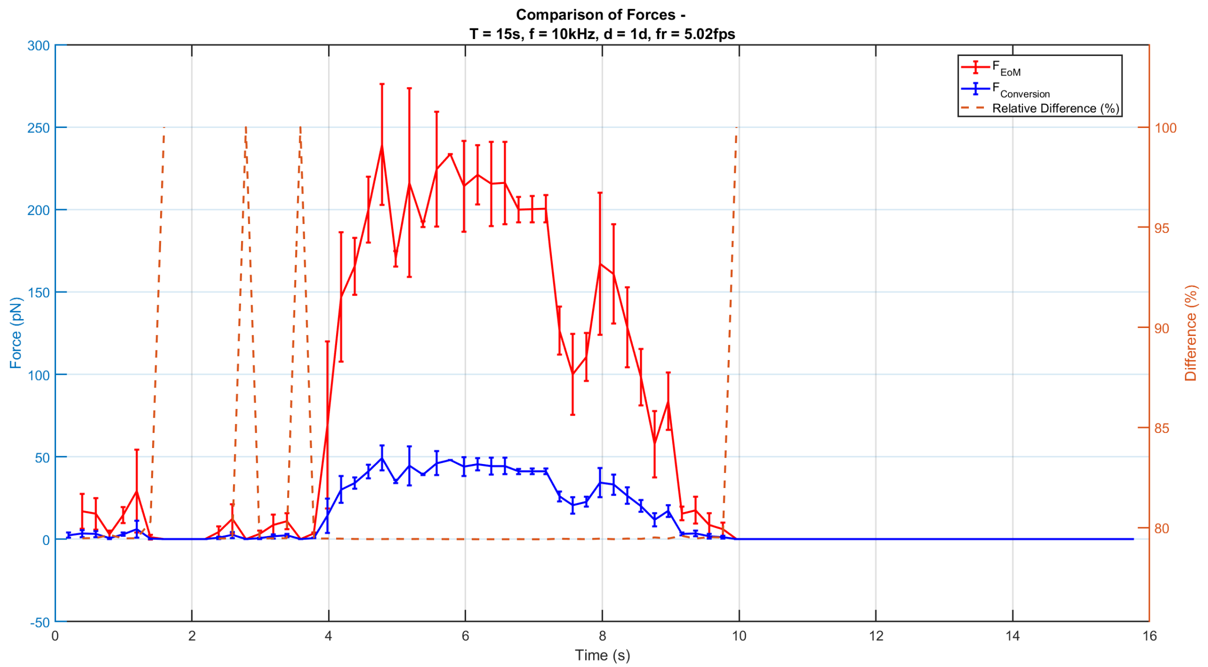

Figure D.200: A comparison of the forces on the microbot calculated using Stokes's law and the conversion coefficient from literature [8]. The relative difference is shown as a dashed orange line. When this dashed orange line is not present, it means that the calculated force is 0 pN. The error bars denote the standard deviation of the measurement. The sweep used for creating the DEP force had a sweep time of 15 seconds and a sweep thickness of 30 pixels. The input voltage of the experiment is 30 V with a frequency of 10 kHz.

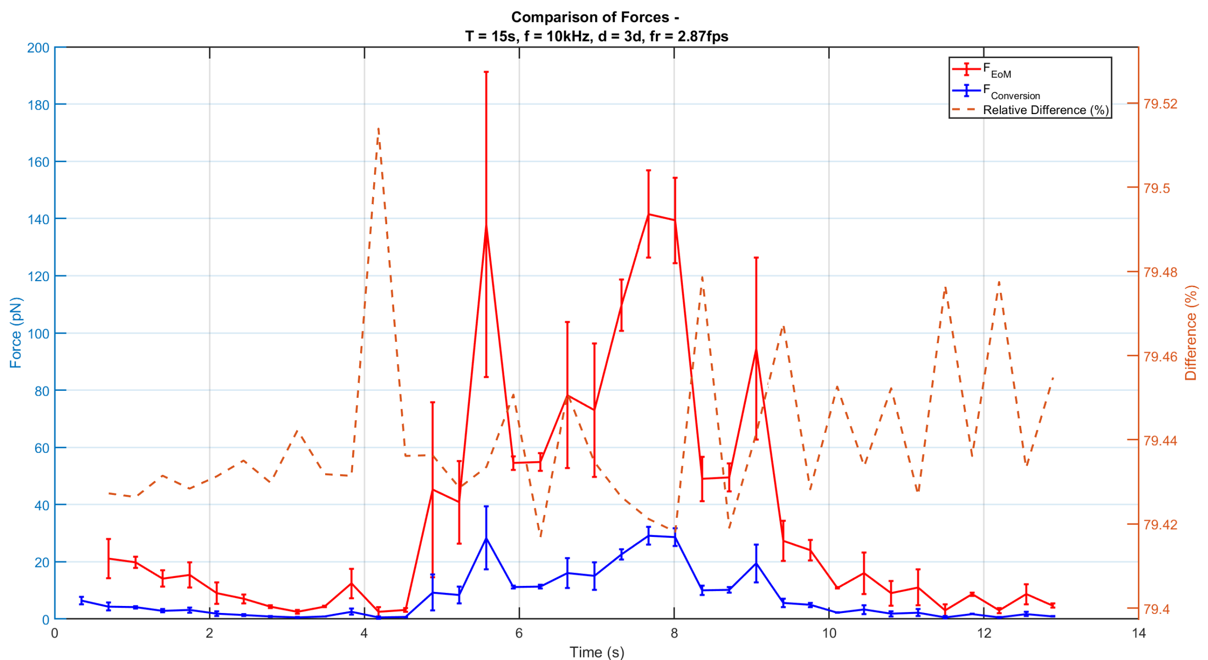

Figure D.201: A comparison of the forces on the microbot calculated using Stokes's law and the conversion coefficient from literature [8]. The relative difference is shown as a dashed orange line. When this dashed orange line is not present, it means that the calculated force is 0 pN. The error bars denote the standard deviation of the measurement. The sweep used for creating the DEP force had a sweep time of 15 seconds and a sweep thickness of 90 pixels. The input voltage of the experiment is 30 V with a frequency of 10 kHz.

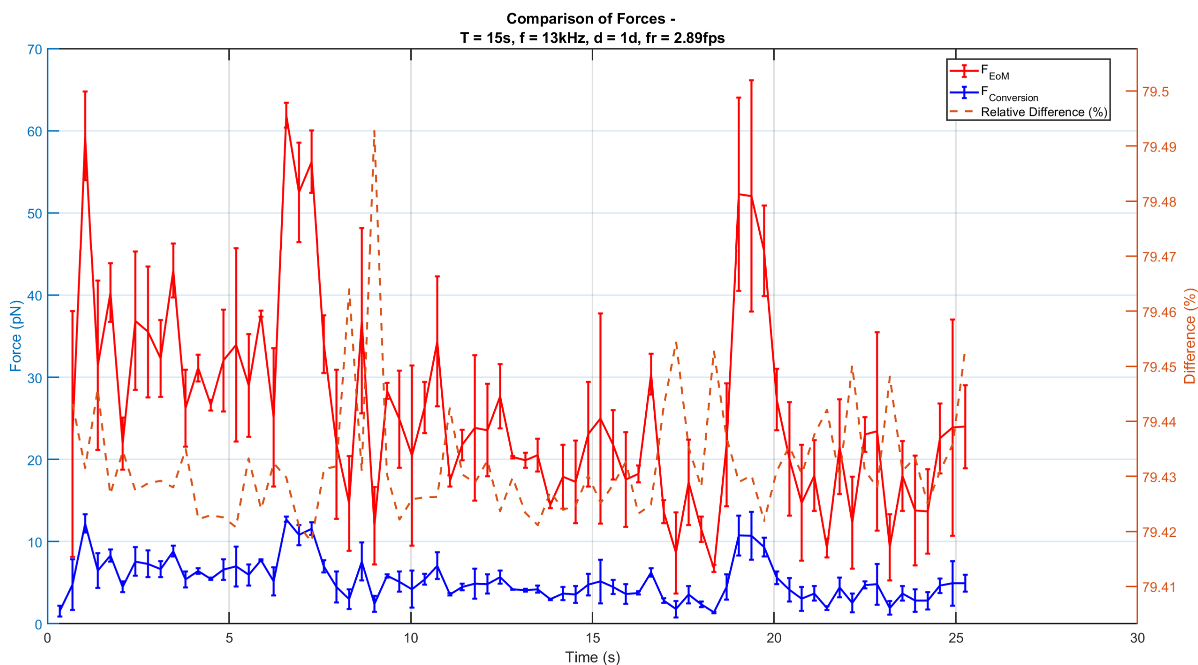

Figure D.202: A comparison of the forces on the microbot calculated using Stokes's law and the conversion coefficient from literature [8]. The relative difference is shown as a dashed orange line. When this dashed orange line is not present, it means that the calculated force is 0 pN. The error bars denote the standard deviation of the measurement. The sweep used for creating the DEP force had a sweep time of 15 seconds and a sweep thickness of 30 pixels. The input voltage of the experiment is 30 V with a frequency of 13 kHz.

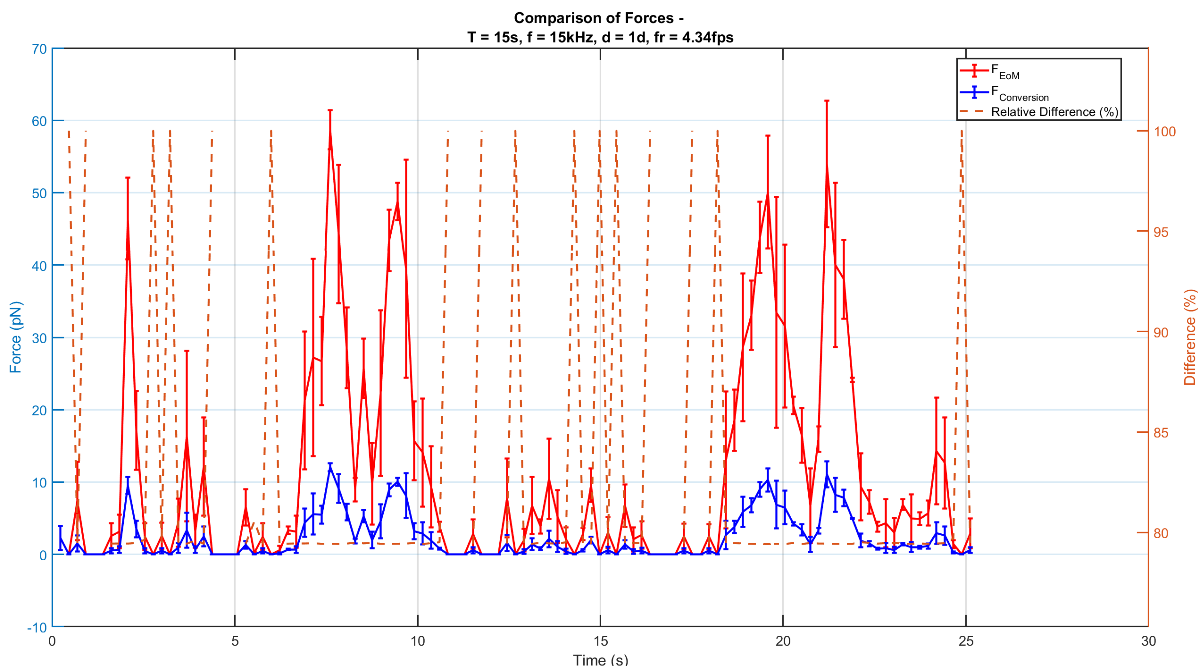

Figure D.203: A comparison of the forces on the microbot calculated using Stokes's law and the conversion coefficient from literature [8]. The relative difference is shown as a dashed orange line. When this dashed orange line is not present, it means that the calculated force is 0 pN. The error bars denote the standard deviation of the measurement. The sweep used for creating the DEP force had a sweep time of 15 seconds and a sweep thickness of 30 pixels. The input voltage of the experiment is 30 V with a frequency of 15 kHz.

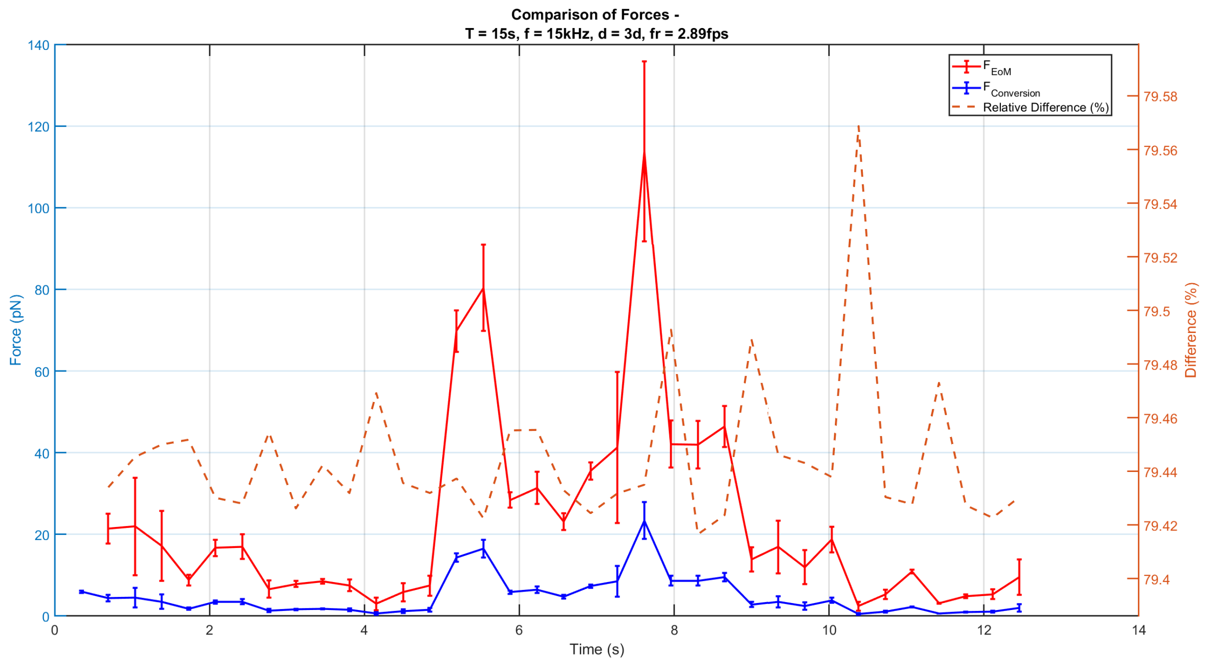

Figure D.204: A comparison of the forces on the microbot calculated using Stokes's law and the conversion coefficient from literature [8]. The relative difference is shown as a dashed orange line. When this dashed orange line is not present, it means that the calculated force is 0 pN. The error bars denote the standard deviation of the measurement. The sweep used for creating the DEP force had a sweep time of 15 seconds and a sweep thickness of 90 pixels. The input voltage of the experiment is 30 V with a frequency of 15 kHz.

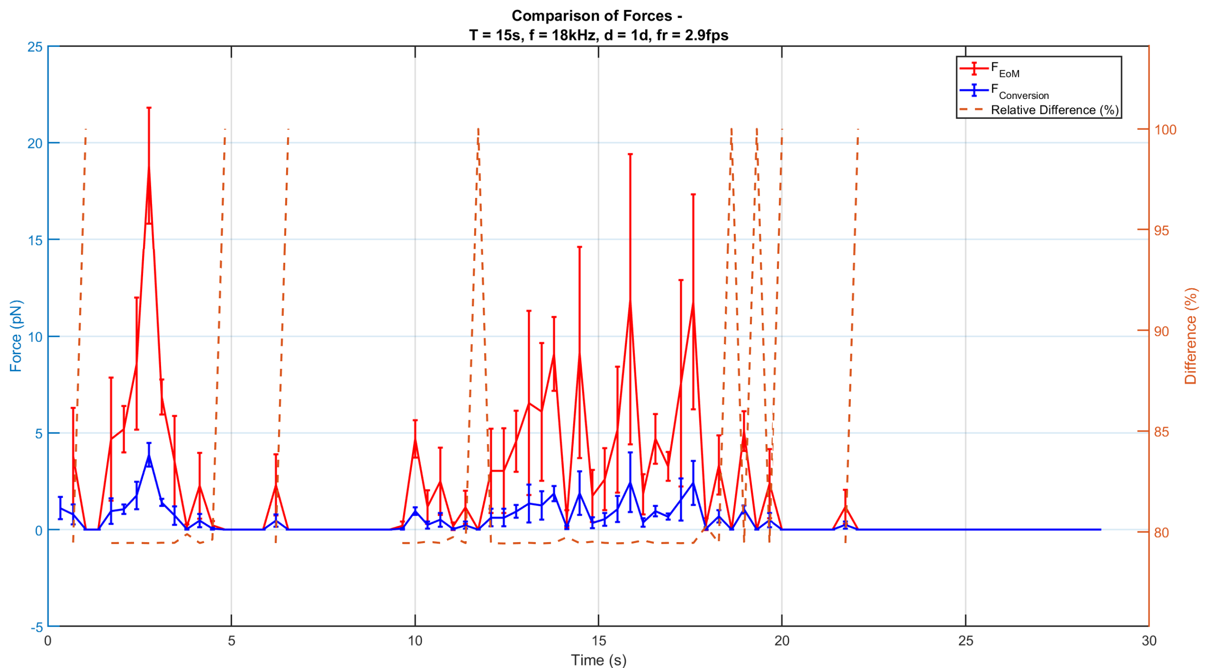

Figure D.205: A comparison of the forces on the microbot calculated using Stokes's law and the conversion coefficient from literature [8]. The relative difference is shown as a dashed orange line. When this dashed orange line is not present, it means that the calculated force is 0 pN. The error bars denote the standard deviation of the measurement. The sweep used for creating the DEP force had a sweep time of 15 seconds and a sweep thickness of 30 pixels. The input voltage of the experiment is 30 V with a frequency of 18 kHz.

D.4. Electrolysis

Limit of Vpp Before Electrolysis in Deionized Water				
	2 V	**10 V**	**20 V**	**35 V**
Chip 1				
Upper limit	N.A.	10 MHz	10 MHz	10 MHz
Lower limit	N.A.	N.A.	10 Hz	100 Hz
Chip 2				
Upper limit	N.A.	10 MHz	10 MHz	100 kHz
Lower limit	N.A.	N.A.	N.A.	100 Hz
Chip 3				
Upper limit	N.A.	10 MHz	1 MHz	1 MHz
Lower limit	N.A.	N.A.	N.A.	100 Hz

Table D.1: Limits of the applied electrical signal frequency before electrolysis occurs for different chips in deionized water at varying voltage levels.

Limit of Vpp Before Electrolysis in Deionized Water + 0.05% Tween-20				
	2 V	**10 V**	**20 V**	**35 V**
Chip 1				
Upper limit	N.A.	10 MHz	10 MHz	1 MHz
Lower limit	N.A.	10 Hz	100 Hz	100 Hz
Chip 2				
Upper limit	N.A.	10 MHz	1 MHz	1 MHz
Lower limit	N.A.	N.A.	10 Hz	100 Hz
Chip 3				
Upper limit	N.A.	10 MHz	10 MHz	1 MHz
Lower limit	N.A.	N.A.	10 Hz	100 Hz

Table D.2: Limits of the applied electrical signal frequency before electrolysis occurs for different chips in deionized water with 0.05% Tween-20 at varying voltage levels.

Limit of Vpp Before Electrolysis in Deionized Water + 5% Tween-20				
	2 V	**10 V**	**20 V**	**35 V**
Chip 1				
Upper limit	N.A.	10 MHz	10 MHz	1 MHz
Lower limit	N.A.	10 Hz	10 Hz	1 kHz
Chip 2				
Upper limit	N.A.	10 MHz	10 MHz	1 MHz
Lower limit	N.A.	10 Hz	10 Hz	100 Hz
Chip 3				
Upper limit	N.A.	10 MHz	10 MHz	1 MHz
Lower limit	N.A.	N.A.	10 Hz	10 Hz

Table D.3: Limits of the applied electrical signal frequency before electrolysis occurs for different chips in deionized water with 5% Tween-20 at varying voltage levels.